Cranfield University

John McKernan

Control of Plane Poiseuille Flow: A Theoretical and Computational Investigation

School of Engineering

PhD Thesis

Cranfield University

Department of Aerospace Sciences,
School of Engineering

PhD Thesis

Academic Year 2005/2006

John M^{c}Kernan

Control of Plane Poiseuille Flow: A Theoretical and Computational Investigation

Supervisor: Dr J.F. Whidborne

April 2006

©Cranfield University, 2006. All Rights reserved. No part of this publication may be reproduced without the written permission of the copyright holder.

Abstract

Control of the transition of laminar flow to turbulence would result in lower drag and reduced energy consumption in many engineering applications. A spectral state-space model of linearised plane Poiseuille flow with wall transpiration actuation and wall shear measurements is developed from the Navier-Stokes and continuity equations, and optimal controllers are synthesized and assessed in simulations of the flow. The polynomial-form collocation model with control by rate of change of wall-normal velocity is shown to be consistent with previous interpolating models with control by wall-normal velocity. Previous methods of applying the Dirichlet and Neumann boundary conditions to Chebyshev series are shown to be not strictly valid. A partly novel method provides the best numerical behaviour after preconditioning.

Two test cases representing the earliest stages of the transition are considered, and linear quadratic regulators (LQR) and estimators (LQE) are synthesized. Finer discretisation is required for convergence of estimators. A novel estimator covariance weighting improves estimator transient convergence. Initial conditions which generate the highest subsequent transient energy are calculated. Non-linear open- and closed-loop simulations, using an independently derived finite-volume Navier-Stokes solver modified to work in terms of perturbations, agree with linear simulations for small perturbations. Although the transpiration considered is zero net mass flow, large amounts of fluid are required locally. At larger perturbations the flow saturates. State feedback controllers continue to stabilise the flow, but estimators may overshoot and occasionally output feedback destabilises the flow.

Actuation by simultaneous wall-normal and tangential transpiration is derived. There are indications that control via tangential actuation produces lower highest transient energy, although requiring larger control effort. State feedback controllers are also synthesized which minimise upper bounds on the highest transient energy and control effort. The performance of these controllers is similar to that of the optimal controllers.

Keywords: Optimal Control, Channel Flow, Navier-Stokes Equations, Spectral Methods, State-Space Model, Finite-Volume Discretisation Method, Linear Matrix Inequality

Acknowledgments

This thesis communicates the results of research carried out under the supervision of Dr James Whidborne during the period October 2002 to December 2003 at King's College London, and from January 2004 to March 2006 at Cranfield University, the author having followed Dr Whidborne there. Funding from the Department of Mechanical Engineering at King's College, and from the School of Engineering at Cranfield University, is gratefully acknowledged.

My grateful thanks to Dr Whidborne for his inspiring and enlightening supervision, and also to Dr George Papadakis of King's College London, for his generous advice on matters of fluid mechanics and the use of his finite volume Navier-Stokes solver. The use of the linear spectral computer code written by Dr Satish Reddy (Oregon State University), to be found in Schmid and Henningson (2001, appendix A), is also acknowledged.

My gratitude is also due to Professor Thomas Bewley (University of California San Diego) and Dr Ole Morten Aamo (Norwegian University of Science and Technology) for copies of their theses, and to Cranfield Students-off-site service for the forwarding of material from the exceptional library. This thesis is typeset in LaTeX 2_ε using MiKTeX and TeXnicCentre.

My deepest thanks to my wife Kate, for her love and support, and to Edward, whose arrival on 14^{th} July 2004, brought with it much joy.

Theydon Bois, March, 2006 John McKernan

Contents

List of Figures

List of Tables

Notation

Variables are real scalars unless stated otherwise. $\mathbb{R}^M$ denotes a real column vector of size M. $\mathbb{C}^{M\times P}$ denotes a complex array of size $M \times P$. For clarity, large dimensions are shown as approximate nominal values. Where the systems are complex $\mathbb{K} \equiv \mathbb{C}$, where they are real $\mathbb{K} \equiv \mathbb{R}$.

For the system generated for test case 1, where complex, the number of state variables M is approximately the discretisation parameter N, the number of inputs P is 2, and the number of outputs Q is 2. For test case 2 the corresponding values are $M \approx 2N$,$P = 2$, and $Q = 4$. When the matrices of case 1 are made real, their dimensions double in size, but those of case 2 do not (see section 2.7).

Variables h, U_{cl}, ρ, μ retain their dimensions, and are used to non-dimensionalise the remainder as described in section 2.2.5, and in so doing introduce the non-dimensional Reynolds number R.

Variables δx and δt retain their dimensions and are used together with μ and dimensionalised velocities to calculate the non-dimensional Courant C and Peclet Pe numbers in section 4.4.7.

Roman Symbols

$a_n \in \mathbb{K}$	:=	multiplying co-efficient for n^{th} Chebyshev polynomial
$\mathbf{a}_v \in \mathbb{K}^N$	:=	co-efficients for velocity
$\mathbf{a}_\eta \in \mathbb{K}^N$	:=	co-efficients for vorticity
C	:=	Courant number, $C = u\delta t/\delta x$
c_i	:=	amplitude of mode i
$\mathbf{Dn} \in \mathbb{R}^{N\times N}$	:=	matrix of n^{th} derivative of Chebyshev polynomials at collocation points
$\mathbf{Dn}_D \in \mathbb{R}^{N\times N}$	:=	modified **Dn** with Dirichlet boundary conditions
$\mathbf{Dn}_{DN} \in \mathbb{R}^{N\times N}$	:=	modified **Dn** with Dirichlet and Neumann boundary conditions
$\mathbf{D} \in \mathbb{R}^{N\times N}$	:=	interpolating basis derivative matrix, $\mathbf{D1D0}^{-1}$
D	:=	y differentiation operator
δx	:=	mesh cell size
δt	:=	timestep
$E(t)$	:=	transient energy, $\mathcal{X}^T\mathcal{Q}\mathcal{X}$, at time t
$E_{Est}(t)$	:=	estimated transient energy, $\hat{\mathcal{X}}^T\mathcal{Q}\hat{\mathcal{X}}$, at time t
$E_{Error}(t)$	:=	error energy $\left(\mathcal{X}-\hat{\mathcal{X}}\right)^T\mathcal{Q}\left(\mathcal{X}-\hat{\mathcal{X}}\right)$, at time t
E_{C1}	:=	E of case 1 worst open-loop perturbation of $\max v = 0.0001$, at $t = 0$, value 8.23×10^{-8}
E_{C2}	:=	E of case 2 worst open-loop perturbation of $\max v = 0.0001$, at $t = 0$, value 2.26×10^{-9}
$E_{pair,bound}$	:=	upper bound on mode pair energy growth
f_l	:=	inhomogeneous function at lower wall
f_u	:=	inhomogeneous function at upper wall
g_l	:=	inhomogeneous gradient function at lower wall
g_u	:=	inhomogeneous gradient function at upper wall
h	:=	channel wall to centre-line separation
$\mathbf{I}$	:=	identity matrix
$\jmath$	:=	$\sqrt{-1}$
k	:=	$\sqrt{\alpha^2+\beta^2}$
$\mathbf{L} \in \mathbb{K}^{M\times M}$	:=	discrete form of Laplacian operator
N	:=	highest Chebyshev polynomial degree used, final collocation point index
Pe	:=	Peclet number, $Pe = \rho u\delta x/\mu$
P	:=	pressure
P_b	:=	steady base flow pressure
p	:=	pressure perturbation

(continued)

Roman Symbols, Continued

$q_l \in \mathbb{K}$	:=	v actuation at lower wall
$q_u \in \mathbb{K}$	:=	v actuation at upper wall
$q_l^u \in \mathbb{K}$	:=	u actuation at lower wall
$q_u^u \in \mathbb{K}$	:=	u actuation at upper wall
$q_l^w \in \mathbb{K}$	:=	w actuation at lower wall
$q_u^w \in \mathbb{K}$	:=	w actuation at upper wall
R	:=	Reynolds number, $R = \rho U_{cl} h/\mu$
r	:=	control weight multiplier
s	:=	measurement noise weight multiplier
$\mathbf{T} \in \mathbb{K}^{M \times M}$	:=	matrix for conversion from state variables to $\tilde{v}, \tilde{\eta}$
$\mathbf{T}_{cp} \in \mathbb{K}^{M \times M}$	:=	invertible matrix for conversion between state variables and $\tilde{v}, \tilde{\eta}$, excludes next-to-wall velocities and vorticities
t	:=	time
x, y, z	:=	streamwise, wall-normal and spanwise co-ordinates
$\vec{U} = (U, V, W)$	:=	fluid velocity vector
U, V, W	:=	fluid velocity in x, y, z directions
$\vec{U_b} = (U_b, V_b, W_b)$	:=	steady base fluid velocity in x, y, z directions
U_{cl}	:=	U_b at centreline
$\vec{u} = (u, v, w)$	:=	fluid velocity perturbation vector
u, v, w	:=	fluid velocity perturbations in x, y, z directions
$\tilde{u}, \tilde{v}, \tilde{w} \in \mathbb{K}$	:=	u, v, w Fourier coefficients at wavenumber pair α, β
$\tilde{v}_l, \tilde{v}_u \in \mathbb{K}$	:=	v Fourier coefficients at lower and upper walls i.e. $\tilde{v}_l(t) = \tilde{v}(y = -1, t)$ & $\tilde{v}_u(t) = \tilde{v}(y = 1, t)$
y_n	:=	y at n^{th} Chebyshev-Gauss-Lobatto collocation point
$\tilde{v}_n$	:=	$\tilde{v}$ at n^{th} Chebyshev-Gauss-Lobatto collocation point
v_h	:=	homogeneous component of wall-normal velocity

Calligraphic Symbols

$\mathcal{A} \in \mathbb{K}^{M \times M}$	:=	system matrix
$\mathcal{B} \in \mathbb{K}^{M \times P}$	:=	input matrix
$\mathcal{C} \in \mathbb{K}^{Q \times M}$	:=	output matrix
$\mathcal{D} \in \mathbb{K}^{Q \times P}$	:=	direct transmission matrix
$\mathcal{E} \in \mathbb{K}^{M \times P}$	:=	input derivative matrix
$\mathcal{G}$	:=	state-space system $(\mathcal{A}, \mathcal{B}, \mathcal{C}, \mathcal{D})$
$\mathcal{K} \in \mathbb{K}^{P \times M}$	:=	state feedback gain matrix
$\mathcal{L} \in \mathbb{K}^{P \times M}$	:=	estimator gain matrix
$\mathcal{P} \in \mathbb{K}^{M \times M}$	:=	solution to algebraic Riccati equations and Lyapunov equations
$\mathcal{Q} \in \mathbb{K}^{M \times M}$	:=	state variable weighting (energy) matrix
$\mathcal{R} \in \mathbb{K}^{P \times P}$	:=	control weighting matrix
$\mathcal{S} \in \mathbb{K}^{M \times M}$	:=	$\mathcal{P}^{-1}$
$\mathcal{T} \in \mathbb{K}^{M \times M}$	:=	balancing transformation
$\mathcal{U} \in \mathbb{K}^{M}$	:=	control vector
$\mathcal{V} \in \mathbb{K}^{Q \times Q}$	:=	measurement noise power spectral density
$\mathcal{W} \in \mathbb{K}^{M \times M}$	:=	process noise power spectral density
$\mathcal{X} \in \mathbb{K}^{M}$	:=	state variable vector
$\hat{\mathcal{X}} \in \mathbb{K}^{M}$	:=	state estimates vector
$\mathcal{X}_{Error} \in \mathbb{K}^{M}$	:=	estimate error vector, $\mathcal{X} - \hat{\mathcal{X}}$
$\mathcal{X}_{Worst} \in \mathbb{K}^{M}$	:=	$\mathcal{X}(t = 0)$ which generates θ
$\mathcal{X}_{Error,Worst} \in \mathbb{K}^{M}$	:=	$\mathcal{X}_{Error}(t = 0)$ which generates θ_{Error}
$\mathcal{X}_{cp} \in \mathbb{K}^{M}$	:=	$\mathcal{X}$ transformed to $\tilde{v}, \tilde{\eta}$ values at collocation points
$\tilde{\mathcal{X}} \in \mathbb{K}^{M}$	:=	state variables transformed to $\mathcal{Q}^{1/2}\mathcal{X}$, thus $E = \tilde{\mathcal{X}}^{T}\tilde{\mathcal{X}}$
$\mathcal{Y} \in \mathbb{K}^{Q}$	:=	measurement vector
$\mathcal{Z} \in \mathbb{K}^{P \times M}$	:=	$\mathcal{K}\mathcal{S}$

Greek Symbols

α	:=	streamwise(x) wave number, cycles per 2π distance
β	:=	spanwise(z) wave number, cycles per 2π distance
$\Gamma_n(y)$	:=	n^{th} Chebyshev polynomial of the first kind, $\cos n(\arccos(y))$
$\Gamma_n^M(y)$	:=	modified n^{th} Chebyshev polynomial
$\Gamma_n^D(y)$	:=	$\Gamma_n^M(y)$ which satisfies Dirichlet boundary conditions $\Gamma_n^M(y=\pm 1)=0$
$\Gamma_n^{DN}(y)$	:=	$\Gamma_n^M(y)$ which satisfies Dirichlet and Neumann boundary conditions $\Gamma_n^M(y=\pm 1)=\Gamma_n^M(y=\pm 1)'=0$
δ_i	:=	Boyd's ordinal difference
$\epsilon(t)$	:=	synchronic transient energy bound at time t
$\epsilon_{Error}(t)$	:=	synchronic error energy bound at time t
ζ	:=	eigenvalue in synchronic transient energy bound eigensystem
$\eta(x,y,z,t)$	:=	wall-normal vorticity perturbation
$\tilde{\eta}(\alpha,\beta,y,t)\in\mathbb{K}$	:=	η Fourier coefficient at wavenumber pair α,β
$\tilde{\eta}_n$	:=	$\tilde{\eta}$ at n^{th} Chebyshev-Gauss-Lobatto collocation point
Θ_n	:=	Γ_n modified to fulfill Dirichlet boundary conditions
θ	:=	diachronic transient energy bound
θ_{Error}	:=	diachronic error energy bound
θ_{Est}	:=	estimated energy bound
θ_u	:=	upper bound on diachronic transient energy bound
κ	:=	condition number
κ_c	:=	controllability
κ_o	:=	observability
$\lambda_i\in\mathbb{C}$	:=	i^{th} eigenvalue
$\Lambda\in\mathbb{C}^{M\times M}$	:=	diagonal eigenvalue matrix
μ	:=	molecular or kinematic viscosity
ν	:=	upper bound on control effort
Ξ_n	:=	Γ_n modified to fulfill Dirichlet and Neumann boundary conditions
ρ	:=	fluid density
$\sigma_i(\mathbf{A})$	:=	i^{th} singular value of $\mathbf{A}$, $i=1$ for largest singular value
$\bar{\sigma}(\mathbf{A})$	:=	spectral norm or largest singular value of $\mathbf{A}$
τ_{yx}	:=	x component of wall shear stress normal to y direction
υ_i	:=	Boyd's intermodal separation
$\Phi^T\in\mathbb{C}^{M\times M}$	:=	matrix of left eigenvectors
$\phi_i^T\in\mathbb{C}^M$	:=	i^{th} left eigenvector
$\chi\in\mathbb{K}^M$	:=	modal amplitude vector, $[c_0,\ldots,c_M]^T$
χ_0	:=	initial χ, at time $t=0$
$\Psi\in\mathbb{C}^{M\times M}$	:=	matrix of right eigenvectors
$\psi_i\in\mathbb{C}^M$	:=	i^{th} right eigenvector
$\omega\in\mathbb{C}$	:=	frequency

Miscellaneous Symbols

$\triangleq$	:=	by definition
f	:=	scalar
$\vec{f}$	:=	vector, (if Cartesian, $f_x\vec{i} + f_y\vec{j} + f_z\vec{k}$)
∇f	:=	grad f, $(\partial/\partial x, \partial/\partial y, \partial/\partial z)$
$\nabla \cdot \vec{f}$	:=	div $\vec{f}$, $\partial f_x/\partial x + \partial f_y/\partial y + \partial f_z/\partial z$
$\nabla \times \vec{f}$	:=	curl $\vec{f}$, $(\partial f_z/\partial y - \partial f_y/\partial z, \partial f_x/\partial z - \partial f_z/\partial x, \partial f_y/\partial x - \partial f_x/\partial y)$
f'	:=	differentiation of f with respect to y
$\dot{f}$	:=	differentiation of f with respect to t
$\mathbf{f}, (f_n)$	:=	array with elements f
$\mathbf{f}^T$	:=	conjugate transpose of $\mathbf{f}$
$\Im(f)$	:=	imaginary part of f
$\Re(f)$	:=	real part of f
$\left\|\vec{f}\right\|_2$	:=	vector 2-norm, $\sqrt{\sum_i \left\|f_i\right\|^2}$
$\|\mathbf{A}\|_{max}$	:=	max element norm, $\max_{i,j} \left\|a_{ij}\right\|$

Acronyms

ARE	:=	Algebraic Riccati Equation
CFD	:=	Computational Fluid Dynamics
FFT	:=	Fast Fourier Transform
LEBU	:=	Large Eddy Breakup device
LMI	:=	Linear Matrix Inequality
LQE	:=	Linear Quadratic Estimator
LQG	:=	Linear Quadratic Gaussian controller
LQR	:=	Linear Quadratic Regulator
MEM	:=	Micro-Electrical Machine
ODE	:=	Ordinary Differential Equation
PDE	:=	Partial Differential Equation

Chapter 1

Introduction

1.1 Introduction

In its widest sense 'flow control' is the manipulation of fluid flow fields, by passive or active means, in order to achieve beneficial results (Gad-el-Hak, 1998, p1), if we exclude the sense associated with the metering of flows. Examples of flow control in this sense are the design of cars to reduce drag, or of aerofoils to maximise lift.

More specifically, practical control of fluid flows involves boundary layer transition delay, separation control and drag reduction. Historically, it has been achieved by experiment and intuition, and has mainly focused upon the introduction of features to achieve steady-state manipulation of boundary layer base flows, i.e. control in a spatial sense, with any temporal disturbances being manipulated in the process. Amongst other successes, this control of flow fields has contributed to the era of modern flight. Such flow control may be passive, for example, separation control by careful shaping (Gad-el-Hak, 1998, p33) or predetermined active control, whereby energy is expended in order to obtain beneficial results, for instance steady suction to remove boundary layers and maintain laminar skin-friction as reviewed by Joslin (1998).

Developments in flow visualisation and simulation have revealed details of the transient behaviour in fluid flow, in particular the structures which appear during the separation of flow and the transition to turbulence, and the disturbances on various length and time-scales in turbulent flow, as shown for example by Van Dyke (1982). Micro-electrical machines (MEMs), as described by Ho and Tai (1998), Gad-el-Hak (1999) and Lofdahl and Gad-el-Hak (1999), have also been developed, and are able to sense and deflect fluid flow on boundaries at the small length scales encountered in flows of engineering interest.

Fluid transient disturbances may be manipulated by passive means, for example by riblets (Bushnell, 2003, p7) or large eddy breakup devices (LEBUs) (Gad-el-Hak, 1998, p65) in turbulent flow, or by ad-hoc active means, for example wave cancellation techniques as described by Gaster (2000) and Sturzebecher and Nitsche (2003) in laminar flow. However, the disturbances may also be altered by means that measure them and react to them. This introduces 'control' in the sense of the usual application of modern systems control theory, i.e. the reactive control of systems in a temporal setting, and this is the sense used in this thesis. Unlike

passive or ad-hoc active flow control, reactive flow control responds appropriately to disturbances as they occur.

Abergel and Temam (1990) were amongst the first to suggest the application of systems control theory to the Navier-Stokes equations. In conjunction with the advent of MEMs devices, systems theory flow control attempts to improve flow control performance over that of passive and ad-hoc active control, for which Collis et al. (2004) note that, to date, progress has been erratic. Systems theory flow control aims to synthesize controllers for flows which provide certain guarantees regarding the stability, performance and robustness of the controlled system. The controllers are synthesized by applying mathematical techniques to a model of the system derived from its physical equations or measured dynamical properties.

The aim of this thesis is to investigate, using systems theory approaches, the control of plane Poiseuille flow in the very earliest stages of transition from laminar flow to turbulence, with an emphasis on modelling the flow, reducing its transient energy growth, and comparing methods of actuation. The application of feedback control to the problem of transition brings the prospect of the attenuation of unknown and variable disturbances in imprecise flow conditions, and mathematical modelling and optimal solution of the problem may lead the way to practical configurations.

Flows which are linearly stable nonetheless undergo transition to turbulence, and the explanation is believed to be the large transient growth of perturbation kinetic energy taking the system into a non-linear regime, for example as described by Trefethen and Embree (2005, p210). In a state-space setting, the transient energy is a weighted sum of the squares of the state variables. Many systems experience initial excursions of transient energy before settling down to stable states. The control of the transient behaviour of systems has recently been investigated by Hinrichsen and Pritchard (2000) and Hinrichsen et al. (2002).

The benefits of laminar fluid flow over turbulent flow include lower skin friction and less noise, and methods of preventing the transition of laminar flow to turbulent flow would yield significantly lower energy costs and carbon emissions in many kinds of transportation, as reviewed by Wood (2003). Gad-el-Hak (1998, p79) estimates that skin friction accounts for 50,90, and 100% of drag on commercial aircraft, underwater vehicles and pipelines respectively, and Joslin (1998, p3) notes that laminar drag can be as low as 10% of turbulent drag.

However, the governing fluid flow equations are infinite dimensional, non-linear and coupled, and exhibit complex behaviour during the transition from smoothly shearing laminar flow to the chaotic limit-cycle type behaviour on various length and timescales that is turbulence. Hogberg and Bewley (2000) note that descriptions of the transition in terms of phenomena are incomplete. The earliest transition behaviour can be modelled by linearisation of the equations, also making the equations amenable to rigorous modern controller synthesis techniques. Furthermore, any control of full turbulence would also need to control the early stages in order to achieve laminar flow, but Hogberg et al. (2003a, p154) note that linear control of the early stages may obviate the need for control of the later non-linear ones. It would also seem reasonable to control the large slow moving disturbances at the beginning of the turbulence cascade (Tritton, 1988, p314) rather than the

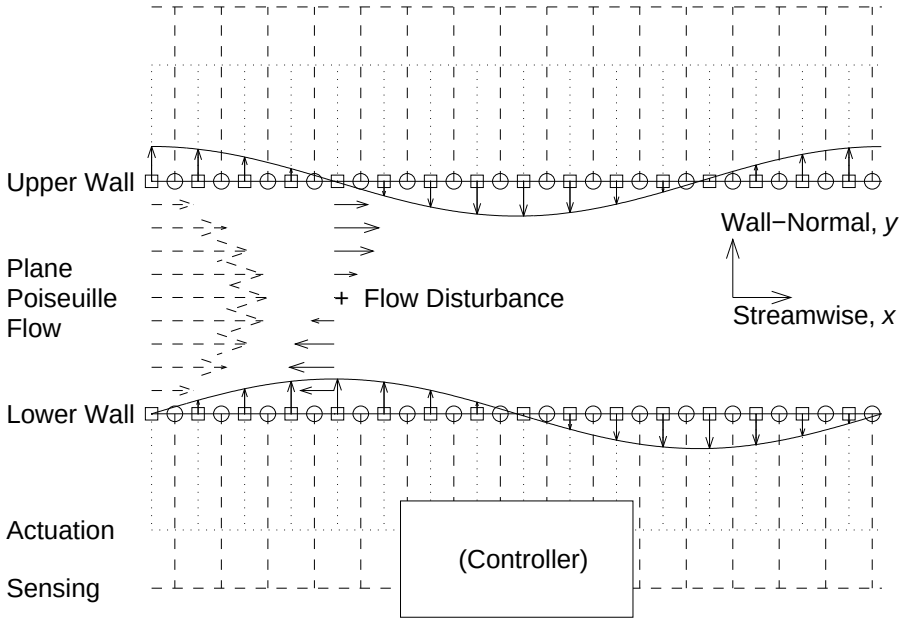

Figure 1.1: The Flow Control Scheme

fast small eddies which finally dissipate energy, and which require many more degrees of freedom to model. Joslin (1998, p2) estimates that the energy requirements for relaminarization could be an order of magnitude greater than those for laminar flow control.

In non-phenomenological terms, controlling the growth of the transient energy of disturbances in laminar flow is crucial to the suppression of non-linear effects and the transition to turbulence. In a linear setting, an upper bound on the growth of the transient energy of disturbances of a system is given by the highest subsequent transient energy possible from initial conditions of unit energy. Transient energy growth is associated with non-normal system eigenvectors, as investigated by Trefethen et al. (1993).

The geometry of the boundary surfaces over which transition to turbulence takes place are many and varied, generally with complex boundary conditions and boundary layer profiles without closed form solutions. Plane Poiseuille (channel) flow has simple flow geometry, boundary conditions and velocity profile, making it a suitable choice for the investigation of flow control. The control of flow separation is another subject, and such separation does not generally occur in channel flow.

The use of MEMs devices providing almost continuous detection of disturbances and variation of the wall boundary conditions of plane Poiseuille flow under control, is depicted schematically in figure 1.1. The figure shows plane Poiseuille flow between two horizontal boundary walls, which contain distributed sensors and actuators. A flow disturbance is sensed, and fed to the controller which computes an appropriate transpiration actuation to render the disturbance stable, with further dynamic properties, e.g. minimised transient energy growth.

1.2 Previous Work

What follows is an overview of recent research in the systems theory feedback control of laminar plane Poiseuille flow. For other more general reviews of flow control research, see the articles by Moin and Bewley (1994), Lumley and Blossey (1998), Bewley (2001) and Collis et al. (2004), and the books by Gad-el-Hak (1998, 2000). Rempfer (2003) provides a review of modelling transition.

Hu and Bau (1994) and Pabiou et al. (2004) demonstrate how the linear stability of plane Poiseuille flow may be modified by proportional feedback control from wall shear stress measurements to wall temperature actuation. Joshi et al. (1995, 1997, 1999) were amongst the first to consider the problem of applying modern control theory to linearised plane Poiseuille flow. Using a stream function formulation, which restricts flow perturbations to the streamwise/wall-normal plane, the authors model the flow spectrally assuming a periodic Fourier series variation in the unbounded streamwise direction, and a Chebyshev series variation in the wall-normal direction. They use a Galerkin method to form a system with Chebyshev coefficients as state variables, and which assumes temporal but not spatial growth of disturbances. As the authors transform their homogeneous system with inhomogeneous boundary conditions into a inhomogeneous system with homogeneous boundary conditions, their control input is via rate of change of wall-normal velocity. Their measurements are wall shear stress. The authors propose distributed actuation and sensing in order to make unmodelled wavenumber dynamics uncontrollable and unobservable respectively, although they employ point sensing in their linear simulations which show the effectiveness of integral and linear optimal controllers with prescribed stability, in terms of shear settling time and the required control effort, from unit initial state variables. Controllers from low-order models are seen to be as effective as those from high order models.

Cortelezzi and Speyer (1998) and Cortelezzi et al. (1998a,b) employ similar methods to those of Joshi et al., and point out that distributed actuation and sensing makes the linearised equations decouple by wavenumber. In their linear quadratic regulator (LQR) controller synthesis the authors chose to minimise the wall shear stress, and like Joshi use the power spectral densities of the estimator in their linear quadratic estimator (LQE) synthesis as design parameters to introduce robustness via the loop transfer matrix. A combined model covering several wavenumbers is used for the synthesis of a controller, which is then reduced by selection of controllable and observable rows and columns from the Jordan canonical form. The authors compute initial conditions which lead to the worst wall shear stress, and achieve a significant reduction in non-linear simulations, but being two-dimensional it does not fully represent turbulence. Lee et al. (2001) extend the controller into the spanwise direction in an ad-hoc manner.

In their seminal paper, Bewley and Liu (1998) adopt a wall-normal velocity-vorticity formulation, capable of representing three-dimensional disturbances, discretised by spectral collocation in the wall-normal direction to yield the state variables as values at collocation points. Unfortunately, although their implementation of the boundary conditions allows control directly by wall-normal velocity, it also introduces spurious system modes. The authors synthesize linear quadratic

Gaussian (LQG) controllers using the transient energy plus control effort as an LQR cost function, seeking to minimise transient energy growth and consequent non-linearity, as a precursor to transition, rather than the immediate but short term benefit of reduced wall shear as sought by Joshi et al. and Cortelezzi et al. The authors also synthesize H_∞ robust controllers, which are insensitive to uncertainties. They compute initial conditions which produce the worst subsequent transient energy growth as derived by Butler and Farrell (1992), and perform linear simulations on two test cases, an unstable two-dimensional flow perturbation, and the stable three-dimensional perturbation which produces the largest overall transient energy growth. The authors emphasize the role of non-modal transient energy growth associated with non-orthogonal system eigenvectors, and show the superiority of modern control methods over more conventional ones. By reformulating the boundary conditions, Aamo (2002) is able to avoid the spurious modes.

Balogh et al. (1999, 2000, 2001) derive controllers for global Lyapunov (non-linear) stabilization of two-dimensional channel flow. The intractability of the problem is shown by the results only being applicable to low Reynolds number, $R < 1/8$, although the flow is known to be stable uncontrolled to $R \approx 1000$, for example as shown by Carlson et al. (1982). The authors' controllers achieve laminar flow in non-linear simulations at much higher Reynolds numbers, $R = 7500$ and 15000. They use tangential actuation with local shear stress measurements and perform non-linear simulations with both finite-volume and spectral Navier-Stokes solvers, from initial random perturbations allowed to grow for some time. Subsequently Aamo et al. (2003) formulate controllers for achieving global Lyapunov stabilization using wall-normal actuation and pressure measurements, which are similarly restricted to low Reynolds numbers but are seen to achieve laminar flow at much higher ones. Reversal of the feedback sign leads to enhanced instability and mixing as compared to open-loop flow. Bewley and Aamo (2004) observe low drag transients in the controlled flow, but find that they are unsustainable, and conjecture that the lowest possible sustainable drag in channel flow is that of laminar flow.

Bamieh and Dahleh (1999, 2001) show that subcritical streamwise constant disturbance energy amplification is $\mathcal{O}(R^3)$ and is due to the coupling between velocity and vorticity, as a consequence of the non-normality of the Orr-Sommerfeld operator. Subsequently Bamieh et al. (2002) demonstrate that optimal controllers inherit the spatial invariance of the plant under a variety of performance criteria, and furthermore that convolution kernels, arising from many controllers at continuous wavenumbers in Fourier space, decay exponentially with physical distance, i.e. only local variables affect the control, thus resulting in localised control.

Hogberg and Bewley (2000), motivated to derive control 'bypassing phenomenological descriptions of transition which are still incomplete', generate convolution kernels for the LQR control of linearised plane Poiseuille flow, and find that they do generally decay exponentially and result in localised control. The authors' flow model is a development of Bewley and Liu (1998), using the differentiation matrix suite of Weideman and Reddy (2000) and, akin to Joshi et al. (1995), forming an inhomogeneous system with homogeneous boundary conditions (as also recommended by Boyd (2001)), the authors use control by rate of change of wall-normal

velocity, and find no spurious modes. Direct numerical simulations on oblique waves (which generate streamwise vortices and thus streaks) and random initial conditions, both of initial energy well above the known transition energy thresholds determined by Reddy et al. (1998), demonstrate that the resulting controllers bring the flow back to the laminar state.

Hogberg et al. (2003a) show that although convolution kernels decay, and truncation does not degrade state feedback control significantly, convolved output feedback performance is degraded. The authors also quantify the improvement in transition thresholds when feedback is applied, by non-linear simulations using the widely cited code of Bewley et al. (2001, p193), which is pseudospectral streamwise and spanwise, and finite difference in the wall-normal direction, with time advancement by hybrid Crank-Nicholson/Runge-Kutta methods. Oblique waves are known to have a lower transition threshold than streamwise vortices or random perturbations in uncontrolled flow as shown by Reddy et al. (1998), and control significantly increases the transition thresholds. Streamwise vortices are seen to have the lowest transition threshold in state feedback controlled flow. The controllers are unable to relaminarize turbulent flow. Hogberg et al. (2003b) report the successful non-linear simulation of relaminarization of turbulent channel flow, using the gain scheduling of linear state feedback kernels derived for different mean flow profiles as the flow field is made laminar.

The importance of the linear transient energy growth mechanism is stressed by Reddy and Henningson (1993, p236). Hogberg and Bewley (2000) note that non-linear terms only redistribute energy. Kim and Lim (2000) and Kim (2003) emphasize the importance of the linear terms in maintaining turbulence.

Bewley et al. (2001) successfully control a turbulent channel flow simulation using non-linear predictive optimal control to optimize actuation over a finite prediction horizon. The method uses a cost function gradient computed from the adjoint flow field, requiring an intensive online calculation. Thus the authors see the result as a benchmark for more practical controllers. Hogberg et al. (2001) compare optimal linear control and non-linear predictive optimal control on oblique waves in channel flow. LQR controller performance is found to be very similar to predictive controller performance, and LQG controller performance is not as good, although it may be improved with better initial estimates. The authors identify the need for estimators with faster convergence.

Bewley and Protas (2004) show that, in theory, measurements of wall shear stresses and pressure over a short interval of time are sufficient to determine the exact state of turbulent flow, and the stresses alone are sufficient for determining the state of linearised flow, without any knowledge of the initial conditions of the flow. However, poor estimator convergence is found in non-linear simulations, and the authors present an adjoint based algorithm which utilises the Navier-Stokes equations as a filter and is better behaved, especially with regard to measurement noise, since it does not perform differentiation. Chevalier et al. (2004) gather statistical data from direct numerical simulations of turbulence in Poiseuille flow, in order to compute the covariance of the process noise. For individual wavenumber pairs and in terms of velocity components, the variance is found to be stronger near the walls, and the covariance decreases as the wall-normal distance between

the points increases. The authors then compute optimal estimator gains for an extended Kalman filter based on the linearised Navier-Stokes equations, and test the resulting estimator on turbulent Poiseuille flow simulations. The estimators show better correlation with simulated turbulent flow than do estimators from previous studies which use a spatially uncorrelated covariance, in terms of maximum correlation and distribution in the channel. Hœpffner et al. (2005, 2006) assume a parameterised covariance which decreases exponentially as the wall-normal distance between the points increases. The authors then compute optimal estimator kernel gains for a Kalman filter for a number of simultaneous wavenumbers, which converge upon grid refinement. The resulting estimators are tuned, in part by physical arguments, and found to be effective in linear and non-linear simulations of perturbed laminar flow. The authors show that extended filters incorporating non-linearity perform better for large disturbances, and that time varying estimator gains lead to faster convergence.

Baker and Christofides (1999), Baker et al. (2000a,b) and Baker and Christofides (2002) synthesize non-linear finite-dimensional output feedback controllers for two-dimensional channel flow. The controllers measure wall shear stresses and generate Lorentz electromagnetic body force actuation, which requires a conducting fluid. The non-linear channel equations are modelled using a stream function formulation, and discretised by a Galerkin method utilising approximate inertial manifolds, assuming periodicity of several wavenumbers in the streamwise direction, and using linear combinations of Chebyshev polynomials in the wall-normal direction that satisfy the homogeneous boundary condition. Controllers are synthesised using geometric methods. The authors also synthesize linear output feedback controllers, and show the superiority of the non-linear control using a transient performance index related to system energy.

Using a two-dimensional modified stream function formulation, Baramov et al. (2000, 2002) model Poiseuille flow with discrete wall shear stress measurements, and both harmonic and panel transpiration, with included actuator dynamics. Since the panel actuation boundary conditions are not harmonic, several wavenumbers are modelled simultaneously. The high order model from a Galerkin discretisation of the linearised Navier-Stokes equations is reduced in order by Hankel-optimal reduction. The flow model consists of an interconnection of the reduced order model and a perturbation, and H_∞ controllers are synthesized using appropriate frequency weightings. The controllers are tested on the high order model with random initial conditions. The controllers satisfy the robust stability condition, and significantly attenuate wall shear stress. Panel actuation introduces an unstable zero and thus has a large H_∞ performance index, but requires less control effort than harmonic actuation. The authors' use of frequency domain analysis provides an alternative insight into the system dynamics to transient analysis, but the existence of non-modal transient energy growth is not as apparent. Jovanovic and Bamieh (2005) find the existence of input-output resonances in linearised plane Poiseuille flow spatial-temporal frequency responses which correspond to the known growth mechanisms of Tollmien-Schlichting waves, streamwise vortices and oblique waves.

Subsequently Baramov et al. (2001, 2003, 2004) model two-dimensional non-

periodic spatially evolving disturbances by coupling systems representing segments of channel. Each segment is a finite difference discretisation of the channel in the streamwise direction with a Chebyshev expansion in the wall-normal direction. Additional segments are added to avoid end effects. Segments are combined using the Redheffer star product on their frequency domain data. A low-order transfer function matrix is fitted to the combined frequency domain data, and a disturbance model is designed and H_∞ controllers are synthesized, using appropriate frequency weights which achieve robust stability. The resulting high order controller is reduced in order by Hankel-optimal reduction. Closed-loop frequency domain tests show that the controller significantly reduces incoming wall shear stress. Further evaluations using a finite-difference non-linear Navier-Stokes solver also show significant shear reduction downstream of the actuation panels, from incoming disturbances.

Veres et al. (2003) iteratively synthesize low order controllers for a similar model of Poiseuille flow by the technique of unfalsification. The forms of a parameterised model and of robust controllers are assumed, and unsuitable parameter vectors are discarded by using a priori knowledge of the physical plant and by assessing the controller robust performance. Bewley et al. (2000) propose a mathematical framework for the robust control of two-dimensional and three-dimensional infinite dimensional linear and non-linear fluid flows, and suggest a numerical algorithm based on repeated computations of an adjoint field.

Researchers have also used techniques developed on Poiseuille flow to model and control spatially developing boundary layers, for example Hogberg and Henningson (2002). This requires a different base flow and the introduction of a free-stream boundary condition. Actuation is solely at the remaining wall and the authors assume that non-parallel flow effects are small.

1.3 Objectives and Methods

1.3.1 Objectives

With the aims of investigating systems theory control of plane Poiseuille flow in the very earliest stages of transition from laminar flow to turbulence, with an emphasis on modelling the flow, reducing its transient energy growth, and comparing methods of actuation, the objectives of this thesis are as follows.

- The first objective is to obtain models of the flow that are in a form suitable for the synthesis and analysis of controllers using standard modern control methods. The available literature shows that the spectral modelling of plane Poiseuille flow for controller synthesis has used a number of different techniques, for example stream function vs. velocity-vorticity formulations, and polynomial vs. interpolating discretisation. Thus, this objective is to combine several of the most beneficial techniques into a single state-space model.

- The next objective is to analyze the physical and numerical properties of the developed models. The correctness of the model dynamics with respect

to previous results is to be established, and appropriate discretisation determined. Regarding wall-normal discretisation of the channel, several ways of applying Dirichlet and Neumann boundary conditions to Chebyshev polynomials have been published. More specifically, this objective is to examine in detail some of these methods of wall-normal discretisation, with particular emphasis on the numerical conditioning of the resulting matrices.

- A further objective is to design feedback controllers using standard control techniques, and to test them using an independent model. Linear quadratic regulators and estimators will be synthesized using the state-space model, as these have been seen to be amongst the feasible controllers in previous work. To date, spectral controllers for linearised plane Poiseuille flow have generally been synthesized and then tested using similar spectral codes, albeit with variations in the order of the synthesis and verification models, and sometimes with non-linear terms included in the verification model. In more detail, this objective is to synthesize linear optimal controllers for the state-space model, and to test the performance of the controllers in non-linear simulations that employ independent methodologies to the spectral synthesis model.

- An additional objective is to investigate whether control can be improved by consideration of alternative actuation. Although to date much work has been performed on flow control via wall-normal transpiration, little has been done on the use of tangential actuation. Although wall-normal actuation acts by convection and might be considered to be more effective than tangential actuation which acts by diffusion, laminar plane Poiseuille flow is dominated by diffusion. To summarise, this objective is to assess the suitability of tangential actuation for flow control of plane Poiseuille flow.

- The final objective is to analyze the transient energy growth of the controlled systems and to consider recent control methods that explicitly reduce this property. Several researchers have identified the highest transient energy growth (over all unit energy initial conditions, and over all subsequent time) as an appropriate index of controller performance, but have synthesized controllers which minimise the time integral of transient energy. Hence this objective is to synthesise controllers which attempt to minimise the highest transient energy growth, and assess their performance in linear and non-linear simulations.

The objectives of this thesis may be summarised as: to generate a state-space model of linearised plane Poiseuille flow, and to investigate the wall-normal discretisation, furthermore to synthesize linear optimal estimators and controllers, and to test their performance in open- and closed-loop independent non-linear simulations, and in addition to investigate tangential actuation, and finally to synthesize and test controllers which minimise the transient energy growth.

1.3.2 Methods

Regarding the methods employed is this thesis in order to reach the objectives, linearised plane Poiseuille flow is modelled spectrally for control synthesis, since spectral methods are known to be the most suitable for modelling flow in simple domains (Ferziger and Peric, 2002, p62). With regard to the techniques employed in the spectral model, a polynomial form of collocation will be employed that allows approximation, on a velocity-vorticity formulation that models three-dimensional disturbances, and the problem will be transformed into an inhomogeneous one with homogeneous boundary conditions to allow the straightforward application of boundary conditions and avoid the introduction of spurious modes. The resulting equations will be transformed into conventional state-space form by inversion of the Laplacian, and integrators will be introduced to regularise the inputs.

For the investigation of wall-normal discretisation, the methods for applying boundary conditions to Chebyshev series by Joshi (1996) and Heinrichs (1989, 1991) are compared with recombinations of Chebyshev series, partly by Weideman and Reddy (2000) and Boyd (2001), and in part novel. The validity of the methods are compared from a linear algebraic viewpoint and subsequently their numerical conditioning is examined by investigation of their maximum and minimum singular values.

LQR controllers and LQE estimators will be synthesized using the state-space model, for various design weightings and model discretisations, and for two test cases. The first test case represents linearly unstable streamwise/wall-normal velocity perturbations, commonly known as Tollmien-Schlichting waves. The second test case represents streamwise vortices, which are linearly stable, but have been shown by Butler and Farrell (1992) to generate the highest subsequent transient energy growth over all initial perturbations and subsequent time.

Although spectral models have been used for controller synthesis then simulation, and finite difference models have been used for synthesis then simulation, little work has been done using finite-volume methods, which are in widespread use in other fields, see for example the work by Yeoh et al. (2004). Thus the performance of the controllers synthesised using a spectral model is determined via non-linear simulations using a finite-volume computational fluid dynamics (CFD) Navier-Stokes solver. The CFD solver is independently derived from the spectral model, and is capable of modelling the flow in simple and complex geometries. Successful implementation of the controllers into such a finite-volume code will provide useful information when the controllers and code are applied to more complicated geometries than the plane channel considered here.

Tangential actuation will be introduced into the state-space model of linearised plane Poiseuille flow by the derivation of the boundary conditions in velocity-vorticity form and the selection of appropriate actuation basis functions that enforce them. Controllers will be synthesised and their performance compared to that of wall-normal actuation controllers in terms of highest transient energy growth. The controllers will also be tested in linear and non-linear simulations.

The largest transient energy growth possible at any particular time may be cast as the square of the spectral norm of the state transition matrix. Hinrichsen

and Pritchard (2000) derive estimates for the maximum over time of the spectral norm of the state transition matrix of a stable system, and show how it can be reduced by state feedback. Hinrichsen et al. (2002) introduce the concept of (M, β) stability, which describes both long term stability and transient behaviour, and Plischke and Wirth (2004) present sufficient conditions for state feedback to satisfy the exponential growth bound. An upper bound for the transient energy growth has been derived by Whidborne et al. (2004), who also provide linear matrix inequality (LMI) methods for synthesizing state feedback controllers which minimise the upper bound. Whidborne et al. (2005) have derived output feedback controllers which minimise the transient energy growth itself.

In order to synthesize controllers which minimise upper bounds on highest transient energy growth and peak control effort, the published system of linear matrix inequalities (LMIs) by Whidborne et al. (2004) will be modified to include a constraint on peak control effort. The system of LMIs is subsequently solved in order to synthesise controllers for the linearised Lorenz equations and the model of plane Poiseuille flow. The controllers are subject to linear and non-linear simulations, and the results for plane Poiseuille flow are compared to those of controllers which minimise the time integral of transient energy.

1.4 Outline of Thesis

The outline of this thesis is as follows. Chapter 2 models plane Poiseuille flow using spectral methods, and examines the resulting model in detail with regard to discretisation, controllability and observability. Chapter 3 investigates wall-normal discretisation in depth, comparing the numerical conditioning of several methods of applying the boundary conditions. In chapter 4 linear optimal controllers are synthesized using the flow model, and detailed linear and non-linear closed-loop simulations performed. Chapter 5 derives generalised wall boundary conditions and synthesizes controllers using tangential actuation, which are subsequently assessed in closed-loop linear and non-linear simulations. In chapter 6 state feedback controllers which minimise upper bounds on the transient energy growth and control effort are derived, and controllers for the Lorenz equations, as an example problem, are synthesised and tested. Minimising controllers for the plane Poiseuille flow model are also synthesized and assessed by further simulations. Finally chapter 7 draws conclusions from the work described in this thesis and suggests possible directions for future work.

1.5 Achievements

The following papers and report have been written to disseminate the results of the research described in this thesis.

McKernan, J., Whidborne, J.F. and Papadakis, G. (2006). Linear Quadratic Control of Plane Poiseuille Flow - the Transient Behaviour, *International Journal of Control*, submitted.

McKernan, J., Whidborne, J.F. and Papadakis, G. (2006). A Linear State-Space Representation of Plane Poiseuille Flow for Control Design - A Tutorial, *International Journal of Modelling, Identification and Control*, accepted.

McKernan, J., Papadakis, G. and Whidborne, J.F. (2006). Wall-normal Discretisation of Linearised Plane Poiseuille Flow for Boundary Control, *Journal of Computational Physics*, to be submitted.

McKernan, J., Whidborne, J.F. and Papadakis, G. (2004). Optimal Control of Plane Poiseuille Flow, *Proc. UKACC International Conference Control 2004, September 2004*, Bath, UK.

McKernan, J., Whidborne, J.F. and Papadakis, G. (2004). Optimal Control of Plane Poiseuille Flow, *Proc. First European Forum on Flow Control, October 2004*, Poitiers, France.

McKernan, J., Whidborne, J.F. and Papadakis, G. (2005). Minimisation of Transient Perturbation Growth in Linearised Lorenz Equations, *Proc. 16th IFAC World Congress, July 2005*, Prague.

McKernan, J., Papadakis, G. and Whidborne, J.F. (2003). Modelling plane Poiseuille flow for feedback control design, *Technical Report EM/2003/01*, Centre for Mechatronics and Manufacturing Systems, Department of Mechanical Engineering, King's College, London.

The major achievements arising from this thesis are:

1. The development of a polynomial-form state-space model of three-dimensional linearised plane Poiseuille flow, with a detailed investigation of convergence with the degree of discretisation, of controllability and observability, and of consistency with a previously published interpolating-form model. The effect of input integrators on state-space system observability and controllability has been derived.

2. The investigation of the numerical conditioning of four methods of basis recombination in order to fulfill Dirichlet and Neumann boundary conditions. A novel recombination is proposed for the simultaneous Neumann and Dirichlet boundary conditions, that extends a published Dirichlet boundary condition method. In association with derived pre-conditioning, this recombination yields the best numerical conditioning of the four methods for inversion of the discrete Laplacian, which is required to form the state-space model.

3. The synthesis of linear quadratic regulators and estimators for the state-space model of plane Poiseuille flow, and the calculation of the worst initial conditions, with investigations of the selection of weighting matrices, and of the convergence with discretisation. A novel estimator weighting is proposed which results in improved convergence over an identity matrix. Subsequent linear simulations show the requirement for large local displacement of transpiration fluid to stabilise the selected test cases. The simulations also show

that the best controllers in terms of lowest transient growth do not change the system eigenvector orthogonality appreciably.

4. Non-linear simulations using an independently derived finite-volume Navier-Stokes solver, modified to model small perturbations accurately, show agreement with open- and closed-loop linear results at low initial perturbation energy levels, and generally saturation and closed-loop stabilisation at larger initial energy levels.

5. The derivation of generalised boundary conditions, allowing simultaneous tangential and wall-normal transpiration, and the synthesis and closed-loop simulation of controllers which utilise tangential actuation. Despite numerical difficulties with tangential actuation, and its equivocal performance as compared to wall-normal actuation, it may be more feasible in practice, since although mechanisms such as rollers have constraints on velocity and acceleration, as do wall-normal jets, unlike jets they have no constraint on displacement.

6. The addition of limited control effort to a system of linear matrix inequalities for synthesizing controllers with a minimised upper bound on transient energy growth, and the resulting generation and closed-loop simulation of such controllers on both the linearised Lorenz equations and the plane Poiseuille flow model. For the latter, the performance of the controllers is close to that of linear optimal controllers. For the Lorenz system, it is again found that transient energy growth does not correlate well with system orthogonality.

Chapter 2

A Linear State-Space Representation of Plane Poiseuille Flow

2.1 Introduction

This chapter derives a linear state-space representation of linear perturbations in plane Poiseuille flow. The representation takes the form

$$\begin{aligned} \dot{\mathcal{X}} &= \mathcal{A}\mathcal{X} + \mathcal{B}\mathcal{U} \\ \mathcal{Y} &= \mathcal{C}\mathcal{X} \end{aligned} \tag{2.1}$$

where $\mathcal{U}$ represents control inputs, $\mathcal{Y}$ represents measurement outputs, $\mathcal{X}$ are state variables, and $\mathcal{A}, \mathcal{B}$ and $\mathcal{C}$ are the system, input and output matrices respectively.

Section 2.2 presents the Navier-Stokes equations and their boundary conditions, as well as the procedure for linearisation about plane Poiseuille (channel) flow. Subsequently the section describes non-dimensionalisation of the linearised equations and the derivation of wall shear stress measurement vector. In section 2.3 appropriate formulations of the linearised Navier-Stokes equations are discussed and the velocity-vorticity formulation selected for the present work. The boundary conditions are restated in this formulation. Section 2.4 describes the spectral discretisation of the linearised equations in the streamwise, spanwise and wall-normal directions. Periodic behaviour is assumed in the spanwise and streamwise directions, and non-periodic behaviour in the wall-normal direction. The wall shear stress measurements are also discretised in this section.

The introduction of wall-transpiration boundary conditions into the discretised equations is described in section 2.5, with the subsequent transformation of the equations into an inhomogeneous or forced form with homogeneous (zero-valued) boundary conditions. The homogeneous boundary conditions are fulfilled by the use of the recombined Chebyshev polynomials described in chapter 3. In section 2.6, the inhomogeneous terms are extracted as the control inputs during manipulation of the equations into state-space form, and the system matrices and variables are identified. Finally the section compares the derivation of the state-space form with a previously published derivation.

Section 2.7 describes two relevant test cases, and the implementations of the state-space model appropriate for each of them such that the minimum number of variables are required. Investigations into the accuracy and convergence of the resulting state-space model are presented and discussed in section 2.8. Comparisons are made with published data, and discrepancies investigated. Finally section 2.9 draws conclusions regarding the development and implementation of the state-space model of linearised plane Poiseuille flow.

2.2 Flow Equations

This section derives the flow equations of linearised plane Poiseuille flow. The Navier-Stokes and continuity equations are introduced, and the perturbation equations developed. The base plane Poiseuille flow is described, and substituted into the perturbation equations. Finally the resulting linearised plane Poiseuille flow equations are non-dimensionalised, and appropriate flow measurements defined.

2.2.1 The Incompressible Navier-Stokes and Continuity Equations

The flow of a Newtonian fluid is described by the Navier-Stokes and continuity equations. The Navier-Stokes equations form a set of three coupled, non-linear, partial differential equations representing conservation of momentum, and the continuity equation is an additional constraint representing the conservation of mass. The equations are infinite dimensional in each spatial direction, in the sense that the fluid is treated as a continuum.

For an incompressible fluid with uniform density ρ and viscosity μ, in the absence of body forces, in cartesian co-ordinates (x, y, z), the Navier-Stokes equations are

$$\frac{\partial \vec{U}}{\partial t} + \left(\vec{U} \cdot \nabla\right) \vec{U} = -\frac{1}{\rho}\nabla P + \frac{\mu}{\rho}\nabla^2 \vec{U} \tag{2.2}$$

where $\vec{U}(x, y, z, t)$ and $P(x, y, z, t)$ are the instantaneous velocity and pressure respectively. The continuity equation for an incompressible fluid in the absence of sources and sinks is

$$\nabla \cdot \vec{U} = 0 \tag{2.3}$$

These equations are accurately representative of the behaviour of many real fluids, such as air and water at normal pressures and temperatures, and low velocities.

The usual boundary conditions specify no slip, i.e. zero relative velocity, normal and tangential, at solid boundaries. Ultimately, for control purposes, a time-dependent velocity is specified on the boundaries, representing the injection or suction of fluid through porous walls known as transpiration.

For a steady base flow $\left(\vec{U}_b, P_b\right)$, $\partial \vec{U}_b / \partial t = 0$ and so the Navier-Stokes and continuity equations (2.2,2.3) become

$$\left(\vec{U}_b \cdot \nabla\right) \vec{U}_b = -\frac{1}{\rho}\nabla P_b + \frac{\mu}{\rho}\nabla^2 \vec{U}_b \tag{2.4}$$

and

$$\nabla \cdot \vec{U}_b = 0 \tag{2.5}$$

respectively.

2.2.2 Perturbations About a Base Flow

Upon substituting a steady base flow ($\vec{U}_b = (U_b, V_b, W_b), P_b$) plus a transient flow perturbation ($\vec{u} = (u, v, w), p$) into the Navier-Stokes and continuity equations (2.2,2.3), they become

$$\frac{\partial\left(\vec{U}_b + \vec{u}\right)}{\partial t} + \left(\left(\vec{U}_b + \vec{u}\right) \cdot \nabla\right)\left(\vec{U}_b + \vec{u}\right) = -\frac{1}{\rho}\nabla\left(P_b + p\right) + \frac{\mu}{\rho}\nabla^2\left(\vec{U}_b + \vec{u}\right) \tag{2.6}$$

$$\nabla \cdot \left(\vec{U}_b + \vec{u}\right) = 0 \tag{2.7}$$

Since the base flow is steady and its terms themselves satisfy the Navier-Stokes and continuity equations (2.4,2.5), these equations may be simplified to

$$\frac{\partial \vec{u}}{\partial t} + \left(\vec{U}_b \cdot \nabla\right)\vec{u} + \left(\vec{u} \cdot \nabla\right)\vec{u} + \left(\vec{u} \cdot \nabla\right)\vec{U}_b = -\frac{1}{\rho}\nabla p + \frac{\mu}{\rho}\nabla^2\vec{u} \tag{2.8}$$

$$\nabla \cdot \vec{u} = 0 \tag{2.9}$$

The boundary condition on perturbation velocities is the no slip condition.

2.2.3 The Base Flow: Plane Poiseuille Flow

There are few exact solutions to the base flow system of equations (2.4,2.5), but one that does exist is that for laminar plane Poiseuille flow, the fully developed plane steady flow between infinite parallel planar stationary boundaries. Assuming flow is in the x-direction, then $V_b = W_b = 0$ and the base flow equations reduce to

$$-\frac{1}{\rho}\frac{\partial P_b}{\partial x} + \frac{\mu}{\rho}\left(\frac{\partial^2 U_b}{\partial y^2}\right) = 0, \quad \frac{\partial P_b}{\partial y} = 0, \quad \frac{\partial P_b}{\partial z} = 0 \tag{2.10}$$

and

$$\frac{\partial U_b}{\partial x} = 0 \tag{2.11}$$

Assuming the planar boundaries are located at $y = \pm h$, the boundary conditions are $\vec{U}_b(x, \pm h, z, t) = 0$. The solution of (2.10) and (2.11) is a parabolic velocity profile in y and a linear pressure gradient in x

$$\vec{U}_b = \left(\left(1 - \frac{y^2}{h^2}\right)U_{cl}, 0, 0\right), \quad \frac{dP_b}{dx} = -\frac{2U_{cl}\mu}{h^2} \tag{2.12}$$

where U_{cl} is the centre-line velocity. This flow may be physically realised at low Reynolds numbers ($R = \rho U_{cl} h/\mu$, based on centreline velocity and channel half-height), when the flow is laminar. At higher Reynolds numbers the flow becomes

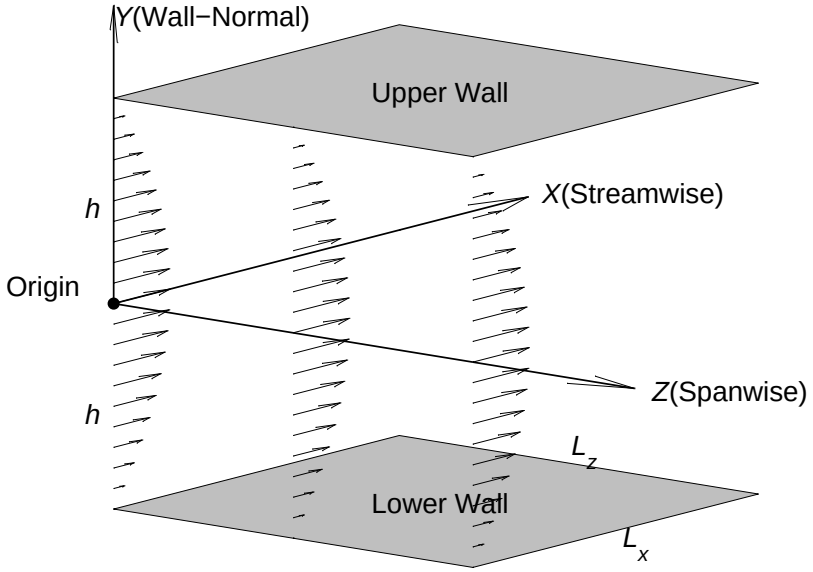

Figure 2.1: Co-ordinate System for Plane Poiseuille Flow

turbulent, with associated large increases in skin friction and heat transfer. The present work is applicable only to laminar flow.

Henceforth the x direction is referred to as the streamwise direction, the y direction is referred to as the wall-normal direction, and the z direction is referred to as the spanwise direction. The coordinate system is shown in figure 2.1.

2.2.4 Linearization About Plane Poiseuille Flow

The Navier-Stokes perturbation equations (2.8), are linearised by discarding the second order quantity $(\vec{u}\cdot\nabla)\,\vec{u}$, which is small compared to $\left(\vec{U}_b\cdot\nabla\right)\vec{u}+(\vec{u}\cdot\nabla)\,\vec{U}_b$ in (2.8) when $\vec{u}\ll\vec{U}_b$, resulting in the linearised Navier-Stokes equations

$$\frac{\partial\vec{u}}{\partial t}+\left(\vec{U}_b\cdot\nabla\right)\vec{u}+(\vec{u}\cdot\nabla)\,\vec{U}_b \;=\; -\frac{1}{\rho}\nabla p+\frac{\mu}{\rho}\nabla^2\vec{u} \tag{2.13}$$

The continuity perturbation equation, $\nabla\cdot\vec{u}=0$ (2.9), is already linear. The boundary condition on perturbation velocities remains the no slip condition. This linearization is the first in a series of approximations. Although the behaviour of a real fluid is non-linear, a linear model can still capture critical unstable behaviour, as noted by Trefethen et al. (1993).

If the plane Poiseuille base flow (2.12) is substituted for $\vec{U}_b$, the equations (2.13) become the Navier-Stokes equations linearised about plane Poiseuille flow

$$\begin{aligned}
\frac{\partial u}{\partial t}+U_b\frac{\partial u}{\partial x}+v\frac{\partial U_b}{\partial y} &= -\frac{1}{\rho}\frac{\partial p}{\partial x}+\frac{\mu}{\rho}\nabla^2 u\\
\frac{\partial v}{\partial t}+U_b\frac{\partial v}{\partial x} &= -\frac{1}{\rho}\frac{\partial p}{\partial y}+\frac{\mu}{\rho}\nabla^2 v\\
\frac{\partial w}{\partial t}+U_b\frac{\partial w}{\partial x} &= -\frac{1}{\rho}\frac{\partial p}{\partial z}+\frac{\mu}{\rho}\nabla^2 w
\end{aligned} \tag{2.14}$$

where $U_b = \left(1 - \frac{y^2}{h^2}\right) U_{cl}$.

2.2.5 Non-Dimensionalisation

Non-dimensionalising length scales by the channel half-height, h, velocities by the centre-line velocity, U_{cl}, pressure by ρU_{cl}^2, such that $p^* = p/\rho U_{cl}^2, t^* = tU_{cl}/h, u^* = u/U_{cl}, \bar{u}^* = \bar{u}/U_{cl}, x^* = x/h$ etc, the Navier-Stokes equations linearised about plane Poiseuille flow (2.14) become

$$\begin{aligned} \frac{\partial u^*}{\partial t^*} + U_b^* \frac{\partial u^*}{\partial x^*} + v^* \frac{\partial U_b^*}{\partial y^*} &= -\frac{\partial p^*}{\partial x^*} + \frac{1}{R}\nabla^2 u^* \\ \frac{\partial v^*}{\partial t^*} + U_b^* \frac{\partial v^*}{\partial x^*} &= -\frac{\partial p^*}{\partial y^*} + \frac{1}{R}\nabla^2 v^* \\ \frac{\partial w^*}{\partial t^*} + U_b^* \frac{\partial w^*}{\partial x^*} &= -\frac{\partial p^*}{\partial z^*} + \frac{1}{R}\nabla^2 w^* \end{aligned} \tag{2.15}$$

where R is the Reynolds number, $\rho U_{cl} h/\mu$. The base velocity profile (2.12) becomes

$$U_b^* = 1 - y^{*2} \tag{2.16}$$

and the continuity equation (2.9) becomes

$$\frac{\partial u^*}{\partial x^*} + \frac{\partial v^*}{\partial y^*} + \frac{\partial w^*}{\partial z^*} = 0 \tag{2.17}$$

The asterisk will be dropped for notational convenience for the remainder of this work. In non-dimensional co-ordinates the upper and lower walls are at $y = \pm 1$ respectively.

2.2.6 Measurement

In a real system, the dimensionalised measurements would be the shear stresses τ_{yx}, τ_{yz} in the x and z directions respectively, on the upper and lower walls, where

$$\tau_{yx} = \mu\left(\frac{\partial u}{\partial y} + \frac{\partial v}{\partial x}\right) \qquad \tau_{yz} = \mu\left(\frac{\partial w}{\partial y} + \frac{\partial v}{\partial z}\right) \tag{2.18}$$

Non-dimensionalising the stresses by ρU_{cl}^2, velocities by U_{cl} and distances by h as previously, the equations become

$$\tau_{yx} = \frac{1}{R}\left(\frac{\partial u}{\partial y} + \frac{\partial v}{\partial x}\right) \qquad \tau_{yz} = \frac{1}{R}\left(\frac{\partial w}{\partial y} + \frac{\partial v}{\partial z}\right) \tag{2.19}$$

Since the velocity v at the walls is set by the boundary conditions, it is known and its derivatives can be subtracted out. Thus it is appropriate to define a measurement vector $\mathbf{y}$ similar to that used by Bewley and Liu (1998)

$$\mathbf{y} = \frac{1}{R}\begin{pmatrix} \left.\frac{\partial u}{\partial y}\right|_{y=+1} \\ \left.\frac{\partial u}{\partial y}\right|_{y=-1} \\ \left.\frac{\partial w}{\partial y}\right|_{y=+1} \\ \left.\frac{\partial w}{\partial y}\right|_{y=-1} \end{pmatrix} \tag{2.20}$$

Strictly speaking, the shear stress measurement on the upper wall should be negated, as these values refer to the lower surface at any shear plane, but this omission has no consequences, as it has been treated consistently.

2.3 Formulation

In this section a suitable formulation of the linearised plane Poiseuille flow equations is selected and developed, and the boundary conditions restated in the selected formulation.

2.3.1 System Formulations

The equations (2.15,2.17) form a system of 4 linear partial differential equations, in four flow variables (u, v, w, p), in which the continuity equation has no time derivative, and acts as a spatial differential constraint. The constraint is enforced by ∇p acting as a Lagrange multiplier, keeping the velocity field divergence free. If ordinary differential equations are formulated from the system by discretisation, they are singular, as noted by Bewley (2001), since the continuity equation has no time derivative and thus the matrix $\mathcal{L}$ in the differential algebraic equation (or DAE, as described by Campbell and Marszalek (1999, p25,p38)) or descriptor form

$$\mathcal{L}\dot{\mathcal{X}} \;=\; \mathcal{A}^{\#}\mathcal{X} + \mathcal{B}^{\#}\mathcal{U} \tag{2.21}$$

where $\mathcal{A}^{\#}$ and $\mathcal{B}^{\#}$ are related forms of $\mathcal{A}$ and $\mathcal{B}$, cannot be inverted to produce the conventional state-space form of equation (2.1). To proceed further the system (2.15,2.17) can be reformulated in terms of only two flow variables, a so-called divergence free basis in which continuity is implicitly enforced. The variables (u, v, w, p) are transformed to eliminate the continuity equation and thus the differential constraint. This eliminates the algebraic constraints in the discretised form (2.21), reduces the order of $\mathcal{X}$ and $\mathcal{L}$ becomes non-singular. There are several possible formulations: vorticity-stream function, velocity-vorticity, and velocity-pressure (provided the continuity equation is used to derive pressure), as described by Peyret (2002). The current work employs a velocity-vorticity formulation as it is convenient for the application of boundary conditions in this simple geometry, as noted by Bewley (2001).

2.3.2 Velocity-Vorticity Formulation

The pressure perturbation is eliminated from the Navier-Stokes perturbation equations by forming its gradient, $(\partial p/\partial x, \partial p/\partial y, \partial p/\partial z)$, from the three perturbation equations (2.15), taking the divergence of the result, and substituting the resulting Laplacian into the Laplacian of the second perturbation equation to yield a 'wall-normal velocity' equation, as described by Schmid and Henningson (2001, p56)

$$\frac{\partial(\nabla^2 v)}{\partial t} + U_b\frac{\partial(\nabla^2 v)}{\partial x} - \frac{\partial^2 U_b}{\partial y^2}\frac{\partial v}{\partial x} - \frac{1}{R}\nabla^2(\nabla^2 v) = 0 \tag{2.22}$$

having employed the continuity perturbation equation (2.17) in the process by substitution. A second equation is required to completely describe a 3-d perturbation. Vorticity is the curl of the velocity field, $\nabla \times \vec{u}$, and defining the wall-normal vorticity, η, as

$$\eta = \frac{\partial u}{\partial z} - \frac{\partial w}{\partial x} \tag{2.23}$$

it represents twice the angular velocity of a fluid particle with respect to an axis in the wall-normal direction. The z differential of the first perturbation equation of (2.15) minus the x differential of the third equation yields a 'wall-normal vorticity' equation

$$\frac{\partial \eta}{\partial t} + \frac{\partial U_b}{\partial y}\frac{\partial v}{\partial z} + U_b\frac{\partial \eta}{\partial x} - \frac{1}{R}\nabla^2\eta = 0 \tag{2.24}$$

The velocity equation (2.22) contains the time derivative of the Laplacian of velocity, which will need to be inverted to produce the form of (2.1). The equations are one-way coupled, in the sense that (2.22) can be solved independently of (2.24), and its solutions for v (including $v = 0$) then used to derive the solution of (2.24) for η.

2.3.3 Boundary Conditions in Velocity-Vorticity Formulation

The no-slip boundary conditions in the velocity-vorticity formulation become

Dirichlet Boundary Conditions on v. The wall-normal velocity at the walls, $v(y = \pm 1)$, is zero in plane Poiseuille flow, and thus the boundary conditions are homogeneous. The introduction of wall transpiration will make the velocities non-zero and thus the boundary conditions inhomogeneous

$$\begin{aligned} v(y = 1) &= q_u \\ v(y = -1) &= q_l \end{aligned} \tag{2.25}$$

where q_u and q_l are determined by the controller.

Homogeneous Neumann Boundary Conditions on v. The equation of continuity at the walls states

$$\left.\frac{\partial u}{\partial x}\right|_{y=\pm 1} + \left.\frac{\partial v}{\partial y}\right|_{y=\pm 1} + \left.\frac{\partial w}{\partial z}\right|_{y=\pm 1} = 0 \tag{2.26}$$

Thus, substituting the zero streamwise (x) and spanwise (z) velocity perturbations, the y derivative of wall-normal velocity perturbations is zero at the walls

$$\left.\frac{\partial v}{\partial y}\right|_{y=\pm 1} = 0 \tag{2.27}$$

Homogeneous Dirichlet Boundary Conditions on η. The streamwise (x) and spanwise (z) velocity perturbations (u, w) are zero at the wall, so the wall-normal vorticity at the walls is also zero

$$\eta(y = \pm 1) = \left.\frac{\partial u}{\partial z}\right|_{y=\pm 1} - \left.\frac{\partial w}{\partial x}\right|_{y=\pm 1} = 0 \tag{2.28}$$

There are four boundary conditions for the fourth order velocity equation, and two boundary conditions for the second order vorticity equation, thus forming a well-posed mathematical problem.

2.4 Discretisation

This section describes the discretisation of the linearised system of equations in the streamwise, spanwise and wall-normal directions.

2.4.1 Introduction

Since the flow problem is infinite dimensional in spatial coordinates, in order to work with a system with a finite number of state variables, the linearized system must be discretised in space, which is the second approximation in the process of generating the plant model, linearisation being the first. Several methods of spatial discretisation of PDE's exist, e.g. spectral, finite difference, finite element, and finite volume methods. The system of partial differential equations is approximated and replaced by a system of ordinary differential equations.

Spectral collocation discretisation methods are used here. Spectral methods belong to the class of weighted residual methods in which the weighted residual from evaluating the PDE using an approximate solution is set to zero. Spectral methods approximate the solution by a truncated series of orthogonal functions. Using a Fourier series for the orthogonal functions assumes a periodic solution, using a Chebyshev polynomial series assumes a non-periodic one. Collocation involves setting the residual to zero at specific points, as compared to the Galerkin method which sets the average residual to zero, as described by Peyret (2002).

2.4.2 Streamwise and Spanwise Discretisation

The variation of the solution in the streamwise and spanwise dimensions is approximated by terms from a truncated Fourier series. The use of a Fourier series assumes a periodic solution for all variables in the dimensions to which it is applied, and Rempfer (2003, p237) notes thats its use in these dimensions assumes a temporally rather than spatially growing perturbation. Truncation of the series approximates infinite dimensional behaviour by finite dimensional behaviour.

For mathematical convenience, complex solutions v_c and η_c are generated for the wall-normal velocity and vorticity equations, bearing in mind that the real

solutions

$$\begin{aligned} v &= \Re(v_c) \\ \eta &= \Re(\eta_c) \end{aligned} \tag{2.29}$$

are ultimately required. Thus solutions to (2.22) and (2.24) are approximated by truncated complex Fourier series

$$v_c(x,y,z,t) = \sum_{n_{st}=0}^{N_{st}} \sum_{n_{sp}=0}^{N_{sp}} \tilde{v}(y,t,n_{st},n_{sp}) e^{2\pi \jmath n_{st} x/L_x} e^{2\pi \jmath n_{sp} z/L_z} \tag{2.30}$$

$$\eta_c(x,y,z,t) = \sum_{n_{st}=0}^{N_{st}} \sum_{n_{sp}=0}^{N_{sp}} \tilde{\eta}(y,t,n_{st},n_{sp}) e^{2\pi \jmath n_{st} x/L_x} e^{2\pi \jmath n_{sp} z/L_z} \tag{2.31}$$

where n_{st} is the streamwise harmonic number, n_{sp} is the spanwise harmonic number, and L_x and L_z are fundamental wavelengths in the streamwise and spanwise directions (see figure 2.1). N_{st} and N_{sp} are finite and represent the truncation of the series.

The linearized equations decouple by harmonic number pair and thus it is possible to treat each harmonic number pair separately, bearing in mind that in so doing, all dependent variables will vary at the selected frequencies in the streamwise and spanwise directions. For convenience, a streamwise wavenumber, $\alpha = 2\pi n_{st}/L_x$, and spanwise wavenumber, $\beta = 2\pi n_{sp}/L_z$, are defined in cycles per 2π distance, and then the solution at each wavenumber pair is assumed to be of the form

$$v_c(x,y,z,t) = \tilde{v}(y,t) e^{\jmath(\alpha x + \beta z)} \tag{2.32}$$

$$\eta_c(x,y,z,t) = \tilde{\eta}(y,t) e^{\jmath(\alpha x + \beta z)} \tag{2.33}$$

where $\tilde{v}(y,t)$ and $\tilde{\eta}(y,t)$ are wall-normal velocity and vorticity perturbation Fourier coefficients, henceforth referred to simply as velocity and vorticity coefficients. These are complex and convey the wall-normal (y) and temporal (t) variation of v_c and η_c at real streamwise and spanwise wavenumber pair α, β.

Substituting the assumed solutions (2.32,2.33) into the partial differential equations for wall-normal velocity (2.22), and wall-normal vorticity (2.24), results in wall-normal velocity perturbation and vorticity perturbation Fourier-space equations in $\tilde{v}$ and $\tilde{\eta}$ respectively

$$\left(-U_b k^2 - \frac{\partial^2 U_b}{\partial y^2} - \frac{k^4}{\jmath R\alpha}\right)\tilde{v} + \left(U_b + \frac{2k^2}{\jmath R\alpha}\right)\frac{\partial^2 \tilde{v}}{\partial y^2} - \left(\frac{1}{\jmath R\alpha}\right)\frac{\partial^4 \tilde{v}}{\partial y^4} = \frac{\jmath}{\alpha}\left(\frac{\partial^3 \tilde{v}}{\partial y^2 \partial t} - k^2 \frac{\partial \tilde{v}}{\partial t}\right) \tag{2.34}$$

and

$$\left(\jmath\alpha U_b + \frac{k^2}{R}\right)\tilde{\eta} - \frac{1}{R}\frac{\partial^2 \tilde{\eta}}{\partial y^2} + \jmath\beta\tilde{v}\frac{\partial U_b}{\partial y} = -\frac{\partial \tilde{\eta}}{\partial t} \tag{2.35}$$

where $k^2 = \alpha^2 + \beta^2$.

These wall-normal velocity and vorticity perturbation Fourier-space equations will henceforth be referred to as the velocity and vorticity equations. If an exponential time variation is assumed, the classical Orr-Sommerfeld (Orr, 1907) and Squire equations result. The fluid mechanics community assume a time variation $\tilde{v} = f_v(y)e^{-\jmath\omega t}, \tilde{\eta} = f_\eta(y)e^{-\jmath\omega t}$, implying a temporal frequency $-\Re(\omega)$, and damping $\Im(\omega)$ but the control community assume a variation $\tilde{v} = f_v(y)e^{\lambda t}, \tilde{\eta} = f_\eta(y)e^{\lambda t}$, and the latter convention is adopted here for all time variations. With the latter time variation, solutions to the Orr-Sommerfeld and Squire equations exist at particular eigenvalues λ_i (damping $\Re(\lambda_i)$ and temporal frequency $\omega = \Im(\lambda_i)$), for the i^{th} eigenfunction pair denoted $(f_v(y), f_\eta(y))_i$.

The velocity and vorticity equations become independent if β is zero. For non-zero β the vorticity equation is driven by solutions of the velocity equation. Solutions with zero velocity are known as Squire modes, those with non-zero velocity as Orr-Sommerfeld modes, as defined in Schmid and Henningson (2001, p58). The Squire modes are all known to be stable, whereas the first Orr-Sommerfeld mode for $R > 5772$ is unstable. Stability is not the only control criterion, as large transient energy growth may invalidate assumptions about linearity and ultimately cause transition to turbulence, as noted by Aamo and Fossen (2002, p42).

Returning to the solutions for v and η, they are given by substituting (2.32,2.33) into (2.29)

$$\begin{aligned} v(x,y,z,t) &= \Re(v_c) = \Re\left(\tilde{v}(y,t)e^{\jmath(\alpha x+\beta z)}\right) && (2.36)\\ \eta(x,y,z,t) &= \Re(\eta_c) = \Re\left(\tilde{\eta}(y,t)e^{\jmath(\alpha x+\beta z)}\right) && (2.37)\end{aligned}$$

The appropriate boundary conditions on v and η (2.25,2.27,2.28) translate to

$$\begin{aligned} v_c(y=1) &= q_u + 0\jmath \\ v_c(y=-1) &= q_l + 0\jmath \\ v_c'(y=\pm 1) &= 0 + 0\jmath \\ \eta_c(y=\pm 1) &= 0 + 0\jmath \end{aligned} \qquad (2.38)$$

on v_c and η_c, since the imaginary solutions $\Im(v_c), \Im(\eta_c)$ are of no interest, and these translate to

$$\begin{aligned} \tilde{v}(y=1) &= \tilde{q}_u \\ \tilde{v}(y=-1) &= \tilde{q}_l \\ \tilde{v}'(y=\pm 1) &= 0 + 0\jmath \\ \tilde{\eta}(y=\pm 1) &= 0 + 0\jmath \end{aligned} \qquad (2.39)$$

on $\tilde{v}$ and $\tilde{\eta}$, where $q_u = \Re(\tilde{q}_u e^{\jmath(\alpha x+\beta z)})$ and $q_l = \Re(\tilde{q}_l e^{\jmath(\alpha x+\beta z)})$ by analogy with (2.32) i.e. the actuation varies sinusoidally in the streamwise and spanwise directions. Although v, η, q_u and q_l are real, $\tilde{v}, \tilde{\eta}, \tilde{q}_u$ and $\tilde{q}_l$ are complex. For the present, until transpiration is introduced in section 2.5, $q_u, q_l, \tilde{q}_u$ and $\tilde{q}_l$ are assumed to be zero.

Useful Relationships

Several useful relationships by Aamo and Fossen (2002, p38) are rederived in the present context. For mathematical convenience, the complex expressions

$$\begin{aligned} u_c(x,y,z,t) &= \tilde{u}(y,t)e^{\jmath(\alpha x+\beta z)} \\ v_c(x,y,z,t) &= \tilde{v}(y,t)e^{\jmath(\alpha x+\beta z)} \\ w_c(x,y,z,t) &= \tilde{w}(y,t)e^{\jmath(\alpha x+\beta z)} \\ \eta_c(x,y,z,t) &= \tilde{\eta}(y,t)e^{\jmath(\alpha x+\beta z)} \end{aligned} \tag{2.40}$$

are assumed, where $u = \Re(u_c), v = \Re(v_c), w = \Re(w_c)$ and $\eta = \Re(\eta_c)$ by extensions of (2.32) and (2.29).

The continuity equation (2.17) states

$$\frac{\partial u}{\partial x} + \frac{\partial v}{\partial y} + \frac{\partial w}{\partial z} = 0 \tag{2.41}$$

Substituting (2.40) into the continuity equation yields

$$\jmath\alpha\tilde{u} + \frac{\partial \tilde{v}}{\partial y} + \jmath\beta\tilde{w} = 0 \tag{2.42}$$

The definition of vorticity (2.23) states

$$\eta = \frac{\partial u}{\partial z} - \frac{\partial w}{\partial x} \tag{2.43}$$

and substituting in (2.40) yields

$$\tilde{\eta}(y,t) = \jmath\beta\tilde{u} - \jmath\alpha\tilde{w} \tag{2.44}$$

Solving (2.40,2.44) for $\tilde{u}$ and $\tilde{w}$ yields

$$\begin{aligned} \tilde{u} &= \frac{\jmath}{\alpha^2+\beta^2}\left(\alpha\frac{\partial\tilde{v}}{\partial y} - \beta\tilde{\eta}\right) \\ \tilde{w} &= \frac{\jmath}{\alpha^2+\beta^2}\left(\beta\frac{\partial\tilde{v}}{\partial y} + \alpha\tilde{\eta}\right) \end{aligned} \tag{2.45}$$

2.4.3 Measurement

In Fourier space the measurement vector (2.20) becomes

$$\tilde{\mathbf{y}} = \frac{1}{R}\begin{pmatrix} \left.\frac{\partial\tilde{u}}{\partial y}\right|_{y=+1} \\ \left.\frac{\partial\tilde{u}}{\partial y}\right|_{y=-1} \\ \left.\frac{\partial\tilde{w}}{\partial y}\right|_{y=+1} \\ \left.\frac{\partial\tilde{w}}{\partial y}\right|_{y=-1} \end{pmatrix} \tag{2.46}$$

Thus for physical measurement of $\tilde{\mathbf{y}}$, a Fourier transform is necessary, since at a particular wavenumber pair, $\partial\tilde{u}/\partial y$ for example, is given by

$$\frac{\partial\tilde{u}(y,t)}{\partial y} = \frac{1}{L_x}\frac{1}{L_z}\int_a^{a+L_x}\int_b^{b+L_z}\frac{\partial u(x,y,z,t)}{\partial y}e^{\jmath\alpha x}e^{\jmath\beta z}dxdz \tag{2.47}$$

which requires distributed sensing of shear stress component $\partial u/\partial y$ and subsequent integration. In practice a number of discrete sensors would be used, and a fast Fourier transform (FFT) performed on their signals. The FFT's are in space rather than the usual application of FFT's in time.

Regarding the development of a measurement equation $\mathcal{Y} = \mathcal{C}\mathcal{X}$, in (2.1) the measurement vector can be expressed in terms of derivatives of $\tilde{v}$ and $\tilde{\eta}$, as performed by Aamo and Fossen (2002). Taking derivatives of (2.45) and substituting into (2.46) leads to

$$\tilde{\mathbf{y}} = \frac{1}{R}\frac{\jmath}{\alpha^2+\beta^2}\begin{pmatrix} \alpha\frac{\partial^2\tilde{v}}{\partial y^2} - \beta\frac{\partial\tilde{\eta}}{\partial y}\Big|_{y=+1} \\ \alpha\frac{\partial^2\tilde{v}}{\partial y^2} - \beta\frac{\partial\tilde{\eta}}{\partial y}\Big|_{y=-1} \\ \beta\frac{\partial^2\tilde{v}}{\partial y^2} + \alpha\frac{\partial\tilde{\eta}}{\partial y}\Big|_{y=+1} \\ \beta\frac{\partial^2\tilde{v}}{\partial y^2} + \alpha\frac{\partial\tilde{\eta}}{\partial y}\Big|_{y=-1} \end{pmatrix} \tag{2.48}$$

which, after taking into account no negation of shear at the upper wall, is consistent with the work of Aamo (2002, p59), but slightly different to that of Bewley and Liu (1998, p311), in respect of the sign of β in the lower two terms.

The wall pressures are also useful measurements, and may be expressed avoiding the inversion of the Laplacian suggested previously by Bewley and Liu (1998, p309), as follows. When represented in Fourier space, such that $p = \tilde{p}e^{\jmath(\alpha x+\beta z)}$ and similarly for $\tilde{u}, \tilde{v}$ and $\tilde{w}$, the linearised x and z-momentum Navier-Stokes equations, from (2.15), become

$$\begin{aligned} \jmath\alpha\tilde{p} &= \frac{1}{R}\left(\frac{\partial^2\tilde{u}}{\partial y^2} - \alpha^2\tilde{u} - \beta^2\tilde{u}\right) - U_b\jmath\alpha\tilde{u} - \tilde{v}\frac{\partial U_b}{\partial y} - \frac{\partial\tilde{u}}{\partial t} \\ \jmath\beta\tilde{p} &= \frac{1}{R}\left(\frac{\partial^2\tilde{w}}{\partial y^2} - \beta^2\tilde{w} - \alpha^2\tilde{w}\right) - \frac{\partial\tilde{w}}{\partial t} \end{aligned} \tag{2.49}$$

Adding, and noting that at the wall $\tilde{u} = \tilde{w} = 0$

$$\jmath\left(\alpha+\beta\right)\tilde{p}\big|_{y=\pm1} = \frac{1}{R}\left(\frac{\partial^2\tilde{u}}{\partial y^2} + \frac{\partial^2\tilde{w}}{\partial y^2}\right) - \tilde{v}\frac{\partial U_b}{\partial y} \tag{2.50}$$

Substituting (2.45) yields

$$\tilde{p}\big|_{y=\pm1} = \frac{1}{\alpha^2+\beta^2}\frac{1}{R}\left(\frac{\partial^3\tilde{v}}{\partial y^3} + \frac{\alpha-\beta}{\alpha+\beta}\frac{\partial^2\tilde{\eta}}{\partial y^2}\right) + \frac{\jmath}{\alpha+\beta}\tilde{v}\frac{\partial U_b}{\partial y} \tag{2.51}$$

Thus the wall pressure contains one higher derivative of $\tilde{v}$ and $\tilde{\eta}$ than the shear stress measurement (2.48).

2.4.4 Polynomial Discretization in the Wall-Normal Direction

Discretisation in the wall-normal direction is based on Chebyshev polynomial series as performed by Joshi et al. (1995) and Schmid and Henningson (2001). These series do not make an assumption of periodicity. Chebyshev polynomials, $\Gamma_n(y)$, of the first kind, are of the form (Råde and Westergren, 1999, p260)

$$\Gamma_n(y) = \cos\left(n \arccos\left(y\right)\right) \tag{2.52}$$

where $-1 \leq y \leq 1$ (conveniently the same as the full non-dimensionalised channel height). So, for instance

$$\Gamma_0(y) = 1 \qquad \Gamma_1(y) = y \qquad \Gamma_2(y) = 2y^2 - 1$$

Chebyshev polynomials have many useful properties e.g. the minimax property of minimising the maximum error when approximating continuous functions, as noted by Fox and Parker (1968), and are recommended by Boyd (2001, p10) where periodic boundary conditions are not applicable. $\tilde{v}$ is approximated by a finite Chebyshev series

$$\tilde{v}(y,t) = \sum_{n=0}^{N} a_{v,n}(t)\Gamma_n(y) \tag{2.53}$$

as is $\tilde{\eta}$

$$\tilde{\eta}(y,t) = \sum_{n=0}^{N} a_{\eta,n}(t)\Gamma_n(y) \tag{2.54}$$

The derivatives of the approximations with respect to y are obtained by differentiating the Chebyshev polynomials, for example

$$\tilde{v}' = \sum_{n=0}^{N} a_{v,n}(t)\Gamma'_n(y) \tag{2.55}$$

Recursion formulae exist for calculating the derivatives of Chebyshev polynomials, e.g. as provided by Schmid and Henningson (2001, p485). The derivatives are known to become large at the ends of the range, for large N and high order derivative, as noted by Boyd (2001, p142).

The partial differential equations are expressed on a grid of $N+1$ Chebyshev-Gauss-Lobatto points (Chebyshev collocation points), y_k, where

$$y_k = \cos(\pi k/N), \quad k = 0, \ldots, N \tag{2.56}$$

in the technique known as collocation. This distribution of points is particularly favourable for spectral accuracy, and appropriately for the present problem, includes the boundary points (Peyret, 2002, p46). On this distribution of points equation (2.53) becomes

$$\begin{pmatrix} \tilde{v}(y_0,t) \\ \vdots \\ \tilde{v}(y_N,t) \end{pmatrix} = \begin{bmatrix} \Gamma_0(1) & \ldots & \Gamma_N(1) \\ \vdots & \ddots & \vdots \\ \Gamma_0(-1) & \ldots & \Gamma_N(-1) \end{bmatrix} \begin{pmatrix} a_{v,0} \\ \vdots \\ a_{v,N} \end{pmatrix} \tag{2.57}$$

and equation (2.55) becomes

$$\begin{pmatrix} \tilde{v}'(y_0,t) \\ \vdots \\ \tilde{v}'(y_N,t) \end{pmatrix} = \begin{bmatrix} \Gamma'_0(1) & \dots & \Gamma'_N(1) \\ \vdots & \ddots & \vdots \\ \Gamma'_0(-1) & \dots & \Gamma'_N(-1) \end{bmatrix} \begin{pmatrix} a_{v,0} \\ \vdots \\ a_{v,N} \end{pmatrix} \tag{2.58}$$

2.4.5 The Interpolating Basis

An alternative use of Chebyshev series is via an interpolating or cardinal function basis, where the series are used to interpolate values of velocity, and in so doing can also provide derivatives, as used by Bewley and Liu (1998). In this basis

$$\begin{pmatrix} \tilde{v}'(y_0,t) \\ \vdots \\ \tilde{v}'(y_N,t) \end{pmatrix} = \mathbf{D} \begin{pmatrix} \tilde{v}(y_0,t) \\ \vdots \\ \tilde{v}(y_N,t) \end{pmatrix} \tag{2.59}$$

where, conceptually

$$\mathbf{D} = \begin{bmatrix} \Gamma'_0(1) & \dots & \Gamma'_N(1) \\ \vdots & \ddots & \vdots \\ \Gamma'_0(-1) & \dots & \Gamma'_N(-1) \end{bmatrix} \begin{bmatrix} \Gamma_0(1) & \dots & \Gamma_N(1) \\ \vdots & \ddots & \vdots \\ \Gamma_0(-1) & \dots & \Gamma_N(-1) \end{bmatrix}^{-1} \tag{2.60}$$

$$\triangleq \begin{bmatrix} D_{0,0} & \dots & D_{0,N} \\ \vdots & \ddots & \vdots \\ D_{N,0} & \dots & D_{N,N} \end{bmatrix} \tag{2.61}$$

although this is not the preferred numerical form, for which see the form by Trefethen (2000, p54).

There is an important distinction between the two forms regarding approximation. The polynomial basis is amenable to approximation. For instance, if two state variables are to be discarded and the derivative of the wall velocities is not to be calculated

$$\begin{pmatrix} \tilde{v}'(y_1,t) \\ \vdots \\ \tilde{v}'(y_{N-1},t) \end{pmatrix} \approx \begin{bmatrix} \Gamma'_0(y_1) & \dots & \Gamma'_{N-2}(y_1) \\ \vdots & \ddots & \vdots \\ \Gamma'_0(y_{N-1}) & \dots & \Gamma'_{N-2}(y_{N-1}) \end{bmatrix} \begin{pmatrix} a_{v,0} \\ \vdots \\ a_{v,N-2} \end{pmatrix} \tag{2.62}$$

whether or not $\tilde{v}$ is homogeneous ($\tilde{v}(y_{0,N} = \pm 1) = 0$)). In the present work, it so happens that the bases used are homogeneous (see section 2.5). The approximation holds because it is just a truncation of the high order terms of the Chebyshev series, and the coefficients decay spectrally. A similar approximation does not hold for the interpolating form

$$\begin{pmatrix} \tilde{v}'(y_1,t) \\ \vdots \\ \tilde{v}'(y_{N-1},t) \end{pmatrix} \neq \begin{bmatrix} D_{1,1} & \dots & D_{1,N-1} \\ \vdots & \ddots & \vdots \\ D_{N-1,1} & \dots & D_{N-1,N-1} \end{bmatrix} \begin{pmatrix} \tilde{v}(y_1,t) \\ \vdots \\ \tilde{v}(y_{N-1},t) \end{pmatrix} \tag{2.63}$$

if $\tilde{v}$ in inhomogeneous ($\tilde{v}(y_{0,N} = \pm 1) \neq 0$)). The reason is that this form performs high order curve fitting on $\tilde{v}(y_k)$, and then algebraic differentiation, as can be seen from (2.60). If $\tilde{v}(y_0)$ or $\tilde{v}(y_N)$ are absent, they are taken to be zero (homogeneous). If this is not correct, for instance in the controlled setting, the curve fitting oscillates wildly, and the derivatives, although algebraic, have very large values. If the missing variables have simply been partitioned to another term in an expression, overall the expression still holds.

Bewley and Liu (1998, p311) partition the terms $\tilde{v}(y_{0,N})$ from the system matrix into the control input matrix, but also discard the terms from the energy matrix. Thus no attempt is made in this thesis to compare any closed loop results with those from this source. See section 4.2.1 for further details.

2.4.6 Resulting Equations

Upon substitution of the Chebyshev polynomial series, the velocity and vorticity equations (2.34,2.35) become those presented by Schmid and Henningson (2001, p488)

$$\left(-U_b k^2 - \frac{\partial^2 U_b}{\partial y^2} - \frac{k^4}{\jmath \alpha R}\right) \sum_{n=0}^{N} a_{v,n}(t)\Gamma_n(y) + \left(U_b + 2\frac{k^2}{\jmath \alpha R}\right) \sum_{n=0}^{N} a_{v,n}(t){\Gamma_n}''(y) - \frac{1}{\jmath R \alpha} \sum_{n=0}^{N} a_{v,n}(t){\Gamma_n}''''(y) = \frac{\jmath}{\alpha}\left(-k^2 \sum_{n=0}^{N} \dot{a}_{v,n}(t)\Gamma_n(y) + \sum_{n=0}^{N} \dot{a}_{v,n}(t){\Gamma_n}''(y)\right) \tag{2.64}$$

and

$$\left(\jmath \alpha U_b + \frac{k^2}{R}\right) \sum_{n=0}^{N} a_{\eta,n}(t)\Gamma_n(y) - \frac{1}{R} \sum_{n=0}^{N} a_{\eta,n}(t){\Gamma_n}''(y) + \jmath \beta \frac{\partial U_b}{\partial y} \sum_{n=0}^{N} a_{v,n}(t)\Gamma_n(y) = -\sum_{n=0}^{N} \dot{a}_{\eta,n}(t)\Gamma_n(y) \tag{2.65}$$

After multiplying the equations by α and $-\jmath$ respectively, and the evaluation of both equations at each of the collocation points y_k, and noting that $U_b = 1 - y^2$, the equations may be assembled as

$$\begin{pmatrix} \mathbf{A}_{11} & \mathbf{A}_{12} \\ \mathbf{A}_{21} & \mathbf{A}_{22} \end{pmatrix} \mathbf{a} = \begin{pmatrix} \mathbf{L}_{11} & \mathbf{L}_{12} \\ \mathbf{L}_{21} & \mathbf{L}_{22} \end{pmatrix} \dot{\mathbf{a}} \tag{2.66}$$

where

$$\mathbf{a} = \begin{pmatrix} a_{v,0} \\ \vdots \\ a_{v,N} \\ a_{\eta,0} \\ \vdots \\ a_{\eta,N} \end{pmatrix} \tag{2.67}$$

and where the following submatrices all have dimensions $N+1$ by $N+1$ and are

$$\begin{aligned}
\mathbf{A}_{11} &= \left(-\alpha\bar{\mathbf{u}}k^2 - \alpha\bar{\mathbf{u}}'' - \frac{\mathbf{I}k^4}{\jmath R}\right)\mathbf{D0} + \left(\alpha\bar{\mathbf{u}} + \frac{2\mathbf{I}k^2}{\jmath R}\right)\mathbf{D2} - \frac{\mathbf{D4}}{\jmath R} \\
\mathbf{A}_{12} &= [0] \\
\mathbf{A}_{21} &= \beta\bar{\mathbf{u}}'\mathbf{D0} \\
\mathbf{A}_{22} &= \left(\alpha\bar{\mathbf{u}} + \frac{\mathbf{I}k^2}{\jmath R}\right)\mathbf{D0} - \frac{\mathbf{D2}}{\jmath R} \\
\mathbf{L}_{11} &= \jmath\left(-k^2\mathbf{D0} + \mathbf{D2}\right) \\
\mathbf{L}_{12} &= [0] \\
\mathbf{L}_{21} &= [0] \\
\mathbf{L}_{22} &= \jmath\mathbf{D0}
\end{aligned} \tag{2.68}$$

Matrix $\mathbf{L}$ is the discrete form of the Laplacian ∇^2 which operates on the wall-normal velocity time derivative in (2.22). The elements of derivative matrices $\mathbf{Dn}$ and diagonal base flow matrices $\bar{\mathbf{u}}, \bar{\mathbf{u}}', \bar{\mathbf{u}}''$ are

$$\begin{aligned}
&D0_{kj} = \Gamma_j(y_k) && D2_{kj} = \Gamma_j(y_k)'' && D4_{kj} = \Gamma_j(y_k)'''' \\
&Ub_{kk} = (1 - y_k^2) && Ub'_{kk} = -2y_k && Ub''_{kk} = -2
\end{aligned} \tag{2.69}$$

2.4.7 Schmid and Henningson Form

Schmid and Henningson (2001, p489) discard equations at and next to the walls and replace them with algebraic equations representing the homogeneous Dirichlet and Neumann conditions, in a technique named 'boundary bordering' by (Boyd, 2001, p111). The technique introduces spurious eigenvalues, which may be moved to highly damped locations in the complex plane by suitable choice of algebraic coefficients. The technique of boundary bordering is not required when the form of wall transpiration to be described shortly is applied.

As Schmid and Henningson solve the Orr-Sommerfeld/Squire equations, they assume a time dependence $e^{-\jmath\omega t}$ for coefficients a and arrive at a final form

$$\begin{pmatrix} \mathbf{A}_{11} & \mathbf{A}_{12} \\ \mathbf{A}_{21} & \mathbf{A}_{22} \end{pmatrix} \mathbf{a} = -\jmath\omega \begin{pmatrix} \mathbf{L}_{11} & \mathbf{L}_{12} \\ \mathbf{L}_{21} & \mathbf{L}_{22} \end{pmatrix} \mathbf{a} \tag{2.70}$$

The solution of this system of equations provides highly accurate eigenvalues and eigenfunctions for periodic linearised plane Poiseuille flow, in the absence of any wall transpiration.

2.4.8 Discretised Measurement

Upon substitution of the Chebyshev series the measurement equation (2.48) becomes

$$\tilde{\mathbf{y}} = \frac{1}{R}\frac{\jmath}{\alpha^2+\beta^2}\begin{pmatrix} \alpha\sum_{n=0}^{N} a_{v,n}(t)\Gamma''_n(y=+1) - \beta\sum_{n=0}^{N} a_{\eta,n}(t)\Gamma'_n(y=+1) \\ \alpha\sum_{n=0}^{N} a_{v,n}(t)\Gamma''_n(y=-1) - \beta\sum_{n=0}^{N} a_{\eta,n}(t)\Gamma'_n(y=-1) \\ \beta\sum_{n=0}^{N} a_{v,n}(t)\Gamma''_n(y=+1) + \alpha\sum_{n=0}^{N} a_{\eta,n}(t)\Gamma'_n(y=+1) \\ \beta\sum_{n=0}^{N} a_{v,n}(t)\Gamma''_n(y=-1) + \alpha\sum_{n=0}^{N} a_{\eta,n}(t)\Gamma'_n(y=-1) \end{pmatrix} \tag{2.71}$$

or

$$\tilde{\mathbf{y}} = \frac{1}{R}\frac{\jmath}{\alpha^2+\beta^2}\begin{pmatrix} \mathbf{C}_{11} & \mathbf{C}_{12} \\ \mathbf{C}_{21} & \mathbf{C}_{22} \end{pmatrix}\mathbf{a} \tag{2.72}$$

where

$$\mathbf{C}_{11} = \alpha\begin{bmatrix} \Gamma''_0(y=+1), & \ldots, & \Gamma''_N(y=+1) \\ \Gamma''_0(y=-1), & \ldots, & \Gamma''_N(y=-1) \end{bmatrix} \tag{2.73}$$

and similarly for $\mathbf{C}_{12}$, $\mathbf{C}_{21}$ and $\mathbf{C}_{22}$.

2.5 Boundary Conditions and the Introduction of Wall Transpiration

Without transpiration the velocity equation (2.34) is homogeneous and thus may be expressed in the form

$$F(\tilde{v}) = 0 \tag{2.74}$$

and has homogeneous boundary conditions

$$\begin{aligned} \tilde{v}(y=\pm1,t) &= 0 \\ \tilde{v}'(y=\pm1,t) &= 0 \end{aligned} \tag{2.75}$$

Non-zero wall-normal velocity due to transpiration introduces inhomogeneous Dirichlet boundary conditions:

$$\begin{aligned} \tilde{v}(y=1,t) &= \tilde{q}_u(t) \\ \tilde{v}(y=-1,t) &= \tilde{q}_l(t) \\ \tilde{v}'(y=\pm1,t) &= 0 \end{aligned} \tag{2.76}$$

where $\tilde{q}_u(t)$ is the upper wall transpiration fluid wall-normal velocity, and $\tilde{q}_l(t)$ the lower. Since it is linear, the homogeneous equation (2.74) with inhomogeneous boundary conditions (2.76) can be transformed to an inhomogeneous equation with homogeneous boundary conditions, by a suitable change of variable, as noted by Boyd (2001, p112). Defining

$$\tilde{v}(y,t) = \tilde{v}_h(y,t) + f_u(y)\tilde{q}_u(t) + f_l(y)\tilde{q}_l(t) \tag{2.77}$$

then providing

$$\begin{aligned} \tilde{v}_h(\pm 1, t) &= \tilde{v}_h'(\pm 1, t) = 0 \\ f_u(y=1) &= f_l(y=-1) = 1 \\ f_u(y=-1) &= f_l(y=1) = 0 \\ f_u'(y=\pm 1) &= f_l'(y=\pm 1) = 0 \end{aligned} \tag{2.78}$$

the boundary conditions (2.76) are satisfied. After the substitution the equation (2.74) becomes inhomogeneous

$$F(\tilde{v}_h) = -F(f_u(y)\tilde{q}_u(t) + f_l(y)\tilde{q}_l(t)) \tag{2.79}$$

and its boundary conditions homogeneous

$$\begin{aligned} \tilde{v}_h(y=\pm 1, t) &= 0 \\ \tilde{v}_h'(y=\pm 1, t) &= 0 \end{aligned} \tag{2.80}$$

Joshi et al. (1995) employed this method on a stream function formulation, and Hogberg et al. (2003a) on a velocity-vorticity formulation using on an interpolating basis.

Polynomials that satisfy the conditions for $f_u(y)$ and $f_l(y)$ (2.78) are

$$f_u(y) = \frac{-y^3 + 3y + 2}{4} \qquad f_l(y) = \frac{y^3 - 3y + 2}{4} \tag{2.81}$$

which are simpler than those used previously by Joshi

$$f_l(y) = \frac{2y^4 + y^3 - 4y^2 - 3y + 4}{4} \tag{2.82}$$

The vorticity equation (2.35) is homogeneous both without and with transpiration

$$F_\eta(\tilde{\eta}) = 0 \tag{2.83}$$

and has homogeneous boundary conditions

$$\tilde{\eta}(y=\pm 1, t) = 0 \tag{2.84}$$

and thus requires no change of variables.

The homogeneous Dirichlet boundary conditions on $\tilde{\eta}$, $(y = \pm 1) = 0$, are implemented by the use of basis functions Γ^D which individually satisfy the homogeneous conditions, i.e.

$$\eta_h(y, t) = \sum_0^N \Gamma_n^D(y) a_{\eta,n}(t) \tag{2.85}$$

where $\Gamma_n^D(y = \pm 1) = 0$, as recommended by Boyd (2001, p114).

The simultaneous homogeneous Dirichlet and Neumann boundary conditions on $\tilde{v}$, $\tilde{v}_h(y=\pm 1,t)=\tilde{v}_h'(y=\pm 1,t)=0$, are also implemented directly, by the use of basis functions Γ^{DN} which individually satisfy the conditions, i.e.

$$\tilde{v}_h(y,t)=\sum_0^N \Gamma_n^{DN}(y)a_{v,n}(t) \tag{2.86}$$

where $\Gamma_n^{DN}(y=\pm 1)=\Gamma_n^{DN}(y=\pm 1)'=0$. Thus the final expressions for velocity and vorticity with wall transpiration present are

$$\tilde{v}(y,t) = \sum_0^N \Gamma_n^{DN}(y)a_{v,n}(t)+f_u(y)\tilde{q}_u(t)+f_l(y)\tilde{q}_l(t) \tag{2.87}$$

$$\tilde{\eta}(y,t) = \sum_0^N \Gamma_n^{D}(y)a_{\eta,n}(t) \tag{2.88}$$

In the present work, Γ^D and Γ^{DN} are the modified Chebyshev polynomials Θ and Ξ, and their derivation is described in chapter 3.

2.5.1 Inhomogeneous Form

After the change of variable (2.77) and substitution of the modified Chebyshev series $\Gamma_n^D, \Gamma_n^{DN}$ in (2.64,2.65), and evaluation of the equations at the collocation points y_k, the equations may be assembled as

$$\begin{pmatrix} \mathbf{A}_{11} & \mathbf{A}_{12} \\ \mathbf{A}_{21} & \mathbf{A}_{22} \end{pmatrix}\mathbf{a}+\begin{pmatrix} \mathbf{B}_{11} & \mathbf{B}_{12} \\ \mathbf{B}_{21} & \mathbf{B}_{22} \end{pmatrix}\mathbf{q}=\begin{pmatrix} \mathbf{L}_{11} & \mathbf{L}_{12} \\ \mathbf{L}_{21} & \mathbf{L}_{22} \end{pmatrix}\dot{\mathbf{a}}+\begin{pmatrix} \mathbf{E}_{11} & \mathbf{E}_{12} \\ \mathbf{E}_{21} & \mathbf{E}_{22} \end{pmatrix}\dot{\mathbf{q}} \tag{2.89}$$

where $\mathbf{q}=(\tilde{q}_u,\tilde{q}_l)^T$. Rearranging, an additional term, as compared to (2.1), due to the rate of change of control $\dot{\mathbf{q}}_u$, becomes apparent

$$\begin{pmatrix} \mathbf{L}_{11} & \mathbf{L}_{12} \\ \mathbf{L}_{21} & \mathbf{L}_{22} \end{pmatrix}\dot{\mathbf{a}}=\begin{pmatrix} \mathbf{A}_{11} & \mathbf{A}_{12} \\ \mathbf{A}_{21} & \mathbf{A}_{22} \end{pmatrix}\dot{\mathbf{a}}+\begin{pmatrix} \mathbf{B}_{11} & \mathbf{B}_{12} \\ \mathbf{B}_{21} & \mathbf{B}_{22} \end{pmatrix}\mathbf{q}-\begin{pmatrix} \mathbf{E}_{11} & \mathbf{E}_{12} \\ \mathbf{E}_{21} & \mathbf{E}_{22} \end{pmatrix}\dot{\mathbf{q}} \tag{2.90}$$

The additional submatrices cf. (2.66) are $N+1$ by 1 vectors and are

$$\begin{aligned}
\mathbf{B}_{11} &= \left(-\alpha\bar{\mathbf{u}}k^2-\alpha\bar{\mathbf{u}}''-\frac{\mathbf{I}k^4}{\jmath R}\right)\mathbf{f}_u+\left(\alpha\bar{\mathbf{u}}+\frac{2k^2\mathbf{I}}{\jmath R}\right)\mathbf{f}_u'' \\
\mathbf{B}_{12} &= \left(-\alpha\bar{\mathbf{u}}k^2-\alpha\bar{\mathbf{u}}''-\frac{\mathbf{I}k^4}{\jmath R}\right)\mathbf{f}_l+\left(\alpha\bar{\mathbf{u}}+\frac{2k^2\mathbf{I}}{\jmath R}\right)\mathbf{f}_l'' \\
\mathbf{B}_{21} &= \beta\bar{\mathbf{u}}'\mathbf{f}_u \\
\mathbf{B}_{22} &= \beta\bar{\mathbf{u}}'\mathbf{f}_l \\
\mathbf{E}_{11} &= \jmath\left(-k^2\mathbf{f}_u+\mathbf{f}_u''\right) \\
\mathbf{E}_{12} &= \jmath\left(-k^2\mathbf{f}_l+\mathbf{f}_l''\right) \\
\mathbf{E}_{21} &= (0) \\
\mathbf{E}_{22} &= (0)
\end{aligned} \tag{2.91}$$

The elements of derivative matrices $\mathbf{Dn}_D$ which replace $\mathbf{Dn}$ previously used in $\mathbf{A}_{22}$ and $\mathbf{L}_{22}$ are

$$D0_{D_{kj}} = \Gamma_j^D(y_k) \qquad D2_{D_{kj}} = \Gamma_j^D(y_k)'' \tag{2.92}$$

The elements of derivative matrices $\mathbf{Dn}_{DN}$ which replace $\mathbf{Dn}$ previously used in the remainder of $\mathbf{A}$ and $\mathbf{L}$ are

$$D0_{DN_{kj}} = \Gamma_j^{DN}(y_k) \qquad D2_{DN_{kj}} = \Gamma_j^{DN}(y_k)'' \qquad D4_{DN_{kj}} = \Gamma_j^{DN}(y_k)'''' \tag{2.93}$$

The elements of the dimension $N+1$ vectors $\mathbf{f}_u, \mathbf{f}_l, \mathbf{f}'_u, \mathbf{f}'_l, \mathbf{f}''_u, \mathbf{f}''_l$ are the values or derivatives of f_u and f_l, for example

$$\begin{aligned} f_{u_k} &= f_u(y_k) \\ f'_{u_k} &= f_u(y_k)' \end{aligned} \tag{2.94}$$

The measurement equation (2.72) becomes

$$\tilde{\mathbf{y}} = \frac{\jmath}{\alpha^2+\beta^2} \begin{pmatrix} \mathbf{C}_{11} & \mathbf{C}_{12} \\ \mathbf{C}_{21} & \mathbf{C}_{22} \end{pmatrix} \mathbf{a} + \frac{\jmath}{\alpha^2+\beta^2} \begin{pmatrix} \mathbf{D}_{11} \\ \mathbf{D}_{21} \end{pmatrix} \mathbf{q} \tag{2.95}$$

where

$$\mathbf{D}_{11} = \frac{\jmath\alpha}{\alpha^2+\beta^2} \begin{bmatrix} f''_u(y=+1) & f''_l(y=+1) \\ f''_u(y=-1) & f''_l(y=-1) \end{bmatrix} \tag{2.96}$$

and

$$\mathbf{D}_{21} = \frac{\jmath\beta}{\alpha^2+\beta^2} \begin{bmatrix} f''_u(y=+1) & f''_l(y=+1) \\ f''_u(y=-1) & f''_l(y=-1) \end{bmatrix} \tag{2.97}$$

Expressing (2.90) and (2.95) more succinctly we have

$$\begin{aligned} \mathbf{L}\dot{\mathbf{a}} &= \mathbf{A}\mathbf{a} + \mathbf{B}\mathbf{q} - \mathbf{E}\dot{\mathbf{q}} \\ \tilde{\mathbf{y}} &= \mathbf{C}\mathbf{a} + \mathbf{D}\mathbf{q} \end{aligned} \tag{2.98}$$

2.5.2 Redundant Equations

The homogeneous vorticity and velocity components are given in terms of the state variable coefficients by (2.85) and (2.86). Chapter 3 shows that the modification of the bases to impose the Dirichlet boundary conditions reduces their size from $0 \ldots N$ to $0 \ldots N-2$. This need not lead to a significant approximation error, since due to the spectral convergence of the Chebyshev series (Fox and Parker, 1968), the values of $a_{v,n}$ and $a_{\eta,n}$ become ever smaller as n increases, and thus the use of slightly fewer terms does not introduce significant error, providing N is large.

This leaves the prototype system matrix $\mathbf{A}$ non-square, and to rectify this, some equations must also be discarded. The inhomogeneous Dirichlet boundary conditions on velocity, and homogeneous Dirichlet boundary conditions on vorticity mean that velocity and vorticity equations at the walls are redundant, since

the vorticity at the walls is zero, and the wall-normal velocity is set by the control input. Therefore it is appropriate to discard these equations.

Chapter 3 shows that the modification of the velocity basis to impose the Neumann boundary conditions reduces its size by a further 2, in the limit of infinitesimal discretisation. Again, due to the spectral convergence of the Chebyshev series, the use of slightly fewer terms does not introduce significant error, providing N is large.

This again leaves the prototype system matrix $\mathbf{A}$ non-square. The homogeneous Neumann boundary conditions on velocity means that the velocity equations next to the walls are in some sense close to redundant if N is large, since the wall-normal velocity at the wall is set by the control input, and its gradient there is zero. After careful examination of the issues in chapter 3, it is considered appropriate to discard these equations also.

2.6 State-Space Representation

This section manipulates the system into conventional state-space from, identifies the state, control and measurement variables, and derives the final form of the system, input and output matrices.

2.6.1 State-Space Form

It is evident that some manipulation is required to achieve the state-space form (2.1) from (2.98). The first step is to invert $\mathbf{L}$

$$\begin{aligned} \dot{\mathbf{a}} &= \mathbf{L}^{-1}\mathbf{A}\mathbf{a} + \mathbf{L}^{-1}\mathbf{B}\mathbf{q} - \mathbf{L}^{-1}\mathbf{E}\dot{\mathbf{q}} \\ \tilde{\mathbf{y}} &= \mathbf{C}\mathbf{a} + \mathbf{D}\mathbf{q} \end{aligned} \tag{2.99}$$

The system now has two input vectors, $\mathbf{q}$ and $\dot{\mathbf{q}}$, which are not independent. Hence the system is recast so that $\mathbf{q}$ is no longer an input vector, but part of the state variable vector, and that the control input is the rate of change of wall velocity $\dot{\mathbf{q}}$, as found by Hogberg et al. (2003a)

$$\begin{aligned} \begin{pmatrix} \dot{\mathbf{a}} \\ \dot{\mathbf{q}} \end{pmatrix} &= \begin{pmatrix} \mathbf{L}^{-1}\mathbf{A} & \mathbf{L}^{-1}\mathbf{B} \\ \mathbf{0} & \mathbf{0} \end{pmatrix} \begin{pmatrix} \mathbf{a} \\ \mathbf{q} \end{pmatrix} + \begin{pmatrix} \mathbf{L}^{-1}\mathbf{E} \\ \mathbf{I} \end{pmatrix} \dot{\mathbf{q}} \\ \tilde{\mathbf{y}} &= \begin{pmatrix} \mathbf{C} & \mathbf{D} \end{pmatrix} \begin{pmatrix} \mathbf{a} \\ \mathbf{q} \end{pmatrix} \end{aligned} \tag{2.100}$$

Comparison of the unrecast system matrix $\mathbf{L}^{-1}\mathbf{A}$ and state variables $\mathbf{a}$ with the recast system matrix

$$\begin{pmatrix} \mathbf{L}^{-1}\mathbf{A} & \mathbf{L}^{-1}\mathbf{B} \\ \mathbf{0} & \mathbf{0} \end{pmatrix} \tag{2.101}$$

and state variables

$$\begin{pmatrix} \mathbf{a} \\ \mathbf{q} \end{pmatrix} \tag{2.102}$$

shows that the recast form has the same eigenvalues, plus two new zero values, since $\mathbf{q}$ has dimension 2×1. The unrecast eigensystem is $\mathbf{L}^{-1}\mathbf{A}\Psi = \Psi\Lambda$, where Λ is a diagonal matrix of eigenvalues and Ψ is the matrix of right eigenvectors, which, being composed solely of state variables $\mathbf{a}$ without $\mathbf{q}$ cannot represent a non-zero wall-normal velocity. The eigensystem of the recast system is

$$\begin{pmatrix} \mathbf{L}^{-1}\mathbf{A} & \mathbf{L}^{-1}\mathbf{B} \\ \mathbf{0} & \mathbf{0} \end{pmatrix} \begin{pmatrix} \Psi & \Psi_a \\ \mathbf{0} & \Psi_q \end{pmatrix} = \begin{pmatrix} \Psi & \Psi_a \\ \mathbf{0} & \Psi_q \end{pmatrix} \begin{pmatrix} \Lambda & \mathbf{0} \\ \mathbf{0} & \mathbf{0} \end{pmatrix} \tag{2.103}$$

The recast form eigenvectors are based on state variables $(\mathbf{a}, \mathbf{q})^T$, and comprise the previous eigenvectors Ψ augmented with zeros, plus new eigenvectors $\left(\Psi_a^T, \Psi_q^T\right)^T$. The new eigenvectors represent transpiration at each wall, since $\mathbf{A}\Psi_a + \mathbf{B}\Psi_q = \mathbf{0}$, and thus Ψ_q^T is non-zero, and are steady-state since the associated new eigenvalues are zero. Thus the system dynamics now include steady-state transpiration modes.

The new form also has a zero direct transmission matrix, which is necessary for the standard linear quadratic Gaussian optimal control problem, e.g. as presented by Skogestad and Postlethwaite (1996, p353).

2.6.2 State Variables

Comparing (2.1) and (2.100) it can be seen that the state variables are given by

$$\mathcal{X} = \begin{pmatrix} \mathbf{a} \\ \mathbf{q} \end{pmatrix} \tag{2.104}$$

These state variables are not unique, and may be transformed by any invertible constant matrix, without changing the system input-output behaviour (Skogestad and Postlethwaite, 1996, p114). A possible choice for the homogeneous part is to use the values of velocity and vorticity at the collocation points, e.g. $\tilde{v}_k = \sum \Gamma_n(y_k) a_n$, by means of an interpolating basis, as used by Weideman and Reddy (2000). The state variables considered here for the homogeneous part are simply the coefficients a_n which multiply the Chebyshev polynomial basis, as used by Schmid and Henningson (2001). Although less intuitive than the collocation point values, the coefficients multiplying Chebyshev polynomials may be reduced in number when required. For example, when the bases are reduced in size due to the modifications necessary for the boundary conditions, the use of slightly fewer terms introduces negligible error, due to the fast convergence of Chebyshev series, as noted by Fox and Parker (1968, p25).

The velocities and vorticities may be recovered from the state variables via

$$\begin{aligned} \begin{pmatrix} \tilde{v}(y_{k1}, t) \\ \tilde{\eta}(y_{k2}, t) \end{pmatrix} &= \begin{pmatrix} \Gamma_{n1}^{DN}(y_{k1}) & \mathbf{0} & f_u(y_{k1}) & f_l(y_{k1}) \\ \mathbf{0} & \Gamma_{n2}^{D}(y_{k2}) & \mathbf{0} & \mathbf{0} \end{pmatrix} \begin{pmatrix} a_{v,n1}(t) \\ a_{\eta,n2}(t) \\ \tilde{q}_u(t) \\ \tilde{q}_l(t) \end{pmatrix} \\ &\triangleq \mathbf{T} \begin{pmatrix} a_{v,n1}(t) \\ a_{\eta,n2}(t) \\ \tilde{q}_u(t) \\ \tilde{q}_l(t) \end{pmatrix} \end{aligned} \tag{2.105}$$

where $k1 = 0 \ldots N$, $k2 = 0 \ldots N$, $n1 = 0 \ldots N-4$, and $n2 = 0 \ldots N-2$. $\mathbf{T}$ is useful for the plotting of eigenvectors and initial conditions, but being $(2N+2) \times (2N-2)$ is not invertible. An invertible form may be made by discarding the next-to-wall velocities and wall vorticities from the output. The wall vorticities are zero, due to the Dirichlet boundary condition, and the next-to-wall velocities are close to those at the wall on account of the Neumann boundary condition and the close spacing of the collocation points at the wall. With this change

$$\begin{aligned} \begin{pmatrix} \tilde{v}(y_{k1}, t) \\ \tilde{\eta}(y_{k2}, t) \end{pmatrix} &= \begin{pmatrix} \Gamma^{DN}_{n1}(y_{k1}) & \mathbf{0} & f_u(y_{k1}) & f_l(y_{k1}) \\ \mathbf{0} & \Gamma^{D}_{n2}(y_{k2}) & \mathbf{0} & \mathbf{0} \end{pmatrix} \begin{pmatrix} a_{v,n1}(t) \\ a_{\eta,n2}(t) \\ \tilde{q}_u(t) \\ \tilde{q}_l(t) \end{pmatrix} \\ &\triangleq \mathbf{T}_{cp} \begin{pmatrix} a_{v,n1}(t) \\ a_{\eta,n2}(t) \\ \tilde{q}_u(t) \\ \tilde{q}_l(t) \end{pmatrix} \end{aligned} \tag{2.106}$$

where $n1 = 0 \ldots N-4$, $n2 = 0 \ldots N-2$ as in (2.105) but $k1 = 0, 2 \ldots N-2, N$, and $k2 = 1 \ldots N-1$. Defining $\mathcal{X}_{cp}$ as the collocation point velocity and vorticity form of the state variables

$$\mathcal{X}_{cp} = \begin{pmatrix} \tilde{v}(y_{k1}, t) \\ \tilde{\eta}(y_{k2}, t) \end{pmatrix} \tag{2.107}$$

(2.106) becomes

$$\mathcal{X}_{cp} = \mathbf{T}_{cp} \mathcal{X} \tag{2.108}$$

$\mathbf{T}_{cp}$ is inverted as

$$\mathbf{T}^{-1}_{cp} = \begin{pmatrix} \Gamma^{DN-1}_{n1}(y_{k1}) \left(\mathbf{I} - f_u(y_{k1}) r_1 - f_l(y_{k1}) r_2\right) & \mathbf{0} \\ \mathbf{0} & \Gamma^{D-1}_{n2}(y_{k2}) \\ r_1 & \mathbf{0} \\ r_2 & \mathbf{0} \end{pmatrix} \tag{2.109}$$

where $r_1 = (1, 0 \ldots 0, 0)$ and $r_2 = (0, 0 \ldots 0, 1)$, both being of size $1 \times (N-1)$.

Figure 2.2 shows the basis functions associated with the state variables. Those functions associated with homogeneous velocity coefficients e.g. Γ^{DN}_0 have Neumann and Dirichlet boundary conditions, those associated with vorticity coefficients e.g. Γ^{D}_0 have Dirichlet boundary conditions, and those associated with control by wall-normal velocity (derivative) e.g. f_u have Neumann boundary conditions.

2.6.3 Control Variables

Comparing (2.1) and (2.100) it can be seen that the control variables are given by

$$\mathcal{U} = \dot{\mathbf{q}} \tag{2.110}$$

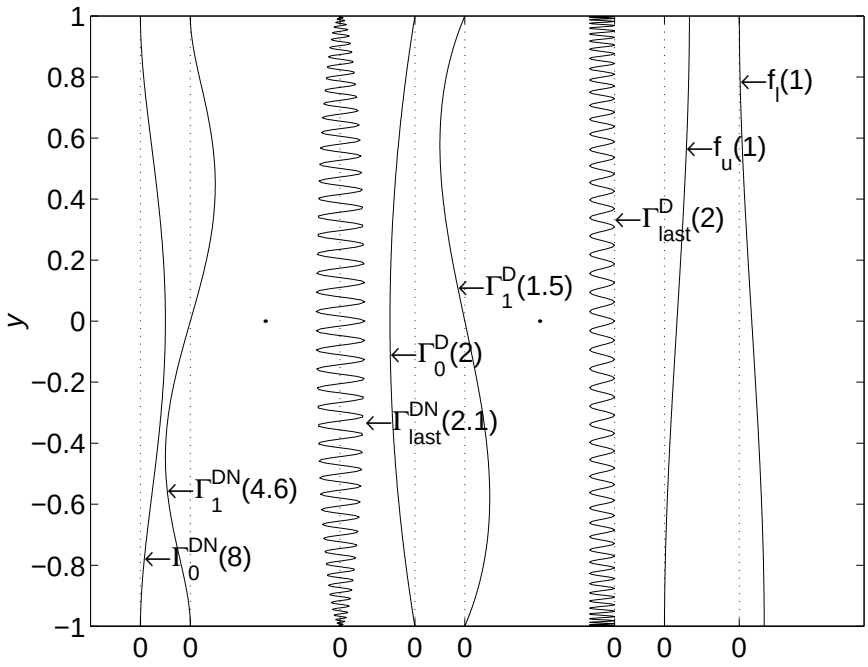

Figure 2.2: The Basis Functions Associated with the State Variables (Peak magnitudes over system for $N = 100$ in parenthesis)

These control variables are the rate of change of wall-normal velocity values on the upper and lower walls, $\dot{\tilde{q}}_u$ and $\dot{\tilde{q}}_l$. As $\tilde{q}_u$ and $\tilde{q}_l$ are Fourier coefficients, physically they correspond to sinusoidal distributions of transpiration velocity in the streamwise and spanwise directions, at the selected wavenumber pair. Since the distributions are sinusoidal, zero-net mass transpiration is achieved.

Control is via the rate of change of wall-normal velocities, as performed by Hogberg et al. (2003a). These signals must be integrated in order to set the wall transpiration velocities.

2.6.4 Measurement Variables

Comparing (2.1) and (2.100) it can be seen that the measurement variables are given by

$$\mathcal{Y} = \tilde{\mathbf{y}} \tag{2.111}$$

Thus the measurement variables in the present work are the wall shear stress Fourier co-efficients on the upper and lower walls, at the selected wavenumber pair.

2.6.5 Bewley's Derivation

It is instructive to compare the derivation of Bewley and Liu (1998) for case 1 (Tollmien-Schlichting waves) with the present one. Bewley's uncontrolled system

uses an interpolating Chebyshev basis, so the state variables are the velocities at the collocation points $\mathbf{v}$

$$\begin{aligned} \mathbf{L}_C\dot{\mathbf{v}} &= \mathbf{A}_C\mathbf{v} \\ \tilde{\mathbf{y}} &= \mathbf{C}_C\mathbf{v} \end{aligned} \tag{2.112}$$

where the subscript $_C$ indicates the use of the interpolating basis. This form is equivalent to the velocity part of (2.66), with the basis interpolating rather than polynomial. Bewley applies the Neumann boundary condition within $\mathbf{L}$ by modification of the differentiation matrix (Bewley and Liu, 1998, p310). Expanding this equation to consider the lower wall velocity v_w separately

$$\begin{pmatrix} \mathbf{L}_{C11} & \mathbf{L}_{C12} \\ \mathbf{L}_{C21} & \mathbf{L}_{C22} \end{pmatrix} \begin{pmatrix} \dot{\mathbf{v}} \\ \dot{v}_w \end{pmatrix} = \begin{pmatrix} \mathbf{A}_{C11} & \mathbf{A}_{C12} \\ \mathbf{A}_{C21} & \mathbf{A}_{C22} \end{pmatrix} \begin{pmatrix} \mathbf{v} \\ v_w \end{pmatrix} \tag{2.113}$$

Bewley inverts the Laplacian $\mathbf{L}_C$ to produce

$$\begin{aligned} \begin{pmatrix} \dot{\mathbf{v}} \\ \dot{v}_w \end{pmatrix} &= \begin{pmatrix} \mathbf{L}_{C11} & \mathbf{L}_{C12} \\ \mathbf{L}_{C21} & \mathbf{L}_{C22} \end{pmatrix}^{-1} \begin{pmatrix} \mathbf{A}_{C11} & \mathbf{A}_{C12} \\ \mathbf{A}_{C21} & \mathbf{A}_{C22} \end{pmatrix} \begin{pmatrix} \mathbf{v} \\ v_w \end{pmatrix} \\ &\equiv \begin{pmatrix} \mathbf{M}_{11} & \mathbf{M}_{12} \\ \mathbf{M}_{21} & \mathbf{M}_{22} \end{pmatrix} \begin{pmatrix} \mathbf{v} \\ v_w \end{pmatrix} \end{aligned} \tag{2.114}$$

and discards the equation at the wall, as it is redundant, leaving

$$\dot{\mathbf{v}} = \begin{pmatrix} \mathbf{M}_{11} & \mathbf{M}_{12} \end{pmatrix} \begin{pmatrix} \mathbf{v} \\ v_w \end{pmatrix} \tag{2.115}$$

and finally partitions out the control, v_w, to form

$$\dot{\mathbf{v}} = \mathbf{M}_{11}\mathbf{v} + \mathbf{M}_{12}v_w \tag{2.116}$$

Now, by the Schur complement (Skogestad and Postlethwaite, 1996, p499)

$$\begin{pmatrix} \mathbf{L}_{C11} & \mathbf{L}_{C12} \\ \mathbf{L}_{C21} & \mathbf{L}_{C22} \end{pmatrix}^{-1} = \begin{pmatrix} \mathbf{L}_{C11}^{-1} + \mathbf{L}_{C11}^{-1}\mathbf{L}_{C12}\mathbf{X}^{-1}\mathbf{L}_{C21}\mathbf{L}_{C11}^{-1} & -\mathbf{L}_{C11}^{-1}\mathbf{L}_{C12}\mathbf{X}^{-1} \\ -\mathbf{X}^{-1}\mathbf{L}_{C21}\mathbf{L}_{C11}^{-1} & \mathbf{X}^{-1} \end{pmatrix} \tag{2.117}$$

if $\mathbf{X}^{-1}$ and $\mathbf{L}_{C11}^{-1}$ are assumed to exist, where $\mathbf{X}$ is the scalar $\left(\mathbf{L}_{C22} - \mathbf{L}_{C21}\mathbf{L}_{C11}^{-1}\mathbf{L}_{C12}\right)$. Thus

$$\begin{aligned} \dot{\mathbf{v}} &= \mathbf{L}_{C11}^{-1}\left(\left(\mathbf{I} + \mathbf{L}_{C12}\mathbf{X}^{-1}\mathbf{L}_{C21}\mathbf{L}_{C11}^{-1}\right)\mathbf{A}_{C11} - \mathbf{L}_{C12}\mathbf{X}^{-1}\mathbf{A}_{C21}\right)\mathbf{v} \\ &+ \mathbf{L}_{C11}^{-1}\left(\left(\mathbf{I} + \mathbf{L}_{C12}\mathbf{X}^{-1}\mathbf{L}_{C21}\mathbf{L}_{C11}^{-1}\right)\mathbf{A}_{C12} - \mathbf{L}_{C12}\mathbf{X}^{-1}\mathbf{A}_{C22}\right)v_w \end{aligned} \tag{2.118}$$

This final form has no explicit integrators.

If applied to Bewley's form, the approach adopted here would first partition out v_w and $\dot{v}_w$ in (2.113)

$$\begin{pmatrix} \mathbf{L}_{C11} \\ \mathbf{L}_{C21} \end{pmatrix} \dot{\mathbf{v}} + \begin{pmatrix} \mathbf{L}_{C12} \\ \mathbf{L}_{C22} \end{pmatrix} \dot{v}_w = \begin{pmatrix} \mathbf{A}_{C11} \\ \mathbf{A}_{C21} \end{pmatrix} \mathbf{v} + \begin{pmatrix} \mathbf{A}_{C12} \\ \mathbf{A}_{C22} \end{pmatrix} v_w \tag{2.119}$$

and then the approach would discard the equation at the wall, as it is redundant, leaving

$$\mathbf{L}_{C11}\dot{\mathbf{v}} + \mathbf{L}_{C12}\dot{v}_w = \mathbf{A}_{C11}\mathbf{v} + \mathbf{A}_{C12}v_w \tag{2.120}$$

The current approach would then invert the Laplacian $\mathbf{L}_{C11}$, and collect control inputs v_w and $\dot{v}_w$ together

$$\dot{\mathbf{v}} = \mathbf{L}_{C11}^{-1}\mathbf{A}_{C11}\mathbf{v} + \mathbf{L}_{C11}^{-1}\mathbf{A}_{C12}v_w - \mathbf{L}_{C11}^{-1}\mathbf{L}_{C12}\dot{v}_w \tag{2.121}$$

The current approach notes that v_w and $\dot{v}_w$ are not independent, and so the next step is to make v_w a state variable, and in so doing introduce an integrator

$$\begin{pmatrix} \dot{\mathbf{v}} \\ \dot{v}_w \end{pmatrix} = \begin{pmatrix} \mathbf{L}_{C11}^{-1}\mathbf{A}_{C11} & \mathbf{L}_{C11}^{-1}\mathbf{A}_{C12} \\ \mathbf{0} & \mathbf{0} \end{pmatrix} \begin{pmatrix} \mathbf{v} \\ v_w \end{pmatrix} + \begin{pmatrix} -\mathbf{L}_{C11}^{-1}\mathbf{L}_{C12} \\ 1 \end{pmatrix} \dot{v}_w \tag{2.122}$$

The integration is not purely on the input signal $\dot{v}_w$, as this would require the term $\mathbf{L}_{C11}^{-1}\mathbf{L}_{C12}$ to be zero. As it is not, the input signal is also utilised unintegrated.

The two forms (2.118) and (2.122) may be reconciled as follows. From (2.114) and (2.117)

$$\dot{v}_w = \mathbf{X}^{-1}\left(\mathbf{A}_{C21} - \mathbf{L}_{C21}\mathbf{L}_{C11}^{-1}\mathbf{A}_{C11}\right)\mathbf{v} + \mathbf{X}^{-1}\left(\mathbf{A}_{C22} - \mathbf{L}_{C21}\mathbf{L}_{C11}^{-1}\mathbf{A}_{C12}\right)v_w \tag{2.123}$$

and substituting this result in (2.118) results in (2.121). Thus the two forms are consistent, up to the point where integrators are introduced in the final stage of the current approach.

It is straightforward to extend the expressions presented here to cover control at both walls, and include the vorticity equation. Numerical experiments with $N = 100$ for case 1 in Matlab (MathWorks Inc., 1998) show a spurious eigenvalue of $-0.024413 + 1.5273\jmath$ for system (2.116), a similar value to one found by Bewley and Liu (1998), as might be expected in a reproduction of their method. However, the system (2.122) is not immune to spurious eigenvalues, for example they occur at $2.9048 + 107.87\jmath$ and $2.8841 + 108.165\jmath$. That is to say, conversion of Bewley's system into integrator form with control by derivative of wall velocity $\dot{v}_w$ as described here does not *per se* remove spurious eigenvalues. Both forms (2.116) and (2.122) produce eigenvalues generally within Orszag's last significant figure. The Schur form (2.118) is not this accurate, although it does serve to show subtle algebraic differences between the two forms (2.116) and (2.122). The extra term $\mathbf{L}_{C11}^{-1}\left(\mathbf{L}_{C12}\mathbf{X}^{-1}\mathbf{L}_{C21}\mathbf{L}_{C11}^{-1}\mathbf{A}_{C11} - \mathbf{L}_{C12}\mathbf{X}^{-1}\mathbf{A}_{C21}\right)$ in Bewley's form system matrix is not negligible, but appears not to influence significantly any of the first 30 genuine modes for case 1, or 110 modes for case 2, for $N = 100$.

Bewley's method performs invert-discard-partition, whereas the approach adopted in the current work performs partition-discard-invert. Discarding the equations and partitioning them are independent stages in reducing their size, so one crucial difference between the methods is whether the equations are inverted then reduced, or reduced then inverted. Another crucial difference is the choice of basis.

Generally the application of a simple Dirichlet boundary condition to a basis makes it singular and requires it to be reduced in order before it can be inverted, but a Neumann condition only makes the basis singular in the limit of infinitesimal discretization, as described in chapter 3. Thus Bewley's introduction of the Neumann boundary condition does allow invert and then reduce. It has been shown here that applying reduction then inversion in Bewley's method does not cure the spurious eigenvalues.

The approach used in this work applies both the Dirichlet and Neumann conditions to the basis, making it singular. Thus the reduction must occur before the inversion, ultimately leading to the current form. The absence of spurious eigenvalues is thought to be due to the basis, and in particular, its treatment of the Neumann boundary condition. The Neumann boundary condition has been identified as the source of the spurious modes by Hogberg et al. (2003a), and Aamo (2002). More information about the basis selected for the present work is given in chapter 3.

2.6.6 State-Space Realization Matrices

System Matrix Comparing (2.1) and (2.100), the system matrix $\mathcal{A}$ is given by

$$\mathcal{A} = \begin{pmatrix} \mathbf{L}^{-1}\mathbf{A} & \mathbf{L}^{-1}\mathbf{B} \\ \mathbf{0} & \mathbf{0} \end{pmatrix} \tag{2.124}$$

The input matrix $\mathcal{B}$ is given by

$$\mathcal{B} = \begin{pmatrix} \mathbf{L}^{-1}\mathbf{E} \\ \mathbf{I} \end{pmatrix} \tag{2.125}$$

The output matrix $\mathcal{C}$ is given by

$$\mathcal{C} = \begin{pmatrix} \mathbf{C} & \mathbf{D} \end{pmatrix} \tag{2.126}$$

The direct transmission matrix $\mathcal{D}$ in $\mathcal{Y} = \mathcal{C}\mathcal{X} + \mathcal{D}\mathcal{U}$ is zero, due to the selection of control by rate of change of wall-normal velocities. This also ensures that the system has integral action.

2.7 Implementation of Model

2.7.1 Test Cases

Two test cases are considered in the present work. The first is Case 1 as used by Bewley and Liu (1998), with Reynolds number ($Re = \rho U_{cl} h/\mu$) of 10^4, and streamwise wavenumber pair (α, β) of $(1, 0)$. For this test case the system matrix has distinct eigenvalues, one of which is unstable (approximately $0.00373967 - 0.23752649\jmath$), and is known as a Tollmien-Schlichting wave (Schmid and Henningson, 2001). Although unstable, this mode grows relatively slowly as compared to non-modal transient growth. This Reynolds number corresponds to centreline base velocity 15 m/s for air (assuming viscosity 0.000018 Pa s, density 1.2 kg/m^3) in a channel

of half-height 0.01m, and 1 m/s for water (assuming viscosity 0.001 Pa s, density 1000 kg/m^3 (Calvert and Farrar, 1999, p7-2)).

For this test case the vorticity equation is decoupled from the velocity equation since $\beta = 0$ in (2.35). Since there is no spanwise variation, if it is assumed that the spanwise velocity w is zero, the vorticity (2.23) is zero, and the vorticity equation may be discarded, reducing the system size to one quarter. The remaining velocity equation represents a two component flow field (u, v) varying in two dimensions (x, y), a problem denoted $2D - 2C$ by Reynolds and Kassinos (1995).

The system matrices are initially complex, due to use of the Fourier method during the assumption of periodicity, and for this case are split into real and imaginary parts to allow the use of Matlab (MathWorks Inc., 1998) state-space models, and enable the solution of the required algebraic Riccati equations (AREs) necessary for controller synthesis. Thus $\dot{\mathcal{X}} = \mathcal{A}\mathcal{X} + \mathcal{B}\mathcal{U}$ becomes

$$\begin{pmatrix} \Re(\dot{\mathcal{X}}) \\ \Im(\dot{\mathcal{X}}) \end{pmatrix} = \begin{bmatrix} \Re(\mathcal{A}) & -\Im(\mathcal{A}) \\ \Im(\mathcal{A}) & \Re(\mathcal{A}) \end{bmatrix} \begin{pmatrix} \Re(\mathcal{X}) \\ \Im(\mathcal{X}) \end{pmatrix} + \begin{bmatrix} \Re(\mathcal{B}) & -\Im(\mathcal{B}) \\ \Im(\mathcal{B}) & \Re(\mathcal{B}) \end{bmatrix} \begin{pmatrix} \Re(\mathcal{U}) \\ \Im(\mathcal{U}) \end{pmatrix} \tag{2.127}$$

using the real representation of a complex matrix given by Hinrichsen and Pritchard (2005, p720). There are now twice as many state variables $(2N - 2)$, 4 inputs (upper and lower wall, real and imaginary wall-normal velocities) and 4 outputs (upper and lower, real and imaginary wall streamwise shears).

This splitting of the equations is equivalent to the addition/subtraction of the conjugate equation, as performed by Aamo (2002, p48), but also provides some information about the dynamics of the system when made real. The eigensystem $\mathcal{A}\Psi = \Psi\Lambda$, where Ψ is the matrix of right eigenvectors and Λ a diagonal matrix of eigenvalues, becomes

$$\begin{bmatrix} \Re(\mathcal{A}) & -\Im(\mathcal{A}) \\ \Im(\mathcal{A}) & \Re(\mathcal{A}) \end{bmatrix} \begin{bmatrix} \Psi & \bar{\Psi} \\ -\jmath\Psi & \jmath\bar{\Psi} \end{bmatrix} = \begin{bmatrix} \Psi & \bar{\Psi} \\ -\jmath\Psi & \jmath\bar{\Psi} \end{bmatrix} \begin{bmatrix} \Lambda & \mathbf{0} \\ \mathbf{0} & \bar{\Lambda} \end{bmatrix} \tag{2.128}$$

Thus the system eigenvalues are joined by their complex conjugates. Since, from (2.106)

$$\begin{pmatrix} \tilde{v}(y_k, t) \\ \tilde{\eta}(y_k, t) \end{pmatrix} = \mathbf{T}\mathcal{X} = \begin{bmatrix} \mathbf{T} & \jmath\mathbf{T} \end{bmatrix} \begin{bmatrix} \Re(\mathcal{X}) \\ \Im(\mathcal{X}) \end{bmatrix} \tag{2.129}$$

the eigenmodes in velocity/vorticity form, $\mathbf{T}\Psi$, become

$$\begin{bmatrix} \mathbf{T} & \jmath\mathbf{T} \end{bmatrix} \begin{bmatrix} \Psi & \bar{\Psi} \\ -\jmath\Psi & \jmath\bar{\Psi} \end{bmatrix} = \begin{bmatrix} 2\mathbf{T}\Psi & \mathbf{0} \end{bmatrix} \tag{2.130}$$

thus the eigenvectors associated with the conjugate modes evaluate to zero velocity/vorticity, leading to a singular right velocity/vorticity form eigenvector matrix. Thus it is not possible to invert this to produce the left velocity/vorticity eigenvectors, which are required for controllability calculations. Also some eigensolvers may fail to compute the conjugate modes correctly, e.g. Matlab returns not the conjugates but the original eigenvectors multiplied by $-\jmath$. The conjugate modes

represent a zero perturbation, and arise purely from creating a real system. However, to avoid the complications they introduce, the complex system is used for the subsequent eigensystem results in section 2.6.6.

The second case is Case 2 as used by Bewley and Liu (1998), with Reynolds number $Re = 5000$, and streamwise wavenumber $\alpha = 0, \beta = 2.044$. For this test case the system matrix has distinct eigenvalues, all of which are stable, and has the largest transient energy growth (named and defined more precisely in section 4.3.1) over α, β and R, as determined by Butler and Farrell (1992).

For this test case the vorticity equation is coupled to the velocity equation since $\beta \neq 0$ in (2.35). Since α is zero, there is no variation in the x direction. The velocity and vorticity equations represent a three component flow field (u, v, w) varying in two dimensions (y, z), a problem denoted $2D - 3C$ by Reynolds and Kassinos (1995).

Although case 2 has the vorticity equation in addition to the velocity equation, it can be reduced to approximately the size of case 1. Like case 1 the system is complex, and must be split into real and imaginary parts to allow the use of Matlab state-space models, and to solve the controller synthesis AREs. By inspection of (2.34) and (2.35), and noting that α is zero, it can be seen that the velocity equation coefficients all have the same phase, and that the vorticity equation coefficients are real, except for the coupling velocity coefficient which is imaginary. Thus it is valid to assume that the velocity and vorticity are $\pi/2$ out of phase, but otherwise of phase determined by the boundary conditions. By applying imaginary velocity boundary conditions, (i.e. making $\mathbf{q}$ imaginary) the velocity can be assumed to be imaginary, and the vorticity real, and the real velocity and imaginary vorticity state variables can be discarded, thus reducing the system size to one quarter. Noting $\alpha = 0$ in (2.45), this choice makes the streamwise velocity $\tilde{u}$ and shear stress $1/R\,\partial\tilde{u}/\partial y$ imaginary, and spanwise velocity $\tilde{w}$ and shear stress $1/R\,\partial\tilde{w}/\partial y$ real.

Case 2 finally has $2N - 2$ state variables, 2 inputs (upper and lower wall imaginary wall-normal velocities) and 4 outputs (upper and lower wall, imaginary streamwise and real spanwise shears).

Both test cases are two-dimensional, since either α or β is zero. Wavenumber pairs in general, with non-zero α and β, result in a three-dimensional problem, with consequent increase in complexity. The present system size could be reduced still further, by assuming either symmetric or asymmetric disturbance behaviour, but this has not been performed.

2.7.2 Software

The Matlab model of plane Poiseuille flow by Schmid and Henningson (2001, p489) was taken as a starting point for the development of the software. The code was written and executed in Matlab version 5.3 (MathWorks Inc., 1998) on a Pentium IV based personal computer.

2.7.3 Balancing

The state-space system (2.1) is balanced by a diagonal similarity transformation $\mathcal{T}$ to produce approximately equal row and column norms in

$$\left[\begin{array}{c|c} \mathcal{T}\mathcal{A}\mathcal{T}^{-1} & \mathcal{T}\mathcal{B} \\ \hline \mathcal{C}\mathcal{T}^{-1} & \mathbf{0} \end{array}\right] \tag{2.131}$$

by using Matlab `ssbal`, in order to reduce the range of numerical values. Such balancing is feasible for stable (case 2) and unstable (case 1) systems. In balanced form the state variables $a_{n,v}, a_{n,\eta}$ do not necessarily display their spectral behaviour, i.e. do not decay with n as fast as in the unbalanced form.

2.8 Results and Discussion

2.8.1 System Size

Variation of Principal Gains with System Size

The state-space system with m inputs and l outputs

$$\begin{aligned} \dot{\mathcal{X}} &= \mathcal{A}\mathcal{X} + \mathcal{B}\mathcal{U} \\ \mathcal{Y} &= \mathcal{C}\mathcal{X} \end{aligned} \tag{2.132}$$

has transfer function form (Skogestad and Postlethwaite, 1996, p115)

$$\begin{aligned} \mathcal{Y}(s) &= \left(\mathcal{C}\left(s\mathcal{I} - \mathcal{A}\right)^{-1}\mathcal{B}\right)\mathcal{U} \\ &= \mathcal{G}(s)\mathcal{U} \end{aligned} \tag{2.133}$$

where the transfer function $\mathcal{G}$ is a function of the Laplace variable s. In the frequency domain, the transfer function becomes $\mathcal{G}(\jmath\omega)$

$$\begin{aligned} \mathcal{Y}(\jmath\omega) &= \left(\mathcal{C}\left(\jmath\omega\mathcal{I} - \mathcal{A}\right)^{-1}\mathcal{B}\right)\mathcal{U} \\ &= \mathcal{G}(\jmath\omega)\mathcal{U} \end{aligned} \tag{2.134}$$

It is possible to perform a singular value decomposition of the matrix $\mathcal{G}(\jmath\omega)$ into

$$\mathcal{G}(\jmath\omega) = \mathbf{U}(\jmath\omega)\Sigma(\jmath\omega)\mathbf{V}^T(\jmath\omega) \tag{2.135}$$

where $\mathbf{U}(\jmath\omega)$ is an $l \times l$ unitary matrix of output singular vectors u_i, $\mathbf{V}(\jmath\omega)$ is an $m \times m$ unitary matrix of input singular vectors v_i, and $\Sigma(\jmath\omega)$ is a unique $l \times m$ matrix consisting of zeros except for $k = min\,(l, m)$ non-negative singular values $\sigma_i(\jmath\omega)$ in descending order on its main diagonal (Skogestad and Postlethwaite, 1996, p72).

A each frequency ω, $\sigma_i(\jmath\omega)$ represents a principal gain, i.e. the gain of a signal entering the system with direction v_i, where the v_i are orthogonal and are the directions which yield the extremal gains (Zhou et al., 1996, p33). Thus a singular value plot of a multiple input multiple output (MIMO) system versus frequency displays the variation of the system principal gains, and provides a useful indicator of the system input-output behaviour. As the model considered here is based on a

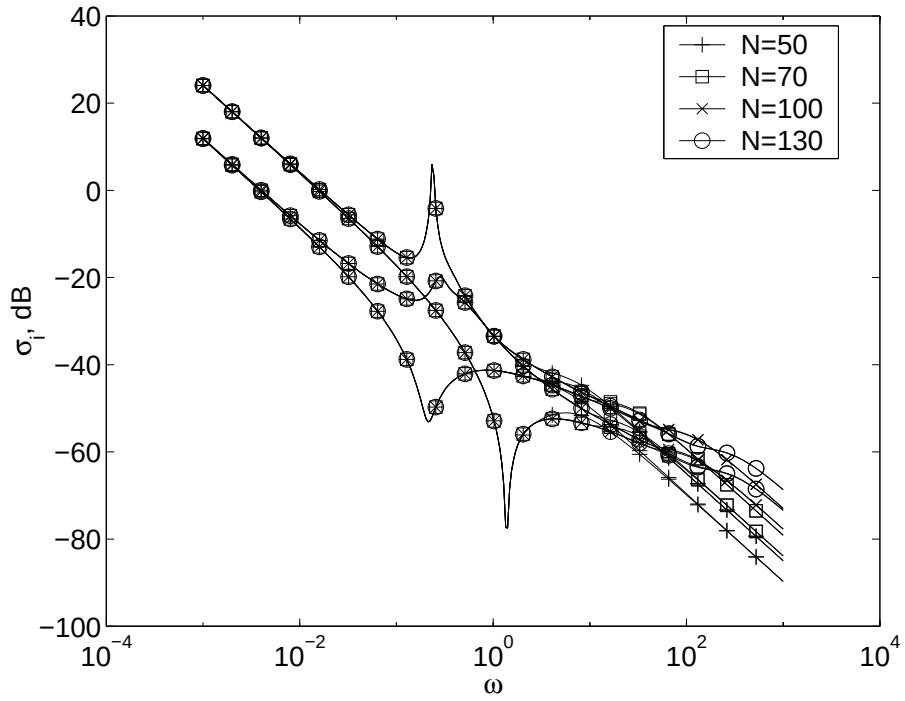

Figure 2.3: Case 1 Open-Loop Singular Values vs Frequency

truncated spectral discretisation in the wall-normal direction, it is to be expected that the system input-output behaviour will converge with an increasing number of terms in the discretisation.

Figure 2.3 shows a plot of singular values in dB ($20log_{10}(\sigma_i(j\omega))$) against logarithm of frequency ($log_{10}(\omega)$) for case 1, for four model discretisations, $N = 50, 70, 100, 130$. Each discretisation has 4 singular values at each frequency, the minimum number of the 4 outputs, and 4 inputs. It can be seen that at low frequencies, all four discretisations agree, and convergence has occurred. Fine detail in shown in figure 2.4 where discretisation $N = 50$ has not converged above approximately 2 rad/s, $N = 70$ has not converged above 10 rad/s and $N = 100$ has not converged above 40 rad/s. It is noteworthy that the lower discretisations consistently underestimate the singular values at high frequencies.

The plot has an underlying gradient of -20 dB per decade of frequency (dB/decade) corresponding to that of the integrator, with a peak at the unstable eigenmode, approximately 0.237 rad/s.

Figure 2.5 shows a singular value plot against frequency for case 2, for the same four model sizes. Each discretisation has 2 singular values at each frequency, the minimum number of the 4 outputs, and 2 inputs. Again, it can be seen that at low frequencies, all four discretisations agree, and convergence has occurred. Fine detail is shown in figure 2.6 where discretisation $N = 50$ has not converged above approximately 5 rad/s, $N = 70$ has not converged above 20 rad/s and $N = 100$ has not converged above 100 rad/s. As with case 1, the coarser discretisations consistently underestimate the singular values at high frequencies.

The plot has a low frequency gradient of approximately -28 dB/decade, and a

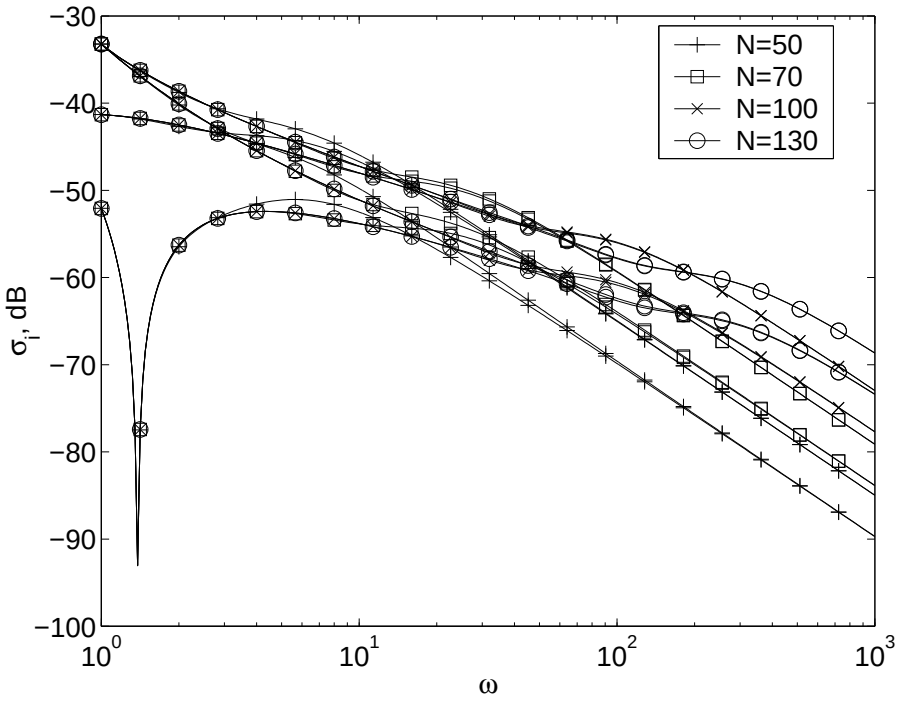

Figure 2.4: Case 1 Open-Loop Singular Values vs Frequency (detail)

high frequency gradient or roll-off of -20 dB/decade corresponding to that of the integrator.

For controller synthesis the plant model should be accurate at frequencies above the closed-loop bandwidth, and here a conservative approach of accuracy at 10 times the bandwidth is used. The closed-loop bandwidth is at this stage unknown, but it needs to be larger than the magnitude of any unstable plant poles for reasonable performance (Skogestad and Postlethwaite, 1996, p185), and another conservative approach of the bandwidth being 10 times larger than the magnitude of the unstable plant pole is applied here.

Case 1 has an unstable pole of magnitude $|0.00373967 - 0.23752649\jmath| \approx 0.2376$. Thus these results indicate that in order to achieve accurate plant model behaviour up to 100 times the unstable eigenvalue magnitude, i.e. approximately 24 rad/s, approximately $N = 100$ terms are required in the wall-normal discretisation.

Discretisation Accuracy

Some explanation for the need for such a fine discretisation can be obtained by examining the process of spectral collocation. Collocation applies the equation being modelled exactly at the collocation points, but only approximately in between. Thus the more points the better the overall accuracy, until rounding effects predominate.

The function $\cos(\pi y) + 1$ has homogeneous Dirichlet and Neumann boundary conditions at the ends of the range $y = \pm 1$. A very good approximation of the function can be obtained with $N = 20$ modified Chebyshev polynomials, with a maximum error of 10^{-15}, slightly larger than machine floating point relative

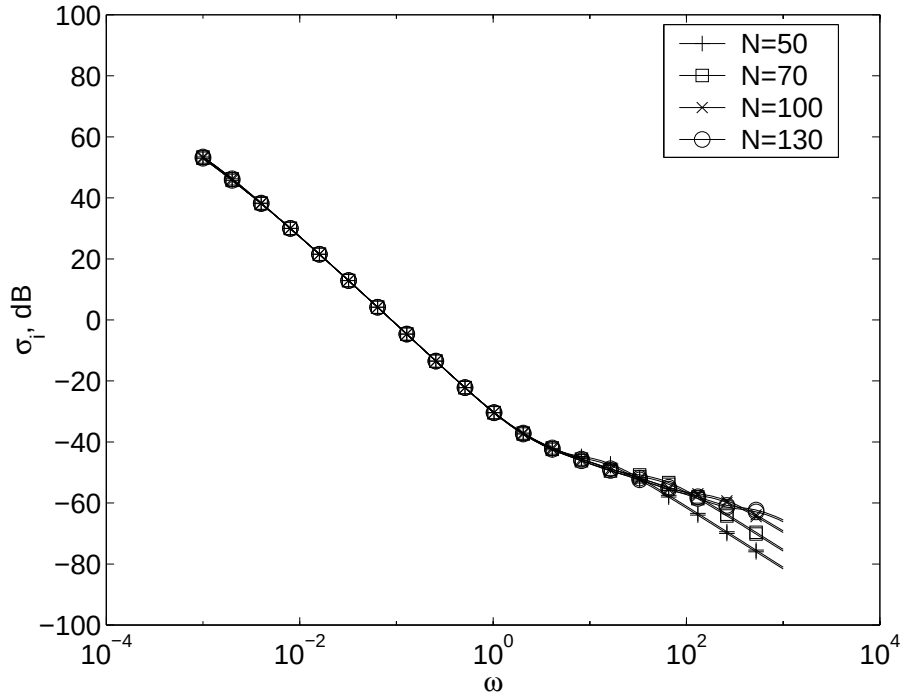

Figure 2.5: Case 2 Open-Loop Singular Values vs Frequency

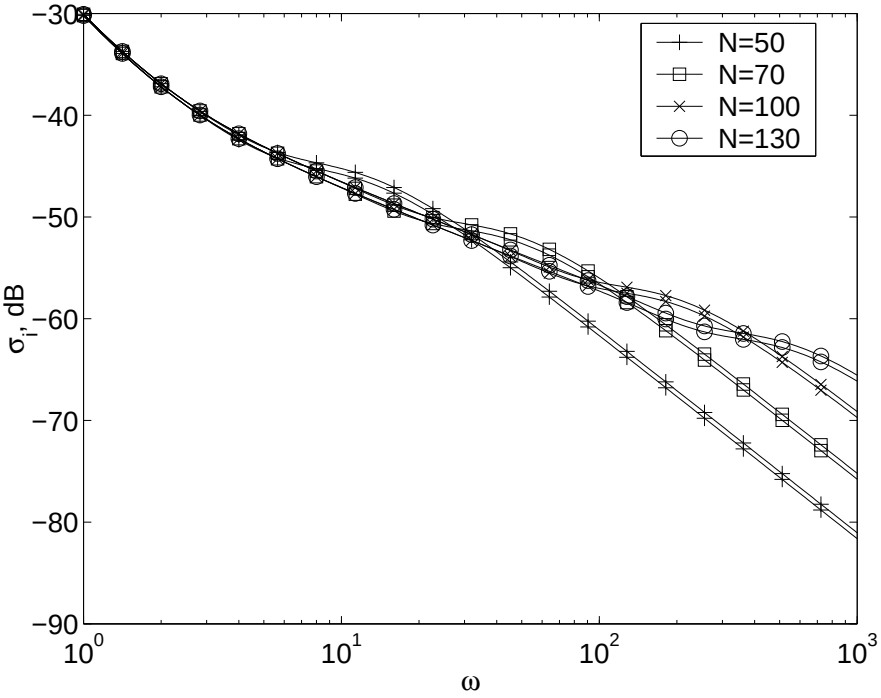

Figure 2.6: Case 2 Open-Loop Singular Values vs Frequency (detail)

accuracy 2×10^{-16} (Matlab `eps`).

For a more complex function $\cos(3\pi y)+1$, with the same boundary conditions, the best accuracy achievable is around 10^{-14} for $N = 32$. However, the accuracy decreases markedly with derivative. The best accuracy of the fourth spectral derivative is 10^{-8} with $N = 36$.

As the velocity equation (2.34) contains the fourth derivative, the results for the simpler equation $\cos(3\pi y)+1$ indicate that a fine level of discretisation is likely to be required.

Eigenvalue Accuracy at $N = 100$

The system gains two integrators when recast to a form with wall-normal velocity derivative control inputs (2.100), which are associated with steady-state modes due to non-zero wall-normal velocities. Thus it is more appropriate to use the eigenvalues of the unconverted system (2.99) when comparing eigenvalues with those of an uncontrolled system, which by definition has zero wall-normal velocities.

Although spectral models are unable to produce more than the lowest $N/2$ eigenvalues accurately, as noted by Boyd (2001, p132), a model size of $N = 100$ Chebyshev polynomials produces very accurate values for these. Figure 2.7 compares case 1 open-loop eigenvalues with the 32 published values of Orszag (1971) plus the additional eigenvalue discovered by Dongarra et al. (1996), as relative fractional error. Also shown is the accuracy of Orszag's calculation, in the form of the fractional error due to one unit in the his least significant digit. The eigenvalues are seen to be close to the results of Orszag to within the computational error quoted, and thus it can be concluded that the physics of linearised plane Poiseuille flow have been modelled correctly.

Boyd (2001, p139) notes that spectral discretisations are susceptible to spurious eigenvalues, for example as found by Bewley and Liu (1998). Typically these eigenvalues are sensitive to N, and have eigenvectors which are not physically realistic due to oscillations. Boyd's ordinal differences δ_i (Boyd, 2001, p138), are a measure of the sensitivity of the eigenvalues λ to N

$$\delta_i = \left|\lambda_i\left(N_1\right) - \lambda_i\left(N_2\right)\right| / \upsilon_i \tag{2.136}$$

where N_1 and $N_2 (> N_1)$ are different values of N and υ_i is the intermodal separation

$$\begin{aligned} \upsilon_1 &= |\lambda_1 - \lambda_2| \\ \upsilon_i &= 0.5\left(|\lambda_i - \lambda_{i-1}| + |\lambda_{i+1} - \lambda_i|\right), \quad 1 < i < N_1 \end{aligned} \tag{2.137}$$

Eigenvalues $i > N_1/2$ are inadequately resolved, and thus show a large sensitivity δ_i, but those $i < N_1/2$ should be resolved well, unless they are spurious.

Figure 2.8 plots the reciprocal of sensitivity δ_i for case 1, with $N_1 = 100$ and $N_2 = 133$, for the complex system (2.98). The figure shows that although sensitivity rises with i, there are no exceptionally sensitive modes below $N_1/2 = 50$. Figure 2.9 plots the reciprocal of sensitivity δ_i for case 2, also from (2.98). For case 2 this system contains both the vorticity and velocity equations, and is thus twice as large as for case 1, for the same N_1. This figure shows low sensitivity for

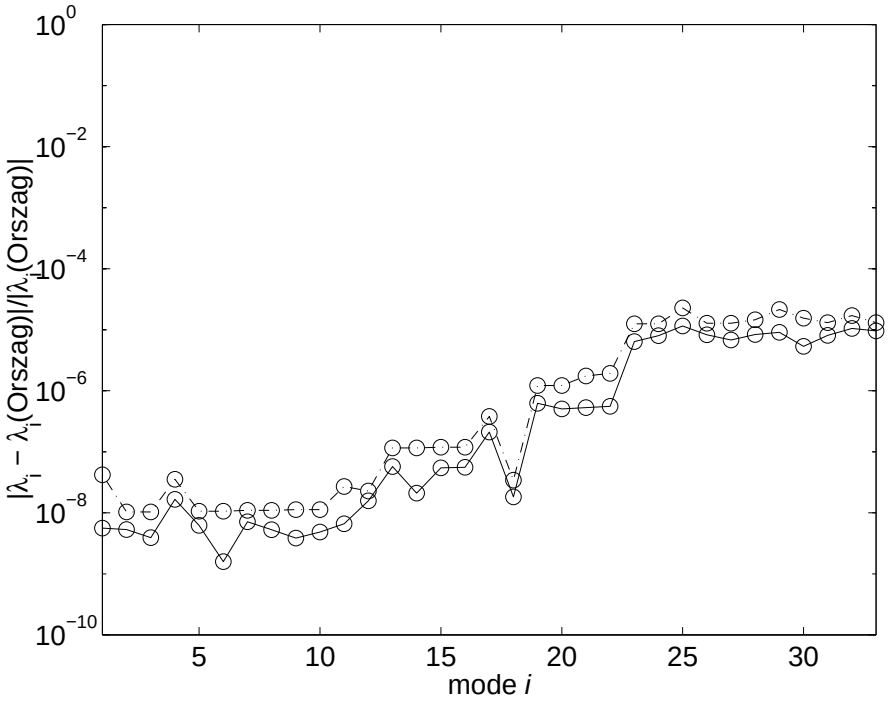

Figure 2.7: Case 1 Error in Open-Loop Eigenvalues (solid) and Accuracy of Reference Data (dotted) vs Mode

all modes below $N_1/2 = 50$. The sensitivity shown in figures 2.8 and 2.9 for modes up to $N_1/2$ indicates that no spurious modes occur in the present test cases.

2.8.2 Model Dynamics

Poles and Zeros

Figure 2.10 shows the poles and zeros for case 1. As sorted by stability, i.e. from right to left, the highest $N/2$ poles (corresponding to $Re(\lambda) < -0.55$) are inaccurate, as is to be expected using spectral methods, as noted by Boyd (2001). The rightmost pole is unstable, within one decimal place of the well-known result $0.00373967, -0.23752649\jmath$ for the Orr-Sommerfeld equations as calculated by Orszag (1971). There are several zeros in the state-space system derived here, but none are unstable. Several zeros are close to cancelling poles, and so the system is close to being non-minimal, as was found by Joshi et al. (1995). The Matlab function `minreal`, which eliminates non-minimal state dynamics, would remove 36 state variables at the default tolerance of 1.5×10^{-8}, but none at a tighter tolerance of 10^{-10}, for $N = 100$.

Figure 2.11 shows poles and zeros for case 2. All poles are real and stable, as found by Bewley and Liu (1998). There are no zeros in the state-space system derived in the present work.

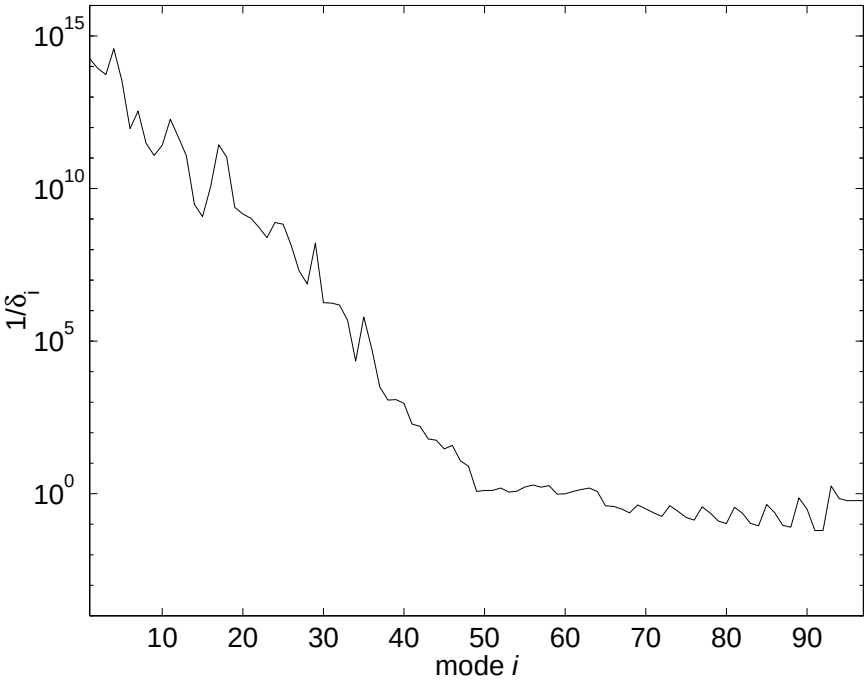

Figure 2.8: Case 1 Reciprocal of Boyd's Ordinal Difference

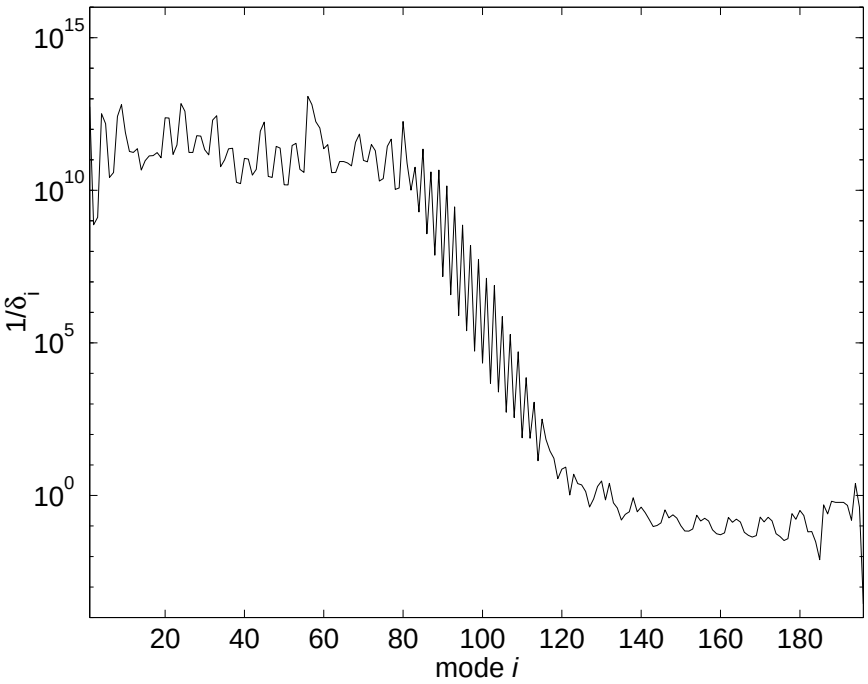

Figure 2.9: Case 2 Reciprocal of Boyd's Ordinal Difference

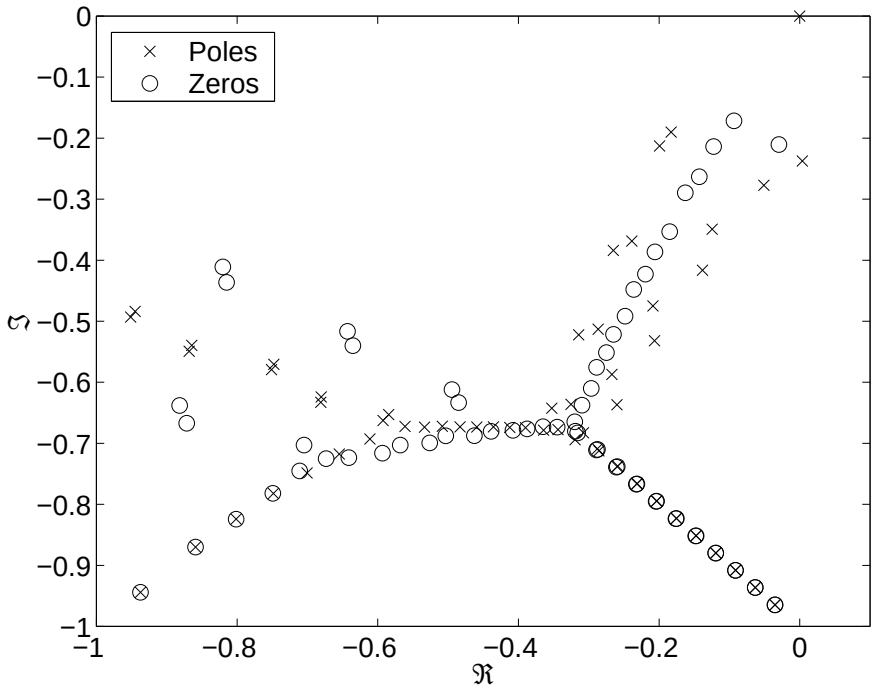

Figure 2.10: Case 1 Pole-Zero Map (detail)

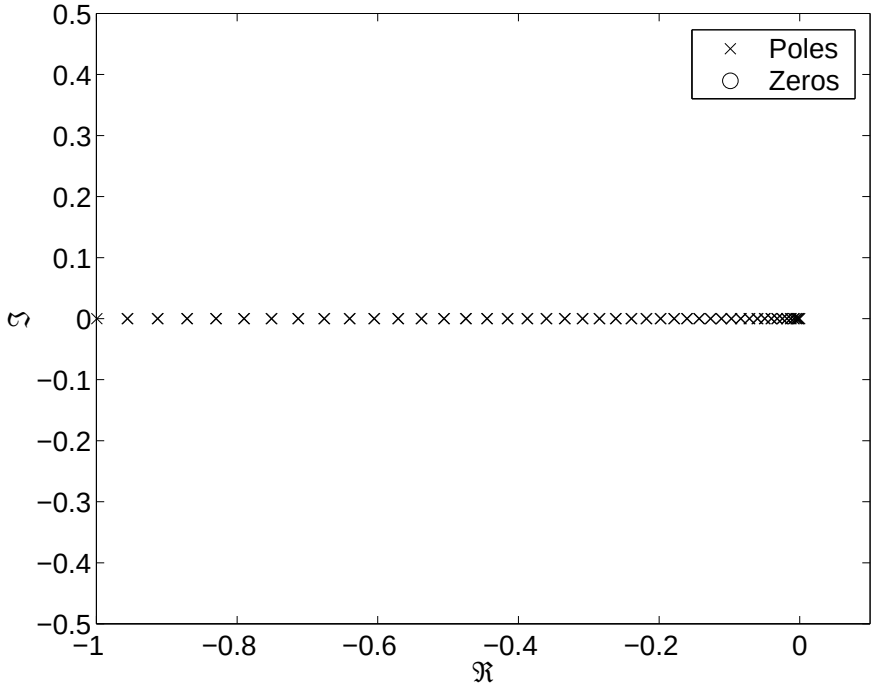

Figure 2.11: Case 2 Pole-Zero Map (detail)

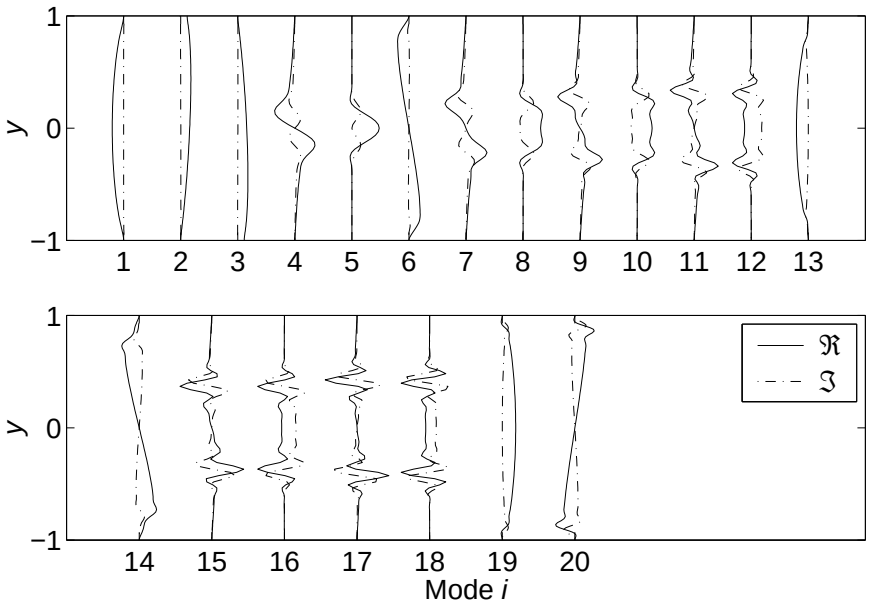

Figure 2.12: Case 1, $N = 100$, $\tilde{v}$ Eigenvectors, Real Part (solid) and Imaginary Part (dot-dashed)

Eigenvectors

Figure 2.12 shows the first twenty wall-normal velocity ($\tilde{v}$) right eigenvectors ψ_i for case 1, normalised consistently as per Bewley and Liu (1998) ($\psi_i^T \psi_i = N/\pi, \forall i$), and generated from the complex system (2.6.6), to avoid introducing the conjugate modes. Both real (solid) and imaginary (dot-dashed) components are shown. Mode 1 is the well-documented unstable mode, symmetrically filling the whole channel height. Modes 2 and 3 are associated with the integrators in (2.100), each representing steady-state transpiration from the upper and lower walls respectively, as shown by the non-zero wall velocities, and thus each is a reflection of the other about the centre-line, ($\tilde{v}_2(+y) = \tilde{v}_3(-y)$). These modes fill the whole channel and are unusual in being real. The following modes are naturally occurring, and are symmetric ($\tilde{v}(+y) = \tilde{v}(-y)$) or antisymmetric ($\tilde{v}(+y) = -\tilde{v}(-y)$), and either fill the whole channel or are concentrated in the central portion.

Figure 2.13 shows the first twenty streamwise perturbation velocity ($\tilde{u}$) eigenvectors for case 1, normalised consistently with the $\tilde{v}$ modes, then uniformly scaled by 1/25. The $\tilde{u}$ modes are generally much larger than the $\tilde{v}$ modes (noting the scaling applied as compared to figure 2.12), and of opposite symmetry, e.g. symmetric $\tilde{v}$ modes are antisymmetric in $\tilde{u}$ and vice versa. Both $\tilde{u}$ and $\tilde{v}$ modes are complex. In figure 2.14 the first and unstable $\tilde{v}$ eigenvector of case 1 normalised to unit magnitude, is compared with that of Thomas (1953). The agreement of both imaginary and real components is very good. Figure 2.15 shows the streamwise (u) and wall-normal velocity (v) flow fields associated with mode 2 in figure 2.12, one of the integrator modes, normalised to unit maximum v for case 1 with $R = 500$. For this figure, the Reynolds number is reduced below the critical value of approximately 5772 (Schmid and Henningson, 2001, p73), below which the system is

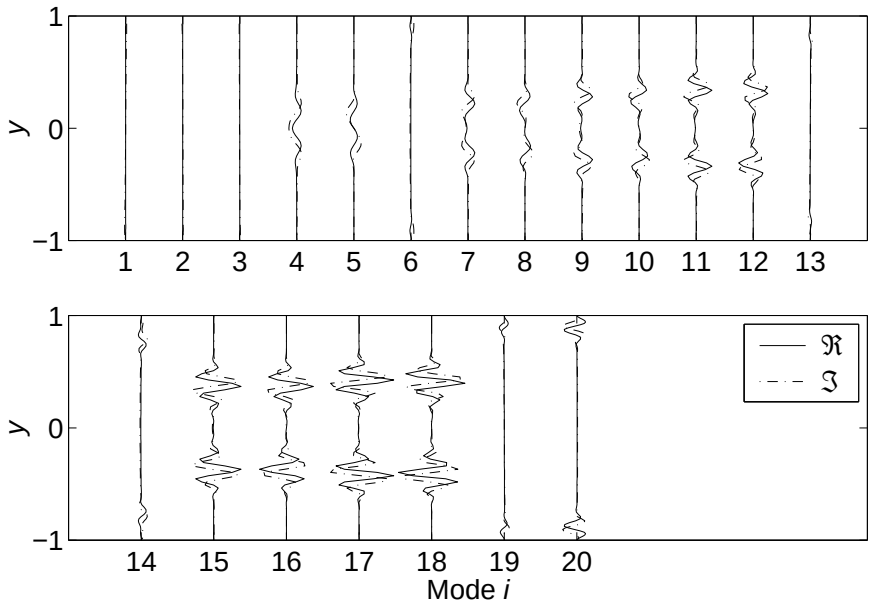

Figure 2.13: Case 1, $N = 100$, $\tilde{u}$ Eigenvectors, Scaled by 1/25 c.f. Figure 2.12, Real Part (solid) and Imaginary Part (dot-dashed)

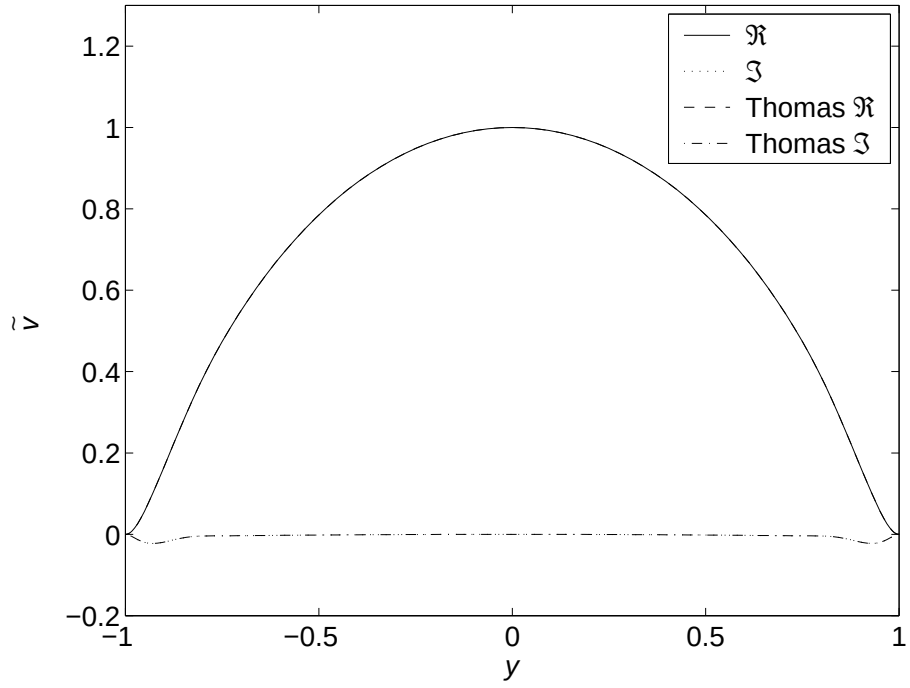

Figure 2.14: Case 1, $N = 100$, Comparison of Unstable Eigenvector with Results of Thomas (1953)

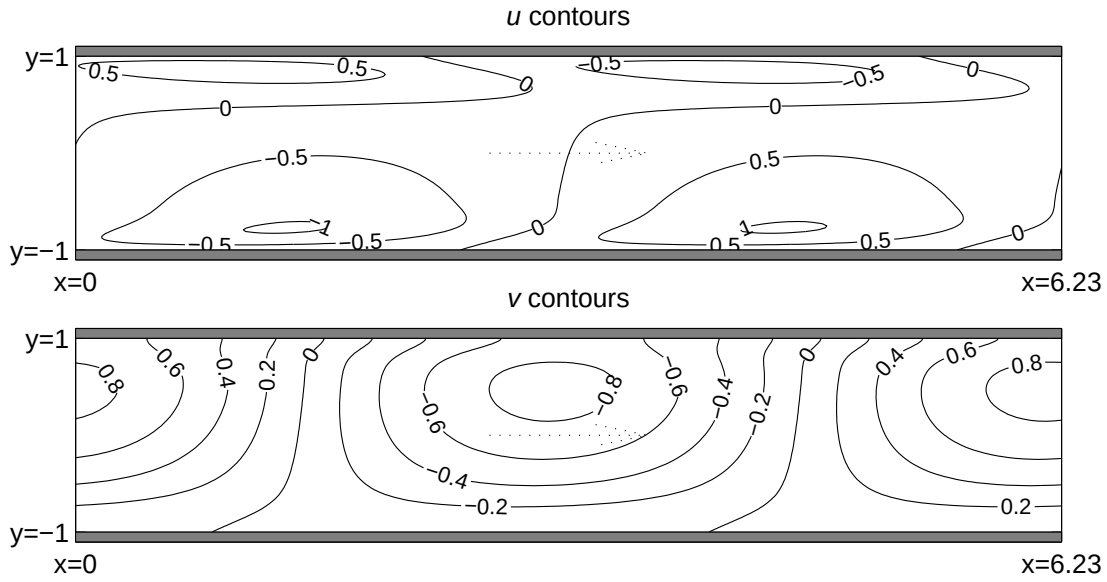

Figure 2.15: Case 1, $N = 100$, Streamwise (upper) and Wall-Normal (lower) Velocity Fields Associated with Zero Value Eigenvalue of State-Space Model, $R = 500$

linearly stable, to assist in comparisons with non-linear simulation results in chapter 4. Sinusoidal transpiration is clearly evident from the upper wall ($y = 1$) in the v contours, as is the periodic behaviour of the flow in the streamwise direction in general.

Figure 2.16 shows the first twenty wall-normal velocity ($\tilde{v}$) eigenvectors for case 2, normalised consistently ($[\tilde{v}_i, \tilde{\eta}_i]^T [\tilde{v}_i, \tilde{\eta}_i] = N/\pi, \forall i$). All the modes are purely imaginary. Modes 1 and 2 are associated with the integrators, each representing steady-state transpiration from the upper and lower walls respectively, and like the transpiration modes in case 1, they fill the whole channel and are unusual in being neither symmetrical nor antisymmetric. The following modes are naturally occurring. Alternate modes have zero velocity, whereas the remainder are symmetric or antisymmetric, and fill the whole channel.

The first twenty vorticity ($\tilde{\eta}$) eigenvectors, normalised consistently with the $\tilde{v}$ modes, then uniformly scaled by 1/550, are shown in figure 2.17. The $\tilde{\eta}$ modes are all purely real and much larger than the $\tilde{v}$ modes (noting the scaling applied as compared to figure 2.16), and none have zero vorticity. Where the $\tilde{v}$ modes are non-zero, the $\tilde{\eta}$ modes are of opposite symmetry. After the two integrator modes, the $\tilde{\eta}$ modes come in almost identical pairs, one associated with a zero velocity mode, the other with a non-zero velocity mode. Bewley and Liu (1998, p329) have explained these near identical pairs in terms of the discretised velocity and vorticity equations (2.66), which are similar after the inversion of the Laplacian, when $\alpha = 0$, differing only in the velocity equation requiring a Neumann boundary condition in addition to the Dirichlet one, and the vorticity equation having a coupling velocity term.

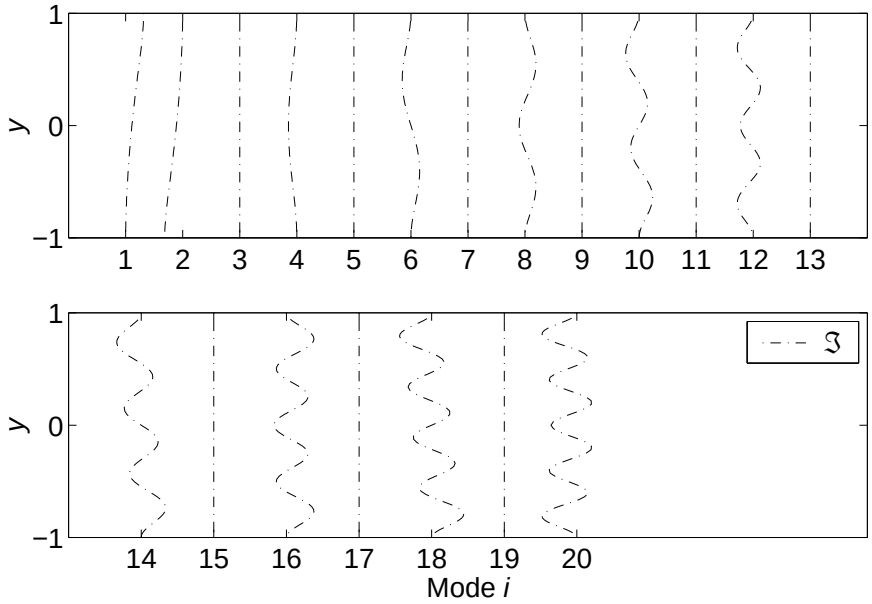

Figure 2.16: Case 2, $N = 100$, $\tilde{v}$ Eigenvectors (imaginary)

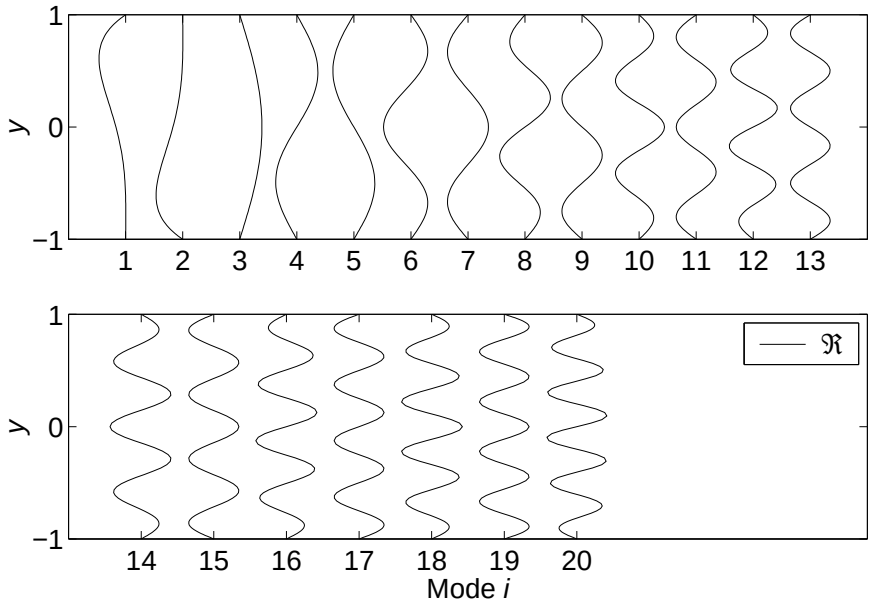

Figure 2.17: Case 2, $N = 100$, $\tilde{\eta}$ Eigenvectors (real), Scaled by 1/550 c.f. Figure 2.16

Model Reduction

Model reduction techniques, to lessen the size of the arrays, which lose the physical relevance of the state variables would need to be applied with care since calculations of the kinetic energy of the system based on the variables are to be performed in subsequent chapters. In theory, the model size could be reduced by performing a balanced realization, and examining its Gramian to determine which state variables in the balanced realization have little effect on its input-output behaviour and could be discarded (Skogestad and Postlethwaite, 1996, p452). The effect of discarding these balanced state variables on the energy calculation would need to be investigated. Also, this procedure is only suitable for stable plant, and thus for case 1 open loop, the unstable modes would have to be factored out beforehand, further complicating the energy calculation. Furthermore the effects of model reduction on non-normal transient energy growth are unclear. The approach adopted in this work is that the discretization process itself can be viewed as model reduction of the infinite dimensional system, and the inspection of convergence with discretisation can achieve a degree of model reduction, without causing difficulties in the calculation of the system energy.

Observability and Controllability

A system is state observable if and only if $\mathcal{C}\psi_i \neq 0, \forall i$, where ψ_i is a right eigenvector, $\mathcal{A}\psi_i = \lambda_i\psi_i$ (Skogestad and Postlethwaite, 1996, p126). The degree to which a mode i is observable may be assessed by examining the magnitude of $\mathcal{C}\psi_i$, since it represents the outputs $\mathcal{Y}$ arising from mode i, i.e. from substituting $\mathcal{X} = \psi_i$ in (2.1). Bewley and Liu (1998) have presented a numerically convenient measure of observability for discretised Poiseuille flow, $\kappa_o = R\sqrt{\psi_i^T\mathcal{C}^T\mathcal{C}\psi_i}$. This measure is based on an eigenvector normalisation which converges with discretisation N, $\psi_i^T\psi_i\pi/N = 1$. Other normalisations which are independent of discretisation are possible e.g $max_i(\psi_i) = 1$. The magnitudes of the right eigenvectors, and thus their observability, depend on the normalisation employed. Here, to facilitate comparison with Bewley's results, his normalisation is used.

Figure 2.18 plots Bewley's observability measure for the present model case 1. The complex model of section 2.6.6 is used to avoid introducing the conjugate modes. The system measurements are based on the wall shear stresses (2.19), and for case 1 matrix $\mathcal{C}$ computes $\partial u/\partial y$ at the upper and lower walls from the state variables. Figure 2.19 shows the upper wall detail of the u modes, normalised as for observability. The u gradient at the wall shows a clear correlation with the observability of figure 2.18. Modes 5,8,10,12,16,18 have small u gradient at the wall, and small observability. These modes are antisymmetric in u, centre-span modes, and thus would be expected to have low wall gradients. Figure 2.18 also shows Bewley's results, where the mode numbering of Bewley's results has been adjusted to allow for the 2 integrators added to the present system for case 1, and it is evident that the agreement with Bewley's results is good.

Figure 2.20 plots the observability results for case 2. For case 2 measurements at the wall are $\partial u/\partial y$ and $\partial w/\partial y$, and figures 2.21 and 2.22 show near-wall detail of the u and w modes respectively, normalised as for observability. Noting the 40

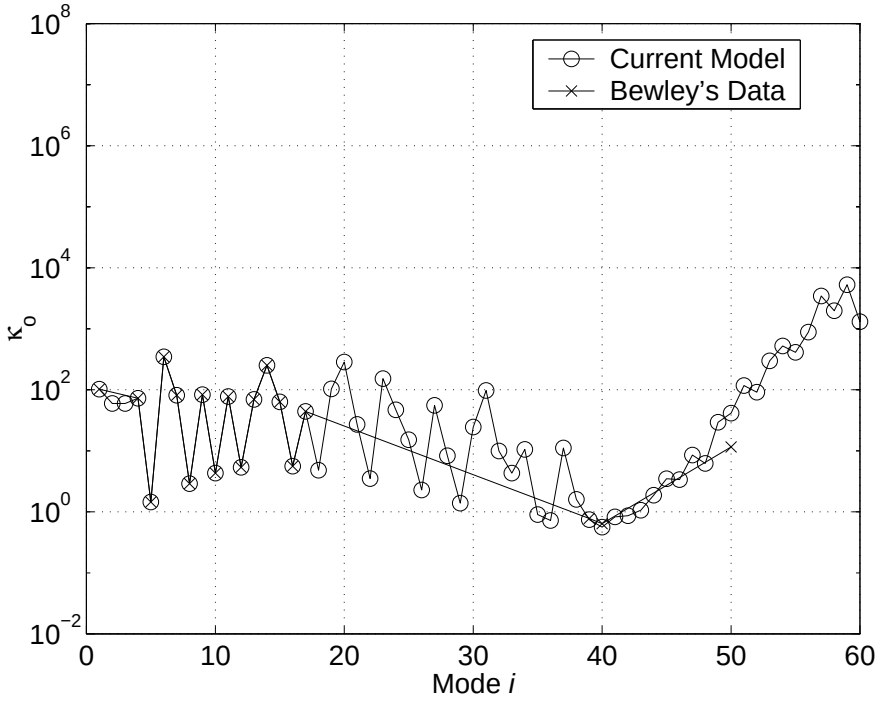

Figure 2.18: Case 1 Observability

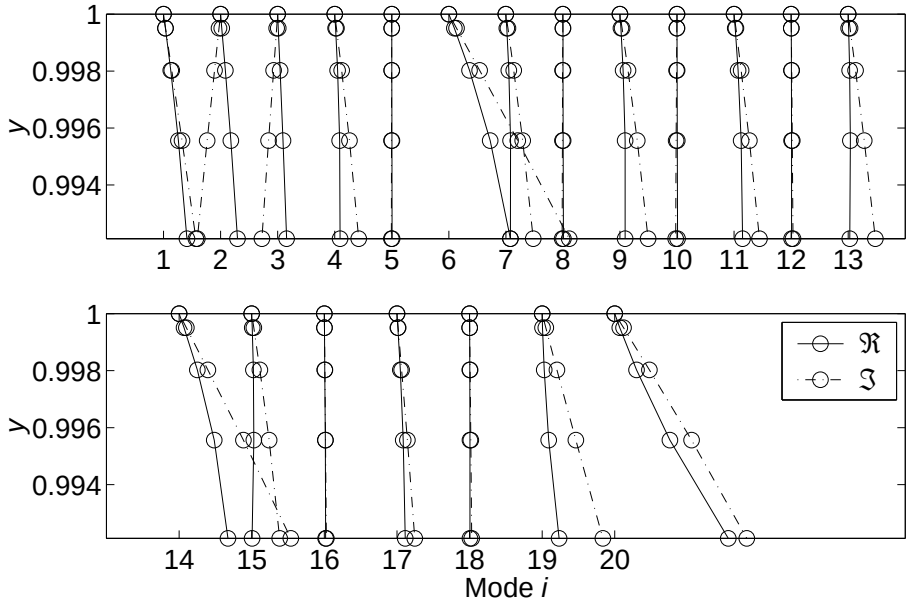

Figure 2.19: Case 1 $\tilde{u}$ Mode Wall Detail, Real Part (solid) and Imaginary Part (dot-dashed)

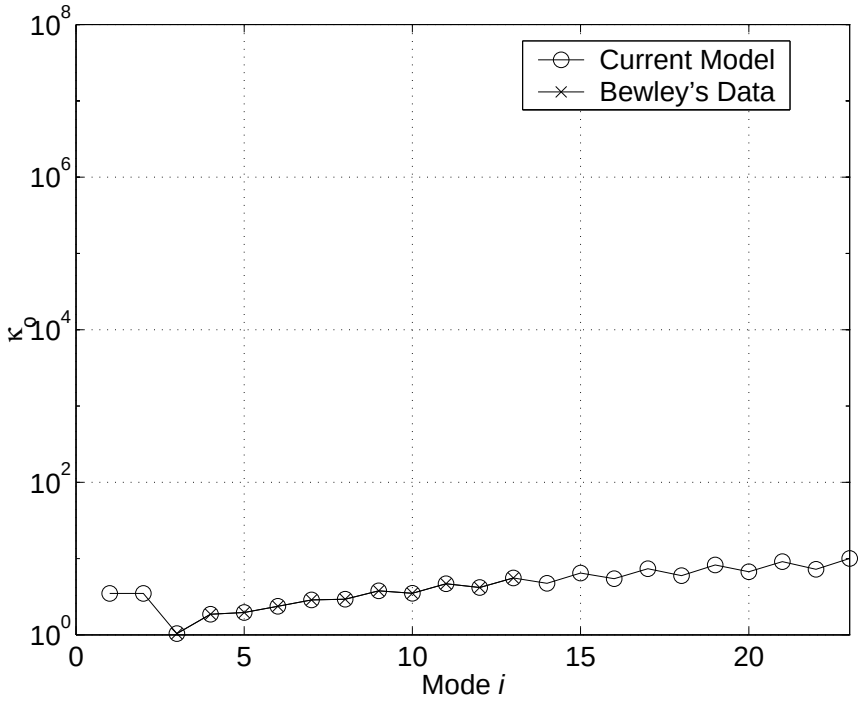

Figure 2.20: Case 2 Observability

times scaling applied to the w modes, it is seen that the w mode gradients are much smaller than the u modes, and contribute comparatively little to the measurements. Integrator mode 1 has a large u gradient at the upper wall, and this correlates with its high observability. Mode 2 has a small upper wall u gradient, but being an integrator mode is asymmetric, and has a high wall gradient at the lower wall (not shown), which accounts for its good observability. The subsequent naturally occurring modes increase in wall u gradient as they become more complex with mode number, as shown in figure 2.16, and this correlates with their increasing observability. Bewley's results, with the mode numbering adjusted to allow for the integrators added to the present system, are also shown. The agreement with Bewley's results is good.

A system is state controllable if and only if $\mathcal{B}^T\phi_i \neq 0, \forall i$, where ϕ_i is a left eigenvector, $\phi_i^T\mathcal{A} = \lambda_i\phi_i^T$ (Skogestad and Postlethwaite, 1996, p122) and the degree to which a mode i is controllable may be assessed by examining the magnitude of $\mathcal{B}^T\phi_i$. This result may be interpreted as follows (Bewley and Liu, 1998, p322). Considering the system (2.1), repeated here

$$\begin{aligned} \dot{\mathcal{X}} &= \mathcal{A}\mathcal{X} + \mathcal{B}\mathcal{U} \\ \mathcal{Y} &= \mathcal{C}\mathcal{X} \end{aligned} \tag{2.138}$$

with left eigensystem $\Phi^T\mathcal{A} = \Lambda\Phi^T$ where Φ^T is the matrix of left eigenvectors ϕ_i^T and Λ a diagonal matrix of eigenvalues λ_i, and right eigensystem $\mathcal{A}\Psi = \Psi\Lambda$ where Ψ is the matrix of right eigenvectors ψ_i. Bewley's eigenvector normalisation which converges with discretisation N is assumed, $\phi_i^T\psi_i\pi/N = 1$ where $\psi_i^T\psi_i\pi/N = 1$. Other normalisations which are independent of discretisation are possible e.g

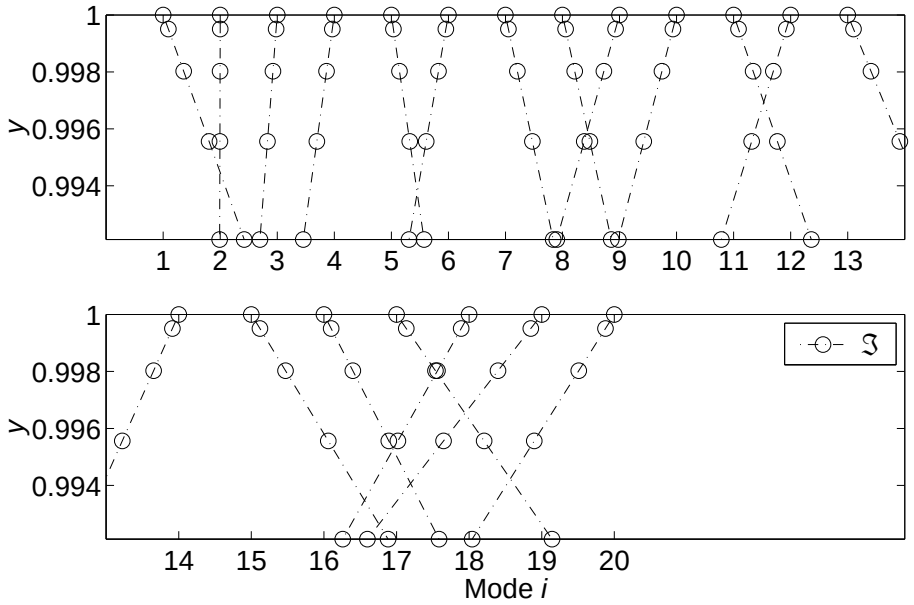

Figure 2.21: Case 2 $\tilde{u}$ Mode Wall Detail (imaginary)

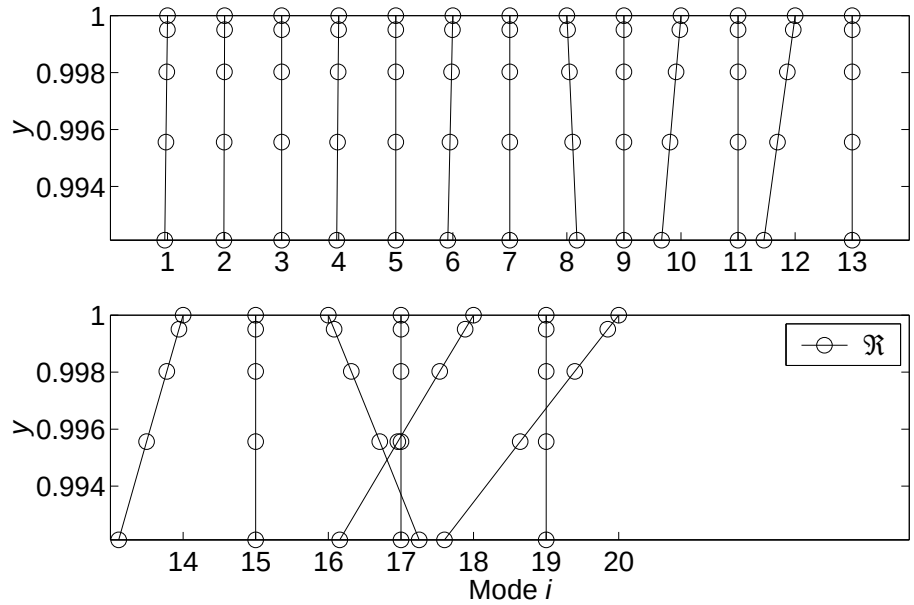

Figure 2.22: Case 2 $\tilde{w}$ Mode Wall Detail (real), Scaled by 40 c.f. Figure 2.21

$max_i(\psi_i) = 1$, $\phi_i^T \psi_i = 1$. The magnitudes of the left and right eigenvectors, and thus their controllability, depend on the normalisation employed. Here, to facilitate comparison with Bewley's results, his normalisation is used.

Any state may be represented

$$\mathcal{X} = \Psi\chi \tag{2.139}$$

where χ is a vector of initial modal amplitudes, $[c_i, \ldots, c_N]^T$. Substituting this expression in the first equation of (2.138) yields

$$\Psi\dot{\chi} = \mathcal{A}\Psi\chi + \mathcal{B}\mathcal{U} \tag{2.140}$$

Since $\mathcal{A}\Psi = \Psi\Lambda$, the equation becomes

$$\Psi\dot{\chi} = \Psi\Lambda\chi + \mathcal{B}\mathcal{U} \tag{2.141}$$

Premultiplying by Φ^T yields

$$\dot{\chi} = \Lambda\chi + \pi/N\Phi^T\mathcal{B}\mathcal{U} \tag{2.142}$$

since $\Phi^T\Psi = N/\pi\mathbf{I}$, due to the normalisation imposed and the orthogonality of left and right eigenvectors. Equation i of this system is

$$\dot{c}_i = \lambda_i c_i + \pi/N\phi_i^T\mathcal{B}\mathcal{U} \tag{2.143}$$

and thus the effect of the input $\mathcal{U}$ on rate of growth of the amplitude of mode i, $\dot{c}_i$, depends upon the magnitude of $\phi_i^T\mathcal{B}$. Bewley and Liu (1998) have presented a convenient measure of controllability

$$\kappa_c = \pi\sqrt{\phi_i^T\mathcal{B}\mathcal{B}^T\phi_i}/N \tag{2.144}$$

for discretised Poiseuille flow.

Figure 2.23 plots this controllability measure for the current model for each mode i for case 1. Considering the initial modes, since high modes are known to be inaccurate, the controllability of whole-span modes (e.g. 1,2,6,13 in figure 2.12) is higher than that of centre-span modes (e.g. 4,5,7,8,9), as might be expected with actuation at the walls. The controllability of the centre-span modes increases with mode number as the the centre-span modes increase in spanwise extent. Asymmetric v centre-span modes (e.g. 4,7,9,11) are more controllable than neighbouring symmetric v centre-span modes (5,8,10,12), which is consistent with their having small magnitudes outside the central of the span, unlike the symmetric modes. The figure also presents Bewley's own results, with the mode numbering adjusted as previously, and shows that the agreement with Bewley's results is good.

Figure 2.24 plots the same results for case 2. The controllability decreases with increasing mode number, which is consistent with the mode shapes becoming more complex. The zero-velocity modes (e.g. 5,7,9,11) are less controllable than their non-zero-velocity similar partners (4,6,8,10), as might be expected with wall velocity actuation. The figure also shows Bewley's own results, with the mode numbering adjusted as previously. The agreement with Bewley's results is poor, the current model being several orders of magnitude more controllable.

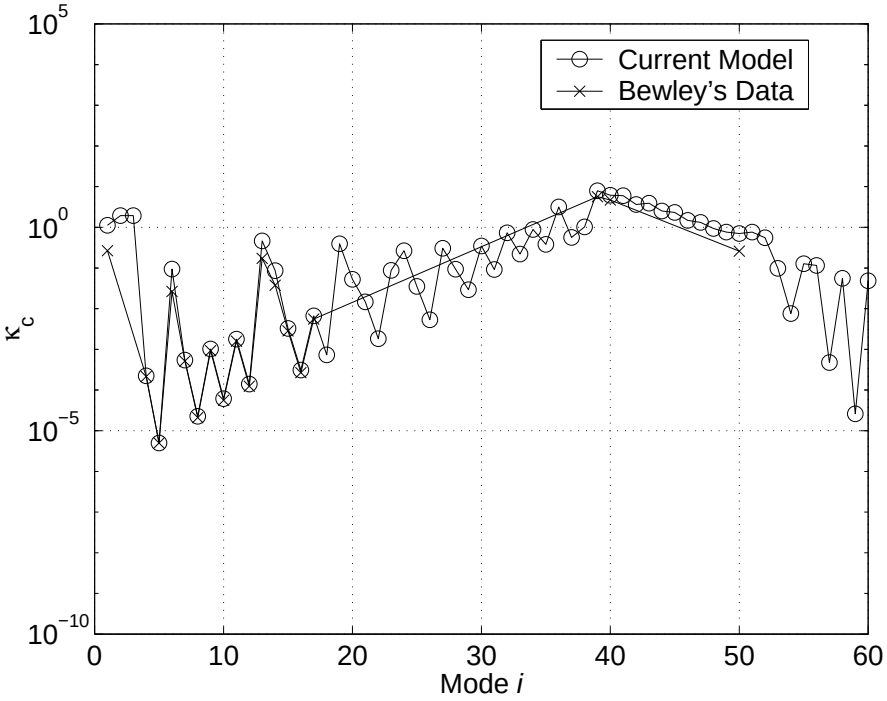

Figure 2.23: Case 1 Controllability

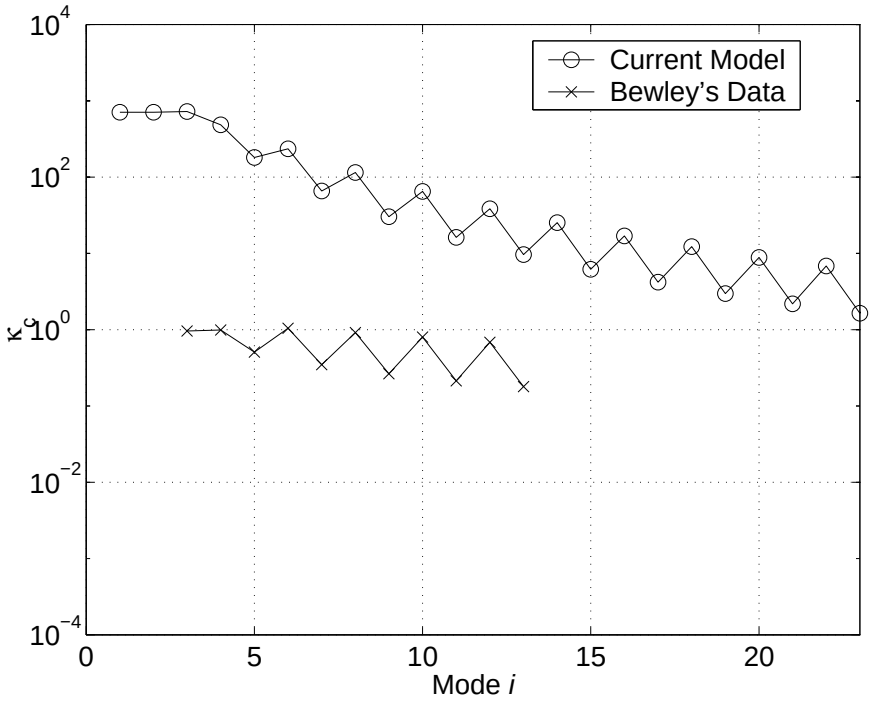

Figure 2.24: Case 2 Controllability

Investigation of the Effect of Integrators on Bewley's Model

It is straightforward to reproduce Bewley's model and open loop results. The spurious modes may be identified by their saw-tooth appearance, oscillating between grid points. For case 1 spurious modes occur at $-0.024413 + 1.5273\jmath$, and for case 2 at -0.00083558, for $N = 100$, which are shifted to $-500, 0\jmath$, with no other spurious modes within the first half eigenvalues. Spurious modes are more difficult distinguish in the second half eigenmodes, as the eigenmodes become discretised less accurately. No attempt is made to adjust any second-half modes, which are known to be inaccurate in a spectral model anyway.

Bewley's model is reproduced to examine the effect of transforming it from the original form (2.118), reproduced here

$$\begin{aligned} \dot{\mathbf{v}} &= \mathbf{L}_{11}^{-1}\left(\left(\mathbf{I}+\mathbf{L}_{12}\mathbf{X}^{-1}\mathbf{L}_{21}\mathbf{L}_{11}^{-1}\right)\mathbf{A}_{11}-\mathbf{L}_{12}\mathbf{X}^{-1}\mathbf{A}_{21}\right)\mathbf{v} \\ &+ \mathbf{L}_{11}^{-1}\left(\left(\mathbf{I}+\mathbf{L}_{12}\mathbf{X}^{-1}\mathbf{L}_{21}\mathbf{L}_{11}^{-1}\right)\mathbf{A}_{12}-\mathbf{L}_{12}\mathbf{X}^{-1}\mathbf{A}_{22}\right)v_w \end{aligned} \tag{2.145}$$

to the integrator form (2.122), also reproduced here

$$\begin{pmatrix} \dot{\mathbf{v}} \\ \dot{v}_w \end{pmatrix} = \begin{pmatrix} \mathbf{L}_{11}^{-1}\mathbf{A}_{11} & \mathbf{L}_{11}^{-1}\mathbf{A}_{12} \\ \mathbf{0} & \mathbf{0} \end{pmatrix}\begin{pmatrix} \mathbf{v} \\ v_w \end{pmatrix} + \begin{pmatrix} -\mathbf{L}_{11}^{-1}\mathbf{L}_{12} \\ 1 \end{pmatrix}\dot{v}_w \tag{2.146}$$

This transformation alters the observability and controllability as follows. Figures 2.25 and 2.26 show how the introduction of the integrators does not affect the the observability of the first half modes of Bewley's model in either case 1 or case 2. Also, the agreement with the current model shows that the presence of the shifted spurious eigenmodes need not necessarily compromise the results of the genuine modes.

Figure 2.27 shows how the introduction of the integrators does not generally affect the the controllability of Bewley's first half modes for case 1. However, the integrators do increase the controllability of the first half modes substantially for case 2, as shown in figure 2.28, and produce values in good agreement with those of the current model. These results show that the discrepancy between the controllability of the current model for case 2 and that of Bewley's results is purely due to the introduction of the integrators. Again, the agreement with the current model shows that the presence of the shifted spurious eigenmodes need not necessarily compromise the results of the genuine modes.

Investigation of the Effect of Integrators on Observability and Controllability

Considering the system

$$\begin{aligned} \dot{\mathcal{X}} &= \mathcal{A}\mathcal{X}+\mathcal{B}\mathcal{U} \\ \mathcal{Y} &= \mathcal{C}\mathcal{X}+\mathcal{D}\mathcal{U} \end{aligned} \tag{2.147}$$

with left eigensystem $\Phi^T\mathcal{A} = \Lambda\Phi^T$ where Φ^T is the matrix of left eigenvectors ϕ_i^T and Λ a diagonal matrix of eigenvalues λ_i, and right eigensystem $\mathcal{A}\Psi = \Psi\Lambda$ where Ψ is the matrix of right eigenvectors. The system has controllability $\pi/N\sqrt{\phi_i^T\mathcal{B}\mathcal{B}^T\phi_i}, l^T \in \Phi^T$ and observability $R\sqrt{\psi_i^T\mathcal{C}^T\mathcal{C}\psi_i}, \psi_i \in \Psi$.

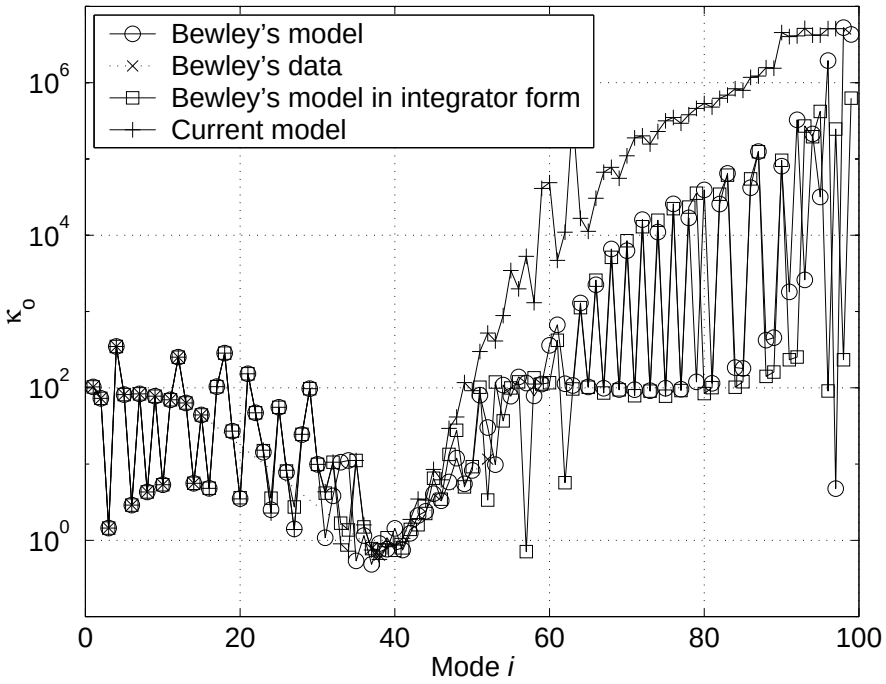

Figure 2.25: Case 1 Observability of Integrator and Non-Integrator Forms

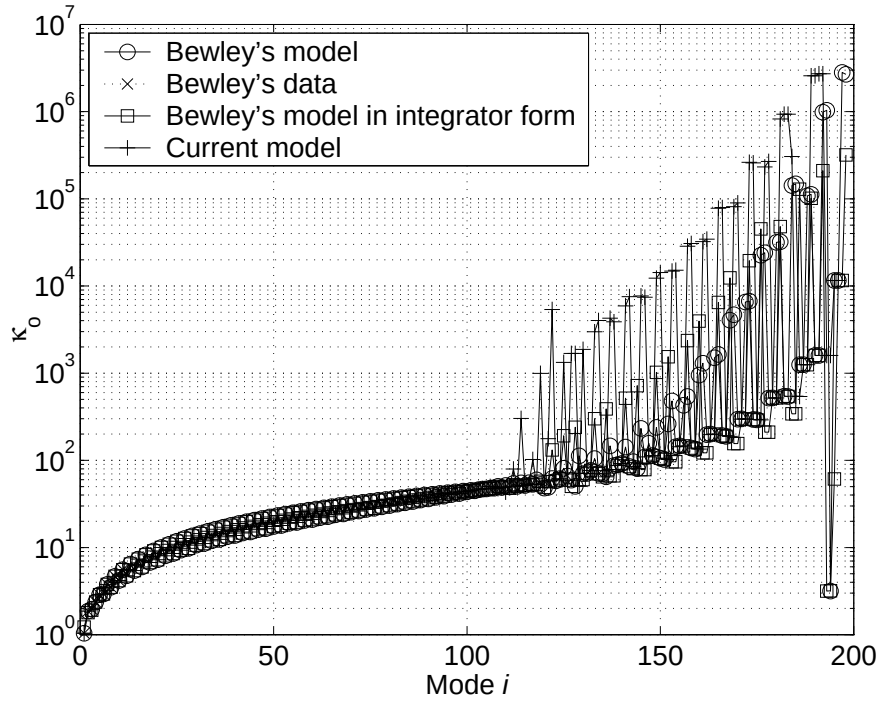

Figure 2.26: Case 2 Observability of Integrator and Non-Integrator Forms

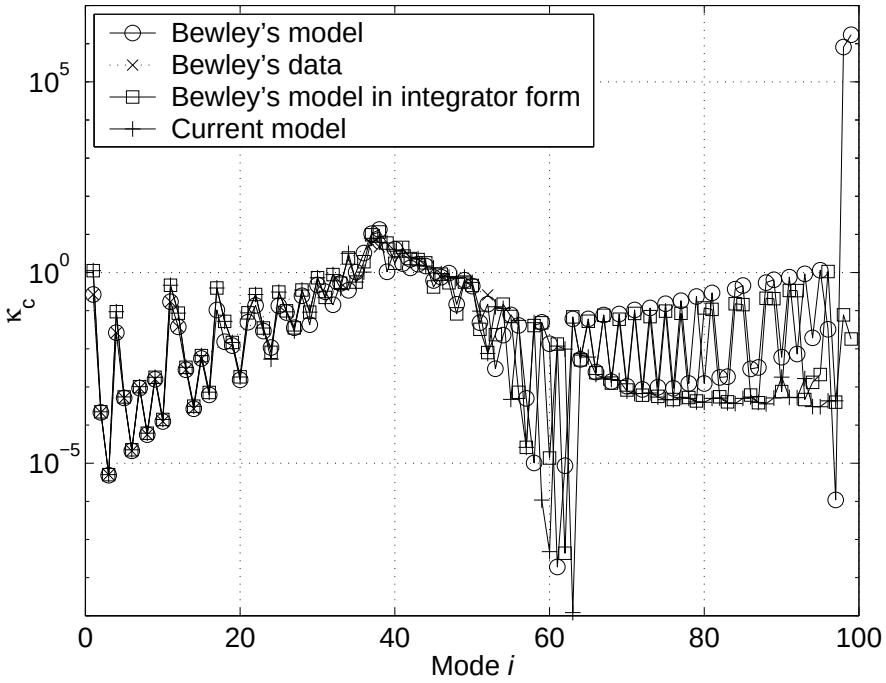

Figure 2.27: Case 1 Controllability of Integrator and Non-Integrator Forms

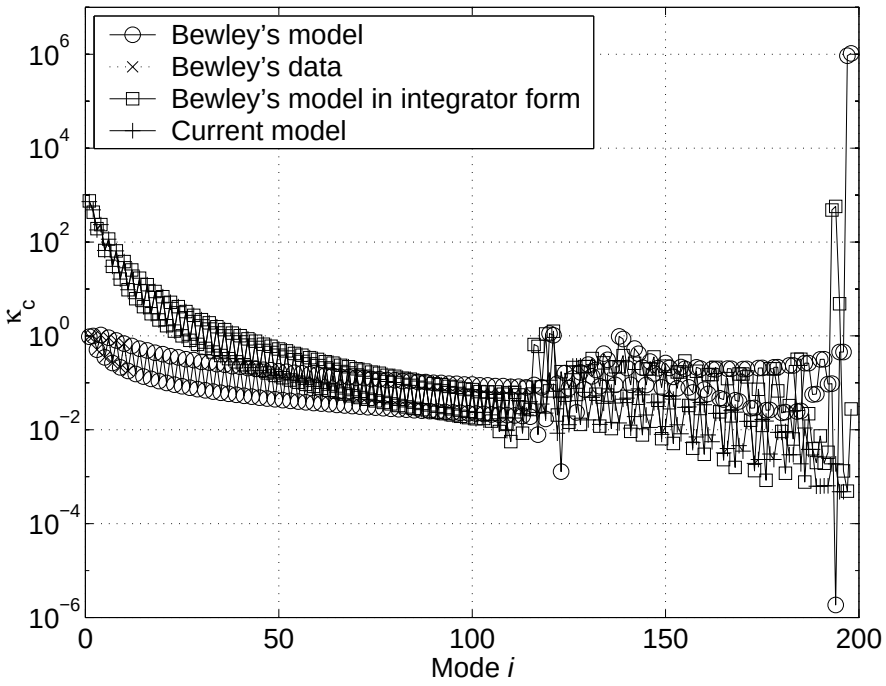

Figure 2.28: Case 2 Controllability of Integrator and Non-Integrator Forms

If integrators are introduced onto the system inputs it becomes

$$\begin{pmatrix} \dot{\mathcal{X}} \\ \dot{\mathcal{U}} \end{pmatrix} = \begin{pmatrix} \mathcal{A} & \mathcal{B} \\ \mathbf{0} & \mathbf{0} \end{pmatrix} \begin{pmatrix} \mathcal{X} \\ \mathcal{U} \end{pmatrix} + \begin{pmatrix} \mathbf{0} \\ \mathbf{I} \end{pmatrix} \dot{\mathcal{U}}$$
$$\mathcal{Y} = \begin{pmatrix} \mathcal{C} & \mathcal{D} \end{pmatrix} \begin{pmatrix} \mathcal{X} \\ \mathcal{U} \end{pmatrix} \tag{2.148}$$

By inspection, the right eigensystem of (2.148) is

$$\begin{bmatrix} \mathcal{A} & \mathcal{B} \\ \mathbf{0} & \mathbf{0} \end{bmatrix} \begin{bmatrix} \Psi & \Psi_1 \\ \mathbf{0} & \Psi_2 \end{bmatrix} = \begin{bmatrix} \Psi & \Psi_1 \\ \mathbf{0} & \Psi_2 \end{bmatrix} \begin{bmatrix} \Lambda & \mathbf{0} \\ \mathbf{0} & \mathbf{0} \end{bmatrix} \tag{2.149}$$

i.e. as compared to (2.147), each eigenvector $\psi_i \in \Psi$ is augmented by as many zeros as inputs, and new integrator modes $\left[\Psi_1^T \Psi_2^T\right]^T$ are added. The observability of non-integrator mode i is

$$R\sqrt{\begin{bmatrix} \psi_i^T & \mathbf{0}^T \end{bmatrix} \begin{bmatrix} \mathcal{C}^T \\ \mathcal{D}^T \end{bmatrix} \begin{bmatrix} \mathcal{C} & \mathcal{D} \end{bmatrix} \begin{bmatrix} \psi_i \\ \mathbf{0} \end{bmatrix}} = R\sqrt{\psi_i^T \mathcal{C}^T \mathcal{C} \psi_i}, \psi_i \in \Psi \tag{2.150}$$

i.e. the observability of the non-integrator mode i is identical to that of the mode in the system without integrators, (2.147). By inspection, the system left eigensystem is

$$\begin{bmatrix} \Phi^T & \Phi_3^T \\ \mathbf{0} & \mathbf{D} \end{bmatrix} \begin{bmatrix} \mathcal{A} & \mathcal{B} \\ \mathbf{0} & \mathbf{0} \end{bmatrix} = \begin{bmatrix} \Lambda & \mathbf{0} \\ \mathbf{0} & \mathbf{0} \end{bmatrix} \begin{bmatrix} \Phi^T & \Phi_3^T \\ \mathbf{0} & \mathbf{D} \end{bmatrix} \tag{2.151}$$

i.e. as compared to (2.147), the left eigenvectors Φ^T are augmented with Φ_3^T , and new integrator modes $[\mathbf{0}, \mathbf{D}]$ added, where the diagonal matrix $\mathbf{D}$ ensures that the new left and right integrator eigenvectors are normalised consistently with the other eigenvectors. The controllability of the non-integrator mode i is given by

$$\frac{\pi}{N}\sqrt{\begin{bmatrix} \phi_i^T & \phi_{3,i}^T \end{bmatrix} \begin{bmatrix} \mathbf{0} \\ \mathbf{I} \end{bmatrix} \begin{bmatrix} \mathbf{0} & \mathbf{I} \end{bmatrix} \begin{bmatrix} \phi_i \\ \phi_{3,i} \end{bmatrix}} \tag{2.152}$$

which simplifies to

$$\frac{\pi}{N}\sqrt{\phi_{3,i}^T \phi_{3,i}} \tag{2.153}$$

Now from (2.151) $\Phi^T \mathcal{B} = \Lambda \Phi_3^T$, so $\phi_{3,i} = \mathcal{B}^T \phi_i / \lambda_i^T$ and so the controllability of mode i is

$$\frac{\pi}{N}\sqrt{\phi_i^T \mathcal{B}\mathcal{B}^T \phi_i / \left(\lambda_i^T \lambda_i\right)} \tag{2.154}$$

Thus compared to the controllability, $\pi/N\sqrt{\phi_i^T \mathcal{B}\mathcal{B}^T \phi_i}$ of (2.147) the controllability of original mode i changes by a factor of $1/\sqrt{\lambda_i^T \lambda_i}$. If the eigenvalue λ_i of a mode has a magnitude smaller than unity, it is possible to improve the controllability by placing integrators on the system inputs.

This simple analysis shows how the introduction of integrators into a system can leave the observability unchanged, and yet alter the controllability. This analysis

is not strictly applicable to Bewley's model, since the control input is related to the state variables by

$$\dot{\mathcal{U}} = \mathcal{E}\mathcal{X} + \mathcal{F}\mathcal{U} \tag{2.155}$$

from (2.123) and the equations become

$$\begin{aligned} \begin{pmatrix} \dot{\mathcal{X}} \\ \dot{\mathcal{U}} \end{pmatrix} &= \begin{pmatrix} \mathcal{A} - \mathcal{B}_2\mathcal{E} & \mathcal{B} - \mathcal{B}_2\mathcal{F} \\ \mathbf{0} & \mathbf{0} \end{pmatrix} \begin{pmatrix} \mathcal{X} \\ \mathcal{U} \end{pmatrix} + \begin{pmatrix} \mathcal{B}_2 \\ \mathbf{I} \end{pmatrix} \dot{\mathcal{U}} \\ \mathcal{Y} &= \begin{pmatrix} \mathcal{C} & \mathcal{D} \end{pmatrix} \begin{pmatrix} \mathcal{X} \\ \mathcal{U} \end{pmatrix} \end{aligned} \tag{2.156}$$

upon introduction of integrators to make $\mathcal{U}$ a state variable. $\mathcal{B}_2$ is the control derivative input matrix, which can be incorporated into the previous controllability analysis in a straightforward manner. However, because the system matrix gains the extra term $\mathcal{B}_2\mathcal{E}$, it is not straightforward to predict the effects on observability and controllability of changing to the integrator form.

Regarding Bewley's model, the extra system matrix term does not alter the first 30 eigenmodes significantly, but does alter the left eigenvectors greatly.

Observability and Discretisation

Figure 2.29 shows the case 1 u mode 1 to 20 wall details for discretisations of N=50,70,100 and 130. It can be seen that the N=100 and 130 results are in agreement and thus N=100 can be taken as converged in terms of wall gradient for modes 1 to 20. It is also evident that from mode 9 on, the N=50 discretization produces wall gradients that are too high, and that the N=70 discretization is not converged at mode 18. This correlates with figure 2.30 of the corresponding observabilities, where the N=100 and N=130 results are converged, as far as mode 40, but the N=50 results are over-estimates of observability from mode 9 onward. (Modes 5 and 8 also have overestimated observability, but its magnitude is too small to detect in figure 2.29.) Discretisation N=70 is not converged in terms of observability above mode 15, which is slightly different to the degree of convergence as measured in terms of wall gradients, and shows greater sensitivity of observability to convergence, as might be expected, since graphical wall gradients are difficult to interpret accurately when near vertical. Both measures indicate non-convergence at mode 18 and beyond.

It may be concluded that accurate measurement modelling is dependent on accurate gradient information close to the wall, and this requires a high level of discretisation, approximately $N = 100$, to accurately represent the gradient of the first 20 modes of case 1. Since pressure measurements (2.51) require higher derivatives at the wall, modelling them accurately is likely to require even higher levels of discretisation.

Investigation of Left Eigenvectors

It can be shown that system non-normality leads to increased magnitudes of the left eigenvectors, and thus, all other things being equal, larger controllability. First a procedure is presented for computing individual left eigenvectors.

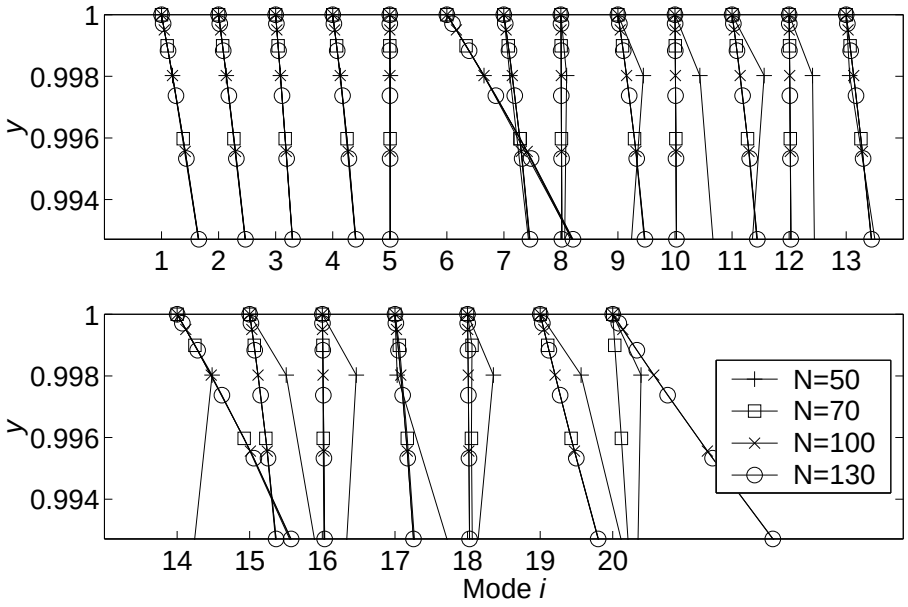

Figure 2.29: Case 1 Open-Loop Variation of $|u|$ Mode Detail at Wall with Discretisation N

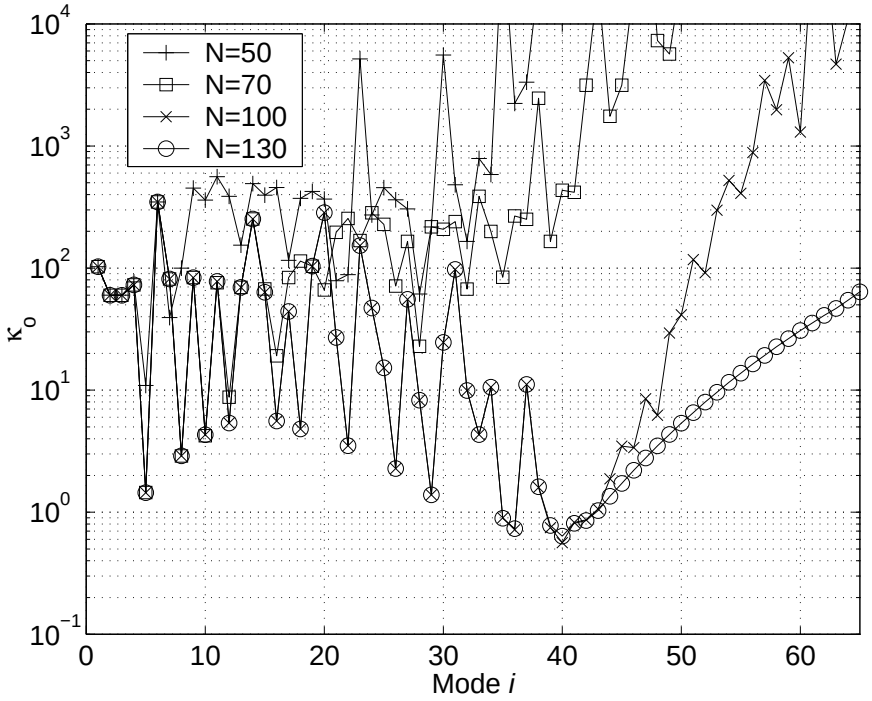

Figure 2.30: Case 1 Open-Loop Variation of Observability with Discretization N

The left eigenvector matrix Φ^T may be computed via the inverse of the right eigenvector matrix, Ψ, since $\Phi^T\Psi = \mathbf{I}N/\pi$. Any individual left eigenvector may also be computed by a procedure akin to Gram-Schmidt orthogonalization (Råde and Westergren, 1999, p104) as follows. Since ϕ_i is perpendicular to all ψ_j, except $j = i$

$$\phi_i = f \prod_{j=1, j\neq i}^{N} \psi_j \tag{2.157}$$

$$\psi_i^T \phi_i = \frac{N}{\pi} \tag{2.158}$$

where f is a normalising scalar, and Π represents the product of $(N-1)$ N-dimensional vectors which is orthogonal to each of them, extending the concept of the vector product beyond 3 dimensions. Premultiplying (2.157) by ψ_i^T, and substituting in (2.158) gives

$$f = \frac{N}{\pi} \frac{1}{\psi_i^T \prod_{j=1, j\neq i}^{N} \psi_j} \tag{2.159}$$

and substituting for f in (2.157) gives an expression for the left eigenvector ϕ_i

$$\phi_i = \frac{N}{\pi} \frac{1}{\psi_i^T \prod_{j=1, j\neq i}^{N} \psi_j} \prod_{j=1, j\neq i}^{N} \psi_j \tag{2.160}$$

The procedure is as follows. First ϕ_i is initialised to $[1, 1, 1, \dots]^T$, and then since ϕ_i is perpendicular to ψ_j, for $j \neq i$, any components in direction ψ_j are subtracted, both from ϕ_i and $\psi_{k,k>j}$

$$\phi_i = \phi_i - \frac{\pi}{N} \psi_j^T \phi_i \psi_j \quad \forall j \neq i \tag{2.161}$$

$$\psi_k = \frac{\psi_k - \psi_j^T \psi_k \psi_j}{\left|\psi_k - \psi_j^T \psi_k \psi_j\right|} \sqrt{\frac{N}{\pi}} \quad \forall k > j \tag{2.162}$$

where π/N appears in (2.161) due to the chosen normalisation of the dot product of left and right eigenvectors, and ψ_k is renormalised in (2.162). Finally ϕ_i must be normalised such that $\phi_i^T \psi_i = N/\pi$. This procedure produces ϕ_i within 10^{-8} of those from matrix inversion.

This approach also shows how the magnitude of left eigenvectors can be greater than the corresponding right eigenvector, $\sqrt{N/\pi}$, when the right eigenvectors are non-normal, as follows. Now

$$\psi_i^T \psi_j = \frac{N}{\pi} \cos(\theta) \tag{2.163}$$

where θ is the angle between ψ_i and ψ_j. Also

$$\phi_i^T \psi_i = \left|\phi_i^T\right| |\psi_i| \cos(\alpha) \tag{2.164}$$

where α is the angle between ϕ_i and ψ_i, but

$$\phi_i^T \psi_i = \frac{N}{\pi} \tag{2.165}$$

and $|\psi_j| = \sqrt{N/\pi}$ from (2.163), thus

$$\left|\phi_i^T\right| = \frac{1}{\cos(\alpha)}\sqrt{\frac{N}{\pi}} \tag{2.166}$$

As ψ_i lies on a cone of semi-angle θ about ψ_j, and yet ϕ_i is perpendicular to ψ_j, then

$$\frac{\pi}{2} - \theta \leq \alpha \leq \frac{\pi}{2} + \theta \tag{2.167}$$

If θ is small

$$\cos\left(\frac{\pi}{2} + \theta\right) \leq \cos(\alpha) \leq \cos\left(\frac{\pi}{2} - \theta\right) \tag{2.168}$$

or

$$-\sin(\theta) \leq \cos(\alpha) \leq \sin(\theta) \tag{2.169}$$

Now from (2.163) and (2.166)

$$\sin(\theta) = \sqrt{1 - \frac{\pi}{N}\psi_i^T\psi_j} \tag{2.170}$$

$$\cos(\alpha) = \frac{1}{|\phi_i^T|}\sqrt{\frac{N}{\pi}} \tag{2.171}$$

Substituting these in (2.169), we have finally

$$|\phi_i| \geq \sqrt{\frac{N}{\pi}}\frac{1}{\sqrt{1 - \psi_i^T\psi_j\pi/N}} \forall j \neq i \tag{2.172}$$

Thus the magnitude of the i^{th} left eigenvector $|\phi_i|$ is greater than that of the right ($|\psi_i| = \sqrt{N/\pi}$), by a factor depending on the highest non-normality of the right eigenvector, and thus, all other things being equal, larger controllability follows from non-normality. In practice this lower bound on $|\phi_i|$ is conservative for the large systems employed here.

2.9 Conclusions

This chapter has derived a linear state-space representation of linear spatially periodic perturbations in plane Poiseuille flow. The Navier-Stokes equations were presented and linearised about the base flow, and suitably reformulated into wall-normal velocity and vorticity form in sections 2.2 and 2.3.

Section 2.4 described the discretisation of the linearised equations in the streamwise, spanwise and wall-normal directions. Following the description of Fourier streamwise and spanwise discretisation of the equations and wall shear stress measurements, the Fourier discretised form of wall pressure measurements avoiding the inversion of a Laplacian was derived. It was seen that pressure measurements involve higher wall-normal derivatives of the velocity and vorticity perturbations than shear stress measurements do. It may be concluded that state-space models

based on pressure measurements will require more careful wall-normal discretisation to achieve the same accuracy as those based on shear stress measurements.

This section also drew an important distinction between interpolating (cardinal function) and polynomial (coefficient) forms of Chebyshev collocation for wall-normal discretisation. The polynomial form and its derivatives are amenable to approximation by truncation of the highest order terms, but derivatives of the interpolating form are very sensitive to the loss of data at any collocation points. The introduction of wall-transpiration boundary conditions into the fully discretised equations was described in section 2.5, and the transformation to an inhomogeneous form with homogeneous boundary conditions. The homogeneous boundary conditions were fulfilled by the use of the recombined Chebyshev polynomials to be presented in chapter 3.

In section 2.6, the inhomogeneous terms were extracted as the control inputs during manipulation of the equations into state-space form. The introduction of integrators during the manipulation was apparent, and their associated eigenvectors were shown to be steady-state modes associated with transpiration from either wall.

The system of state-space equations was generated by partitioning, then inversion of the Laplacian operator. This manipulation of the equations was also performed on the interpolating model of Bewley and Liu (1998) as an alternative to inversion then partitioning, and the two manipulations were shown to be consistent, even though the latter generates no integrator modes. The application of partitioning then inversion to the form produced by Bewley did not remove the spurious eigenvalues associated with that form. This is consistent with the accepted view that the spurious eigenvalues found by Bewley are caused by the particular application of the Neumann boundary conditions.

Section 2.7 described the two test cases. A real state-space model for case 1 was implemented by splitting the equations into real and imaginary parts, and it was demonstrated that the split caused the system eigenvalues to be joined by their conjugates, and expressions for the eigenvectors of the split system were derived. Furthermore, it was shown how the eigenvectors associated with the conjugate modes evaluate as zero in terms of velocity and vorticity. Regarding test case 2, section 2.7 showed how it may be implemented as a real system in terms of imaginary velocity and real vorticity components, thus reducing the system size from approximately $(2N) \times (2N)$ to $N \times N$.

Section 2.8 showed how the singular values of the state-space system generated converge up to ever higher frequencies as the wall-normal discretisation N is refined. The first 32 system eigenvalues for discretisation $N = 100$ on case 1 were found to compare well with published data, as compared to the 15 quoted in earlier works, and the use of Boyd's ordinal differences (Boyd, 2001, p139) showed that no spurious modes were present. The eigenvector of the case 1 unstable mode was found to compare well with published data, and the velocity flow-field from the integrator modes was plotted to confirm that they do represent steady transpiration.

Although many techniques exist for the reduction of model size, for example balanced residualisation and truncation (Skogestad and Postlethwaite, 1996, p452),

none have been applied here, since the controller performance criteria to be applied is the minimisation of the energy growth of the system, and the calculation of the system energy requires that the state variables remain physically meaningful.

Taking the extra integrator modes into account, good agreement with Bewley's observability (Bewley and Liu, 1998), based on right eigenvectors, was shown for both test cases, and a clear correlation established between eigenmode wall gradient and its observability. Good agreement was also achieved for case 1 with Bewley's controllability, based on left eigenvectors, but not for case 2.

Bewley's model and open loop results were reproduced. When his model was recast into partition-then-inversion form, with its associated integrators, it was found to produce observability and controllability in good agreement with the model here developed, demonstrating that the form was the cause of the discrepancy in case 2 controllability.

This section also showed that convergence of wall-gradients and of observability requires a high level of discretisation N, the wall gradient being accurate only with collocation points very close to the wall. The poor detection of modes in the centre of the channel via measurements very close to the channel walls was found by Bewley and Liu (1998, p328), and these results quantify the discretisation required. For case 2, the gradient of $\partial w/\partial y$ at the wall was found to be small and contribute little to observability. This explains the lack of consequences from the discrepancy found in the measurements, in terms of wall-normal velocity and vorticity, in equation (2.48).

Section 2.8 also investigated the effect of input integrators on system controllability and observability. It was demonstrated how integrators have no effect on the observability of the mode i, but alter its controllability by a factor $1/\sqrt{\lambda_i^T \lambda_i}$, where λ_i is its eigenvalue. This result is believed to be novel but is not applicable to the current systems, since the integrators do not act purely on the inputs.

Finally this section introduced a procedure for the calculation of individual left eigenvectors, and it was demonstrated that the magnitude of left eigenvectors is greater than that of the right, when the right eigenvectors are non-normal. All other things being equal, this would lead to larger controllability in non-normal systems.

Thus this chapter has described the development of a polynomial-form spectral state-space model of linearised plane Poiseuille flow which is free of spurious modes and which has been shown to be consistent with previous models in terms of eigenvalues, observability and controllability and yet is also amenable to approximation by truncation of the polynomial coefficients, for use in controller synthesis and simulation in chapter 4. The zero eigenvalue modes of the model have been shown to correspond to steady-state sinusoidal transpiration, and thus the flow-field of linearised transpiration has been determined, as an aid to verifying subsequent computational fluid dynamics calculations. The convergence of the model dynamics with discretisation has been investigated, and the slow convergence of observability traced to the need for fine discretization of the velocity profile at the wall, in order to determine the appropriate discretisation for use in chapter 4. Pressure measurements have been derived and shown to require still finer discretisation than wall shear stress measurements. A method for halving the dimensions

of the discretised model for test case 2, in order to reduce the resources required for subsequent controller synthesis and simulation, has also been presented.

Chapter 3

Wall-Normal Direction Discretisation

3.1 Introduction

This chapter describes in detail the discretisation of the model in the wall-normal direction, as introduced in section 2.4.4. For plane Poiseuille flow, the wall-normal direction is bounded, unlike the streamwise and spanwise directions. The inhomogeneous (non-zero at the walls) component of wall-normal velocity is extracted to form the control input. Whereas for the streamwise and spanwise boundaries periodic boundary conditions on velocity and vorticity suffice, for the wall boundaries the boundary conditions on the vorticity are Dirichlet, and on the remaining homogeneous component of wall-normal velocity they are Dirichlet and Neumann. The non-periodic behaviour in the wall-normal direction is not decoupled by wavenumber but rather represented by a modified Chebyshev basis evaluated at a number of collocation points, in order to form a system of equations.

Section 3.2 presents the equations to be discretised, and proceeds to discretise them by spectral collocation. In section 3.3 the requirements of a valid linear algebraic basis are stated, and Chebyshev basis functions are described. Basis modification in order to impose the boundary conditions is then introduced. The tools used for basis modification, namely matrix operations and partitioning, are described in section 3.4.

In section 3.5 four methods of basis modification are described. The first is due to Heinrichs (1989) and the second by Joshi (1996). The third is a combined method, partly as described by Boyd (2001, p113,143) and partly believed to be novel. The fourth and final method is also a combined method, partly as described by Boyd (2001, p113,143) and partly as described by Weideman and Reddy (2000, p499).

Section 3.6 compares condition numbers of various derivative matrices which arise in the discretised system, for each of the four methods. Finally section 3.7 draws conclusions about the methods of basis modification.

3.2 Spectral Collocation

3.2.1 Equations Discretised in Streamwise and Spanwise Directions

Once the Fourier assumption has been applied in the x and z dimensions, the linearised plane Poiseuille flow problem reduces to one spatial dimensional variation, in the wall-normal (y) direction, plus time variation, as shown in equations (2.34) and (2.35), rearranged here with the time variations on the left as

$$\frac{\jmath}{\alpha}\left(\frac{\partial^3\tilde{v}}{\partial y^2\partial t}-k^2\frac{\partial\tilde{v}}{\partial t}\right) = \left(-U_b k^2-\frac{\partial^2 U_b}{\partial y^2}-\frac{k^4}{\jmath R\alpha}\right)\tilde{v}+\left(U_b+\frac{2k^2}{\jmath R\alpha}\right)\frac{\partial^2\tilde{v}}{\partial y^2}-\frac{1}{\jmath R\alpha}\frac{\partial^4\tilde{v}}{\partial y^4} \tag{3.1}$$

$$-\frac{\partial\tilde{\eta}}{\partial t} = \left(\jmath\alpha U_b+\frac{k^2}{R}\right)\tilde{\eta}-\frac{1}{R}\frac{\partial^2\tilde{\eta}}{\partial y^2}+\jmath\beta\tilde{v}\frac{\partial U_b}{\partial y} \tag{3.2}$$

The equations may be written more succinctly, using D to represent the operator $\partial/\partial y$ and $\dot{}$ to represent $\partial/\partial t$

$$\begin{aligned}\left(D^2-k^2\right)\dot{\tilde{v}} &= \left(f_1+f_2D^2+f_3D^4\right)\tilde{v}\\ \dot{\tilde{\eta}} &= \left(f_4+f_5D^2\right)\tilde{\eta}+f_6\tilde{v}\end{aligned} \tag{3.3}$$

where $f_1,\ldots,f_6$ are known functions of parameters α,β,R and dimension y alone.

3.2.2 Subscript Convention

The collocation may be expressed in a polynomial function basis or a cardinal function (interpolating) basis. The usual subscript convention for collocation is $n=0$ to N. However, for the remainder of this chapter the convention $m=1$ to M is used, to assist in the application of linear algebra, where m in $\mathbb{R}^m$ is conventionally 1 for a one-dimensional space. Thus $m=n+1$ and $M=N+1$.

3.2.3 Cardinal or Interpolating Function Basis

In the spectral collocation cardinal function method the variables $\tilde{v}$ and $\tilde{\eta}$ are interpolated at the collocation points y_m, chosen to enhance the accuracy of the procedure, by the M cardinal functions C_m e.g.

$$\begin{aligned}\tilde{v}_M &= \sum_{m=1}^{M} C_m(y)\tilde{v}(y_m)\\ \tilde{\eta}_M &= \sum_{m=1}^{M} C_m(y)\tilde{\eta}(y_m)\end{aligned} \tag{3.4}$$

as described by Gottlieb et al. (1984, p13) where $\tilde{v}_M$ and $\tilde{\eta}_M$ are approximations to $\tilde{v}$ and $\tilde{\eta}$ respectively, and the unknowns become the interpolated values $\tilde{v}(y_m)$.

3.2.4 Polynomial Basis

In the spectral collocation polynomial function method the variables $\tilde{v}$ and $\tilde{\eta}$ are approximated by a sum of $m = 1, \ldots, M$ spectral basis functions $\Gamma_m(y)$, weighted by unknown spectral coefficients a_m e.g.

$$\begin{aligned} \tilde{v}_M &= \sum_{m=1}^{M} \Gamma_m(y) a_{v,m} \\ \tilde{\eta}_M &= \sum_{m=1}^{M} \Gamma_m(y) a_{\eta,m} \end{aligned} \tag{3.5}$$

A zero residual is enforced at a number of collocation points y_m and the unknowns become the spectral coefficients.

The cardinal and polynomial methods are equivalent (Boyd, 2001, p 115), although they lead to different state variables in the state-space form, with important consequences (see section 4.2.1). Here the polynomial method is used, with Chebyshev spectral basis functions.

$\tilde{v}_M(y_m)$ and $\tilde{\eta}_M(y_m)$ are good approximations to $\tilde{v}(y_m)$ and $\tilde{\eta}(y_m)$ in (3.4) and (3.5), since these equations just interpolate them. This good approximation is not necessarily the case for the solution of (3.1) and (3.2) where, for example, convergence with M, and accurate derivatives, are required for accurate results.

3.2.5 Chebyshev Functions

Here, the y variation is aperiodic, and so Chebyshev polynomials

$$\Gamma_m(y) = \cos\left((m-1)\arccos(y)\right) \tag{3.6}$$

are a suitable choice of basis function (Boyd, 2001), here presented using the current non-standard subscript convention. The Gauss-Lobatto points

$$y_m = \cos\left((m-1)\pi/(M-1)\right), m = 1, \ldots, M \tag{3.7}$$

are an appropriate choice for collocation. These points have range $-1 \leq y \leq 1$, since $y_1 = 1, y_M = -1$. This range is conveniently the same as the full non-dimensionalised channel height. This distribution is particularly favourable for spectral accuracy, and appropriately for the present problem, includes the boundary points (Peyret, 2002, p46).

The first four Chebyshev polynomials are

$$\begin{aligned} \Gamma_{m=1}(y) &= 1 \\ \Gamma_{m=2}(y) &= y \\ \Gamma_{m=3}(y) &= 2y^2 - 1 \\ \Gamma_{m=4}(y) &= 4y^3 - 3y \end{aligned}$$

Some Chebyshev polynomials and their derivatives are shown in figure 3.1. Their peak magnitudes, over all the collocation points for the domain, are also given.

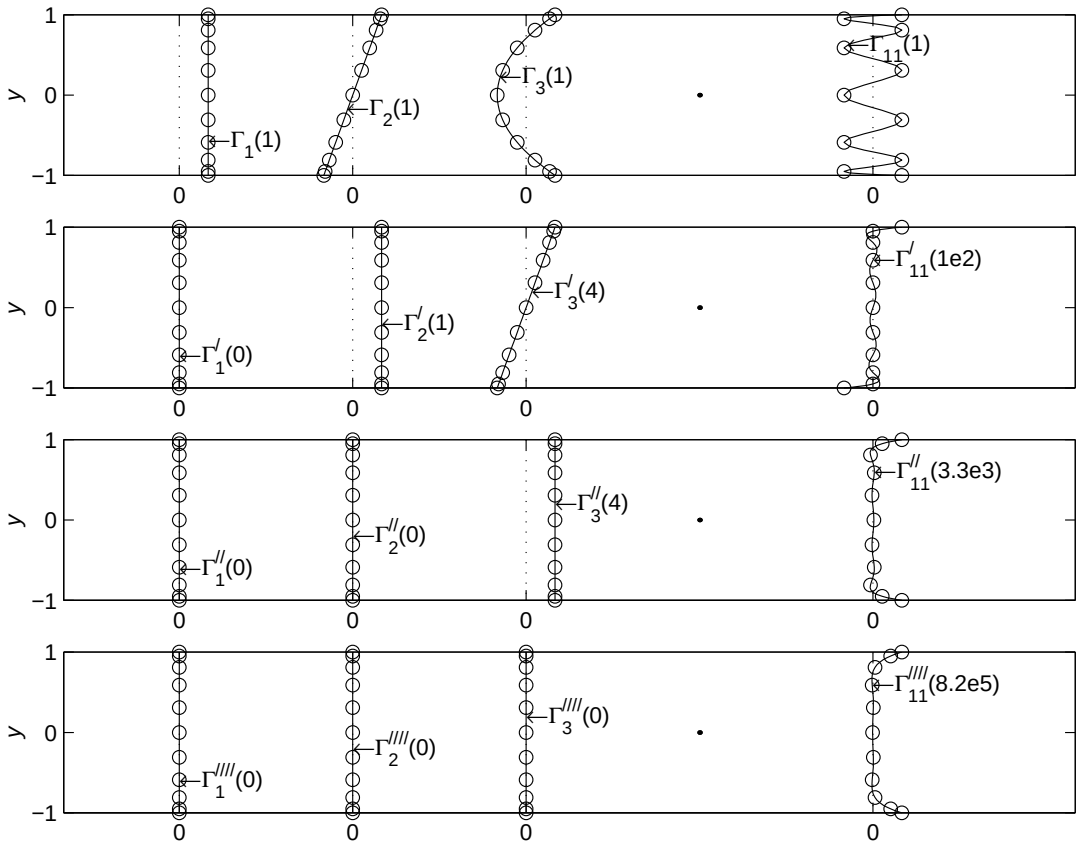

Figure 3.1: Chebyshev Basis Functions and Their Derivatives (Peak magnitudes over circled collocation points for $M = 11$ in parenthesis)

3.2.6 Evaluation at Collocation Points

The discretised form of $\tilde{v}$ is the values at the collocation points

$$\begin{pmatrix} \tilde{v}_M(y_1,t) \\ \vdots \\ \tilde{v}_M(y_m,t) \\ \vdots \\ \tilde{v}_M(y_M,t) \end{pmatrix} = \begin{bmatrix} \Gamma_1(y_1) & \dots & \Gamma_m(y_1) & \dots & \Gamma_M(y_1) \\ \vdots & \ddots & \vdots & \ddots & \vdots \\ \Gamma_1(y_m) & \dots & \Gamma_m(y_m) & \dots & \Gamma_M(y_m) \\ \vdots & \ddots & \vdots & \ddots & \vdots \\ \Gamma_1(y_M) & \dots & \Gamma_m(y_M) & \dots & \Gamma_M(y_M) \end{bmatrix} \begin{pmatrix} a_{v,1} \\ \vdots \\ a_{v,m} \\ \vdots \\ a_{v,M} \end{pmatrix}$$

$$\text{or} \quad \vec{\tilde{v}}_M = \mathbf{D0}\,\mathbf{a}_v(t) \tag{3.8}$$

and similarly for $\tilde{\eta}$

$$\begin{pmatrix} \tilde{\eta}_M(y_1,t) \\ \vdots \\ \tilde{\eta}_M(y_m,t) \\ \vdots \\ \tilde{\eta}_M(y_M,t) \end{pmatrix} = \begin{bmatrix} \Gamma_1(y_1) & \dots & \Gamma_m(y_1) & \dots & \Gamma_M(y_1) \\ \vdots & \ddots & \vdots & \ddots & \vdots \\ \Gamma_1(y_m) & \dots & \Gamma_m(y_m) & \dots & \Gamma_M(y_m) \\ \vdots & \ddots & \vdots & \ddots & \vdots \\ \Gamma_1(y_M) & \dots & \Gamma_m(y_M) & \dots & \Gamma_M(y_M) \end{bmatrix} \begin{pmatrix} a_{\eta,1} \\ \vdots \\ a_{\eta,m} \\ \vdots \\ a_{\eta,M} \end{pmatrix}$$

$$\text{or} \quad \vec{\tilde{\eta}}_M = \mathbf{D0}\,\mathbf{a}_\eta(t) \tag{3.9}$$

3.2.7 Derivatives at Collocation Points

The derivatives of the discretised variables with respect to y are obtained by differentiating the Chebyshev polynomials, for example (2.55), repeated here

$$\begin{pmatrix} \tilde{v}'_M(y_1,t) \\ \vdots \\ \tilde{v}'_M(y_m,t) \\ \vdots \\ \tilde{v}'_M(y_M,t) \end{pmatrix} = \begin{bmatrix} \Gamma_1(y_1)' & \dots & \Gamma_m(y_1)' & \dots & \Gamma_M(y_1)' \\ \vdots & \ddots & \vdots & \ddots & \vdots \\ \Gamma_1(y_m)' & \dots & \Gamma_m(y_m)' & \dots & \Gamma_M(y_m)' \\ \vdots & \ddots & \vdots & \ddots & \vdots \\ \Gamma_1(y_M)' & \dots & \Gamma_m(y_M)' & \dots & \Gamma_M(y_M)' \end{bmatrix} \begin{pmatrix} a_{\eta,1} \\ \vdots \\ a_{\eta,m} \\ \vdots \\ a_{\eta,M} \end{pmatrix}$$

$$\text{or} \quad \vec{\tilde{v}}'_M = \mathbf{D1}\,\mathbf{a}_\eta(t) \tag{3.10}$$

and similarly for higher derivatives **D2** and **D4**. Recursion formulae are used for accurately calculating the derivatives of Chebyshev polynomials, e.g. as presented by Schmid and Henningson (2001, p485).

3.2.8 Discretised Form of Equations

In discretised form the equations (3.3) become

$$\begin{aligned} \left(\mathbf{D2} - k^2\mathbf{D0}\right)\dot{\mathbf{a}}_v &= \left(\mathbf{F}_1\mathbf{D0} + \mathbf{F}_2\mathbf{D2} + \mathbf{F}_3\mathbf{D4}\right)\mathbf{a}_v \\ \mathbf{D0}\dot{\mathbf{a}}_\eta &= \left(\mathbf{F}_4\mathbf{D0} + \mathbf{F}_5\mathbf{D2}\right)\mathbf{a}_\eta + \mathbf{F}_6\mathbf{D0}\mathbf{a}_v \end{aligned} \tag{3.11}$$

where $\mathbf{F}_1, \dots, \mathbf{F}_6$ are $\mathrm{diag}(f_1(y_m), m = 1, \dots, M), \dots, \mathrm{diag}(f_6(y_m), m = 1, \dots, M)$ respectively. The Laplacian term $\mathbf{L} = (\mathbf{D2} - k^2\mathbf{D0})$ is very poorly conditioned without boundary conditions applied, as noted by Bewley (2001, p23). In the

present context this is due to some of its columns being almost linearly dependent. For example and noting the present subscript convention and domain $-1 \leq y \leq 1$, for test case 1 $k = 1$, and thus column 1 is $\Gamma_1'' - \Gamma_1 = -1$, and column 3 is $\Gamma_3'' - \Gamma_3 = 5 - 2y^2$, similarly column 2 is $\Gamma_2'' - \Gamma_2 = -y$ and column 4 is $\Gamma_4'' - \Gamma_4 = 27y - 4y^3$, with the result that the condition number is around 10^{19} for $M = 100$ in double precision arithmetic. Here the poor conditioning arises inevitably since double differentiation of high order Chebyshev polynomials yields large magnitude polynomials of lower degree (e.g. $\Gamma_4'' = 24y$), which are similar in shape to other lower order undifferentiated Chebyshev polynomials ($\Gamma_2 = y$), which themselves have small double differentials on account of their lower order ($\Gamma_2'' = 0$).

3.3 Linear Algebraic Bases

3.3.1 The Requirements of a Basis

When the basis functions are evaluated at the M collocation points, they generate a basis of vector space $\mathbb{R}^M$ in the linear algebraic sense. In this sense, bases fulfill several properties. If V is any vector space, and $B = \left\{\vec{b}_1, \ldots, \vec{b}_m, \ldots, \vec{b}_M\right\}$, then B is a basis for V if (Anton, 1991, p181)

1. B is linearly independent i.e.

$$\sum_{m=1}^{M} \alpha_m \vec{b}_m = \mathbf{0} \text{ only if } \alpha_m = 0 \forall m \tag{3.12}$$

2. B spans V, that is, every vector in V is expressible as a linear combination of the vectors $\vec{b}_m$ of B.

If follows that any vector $\vec{v} \in V$ is a unique weighted sum of the elements of B. All bases of the vector space $\mathbb{R}^M$ have M vectors of size $(M \times 1)$ i.e. are of dimension M, and any linearly independent set of M vectors in $\mathbb{R}^M$ span $\mathbb{R}^M$ and form a basis. The vectors of a basis need not be orthogonal, i.e. $\vec{b}_i^T \vec{b}_j = 0$ is not required.

3.3.2 The Unmodified Chebyshev Basis

D0 in the velocity and vorticity discretisation systems of equations (3.8,3.9) is represented in column form as

$$\left[\vec{\Gamma}_1(\mathbf{y}), \ldots, \vec{\Gamma}_M(\mathbf{y})\right] \tag{3.13}$$

where $\mathbf{y} = (y_1 \ldots y_M)^T$. Now the vectors $\text{diag}(1/2, 1, \ldots, 1, 1/2)\vec{\Gamma}_m(\mathbf{y}), m = 1, \ldots, M$ are orthogonal (Hamming, 1973) and thus linearly independent. Multiplication by $\text{diag}(1/2, 1, \ldots, 1, 1/2)$ is valid matrix row operation (see section 3.4) and thus the vectors $\vec{\Gamma}_m(\mathbf{y})$ are also linearly independent and therefore form a basis of $\mathbb{R}^M$. Thus they span the whole of vector space $\mathbb{R}^M$, any distribution of $\tilde{v}_M(\mathbf{y}, t)$ over the points $\mathbf{y}$ may be represented by the coefficients $\mathbf{a}_v$, and similarly for $\tilde{\eta}_M(\mathbf{y}, t)$.

3.3.3 Boundary Conditions and Basis Modification

In the uncontrolled channel, the boundary conditions are homogeneous Dirichlet conditions on $\tilde{\eta}$, and homogeneous Dirichlet and Neumann conditions on $\tilde{v}$

$$\begin{aligned} \tilde{\eta}(y_1,t) &= \tilde{\eta}(y_M,t) = 0 \\ \tilde{v}(y_1,t) &= \tilde{v}(y_M,t) = 0 \\ \frac{\partial \tilde{v}(y_1,t)}{\partial y} &= \frac{\partial \tilde{v}(y_M,t)}{\partial y} = 0 \end{aligned} \tag{3.14}$$

In the controlled channel, the boundary condition on $\tilde{v}$ is inhomogeneous, but may be converted to a homogeneous form by a change of variable, see section 2.5.1.

The boundary conditions require the equations (3.11) to be modified to

$$\begin{aligned} \left(\mathbf{D2}_{DN} - k^2\mathbf{D0}_{DN}\right)\dot{\mathbf{a}}_v &= \left(\mathbf{F}_1\mathbf{D0}_{DN} + \mathbf{F}_2\mathbf{D2}_{DN} + \mathbf{F}_3\mathbf{D4}_{DN}\right)\mathbf{a}_v \\ \mathbf{D0}_D\dot{\mathbf{a}}_\eta &= \left(\mathbf{F}_4\mathbf{D0}_D + \mathbf{F}_5\mathbf{D2}_D\right)\mathbf{a}_\eta + \mathbf{F}_6\mathbf{D0}_{DN}\mathbf{a}_v \end{aligned} \tag{3.15}$$

where subscripts $_D$ and $_N$ show matrices where the Dirichlet and Neumann boundary conditions are required respectively. When a cardinal function basis is used, it is recommended practice to only apply the Dirichlet boundary conditions to the term $(\mathbf{D2}_{DN} - k^2\mathbf{D0}_{DN})$ of the velocity equation in (3.15), as this term is only second order (Boyd, 2001, p141). This is not appropriate when the polynomial basis is used, as the spectral coefficients must be consistent throughout the system.

There are two strategies for imposing these homogeneous boundary conditions, boundary bordering and basis modification, as described by Boyd (2001, p110). Boundary bordering involves the replacement of equations at the boundaries, $m = 1, m = M$, with equations that explicitly enforce the boundary conditions. Since the homogeneous boundary conditions are time invariant, this leads to the addition of algebraic constraints to the system, and can lead to spurious eigenvalues, for example see Schmid and Henningson (2001, p489).

Basis modification involves the replacement of the original basis functions with modified ones that each satisfy the homogeneous boundary conditions, and is the method adopted in the present work.

The Basis Modification Required on the Vorticity Representation

The first requirement of basis modification is to produce a vorticity system in which $\tilde{\eta}_M(y_1,t) = 0, \tilde{\eta}_M(y_M,t) = 0, \forall \mathbf{a}_\eta$, that is, the span of the new vorticity basis Θ is reduced to $\mathbb{R}^{M-2}$, a subspace of $\mathbb{R}^M$

$$\begin{aligned} \begin{pmatrix} \tilde{\eta}_M(y_1,t) = 0 \\ \tilde{\eta}_M(y_2,t) \\ \vdots \\ \tilde{\eta}_M(y_{M-1},t) \\ \tilde{\eta}_M(y_M,t) = 0 \end{pmatrix} &= \begin{bmatrix} \Theta_1(y_1) & \dots & \Theta_m(y_1) & \dots & \Theta_M(y_1) \\ \vdots & \ddots & \vdots & \ddots & \vdots \\ \Theta_1(y_m) & \dots & \Theta_m(y_m) & \dots & \Theta_M(y_m) \\ \vdots & \ddots & \vdots & \ddots & \vdots \\ \Theta_1(y_M) & \dots & \Theta_m(y_M) & \dots & \Theta_M(y_M) \end{bmatrix} \begin{pmatrix} a_{\eta,1} \\ \vdots \\ a_{\eta,m} \\ \vdots \\ a_{\eta,M} \end{pmatrix} \\ &\triangleq \mathbf{D0}_D\,\mathbf{a}_\eta(t) \end{aligned} \tag{3.16}$$

This may be achieved by ensuring $\Theta_m(y_1) = \Theta_m(y_M) = 0, \forall m$. In chapter 2, Θ is denoted Γ^D.

The Basis Modification Required on the Velocity Representation

The second requirement of basis modification is to produce a velocity system in which $\tilde{v}_M(y_1,t)=0, \tilde{v}_M(y_M,t)=0, \tilde{v}_M(y_1,t)'=0, \tilde{v}_M(y_M,t)'=0, \forall \mathbf{a}_v$ i.e.

$$\begin{pmatrix} \tilde{v}_M(y_1,t)=0 \\ \tilde{v}_M(y_2,t) \\ \vdots \\ \tilde{v}_M(y_{M-1},t) \\ \tilde{v}_M(y_M,t)=0 \end{pmatrix} = \begin{bmatrix} \Xi_1(y_1) & \dots & \Xi_m(y_1) & \dots & \Xi_M(y_1) \\ \vdots & \ddots & \vdots & \ddots & \vdots \\ \Xi_1(y_m) & \dots & \Xi_m(y_m) & \dots & \Xi_M(y_m) \\ \vdots & \ddots & \vdots & \ddots & \vdots \\ \Xi_1(y_M) & \dots & \Xi_m(y_M) & \dots & \Xi_M(y_M) \end{bmatrix} \begin{pmatrix} a_{v,1} \\ \vdots \\ a_{v,m} \\ \vdots \\ a_{v,M} \end{pmatrix}$$
$$\triangleq \mathbf{D0}_{DN}\,\mathbf{a}_v(t) \tag{3.17}$$

and

$$\begin{pmatrix} \tilde{v}_M(y_1,t)'=0 \\ \tilde{v}_M(y_2,t)' \\ \vdots \\ \tilde{v}_M(y_{M-1},t)' \\ \tilde{v}_M(y_M,t)'=0 \end{pmatrix} = \begin{bmatrix} \Xi_1(y_1)' & \dots & \Xi_m(y_1)' & \dots & \Xi_M(y_1)' \\ \vdots & \ddots & \vdots & \ddots & \vdots \\ \Xi_1(y_m)' & \dots & \Xi_m(y_m)' & \dots & \Xi_M(y_m)' \\ \vdots & \ddots & \vdots & \ddots & \vdots \\ \Xi_1(y_M)' & \dots & \Xi_m(y_M)' & \dots & \Xi_M(y_M)' \end{bmatrix} \begin{pmatrix} a_{v,1} \\ \vdots \\ a_{v,m} \\ \vdots \\ a_{v,M} \end{pmatrix}$$
$$\triangleq \mathbf{D1}_{DN}\,\mathbf{a}_v(t) \tag{3.18}$$

This may be achieved by ensuring $\Xi_m(y_1)=\Xi_m(y_M)=\Xi_m(y_1)'=\Xi_m(y_M)'=0, \forall m$. It is evident that the span of the new velocity basis Ξ is reduced to $\mathbb{R}^{M-2}$, by the Dirichlet conditions, $\tilde{v}_M(y_1,t)=0, \tilde{v}_M(y_M,t)=0$. In the limit $M\to\infty$ the Neumann conditions, $\tilde{v}_M(y_1,t)'=0, \tilde{v}_M(y_M,t)'=0$, produce $\tilde{v}_M(y_2,t)=0, \tilde{v}_M(y_{M-1},t)=0$, so new velocity basis Ξ is required to be reduced by a further 2 to $\mathbb{R}^{M-4}$ in the limiting case. In chapter 2, Ξ is denoted Γ^{DN}.

3.4 The Tools of Basis Modification

Basis modification is achieved by the sequential execution of a series of elementary matrix operations and partitions/deletions on the system.

3.4.1 Basis Modification via Elementary Matrix Operations

The elementary matrix row operations are (Cameron, 1998, p120)

1. Multiplication of a row by a non-zero constant.
2. Interchange of two rows.
3. Addition of a multiple of one row to another.

These operations represent manipulation of individual equations. The elementary matrix column operations are (Cameron, 1998, p125)

1. Multiplication of a column by a non-zero constant.

2. Interchange of two columns.

3. Addition of a multiple of one column to another.

These operations represent substitution of variables.

The elementary matrix operations produce an equivalent system, in the sense that the results of the modified system are the same as those of the original. Thus the elementary matrix operations do not modify the span of the basis or the linear independence of their vectors, although they may modify the directions of the vectors. In the present context this means that the elementary operations do not alter the distribution of $\tilde{v}_M(y_m, t)$ over the points y_m that may be represented by the coefficients $\mathbf{a}_v$, although the directions of $\Gamma_m(y_m), m = 1, \ldots, M$ change and also the values of $\mathbf{a}_v$ required to represent any particular distribution change, and similarly for $\tilde{\eta}_M(y_m, t)$.

It is noteworthy that the operations are applied sequentially, not simultaneously. For instance, simultaneously subtracting two rows or columns from one another will make any matrix singular.

3.4.2 Partitioning of Bases

If the elementary matrix operations are able to manipulate the vectors of a basis such that one vector alone is capable of producing an output at a particular y location, for instance

$$\begin{pmatrix} \tilde{v}_M(y_1,t) \\ \tilde{v}_M(y_2,t) \\ \vdots \\ \tilde{v}_M(y_M,t) \end{pmatrix} = \begin{bmatrix} \Xi_1(y_1) & 0 & \ldots & 0 \\ \Xi_1(y_2) & \Xi_2(y_2) & \ldots & \Xi_M(y_2) \\ \vdots & \vdots & \ddots & \vdots \\ \Xi_1(y_M) & \Xi_2(y_M) & \ldots & \Xi_M(y_M) \end{bmatrix} \begin{pmatrix} a_{v,1} \\ a_{v,2} \\ \vdots \\ a_{v,M} \end{pmatrix} \tag{3.19}$$

where modified vector $(\Xi_1(y_1) \ldots \Xi_1(y_m) \ldots \Xi_1(y_M))^T$ alone may cause $\tilde{v}_M(y_1, t)$ to be non-zero, it is possible to partition the system into

$$\begin{pmatrix} \tilde{v}_M(y_1,t) \end{pmatrix} = \begin{bmatrix} \Xi_1(y_1) \end{bmatrix} \begin{pmatrix} a_{v,1} \end{pmatrix} \tag{3.20}$$

and

$$\begin{pmatrix} \tilde{v}_M(y_2,t) \\ \vdots \\ \tilde{v}_M(y_M,t) \end{pmatrix} = \begin{bmatrix} \Xi_1(y_2) & \ldots & \Xi_M(y_2) \\ \vdots & \ddots & \vdots \\ \Xi_1(y_M) & \ldots & \Xi_M(y_M) \end{bmatrix} \begin{pmatrix} a_{v,1} \\ \vdots \\ a_{v,M} \end{pmatrix} \tag{3.21}$$

Now if $\tilde{v}_M(y_1, t)$ is required to be zero, $a_{v,1} = 0$ and system (3.20) is simply discarded. System (3.21) becomes

$$\begin{pmatrix} \tilde{v}_M(y_2,t) \\ \vdots \\ \tilde{v}_M(y_M,t) \end{pmatrix} = \begin{bmatrix} \Xi_2(y_2) & \ldots & \Xi_M(y_2) \\ \vdots & \ddots & \vdots \\ \Xi_2(y_M) & \ldots & \Xi_M(y_M) \end{bmatrix} \begin{pmatrix} a_{v,2} \\ \vdots \\ a_{v,M} \end{pmatrix} \tag{3.22}$$

Now since the array in (3.19) is square, the remaining condition for it to be a valid basis is linear independence (3.12), i.e. the only solutions of

$$\begin{bmatrix} \Xi_1(y_1) & 0 & \dots & 0 \\ \Xi_1(y_2) & \Xi_2(y_2) & \dots & \Xi_M(y_2) \\ \vdots & \vdots & \ddots & \vdots \\ \Xi_1(y_M) & \Xi_2(y_M) & \dots & \Xi_M(y_M) \end{bmatrix} \begin{pmatrix} \alpha_1 \\ \alpha_2 \\ \vdots \\ \alpha_M \end{pmatrix} = \begin{pmatrix} 0 \\ 0 \\ \vdots \\ 0 \end{pmatrix} \tag{3.23}$$

are $\alpha_i = 0, \forall i$. Inspection shows $\alpha_1 = 0$, and substituting this gives

$$\begin{bmatrix} \Xi_2(y_2) & \dots & \Xi_M(y_2) \\ \vdots & \ddots & \vdots \\ \Xi_2(y_M) & \dots & \Xi_M(y_M) \end{bmatrix} \begin{pmatrix} \alpha_2 \\ \vdots \\ \alpha_M \end{pmatrix} = \begin{pmatrix} 0 \\ \vdots \\ 0 \end{pmatrix} \tag{3.24}$$

which must have only the solution $\alpha_i = 0, \forall i$. Now this is the same condition that (3.22) requires to be linearly independent, and thus a basis for $\mathbb{R}^{M-1}$. That is to say if (3.19) is a valid basis for $\mathbb{R}^M$, then (3.22) is for $\mathbb{R}^{M-1}$.

Partitioning operations also maintain equivalence of the system of equations, but the deletion of equations may lead to approximations. Assuming $\tilde{v}_M(y_1, t) = 0$ is required, no approximation is involved here.

3.4.3 State-Space Form

To form the state-space form the equations (3.15) must be inverted to

$$\begin{aligned} \dot{\mathbf{a}}_v &= \mathbf{L}^{-1} \left(\mathbf{F}_1 \mathbf{D0}_{DN} + \mathbf{F}_2 \mathbf{D2}_{DN} + \mathbf{F}_3 \mathbf{D4}_{DN} \right) \mathbf{a}_v \\ \dot{\mathbf{a}}_\eta &= \mathbf{D0}_D^{-1} \left(\mathbf{F}_4 \mathbf{D0}_D + \mathbf{F}_5 \mathbf{D2}_D \right) \mathbf{a}_\eta + \mathbf{D0}_D^{-1} \mathbf{F}_6 \mathbf{D0}_{DN} \mathbf{a}_v \end{aligned} \tag{3.25}$$

Where the conditioning of $\mathbf{L} = (\mathbf{D2}_{DN} - k^2 \mathbf{D0}_{DN})$ is improved over that in (3.11) by the application of boundary conditions. The degree of improvement is the subject of the present study.

3.5 Methods of Basis Modification Considered

Four methods of basis modification are considered

3.5.1 Heinrichs' Method

Elementary Matrix Operations

The method described by Heinrichs (1989, 1991), involves multiplying each Chebyshev polynomial by another function f which has the required number of roots at $y = \pm 1$: one root for the Dirichlet boundary condition, two for the simultaneous Neumann and Dirichlet boundary conditions, and no other real roots in $[-1, 1]$. This multiplication is an invalid application of elementary matrix row operation 1, multiplication of a row by a non-zero constant. The fact that the constant is zero at the walls $y = \pm 1$, requires special consideration.

The simplest functions are $(1-y^2)$ for the Dirichlet condition, and $(1-y^2)^2$ for the Neumann condition also, although many other functions would suffice e.g. $(1-y^{2k})$ and $(1-y^{2k})^2$.

Using the simplest functions, the modified Chebyshev polynomials Θ and Ξ which enforce the Dirichlet and Dirichlet/Neumann boundary conditions respectively are

$$\begin{aligned} \Theta_m &= (1-y^2)\Gamma_m \\ \Xi_m &= (1-y^2)^2\Gamma_m \end{aligned} \tag{3.26}$$

These new bases are normalised to a peak value of approximately 1 at high m, since its components Γ_m and $(1-y^2)$ are so normalised.

The new basis has first derivatives

$$\begin{aligned} \Theta'_m &= -2y\Gamma_m + (1-y^2)\Gamma'_m \\ \Xi'_m &= 4y(y^2-1)\Gamma_m + (1-y^2)^2\Gamma'_m \end{aligned} \tag{3.27}$$

and second derivatives

$$\begin{aligned} \Theta''_m &= -2\Gamma_m - 4y\Gamma'_m + (1-y^2)\Gamma''_m \\ \Xi''_m &= (12y^2-4)\Gamma_m + 8y(y^2-1)\Gamma'_m + (1-y^2)^2\Gamma''_m \end{aligned} \tag{3.28}$$

Thus at the ends of the domain, $(y=\pm 1)$, the second derivatives become

$$\begin{aligned} \Theta''_m(\pm 1) &= -2\Gamma_m(\pm 1) \mp 4y\Gamma'_m(\pm 1) \\ \Xi''_m(\pm 1) &= 8\Gamma_m(\pm 1) \end{aligned} \tag{3.29}$$

It is noteworthy that $|\Xi_m(\pm 1)''|$ is a constant, for all m (see equation (3.40)).

The Span of the Transformed Basis

For the Dirichlet boundary condition, the new basis Θ has been generated by multiplying the rows of Γ by $1-y^2$. This is zero at the walls, and violates the condition of requiring a non-zero multiplicand, thus the span of the new basis may be less than $\mathbb{R}^M$. Inspection shows that the new column span is $\mathbb{R}^{M-2}$ at most, since no non-zero wall values can be generated. Similarly, the Dirichlet and Neumann basis Ξ has been generated by multiplication by $(1-y^2)^2$, which is zero at the walls, and inspection shows its span is $\mathbb{R}^{M-2}$ at most.

Partitioning Operations

The equations at the walls can be discarded, since the boundary condition is implicitly enforced, and thus the solution at the walls is already known. Thereafter Θ is an invalid basis, since it contains M vectors of length $(M-2)$, which cannot be linearly independent. An attempt to remedy this is made by discarding the highest two basis vectors, although this may not render the remaining vectors linearly independent. Thus the final span of the new basis may still be less than $\mathbb{R}^{M-2}$. The same reasoning is applied to the simultaneous Dirichlet and Neumann basis Ξ.

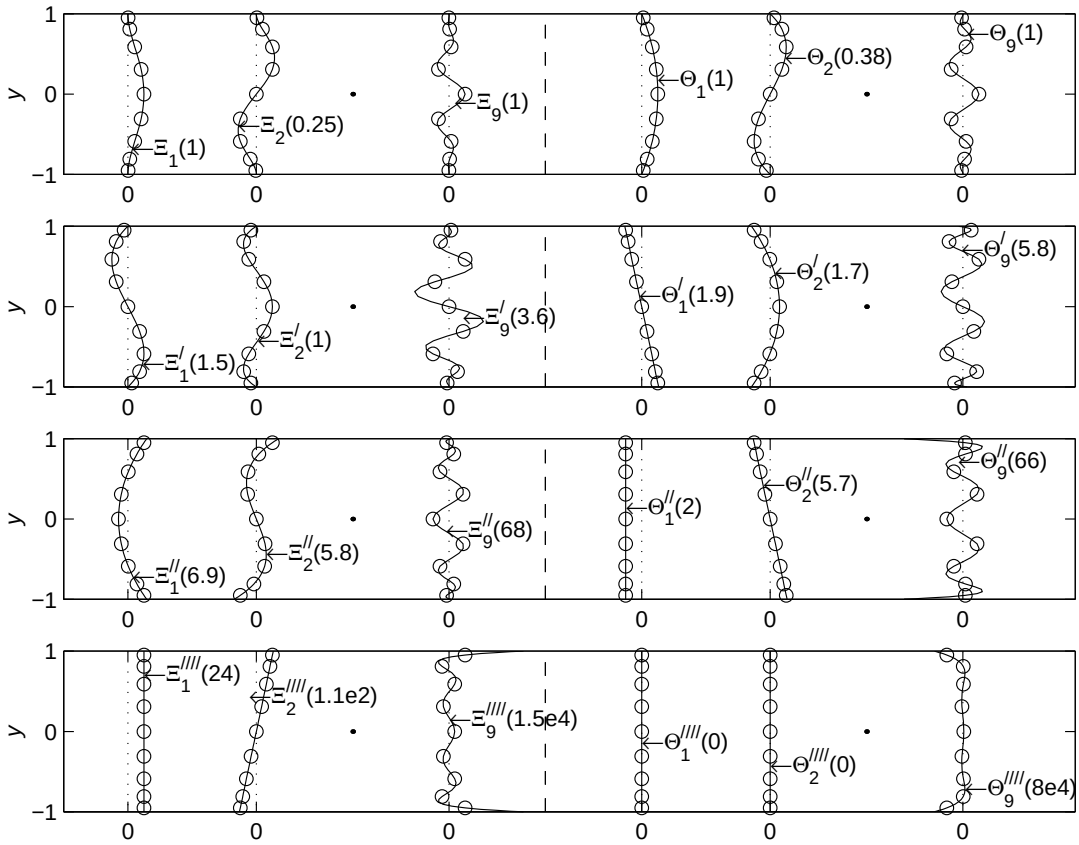

Figure 3.2: Heinrichs' Basis Functions and Their Derivatives (Peak magnitudes over circled relevant collocation points for $M = 11$ in parenthesis)

Derivative Matrices

Thus for this basis modification after partitioning, the zero derivative matrices of the state-space form (3.25) in terms of the basis functions are

$$\begin{aligned} \mathbf{D0}_D &= \begin{bmatrix} \Theta_1(y_2) & \dots & \Theta_{M-2}(y_2) \\ \vdots & \ddots & \vdots \\ \Theta_1(y_{M-1}) & \dots & \Theta_{M-2}(y_{M-1}) \end{bmatrix} \\ \mathbf{D0}_{DN} &= \begin{bmatrix} \Xi_1(y_2) & \dots & \Xi_{M-2}(y_2) \\ \vdots & \ddots & \vdots \\ \Xi_1(y_{M-1}) & \dots & \Xi_{M-2}(y_{M-1}) \end{bmatrix} \end{aligned} \tag{3.30}$$

and differentiation of Θ and Ξ by y yields the required higher derivative matrices, **D1**,**D2** and **D4**. Some of the basis functions and their derivatives are shown in figure 3.2.

3.5.2 Joshi's Method

Elementary Matrix Operations

The method described by Joshi (1996) applies only to the simultaneous Dirichlet and Neumann boundary conditions, and involves performing a recombination of sequences of 5 consecutive polynomials

$$\Xi_m \;=\; A\Gamma_m + B\Gamma_{m+1} + C\Gamma_{m+2} + D\Gamma_{m+3} + \Gamma_{m+4} \tag{3.31}$$

The coefficients A, B, C, D can be obtained by solving a linear system which enforces the Dirichlet and Neumann boundary conditions

$$\begin{bmatrix} \Gamma_m(y_1) & \Gamma_{m+1}(y_1) & \Gamma_{m+2}(y_1) & \Gamma_{m+3}(y_1) \\ \Gamma_m(y_1)' & \Gamma_{m+1}(y_1)' & \Gamma_{m+2}(y_1)' & \Gamma_{m+3}(y_1)' \\ \Gamma_m(y_M) & \Gamma_{m+1}(y_M) & \Gamma_{m+2}(y_M) & \Gamma_{m+3}(y_M) \\ \Gamma_m(y_M)' & \Gamma_{m+1}(y_M)' & \Gamma_{m+2}(y_M)' & \Gamma_{m+3}(y_M)' \end{bmatrix} \begin{pmatrix} A \\ B \\ C \\ D \end{pmatrix} = - \begin{pmatrix} \Gamma_{m+4}(y_1) \\ \Gamma_{m+4}(y_1)' \\ \Gamma_{m+4}(y_M) \\ \Gamma_{m+4}(y_M)' \end{pmatrix} \tag{3.32}$$

Some of Joshi's coefficients A, B, C, D are reproduced in table 3.1. Odd and even Chebyshev polynomials are uncoupled in the sense that the odd ones are symmetric and even ones are asymmetric (in the current subscript convention), thus coefficients B and D of opposite parity to A are always zero. Thus a combination of three polynomials of the same parity suffices to form Ξ in (3.31). By inspection it can be seen that $A = (m+2)/m, B = 0, C = -(2m+2)/m, D = 0$, and this can be verified since $\Gamma_m 1 = (m-1)^2$ and so the start gradient becomes $(m-1)^2(m+2)/m - (m+1)^2(2m+2)/m + (m+3)^2$ which equates to zero.

The basis modification appears to correspond to elementary matrix column operation 3, addition of a multiple of one column to another, but does not apply it validly, since the operations are not applied sequentially, but simultaneously: all of the original basis vectors are simultaneously transformed to the new basis vectors.

The final recombinations also present some difficulties. Joshi (1996) took no special measures, and used the procedure for Ξ_M (3.31) using $\Gamma_M, \ldots, \Gamma_{M+4}$ on

m	A	B	C	D
1	3	0	-4	0
2	2	0	-3	0
3	5/3	0	-8/3	0
4	3/2	0	-5/2	0
5	7/5	0	-12/5	0
6	4/3	0	-7/3	0
⋮	⋮	⋮	⋮	⋮
240	121/120	0	-241/120	0
241	243/241	0	-484/241	0

Table 3.1: Joshi's Coefficients

M collocation points. However, regarding the discretised equations, the values of Γ_{M+1} at collocation points $y_m = \cos\left((m-1)\pi/(M-1)\right), m = 1, \ldots, M$ are identical to those of Γ_{M-1}, as Γ_{M+1} aliases Γ_{M-1} at these points, and similarly $\Gamma_{M+2}, \Gamma_{M+3}, \Gamma_{M+4}$ alias $\Gamma_{M-2}, \Gamma_{M-3}, \Gamma_{M-4}$. This aliasing invalidates the basis, since not all vectors are linearly independent, and it makes $\mathbf{D0}_{DN}$ singular, and thus it is not possible to transform spectral velocity coefficients $a_{v,m}$ to velocities $v_M(y_m)$.

It is more appropriate to cycle the recombinations, for example such that

$$\Xi_{M-1} = A\Gamma_{M-1} + B\Gamma_M + C\Gamma_1 + D\Gamma_2 + \Gamma_3 \tag{3.33}$$

$$\Xi_M = A\Gamma_M + B\Gamma_1 + C\Gamma_2 + D\Gamma_3 + \Gamma_4 \tag{3.34}$$

and thus the use of Γ_m where $m > M$ is avoided, and $\mathbf{D0}_{DN}$ is not singular. This recycling is incorporated into the present work.

This basis modification is approximately $\Gamma_m - 2\Gamma_{m+2}$ at high m, and is normalised to a peak value of approximately 4 as shown by inspection of plots of the basis functions at the collocation points for high m (not shown).

The Span of the Transformed Basis

The use of an invalid sequence of elementary matrix operations produces no guarantees regarding the span of the new basis. This is a consequence of operating on all the basis vectors simultaneously. Inspection shows that the span is $\mathbb{R}^{M-2}$ at most because all vectors have zero first and last elements, due to the Dirichlet boundary condition, and is unable to represent velocity fields with non-zero wall velocities.

Partitioning Operations

The equations at the walls can be discarded, since the boundary condition is implicitly enforced, and thus the solution at the walls is already known. The highest two basis vectors are also discarded. There is no guarantee that the remaining vectors are linearly independent, and thus the final span of the basis may be less than $\mathbb{R}^{M-2}$.

Derivative Matrices

In terms of the basis functions, for this basis modification, the zero derivative matrices of the state-space form (3.25) are

$$\mathbf{D0}_{DN} = \begin{bmatrix} \Xi_1(y_2) & \ldots & \Xi_{M-2}(y_2) \\ \vdots & \ddots & \vdots \\ \Xi_1(y_{M-1}) & \ldots & \Xi_{M-2}(y_{M-1}) \end{bmatrix} \tag{3.35}$$

and differentiation yields the higher derivative matrices. Some of the basis functions and their derivatives are shown in figure 3.3. Unlike the other plots in this chapter, this plot uses linear interpolation between the collocation points. The other plots employ the lower basis functions from a higher order system to obtain

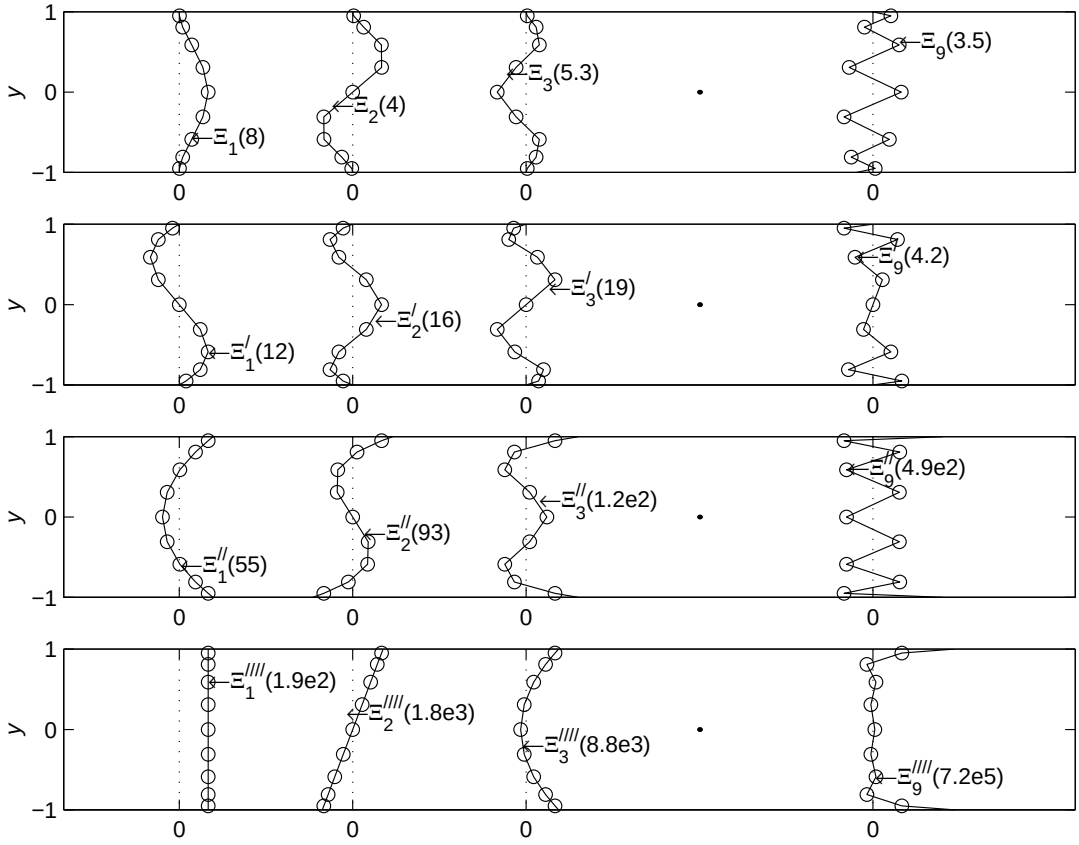

Figure 3.3: Joshi's Basis Functions and Their Derivatives (Peak magnitudes over circled relevant collocation points for $M = 11$ in parenthesis)

the spectral interpolation as this gives the data at more collocation points. However, for the present implementation of Joshi's method a particular basis function changes depending on whether it is the final one or not, so a basis function from a higher order system is not the same as when it is the last basis function in a lower order system.

3.5.3 Combined Method 1

The first combined method uses a standard method for the Dirichlet boundary condition, and derives a method for the combined Dirichlet and Neumann conditions as follows.

Elementary Matrix Operations

For the Dirichlet boundary condition, this recombination by Boyd (2001, p113,143) is used

$$\begin{aligned}
\Theta_1 &= \Gamma_{m=1} = 1 && (3.36)\\
\Theta_2 &= \Gamma_{m=2} = y && (3.37)\\
\Theta_{m>1,odd} &= \Gamma_m - \Gamma_1 && (3.38)\\
\Theta_{m>2,even} &= \Gamma_m - \Gamma_2 && (3.39)
\end{aligned}$$

This recombination employs elementary matrix column operation 3 on **D0**, addition of a multiple of one column to another, and thus yields a valid basis of $\mathbb{R}^M$. The basis is normalised to a peak value of approximately 2 at high m, by inspection of its components, and satisfies the homogeneous Dirichlet boundary condition for $m > 2$ since

$$\Gamma_m(\pm 1) = (\pm 1)^{m-1} \quad (3.40)$$

as shown by Gottlieb and Orszag (1993, p159) (with a change of parity associated with the present subscript convention), so

$$\begin{aligned}
\Gamma_{m_{odd}}(\pm 1) &= \Gamma_1(\pm 1)\\
\Gamma_{m_{even}}(\pm 1) &= \Gamma_2(\pm 1) && (3.41)
\end{aligned}$$

and thus

$$\Theta_{m>2}(\pm 1) = 0 \quad (3.42)$$

Boyd (2001, p143) points out that this recombination's second derivative is another Chebyshev polynomial, which may lead to poor conditioning. For the simultaneous Neumann and Dirichlet boundary conditions, this recombination is proposed, which extends Boyd's method for the Dirichlet boundary condition

$$\begin{aligned}
\Xi_1 &= \Gamma_1 && (3.43)\\
\Xi_2 &= \Gamma_2 && (3.44)\\
\Xi_3 &= \Gamma_3 - \Gamma_1 && (3.45)\\
\Xi_4 &= \Gamma_4 - \Gamma_2 && (3.46)\\
\Xi_{m>4,odd} &= (\Gamma_m - \Gamma_1) - \frac{(m-1)^2\,(\Gamma_{m-2} - \Gamma_1)}{(m-3)^2} && (3.47)\\
\Xi_{m>4,even} &= (\Gamma_m - \Gamma_2) - \frac{((m-1)^2 - 1)\,(\Gamma_{m-2} - \Gamma_2)}{(m-3)^2 - 1} && (3.48)
\end{aligned}$$

This recombination employs elementary matrix column operation 3, addition of a multiple of one column to another, which can be applied sequentially starting at Γ_M, and thus yields a valid basis. For $m > 2$, this recombination satisfies the homogeneous Dirichlet boundary conditions, since it is composed of terms from (3.39). For $m > 4$ it satisfies the homogeneous Neumann boundary condition since

$$\begin{aligned}
\Gamma_1'(\pm 1) &= 0\\
\Gamma_{m>1}'(\pm 1) &= (\pm 1)^{m-2}(m-1)^2 && (3.49)
\end{aligned}$$

as shown by Gottlieb and Orszag (1993, p159), so

$$\Xi'_{m>4,odd}(\pm 1) = (\pm 1)^{m-2}(m-1)^2 - \frac{(m-1)^2(\pm 1)^{m-4}(m-3)^2}{(m-3)^2} \quad (3.50)$$

$$\Xi'_{m>4,even}(\pm 1) = \left((m-1)^2 - 1\right) - \frac{\left((m-1)^2-1\right)\left((m-3)^2-1\right)}{(m-3)^2-1} \quad (3.51)$$

and thus

$$\Xi'_{m>4}(\pm 1) = 0 \quad (3.52)$$

For $m \leq 4$

$$\begin{aligned}
\Xi_1(\pm 1) &= 1 \\
\Xi_2(\pm 1) &= \pm 1 \\
\Xi_3(\pm 1) &= 0 \\
\Xi_4(\pm 1) &= 0 \\
\Xi'_1(\pm 1) &= 0 \\
\Xi'_2(\pm 1) &= 1 \\
\Xi'_3(\pm 1) &= \pm 4 \\
\Xi'_4(\pm 1) &= 8
\end{aligned} \quad (3.53)$$

This basis modification is approximately $\Gamma_m - \Gamma_{m-2}$ at high m, and is normalised to a peak value of approximately 2 as shown by inspection of plots of the basis functions at the collocation points for high m (not shown).

The Span of the Transformed Bases

The use of a valid sequence of elementary matrix operations guarantees that the span of the new bases are both $\mathbb{R}^M$.

Partitioning Operations

Both recombinations lead to valid bases, but neither fully enforce the boundary conditions, since

$$\begin{aligned}
&\Theta_{m\leq 2}(\pm 1) \neq 0 \\
&\Xi_{m\leq 2}(\pm 1) \neq 0 \\
&\Xi'_{m\leq 4}(\pm 1) \neq 0
\end{aligned} \quad (3.54)$$

Both $\Theta_{m\leq 2}$ and $\Xi_{m\leq 2}$ are the only vectors in their respective bases that generate non-zero wall vorticities and velocities. This presents an opportunity to form a basis for subspace $\mathbb{R}^{M-2}$ of $\mathbb{R}^M$, using partitioning as described in section 3.4.2. For vorticity the system becomes

$$\begin{pmatrix} \tilde{\eta}_M(y_2,t) \\ \vdots \\ \tilde{\eta}_M(y_{M-1},t) \end{pmatrix} = \begin{bmatrix} \Theta_3(y_2) & \dots & \Theta_M(y_2) \\ \vdots & \ddots & \vdots \\ \Theta_3(y_{M-1}) & \dots & \Theta_M(y_{M-1}) \end{bmatrix} \begin{pmatrix} a_{\eta,3} \\ \vdots \\ a_{\eta,M} \end{pmatrix} \quad (3.55)$$

and for velocity

$$\begin{pmatrix} \tilde{v}_M(y_2,t) \\ \vdots \\ \tilde{v}_M(y_{M-1},t) \end{pmatrix} = \begin{bmatrix} \Xi_3(y_2) & \dots & \Xi_M(y_2) \\ \vdots & \ddots & \vdots \\ \Xi_3(y_{M-1}) & \dots & \Xi_M(y_{M-1}) \end{bmatrix} \begin{pmatrix} a_{v,3} \\ \vdots \\ a_{v,M} \end{pmatrix} \tag{3.56}$$

These reduced new bases enforce the Dirichlet boundary condition, since Θ_1 and Θ_2 and Ξ_1 and Ξ_2 are absent. The system has lost the equations at the walls, but these are redundant, since $\tilde{v}$ and $\tilde{\eta}$ are zero there whether or not the equations are solved.

The reduced velocity basis Ξ does not enforce the required Neumann boundary condition, since Ξ_3 and Ξ_4 are still present. However, values of $\Xi_5(y_1)$ to $\Xi_M(y_1)$, and $\Xi_5(y_{M-1})$ to $\Xi_M(y_{M-1})$ are small for high M due to Ξ_5 to Ξ_M enforcing the Neumann boundary condition, and y_2 and y_{M-1} being very close to y_1 and y_M respectively, where the Dirichlet boundary condition is enforced. So the velocity system is actually

$$\begin{pmatrix} \tilde{v}_M(y_2,t) \\ \vdots \\ \tilde{v}_M(y_m,t) \\ \vdots \\ \tilde{v}_M(y_{M-1},t) \end{pmatrix} =$$

$$\begin{bmatrix} \Xi_3(y_2) & \Xi_4(y_2) & \Xi_5(y_2) \approx 0 & \dots & \Xi_M(y_2) \approx 0 \\ \Xi_3(y_3) & \Xi_4(y_3) & \Xi_5(y_3) & \dots & \Xi_M(y_3) \\ \vdots & \vdots & \vdots & \ddots & \vdots \\ \Xi_3(y_{M-2}) & \Xi_4(y_{M-2}) & \Xi_5(y_{M-2}) & \dots & \Xi_M(y_{M-1}) \\ \Xi_3(y_{M-1}) & \Xi_4(y_{M-1}) & \Xi_5(y_{M-1}) \approx 0 & \dots & \Xi_M(y_{M-1}) \approx 0 \end{bmatrix} \begin{pmatrix} a_{v,3} \\ \vdots \\ a_{v,m} \\ \vdots \\ a_{v,M} \end{pmatrix} \tag{3.57}$$

Now if $\Xi_5(y_2)$ to $\Xi_M(y_2)$, and $\Xi_5(y_{M-1})$ to $\Xi_M(y_{M-1})$ are small enough, then using partitioning as described in section 3.4.2 to produce

$$\begin{pmatrix} \tilde{v}_M(y_3,t) \\ \vdots \\ \tilde{v}_M(y_{M-2},t) \end{pmatrix} = \begin{bmatrix} \Xi_5(y_3) & \dots & \Xi_M(y_3) \\ \vdots & \ddots & \vdots \\ \Xi_5(y_{M-2}) & \dots & \Xi_M(y_{M-2}) \end{bmatrix} \begin{pmatrix} a_{v,5} \\ \vdots \\ a_{v,M} \end{pmatrix} \tag{3.58}$$

will be a valid basis for $\mathbb{R}^{M-4}$.

Now $y_1 - y_2 = 1 - \cos(\pi/(M-1))$ from (3.7), so for large M then $y_1 - y_2 \approx (\pi/(M-1))^2/2$ e.g. for $M = 101$ when $y_1 - y_2 \approx 5 \times 10^{-4}$, and so the approximation would seem reasonable. Thus the reduced basis is therefore adopted, and in so doing the next-to-wall equations are also discarded and thus the residual is not forced to zero at the y_2 and y_{M-1} collocation points, but since they are so close to the walls, the effect on the system of discretised equations is small.

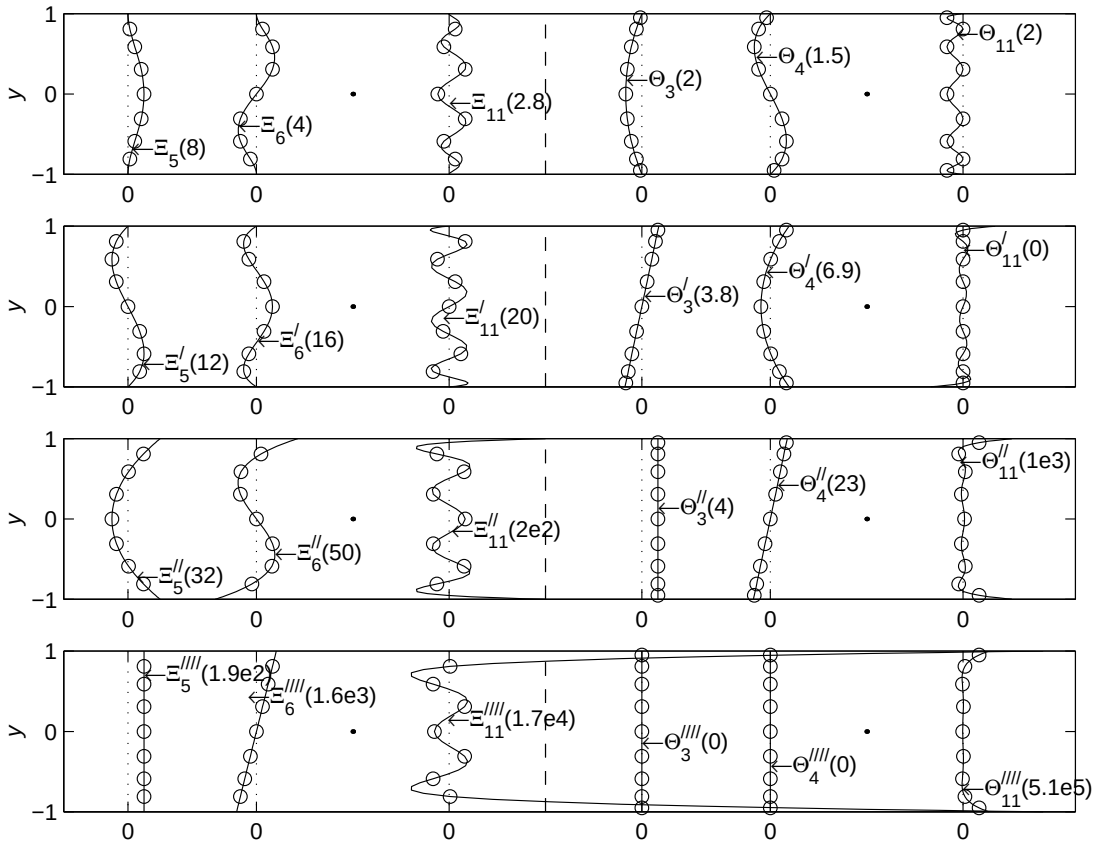

Figure 3.4: Combination 1 Basis Functions and Their Derivatives (Peak magnitudes over circled relevant collocation points for $M = 11$ in parenthesis)

Derivative Matrices

In terms of the basis functions, for this basis modification, the zero derivative matrices of the state-space form (3.25) are

$$\begin{aligned} \mathbf{D0}_D &= \begin{bmatrix} \Theta_3(y_2) & \dots & \Theta_M(y_2) \\ \vdots & \ddots & \vdots \\ \Theta_3(y_{M-1}) & \dots & \Theta_M(y_{M-1}) \end{bmatrix} \\ \mathbf{D0}_{DN} &= \begin{bmatrix} \Xi_5(y_3) & \dots & \Xi_M(y_3) \\ \vdots & \ddots & \vdots \\ \Xi_5(y_{M-2}) & \dots & \Xi_M(y_{M-2}) \end{bmatrix} \end{aligned} \tag{3.59}$$

and differentiation yields the higher derivative matrices. Some of the basis functions and their derivatives are shown in figure 3.4. The first derivative of the final Dirichlet basis is zero at the interior collocation points, since the collocation points are at the ends and extrema of the undifferentiated basis. This makes the $\mathbf{D1}_D$ singular, but this matrix is not used in either of the velocity or vorticity equations in (3.25).

3.5.4 Combined Method 2

Its is evident that a weakness in the formulation of the bases created using methods from Heinrichs and Joshi is the arbitrary final partitioning during which the equations at the wall and the two highest basis coefficients are discarded. Combined method 1 has shown a more rigorous derivation of the Dirichlet basis (3.55), and this will be used here.

Weideman and Reddy (2000, p499), working on an interpolating scheme rather than a polynomial scheme, are able to avoid any final partitioning by applying Heinrichs method to a reduced basis on the interior points. Now the rigorous Dirichlet basis is a valid basis of $\mathbb{R}^{M-2}$ on the interior points. Thus here Heinrichs' method is applied to the rigorous Dirichlet basis in order to form a Dirichlet and Neumann basis.

Elementary Matrix Operations

The basis (3.55) does not include the wall locations, although the polynomials from which it was formed (3.39) evaluate to zero at the walls. For these polynomials to also fulfill the Neumann boundary condition at the wall, they require further roots there. This may be achieved by multiplication by $(1-y^2)$ as per Heinrichs (1989), thus

$$\Xi_m = (1-y^2)\Theta_m \tag{3.60}$$

This new basis function is normalised to a peak value of approximately 2 at high n, since Θ_m is so normalised.

Now since the basis (3.55) does not include the walls, it is a valid elementary matrix operation to multiply by $(1-y^2)$, since this is now never zero, resulting in a new basis for velocity which fulfills the Neumann and Dirichlet boundary conditions

$$\begin{aligned}
\begin{pmatrix} \tilde{v}_M(y_2,t) \\ \vdots \\ \tilde{v}_M(y_{M-1},t) \end{pmatrix} & \\
&= \begin{bmatrix} \Theta_3(y_2)(1-y_2^2) & \dots & \Theta_M(y_2)(1-y_2^2) \\ \vdots & \ddots & \vdots \\ \Theta_3(y_{M-1})(1-y_{M-1}^2) & \dots & \Theta_M(y_{M-1})(1-y_{M-1}^2) \end{bmatrix} \begin{pmatrix} a_{v,3} \\ \vdots \\ a_{v,M} \end{pmatrix} \\
&= \begin{bmatrix} \Xi_3(y_2) & \dots & \Xi_M(y_2) \\ \vdots & \ddots & \vdots \\ \Xi_3(y_{M-1}) & \dots & \Xi_M(y_{M-1}) \end{bmatrix} \begin{pmatrix} a_{v,3} \\ \vdots \\ a_{v,M} \end{pmatrix}
\end{aligned} \tag{3.61}$$

This basis continues to span $\mathbb{R}^{M-2}$, as the matrix operation is valid. Some of the basis functions and their derivatives are shown in figure 3.5.

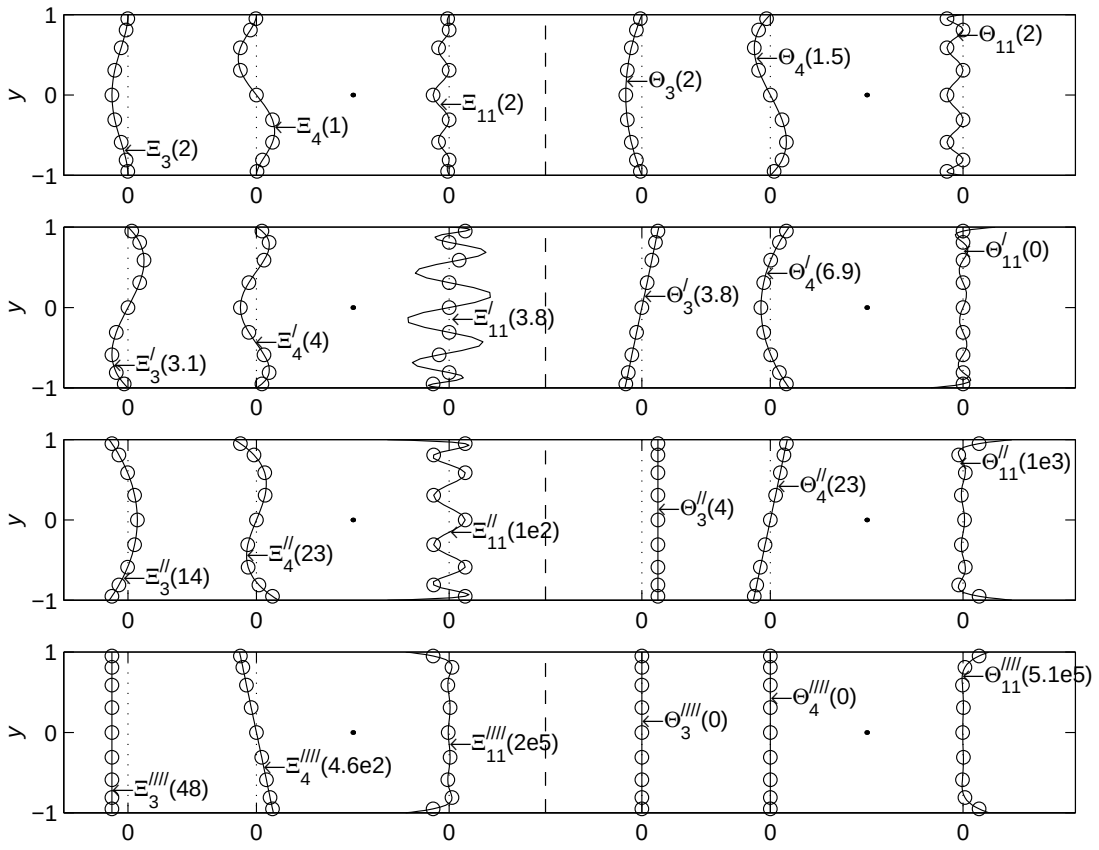

Figure 3.5: Combination 2 Basis Functions and Their Derivatives (Peak magnitudes over circled relevant collocation points for $M = 11$ in parenthesis)

3.5.5 Preconditioning

The magnitude of values of the derivatives of Γ_m are known to be large, for example the end values (at $y = \pm 1$) of the derivatives have a magnitude

$$\left| \frac{d^p \Gamma_M}{dx^p} (\pm 1) \right| \approx (M-1)^{2p} \prod_{k=1}^{p} \frac{1}{2k+1} \left(1 + O\left(1/(M-1)^2\right)\right) \tag{3.62}$$

where p is the order of derivation, and thus can be very large as shown by Boyd (2001, p142). Boyd shows that Heinrichs' method reduces end 2nd derivatives from $(m-1)^4$ to $(m-1)^2$ behaviour. However, in the present work, the ends of the range are the wall values and these equations are discarded. Thus the maximum magnitude of the derivative matrix elements lies somewhere between that at the ends and in the interior.

For the derivatives of $\Gamma_m(y)$ on the interior of the domain

$$\begin{aligned} \Gamma_m &= \cos\left((m-1)\,x\right) \\ i.e.\ \Gamma_m &= \frac{e^{i(m-1)x} + e^{-i(m-1)x}}{2} \\ \text{so } \frac{d^p \Gamma_m}{dx^p} &= \frac{(i\,(m-1)\,x)^p e^{i(m-1)x} + (-i\,(m-1)\,x)^p e^{-i(m-1)x}}{2} \end{aligned} \tag{3.63}$$

where $y = \cos(x)$. Now so long as $dy^n/dx^n \neq 0$ i.e. $y \neq 0, \pm 1$

$$\begin{aligned} \frac{d\Gamma_m}{dy} &= \frac{d\Gamma_m}{dx}\frac{dx}{dy} \\ \frac{d^2\Gamma_m}{dy^2} &= \frac{d^2\Gamma_m}{dx\,dy}\frac{dx}{dy} + \frac{d\Gamma_m}{dx}\frac{d^2x}{dy^2} \\ \frac{d^3\Gamma_m}{dy^3} &= \frac{d^3\Gamma_m}{dx\,dy^2}\frac{dx}{dy} + 2\frac{d^2\Gamma_m}{dx\,dy}\frac{d^2x}{dy^2} + \frac{d\Gamma_m}{dx}\frac{d^3x}{dy^3} \end{aligned} \tag{3.64}$$

and so on. Thus the interior derivatives are proportional to $d^p\Gamma_m/dx^p$, i.e. to $(m-1)^p$, in general, i.e. not specifically at collocation points since the latter are the extrema of the highest polynomial Γ_M but not of the lower ones. This result is not unexpected, since Γ_m has a leading term proportional to y^{m-1}, and y^{m-1} has a p^{th} derivative $(m-1)\ldots(m-p)y^{m-1-p}$ for $p > 1$, which is therefore proportional to m^p.

Now the numerical conditioning of a matrix is partly dependent on the maximum singular value, for which a good approximation is the maximum magnitude matrix element (Skogestad and Postlethwaite, 1996, p521). Therefore it may be possible to improve the conditioning of an array, or any subarray of,

$$\begin{bmatrix} \Gamma_1(y_1)'' & \ldots & \Gamma_M(y_1)'' \\ \vdots & \ddots & \vdots \\ \Gamma_1(y_M)'' & \ldots & \Gamma_M(y_M)'' \end{bmatrix} \tag{3.65}$$

by reducing the magnitude of the maximum element by postmultiplying by $\mathrm{diag}([1, 1/\left(m-1\right)^4_{m=2:M}])$ (henceforth the 'wall preconditioning') or

$\text{diag}([1, 1/(m-1)^2_{m=2:M}])$ (henceforth the 'interior preconditioning') depending on whether the wall or interior derivatives predominate, and similarly improve

$$\begin{bmatrix} \Gamma_1(y_1)'''' & \dots & \Gamma_M(y_1)'''' \\ \vdots & \ddots & \vdots \\ \Gamma_1(y_M)'''' & \dots & \Gamma_M(y_M)'''' \end{bmatrix} \tag{3.66}$$

by postmultiplying by $\text{diag}([1, 1/(m-1)^8_{m=2:M}])$ or $\text{diag}([1, 1/(m-1)^4_{m=2:M}])$. This preconditioning is likely to assist Joshi's and the combined method, as they are composed of sums of Chebyshev polynomials of similar m. The interior preconditioning may possibly assist Heinrichs' method away from the walls, as the $(1-y^2)$ and $(1-y^2)^2$ factors do not alter the interior derivative variation with m.

3.6 Conditioning Results and Discussion

This section investigates the numerical conditioning of the bases generated, with particular reference to the square matrices required in (3.15). The condition number $\kappa(\mathbf{A})$ of an $M \times M$ matrix $\mathbf{A}$ employed here is the ratio of the maximum and minimum singular values $\sigma_1(\mathbf{A})/\sigma_M(\mathbf{A})$. The singular values are interpreted in this section as the M extremal matrix gains from an input of unit magnitude (Skogestad and Postlethwaite, 1996, p72-74), i.e. $\sigma_i = \|\mathbf{A}\vec{x}_i\|_2 / \|\vec{x}_i\|_2$, for non-zero principal input directions $\vec{x}_i$.

A large condition number indicates sensitivity in the inversion of $\mathbf{A}$ with regard to any errors in $\mathbf{A}$, and in the evaluation of $\vec{x}$ in $\mathbf{A}\vec{x} = \vec{b}$ with regard to errors in $\mathbf{A}$ or $\vec{b}$ (Horn and Johnson, 1985, pp336–338). Since the condition number chosen here also measures the elongation of the hyperellipsoid $\{\mathbf{A}\vec{x} : \|\vec{x}\|_2 = 1\}$ (Golub and Van Loan, 1990, p81), it also indicates sensitivity in the evaluation of $\mathbf{A}\vec{x}$ to errors in $\mathbf{A}$ and $\vec{x}$.

Singular matrices contain linearly dependent vectors which do not span $\mathbb{R}^M$. That is to say, a unit magnitude input or linear combination of those linearly dependent vectors produces zero output. Hence one or more minimum singular values are zero, $\sigma_M(\mathbf{A}) = 0$, and the condition number is infinite. Near singular matrices are capable of producing a small output from a unit magnitude input, and thus have a small minimum singular value $\sigma_M(\mathbf{A})$ and a large condition number, and are prone to significant inaccuracy during inversion. A matrix will typically loose around $\log_{10}(\kappa)$ digits of accuracy during inversion (MathWorks Inc., 1998).

A matrix with a zero row is able to generate a zero output, since the reduced homogeneous system without the row, $\mathbf{A}'\vec{x} = 0$, has a solution which depends upon a free variable (Råde and Westergren, 1999, p92). The free variable becomes set once the input $\vec{x}$ is normalised to unit magnitude, and the system has a zero minimum singular value. Similarly, matrices with small rows have small minimum singular values and thus large condition numbers. Matrices with a zero column can produce zero output, and thus have a zero minimum singular value. A matrix with a small column $\delta_1, \dots, \delta_M$ can produce a small output with gain $\|\delta_1, \dots, \delta_M\|_2$, and thus have a similar minimum singular value. Since $\sigma_i(A) = \sigma_i(A^T)$, the

result confirms that for matrices with a small row. More general row and column degeneracies leading to loss of linear independence are harder to analyze, other than through the minimum singular value itself.

Matrices with large magnitude elements have large maximum singular values $\sigma_1(\mathbf{A})$, since (Skogestad and Postlethwaite, 1996, p520)

$$\|\mathbf{A}\|_{max} \leq \sigma_1(\mathbf{A}) \leq \sqrt{lm}\,\|\mathbf{A}\|_{max} \tag{3.67}$$

where $\|\mathbf{A}\|_{max}$ is the largest magnitude element in $l \times m$ matrix $\mathbf{A}$. Thus such matrices will tend to have large condition numbers (providing their minimum singular value is not equally as large), and show sensitivity in the evaluation of products $\mathbf{A}\vec{x}$.

The lower inequality in (3.67) is approached when the matrix has an element much larger in magnitude than the others, for example

$$\sigma_1 \begin{pmatrix} 10^4 & 1 \\ 1 & 1 \end{pmatrix} = 1.00000001 \times 10^4 \tag{3.68}$$

for which $\|\mathbf{A}\|_{max} = 10^4$, whereas the upper inequality is reached when all elements have a similar magnitude, e.g.

$$\sigma_1 \begin{pmatrix} 10^4 & 10^4 \\ 10^4 & 10^4 \end{pmatrix} = 2 \times 10^4 \tag{3.69}$$

In other words, for a given $\|\mathbf{A}\|_{max}$, the 'flatter' the matrix peak values, the higher the maximum singular value. An $M \times M$ matrix with a maximum element magnitude proportional to M^a with therefore have a maximum singular value which varies between M^a and M^{a+1}.

3.6.1 Conditioning of Spectral Coefficient Conversions

Since the spectral coefficients need to be transformed to velocities and vorticities, for example during the calculation of worst initial conditions for CFD simulations (section 4.3.1), and vice versa, for example during the operation of a state-space controller (section 4.3.3), the numerical conditioning of matrix $\mathbf{D0}_D$ and $\mathbf{D0}_{DN}$ are of interest.

Table 3.2 shows the variation in the maximum matrix element magnitude $\|\mathbf{A}\|_{max}$, maximum singular value σ_1, minimum row and column magnitudes, minimum singular value σ_M and condition condition number κ of the Dirichlet boundary condition matrix $\mathbf{D0}_D$ with problem size M, for Chebyshev polynomials Γ, and the three basis modification methods which provide $\mathbf{D0}_D$.

The variations are calculated by linear regression on the logarithm of the raw data, for M between approximately 16 and 160. The raw data for all the tables in this chapter are plotted in appendix A. For $M \approx 100$ the relative conditioning between methods is dominated by the growth rate of M rather than the constant factor. All methods for basis modification show the expected variation of $\|\mathbf{A}\|_{max}$, given by the normalisation of the polynomials. All methods have a similar variation in maximum singular value, bounded between that of $\|\mathbf{A}\|_{max}$ and M times as great. For $\mathbf{D0}_D$, combination 2 is identical to combination 1.

Method	$\|\mathbf{A}\|_{max}$	σ_1	min row mag	min col mag	σ_M	κ
Γ	1 $\times M^0$	1.2 $\times M^{0.47}$	0.76 $\times M^{0.49}$	0.76 $\times M^{0.49}$	0.65 $\times M^{0.52}$	1.8 $\times M^{-0.044}$
Heinrichs	1 $\times M^0$	0.72 $\times M^{0.52}$	7.1 $\times M^{-1.5}$	0.23 $\times M^{0.52}$	5 $\times M^{-1.5}$	0.14 $\times M^{2.1}$
Comb'n 1	2 $\times M^0$	0.66 $\times M^1$	0.96 $\times M^{0.51}$	0.93 $\times M^{0.52}$	0.65 $\times M^{0.52}$	1 $\times M^{0.5}$
Comb'n 2	2 $\times M^0$	0.66 $\times M^1$	0.96 $\times M^{0.51}$	0.93 $\times M^{0.52}$	0.65 $\times M^{0.52}$	1 $\times M^{0.5}$

Table 3.2: Conditioning of $\mathbf{D0}_D$ for the Various Basis Modification Methods

Method	$\|\mathbf{A}\|_{max}$	σ_1	min row mag	min col mag	σ_M	κ
Γ	1 $\times M^0$	1.2 $\times M^{0.47}$	0.76 $\times M^{0.49}$	0.76 $\times M^{0.49}$	0.65 $\times M^{0.52}$	1.8 $\times M^{-0.044}$
Heinrichs	1 $\times M^0$	0.69 $\times M^{0.52}$	92 $\times M^{-3.6}$	0.15 $\times M^{0.52}$	65 $\times M^{-3.6}$	0.011 $\times M^{4.1}$
Comb'n 1	8 $\times M^0$	3.9 $\times M^{0.52}$	21 $\times M^{-0.61}$	1.6 $\times M^{0.4}$	16 $\times M^{-0.58}$	0.25 $\times M^{1.1}$
Comb'n 2	2 $\times M^0$	0.46 $\times M^{0.99}$	16 $\times M^{-1.6}$	0.33 $\times M^{0.52}$	11 $\times M^{-1.6}$	0.042 $\times M^{2.6}$

Table 3.3: Conditioning of $\mathbf{D0}_{DN}$ for the Various Basis Modification Methods

Heinrichs' method has a lower minimum row magnitude variation with M than the other methods, and this correlates with a lower minimum singular value and higher condition number variation with M. Boyd (2001, p144) also notes that Heinrichs' method causes the conditioning of the undifferentiated ($\mathbf{D0}_D$) basis to deteriorate as compared to the Chebyshev basis. The basis becoming closer to singular may be due to the modulation of all the basis functions by the factor $(1-y^2)$, or by the present implementation of Heinrichs' method failing to select a reduced basis of linearly independent basis vectors. Modulation of all the basis functions by multiplication by $(1-y^2)$ causes them to become more similar, and thus they become less linearly independent. In addition, matrix rows close to the walls may become small, leading to a small minimum row magnitude and thus smaller minimum singular value. As Heinrich's method does have a deterioration in minimum row magnitude, this would indicate that the increased singularity is probably due to modulation.

Table 3.3 shows the same results for the Dirichlet and Neumann matrix $\mathbf{D0}_{DN}$ with problem size M. The expected variation of $\|\mathbf{A}\|_{max}$, is again given by the normalisation of the polynomials. The basis for combination 1 is normalised to 2 at high m, but reaches 8 for $m = 1$, as shown in figure 3.4. Again, all methods have a similar variation in maximum singular value, bounded between that of $\|\mathbf{A}\|_{max}$ and M times as great.

Heinrichs' methods now shows greater deterioration in minimum row mag-

Method	$\|\mathbf{A}\|_{max}$	σ_1	min row mag	min col mag	σ_M	κ
Heinrichs	$0.38 \times M^{2.2}$	$0.2 \times M^{2.8}$	$0.12 \times M^{2.7}$	$1.7 \times M^{0.53}$	$1.5 \times M^{0.52}$	$0.13 \times M^{2.3}$
Comb'n 1	$0.057 \times M^{4.1}$	$0.035 \times M^{4.6}$	$0.31 \times M^{2.5}$	$3.4 \times M^{0.53}$	$2.6 \times M^{0.52}$	$0.013 \times M^{4}$
Comb'n 2	$0.057 \times M^{4.1}$	$0.035 \times M^{4.6}$	$0.31 \times M^{2.5}$	$3.4 \times M^{0.53}$	$2.6 \times M^{0.52}$	$0.013 \times M^{4}$
Heinrichs (i)	$5.6 \times M^{0.016}$	$3.2 \times M^{0.59}$	$1.1 \times M^{0.41}$	$0.46 \times M^{0.58}$	$1.7 \times M^{0.015}$	$1.8 \times M^{0.57}$
Comb'n 1(i)	$0.23 \times M^{1.8}$	$0.22 \times M^{2.3}$	$3.9 \times M^{0.2}$	$3.4 \times M^{0.53}$	$2 \times M^{0.28}$	$0.11 \times M^{2}$
Comb'n 2(i)	$0.23 \times M^{1.8}$	$0.22 \times M^{2.3}$	$3.9 \times M^{0.2}$	$3.4 \times M^{0.53}$	$2 \times M^{0.28}$	$0.11 \times M^{2}$

Table 3.4: Conditioning of $\mathbf{D2}_D$ for the Various Basis Modification Methods.(i) indicates interior preconditioning.

nitude with increasing M than for matrix $\mathbf{D0}_D$, and a greater deterioration in minimum singular value. The increased singularity of the matrix with Dirichlet and Neumann boundary conditions correlates with the stronger modulations of the basis functions by $(1-y^2)^2$ as compared to $(1-y^2)$ for the Dirichlet boundary condition.

Combination 2, which selects a rigorous reduced basis before the application of modulating factor $(1-y^2)$, shows a deterioration in conditioning approximately midway between Heinrichs and the unmodified Chebyshev basis, and deterioration of the minimum singular value is similarly reduced, indicating reduced singularity. Despite the approximation in the selection of the reduced basis for combination 1, its minimum singular value variation remains closer to that of the unmodified Chebyshev basis, indicating little increase in singularity.

For the spectral conversion conditioning, and indeed all the higher derivative matrices, Joshi's method, as implemented here, produces results in between those of Heinrichs' method and combination 1. For the spectral conversion and most of the higher derivative matrices removal of the next-to-wall equations from combination 2 produces a small beneficial effect on conditioning (not shown), not nearly so large as to make it comparable with combination 1. Thus the performance of combination 1 is not believed to be due to its loss of the next-to-wall equations.

3.6.2 Conditioning of the Second Derivative

Table 3.4 shows the variation in the condition number κ of the matrix $\mathbf{D2}_D$ with problem size M. For $\mathbf{D2}_D$, combination 2 is identical to combination 1. $\|\mathbf{A}\|_{max}$ of combination 1 grows close the expected rate for the end derivatives M^4, whereas Heinrichs' method grows close to the predicted rate of M^2. Their singular values grow a little faster, but within the bounds predicted. Neither method shows any

Method	$\|\mathbf{A}\|_{max}$	σ_1	min row mag	min col mag	σ_M	κ
Heinrichs	0.4 $\times M^{2.2}$	0.19 $\times M^{2.7}$	7.3 $\times M^{0.55}$	2.7 $\times M^{0.59}$	7.5 $\times M^{-1.1}$	0.026 $\times M^{3.8}$
Comb'n 1	0.18 $\times M^{3}$	0.11 $\times M^{3.5}$	0.64 $\times M^{2.5}$	15 $\times M^{0.7}$	15 $\times M^{0.5}$	0.0077 $\times M^{3}$
Comb'n 2	0.8 $\times M^{2}$	0.71 $\times M^{2.6}$	0.33 $\times M^{2.5}$	7 $\times M^{0.57}$	3.8 $\times M^{0.64}$	0.18 $\times M^{1.9}$
Heinrichs (i)	6.4 $\times M^{0.049}$	3.5 $\times M^{0.57}$	2.7 $\times M^{0.11}$	0.51 $\times M^{0.46}$	92 $\times M^{-3.1}$	0.039 $\times M^{3.7}$
Comb'n 1(i)	29 $\times M^{0.33}$	20 $\times M^{0.76}$	32 $\times M^{0.07}$	5.7 $\times M^{0.27}$	47 $\times M^{-0.58}$	0.42 $\times M^{1.3}$
Comb'n 2(i)	20 $\times M^{0.1}$	11 $\times M^{0.6}$	7.1 $\times M^{0.11}$	0.71 $\times M^{0.5}$	8.7 $\times M^{-1.3}$	1.2 $\times M^{1.9}$

Table 3.5: Conditioning of $\mathbf{L}$ for the Various Basis Modification Methods. (i) indicates interior preconditioning.

particular deterioration in row or column magnitude, and the condition number is dominated by $\|\mathbf{A}\|_{max}$.

Interior preconditioning by $\text{diag}(1/(m-1)^2)$ reduces the growth of $\|\mathbf{A}\|_{max}$ of both methods by approximately M^2, and that of σ_1 by a similar amount. It causes no deterioration in the minimum row and column magnitudes. Thus Heinrichs condition number grows as $M^{0.57}$, whereas combination 1 grows as M^2.

3.6.3 Conditioning of the Discrete Laplacian

The variation in the condition number κ of the matrix $\mathbf{D2}_{DN}$ with problem size M is almost identical to that of the Laplacian $\mathbf{L} = \mathbf{D2}_{DN} - \mathbf{D0}_{DN}$ which is now considered. Since the discrete Laplacian operator $\mathbf{L}$ has to be inverted in order to generate the state-space system, its numerical conditioning is of particular interest. Table 3.5 shows the variation in the condition number κ and associated data for the matrix with problem size M.

$\|\mathbf{A}\|_{max}$ of combination 1 grows at M^3, lower than the expected rate for the end derivatives M^4, and closer to the rate of the interior derivatives M^2, possibly since the end derivatives have a Neumann condition. Heinrichs' method grows close to its predicted rate of M^2. Their singular values grow at little faster, but within the bounds predicted. Neither method shows any particular deterioration in row or column magnitude, but the minimum singular value of Heinrich's method deteriorates. Heinrich's matrix becomes more singular with M but not via small rows or columns, but a more general loss of linear independence possibly due to the modulating effect of the factor $(1-y^2)^2$ on the basis. Combination 2 has the lowest $\|\mathbf{A}\|_{max}$ growth of the recombinations, lower even than Heinrichs' upon which it is partly based, and uses only a modulation of $(1-y^2)$ leading to reasonable growth of minimum singular value, and the best overall conditioning for this matrix.

Method	$\|\mathbf{A}\|_{max}$	σ_1	min row mag	min col mag	σ_M	κ
Heinrichs	0.8 $\times M^{4.2}$	0.47 $\times M^{4.7}$	0.079 $\times M^{4.7}$	20 $\times M^{0.53}$	16 $\times M^{0.52}$	0.029 $\times M^{4.1}$
Comb'n 1	0.0004 $\times M^{7.5}$	0.00049 $\times M^{7.7}$	0.29 $\times M^{4.6}$	$1.3e2$ $\times M^{0.57}$	$1.2e2$ $\times M^{0.52}$	$4.1e-6$ $\times M^{7.2}$
Comb'n 2	0.081 $\times M^{6.2}$	0.048 $\times M^{6.6}$	0.25 $\times M^{4.5}$	41 $\times M^{0.53}$	30 $\times M^{0.52}$	0.0016 $\times M^{6}$
Heinrichs (i)	$1.1e2$ $\times M^{0.016}$	66 $\times M^{0.56}$	24 $\times M^{0.02}$	3.6 $\times M^{0.1}$	3 $\times M^{0.013}$	22 $\times M^{0.54}$
Comb'n 1(i)	85 $\times M^{1}$	48 $\times M^{1.5}$	$2.2e2$ $\times M^{0.0023}$	0.25 $\times M^{1.9}$	22 $\times M^{-0.069}$	2.2 $\times M^{1.6}$
Comb'n 2(i)	37 $\times M^{0.86}$	25 $\times M^{1.4}$	53 $\times M^{0.0063}$	14 $\times M^{0.75}$	6.5 $\times M^{0.032}$	3.8 $\times M^{1.3}$

Table 3.6: Conditioning of $\mathbf{D4}_{DN}$ for the Various Basis Modification Methods. (i) indicates interior preconditioning.

Interior preconditioning by $\text{diag}(1/(m-1)^2)$ reduces the growth of $\|\mathbf{A}\|_{max}$ of all methods to less than M^1, and the maximum singular value stays within this also. The preconditioning causes deterioration of minimum row magnitude, and this is reflected in deterioration of the minimum singular values, particularly for Heinrichs' method. Overall there is no benefit for Heinrichs' method, or for combination 2, but a reasonable improvement for combination 1, which then achieves the best overall conditioning for $\mathbf{L}$.

3.6.4 Conditioning of the Fourth Derivative Matrix

High derivatives of Chebyshev polynomials are prone to be ill-conditioned, and the interior derivatives scale as $(M-1)^p$, where p is the order of the derivative, as derived in section 3.5.5. Matrix $\mathbf{D4}_{DN}$ appears in the right hand side of the state-space form (3.25), where inaccuracies in $\mathbf{a}_v$ are magnified by any ill-conditioning it may have. Table 3.6 shows the variation in the condition number κ of the matrix $\mathbf{D4}_{DN}$ with problem size M.

The strength of Heinrichs' method for high derivatives is shown in variation of $\|\mathbf{A}\|_{max}$ close to M^4, as compared to almost M^8 for combination 1. There is no deterioration in minimum row or column magnitude for either method, and the overall condition number reflects $\|\mathbf{A}\|_{max}$. Combination 2, which uses only factor $(1-y^2)$, lies between Heinrichs' and combination 1, as might be expected.

Interior preconditioning by postmultiplying by $\text{diag}(1/(m-1)^4)$ has a remarkable effect on the $\|\mathbf{A}\|_{max}$ of all methods, reducing Heinrichs' from $M^{4.20}$ to $M^{0.016}$, and combination 1 from $M^{7.50}$ to M^1, with maximum singular values growing slightly faster. There is some deterioration in minimum row magnitude and minimum singular values, but overall conditioning reflects the maximum singular values, leaving Heinrichs' method with the best conditioning.

Method	$\|\mathbf{A}\|_{max}$	σ_1	min row mag	min col mag	σ_M	κ
Heinrichs	0.38 $\times M^{2.2}$	0.2 $\times M^{2.8}$	0.12 $\times M^{2.7}$	1.7 $\times M^{0.53}$	1.5 $\times M^{0.52}$	0.13 $\times M^{2.3}$
Comb'n 1	0.057 $\times M^{4.1}$	0.035 $\times M^{4.6}$	0.31 $\times M^{2.5}$	3.4 $\times M^{0.53}$	2.6 $\times M^{0.52}$	0.013 $\times M^{4}$
Comb'n 2	0.057 $\times M^{4.1}$	0.035 $\times M^{4.6}$	0.31 $\times M^{2.5}$	3.4 $\times M^{0.53}$	2.6 $\times M^{0.52}$	0.013 $\times M^{4}$
Heinrichs (i)	5.6 $\times M^{0.016}$	3.2 $\times M^{0.59}$	1.1 $\times M^{0.41}$	0.46 $\times M^{0.58}$	1.7 $\times M^{0.015}$	1.8 $\times M^{0.57}$
Comb'n 1(i)	0.23 $\times M^{1.8}$	0.22 $\times M^{2.3}$	3.9 $\times M^{0.2}$	3.4 $\times M^{0.53}$	2 $\times M^{0.28}$	0.11 $\times M^{2}$
Comb'n 2(i)	0.23 $\times M^{1.8}$	0.22 $\times M^{2.3}$	3.9 $\times M^{0.2}$	3.4 $\times M^{0.53}$	2 $\times M^{0.28}$	0.11 $\times M^{2}$
Heinrichs (w)	5.6 $\times M^{0.016}$	3.3 $\times M^{0.55}$	2 $\times M^{7.8e-6}$	1.3 $\times M^{-1.6}$	4.2 $\times M^{-2.1}$	0.79 $\times M^{2.7}$
Comb'n 1(w)	22 $\times M^{0.016}$	13 $\times M^{0.55}$	4.1 $\times M^{3.3e-6}$	0.66 $\times M^{-0.31}$	9.5 $\times M^{-2}$	1.4 $\times M^{2.6}$
Comb'n 2(w)	22 $\times M^{0.016}$	13 $\times M^{0.55}$	4.1 $\times M^{3.3e-6}$	0.66 $\times M^{-0.31}$	9.5 $\times M^{-2}$	1.4 $\times M^{2.6}$

Table 3.7: Wall Pre-conditioning of $\mathbf{D2}_D$ for the Various Basis Modification Methods.(i) and (w) indicate interior and wall preconditioning respectively.

3.6.5 Wall Preconditioning

The wall preconditioning, $\text{diag}(1/(m-1)^{2p})$, where p is the order of the derivative, is also applied. It is found to reduce the maximum singular values, but the minimum singular values fall drastically. The explanation is that such heavy preconditioning causes falling minimum column magnitudes. For Heinrichs' method the wall derivatives only grow at m^p. For the other methods the peak matrix derivatives do not usually grow as fast as m^{2p} since the wall equations are discarded. Overall, this preconditioning occasionally improves matrix conditioning over that of a non-preconditioned matrix, but never achieves the results of interior preconditioning, as shown in tables 3.7, 3.8 and 3.9.

3.6.6 Conditioning of the Eigensystem

Figure 3.6 shows Boyd's 'ordinal differences' presentation of eigenvalue numerical stability (Boyd, 2001, p138), as described in section 2.8.1. In the figure the abscissa is the mode number, as ordered by increasing dynamical stability, and the ordinate is the eigenvalue spacing divided by the absolute difference in eigenvalue from calculations with 101 and 134 polynomials. Large ordinates indicate good numerical stability, since the eigenvalues change little when the number of

Method	$\|\mathbf{A}\|_{max}$	σ_1	min row mag	min col mag	σ_M	κ
Heinrichs	0.4 $\times M^{2.2}$	0.19 $\times M^{2.7}$	7.3 $\times M^{0.55}$	2.7 $\times M^{0.59}$	7.5 $\times M^{-1.1}$	0.026 $\times M^{3.8}$
Comb'n 1	0.18 $\times M^{3}$	0.11 $\times M^{3.5}$	0.64 $\times M^{2.5}$	15 $\times M^{0.7}$	15 $\times M^{0.5}$	0.0077 $\times M^{3}$
Comb'n 2	0.8 $\times M^{2}$	0.71 $\times M^{2.6}$	0.33 $\times M^{2.5}$	7 $\times M^{0.57}$	3.8 $\times M^{0.64}$	0.18 $\times M^{1.9}$
Heinrichs (i)	6.4 $\times M^{0.049}$	3.5 $\times M^{0.57}$	2.7 $\times M^{0.11}$	0.51 $\times M^{0.46}$	92 $\times M^{-3.1}$	0.039 $\times M^{3.7}$
Comb'n 1(i)	29 $\times M^{0.33}$	20 $\times M^{0.76}$	32 $\times M^{0.07}$	5.7 $\times M^{0.27}$	47 $\times M^{-0.58}$	0.42 $\times M^{1.3}$
Comb'n 2(i)	20 $\times M^{0.1}$	11 $\times M^{0.6}$	7.1 $\times M^{0.11}$	0.71 $\times M^{0.5}$	8.7 $\times M^{-1.3}$	1.2 $\times M^{1.9}$
Heinrichs (w)	6.4 $\times M^{0.049}$	3.5 $\times M^{0.57}$	3.8 $\times M^{-0.1}$	2 $\times M^{-1.8}$	$4.1e2$ $\times M^{-5.2}$	0.0087 $\times M^{5.8}$
Comb'n 1(w)	29 $\times M^{0.33}$	20 $\times M^{0.75}$	37 $\times M^{-0.097}$	39 $\times M^{-2.1}$	78 $\times M^{-2.4}$	0.26 $\times M^{3.1}$
Comb'n 2(w)	20 $\times M^{0.1}$	11 $\times M^{0.59}$	9.3 $\times M^{-0.097}$	3 $\times M^{-1.8}$	35 $\times M^{-3.5}$	0.31 $\times M^{4.1}$

Table 3.8: Wall Pre-conditioning of **L** for the Various Basis Modification Methods.(i) and (w) indicate interior and wall preconditioning respectively.

Method	$\|\mathbf{A}\|_{max}$	σ_1	min row mag	min col mag	σ_M	κ
Heinrichs	0.8 $\times M^{4.2}$	0.47 $\times M^{4.7}$	0.079 $\times M^{4.7}$	20 $\times M^{0.53}$	16 $\times M^{0.52}$	0.029 $\times M^{4.1}$
Comb'n 1	0.0004 $\times M^{7.5}$	0.00049 $\times M^{7.7}$	0.29 $\times M^{4.6}$	$1.3e2$ $\times M^{0.57}$	$1.2e2$ $\times M^{0.52}$	$4.1e-6$ $\times M^{7.2}$
Comb'n 2	0.081 $\times M^{6.2}$	0.048 $\times M^{6.6}$	0.25 $\times M^{4.5}$	41 $\times M^{0.53}$	30 $\times M^{0.52}$	0.0016 $\times M^{6}$
Heinrichs (i)	$1.1e2$ $\times M^{0.016}$	66 $\times M^{0.56}$	24 $\times M^{0.02}$	3.6 $\times M^{0.1}$	3 $\times M^{0.013}$	22 $\times M^{0.54}$
Comb'n 1(i)	85 $\times M^{1}$	48 $\times M^{1.5}$	$2.2e2$ $\times M^{0.0023}$	0.25 $\times M^{1.9}$	22 $\times M^{-0.069}$	2.2 $\times M^{1.6}$
Comb'n 2(i)	37 $\times M^{0.86}$	25 $\times M^{1.4}$	53 $\times M^{0.0063}$	14 $\times M^{0.75}$	6.5 $\times M^{0.032}$	3.8 $\times M^{1.3}$
Heinrichs (w)	$1.1e2$ $\times M^{0.016}$	66 $\times M^{0.55}$	24 $\times M^{0}$	28 $\times M^{-4.3}$	24 $\times M^{-4.4}$	2.8 $\times M^{4.9}$
Comb'n 1(w)	$1.4e3$ $\times M^{0.066}$	$6.6e2$ $\times M^{0.65}$	$1.9e2$ $\times M^{0}$	2.2 $\times M^{-2.4}$	$9.7e2$ $\times M^{-4.8}$	0.69 $\times M^{5.5}$
Comb'n 2(w)	$4.5e2$ $\times M^{0.016}$	$2.6e2$ $\times M^{0.55}$	48 $\times M^{0}$	7 $\times M^{-2.7}$	$1e2$ $\times M^{-4.5}$	2.6 $\times M^{5.1}$

Table 3.9: Wall Pre-Conditioning of $\mathbf{D4}_{DN}$ for the Various Basis Modification Methods. (i) and (w) indicate interior and wall preconditioning respectively.

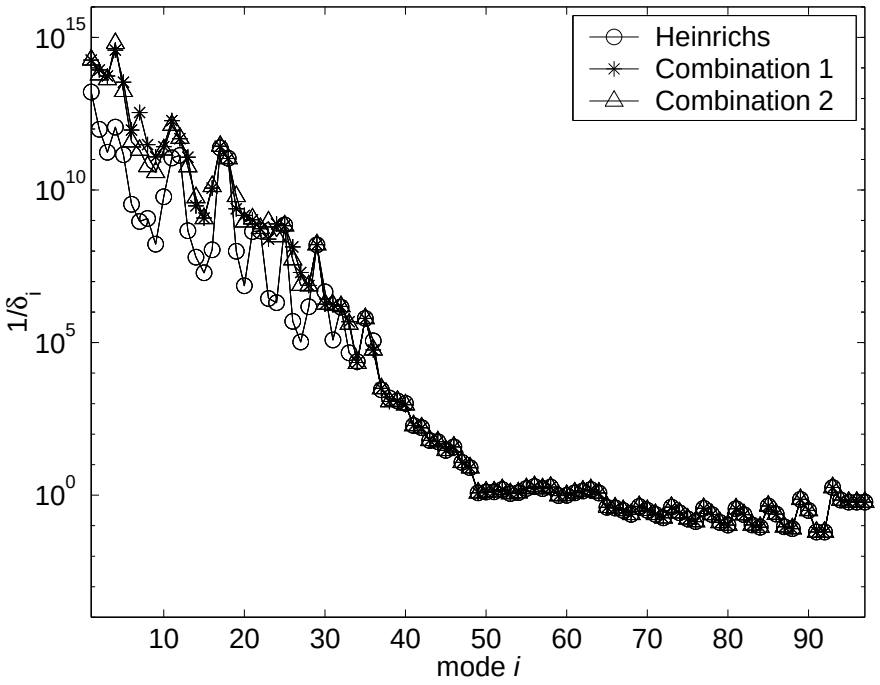

Figure 3.6: Eigenvalue Ordinal Differences Presentation

polynomials is increased.

Results from all methods except Joshi's are shown in figure 3.6. All three show an increasing sensitivity with mode number, but all methods have sensitivity less than 1 part in 1000 for the first 40 modes between bases with $M = 101$ and $M = 134$ vectors. It is therefore reasonable to assume that no spurious modes are present in the first 40 modes. The combined methods are the least sensitive over the first 40 modes, but all methods are very insensitive. Modes over $M/2$ are known to be inaccurate for spectral methods, so the large sensitivity for modes over 50 is to be expected.

Figure 3.7 shows the relative magnitude of the difference between the first 33 eigenvalues and the 32 published values of Orszag (1971) plus the additional eigenvalue discovered by Dongarra et al. (1996), for all three methods. Also shown is the accuracy of Orszag's calculation, in the form of the fractional error due to one unit in the his least significant digit. All methods produce eigenvalues which deviate less than one unit, in Orszag's least significant digit, from his results. The existence of errors in the code implementing the methods is thus unlikely.

3.7 Conclusions

This chapter has investigated in detail the wall-normal discretisation of the linearised Navier-Stokes equations by spectral collocation, examining in particular the numerical conditioning of terms in the resulting system of equations.

Section 3.2 described the discretisation of the linearised Navier-Stokes equations by spectral collocation. Section 3.3 stated the requirements of a valid linear

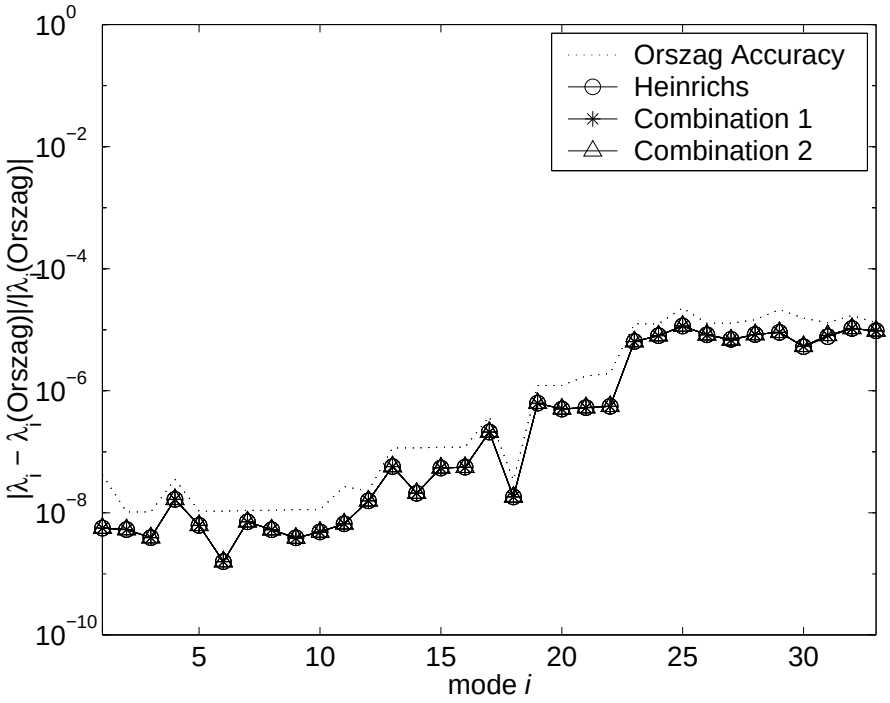

Figure 3.7: Eigenvalues Compared with Orszag (1971) and Dongarra et al. (1996)

algebraic basis, and introduced Chebyshev basis functions and basis modification in order to impose the boundary conditions. The use of matrix operations and partitioning for basis modification were described in section 3.4.

Section 3.5 described four methods of basis modification. The first was by Heinrichs (1989) and the second by Joshi (1996). The third was a combined method, having the Dirichlet condition as by Boyd (2001, p113,143) with a novel extension for the simultaneous Neumann boundary condition, and the fourth method was partly due to Boyd (2001, p113,143) and partly as described by Weideman and Reddy (2000, p499). Only the combined methods led to a strictly correct basis of $\mathbb{R}^{M-2}$ for the Dirichlet boundary condition, and only the second combined method led to a strictly accurate basis of $\mathbb{R}^{M-4}$ for the Dirichlet and Neumann boundary condition. The first combined method was rigorous in the sense that the source of the approximation was identified, whereas the present implementation of Joshi's and Heinrichs' methods arbitrarily discarded supernumerary basis vectors, albeit a tiny fraction of the dimension at large M.

Section 3.6 compared the condition numbers of the various derivative matrices which arose in the discretised system, for three of the four methods. The results from Joshi's method generally fell in the midst of the others and thus were not described. The analysis of the results showed a complex interplay of interior and wall derivative magnitudes, and of minimum and maximum singular values. Combination 1 conditioning was superior for matrices $\mathbf{D0}_D$ and $\mathbf{D0}_{DN}$, primarily because it avoided the growth in singularity that accompanied modulation of the basis vectors in Heinrichs' method and combined method 2.

The strength of Heinrichs' method for specific high derivative matrices was

apparent in the conditioning of $\mathbf{D2}_D$ and $\mathbf{D4}_{DN}$, but for other derivatives of the matrices other methods were superior. For $\mathbf{D2}_{DN}$ and $\mathbf{L}$, combined method 2 had the lowest conditioning.

Preconditioning by postmultiplying by $\mathrm{diag}([1, 1/(m-1)^{\text{derivative order}}_{m=2:M}])$ helped remarkably in high derivative cases, possibly as the interior derivative was proportional to $(m-1)^{\text{derivative order}}$, and thus the overall matrix derivative was at least this large. For low derivatives, the preconditioning helped only the first combined method, making it the superior choice for the inversion of the discrete Laplacian $\mathbf{L}$. Preconditioning by postmultiplying by $\mathrm{diag}([1, 1/(m-1)^{2\times\text{derivative order}}_{m=2:M}])$ was generally not as successful. The peak matrix derivatives did not generally grow at the rate of the wall-derivatives, and undue reduction of the column magnitude seemed to occur, leading to a growth in singularity and not such a large improvement in conditioning as interior preconditioning achieved.

All methods produced eigenvalues in close agreement with all 32 calculated by Orszag (1971), if the extra eigenvalue found by Dongarra et al. (1996) was also included in the comparison.

To summarise, this chapter has investigated four methods of modification of the Chebyshev basis for the imposition of Dirichlet and Neumann boundary conditions. The boundary conditions are required in the state-space model of plane Poiseuille flow developed in chapter 2, and here the operations applied during the methods, and the conditioning of the resulting matrices and derivative matrices have been examined in particular. It was found that the operations must be applied with care in order to strictly produce modified bases with the required span. Analysis of the conditioning of the resulting matrices showed a complex interplay of high element magnitudes and low row and column magnitudes. Preconditioning was able to reduce condition numbers significantly, and thus assist in the inversion of the Laplacian, which is required to form the state-space model. A method comprising preconditioning of a novel extension of the Dirichlet boundary condition to cover the Neumann condition was found to produce the lowest conditioning of the Laplacian of any of the four methods.

Chapter 4

Linear Quadratic Controller Synthesis and Simulations

4.1 Introduction

This chapter describes the synthesis of controllers and estimators for the linear state-space representation of plane Poiseuille flow developed in chapter 2, and subsequent linear and non-linear simulations of the open- and closed-loop systems.

Section 4.2 describes the synthesis of optimal state feedback controllers and optimal state estimators. The controllers are linear quadratic regulators (LQR), which are optimal in the sense of minimising a quadratic cost functional of the weighted state variables and control inputs. The estimators are linear quadratic estimators (LQE), which are optimal in the sense of minimising the expectation of the state estimation errors, given weighting matrices which represent the process and measurement noise covariances. The section also describes the selection of appropriate weighting matrices.

In section 4.3 the linear and non-linear simulations undertaken on the open- and closed-loop systems are described. The open-loop (OL) systems comprise the plant model with an LQE state estimator and the closed-loop systems comprise the plant model with state feedback LQR control, and with output feedback linear quadratic Gaussian (LQG) control, the latter formed by employing both the LQE estimator and LQR controller.

The performance of the controllers is to be judged by examining the growth of the system open- and closed-loop transient kinetic energy density, which also depends on the simulation initial conditions. For an unstable system the highest growth of transient energy is unbounded, but for a stable system methods exist for computing the highest transient energy growth. The highest transient energy that a system may reach at a particular time from initial conditions of unit energy is here termed the *synchronic transient energy bound*, and the maximum transient energy that a stable system may reach over all time from initial conditions with unit energy is here termed the *diachronic transient energy bound*. In flow control this is a measure which is often considered in connection with non-linear effects triggering transition to turbulence. Here, the initial conditions which generate the diachronic transient energy bound are calculated, using results from Butler and

Farrell (1992).

Next section 4.3 describes the code modifications and data preparation necessary for the open and closed-loop non-linear computational fluid dynamics (CFD) simulations. The code used is a finite-volume Navier-Stokes solver, which makes no assumption of spectral behaviour, and solves the full non-linear Navier-Stokes equations, being completely independent of the linear code used for the controller synthesis and linear simulations.

Section 4.4 presents and discusses the results obtained during the synthesis of controllers and estimators and from the linear simulations. The results of non-linear simulations on small initial perturbations are compared to the linear simulation results. Work undertaken to ensure the accuracy of the non-linear simulations is presented, followed by analysis of the results of the non-linear simulations on larger perturbations. Finally section 4.5 draws conclusions regarding the controller and estimator synthesis, and the controller and estimator performance in the linear and non-linear simulations.

4.2 Controller Synthesis

4.2.1 Optimal State Feedback

The standard LQR control problem states that given the real open-loop system or 'plant'

$$\begin{aligned} \dot{\mathcal{X}} &= \mathcal{A}\mathcal{X} + \mathcal{B}\mathcal{U} \\ \mathcal{Y} &= \mathcal{C}\mathcal{X} \end{aligned} \tag{4.1}$$

the feedback control signal that minimizes

$$\int_0^\infty \left(\mathcal{X}(t)^T \mathcal{Q}\mathcal{X}(t) + \mathcal{U}(t)^T \mathcal{R}\mathcal{U}(t)\right) dt \tag{4.2}$$

where $\mathcal{Q} = \mathcal{Q}^T \geq 0$ and $\mathcal{R} = \mathcal{R}^T > 0$ are weighting matrices, is given by $\mathcal{U} = -\mathcal{K}\mathcal{X}$ where $\mathcal{K} = \mathcal{R}^{-1}\mathcal{B}^T\mathcal{P}$ and $\mathcal{P} = \mathcal{P}^T \geq 0$ is the solution of the algebraic Riccati equation

$$\mathcal{A}^T\mathcal{P} + \mathcal{P}\mathcal{A} - \mathcal{P}\mathcal{B}\mathcal{R}^{-1}\mathcal{B}^T\mathcal{P} + \mathcal{Q} = 0 \tag{4.3}$$

The closed-loop state feedback LQR system is

$$\begin{aligned} \dot{\mathcal{X}} &= (\mathcal{A} - \mathcal{B}\mathcal{K})\,\mathcal{X} \\ \mathcal{Y} &= \mathcal{C}\mathcal{X} \end{aligned} \tag{4.4}$$

The state feedback controller $\mathcal{K}$ is the optimal for all initial conditions (Skogestad and Postlethwaite, 1996, p354). The controller has no prescribed degree of stability, but this could be added by modifying the cost functional (4.2), as performed by Joshi et al. (1999). Figure 4.1 shows a block diagram of LQR state feedback.

In most problems the weighting matrices are tuned by hand. However, for a fluid system this is not practical because of the large number of state variables.

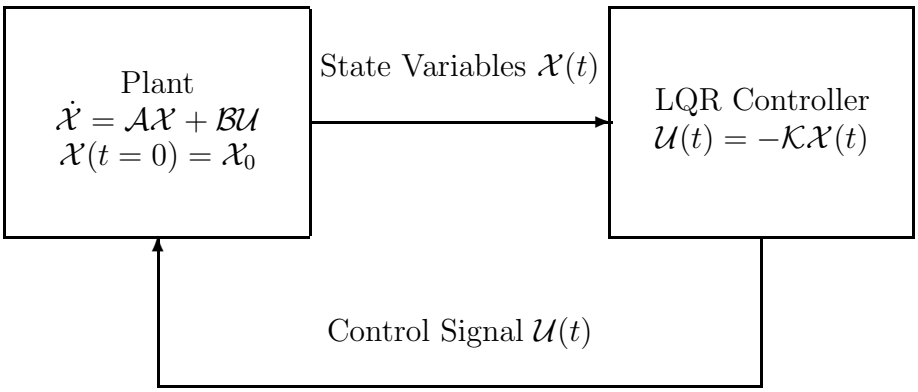

Figure 4.1: A Block Diagram of LQR State Feedback

Furthermore, it is useful to employ a weighting matrix $\mathcal{Q}$ that is defined independently of the chosen state basis since then the there is freedom to alter either. It is also helpful if the weights are defined independently of the level of discretisation, in order to make interpretation of results easier, as noted by Lauga and Bewley (2004). It is suggested by Bewley and Liu (1998) that a natural choice for the matrix $\mathcal{Q}$ is such that $\mathcal{X}^T\mathcal{Q}\mathcal{X}$ equals the transient energy E,

$$E = \frac{1}{V}\int_{vol=V} \rho \frac{\vec{u}^T\vec{u}}{2}\, dvol \tag{4.5}$$

where E has dimensions energy per unit volume, and $\vec{u}$ is the perturbation velocity vector. This choice of $\mathcal{Q}$ is independent of the definition of the state variables, is independent (in the limiting case) of the discretisation N, and also means that the LQR problem (4.2) minimises E in some sense. Furthermore no particular fluid flow phenomena are assumed. In the linearised Navier-Stokes equations (2.13), the base flow provides energy via $\vec{U}_b$, and the viscosity term dissipates energy. Expanding (4.5) in terms of velocity components, the energy density E of a flow perturbation at wave numbers α, β, as performed by Bewley and Liu (1998, p312), is

$$E = \frac{1}{V}\int_{y=-1}^{1}\int_{x=0}^{2\pi/\alpha}\int_{z=0}^{2\pi/\beta} \frac{(u^2+v^2+w^2)}{2} dz\, dx\, dy \tag{4.6}$$

assuming a unit mass density ρ, as did Butler and Farrell (1992). The volume V is that of one streamwise period, by one spanwise period, by the channel full-height

$$V = 8\pi^2/(\alpha\beta), \quad \alpha\beta \neq 0 \tag{4.7}$$

When α is zero, $2\pi/\alpha$ can be replaced by any finite length in the both expressions (4.6,4.7), since there is no streamwise variation, and similarly for β. Now from (2.36)

$$v \;=\; \Re\left(\tilde{v}(y,t)e^{\jmath(\alpha x+\beta z)}\right) \tag{4.8}$$

Thus

$$v^2 = \frac{2\tilde{v}\tilde{v}^T + \tilde{v}\tilde{v}e^{2\jmath(\alpha x+\beta z)} + \tilde{v}^T\tilde{v}^T e^{-2\jmath(\alpha x+\beta z)}}{4} \tag{4.9}$$

and

$$\int_{x=0}^{2\pi/\alpha}\int_{z=0}^{2\pi/\beta}\frac{v^2}{2}dz\,dx = \frac{\pi^2\tilde{v}\tilde{v}^T}{\alpha\beta} \tag{4.10}$$

with similar results for u and w. Thus the energy density becomes

$$E = \frac{1}{V}\int_{y=-1}^{1}\pi^2\frac{\left(\tilde{u}\tilde{u}^T + \tilde{v}\tilde{v}^T + \tilde{w}\tilde{w}^T\right)}{\alpha\beta}dy = \frac{1}{8}\int_{y=-1}^{1}\left(\tilde{u}\tilde{u}^T + \tilde{v}\tilde{v}^T + \tilde{w}\tilde{w}^T\right)dy \tag{4.11}$$

Now $\tilde{u}$ and $\tilde{w}$ are functions of $\tilde{v}$ and $\tilde{\eta}$ from (2.45)

$$\tilde{u} = \frac{\jmath}{\alpha^2+\beta^2}\left(\alpha\frac{\partial\tilde{v}}{\partial y} - \beta\tilde{\eta}\right) \tag{4.12}$$

$$\tilde{w} = \frac{\jmath}{\alpha^2+\beta^2}\left(\beta\frac{\partial\tilde{v}}{\partial y} + \alpha\tilde{\eta}\right) \tag{4.13}$$

So

$$\tilde{u}\tilde{u}^T + \tilde{w}\tilde{w}^T = \frac{\frac{\partial\tilde{v}}{\partial y}^T\frac{\partial\tilde{v}}{\partial y} + \tilde{\eta}^T\tilde{\eta}}{\alpha^2+\beta^2} \tag{4.14}$$

and the energy density becomes

$$E = \frac{1}{8k^2}\int_{-1}^{1}(k^2\tilde{v}^T\tilde{v} + \frac{\partial\tilde{v}}{\partial y}^T\frac{\partial\tilde{v}}{\partial y} + \tilde{\eta}^T\tilde{\eta})dy \tag{4.15}$$

Curtis-Clenshaw quadrature employs a set of abscissa $y_n = \cos(\pi n/N), n = 1, N-1$ for approximate evaluation of the integral (as described by Boyd (2001, p456), but here the limits are 1 and $N-1$, since here the collocation points run from 0 to N)

$$\int_{-1}^{1}f(y)dy \approx \sum_{1}^{N-1}w_n f(y_n) \tag{4.16}$$

These abscissa are equal to the internal Gauss Lobatto points, at which evaluation of the system equations has been performed. The weights w_n are

$$w_n = \frac{2}{N}\sqrt{1-y_n^2}\sum_{m=1}^{N-1}\frac{1}{m}\sin(m\pi n/N)\left(1-\cos(m\pi)\right), \quad n = 1,\ldots,N-1 \tag{4.17}$$

Thus

$$\int_{-1}^{1}\tilde{v}^T\tilde{v}dy \approx \sum_{0}^{N}\tilde{v}^T(y_n)\tilde{v}(y_n)w_n \tag{4.18}$$

if boundary weights $w_0 = w_N = 0$ are defined. In discretised form E becomes

$$E = \frac{(\tilde{v}_n)^T \mathbf{Q} (\tilde{v}_n) + (\partial\tilde{v}_n/\partial y)^T \mathbf{Q} (\partial\tilde{v}_n/\partial y) + (\tilde{\eta}_n)^T \mathbf{Q} (\tilde{\eta}_n)}{8k^2}, \quad n = 0, \ldots, N \tag{4.19}$$

where $\mathbf{Q}$ contains the quadrature weights

$$\mathbf{Q} = \begin{pmatrix} w_0 & & 0 \\ & \ddots & \\ 0 & & w_N \end{pmatrix} \tag{4.20}$$

The velocity and vorticity are available from (2.105)

$$\begin{pmatrix} \tilde{v}(y_k, t) \\ \tilde{\eta}(y_k, t) \end{pmatrix} = \mathbf{T} \begin{pmatrix} a_{v,n}(t) \\ a_{\eta,n}(t) \\ q_u(t) \\ q_l(t) \end{pmatrix} \tag{4.21}$$

and $(\partial\tilde{v}_n/\partial y)$ from its y derivative

$$\begin{pmatrix} \partial\tilde{v}(y_k, t)/\partial y \\ \partial\tilde{\eta}(y_k, t)/\partial y \end{pmatrix} = \frac{\partial \mathbf{T}}{\partial y} \begin{pmatrix} a_{v,n}(t) \\ a_{\eta,n}(t) \\ q_u(t) \\ q_l(t) \end{pmatrix} \tag{4.22}$$

Thus

$$\begin{aligned} E &= \frac{1}{8k^2} \mathcal{X}^T \left(\mathbf{T}^T \begin{bmatrix} \mathbf{Q} & \mathbf{0} \\ \mathbf{0} & \mathbf{Q} \end{bmatrix} \mathbf{T} + (\partial\mathbf{T}/\partial y)^T \begin{bmatrix} \mathbf{Q} & \mathbf{0} \\ \mathbf{0} & \mathbf{0} \end{bmatrix} (\partial\mathbf{T}/\partial y) \right) \mathcal{X} \\ &\triangleq \mathcal{X}^T \mathcal{Q} \mathcal{X} \end{aligned} \tag{4.23}$$

Independent analytical and numerical tests validate this expression for various distributions of velocity and vorticity with the appropriate boundary conditions.

$\mathcal{R}$ is set as $\mathcal{R} = r^2\mathbf{I}$, thus allowing variation of control magnitude, while maintaining equivalent real and imaginary control effect on both walls.

Bewley's Energy Matrix

The energy calculation by Bewley and Liu (1998, p312) is based on the interpolating Chebyshev form

$$\frac{1}{8} \begin{pmatrix} \tilde{v}^T & \tilde{\eta}^T \end{pmatrix} \begin{pmatrix} \Omega + \frac{1}{k^2} \mathcal{D}_c^T \Omega \mathcal{D}_c & \mathbf{0} \\ \mathbf{0} & \frac{1}{k^2}\Omega \end{pmatrix} \begin{pmatrix} \tilde{v} \\ \tilde{\eta} \end{pmatrix} \tag{4.24}$$

where Ω is a matrix of quadrature weights and $\mathcal{D}_c$ is a derivative matrix with the wall values omitted. Truncating the matrix when the wall values are not zero leads to the high order interpolation assuming zero wall values, and this produces large and inaccurate derivatives throughout the domain (see 2.4.5). For this reason no meaningful comparison can be made with Bewley's closed-loop results.

4.2.2 Optimal Estimation

The standard LQE control problem assumes that the system has disturbance and measurement noise input processes w_d and w_n respectively

$$\begin{aligned} \dot{\mathcal{X}} &= \mathcal{A}\mathcal{X} + \mathcal{B}\mathcal{U} + w_d \\ \mathcal{Y} &= \mathcal{C}\mathcal{X} + w_n \end{aligned} \tag{4.25}$$

and that the noise inputs are uncorrelated, zero-mean, Gaussian stochastic processes with constant power spectral density matrices $\mathcal{V}$ and $\mathcal{W}$ (Skogestad and Postlethwaite, 1996, p353). Thus w_d and w_n are white noise processes with covariances

$$\begin{aligned} Exp\left\{w_d^T w_d\right\} &= \mathcal{W}\delta(t-\tau) \\ Exp\left\{w_n^T w_n\right\} &= \mathcal{V}\delta(t-\tau) \\ Exp\left\{w_d^T w_n\right\} &= \mathbf{0} \\ Exp\left\{w_n^T w_d\right\} &= \mathbf{0} \end{aligned} \tag{4.26}$$

where δ is a delta function and Exp is the expectation operator. The theory states that for an LQE state estimator

$$\dot{\hat{\mathcal{X}}} = \mathcal{A}\hat{\mathcal{X}} + \mathcal{B}\mathcal{U} + \mathcal{L}\left(\mathcal{Y} - \mathcal{C}\hat{\mathcal{X}}\right) \tag{4.27}$$

where $\hat{\mathcal{X}}$ are the estimated state variables, the optimal estimator gain $\mathcal{L}$ that minimizes

$$Exp\left\{\left[\hat{\mathcal{X}} - \mathcal{X}\right]^T \left[\hat{\mathcal{X}} - \mathcal{X}\right]\right\} \tag{4.28}$$

is given by $\mathcal{L} = \mathcal{P}\mathcal{C}^T\mathcal{V}^{-1}$ where $\mathcal{P} = \mathcal{P}^T \geq 0$ is the solution of the algebraic Riccati equation

$$\mathcal{P}\mathcal{A}^T + \mathcal{A}\mathcal{P} - \mathcal{P}\mathcal{C}^T\mathcal{V}^{-1}\mathcal{C}\mathcal{P} + \mathcal{W} = 0 \tag{4.29}$$

Figure 4.2 shows a block diagram of LQE state estimation. For open-loop simulations the input $\mathcal{U}$ is zero.

The statistical properties of the noise inputs on the present system are unknown, and the matrices $\mathcal{V}$ and $\mathcal{W}$ can be treated as tuning parameters, in order to achieve an estimator of acceptable performance. A general rule of thumb is that for acceptable estimator accuracy, the slowest estimator pole should be 5-10 times faster than the fastest system pole, for example see Lewis and Syrmos (1995, p456). Unfortunately, the present system has a large number of poles, the faster half of which are known to be inaccurate due to the use of a spectral method, and are unlikely to be excited. It is impractical to attempt to make the large number of estimator poles all faster than these.

Reasonable tuning assumptions can be made if the system state variables $\mathcal{X}$ are transformed from velocity and vorticity Chebyshev coefficients into velocity

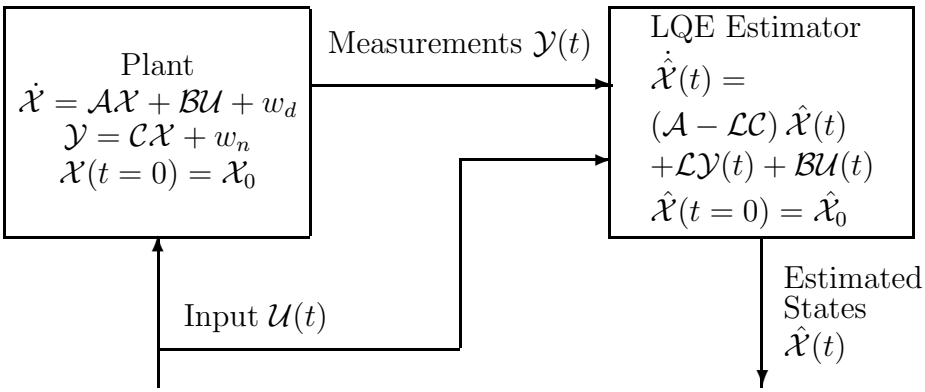

Figure 4.2: A Block Diagram of LQE State Estimation

and vorticity values at the collocation points $\mathcal{X}_{cp}$ by means of the transformation $\mathbf{T}_{cp}$ (2.106). The system becomes

$$\begin{aligned} \dot{\mathcal{X}}_{cp} &= \mathbf{T}_{cp}\mathcal{A}\mathbf{T}_{cp}^{-1}\mathcal{X}_{cp} + \mathbf{T}_{cp}\mathcal{B}\mathcal{U} + w_d \\ \mathcal{Y} &= \mathcal{C}\mathbf{T}_{cp}^{-1}\mathcal{X}_{cp} + w_n \end{aligned} \tag{4.30}$$

In general it is reasonable to assume that the process noise power spectral density $\mathcal{W}$ is a unit matrix, and estimators synthesized using this assumption will be referred to as 'uniform' estimators. These estimators, as used by Bewley and Liu (1998), assume a spatially uncorrelated disturbance model.

A more informed choice is

$$\mathcal{W} = \begin{bmatrix} (1-y_{k1})^2(1-y_{k2})^2 & \mathbf{0} \\ \mathbf{0} & (1-y_{k1})^2(1-y_{k2})^2 \end{bmatrix} \tag{4.31}$$

Since $\mathcal{W}$ operates on the transformed state variables $\mathcal{X}_{cp}$, this choice implies that the covariance between velocity state variables is $(1-y_{k1})^2(1-y_{k2})^2$, where y_{k1}, y_{k2} are the locations of the state variables, and similarly between vorticity state variables. Estimators synthesized using this assumption will henceforth be referred to as 'tuned' estimators.

For tuned estimators, when $k1 = k2$, $\mathcal{W}$ represents the variance of the noise on a single state variable, which therefore varies as $(1-y_{k1})^4$. Thus disturbances on a single state variable have a higher standard deviation (the positive square root of variance) at the centreline ($y = 0$), than near the walls ($y = \pm 1$). These variances are compatible with velocity disturbances near the centreline being more variable than those near the walls and similarly for vorticity disturbances. At the walls, the velocities are set reasonably accurately by the controller, so they are given small variance (10^{-3}).

When $k1 \neq k2$, $\mathcal{W}$ represents the covariance of a pair of state variables. Pairs close to the walls have low covariances, whereas pairs close to the centreline ($y = 0$) have high covariances. Pairs where one state variable is near a wall, and the other near the centreline have covariances in between. These covariances are compatible with velocity disturbances near the centreline being physically larger than those

near the walls and similarly for vorticity disturbances. The covariance between velocity and vorticity state variables is set to zero.

These covariances vary smoothly over the collocation point state variables, and many other such distributions are possible e.g. the exponential variations used by Hœpffner et al. (2005, p271). Chevalier et al. (2004) calculate covariances from non-linear simulations of turbulent channel flow. These simulations differ qualitatively from the assumptions for the tuned estimator made here, since here estimation is of the earliest stages of transition.

By the symmetry and independence of the measurements (upper and lower wall, real and imaginary Fourier components of shear stress), it is reasonable to assume that the measurement noise covariance is $\mathcal{V} = s\mathbf{I}$, where s is a positive tuning parameter, which scales the measurement noise against the process noise.

An estimator $\mathcal{L}$ designed in terms of these velocity and vorticity state variables, may be transformed back for use on the untransformed state variables as $\mathbf{T}_{cp}^{-1}\mathcal{L}$.

4.2.3 Optimal Output Feedback

The combined plant, LQR controller and LQE estimator may be combined into an LQG output feedback system, with dynamics

$$\begin{bmatrix} \dot{\mathcal{X}} \\ \dot{\hat{\mathcal{X}}} \end{bmatrix} = \begin{bmatrix} \mathcal{A} & -\mathcal{B}\mathcal{K} \\ \mathcal{L}\mathcal{C} & \mathcal{A} - \mathcal{B}\mathcal{K} - \mathcal{L}\mathcal{C} \end{bmatrix} \begin{bmatrix} \mathcal{X} \\ \hat{\mathcal{X}} \end{bmatrix} + \begin{bmatrix} \mathbf{I} & \mathbf{0} \\ \mathbf{0} & \mathcal{L} \end{bmatrix} \begin{bmatrix} \omega_d \\ \omega_n \end{bmatrix} \tag{4.32}$$

where the estimate and state dynamics are not independent but are intentionally coupled. If the system is recast in terms of estimator error $\mathcal{X}_{Error} = \mathcal{X} - \hat{\mathcal{X}}$ they become

$$\begin{bmatrix} \dot{\mathcal{X}} \\ \dot{\mathcal{X}} - \dot{\hat{\mathcal{X}}} \end{bmatrix} = \begin{bmatrix} \mathcal{A} - \mathcal{B}\mathcal{K} & \mathcal{B}\mathcal{K} \\ \mathbf{0} & \mathcal{A} - \mathcal{L}\mathcal{C} \end{bmatrix} \begin{bmatrix} \mathcal{X} \\ \mathcal{X} - \hat{\mathcal{X}} \end{bmatrix} + \begin{bmatrix} \mathbf{I} & \mathbf{0} \\ \mathbf{I} & -\mathcal{L} \end{bmatrix} \begin{bmatrix} \omega_d \\ \omega_n \end{bmatrix} \tag{4.33}$$

and thus the estimator error dynamics are independent of the state dynamics, as predicted by the separation theorem (Skogestad and Postlethwaite, 1996, p353). Figure 4.3 shows a block diagram of LQG output feedback.

4.3 Simulations

4.3.1 Initial Conditions

Plant Worst Initial Conditions

The maximum transient energy that a stable system achieves over all time from all possible initial conditions with unit energy is here termed the *diachronic*[1] *transient energy bound*. In flow control this is a measure which is often considered in connection with non-linear effects triggering transition to turbulence. Here, the initial conditions which generate the diachronic transient energy bound are calculated, as performed by Bewley and Liu (1998) using results from Butler and Farrell (1992).

[1] diachronic: From the Greek *dia* through, *chronos* time, from linguistics (Sykes, 1976)

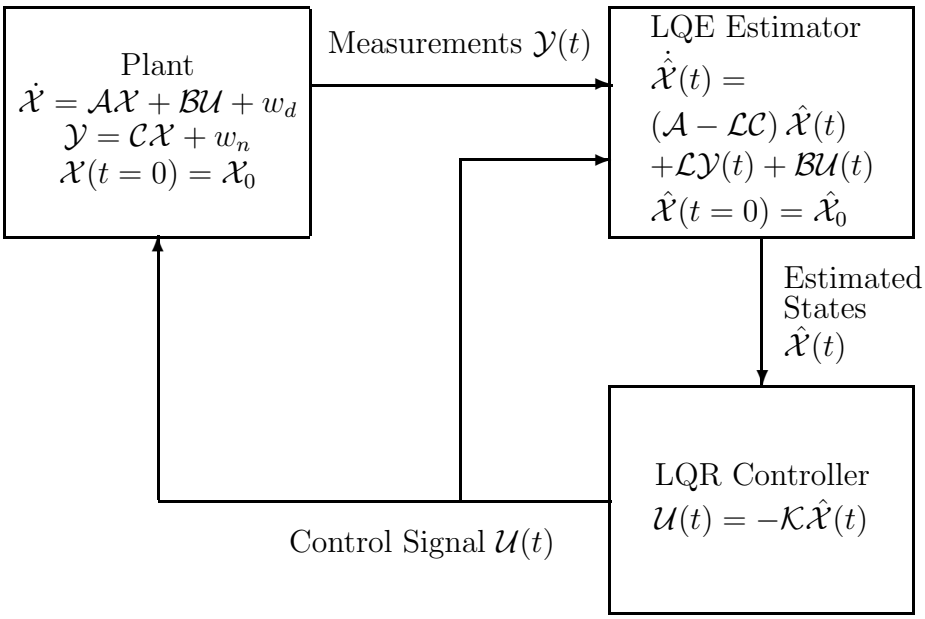

Figure 4.3: A Block Diagram of LQG Output Feedback

Following these derivations, the transient energy

$$E(t) = \mathcal{X}^T(t)\mathcal{Q}\mathcal{X}(t) \tag{4.34}$$

is defined as measure of how far the state is from the equilibrium point, since it considers all the state variables (in a weighted sum of squares sense). The largest possible value at time t after starting from unit initial transient energy but otherwise unknown state variables $\mathcal{X}(0)$

$$\epsilon(t) = \max_{E(0)=1} E(t) \tag{4.35}$$

is here termed the *synchronic*[2] *transient energy bound*. The diachronic transient energy bound θ is defined as the largest synchronic transient energy bound possible over all time

$$\theta = \max_{t \geq 0} \epsilon(t) \tag{4.36}$$

This may be determined as follows. If the system is diagonalizable, which the state-space models generated in chapter 2 are, the state variables evolve with time t as

$$\mathcal{X}(t) = \Psi e^{\Lambda t}\chi_0 \tag{4.37}$$

where Λ is a diagonal matrix of the eigenvalues, Ψ is the right eigenvector matrix, and χ_0 is a vector of unknown initial modal amplitudes.

[2]synchronic: From the Greek *syn* alike, *chronos* time, from linguistics (Sykes, 1976)

Thus

$$\epsilon(t) = \max_{\chi_0^T \Psi^T \mathcal{Q} \Psi \chi_0 = 1} \chi_0^T e^{\Lambda^T t} \Psi^T \mathcal{Q} \Psi e^{\Lambda t} \chi_0 \tag{4.38}$$

and $\epsilon(t)$ is given by a solution of

$$\partial / \partial \chi_0 \left(\chi_0^T e^{\Lambda^T t} \Psi^T \mathcal{Q} \Psi e^{\Lambda t} \chi_0 - \zeta \left(\mathcal{X}^T(0) \mathcal{Q} \mathcal{X}(0) - 1 \right) \right) = 0 \tag{4.39}$$

by the method of Lagrange multipliers, where ζ is the multiplier of the constraint equation. After differentiation by χ_0

$$\left(e^{\Lambda^T t} \Psi^T \mathcal{Q} \Psi e^{\Lambda t} \chi_0 + \left(\chi_0^T e^{\Lambda^T t} \Psi^T \mathcal{Q} \Psi e^{\Lambda t} \right)^T \right) - \zeta \left(\Psi^T \mathcal{Q} \Psi \chi_0 + \left(\chi_0^T \Psi^T \mathcal{Q} \Psi \right)^T \right) = 0 \tag{4.40}$$

Noting $\mathcal{Q}$ is symmetric, the final form is a generalised eigenproblem with eigenvector $\chi_{0,i}$ and eigenvalue ζ_i

$$e^{\Lambda^T t} \Psi^T \mathcal{Q} \Psi e^{\Lambda t} \chi_{0,i} = \zeta_i \Psi^T \mathcal{Q} \Psi \chi_{0,i} \tag{4.41}$$

Premultiplying by $\chi_{0,i}^T$, it is evident that $\epsilon(t) = \max_i \zeta_i$. The initial state variables which generate this synchronic transient energy bound are given by $\mathcal{X}_{worst} = \Psi \chi_{0,i}$.

The synchronic transient energy bound may also be cast as the square of the spectral norm of the state transition matrix $e^{\mathbf{A}t}$, as noted by Lim and Kim (2004) and Whidborne et al. (2004),

$$\epsilon(t) = \bar{\sigma}^2 \left(e^{\mathbf{A}t} \right) \tag{4.42}$$

where $\mathbf{A} = \mathcal{Q}^{1/2} \mathcal{A} \mathcal{Q}^{-1/2}$. This form requires full matrix exponential evaluations, which Moler and Van Loan (2003) show may be unreliable, whereas in (4.41) Λ is diagonal, and the terms of the exponential matrix may be evaluated as scalars.

For a stable system the diachronic transient energy bound θ of $\epsilon(t)$ over all time t, can be found by a search technique. Henceforth the associated initial conditions are referred to as the "worst" initial conditions. Difficulties arise for an unstable system since the synchronic transient energy bound $\epsilon(t)$ increases with time without bound. In practice, for the unstable open-loop case 1 system described here, the long term behaviour is dominated by the single unstable eigenvalue, so for large times, the worst initial conditions are independent of t. These initial conditions are not simply the unstable eigenvector, as other modes may be present initially.

For the open-loop system worst initial conditions, Λ and Ψ are the eigenvalues and eigenvectors of the system matrix $\mathcal{A}$. To prevent the involvement of the steady-state transpiration modes, the system matrix must be taken from the initial form (2.99) rather than the recast form (2.100), since the latter gains integrator modes representing steady-state transpiration. For the state feedback system, Λ and Ψ are the eigenvalues and eigenvectors of the closed-loop system matrix $(\mathcal{A} - \mathcal{B}\mathcal{K})$.

Estimator Energy

In a similar manner to the transient energy (4.34), the estimated transient energy may be defined

$$E_{Est}(t) = \hat{\mathcal{X}}^T(t)\mathcal{Q}\hat{\mathcal{X}}(t) \tag{4.43}$$

as a measure of the energy that the estimates $\hat{\mathcal{X}}$ represent. The growth of the estimates is related to the growth of the state variables they attempt to reproduce (4.32), and this measure of estimator performance is used in the presentation of simulation results. Proximity of plant energy and estimated energy does not guarantee that their states are also close.

The error energy may be defined

$$E_{Error}(t) = \mathcal{X}_{Error}^T(t)\mathcal{Q}\mathcal{X}_{Error}(t) \tag{4.44}$$

as a measure of how far the estimates $\hat{\mathcal{X}}$, are from the actual state variables $\mathcal{X}$, where $\mathcal{X}_{Error} = \mathcal{X} - \hat{\mathcal{X}}$. The growth of the estimator errors $\mathcal{X}_{Error}$ and thus of E_{Error} is independent of the growth of the state variables that the estimator attempts to reproduce (4.33). This measure of estimator performance is used in the tuning of estimator weights.

Estimator Zero Initial Conditions

The Estimated Energy Bound θ_{Est} is defined as the largest error energy E_{Error} during a simulation of the system from the worst plant initial conditions $\mathcal{X}_{Worst}$, and zero estimator initial conditions, $\hat{\mathcal{X}}(0) = \mathbf{0}$, that is $\mathcal{X}_{Error}(0) = \mathcal{X}_{Worst}(0)$.

Estimator Worst Initial Conditions

The largest possible value of error energy E_{Error} at time t after starting from unit initial error energy but with otherwise unknown estimator error $\mathcal{X}(0)_{Error}$ is given by the synchronic error energy bound

$$\epsilon_{Error}(t) = \max_{E_{Error}(0)=1} E_{Error}(t) \tag{4.45}$$

The Diachronic Error Energy Bound θ_{Error} is defined as the largest synchronic error energy bound growth possible over all time

$$\theta_{Error} = \max_{t\geq 0} \epsilon_{Error}(t) \tag{4.46}$$

The synchronic error energy bound may be determined from the generalised eigenproblem with eigenvector $\chi_{0,i}$ and eigenvalue ζ_i

$$e^{\Lambda^T t}\Psi^T\mathcal{Q}\Psi e^{\Lambda t}\chi_{0,i} = \zeta_i\Psi^T\mathcal{Q}\Psi\chi_{0,i} \tag{4.47}$$

where Ψ and Λ are the right eigenvectors and eigenvalues respectively of the estimator system matrix $\mathcal{A}-\mathcal{L}\mathcal{C}$. The synchronic error energy bound ϵ_{Error} is $\max_i \zeta_i$ and the initial estimator errors which generate this are given by $\mathcal{X}_{Error,Worst} = \Psi\chi_{0,i}$.

The diachronic error energy bound θ_{Error} may be determined by a similar search of ϵ_{Error} over time to that used for the diachronic transient energy bound θ.

Modal and Non-Modal Components of Kinetic Energy Density in a System Transformed such that $\mathcal{Q} = \mathbf{I}$

If the state variables $\mathcal{X}$ are transformed to $\tilde{\mathcal{X}}$ such that

$$E(t) = \tilde{\mathcal{X}}^T \tilde{\mathcal{X}} \tag{4.48}$$

then

$$\tilde{\mathcal{X}} = \mathcal{Q}^{1/2} \mathcal{X} \tag{4.49}$$

and the state-space form (4.1) becomes

$$\begin{aligned} \dot{\tilde{\mathcal{X}}} &= \mathcal{Q}^{1/2} \mathcal{A} \mathcal{Q}^{-1/2} \tilde{\mathcal{X}} + \mathcal{B}\mathcal{U} \\ \mathcal{Y} &= \mathcal{C}\mathcal{Q}^{-1/2} \tilde{\mathcal{X}} \end{aligned} \tag{4.50}$$

Substituting the expression for the evolution of state variables (4.37) into the expression for perturbation energy (4.34) produces

$$E(t) = \tilde{\chi}_0^T e^{\Lambda^T t} \Psi^T \Psi e^{\Lambda t} \tilde{\chi}_0 \tag{4.51}$$

where Ψ is the matrix of right normalised eigenvectors ψ_i of $\mathcal{Q}^{1/2}\mathcal{A}\mathcal{Q}^{-1/2}$, and Λ is a diagonal matrix containing the eigenvalues λ_i, which are all assumed stable. If these eigenvectors are orthogonal, i.e. $\Psi^T\Psi = \mathbf{I}$, then

$$E(t) = \tilde{\chi}_0^T e^{\left(\Lambda^T + \Lambda\right)t} \tilde{\chi}_0 \tag{4.52}$$

which decays monotonically for all χ_0, as the eigenvalues Λ are stable, and thus the diachronic transient energy bound θ is unity as shown by Whidborne et al. (2004). If the eigenmodes are not orthogonal

$$\Psi^T\Psi = \begin{pmatrix} 1 & (\psi_1 \cdot \psi_2) & (\psi_1 \cdot \psi_3) & \dots \\ (\psi_2 \cdot \psi_1) & 1 & (\psi_2 \cdot \psi_3) & \dots \\ (\psi_3 \cdot \psi_1) & (\psi_3 \cdot \psi_2) & 1 & \dots \\ \vdots & \vdots & \vdots & \ddots \end{pmatrix} \tag{4.53}$$

where $(\psi_i \cdot \psi_j) = \psi_i^T \psi_j$. The energy can then be represented as

$$E(t) = \sum_{i=1}^{N} c_i^T c_i e^{\left(\lambda_i^T + \lambda_i\right)t} + \sum_{i=1}^{N} \sum_{j=1}^{N, j \neq i} c_i^T c_j (\psi_i \cdot \psi_j) e^{\left(\lambda_i^T + \lambda_j\right)t} \tag{4.54}$$

where $\tilde{\chi}_0 = (c_0, \dots, c_N)^T$. The terms of the first summation of (4.54)

$$\sum_{i=1}^{N} c_i^T c_i e^{\left(\lambda_i^T + \lambda_i\right)t} \tag{4.55}$$

are the modal terms. They are positive for all c_i and decay monotonically, and cannot lead to any energy increase. The terms of the second summation

$$\sum_{i=1}^{N} \sum_{j=1}^{N, j \neq i} c_i^T c_j (\psi_i \cdot \psi_j) e^{\left(\lambda_i^T + \lambda_j\right)t} \tag{4.56}$$

are non-modal. They decay in magnitude, at different rates to the first summation, and can lead to energy increase when either

i) they are negative, that is if $c_i^T c_j(\psi_i \cdot \psi_j)$ is negative. The second term in (4.54) provides an upper bound $E_{pair,bound} = \max(0, -\Re(c_i^T c_j(\psi_i \cdot \psi_j)))$ on the energy growth possible from ordered mode pair i, j.

ii) they oscillate, that is if $\Im(\lambda_i^T + \lambda_j) \neq 0$. The second term in (4.54) provides an upper bound $E_{pair,bound} = \left|c_i^T c_j(\psi_i \cdot \psi_j)\right|$ on the energy growth possible from ordered mode pair i, j.

Of course, all dissimilar-mode pairs in the system may contribute to the aggregate energy growth, or reduce energy growth by simply decaying, as all the individual modes do, and, in the absence of repeated eigenvalues, all at different time constants.

It is noteworthy that if the system eigenvectors cannot be made accurately orthogonal by the introduction of control, selecting instead a system with the lowest dot products $(\psi_i \cdot \psi_j)$ will not necessarily lead to the lowest diachronic transient energy bound due to the presence of the other factors $c_i^T c_j$ and $e^{\left(\lambda_i^T + \lambda_j\right)t}$ in (4.54), and since, for the bound, c_i are selected to maximise the transient energy growth, within the overall constraint $E(0) = (c_0, \ldots, c_N)\Psi^T\Psi(c_0, \ldots, c_N) = 1$.

Differentiating (4.55) the modal energy growth rate terms are

$$\sum_{i=1}^{N} c_i^T c_i \left(\lambda_i^T + \lambda_i\right) e^{\left(\lambda_i^T + \lambda_i\right)t} \tag{4.57}$$

which have an upper bound of zero, whereas the non-modal growth rate terms are

$$\sum_{i=1}^{N} \sum_{j=1}^{N, j \neq i} c_i^T c_j(\psi_i \cdot \psi_j) \left(\lambda_i^T + \lambda_j\right) e^{\left(\lambda_i^T + \lambda_j\right)t} \tag{4.58}$$

which are not bounded above by zero.

Modal and Non-Modal Components of Kinetic Energy Density in a System with $\mathcal{Q} \neq \mathbf{I}$

If the state variables $\mathcal{X}$ are not transformed, then substituting the expression for the evolution of state variables (4.37) into the expression for perturbation energy (4.34) produces

$$E(t) = {\chi_0}^T e^{\Lambda^T t} \Psi^T \mathcal{Q} \Psi e^{\Lambda t} \chi_0 \tag{4.59}$$

where Ψ is the matrix of right normalised eigenvectors ψ_i of $\mathcal{A}$, and Λ is a diagonal matrix containing the eigenvalues λ_i, which are all assumed stable. The condition which guarantees modal and therefore monotonic decay is $\Psi^T \mathcal{Q} \Psi = \mathrm{diag}(d_1, \ldots, d_N), d_i > 0 \, \forall i$, since then

$$\begin{aligned} E(t) &= {\chi_0}^T e^{\Lambda^T t} \mathrm{diag}(d_1, \ldots, d_N) e^{\Lambda t} \chi_0 \\ &= \sum_{i=1}^{N} c_i^T e^{\lambda_i^T t} d_i e^{\lambda_i t} c_i \end{aligned} \tag{4.60}$$

which decays monotonically for all χ_0. This may be interpreted as $\Psi^T \mathcal{Q} \Psi$ not coupling any modes by being diagonal and thus preventing non-modal behaviour, and also being positive definite, and thus ensuring modal energy decay rather than growth.

4.3.2 Linear Simulations

The state-space model is coded in Matlab, and controllers and estimators synthesized for a range of weighting parameters for both test cases 1 and 2. Final controllers and estimators are selected for each test case on the grounds of lowest energy bounds. Detailed linear simulations are performed for the open-loop, state feedback and output feedback systems, from the worst initial conditions, using the Matlab function `lsim`.

4.3.3 Non-Linear Simulations

A finite-volume computational fluid dynamics (CFD) Navier-Stokes solver is used for the non-linear simulations. This solver makes no assumption of spectral behaviour, solves the full non-linear Navier-Stokes equations, and is completely independent of the spectral code used for the controller synthesis and linear simulations.

Code

The full Navier-Stokes solver employs an unstructured, collocated grid, and is capable of representing complex geometry, for example as utilised by Yeoh et al. (2004), although a simple structured mesh of the channel is used in the present work. A second order central differencing scheme is used to discretise the spatial terms and first and second order Euler implicit schemes are used for time marching. These schemes are unconditionally stable (Ferziger and Peric, 2002, p148), although the second order scheme is more accurate in time. The schemes may produce oscillatory solutions for large cell Peclet numbers in the presence of large solution gradients, where the cell Peclet number Pe is

$$Pe = \frac{\rho u}{\mu / \delta x} \tag{4.61}$$

for the x-direction, and similarly for the y- and z-directions, and is a measure of the relative strengths of convection and diffusion at work in a mesh cell of side δx (Versteeg and Malalasekera, 1995, p112). The PISO algorithm is used to handle pressure-velocity coupling.

Modifications to the Code

It is difficult, even with the code converted to double precision and very fine meshes, to get agreement between linear and non-linear results for small perturbations if the solution algorithm provides the total velocity components $\vec{U} = \vec{U}_b + \vec{u}$. This occurs even for a static simulation of channel flow with transpiration. The reason is that the discretisation errors in $\vec{U}_b$ are of the same order of magnitude

as $\vec{u}$. Therefore the existing full Navier-Stokes CFD code is modified to solve for the non-linear perturbation (2.8,2.9) by the addition of extra convection terms $\left(\vec{U}_b \cdot \nabla\right) \vec{u}$ and $\left(\vec{u} \cdot \nabla\right) \vec{U}_b$. These are incorporated as convection and source terms respectively in the finite-volume scheme, as follows.

The Navier-Stokes equations in conservative or divergence form (Versteeg and Malalasekera, 1995, p24), for an incompressible fluid are

$$\begin{aligned}
\dot{U} + \nabla \cdot \left(U\vec{U}\right) &= -\frac{1}{\rho}\frac{\partial P}{\partial x} + \frac{\mu}{\rho}\nabla \cdot (\nabla U) \\
\dot{V} + \nabla \cdot \left(V\vec{U}\right) &= -\frac{1}{\rho}\frac{\partial P}{\partial y} + \frac{\mu}{\rho}\nabla \cdot (\nabla V) \\
\dot{W} + \nabla \cdot \left(W\vec{U}\right) &= -\frac{1}{\rho}\frac{\partial P}{\partial z} + \frac{\mu}{\rho}\nabla \cdot (\nabla W)
\end{aligned} \tag{4.62}$$

Integrating over a control volume Ω yields the finite volume form

$$\begin{aligned}
\int_\Omega \dot{U} d\Omega + \int_\Omega \nabla \cdot \left(U\vec{U}\right) d\Omega &= -\int_\Omega \frac{1}{\rho}\frac{\partial P}{\partial x} d\Omega + \int_\Omega \frac{\mu}{\rho}\nabla \cdot (\nabla U)\, d\Omega \\
\int_\Omega \dot{V} d\Omega + \int_\Omega \nabla \cdot \left(V\vec{U}\right) d\Omega &= -\int_\Omega \frac{1}{\rho}\frac{\partial P}{\partial y} d\Omega + \int_\Omega \frac{\mu}{\rho}\nabla \cdot (\nabla V)\, d\Omega \\
\int_\Omega \dot{W} d\Omega + \int_\Omega \nabla \cdot \left(W\vec{U}\right) d\Omega &= -\int_\Omega \frac{1}{\rho}\frac{\partial P}{\partial z} d\Omega + \int_\Omega \frac{\mu}{\rho}\nabla \cdot (\nabla W)\, d\Omega
\end{aligned} \tag{4.63}$$

Gauss' Theorem states that the integral of a divergence of a continuously differentiable vector $\vec{F}$ over a volume Ω is equal to the integral of the normal component of $\vec{F}$ over the surface S of Ω

$$\int_\Omega \nabla \cdot \vec{F} \quad d\Omega = \int_S \vec{F} \cdot \vec{n} \quad ds \tag{4.64}$$

where unit vector $\vec{n}$ is normal to surface element ds, and points outwards from Ω. After applying Gauss' Theorem to the integrals of a divergence in (4.63)

$$\begin{aligned}
\int_\Omega \dot{U} d\Omega + \int_S \left(U\vec{U}\right) \cdot \vec{n} \quad ds &= -\int_\Omega \frac{1}{\rho}\frac{\partial P}{\partial x} d\Omega + \int_S \frac{\mu}{\rho} (\nabla U) \cdot \vec{n} \quad ds \\
\int_\Omega \dot{V} d\Omega + \int_S \left(V\vec{U}\right) \cdot \vec{n} \quad ds &= -\int_\Omega \frac{1}{\rho}\frac{\partial P}{\partial y} d\Omega + \int_S \frac{\mu}{\rho} (\nabla V) \cdot \vec{n} \quad ds \\
\int_\Omega \dot{W} d\Omega + \int_S \left(W\vec{U}\right) \cdot \vec{n} \quad ds &= -\int_\Omega \frac{1}{\rho}\frac{\partial P}{\partial z} d\Omega + \int_S \frac{\mu}{\rho} (\nabla W) \cdot \vec{n} \quad ds
\end{aligned} \tag{4.65}$$

Since U, V, W are scalars

$$\begin{aligned}
\int_\Omega \dot{U} d\Omega + \int_S U \left(\vec{U} \cdot \vec{n}\right) ds &= -\int_\Omega \frac{1}{\rho}\frac{\partial P}{\partial x} d\Omega + \int_S \frac{\mu}{\rho} (\nabla U) \cdot \vec{n} \quad ds \\
\int_\Omega \dot{V} d\Omega + \int_S V \left(\vec{U} \cdot \vec{n}\right) ds &= -\int_\Omega \frac{1}{\rho}\frac{\partial P}{\partial y} d\Omega + \int_S \frac{\mu}{\rho} (\nabla V) \cdot \vec{n} \quad ds \\
\int_\Omega \dot{W} d\Omega + \int_S W \left(\vec{U} \cdot \vec{n}\right) ds &= -\int_\Omega \frac{1}{\rho}\frac{\partial P}{\partial z} d\Omega + \int_S \frac{\mu}{\rho} (\nabla W) \cdot \vec{n} \quad ds
\end{aligned} \tag{4.66}$$

If the finite volumes are polyhedral cells, the volume integrals may be approximated by the value at the centroid (subscript $_p$) multiplied by the cell volume vol, and the surface integrals may be approximated by the sum of the values at the face centres (subscript $_f$) multiplied by the face areas $area_f$

$$\begin{aligned}
\dot{U}_p vol + \sum_{facesf} U_f \left(\vec{U}_f \cdot \vec{n}_f\right) area_f &= -\frac{1}{\rho}\frac{\partial P_p}{\partial x} vol + \sum_{facesf} \frac{\mu}{\rho} (\nabla U_f) \cdot \vec{n}_f \quad area_f \\
\dot{V}_p vol + \sum_{facesf} V_f \left(\vec{U}_f \cdot \vec{n}_f\right) area_f &= -\frac{1}{\rho}\frac{\partial P_p}{\partial y} vol + \sum_{facesf} \frac{\mu}{\rho} (\nabla V_f) \cdot \vec{n}_f \quad area_f \\
\dot{W}_p vol + \sum_{facesf} W_f \left(\vec{U}_f \cdot \vec{n}_f\right) area_f &= -\frac{1}{\rho}\frac{\partial P_p}{\partial z} vol + \sum_{facesf} \frac{\mu}{\rho} (\nabla W_f) \cdot \vec{n}_f \quad area_f
\end{aligned} \tag{4.67}$$

The common terms $\left(\vec{U}_f \cdot \vec{n}_f\right) area_f$ are the convective fluxes through each cell face, $conv_f$

$$\begin{aligned}
\dot{U}_p vol + \sum_{facesf} U_f conv_f &= -\frac{1}{\rho}\frac{\partial P_p}{\partial x} vol + \sum_{facesf} \frac{\mu}{\rho} (\nabla U_f) \cdot \vec{n}_f \quad area_f \\
\dot{V}_p vol + \sum_{facesf} V_f conv_f &= -\frac{1}{\rho}\frac{\partial P_p}{\partial y} vol + \sum_{facesf} \frac{\mu}{\rho} (\nabla V_f) \cdot \vec{n}_f \quad area_f \\
\dot{W}_p vol + \sum_{facesf} W_f conv_f &= -\frac{1}{\rho}\frac{\partial P_p}{\partial z} vol + \sum_{facesf} \frac{\mu}{\rho} (\nabla W_f) \cdot \vec{n}_f \quad area_f
\end{aligned} \tag{4.68}$$

Now the Navier-Stokes perturbation equations in conservative form are

$$\begin{aligned}
\dot{u} + \nabla \cdot \left((U_b + u)\left(\vec{U}_b + \vec{u}\right)\right) &= -\frac{1}{\rho}\frac{\partial p}{\partial x} + \frac{\mu}{\rho}\nabla \cdot (\nabla u) \\
\dot{v} + \nabla \cdot \left(v\left(\vec{U}_b + \vec{u}\right)\right) &= -\frac{1}{\rho}\frac{\partial p}{\partial y} + \frac{\mu}{\rho}\nabla \cdot (\nabla v) \\
\dot{w} + \nabla \cdot \left(w\left(\vec{U}_b + \vec{u}\right)\right) &= -\frac{1}{\rho}\frac{\partial p}{\partial z} + \frac{\mu}{\rho}\nabla \cdot (\nabla w)
\end{aligned} \tag{4.69}$$

simplifying, noting $\nabla \cdot \left(U_b \vec{U}_b\right) = 0$

$$\begin{aligned}
\dot{u} + \nabla \cdot (U_b \vec{u}) + \nabla \cdot \left(u\vec{U}_b\right) + \nabla \cdot (u\vec{u}) &= -\frac{1}{\rho}\frac{\partial p}{\partial x} + \frac{\mu}{\rho}\nabla \cdot (\nabla u) \\
\dot{v} + \nabla \cdot \left(v\vec{U}_b\right) + \nabla \cdot (v\vec{u}) &= -\frac{1}{\rho}\frac{\partial p}{\partial y} + \frac{\mu}{\rho}\nabla \cdot (\nabla v) \\
\dot{w} + \nabla \cdot \left(w\vec{U}_b\right) + \nabla \cdot (w\vec{u}) &= -\frac{1}{\rho}\frac{\partial p}{\partial z} + \frac{\mu}{\rho}\nabla \cdot (\nabla w)
\end{aligned} \tag{4.70}$$

Comparing the conservative form of the Navier-Stokes equations in U, V, W, P (4.62) with the conservative form of the Navier-Stokes perturbation equations in

u, v, w, p (4.70), it is evident that there are extra terms in the perturbation form. The x-momentum perturbation equation has the extra terms

$$\nabla \cdot (U_b \vec{u}) + \nabla \cdot \left(u \vec{U_b} \right) \tag{4.71}$$

The y-momentum perturbation equation has the extra term

$$\nabla \cdot \left(v \vec{U_b} \right) \tag{4.72}$$

The z-momentum perturbation equation has the extra term

$$\nabla \cdot \left(w \vec{U_b} \right) \tag{4.73}$$

Now in (4.71)

$$\begin{aligned} \nabla \cdot (U_b \vec{u}) &= \frac{\partial U_b u}{\partial x} + \frac{\partial U_b v}{\partial y} + \frac{\partial U_b w}{\partial z} \\ &= U_b \frac{\partial u}{\partial x} + U_b \frac{\partial v}{\partial y} + U_b \frac{\partial w}{\partial z} + u \frac{\partial U_b}{\partial x} + v \frac{\partial U_b}{\partial y} + w \frac{\partial U_b}{\partial z} \\ &= U_b \left(\frac{\partial u}{\partial x} + \frac{\partial v}{\partial y} + \frac{\partial w}{\partial z} \right) + u \frac{\partial U_b}{\partial x} + v \frac{\partial U_b}{\partial y} + w \frac{\partial U_b}{\partial z} \\ &= v \frac{\partial U_b}{\partial y} \end{aligned} \tag{4.74}$$

on expanding, and applying the perturbation continuity equation (2.9), and noting that U_b only varies with y. Employing this result and integrating over a control volume Ω, the x-momentum extra terms (4.71) are

$$\int_\Omega v \frac{\partial U_b}{\partial y} d\Omega + \int_\Omega \nabla \cdot \left(u \vec{U_b} \right) d\Omega \tag{4.75}$$

and the y-momentum extra term (4.72) and z-momentum extra term (4.73) are

$$\int_\Omega \nabla \cdot \left(v \vec{U_b} \right) d\Omega \tag{4.76}$$

$$\int_\Omega \nabla \cdot \left(w \vec{U_b} \right) d\Omega \tag{4.77}$$

respectively.

Gauss' theorem is applied to the extra terms containing $\nabla \cdot \left(u_i \vec{U_b} \right)$. The x-momentum extra terms (4.75) are then

$$\int_\Omega v \frac{\partial U_b}{\partial y} d\Omega + \int_S u \left(\vec{U_b} \cdot \vec{n} \right) ds \tag{4.78}$$

and the y-momentum extra term (4.76) and z-momentum extra term (4.77) are

$$\int_S v \left(\vec{U_b} \cdot \vec{n} \right) ds \tag{4.79}$$

$$\int_S w \left(\vec{U}_b \cdot \vec{n} \right) \, ds \tag{4.80}$$

respectively.

For polyhedral cells, the extra term volume and surface integrals are approximated as previously in (4.67). The x-momentum extra terms (4.78) are then

$$v_p \left. \frac{\partial U_b}{\partial y} \right|_p vol + \sum_{facesf} u_f \left(\vec{U}_b \cdot \vec{n} \right)_f area_f \tag{4.81}$$

and the y-momentum extra term (4.79) and z-momentum extra term (4.80) are

$$\sum_{facesf} v_f \left(\vec{U}_b \cdot \vec{n} \right)_f area_f \tag{4.82}$$

$$\sum_{facesf} w_f \left(\vec{U}_b \cdot \vec{n} \right)_f area_f \tag{4.83}$$

respectively. The extra terms in (4.81,4.82,4.83)

$$\sum_{facesf} u_f \left(\vec{U}_b \cdot \vec{n} \right)_f area_f, \sum_{facesf} v_f \left(\vec{U}_b \cdot \vec{n} \right)_f area_f, \sum_{facesf} w_f \left(\vec{U}_b \cdot \vec{n} \right)_f area_f \tag{4.84}$$

may be incorporated by augmenting the convective flux in (4.68)

$$conv_f = \left(\vec{U}_f \cdot \vec{n}_f \right) area_f \tag{4.85}$$

to perturbation form

$$conv_f = \left(\left(\vec{u}_f + \vec{U}_b \right) \cdot \vec{n}_f \right) area_f \tag{4.86}$$

Since $\vec{U}_b = (U_b, 0, 0)$ this becomes

$$conv_f = \left(\vec{u}_f \cdot \vec{n}_f \right) area_f + U_{b,f} n_{f,x} area_f \tag{4.87}$$

where $\vec{n}_f = (n_{f,x}, n_{f,y}, n_{f,z})$. The extra term

$$v_p \left. \frac{\partial U_b}{\partial y} \right|_p vol \tag{4.88}$$

is incorporated with the other (4.68) x-momentum right hand side terms (so-called 'source' terms), so they become

$$-v_p \left. \frac{\partial U_b}{\partial y} \right|_p vol - \frac{1}{\rho} \frac{\partial p_p}{\partial x} vol + \sum_{facesf} \frac{\mu}{\rho} \left(\nabla u_f \right) \cdot \vec{n}_f \quad area_f \tag{4.89}$$

Comparing the conservative form of the continuity equation in U, V, W

$$\nabla \cdot \bar{U} = 0 \tag{4.90}$$

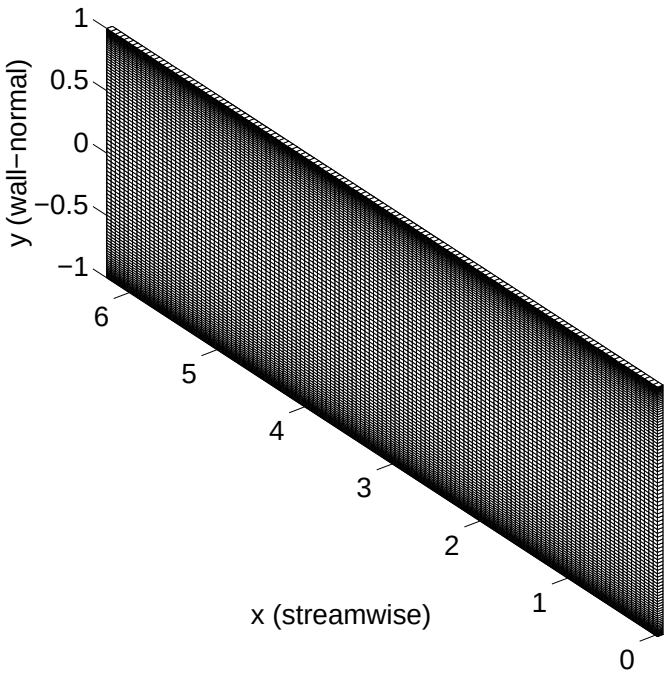

Figure 4.4: External View of Case 1 CFD Mesh

with the conservative form of the continuity perturbation equation in u, v, w

$$\nabla \cdot \bar{u} = 0 \tag{4.91}$$

it is evident that there are no extra terms in the perturbation form to be incorporated.

The code is also modified to calculate the channel perturbation mass flow and momentum accurately by integration, for use in normalising the iteration residuals, and to non-dimensionalise the results prior to writing them out, as in section 2.2.5.

Meshes

The meshes employed here are structured, and nominally two-dimensional, the third dimension being only one cell deep, since both test cases are two-dimensional. Since the meshes are so simple, they are created by a short Fortran program.

The mesh for case 1 is shown in figure 4.4, and covers one streamwise period, $x = 0, 2\pi$, with $2^7 = 128$ uniform cells, an appropriate scheme for fast Fourier transform data, and contains 99 cells in the wall-normal direction, $-h \leq y \leq h$, based on the Gauss-Lobatto collocation points ($h = 1$), thus producing cell refinement in the near wall region, and also avoiding the need for interpolation onto the location of the state variables. The mesh covers only one cell in the spanwise direction, since there is no flow in this direction, with a cell width equal to that in the streamwise direction. The maximum cell aspect ratio is 49.7, at the wall.

The mesh for case 2 is shown in figure 4.5, and covers one spanwise period, $z = 0, 2\pi/2.044$, with $2^6 = 64$ uniform cells, also an appropriate scheme for fast

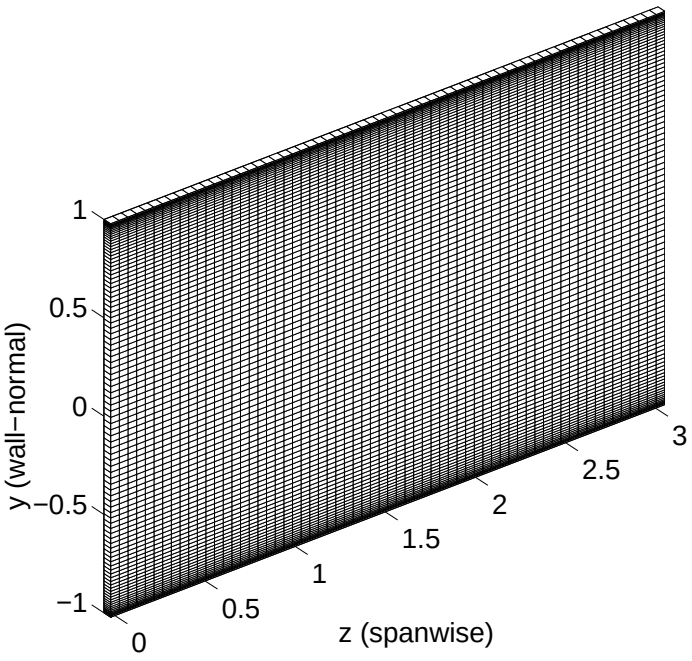

Figure 4.5: External View of Case 2 CFD Mesh

Fourier transform data, and also contains 99 cells in the wall-normal direction. The mesh covers only one cell in the streamwise direction, since there is no variation in this direction. The maximum cell aspect ratio for this mesh is 48.7.

Neither of the non-linear simulations of test cases 1 and 2 may lead to true turbulence, since the meshes are effectively two-dimensional.

Fluid Properties and Initial Conditions

The CFD input data is dimensionalised, and represents a fluid with density 1kg/m^3, viscosity 0.003 Pa s, flowing between walls 2m apart. The base flow centreline velocity is 30m/s for test case 1, and 15m/s for test case 2. The worst initial conditions calculated from the spectral code are dimensionalised and assigned to the cell centroids and boundary faces.

Boundary Conditions

The boundary conditions for case 1 are shown in figure 4.6, and are cyclic in the streamwise direction, allowing not just the fundamental streamwise mode but also harmonics, and are symmetric in the spanwise direction. The wall boundary conditions are modified to simulate wall transpiration, using inlet type boundary conditions.

The boundary conditions for case 2 are shown in figure 4.7, and are cyclic in the streamwise direction, which enforces zero gradient, as the mesh is only one cell wide in this direction, and are cyclic in the spanwise direction. Again the wall boundary conditions are modified to simulate wall transpiration, using inlet type boundary conditions.

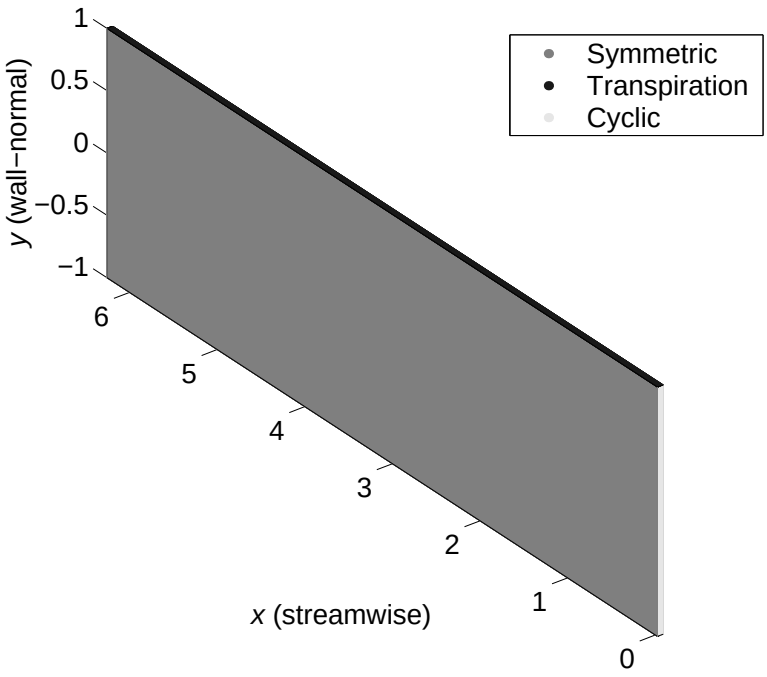

Figure 4.6: External View of Case 1 CFD Boundary Conditions

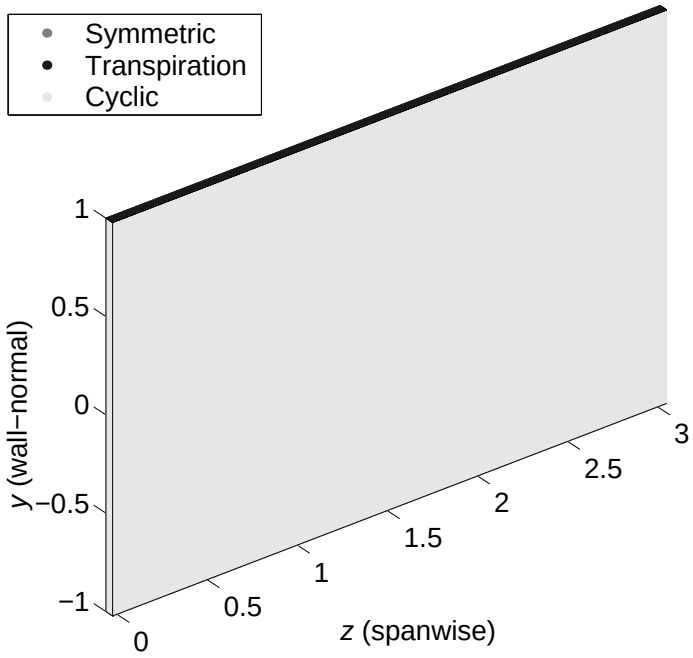

Figure 4.7: External View of Case 2 CFD Boundary Conditions

Implementation of the Controller in the Non-linear Simulation

The full Navier-Stokes CFD code is further modified to initially store the controller matrix $\mathcal{K}$, estimator matrices $\mathcal{A}, \mathcal{B}, \mathcal{C}, \mathcal{L}$ and the matrices necessary for calculating the state variables and energy from the flow-field, $\mathbf{T}, \mathcal{T}, \mathcal{Q}$.

At each timestep the code provides a velocity flow-field. The measured wall shears, $1/R\,(\partial u/\partial y)$ and $1/R\,(\partial w/\partial y)$, are calculated by a first order finite difference method, as the collocation points are very closely spaced at the walls, and for case 2 the vorticity flow-field is calculated by a second order method (Råde and Westergren, 1999, p393), since in the interior of the channel the points are further apart.

Fast Fourier transforms are then performed on the velocity and vorticity flow-fields and wall shears, in the streamwise direction for case 1, and spanwise direction for case 2. Pairs of transforms are performed simultaneously using subroutine `TWOFFT` from Press et al. (1986, p398). The Fourier coefficients $\tilde{v}(y_k)$, $\tilde{\eta}(y_k)$ at the non-zero streamwise or spanwise wavenumbers α or β are selected from the results. The measurement vector $\tilde{\mathbf{y}}$ is also composed from the results of fast Fourier transforms on the wall shears (2.46,2.47).

The state variables $\mathcal{X}$ are then calculated from $\tilde{v}(y_k)$, $\tilde{\eta}(y_k)$ using the inverse of matrix $\mathbf{T}_{cp}$ (2.106), and from these the transient energy $E = \mathcal{X}^{\mathcal{T}}\mathcal{Q}\mathcal{X}$. Estimated state variables $\hat{\mathcal{X}}$ are calculated from the measurement vector $\tilde{\mathbf{y}}$, and control vector $\mathcal{U}$ by integrating (4.27), using the initial estimated state variables $\hat{\mathcal{X}}(t=0)$ as the constant of integration, via an implicit method (Press et al., 1986, p575), as the equation system was found to be stiff for case 2.

For state feedback the control signals $\dot{\tilde{v}}_u, \dot{\tilde{v}}_l$ are calculated as $\mathcal{U} = -\mathcal{K}\mathcal{X}$, whereas for output feedback they are calculated as $\mathcal{U} = -\mathcal{K}\hat{\mathcal{X}}$. The control signals are integrated to become $\tilde{v}_u, \tilde{v}_l$, using the initial conditions $\tilde{v}_u(0)$ and $\tilde{v}_l(0)$, and the wall transpiration velocities v_u, v_l are set as

$$\begin{aligned} v_u(x,z) &= \Re\left(\tilde{v}_u e^{\jmath(\alpha x+\beta z)}\right) \\ v_l(x,z) &= \Re\left(\tilde{v}_l e^{\jmath(\alpha x+\beta z)}\right) \end{aligned} \tag{4.92}$$

for the duration of the subsequent time step, using (2.32,2.29).

4.4 Results and Discussion

This section describes the results of controller and estimator synthesis, and linear and non-linear simulations of the open-loop, state feedback and output feedback systems from the worst initial conditions. A wall-normal discretisation of $N = 100$ is used, to ensure convergence with N, except where the issue of convergence itself is investigated.

4.4.1 Controller synthesis

LQR controllers are synthesized for a range of control weights r, by solving the algebraic Riccati equation (ARE) (4.3) with $\mathcal{R} = r^2\mathbf{I}$, for discretisation $N = 100$.

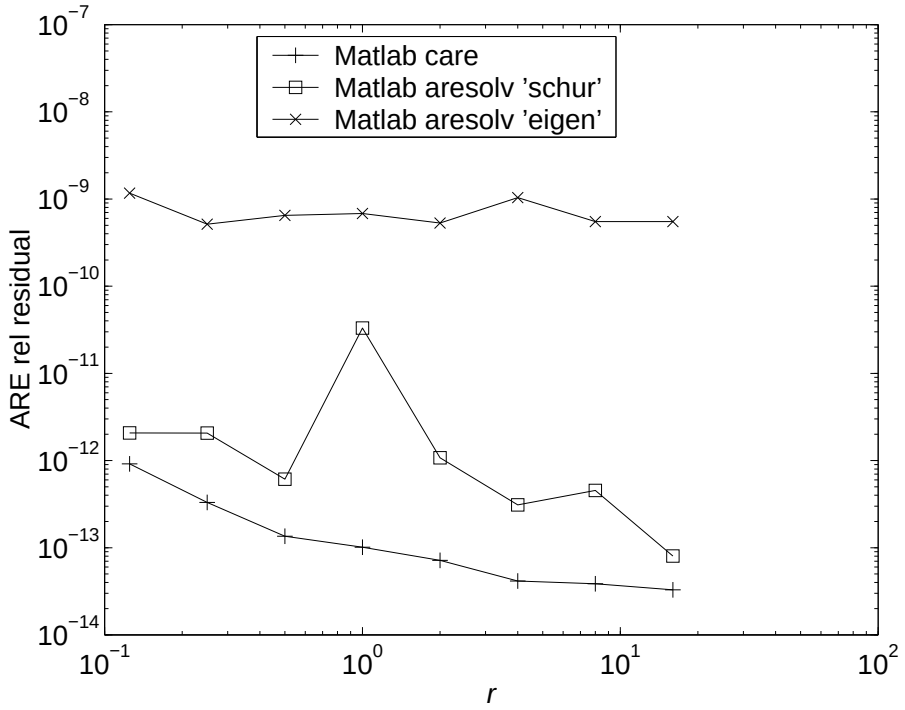

Figure 4.8: Case 1 LQR ARE Relative Residual vs Control Weight r, $N = 100$

The Matlab Release 11 functions `care` (called via `lqr`) and `aresolv`, with both `eigen` and `schur` options, are used to investigate which performs best on such a large system. For case 1, the Matlab function `care`, based on the Hamiltonian matrix, produces the lowest relative residuals i.e. the Frobenius norm of the residual divided by that of the solution $\|ric(\mathcal{P})\|_F / \|\mathcal{P}\|_F$. These residuals are shown in figure 4.8, and are of acceptably small magnitude, implying no particular problems solving the equation for such a large system, at least for this system and range of weights, although numerical problems arise outside this range. Other library routines, such as Slicot `slcares` (Benner et al., 1999; Van Huffel et al., 2004), and newer techniques, such as those of Morris and Navasca (2005), may be able to extend the range of weights.

The variation of diachronic transient energy bound with control weight r for case 1 is shown in figure 4.9, for several discretizations $N = 30, 40, 50, 70, 100$. Convergence with N is relatively fast, and has occurred by $N = 30$. The continued convergence at high N again demonstrates the existence of few problems solving this particular system when very large. The range of weights is appropriate for controller synthesis, since it covers convergence at low r, where the control effort is large and the energy is small. As the control weight rises, the control effort falls, and thus the energy bound rises. The variation here is monotonic, but need not be if very high control (very low weight) itself increases transient energy, as further investigated in section 6.3.2. A value of $r = 0.25$ is selected for subsequent simulations, as this produces almost the lowest diachronic transient energy bound, without being unnecessarily small, which would lead to unnecessarily large control effort. Low diachronic transient energy bound implies low transient energy over

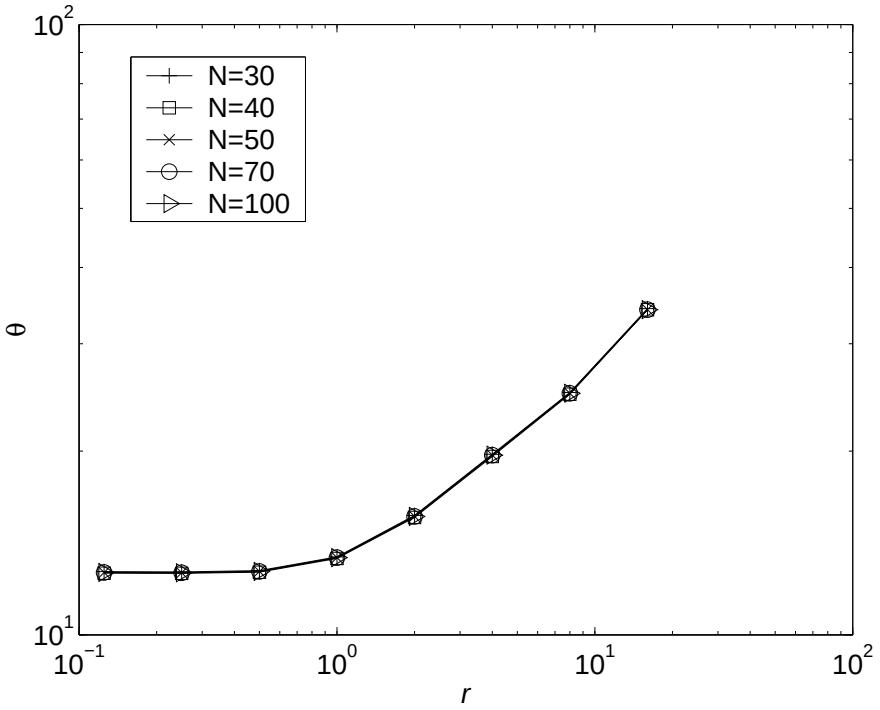

Figure 4.9: Case 1 LQR Diachronic Transient Energy Bound θ vs Control Weight r, for Different Discretisations N

all unit energy initial conditions and all time, thus reducing the possibility of non-linear behaviour and transition to turbulence.

For case 2, the Matlab function `care` generally produces the lowest relative residuals. These residuals are shown in figure 4.10, and are again of acceptably small magnitude, and the function reports that the problem is well posed. The variation of diachronic transient energy bound with control weight r for case 2 is shown in figure 4.11. Several discretisations N are shown, and, as for case 1, convergence has occurred by $N = 30$. A control weight of $r = 128.0$ is selected for further work, as this produces almost the lowest diachronic transient energy bound.

4.4.2 Estimator synthesis

Residuals

LQE estimators are synthesized for a range of measurement noise weights s, by solving the algebraic Riccati equation (ARE) (4.29) with $\mathcal{V} = s\mathbf{I}$, using the Matlab functions `care` (called via `lqe`) and `aresolv`, with both `eigen` and `schur` options, for $N = 100$. For case 1, the Matlab function `care` generally produces the lowest relative residuals, as shown in figure 4.12 for the tuned estimator. The residuals are of acceptably small magnitude, but not as small as those found during the synthesis of controllers.

For case 2, the Matlab function `aresolv` option `eigen` generally produces the lowest relative residuals, as shown in figure 4.13 for the tuned estimator, and

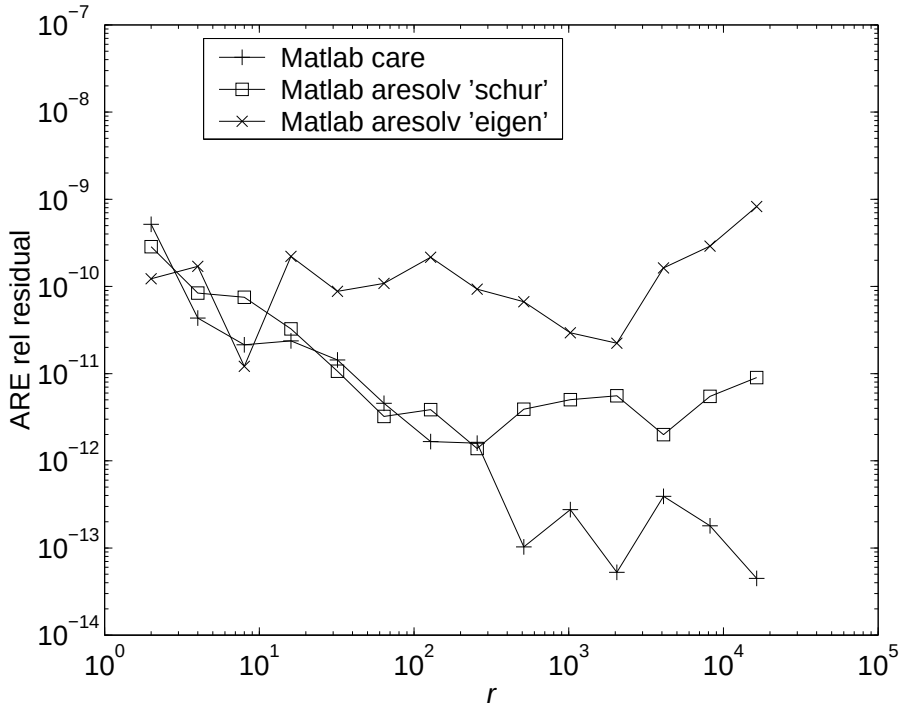

Figure 4.10: Case 2 LQR ARE Relative Residual vs Control Weight r, $N = 100$

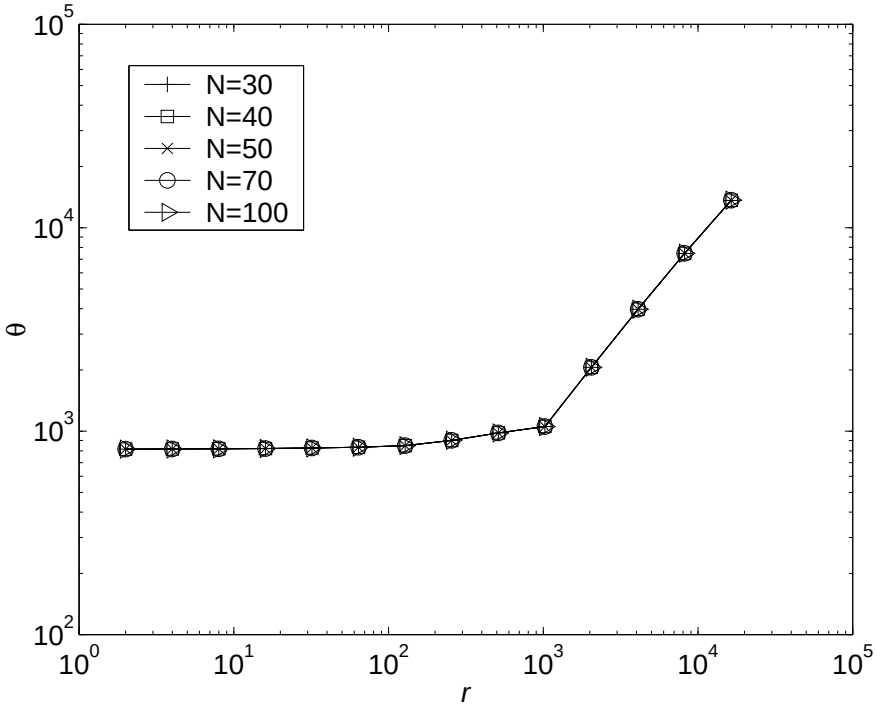

Figure 4.11: Case 2 LQR Diachronic Transient Energy Bound θ vs Control Weight r, for Different Discretisations N

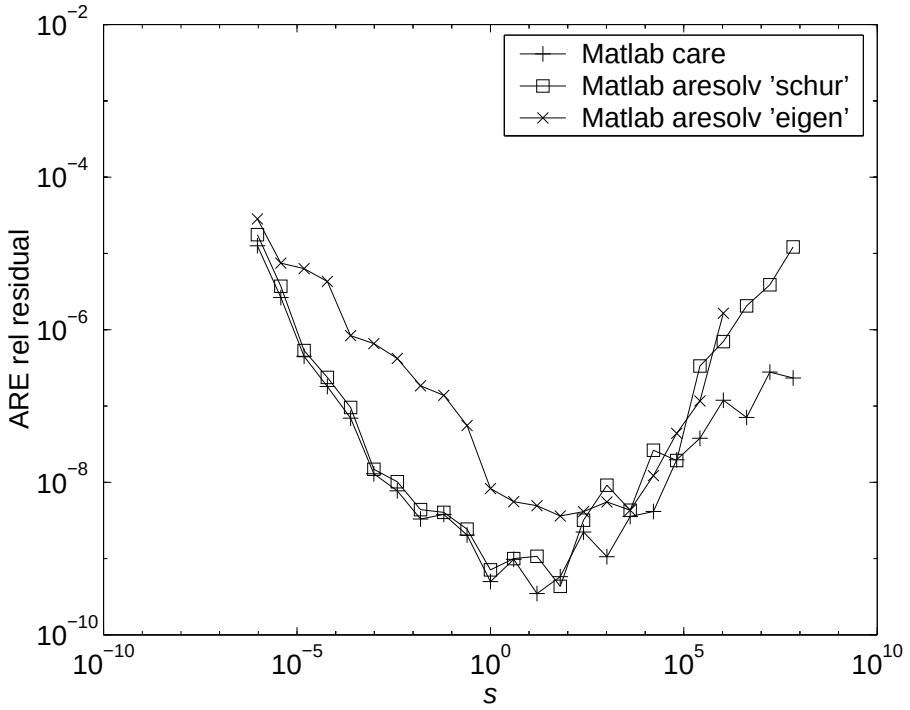

Figure 4.12: Case 1 LQE ARE Relative Residual vs Measurement Noise Weight s, for Tuned Estimator, $N = 100$

again are of acceptably small magnitude, and the function reports that the problem is well posed.

Poles

The variation of the maximum real part of the estimator poles with measurement noise weight s for case 1 is shown in figure 4.14, for both uniform and tuned estimators. Case 2 is shown in figure 4.15. The maximum real part of the estimator poles corresponds to the slowest estimator convergence rate.

Good estimator performance requires that the estimator poles be faster (real part more negative) than the plant poles. However, the current plant has a large number of poles, the faster ones of which are not known accurately, and it is not feasible to make the slowest estimator poles faster than these. At small s, the slowest pole of the tuned estimator is faster than that of the uniform estimator for case 1, but not quite as fast for case 2. Small s represents low measurement noise i.e. reliable measurements.

Estimated Energy Bound θ_{Est} from Estimator Zero Initial Conditions

The variation of estimated energy bound with measurement noise weight for the case 1 tuned estimator is shown in figure 4.16. The initial conditions are zero estimated state variables, and plant worst diachronic transient energy bound initial state variables. Thus the initial estimator error is equal to the plant worst initial conditions. Several different discretisations N are shown. Convergence with N is

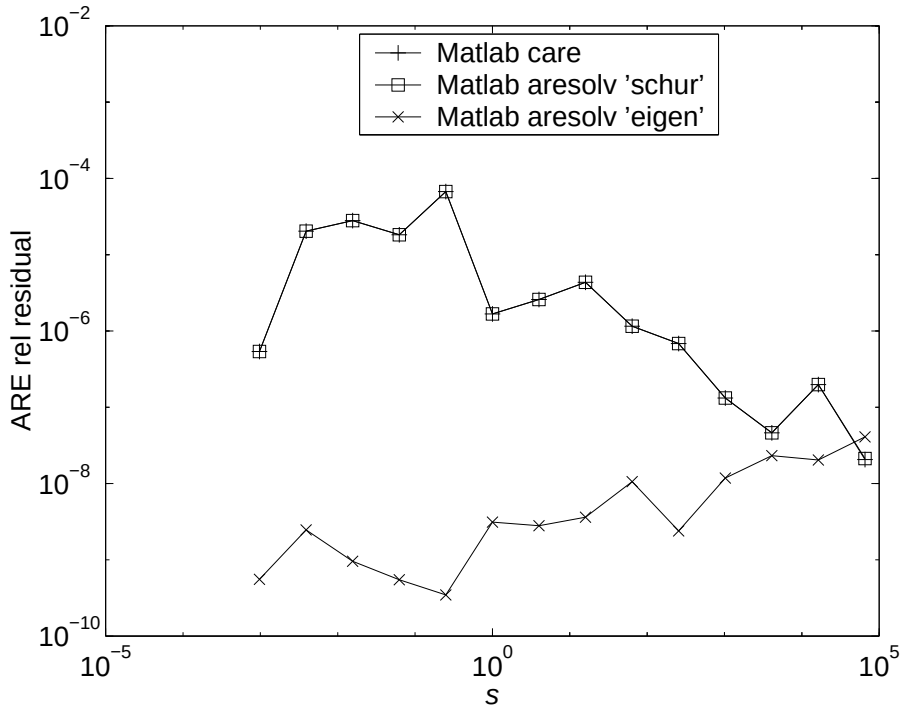

Figure 4.13: Case 2 LQE ARE Relative Residual vs Measurement Noise Weight s, for Tuned Estimator, $N = 100$

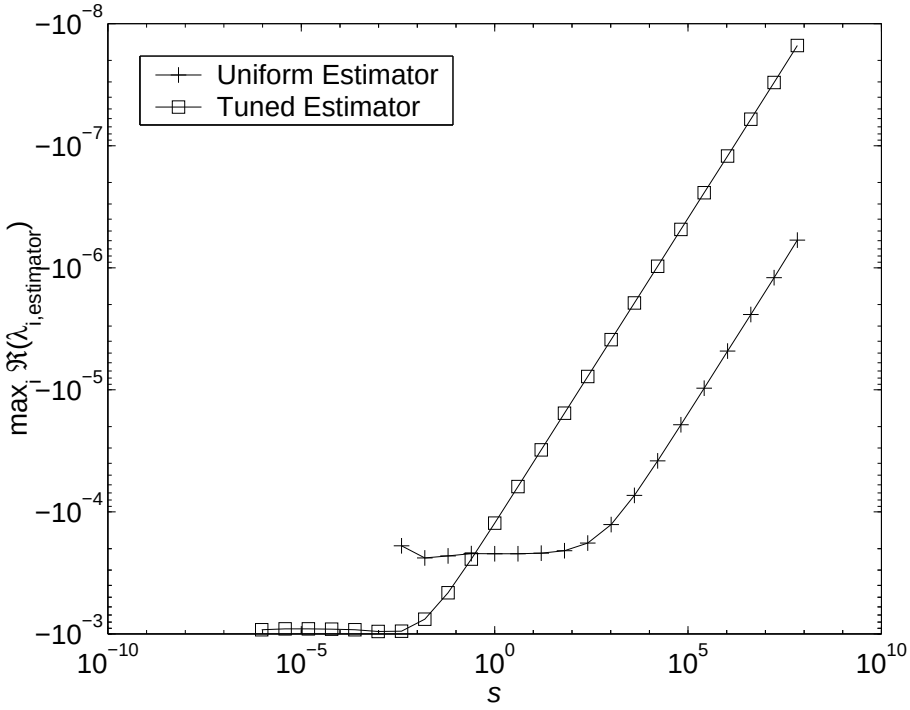

Figure 4.14: Case 1 LQE $\max_i(\Re(\lambda_{i,estimator}))$ vs Measurement Noise Weight s, $N = 100$

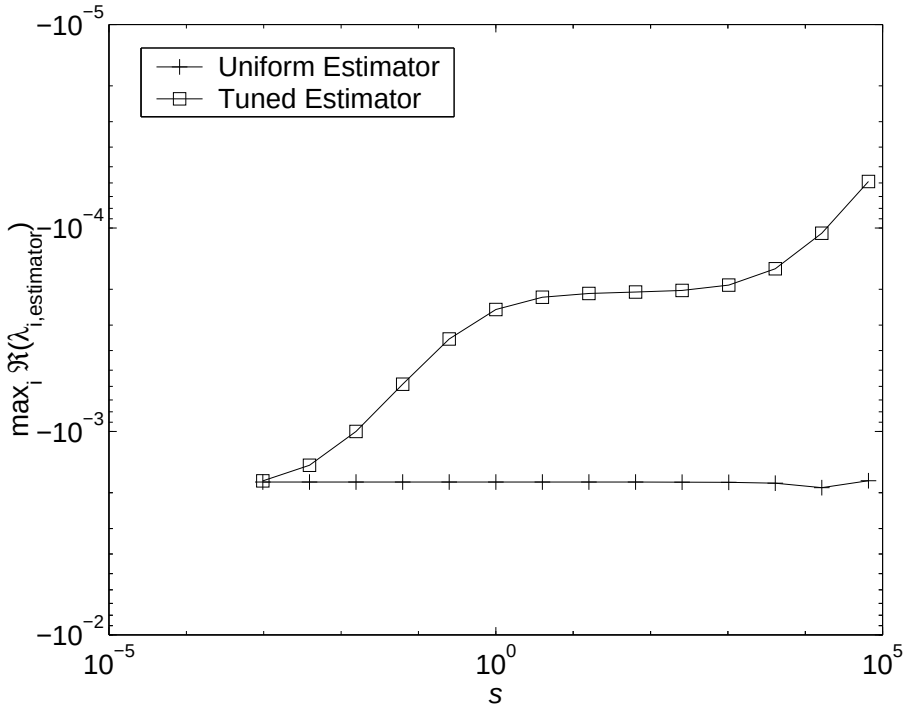

Figure 4.15: Case 2 LQE $\max_i(\Re(\lambda_{i,estimator}))$ vs Measurement Noise Weight s, $N = 100$

relatively slow, as compared to that of the controller in figure 4.9, and does not occur until $N = 70$, which is consistent with the behaviour of the wall eigenvector gradients used for observation in section 2.8.2.

The same variation for case 2 is shown in figure 4.17, from equivalent initial conditions. Convergence with N is better than for case 1, but does not fully occur until $N = 70$.

The variation of estimated energy bound with measurement noise weight for case 1 uniform and tuned estimators is shown in figure 4.18. This variation for case 2 is shown in figure 4.19. At low measurement noise weight, corresponding to more reliable measurements, the tuned estimator provides a significantly smaller estimated energy bound than the uniform estimator for both test cases. This implies that if the estimators are initialised with zero estimates, and the plant is initialised with its worst initial conditions, the tuned estimates will diverge less than the uniform estimates from the plant state variables, in terms of error energy. At high measurement noise weight, the two estimators perform similarly.

Diachronic Error Energy Bound θ_{Error} from Estimator Worst Initial Conditions

The variation of Diachronic Error Energy Bound θ_{Error} with measurement noise weight for cases 1 and 2 are shown in figures 4.20 and 4.21 respectively, starting from the worst initial estimator error conditions. At low measurement noise weight the tuned estimator produces considerably higher Diachronic Error Energy Bound θ_{Error} than the uniform estimator for both test cases. This implies that the tuned

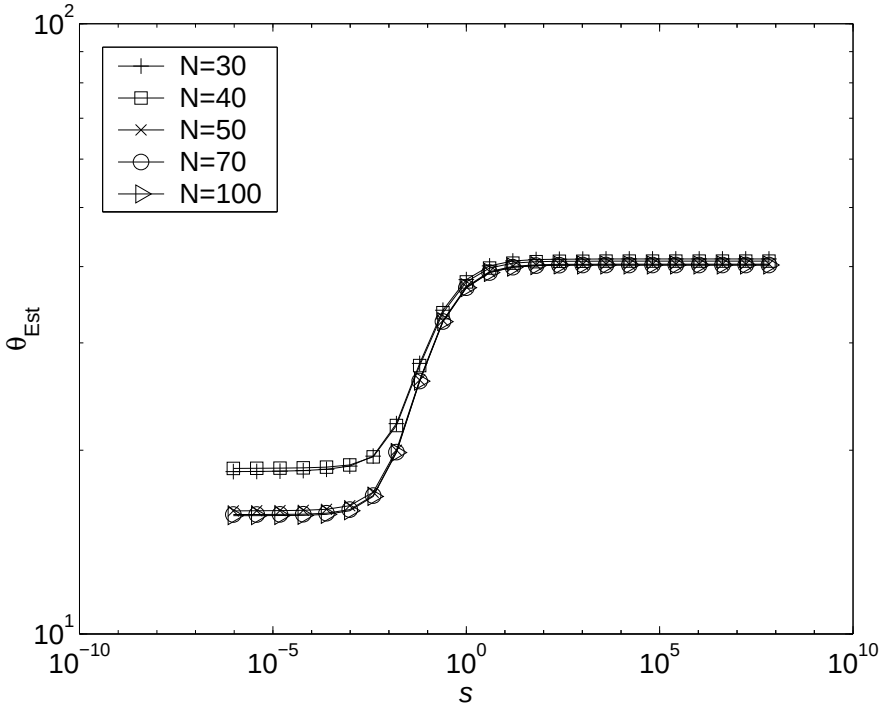

Figure 4.16: Case 1 Tuned LQE Estimated Energy Bound θ_{Est} vs Measurement Noise Weight s, for Discretisations N, from zero estimates i.e. $\hat{\mathcal{X}} = \mathbf{0}$, $\mathcal{X}_{Error} = \mathcal{X}_{Worst}$

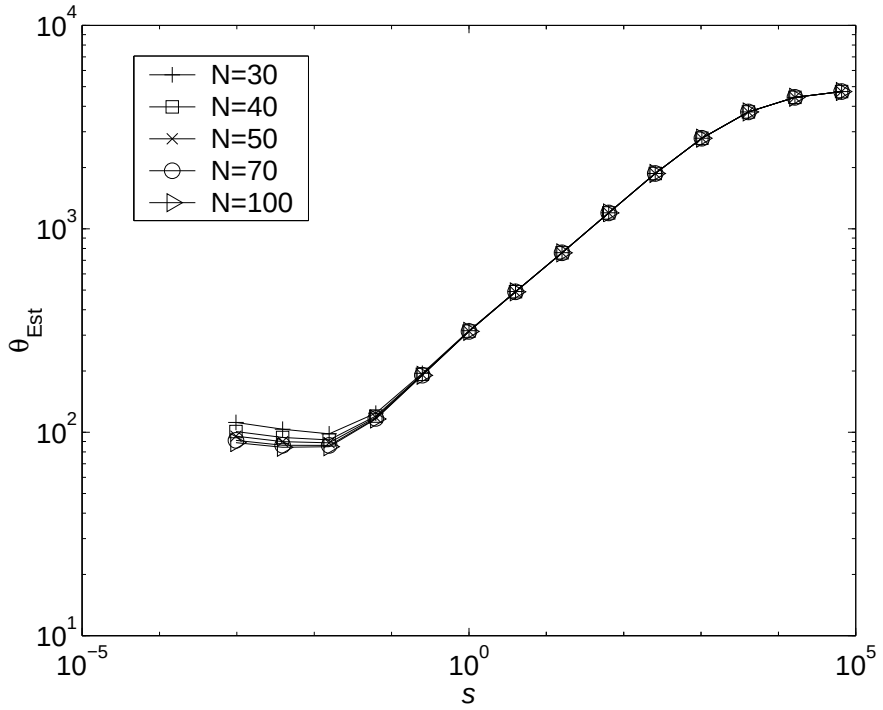

Figure 4.17: Case 2 Tuned LQE Estimated Energy Bound θ_{Est} vs Measurement Noise Weight s, for Discretisations N, from zero estimates i.e. $\hat{\mathcal{X}} = \mathbf{0}$, $\mathcal{X}_{Error} = \mathcal{X}_{Worst}$

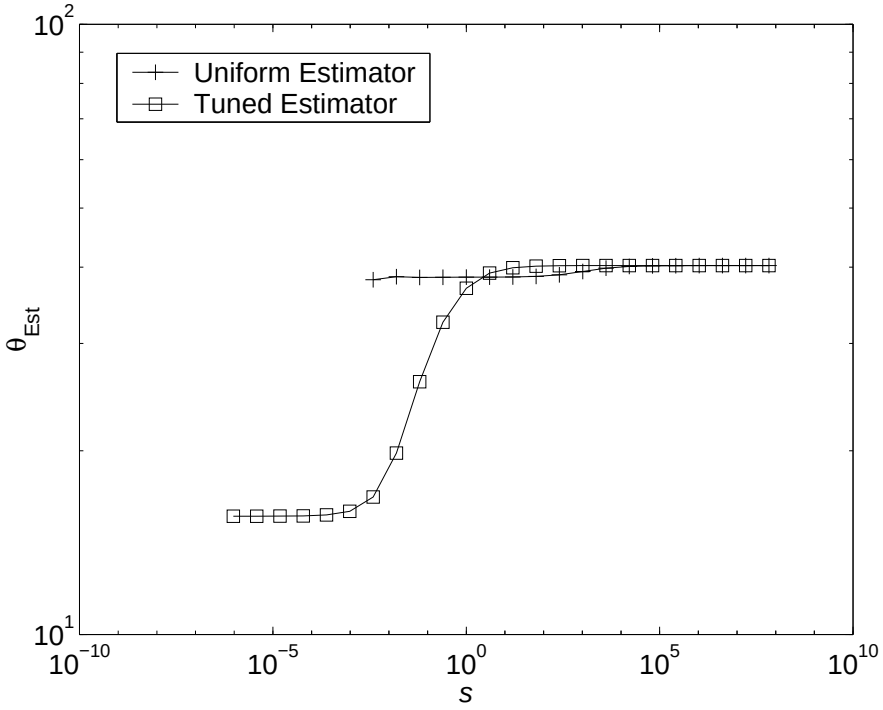

Figure 4.18: Case 1 LQE Estimated Energy Bound θ_{Est} vs Measurement Noise Weight s, from zero estimates i.e. $\hat{\mathcal{X}} = \mathbf{0}$, $\mathcal{X}_{Error} = \mathcal{X}_{Worst}$, $N = 100$

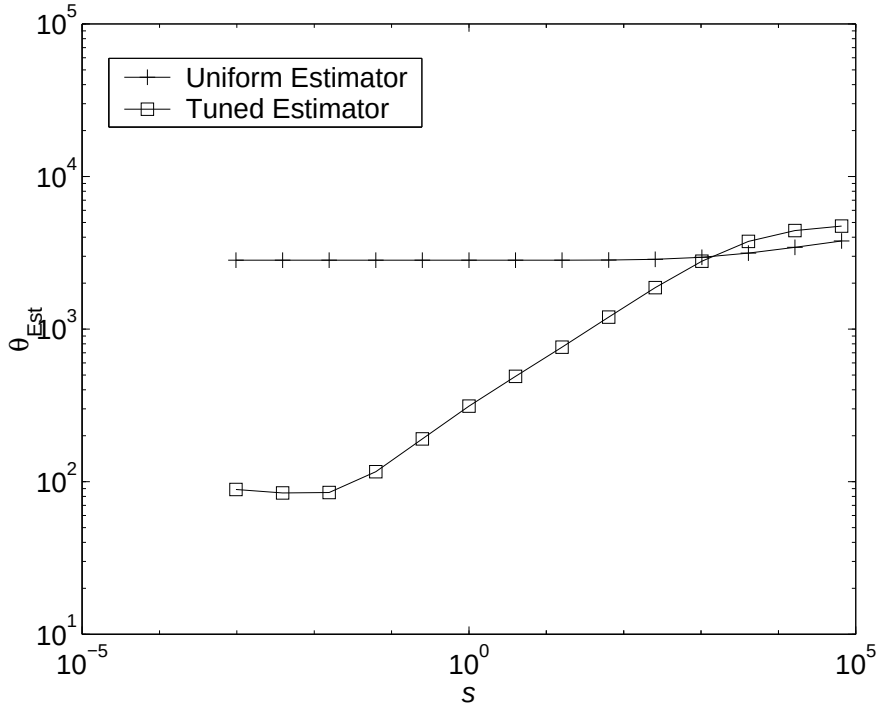

Figure 4.19: Case 2 LQE Estimated Energy Bound θ_{Est} vs Measurement Noise Weight s, from zero estimates i.e. $\hat{\mathcal{X}} = \mathbf{0}$, $\mathcal{X}_{Error} = \mathcal{X}_{Worst}$, $N = 100$

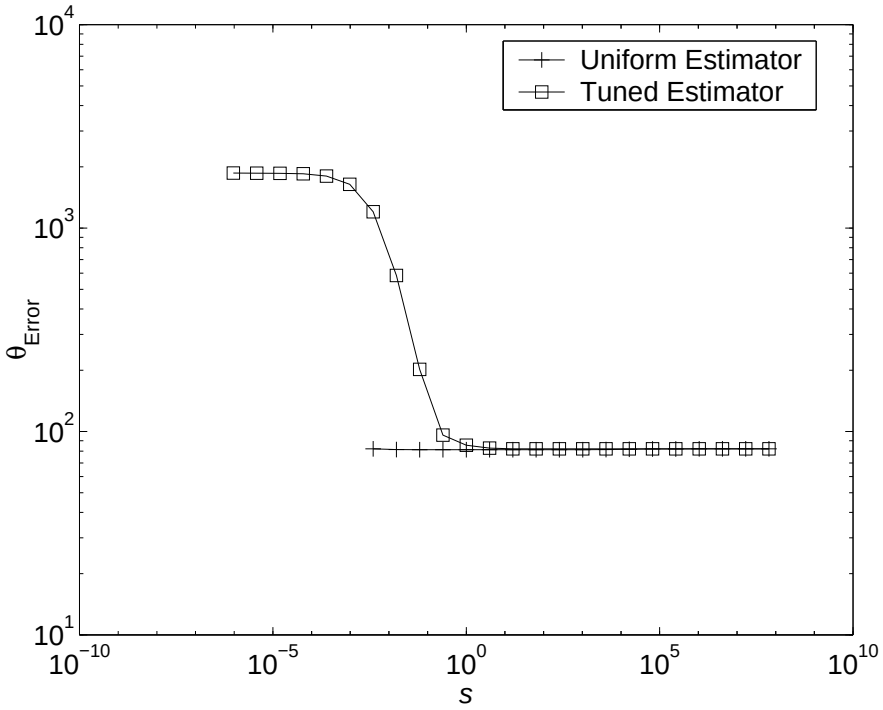

Figure 4.20: Case 1 LQE Diachronic Error Energy Bound θ_{Error} vs Measurement Noise Weight s, from worst estimates $\mathcal{X}_{Error} = \mathcal{X}_{Error,Worst}$, $N = 100$

estimator is capable of diverging further from the plant state variables than the uniform estimator would diverge, if each is initialised with their worst estimator state variables of unit error energy.

Discussion

The worst estimator initial error conditions $\mathcal{X}_{Error,Worst}$ are considered very exacting, since they lead to growth of diachronic error energy bound θ_{Error} of comparable magnitude to the plant diachronic transient energy bound, if not greater. Since the estimators are stable and their state variables converge upon the plant state variables, it is difficult to see how such estimator initial conditions could occur. In contrast, zero estimates $\hat{\mathcal{X}} = \mathbf{0}$, as used by Hogberg et al. (2003a, p169), are to be expected upon initialisation of the estimators, implying initial errors equal to the plant initial conditions, $\mathcal{X}_{Error} = \mathcal{X}_{Worst}$.

Furthermore, for the LQG controller, both plant and estimator initial conditions need to be selected. It is not clear how to select the relative magnitudes of the initial plant energy and estimator error energy, since the plant energy is a physical quantity which leads to transition, whereas the estimator error energy is not. Again, zero initial estimates are a reasonable assumption to make.

Accordingly, zero initial estimates are selected in preference to the worst estimator initial error conditions for further simulations in the present work. Discounting the diachronic error energy bound produced from the worst estimator initial conditions, the remaining plots of estimated energy bound and slowest estimator pole

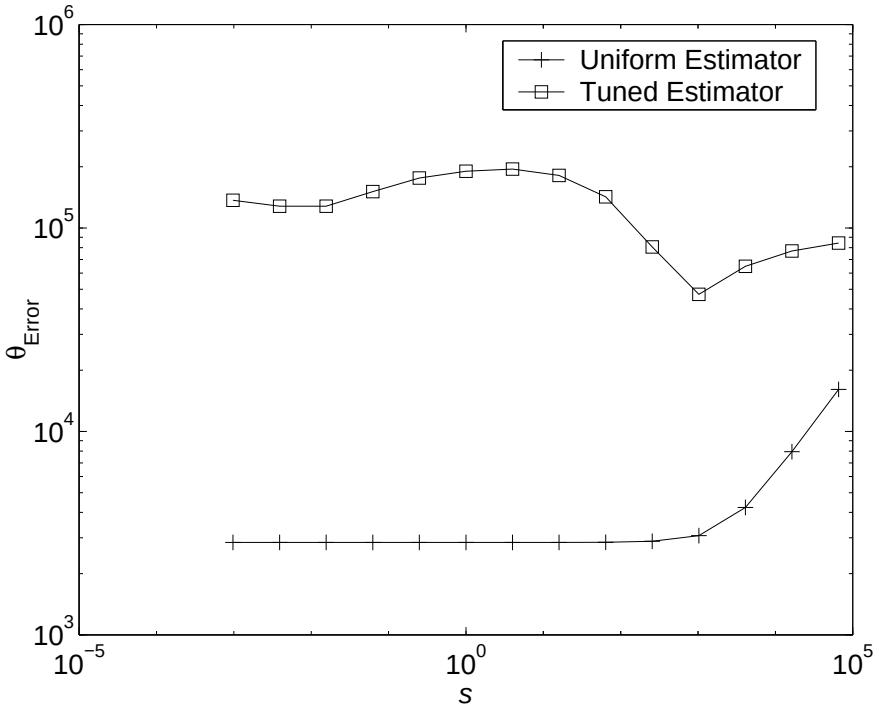

Figure 4.21: Case 2 LQE Diachronic Error Energy Bound θ_{Error} vs Measurement Noise Weight s, from worst estimates $\mathcal{X}_{Error} = \mathcal{X}_{Error,Worst}$, $N = 100$

favour the use of the tuned estimator over the uniform estimator, at low measurement noise. For case 1, a weight of $s = 2^{-10} \approx 10^{-3}$ is selected for further work, as this produces close to the lowest estimated energy bound and similarly for case 2, a weight of $s = 2^{-6} \approx 0.0156$ is chosen.

4.4.3 Initial Conditions

The correct calculation of diachronic transient energy bound and the associated initial conditions are critical in the present work. For example, if the location of the maximum of the synchronic transient energy bound is incorrectly identified, simulations starting from those initial conditions will simply repeat the same erroneous energy growth.

Synchronic Transient Energy Bound ϵ vs Time

Two plots of synchronic transient energy bound against time are presented to provide some insight into the diachronic transient energy bound calculation.

Figure 4.22 shows a logarithmic plot of case 1 open-loop synchronic transient energy bound, $\epsilon(t)$, against time. $\epsilon(t)$ always has unit value at time zero, and in this case increases without bound as the system is unstable. After a short time the rate of increase of $log(\epsilon(t))$ is linear, and corresponds to the energy growth of the single unstable mode. Since the plot has no maximum, no value can be assigned to the diachronic transient energy bound θ, although the initial

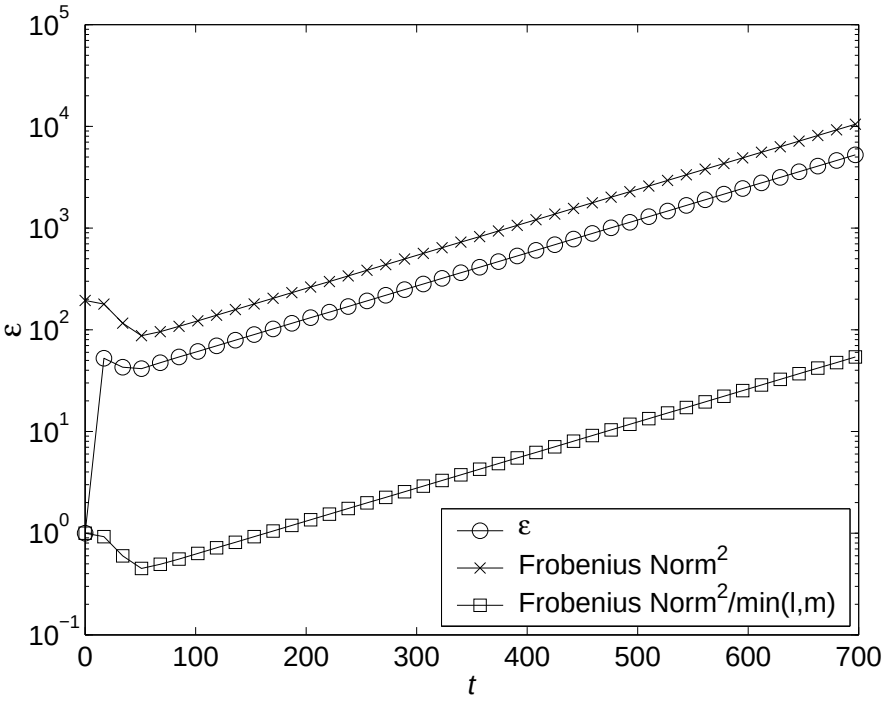

Figure 4.22: Case 1 Open-Loop Synchronic Transient Energy Bound ϵ vs Time t, $N = 100$

conditions which produce the highest synchronic transient energy bound after a long time ($E(t = 700) = 5369.0$) can be extracted. They are found not to vary with the precise time.

As shown from (4.42), the synchronic transient energy bound can be expressed as the square of the spectral norm of the state transition matrix

$$\epsilon(t) = \bar{\sigma}^2 \left(e^{\mathcal{Q}^{1/2}\mathcal{A}\mathcal{Q}^{-1/2}t} \right) \tag{4.93}$$

where $\bar{\sigma}$ is the spectral norm. The Frobenius norm (Skogestad and Postlethwaite, 1996, p517) is defined

$$\|\mathbf{A}\|_F = \sqrt{\sum_{ij} \left| a_{ij}^2 \right|} \tag{4.94}$$

The Frobenius norm and the spectral norm $\bar{\sigma}(\mathbf{A})$ obey

$$\bar{\sigma}(\mathbf{A}) \leq \|\mathbf{A}\|_F \leq \sqrt{\min(l, m)}\bar{\sigma}(\mathbf{A}) \tag{4.95}$$

where $\mathbf{A}$ is $(l \times m)$ (Skogestad and Postlethwaite, 1996, p520). Thus the Frobenius norm squared provides a upper bound on the synchronic transient energy bound, and $1/\min(l, m)$ times the Frobenius norm squared provides a lower bound. Figure 4.22 also shows the Frobenius norm of the state transition matrix

$$\left\| e^{\mathcal{Q}^{1/2}\mathcal{A}\mathcal{Q}^{-1/2}t} \right\|_F \tag{4.96}$$

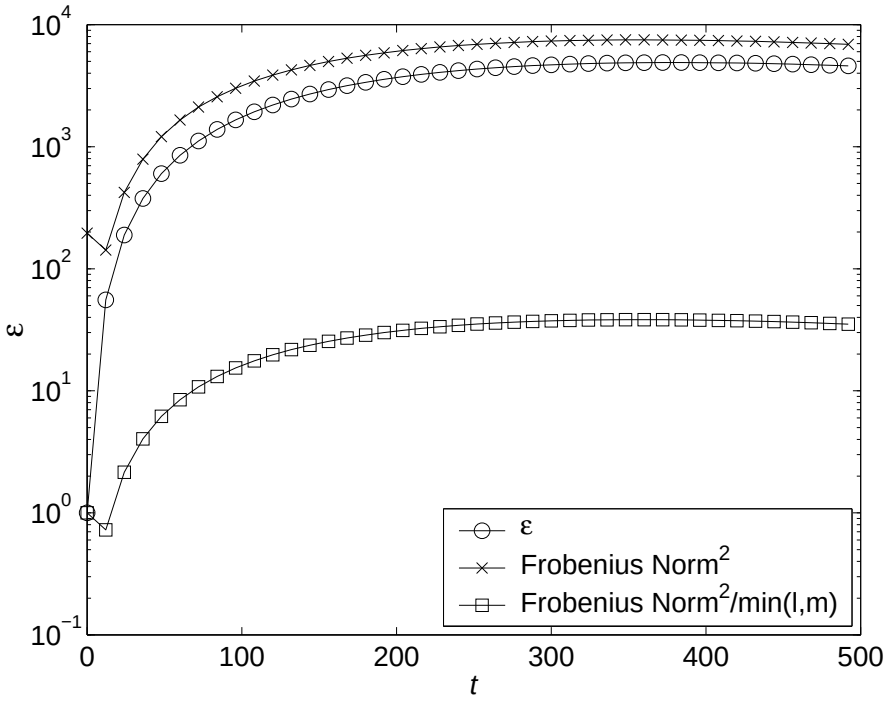

Figure 4.23: Case 2 Open-Loop Synchronic Transient Energy Bound ϵ vs Time t, $N = 100$

and it can be seen that the synchronic transient energy bound $\epsilon(t)$ lies within the correct bounds. Since the Frobenius norm is independent of direction, whereas the spectral norm computes an optimal direction, a comparison between the two norms provides an insight into the direction dependence of the initial conditions. Here the Frobenius norm squared is at least twice as large as the spectral norm squared, showing that the initial conditions are slightly sensitive to direction.

Figure 4.23 shows case 2 open-loop synchronic transient energy bound, $\epsilon(t)$, against time. As the eigenvalues in the case are real and stable, the only mechanism for growth is non-modal, and this is confirmed by the non-linear nature of the logarithmic plot. The graph of the synchronic transient energy bound against time is convex, and so there are no root bracketing problems. A golden section search (Press et al., 1986, p277) produces a maximum at 4896.94 at $t = 379.16$ and thus $\theta = 4896.94$. This value compares well with $\theta = 4897$ at $t = 379$ as reported by Butler and Farrell (1992, p1647). A binary search based on the criteria $\mathcal{X}^T\mathcal{A}\mathcal{X} = 0$, as described by Whidborne et al. (2004), proves inaccurate in this case. The plot also shows that the Frobenius norm squared is at least 1.4 times as large as the spectral norm squared, showing that the initial conditions are slightly sensitive to direction. The corresponding plots for the LQR controlled systems are qualitatively similar to figure 4.23.

Summary of Diachronic Transient Energy Bound θ Results

Table 4.1 shows a summary of the diachronic transient energy bound values of the open-loop and LQR state feedback systems. The LQR controller stabilises case

Table 4.1: Open-Loop and LQR Diachronic Transient Energy Bound θ, $N = 100$

Test case	Open-Loop	LQR
1	(unstable)	12.65
2	4896.94	848.81

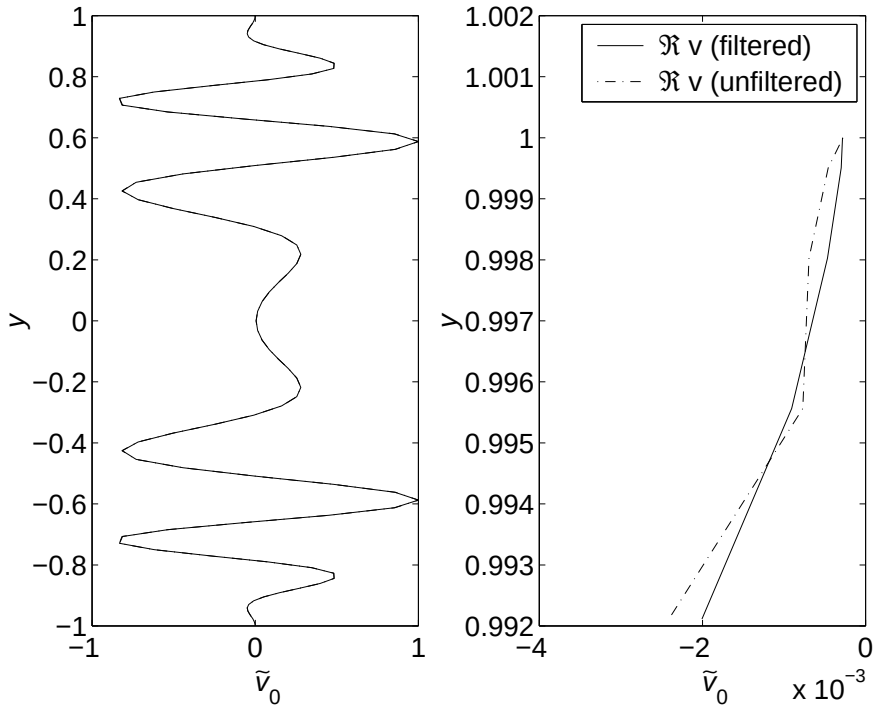

Figure 4.24: (Left) Case 1 LQR Worst $\Re(\tilde{v}(t=0))$ vs y, (Right) Detail Near $y = 1$, $N = 100$, Before and After Filtering

1 and produces a diachronic transient energy bound of 12.65. Case 2 is open-loop stable, and the controller reduces the diachronic transient energy bound from 4896.94 to 848.81.

Inspection of Worst Initial States

The left plot of figure 4.24 shows the initial real wall-normal velocity conditions ($\Re(\tilde{v}(t=0))$ vs y) associated with the diachronic transient energy bound of case 1 with LQR state feedback, normalised to a maximum wall-normal velocity of $(1 + 0\jmath)$. These worst initial conditions are a complicated perturbation flow-field composed of many eigenvectors. The right plot (marked unfiltered) shows a detailed view near the upper wall $y = 1$, and it can be seen that the wall-normal velocity at the wall is not zero. This is because the state-feedback controller acts on the non-zero state variables at time zero, and provides control at the walls.

The left plot of figure 4.25 shows the initial real streamwise velocity conditions ($\Re(\tilde{u}(t=0))$ vs y). The right plot (marked unfiltered) shows a detailed view near the upper wall and it can be seen that the streamwise velocity at the wall is zero due to the non-slip boundary condition on u. These plots interpolate

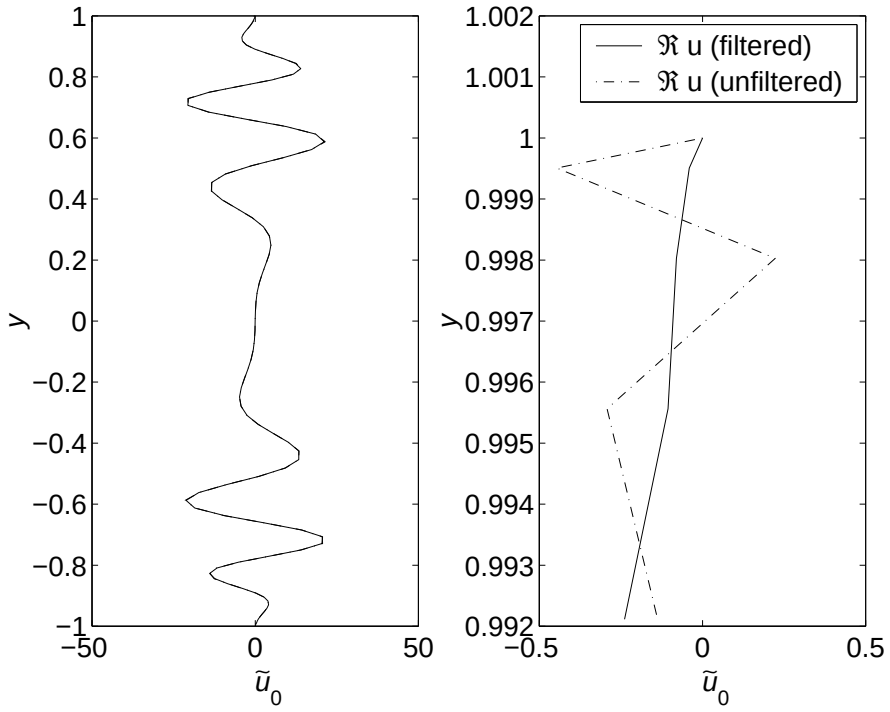

Figure 4.25: (Left) Case 1 LQR Worst $\Re(\tilde{u}(t=0))$ vs y, (Right) Detail Near $y=1$, $N=100$, Before and After Filtering

linearly the velocity values at the collocation points, and spectral interpolation, as assumed in the solution of the equations, would produce a smoother result in the interior of the domain. However, some oscillation is apparent in the results close to the wall, which is non-physical, since it changes sign at alternate grid points, and thus has wavelength twice the local grid spacing, being the so-called 'two-h waves' described by Boyd (2001, p206). The oscillations do not appear on the low frequency system eigenvectors shown in figure 4.26, but are peculiar to the solution of the eigensystem (4.41).

The oscillation causes inaccuracy in the calculation of the wall shear stress in finite difference schemes, since to first order the stress depends on the values of $\tilde{u}$ at the wall and next-to-wall-collocation points. This inaccuracy is reflected in the performance of the output feedback controller in subsequent non-spectral simulations described in section 4.3.3. The non-physical oscillation is removed by filtering or anti-aliasing the spectral results (Boyd, 2001, p212) using the two-thirds rule, which sets the upper 1/3 real and imaginary spectral coefficients to zero. Figure 4.27 shows the magnitude of the unbalanced state variables. There are $(N-1)$ real state variables ($(N-3)$ Chebyshev coefficients, plus two wall velocities), followed by $(N-1)$ imaginary ones. Some of the upper 1/3 real and imaginary Chebyshev coefficients (shown in dash-dot) are showing non-spectral behaviour by increasing in magnitude with (recombined) Chebyshev polynomial n, and are zeroed by the filtering (filtered state variables shown solid). The total energy content of the initial conditions is changed by no more than 0.01% by the filtering for the stable systems, and no more than 1% for the unstable open-loop

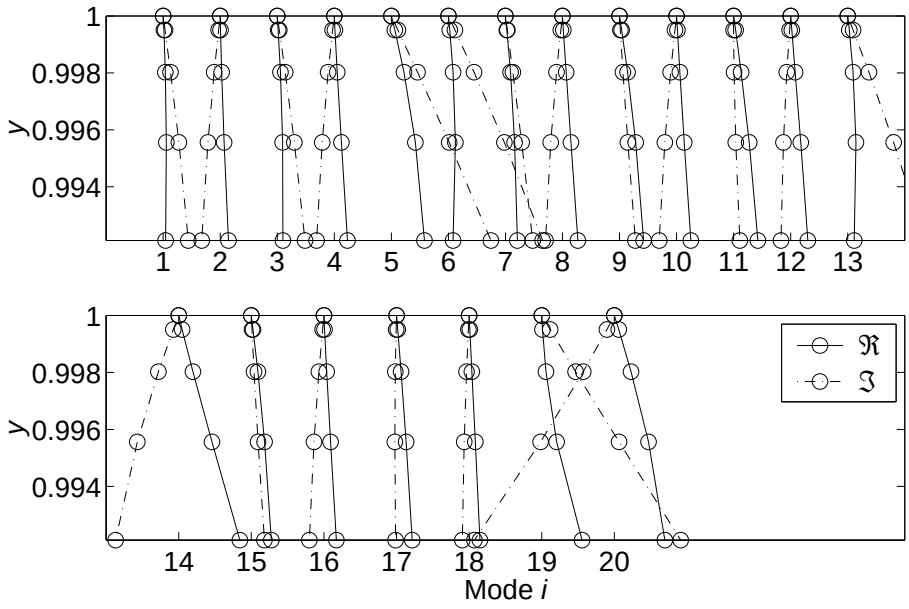

Figure 4.26: Case 1 LQR u Eigenvectors at Upper Wall

case 1 system.

The smoothing effect of the filtering on the velocity profiles at the walls is shown in the filtered results in figures 4.24 and 4.25. No changes occur in the interior of the domain. Filtering is also required on the case 2 initial conditions (not shown).

Investigation of Case 2 Open-Loop and Closed-Loop Diachronic Transient Energy Bound θ

Investigations of the modes which lead to maximum open-loop diachronic transient energy bound are not appropriate for case 1, since although many modes are present initially, only the unstable mode ultimately remains, and its energy growth is unbounded. Investigations for case 2 are appropriate as no modes are unstable. For the remainder of this section, the state variables employed are transformed to $\tilde{\mathcal{X}}$, as defined in section 4.3.1 such that $E = \tilde{\mathcal{X}}\tilde{\mathcal{X}}$, and the eigenvectors are expressed in the same state variables, and normalised to unit magnitude, unless stated otherwise.

Figure 4.28 shows a bar chart of the dot product between pairs of modes from 1 to 25. The main diagonal has unit magnitude, due to the normalisation chosen. The next highest dot products are on the adjacent diagonals, corresponding to mode pairs comprising alternative consecutive modes. The dot products of consecutive open-loop $\tilde{\mathcal{X}}$ modes, together with the vorticity $\tilde{\eta}$ eigenvectors (the velocity eigenvectors are much smaller in magnitude) appear in figure 4.29. It can be seen that a high dot product corresponds to vorticity eigenvectors of similar shape (within reflection), which is to be expected since similar mode shapes imply similar state variable vectors, and thus high dot products.

Figure 4.30 shows the same plot for the LQR system, for which the diachronic

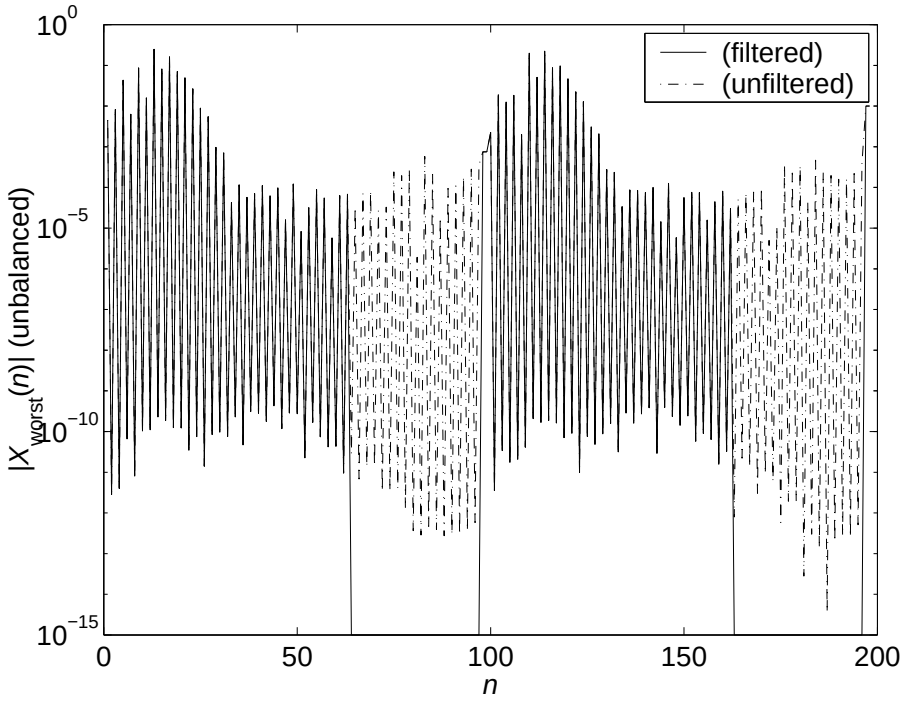

Figure 4.27: Case 1 LQR Worst Initial State $\mathcal{X}_{Worst}$ (unbalanced), Before and After filtering, $N = 100$

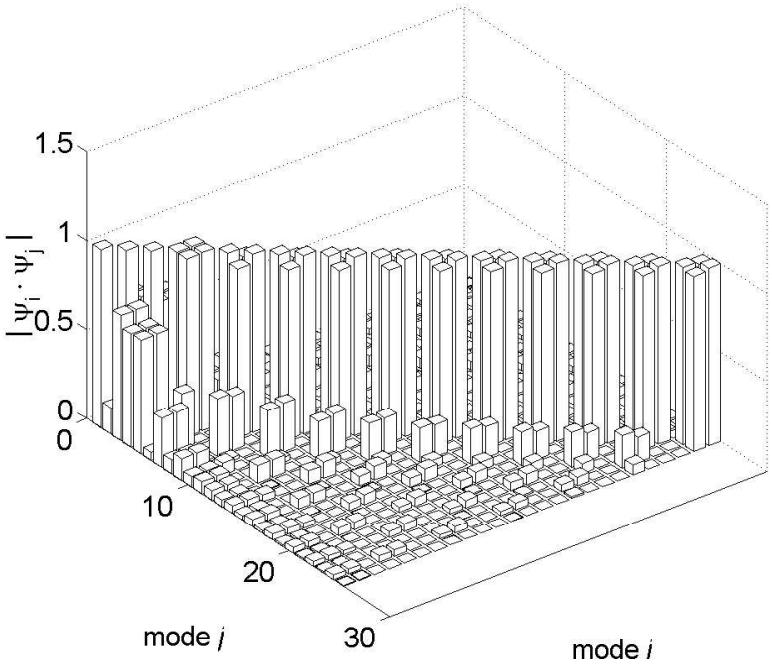

Figure 4.28: Case 2 Open-Loop Bar Chart of Mode Pair Dot Products, $N = 100$

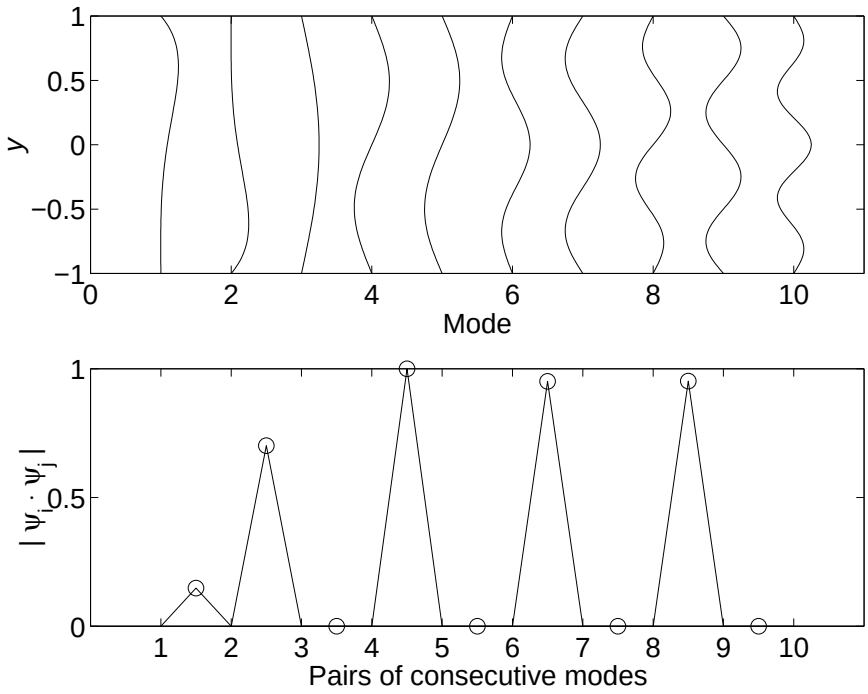

Figure 4.29: Case 2 Open-Loop: Upper Plot - Vorticity Eigenvectors, Lower Plot - Dot Product of Consecutive $\tilde{\mathcal{X}}$ Eigenvectors, $N = 100$

transient energy bound is reduced. It can be seen that in general the modes have comparable dot-products as in the open-loop figure 4.29 and thus remain as non-normal or non-orthogonal as in the open-loop case. The diachronic transient energy bound is known to be minimised to a value of unity when the modes are made precisely orthogonal but when precise orthogonality is not achieved, as here, the effect of increasing orthogonality may not produce the lowest energy, as shown in section 4.3.1. Thus the absence of a distinct reduction of non-normality is not surprising, although the LQR controller failing to directly affect the modal orthogonality is contrary to the discussion of Bewley and Liu (1998, p343). Figure 4.31 shows a bar chart of the dot product between pairs of LQR modes from 1 to 25. As compared to the open-loop chart, figure 4.28, the low alternative consecutive mode pairs on the superdiagonal are not significantly less parallel, although some of the higher pairs ($i, j \geq 12$) are less parallel. The particular structure of the non-normality shown in figure 4.28 has been lost by applying control, with increased non-normality away from the main diagonals.

The upper bounds on mode pair energy growth $E_{pair,bound}$, calculated using the expressions derived in section 4.3.1, from the worst initial conditions, are presented in figure 4.32. As would be expected, the chart is symmetrical. Few mode pairs appear to have a significant potential for transient energy growth, with the exception of pair 4,5.

Figure 4.33 shows the upper bounds on mode pair energy growth for case 2 after the application of LQR control, from the worst initial conditions. More mode pairs have a significant potential for transient energy growth, those with

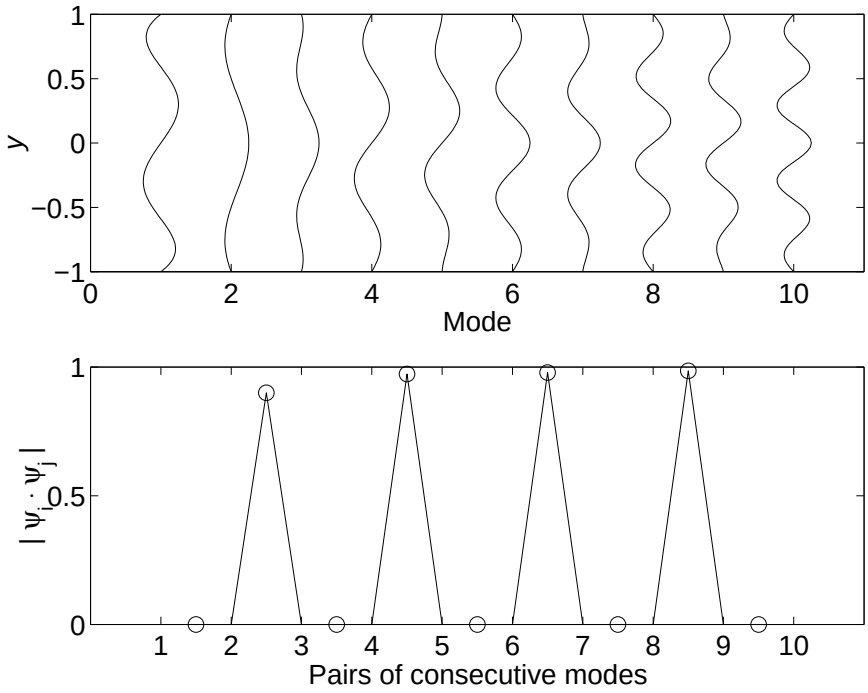

Figure 4.30: Case 2 LQR: Upper Plot - Vorticity Eigenvectors, Lower Plot - Dot Product of Consecutive $\tilde{\mathcal{X}}$ Eigenvectors, $N = 100$

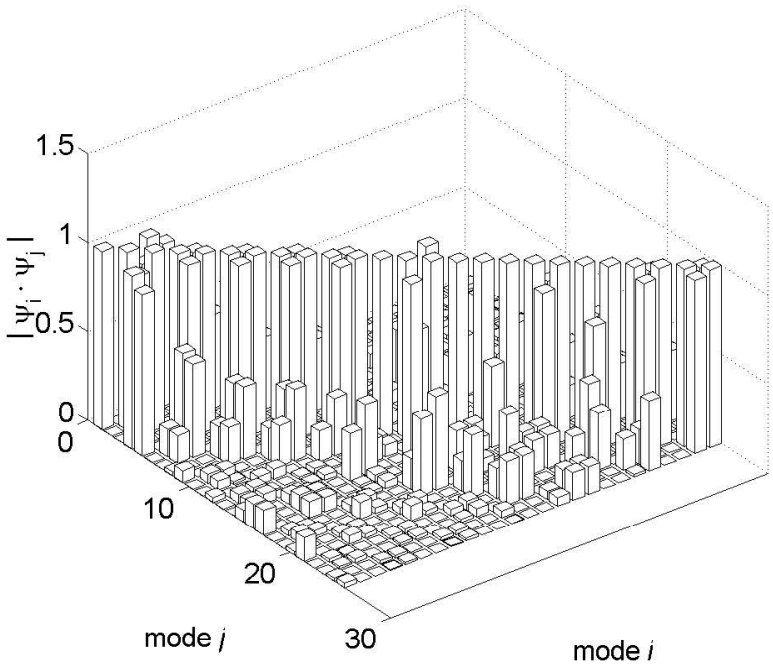

Figure 4.31: Case 2 LQR Bar Chart of Mode Pair Dot Products, $N = 100$

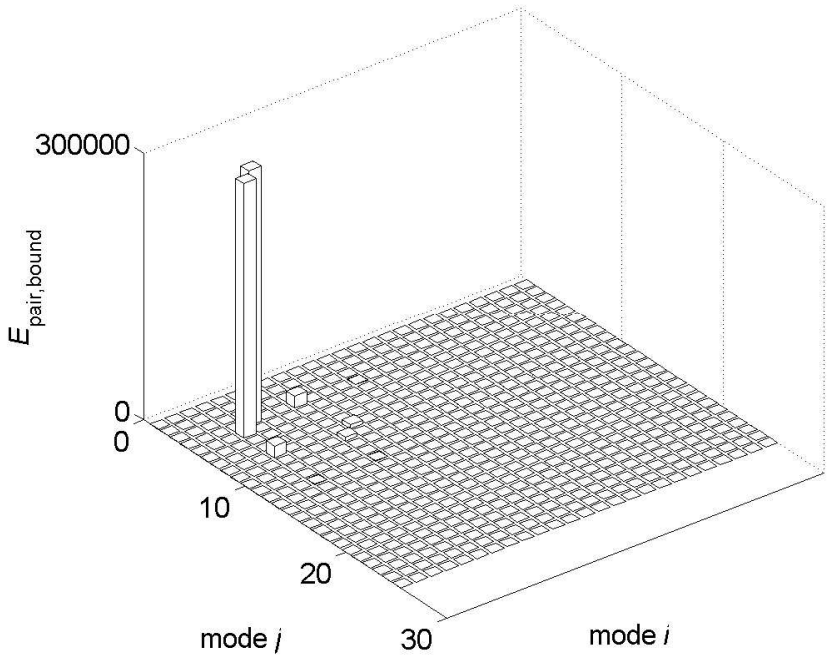

Figure 4.32: Case 2 Open-Loop Upper Bound on Mode Pair Energy Growth $E_{pair,bound}$, $N = 100$

the largest potential being 1,5 and 1,4. These significant pairs are not consecutive modes, unlike the open loop significant pair 4,5. The largest upper bound of all the pairs has fallen from approximately 2.5×10^5 to 3×10^3, due to the application of LQR control.

The cumulative energy of the state variables at the time of open-loop diachronic transient energy bound, for discretisation $N = 100$, are displayed in figure 4.34. Highly spectral behaviour can be seen, the energy converging after less than 10 state variables.

4.4.4 Linear Simulations

The results of linear simulations on the open- and closed-loop systems are investigated in detail in this section. Plots of transient energy against time are presented with linear rather than logarithmic energy axes, as these axes show the peak energy growth in more detail, for convergence and comparison purposes. Later, in section 4.4.7, plots with logarithmic axes are used for the presentation of non-linear simulation results from large initial perturbations.

Case 1 Open-Loop Linear Simulation

Figure 4.35 shows case 1 open-loop transient energy against time. Five different discretisations $N = 10, 20, 30, 40, 50$ are shown and the results are converged at $N = 30$, showing that a relatively low discretisation of $N = 30$ is adequate to simulate case 1 open-loop. The transient energy starts on a minimum, as would be expected since the initial conditions are those which generate maximum transient

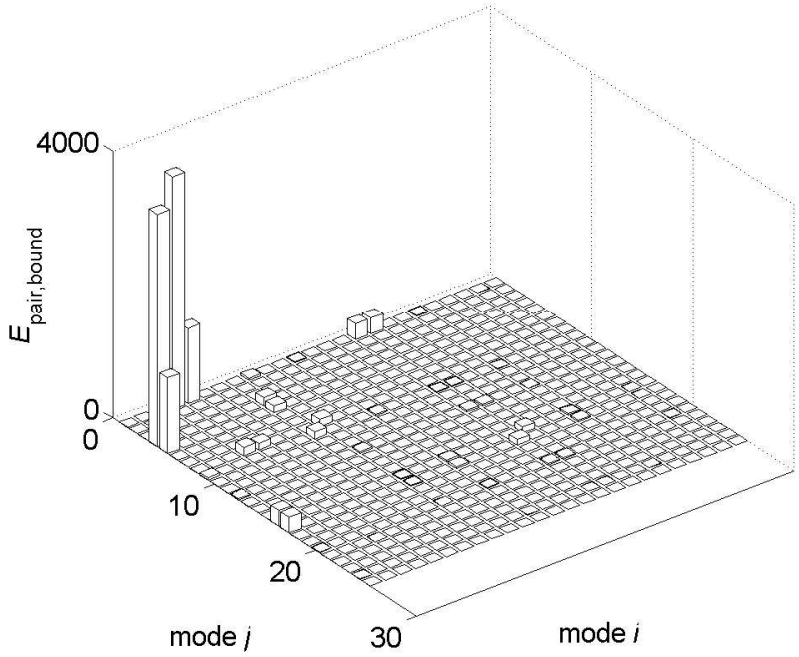

Figure 4.33: Case 2 LQR Upper Bound on Mode Pair Energy Growth $E_{pair,bound}$, $N = 100$

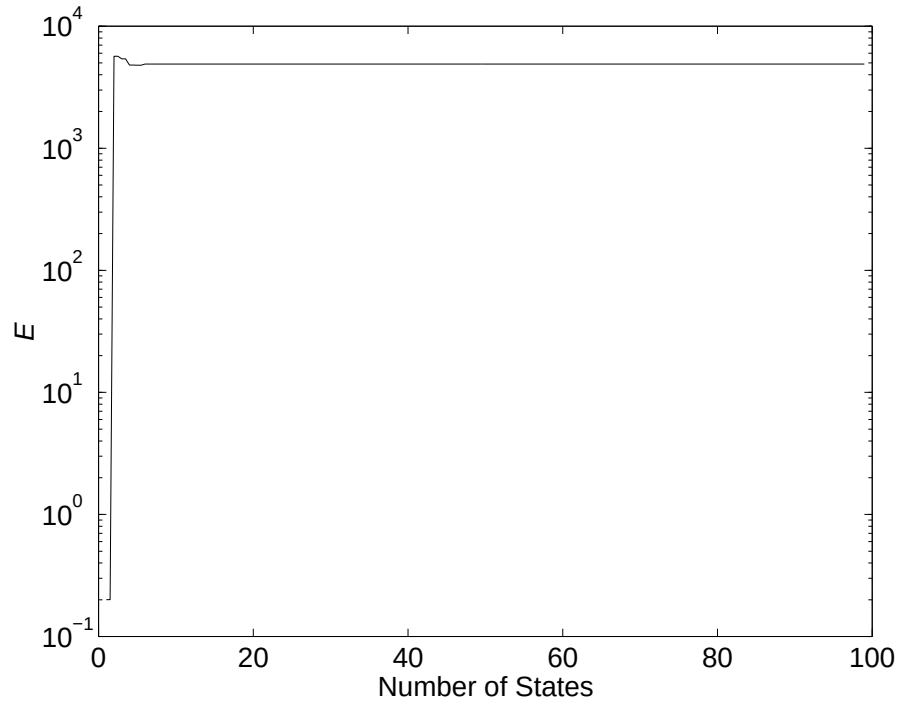

Figure 4.34: Case 2 Open-Loop Cumulative Transient Energy E vs Number of States, for Diachronic Transient Energy Bound θ, $N = 100$

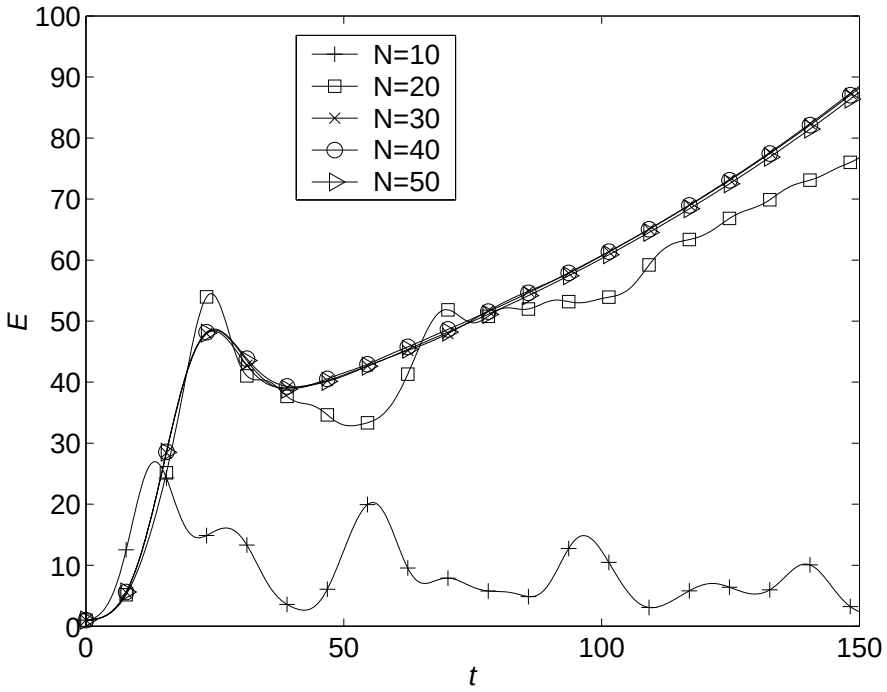

Figure 4.35: Case 1 Open-Loop Transient Energy E vs Time t, for Various Discretisations N, from Initial Conditions $\mathcal{X}_{worst}$ Scaled to $E = 1$

energy at time $t = 700$. The transient energy rises quickly, at a rate much faster than the unstable mode would produce alone, due to non-normal growth. Finally the transient energy grows at the rate dictated by the unstable mode.

The magnitudes of the case 1 open-loop initial modes ranked against pole magnitude are shown in figure 4.36, for eigenvectors normalised to unit magnitude. A large spectrum of modes are present, with very large (but opposing) magnitudes, to enable the largest diachronic transient energy bound to occur. It can be seen that no mode present to any degree has a magnitude much faster than 1 radian per second. For case 2 (not shown), magnitudes are lower, and no modes are present to any degree with a magnitude much faster than 0.1 radian per second.

Case 2 Open-Loop Linear Simulation

Figure 4.37 displays case 2 open-loop wall-normal velocity Fourier coefficient $\tilde{v}$ against time. The coefficient is zero at the walls, due to the Dirichlet boundary condition. In the interior of the channel the coefficient decays smoothly with time, as, in conjunction with spanwise velocity w, it represents decaying streamwise vortices.

The case 2 open-loop streamwise velocity Fourier coefficient $\tilde{u}$ versus time is shown in figure 4.38. The coefficient is zero at the walls, due to the Dirichlet boundary condition, and is initially very small throughout the domain, being less than 1% of the $\tilde{v}$ magnitude at $t = 0$. It grows quickly however, as the wall-normal velocity field moves fluid around in the base flow profile. The base flow is streamwise and varies parabolically in the wall-normal direction. Thus any

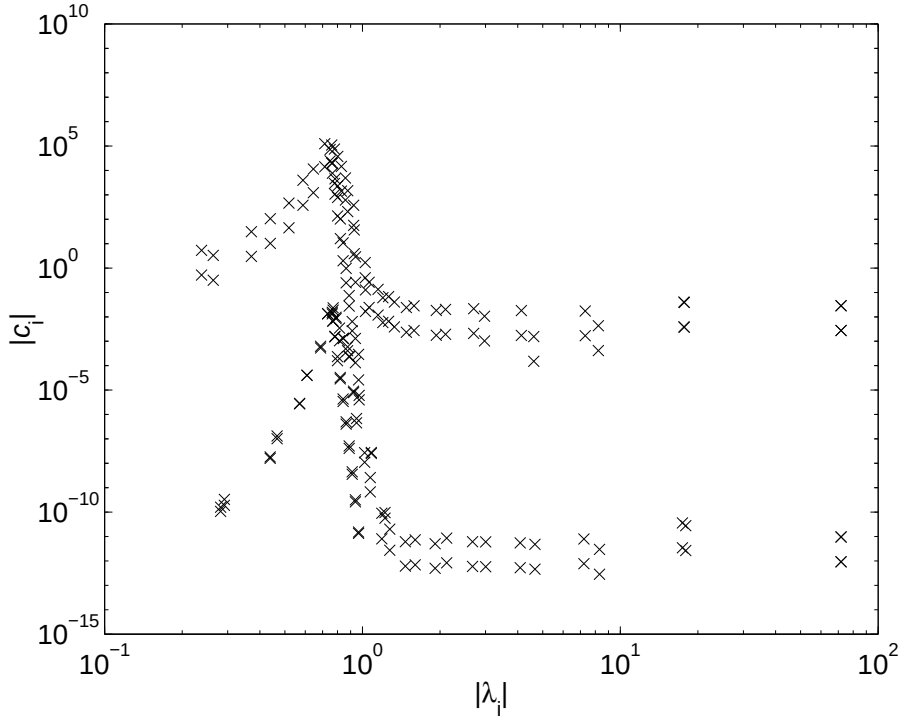

Figure 4.36: Case 1 Open-Loop Initial Mode Amplitudes, from Initial Conditions $\mathcal{X}_{worst}$ Scaled to $E = 1$, $N = 100$

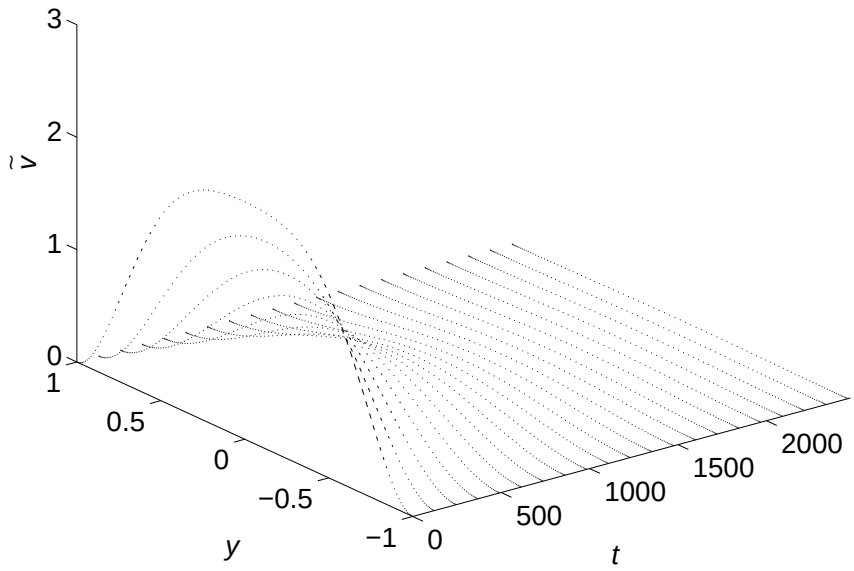

Figure 4.37: Case 2 Open-Loop $\tilde{v}(y)$ (imaginary) vs Time t, from Initial Conditions $\mathcal{X}_{worst}$ Scaled to $E = 1$, $N = 100$

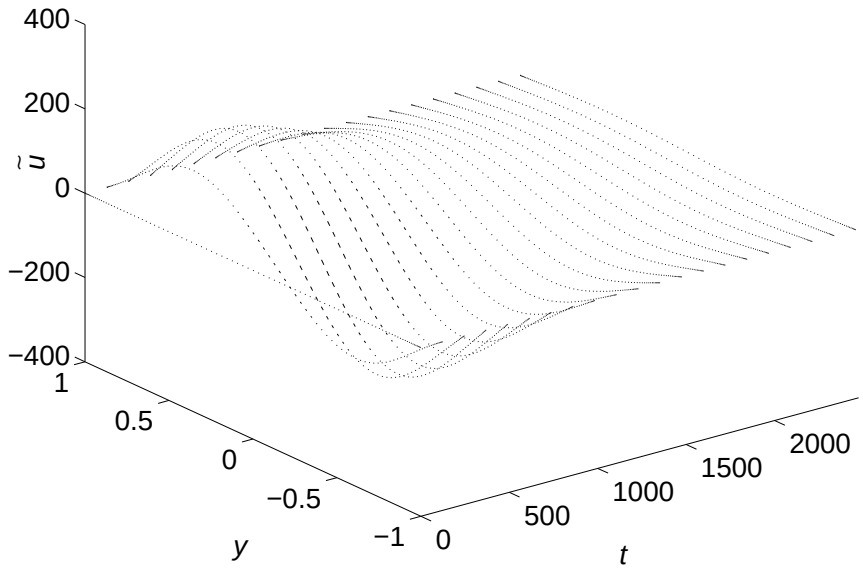

Figure 4.38: Case 2 Open-Loop $\tilde{u}(y)$ (imaginary) vs Time t, from Initial Conditions $\mathcal{X}_{worst}$ Scaled to $E = 1$, $N = 100$

movement of packets of fluid in the wall-normal direction causes them to have a large additional u perturbation velocity generated by the difference in base flow at the old and new locations, resulting in u perturbation velocities much larger than the v values. This so-called lift up effect causes high energy streaks as described by Schmid and Henningson (2001, p120).

Five different plant discretisations, $N = 10, 20, 30, 40, 50$, are simulated and the results are presented in figure 4.39, of case 2 open-loop transient energy against time. The results are converged at $N = 20$ and above, showing that a low discretisation of $N = 20$ is adequate to simulate case 2 open-loop. As for case 1, the transient energy starts at a minimum. Here the transient energy reaches the diachronic transient energy bound value of 4896.94 at time 379.5, close to the predicted value of 4896.94 at time 379.16 from section 4.4.3, before decaying to zero. The small discrepancy is caused by the linear simulation results being provided at discrete timesteps.

Figure 4.40 displays the time histories of those modes which provide more than 10% of the diachronic transient energy bound, calculated using (4.54). Modes 4 and 5 (numbered including the integrators) individually provide substantial decay of transient energy, but mode pair $(4, 5)$ provides substantial growth of transient energy in the form of decay of negative energy, as predicted in figure 4.32. The aggregate transient energy, marked 'All' in figure 4.40, is much less than any of the components, and barely discernible on the same scale. The symbol $\times$ marks the time of the peak aggregate transient energy.

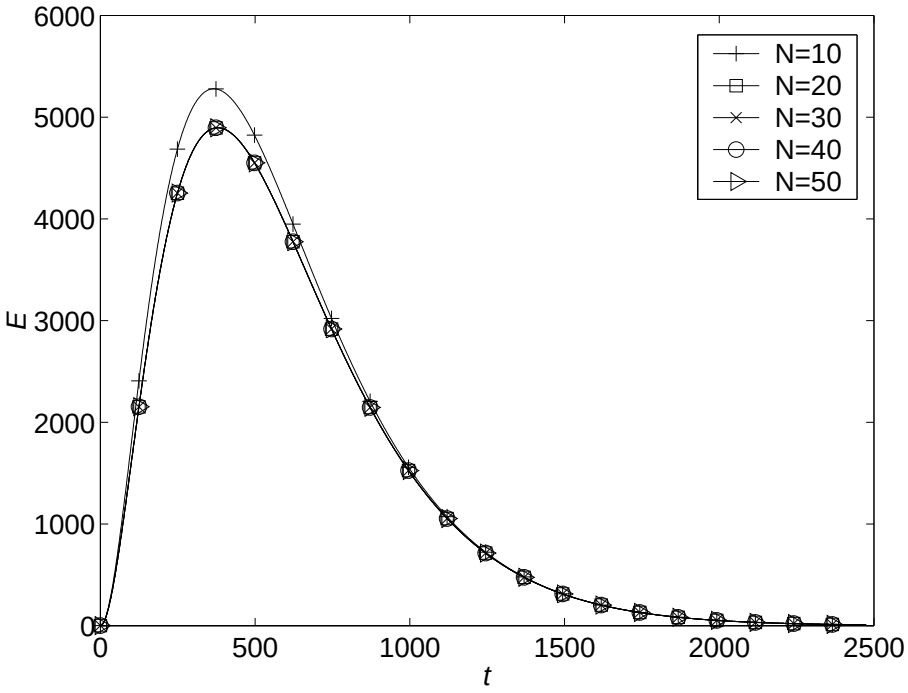

Figure 4.39: Case 2 Open-Loop Transient Energy E vs Time t, for Various Discretisations N, from Initial Conditions $\mathcal{X}_{worst}$ Scaled to $E = 1$

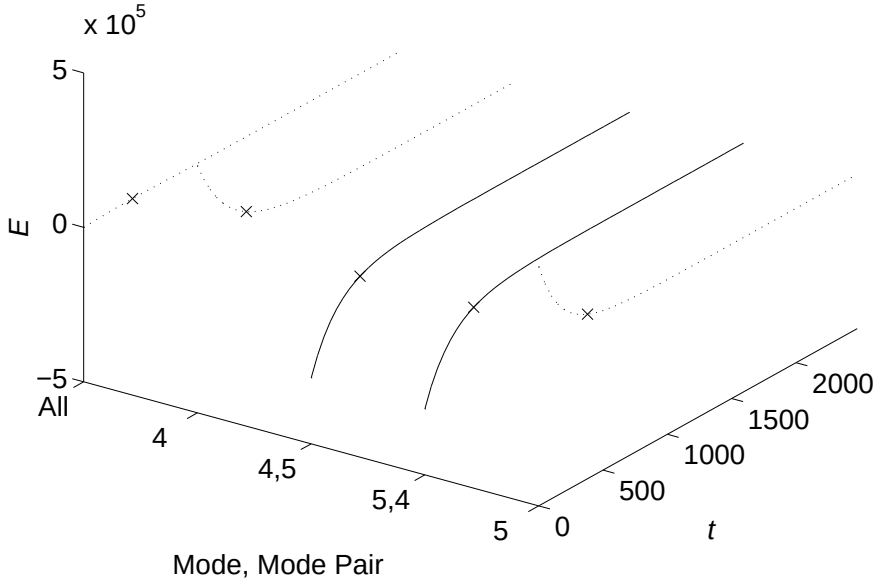

Figure 4.40: Case 2 Open-Loop Mode Transient Energy E Components vs Time t, from Initial Conditions $\mathcal{X}_{worst}$ Scaled to $E = 1$, $N = 100$. $\times$ denotes time of peak overall E.

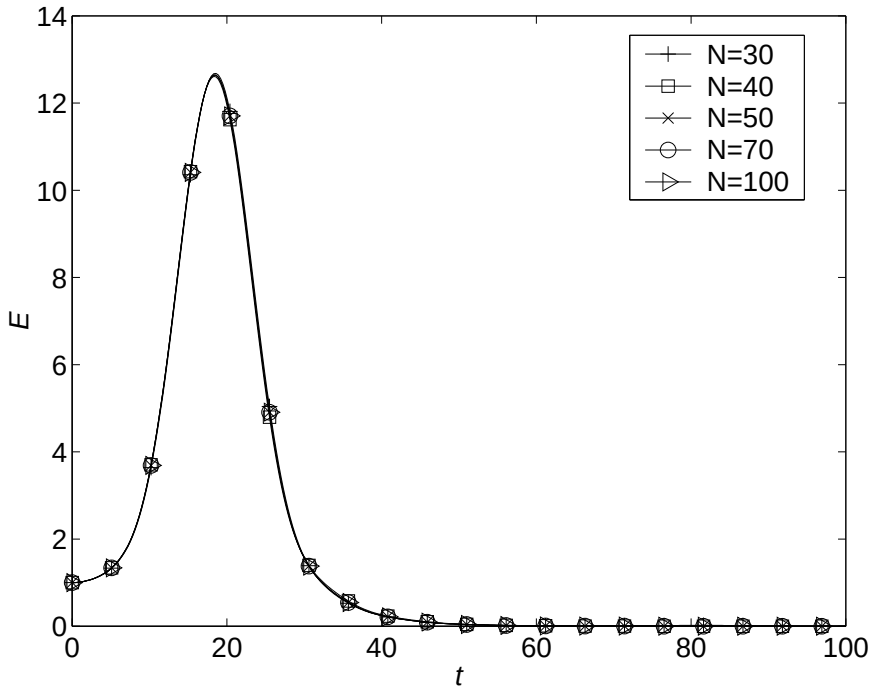

Figure 4.41: Case 1 LQR Transient Energy E vs Time t, for Various Discretisations N, from Initial Conditions $\mathcal{X}_{worst}$ Scaled to $E = 1$

Case 1 LQR State Feedback Linear Simulation

Case 1 LQR transient energy against time, from the closed-loop worst initial conditions, appears in figure 4.41. The controller is able to stabilise the flow, and limit the transient energy to 12.64, which is consistent with figure 4.9. The LQR controller limits the growth of the worst case 1 disturbances. Several different discretisations N are shown, and convergence has occurred for even the lowest, $N = 30$.

Figure 4.42 shows case 1 LQR initial modes. For case 1 the open-loop and LQR initial conditions differ significantly. However, as in the open-loop system, a large spectrum of modes are present, with very large magnitudes, and no mode present to any degree has a magnitude much faster than 1 radian per second.

As the $\tilde{v}$ initial conditions are symmetrical about the centreline (see figure 4.24), the control signal at the lower wall $\dot{\tilde{v}}(y = -1)$ is identical to that at the upper wall. However, as the sense of the upper and lower wall boundaries are reversed, transpiration suction at the upper wall, $\tilde{v}(y = 1) > 0$, corresponds to blowing at the lower wall. Figure 4.43 shows the case 1 LQR control signal at the upper wall $\dot{\tilde{v}}(y = 1)$ against time.

Figure 4.44 displays the time integral of the case 1 LQR control signal at the upper wall, namely the Fourier coefficient of the upper wall velocity. The coefficient magnitude peaks at approximately 2.8, i.e. 2.8 times the base flow centreline velocity. However, this figure is for a unit initial transient energy. The

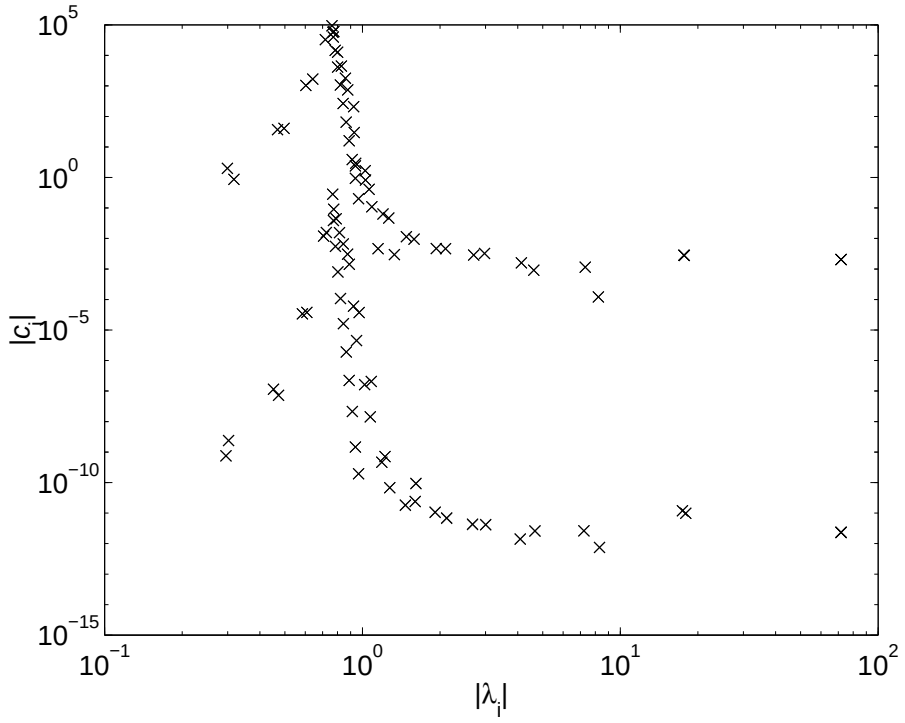

Figure 4.42: Case 1 LQR Initial Mode Amplitudes, from Initial Conditions $\mathcal{X}_{worst}$ Scaled to $E = 1$, $N = 100$

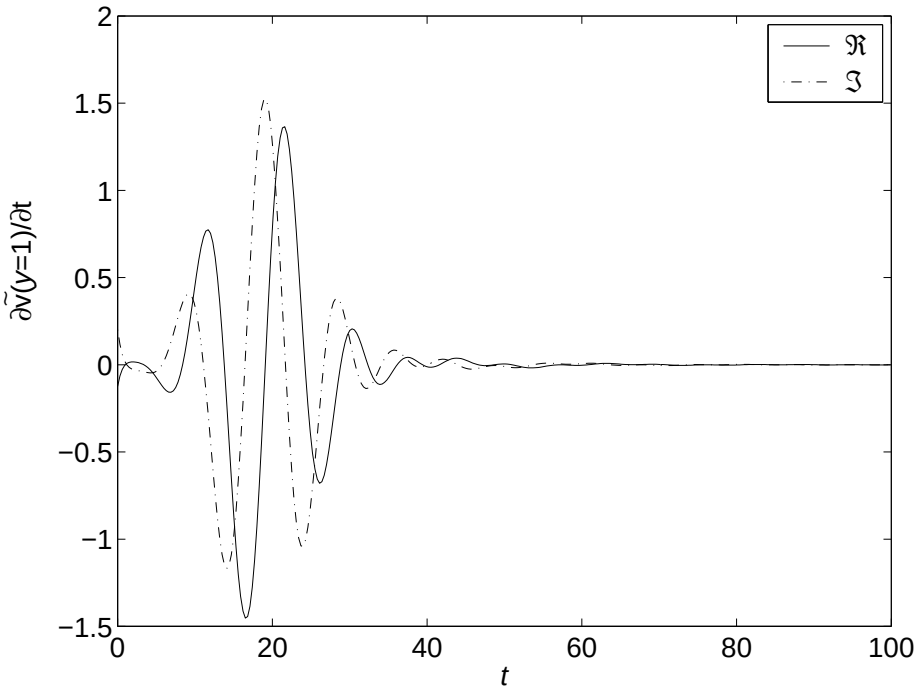

Figure 4.43: Case 1 LQR Upper Wall Control $\mathcal{U}(1)$ vs Time t, from Initial Conditions $\mathcal{X}_{worst}$ Scaled to $E = 1$, $N = 100$

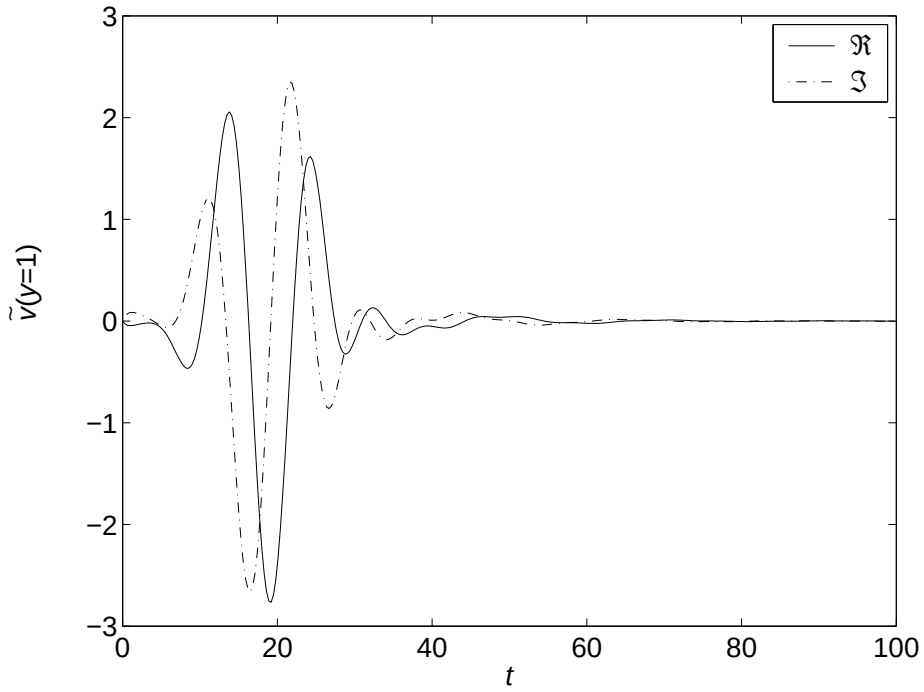

Figure 4.44: Case 1 LQR Wall Velocity Coefficient, $\tilde{v}(y = 1)$ vs Time t, from Initial Conditions $\mathcal{X}_{worst}$ Scaled to $E = 1$, $N = 100$

kinetic energy density of the base flow is

$$\frac{1}{Volume}\int^{Volume}\frac{1}{2}\rho U_b^2\left(y\right)dvol = \frac{1}{4}\int_{y=-1}^{y=1}\left(1-y^2\right)^2 dy \tag{4.97}$$

where $Volume$ corresponds to that of a unit streamwise length of channel, which expression evaluates to $4/15 \approx 0.2667$. For an initial perturbation energy of 10% of the base flow energy, the upper wall velocity would peak at around $2.8 \times \sqrt{0.02667}$, approximately 0.45, and for a perturbation energy of 1% of base flow, the velocity would peak at approximately 0.14 times the base flow centreline velocity. This represents the transpiration at comparatively high velocity.

The double time integral of the case 1 LQR control signal at the upper wall, namely the Fourier coefficient of the upper wall fluid quantity transpired, versus time is displayed in figure 4.45. Although the net amount of fluid transpired is zero since the distribution is sinusoidal, this coefficient represents the magnitude of the sinusoidal distribution. The coefficient magnitude peaks at around 5.8, i.e. 5.8 times the channel half-height, for a unit energy initial perturbation. For an initial perturbation energy 1% of that of the base flow, the quantity would peak at approximately 0.30 times the channel half-height. This represents the transpiration of a comparatively large amount of fluid, requiring a large associated reservoir or distribution system. These significant transpiration fluid velocities and quantities indicate the need for further investigations of actuation. The final coefficient is close to zero, representing the absence of any permanent transport of transpiration fluid within each spatial period, and thus any reservoirs return to their initial level.

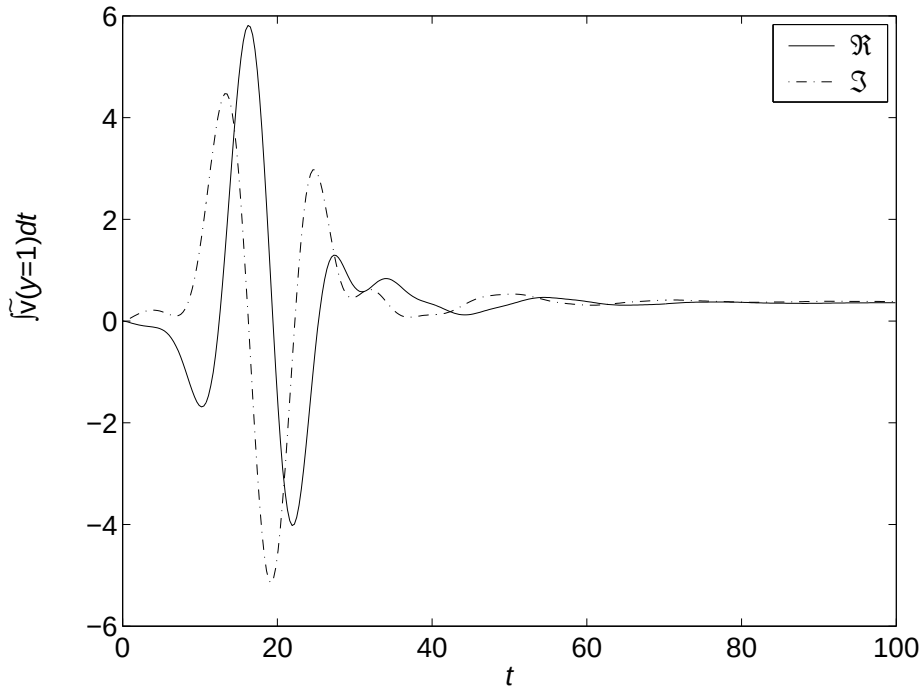

Figure 4.45: Case 1 LQR Fluid Depth Transpired on Upper Wall vs Time t, from Initial Conditions $\mathcal{X}_{worst}$ Scaled to $E = 1$, $N = 100$

Case 2 LQR State Feedback Linear Simulation

Figure 4.46 shows case 2 LQR wall-normal velocity Fourier coefficient $\tilde{v}$ against time. The coefficient is not zero at the walls, due to the control boundary condition. Figure 4.47 shows case 2 LQR streamwise velocity Fourier coefficient $\tilde{u}$ against time. As compared to the open-loop behaviour in figure 4.38, the u velocity is much reduced.

Figure 4.48 displays the time integral of the LQR control signal at the upper wall, namely the Fourier coefficient of the upper wall transpiration velocity. The coefficient magnitude peaks at approximately 1.75, i.e. 1.75 times the base flow centreline velocity. However, this figure is for a unit initial transient energy. As for case 1, the non-dimensionalised kinetic energy density of the base flow for case 2 is $4/15 \approx 0.2667$. For an initial perturbation energy of 1% of base flow, the velocity would peak at approximately 0.090 times the base flow centreline velocity. This represents transpiration at reasonable velocity.

The double time integral of the LQR control signal at the upper wall versus time is displayed in figure 4.49. This coefficient represents the magnitude of the sinusoidal transpiration fluid quantity spanwise distribution. The coefficient magnitude finally peaks at around 515, i.e. 515 times the channel half-height, for a unit energy initial perturbation. For an initial perturbation energy 1% of that of the base flow, the quantity would peak at approximately 26.6 times the channel half-height. As found for case 1, this represents the transpiration of a comparatively large amount of fluid, requiring a large associated reservoir or distribution system, and again indicates the need for further investigations of actuation. Fur-

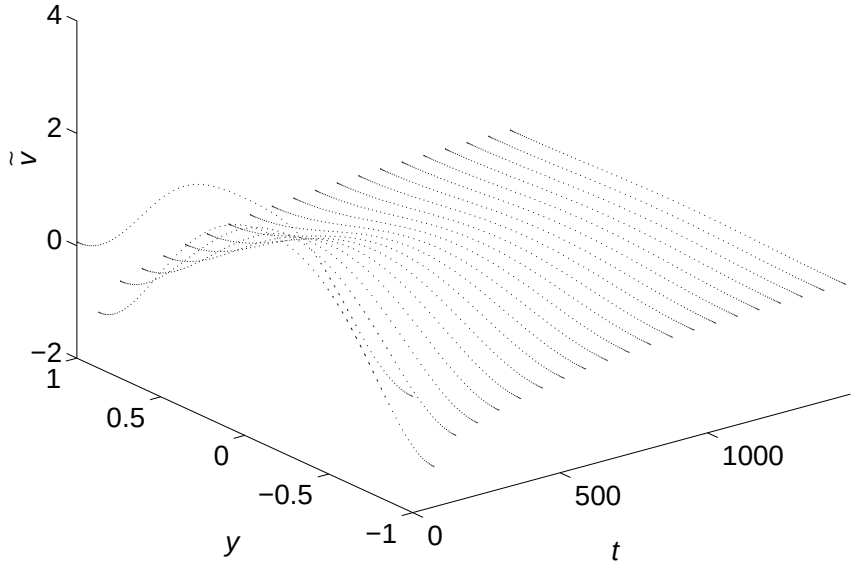

Figure 4.46: Case 2 LQR $\tilde{v}(y)$ (imaginary) vs Time t, from Initial Conditions $\mathcal{X}_{worst}$ Scaled to $E = 1$, $N = 100$

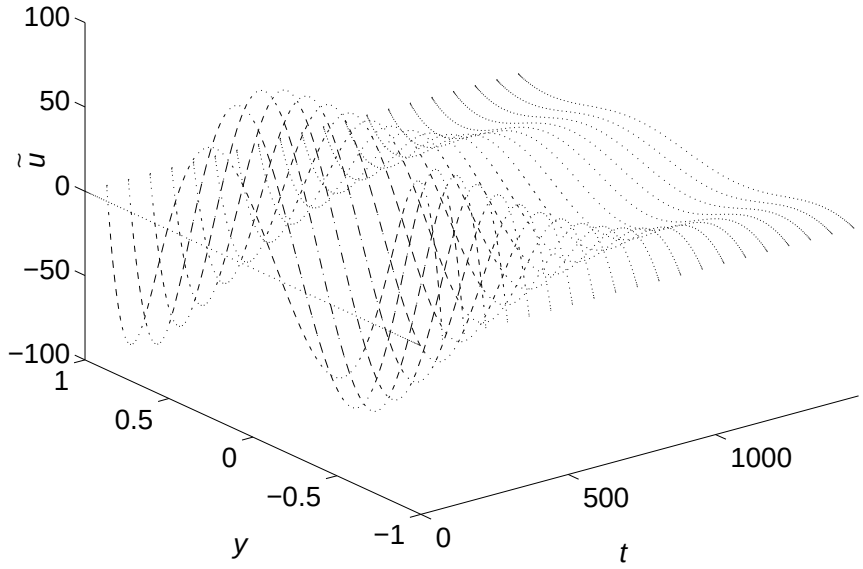

Figure 4.47: Case 2 LQR $\tilde{u}(y)$ (imaginary) vs Time t, from Initial Conditions $\mathcal{X}_{worst}$ Scaled to $E = 1$, $N = 100$

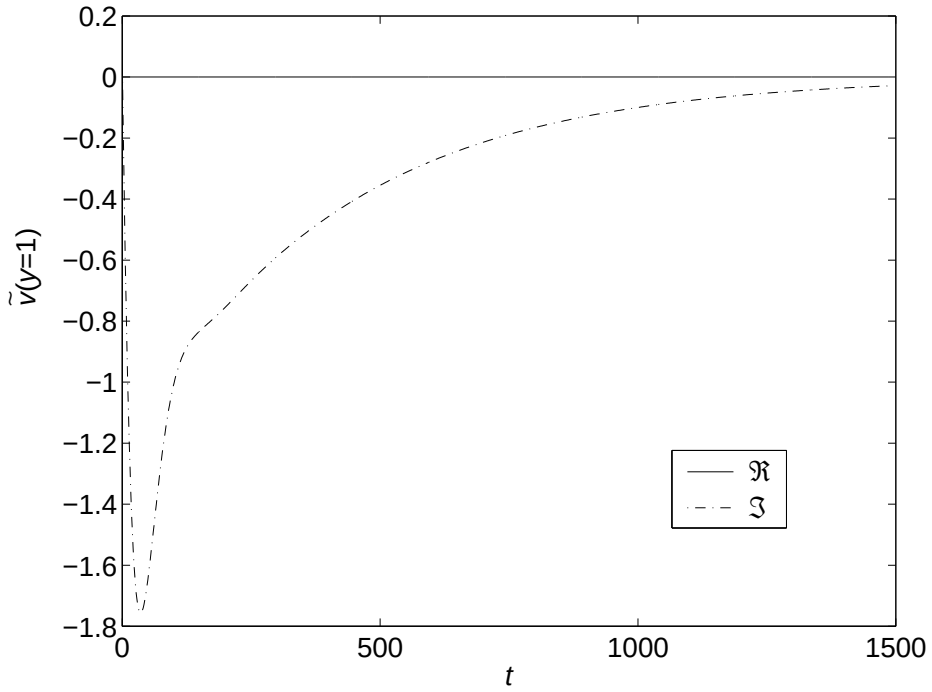

Figure 4.48: Case 2 LQR Wall Velocity Coefficient, $\tilde{v}(y = 1)$ vs Time t, from Initial Conditions $\mathcal{X}_{worst}$ Scaled to $E = 1$, $N = 100$

thermore, here the final coefficient is not zero, representing a permanent transport of transpiration fluid within each spatial period, and thus any reservoirs do not return to their initial level.

Figure 4.50 presents case 2 LQR transient energy against time. The controller is able to limit the transient energy to 848.80, which is consistent with the value of 848.81 from figure 4.11, as compared to the open-loop value of 4896.94. Thus the controller effectively limits the growth of the worst case 2 disturbance. Three different discretisations N are shown, and convergence has occurred for even the lowest $N = 30$.

The LQR controller minimises the *time integral* of the transient energy plus weighted control effort, from all initial conditions, rather than the diachronic transient energy bound itself, although the diachronic transient energy bound has been reduced from 4896.94 to 848.80 as a consequence.

The time histories of those modes which provide more than 10% of the diachronic transient energy bound are presented in figure 4.51. Modes 1 and 4 individually provide substantial decay of transient energy, but mode pairs $(1, 4)$ and $(1, 5)$ provide substantial growth of transient energy in the form of decay of negative energy, as predicted in figure 4.33, although all terms are an order of magnitude less than for the open-loop system (figure 4.40). The aggregate transient energy, marked 'All' in figure 4.51, is much less than any of the components, and less than the open loop aggregate. The symbol $\times$ marks the time of the peak aggregate transient energy.

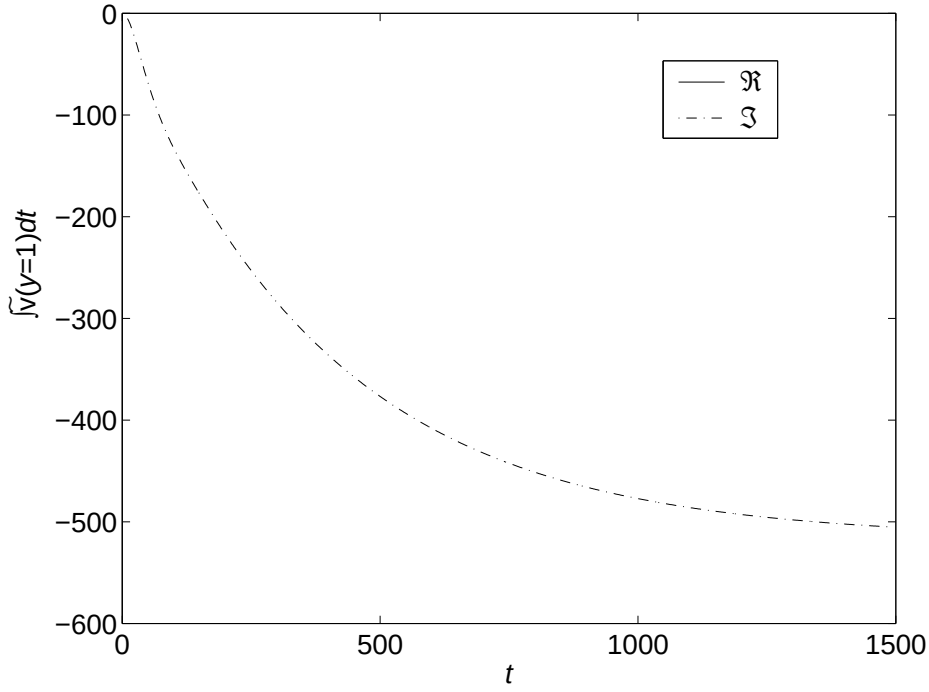

Figure 4.49: Case 2 LQR Fluid Depth Transpired on Upper Wall vs Time t, from Initial Conditions $\mathcal{X}_{worst}$ Scaled to $E = 1$, $N = 100$

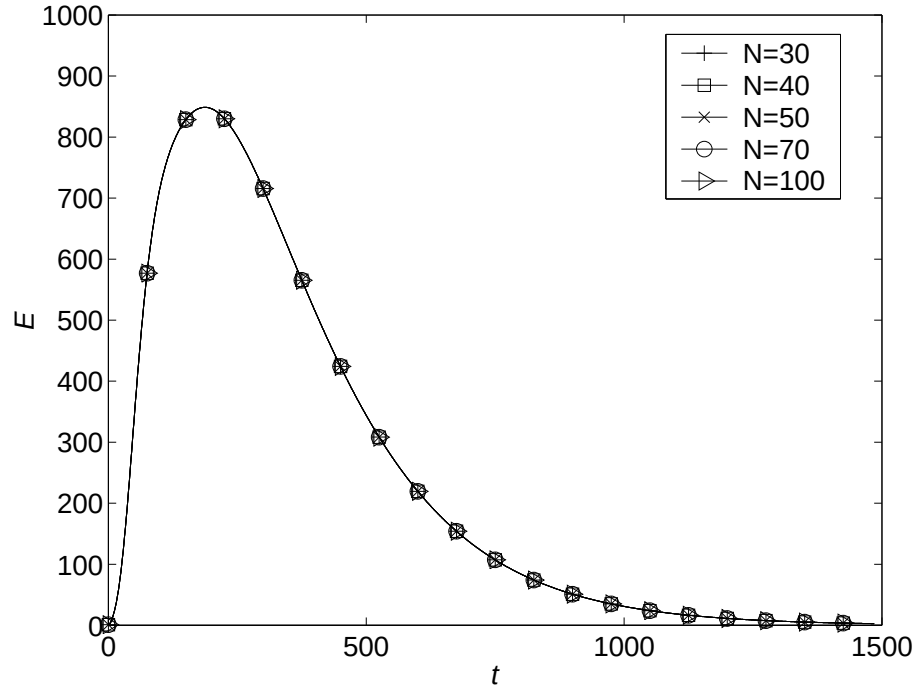

Figure 4.50: Case 2 LQR Transient Energy E vs Time t, for Various Discretisations N, from Initial Conditions $\mathcal{X}_{worst}$ Scaled to $E = 1$

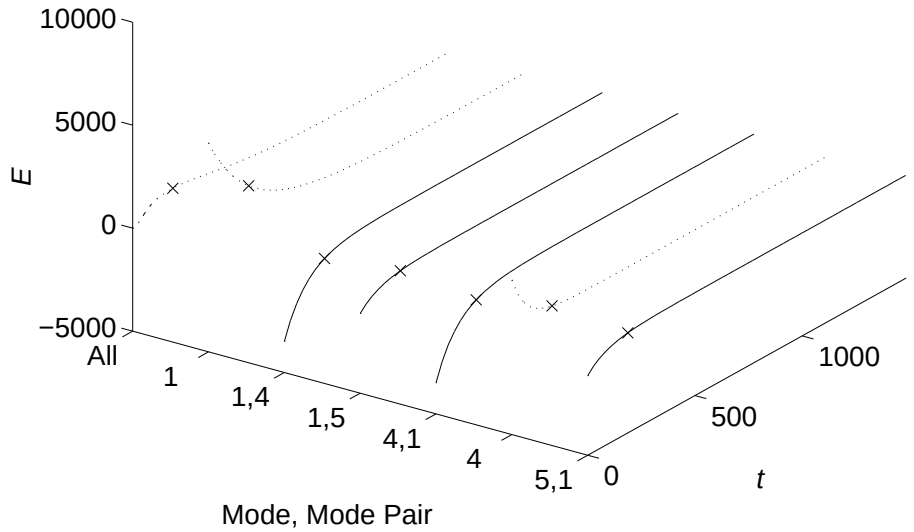

Figure 4.51: Case 2 LQR Mode Transient Energy E Components vs Time t, from Initial Conditions $\mathcal{X}_{worst}$ Scaled to $E = 1$, $N = 100$. $\times$ denotes time of peak overall E.

Case 1 Open-Loop LQE State Estimation Linear Simulation

Figure 4.52 shows case 1 LQE transient energy against time, showing both the plant energy from the open-loop worst initial conditions, and the estimated transient energy E_{Est} from zero initial estimates. For good performance the estimated energy must converge with the plant energy quickly, which is itself growing quickly due to non-normal growth. It can be seen that the tuned estimator converges on the plant energy much faster than the uniform estimator does. The uniform estimator appears less able to follow the non-normal growth that the plant displays, and its energy grows at the relatively slow rate of the plant final unstable eigenvector.

Figure 4.53 displays case 1 LQE estimated transient energy against time, for the tuned estimator, for several discretisations N. It can be seen than behaviour of the estimator is not fully converged below approximately $N = 50$.

Case 2 Open-Loop LQE State Estimation Linear Simulation

Case 2 LQE estimated transient energy against time is presented in figure 4.54. As for case 1, the tuned estimator converges on the plant energy much faster than the uniform estimator. Figure 4.55 shows case 2 LQE transient energy against time, for the tuned estimator, for several discretisations N. It is evident that the behaviour of the estimator is not fully converged below approximately $N = 50$.

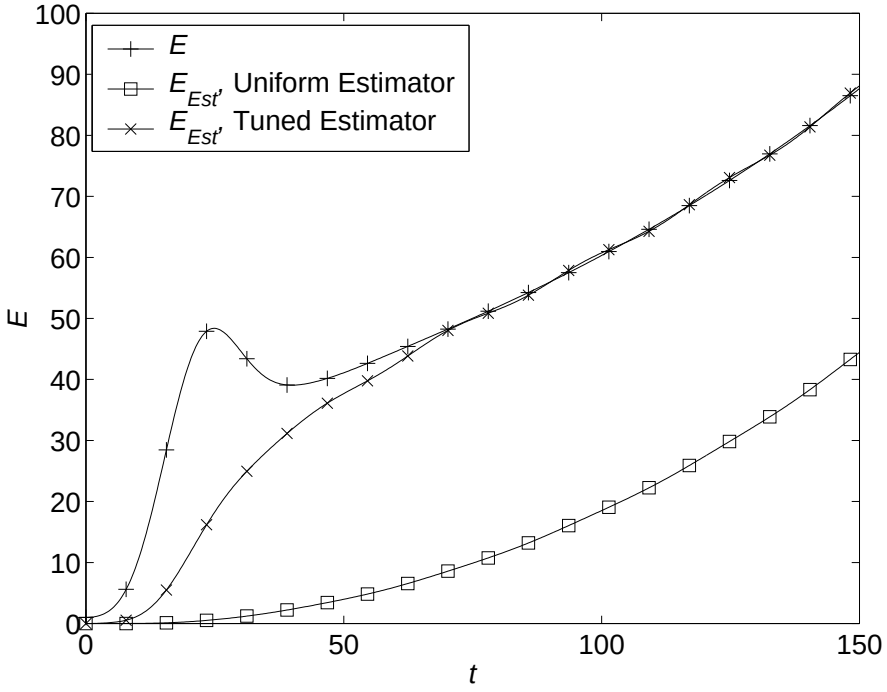

Figure 4.52: Case 1 Uniform vs Tuned LQE Transient Energy E vs Time t, from Initial Conditions $\mathcal{X}_{worst}$ Scaled to $E = 1$, $N = 100$

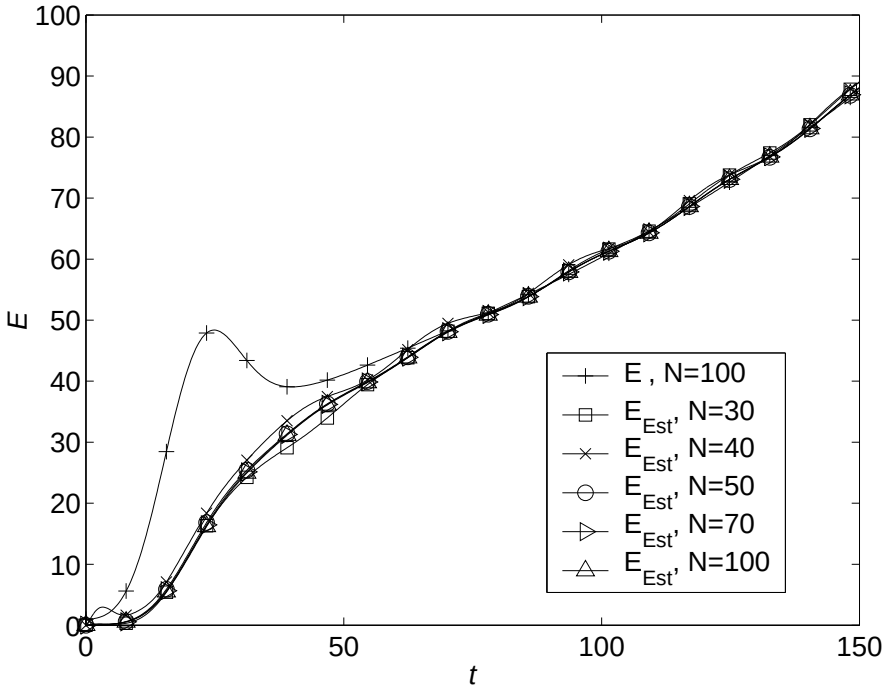

Figure 4.53: Case 1 LQE Transient Energy E vs Time t, for Several Discretisations N, from Initial Conditions $\mathcal{X}_{worst}$ Scaled to $E = 1$

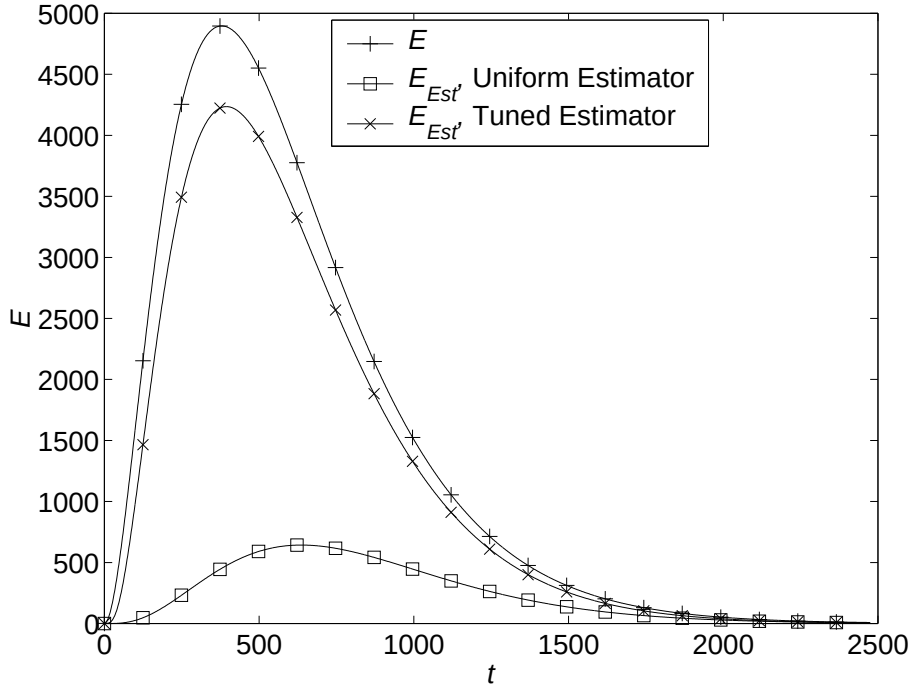

Figure 4.54: Case 2 Uniform vs Tuned LQE Transient Energy E vs Time t, from Initial Conditions $\mathcal{X}_{worst}$ Scaled to $E = 1$, $N = 100$

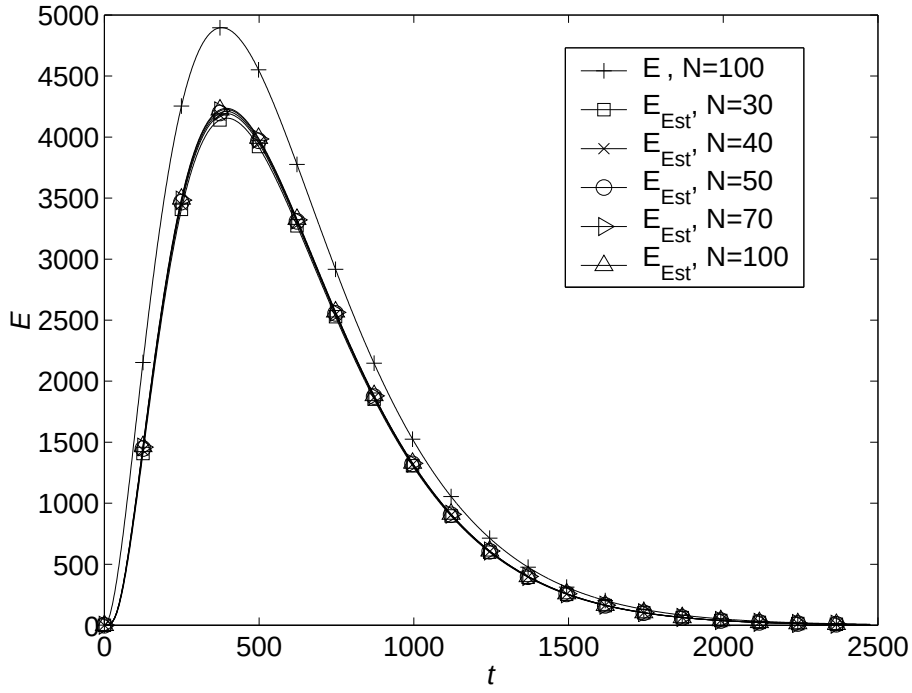

Figure 4.55: Case 2 LQE Transient Energy E vs Time t, for Several Discretisations N, from Initial Conditions $\mathcal{X}_{worst}$ Scaled to $E = 1$

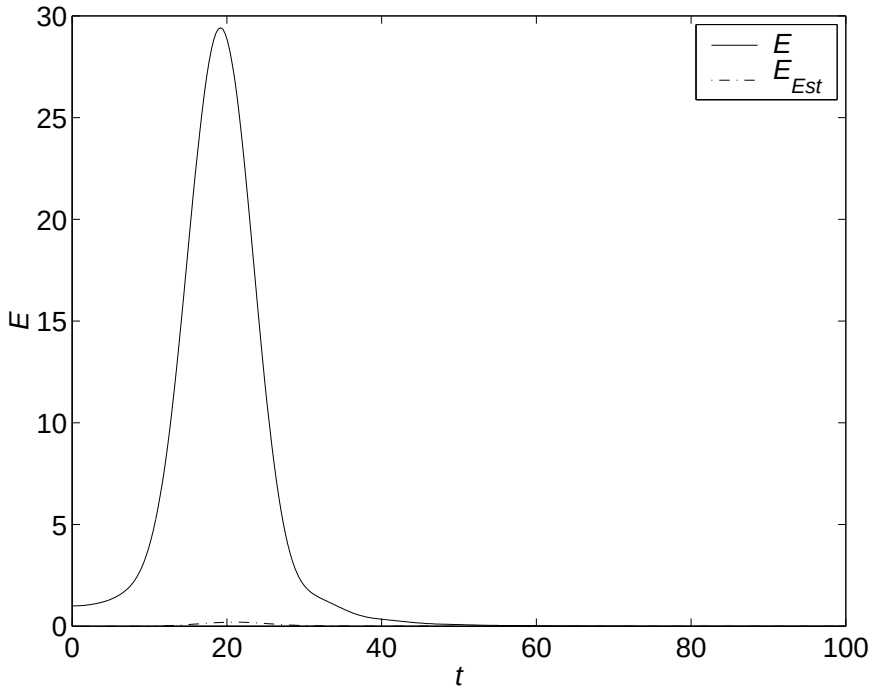

Figure 4.56: Case 1 LQG Transient Energy E vs Time t, from Initial Conditions $\mathcal{X}_{worst}$ Scaled to $E = 1$, $N = 100$

Case 1 LQG Output Feedback Linear Simulation

Results from simulations combining the state feedback LQR controller with the tuned LQE state estimator, and starting from the LQR worst initial state variables and zero initial estimates are displayed in figure 4.56 which shows case 1 LQG transient energy against time. The estimated energy amounts to only a small fraction of the energy of the plant state variables themselves, but nonetheless the controller is able to stabilise the flow, albeit with an diachronic transient energy bound of 29.42, significantly larger than the LQR state feedback value of 12.64.

Figure 4.57 presents the case 1 LQG control signal at the upper wall against time. Even though the estimated energy is very small, actuation levels are higher for the LQG controller than the LQR controller shown in figure 4.43. This implies even higher transpiration velocities and fluid quantities than for the LQR controller.

Case 2 LQG Output Feedback Linear Simulation

Figure 4.58 shows case 2 LQG transient energy and estimated transient energy against time. The case 2 estimator performs significantly better than the case 1 estimator, in their respective LQG systems. The controller is able to stabilise the flow, with a diachronic transient energy bound of approximately 934.00, only slightly larger than the LQR state feedback value of 848.80.

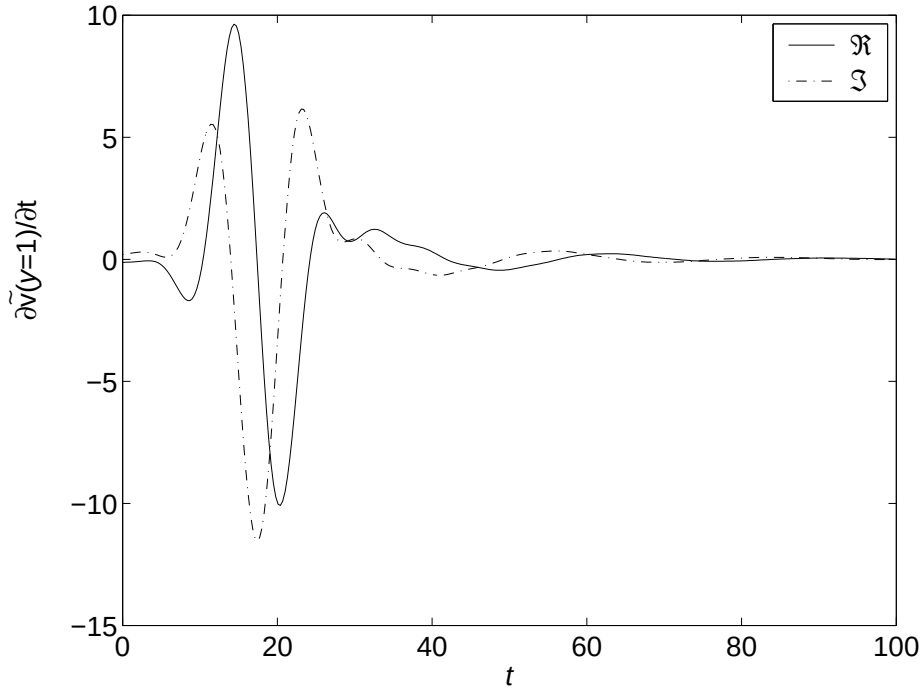

Figure 4.57: Case 1 LQG Upper Wall Control $\mathcal{U}(1)$ vs Time t, from Initial Conditions $\mathcal{X}_{worst}$ Scaled to $E = 1$, $N = 100$

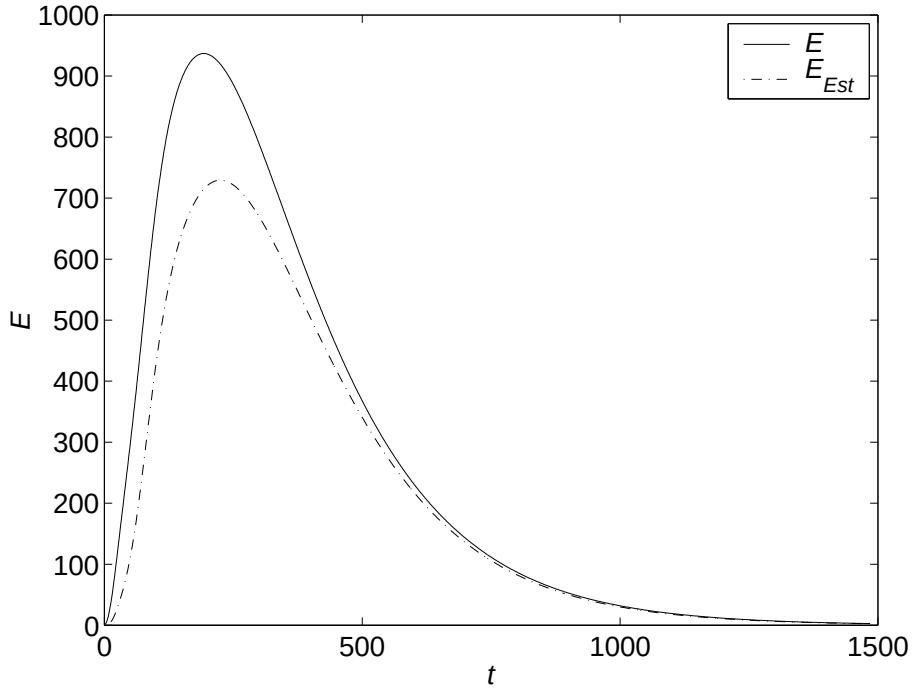

Figure 4.58: Case 2 LQG Transient Energy E vs Time t, from Initial Conditions $\mathcal{X}_{worst}$ Scaled to $E = 1$, $N = 100$

Table 4.2: Open-Loop and LQR Diachronic Transient Energy Bound θ by Eigensystem Calculation (4.41) and Linear Simulation

	Eigensystem Calculation (4.41)				Linear Simulation			
Case	OL	Time	LQR	Time	OL	Time	LQR	Time
1	unstable	-	12.65	18.43	unstable	-	12.64	18.3
2	4896.94	379.16	848.81	187.03	4896.94	379.5	848.80	187.5

Table 4.3: Diachronic Transient Energy Bound θ for All Open- and Closed-Loop Systems, by Linear Simulation (The bracketed values are on unstable systems, and require a time in order to define a nominal value.)

Case	OL θ	LQR θ	OL LQE θ_{Est}	LQG θ	LQE θ_{Est} in LQG
1	(87.67@t=150)	12.64	(88.12@t=150)	29.42	0.20
2	4896.94	848.80	4235.73	937.00	729.30

4.4.5 Summary of Diachronic Transient Energy Bound θ Results

As a check, table 4.2 exhibits a summary of the diachronic transient energy bound values of the open-loop and LQR state feedback systems, from both the diachronic transient energy bound eigensystem (4.41), and the linear simulation from the worst initial conditions. The small discrepancies are thought to be due to numerical inaccuracies, amongst which are the discrete time steps used in the linear simulations.

Table 4.3 shows a summary of the diachronic transient energy bound values from the open-loop and feedback systems, and also includes the estimated energy bound achieved by the LQE estimator on the open-loop and LQG systems, from zero initial estimates.

4.4.6 Choice of Controller Discretisation in Non-Linear Simulations

The non-linear simulations require significantly more computing time than the linear ones, in the order of days rather than minutes, on a Pentium 4^{TM} personal computer. It is appropriate to consider the choice of discretisation for the controllers to be applied to the non-linear models. Since no controller reduction is employed, this equates to the discretisation of the spectral model used for the controller synthesis. The issue of discretisation of the non-linear model itself is considered in section 4.4.7.

Many results regarding the convergence of the discretisation N have been presented thus far. For the controller synthesis model to achieve the high level of accuracy of eigenvalues published by the fluid dynamics community, $N = 100$ is required (section 2.8.1), although there may be no need for it replicate this high level of eigenvalue accuracy for the purposes of controller synthesis. For convergence of the plant model singular values beyond the estimated closed-loop bandwidth

a discretisation of $N = 100$ is required (section 2.8.1). For the observability and wall gradients of case 1 to have converged for the first 20 modes, approximately $N = 100$ is required (section 2.8.2).

For the LQR controller synthesis to converge $N = 30$ is sufficient (section 4.4.1), and for the LQE estimator synthesis $N = 70$ is sufficient (section 4.4.2). The linear simulations require $N = 30$ for the LQR system and $N = 50$ for the LQE system (section 4.4.4). The more exacting requirement of LQE is thought to be related to the convergence of the wall gradients and observability.

The major factor in determining the discretisation to be used appears to be the accuracy of the wall gradients in the estimator model of the plant. The need for fine discretisation at the wall is well known within the fluid dynamics community. Accordingly, controllers synthesized using a spectral model with $N = 100$ are used within the non-linear simulations.

4.4.7 Non Linear Simulations

A linear controller synthesized using a linearisation of a non-linear model will be able to stabilise the full model given initial conditions near the linearisation equilibrium point, and provided the trajectories do not stray far from the equilibrium point. However, if large transients take trajectories far away from the equilibrium point, non-linear effects may predominate and the system may not be stable.

This section explores the performance of the controllers on a non-linear model of the plant, from small and large initial perturbations. The non-linear simulations presented here cannot become fully turbulent as they are not three-dimensional, but they are capable of accurately modelling the initial evolution of instabilities.

Magnitude of Linear Perturbations

To estimate the size of initial perturbations that can be expected to behave linearly, the magnitude of the non-linear terms $(\vec{u} \cdot \nabla)\,\vec{u}$ omitted during linearisation (2.13) are calculated for the worst initial conditions.

The non-linearity in the y momentum equation, in a worst initial perturbation of maximum v amplitude 10^{-4} of U_{cl}, for open-loop case 1 is presented in figure 4.59. The regions with non-linearity greater than 10^{-2} are confined to small areas totalling less than 10%, near the walls. The plot contours scale directly with perturbation, so for a $10^{-2}U_{cl}$ perturbation, the regions with the same degree of non-linearity would cover around 45% of the area. The results for x momentum are similar.

Thus it would appear that a $10^{-4}U_{cl}$ initial perturbation would produce significantly more linear behaviour than a $10^{-2}U_{cl}$ one. A case 1 $10^{-4}U_{cl}$ perturbation has initial transient energy of 8.23×10^{-8}, hereafter denoted by E_{C1}, and the value for case 2 is 2.26×10^{-9}, denoted by E_{C2}. E_{C2} is approximately one hundredth of the open-loop streamwise vortices transition threshold for the test case, $2.56 - 2.65 \times 10^{-7}$, as determined by Reddy et al. (1998, p292), further confirming that transition and its associated non-linear behaviour should not occur from this initial energy level of the case 2 initial conditions. The transition threshold

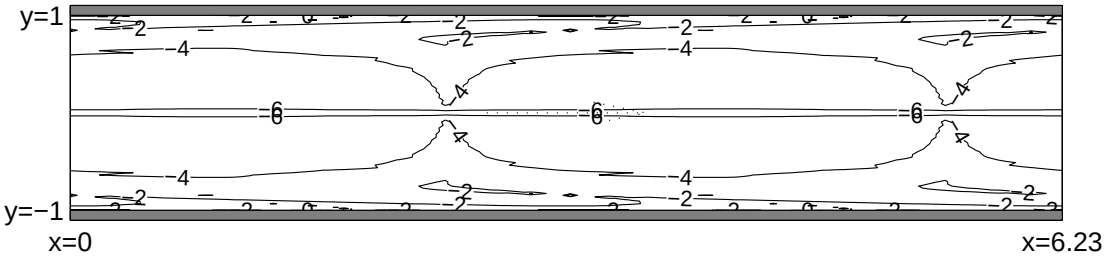

Figure 4.59: Contours of the Non-linearity in the y-momentum Equation, $log_{10}\left|(\vec{u}\cdot\nabla v)\,/\left(\vec{U}_b\cdot\nabla v\right)\right|$, in Case 1 Worst Initial Perturbation of Amplitude $v_{max}=10^{-4}U_{cl}$

for oblique waves is slightly lower at $1.14-1.19\times10^{-7}$, and is the lowest of the scenarios investigated by Reddy et al. (1998, p292).

Steady Transpiration Results

Figure 4.60 displays the steady u and v perturbation contours for $10^{-4}U_{cl}$ amplitude sinusoidal transpiration from the upper wall, at a base flow corresponding to a stable Reynolds number of 500, from both linear and non-linear simulations. The linear results are the eigenvector of the zero eigenvalue which represents control actuation at the upper wall, transformed from Fourier space to physical space, as in figure 2.15 but scaled to $10^{-4}U_{cl}$ amplitude sinusoidal transpiration. The linear and non-linear results are identical for both u and v flow-fields. Thus it can be concluded that the boundary conditions have been implemented correctly into the CFD code, and that the code and mesh are capable of accurately modelling perturbations small enough to be linear.

Small Perturbation Results

Results from worst but small magnitude initial perturbations in non-linear simulations are now presented. The open-loop initial maximum $\tilde{v}$ is $10^{-4}U_{cl}$, corresponding to an initial transient energy of E_{C1} (8.23×10^{-8}) for case 1 and E_{C2} (2.26×10^{-9}) for case 2. Closed-loop worst initial conditions of equal transient energy to the corresponding open-loop case are used. Simulation of linear sized perturbations is less exacting than for larger perturbations, so details of the mesh and timestep sensitivity study are given later in section 4.4.7. The base flow energy density is $4/15\approx0.2667$. Thus E_{C1} has approximately 3.1×10^{-7}, and E_{C2} has 8.5×10^{-9}, of the base flow energy density.

The case 1 open-loop transient energy from this small initial perturbation, for both linear (dotted) and non-linear (solid) simulations, is exhibited in figure 4.61. The results from the linear and non-linear simulations agree well, as might be expected from the initial small degree of non-linearity, and the same is true for case 2, shown in figure 4.62. Thus it may be assumed that the non-linear finite volume and linear spectral simulations are both modelling the linear terms of the

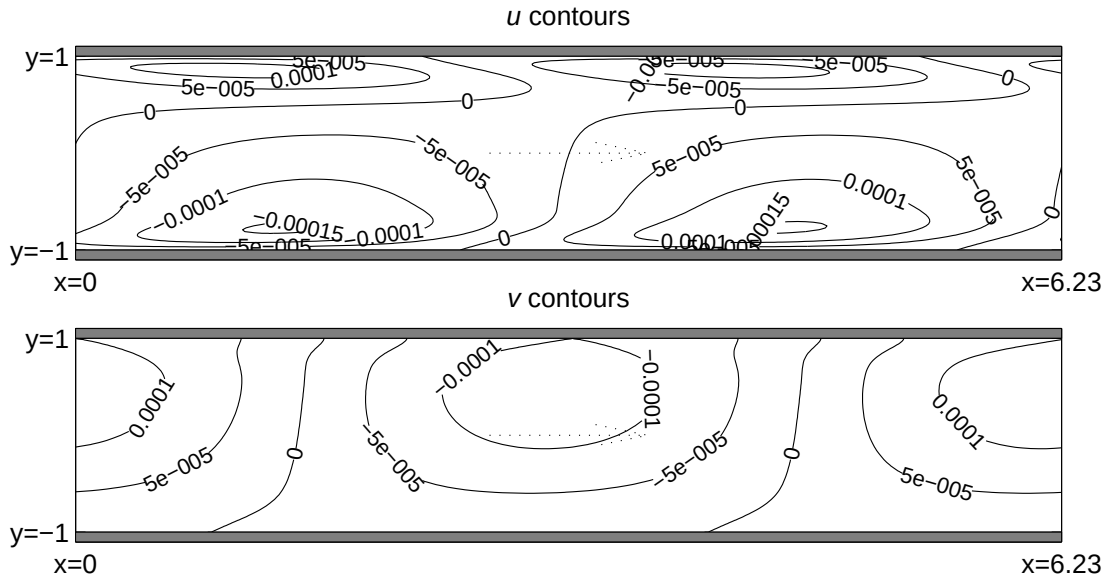

Figure 4.60: u and v Perturbation Contours from Sinusoidal Upper Wall Transpiration of Amplitude $v_{max} = 10^{-4}U_{cl}, R = 500$, Showing Linear (dashed) and Non-linear (solid) Simulation Results. (The linear and non-linear results appear identical.)

uncontrolled flow correctly. The final case 1 flow field (not shown) corresponds to the unstable eigenvector shown in figure 2.14, and is a Tollmien-Schlichting wave (Schmid and Henningson, 2001, p64).

Figure 4.61 also shows the behaviour of the tuned estimator on the worst initial open-loop conditions of energy E_{C1}, for case 1. The non-linear simulation energy estimate agrees well with the linear simulation. For the case 2 tuned estimator on worst initial conditions of energy E_{C2}, the agreement is not as good, as shown in figure 4.62. A discrepancy between the linear and non-linear results grows with time, until the disturbance begins to decay. This discrepancy may be due to the use of implicit code to integrate the estimates in the non-linear simulation, to avoid problems with stiffness. The scheme is stable but possibly inaccurate at the timestep used.

Figures 4.63 and 4.64 present the closed-loop LQR state feedback transient energy, from worst initial perturbations of equal energy to their respective open-loop cases, for both linear (solid) and non-linear (dotted) simulations, for cases 1 and 2 respectively. The results from both the linear and non-linear simulations again agree well, and both show the stabilization of the flow by the LQR controller. Thus it may be assumed that the non-linear finite volume and linear spectral simulations are both modelling the linear terms of the flow controlled by state feedback correctly, and that the controllers have been correctly implemented in the CFD code. By integration, the magnitude of the harmonic transpiration fluid quantity required for case 2 was found to be 0.0243, as compared to 0.0245 by scaling of the linear simulation results to energy E_{C2}.

These small perturbation non-linear simulations show agreement between peak

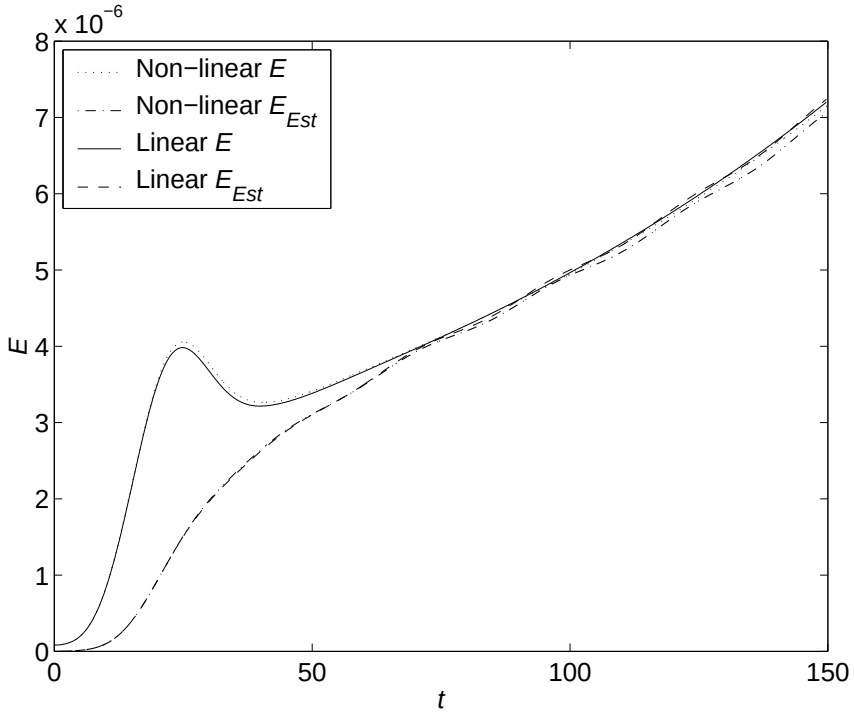

Figure 4.61: Case 1 Open-Loop Transient Energy E vs Time t from Initial Conditions $\mathcal{X}_{Worst}$ Scaled to Energy E_{C1}

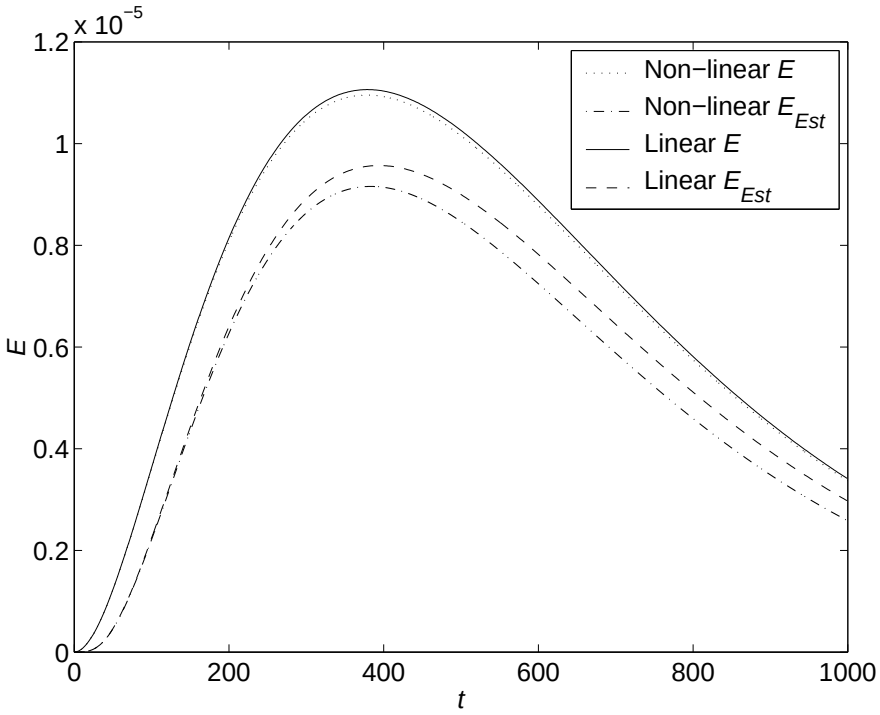

Figure 4.62: Case 2 Open-Loop Transient Energy E vs Time t from Initial Conditions $\mathcal{X}_{Worst}$ Scaled to Energy E_{C2}

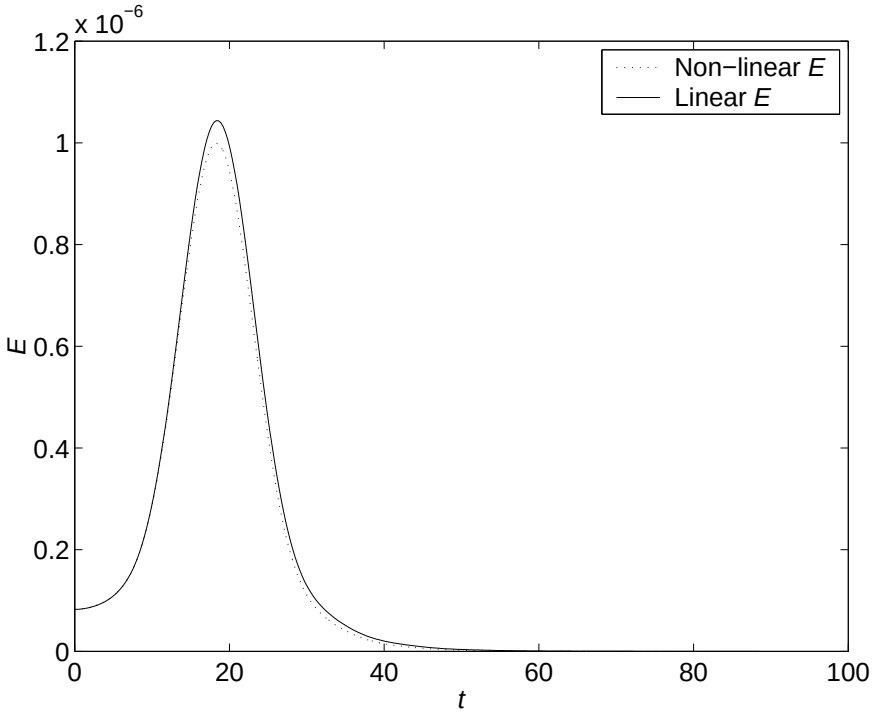

Figure 4.63: Case 1 LQR Transient Energy E vs Time t from Initial Conditions $\mathcal{X}_{Worst}$ Scaled to Energy E_{C1}

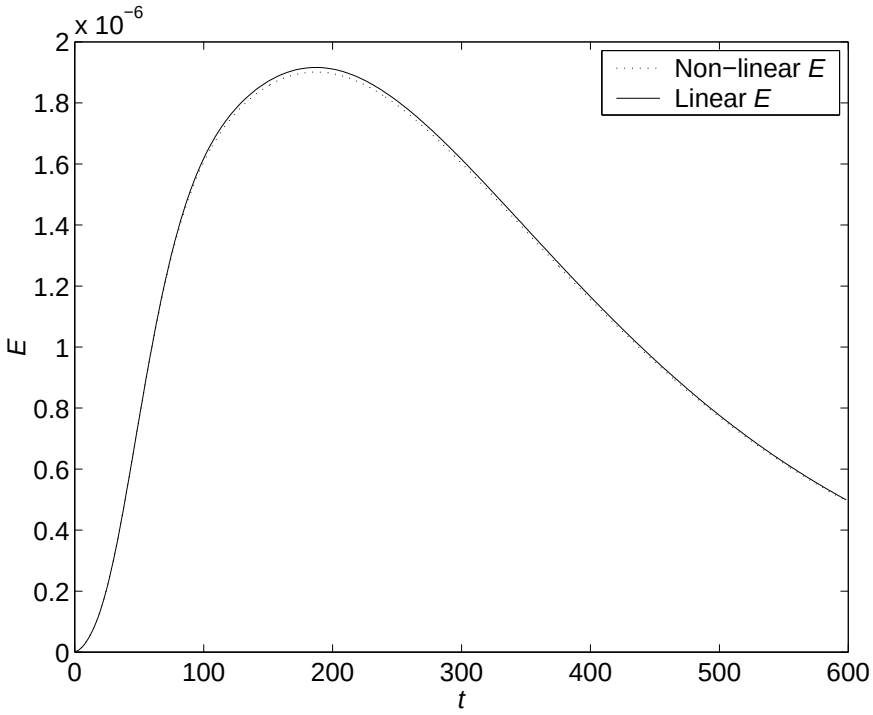

Figure 4.64: Case 2 LQR Transient Energy E vs Time t from Initial Conditions $\mathcal{X}_{Worst}$ Scaled to Energy E_{C2}

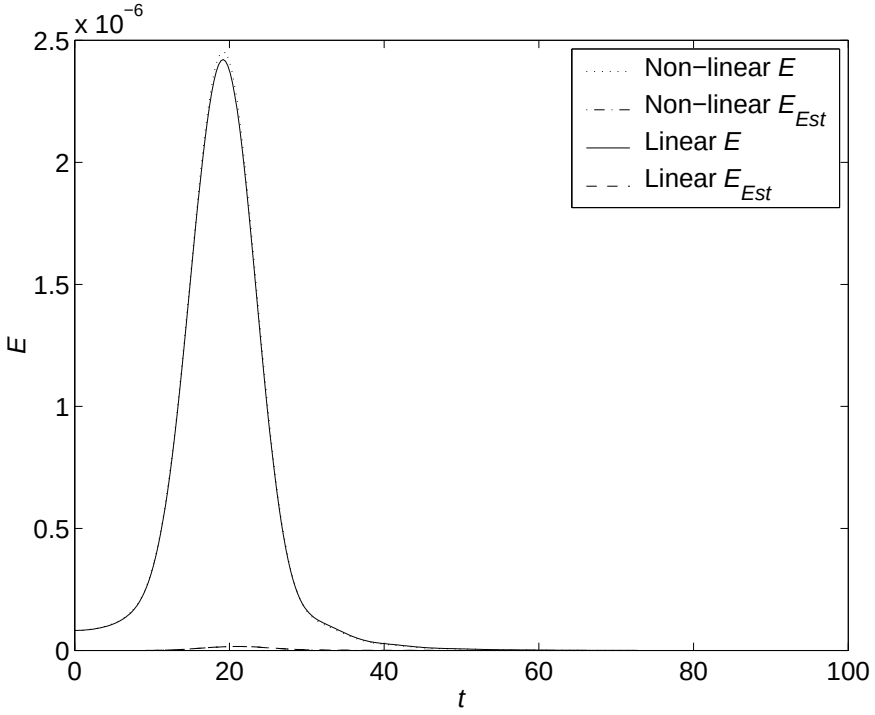

Figure 4.65: Case 1 LQG Transient Energy E vs Time t from Initial Conditions $\mathcal{X}_{Worst}$ Scaled to Energy E_{C1}

transient energy as computed from the state variables by $E = \mathcal{X}^T \mathcal{Q} \mathcal{X}$ from (4.23) and as calculated by direct integration over the mesh using (4.5), repeated here

$$E = \frac{1}{V} \int_{vol=V} \rho \frac{\vec{u}^T \vec{u}}{2} \, dvol \tag{4.98}$$

to within 0.3% for both case 1 and case 2 LQR systems. This result shows that the calculation of the state variables is substantially correct, and also that the energy matrix $\mathcal{Q}$ is correctly formulated. As a further check, integration of case 2 fluid quantity transpired in the non-linear simulation is found to closely agree with that from linear simulation, to within 1%.

The behaviour of the combined tuned LQE estimator and state feedback LQR controller on the plant from worst initial conditions of energy E_{C1}, for case 1, appears in figure 4.65. The non-linear simulation energy estimates agree well with the linear simulation, for both the plant and estimator transient energy. The agreement is not good for the case 2 estimator from plant initial energy E_{C2}, as shown in figure 4.62, where again a discrepancy between the linear and non-linear results grows with time, until the disturbance begins to decay. Although the behaviour of the estimator in the non-linear simulation differs from that in the linear simulation, the plant energies agree well. This indicates that the exact behaviour of the estimator is not critical.

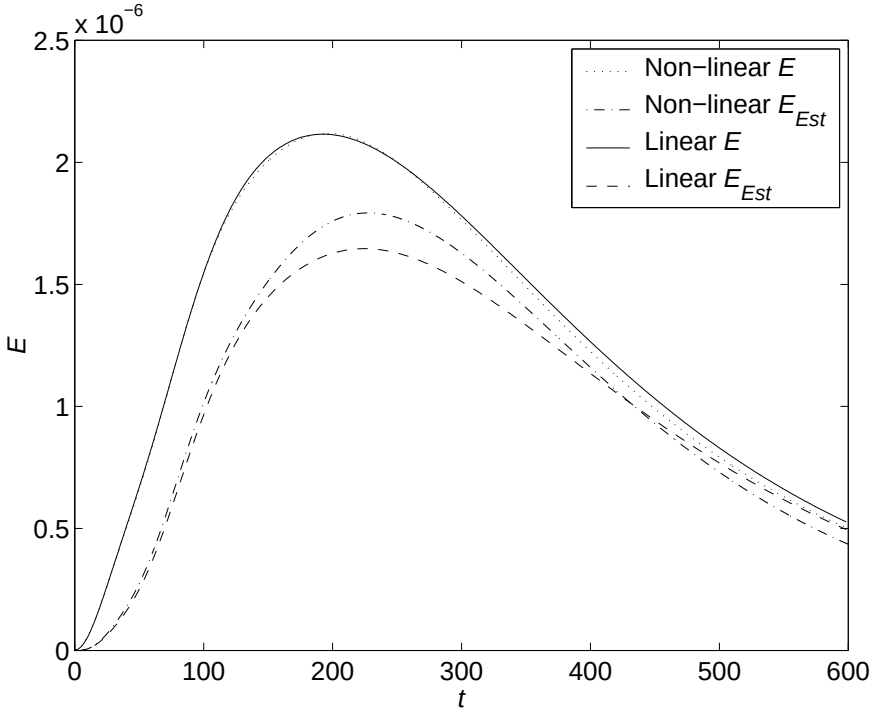

Figure 4.66: Case 2 LQG Transient Energy E vs Time t from Initial Conditions $\mathcal{X}_{Worst}$ Scaled to Energy E_{C2}

Large Perturbation Mesh Sensitivity Results

Large perturbations which produce significant non-linear terms are much harder to simulate accurately, and the linear spectral results are of no use for comparison purposes. Accordingly, mesh and timestep sensitivity studies are performed to demonstrate that the discretisation is appropriate for the flow under simulation (Drikakis, 2001). Only open-loop sensitivity studies are performed, which are more demanding, since closed-loop simulations will be stable and of lower peak energy levels than the open-loop ones. The initial conditions used are worst perturbations with energies of $10^4 E_{C1}$ and $10^4 E_{C2}$, for cases one and two respectively.

A second order central differencing scheme is used to discretise the spatial terms, and a first order implicit Euler scheme is used for time marching in case 2. Ferziger and Peric (2002, p148) note that this scheme is unconditionally stable, but its accuracy is only first order in time, and it is found useful to employ a second order implicit Euler scheme for case 1, where time variations are faster. The schemes may produce oscillatory solutions in space, but nonetheless stable solutions, where large solution gradients exist and the cell Peclet number (also known as the cell Reynolds number) is high, for example $Pe > 2$ on a three-level fully implicit scheme for the transport equation, as noted by Fletcher (1991, p303).

The cell Peclet number (Versteeg and Malalasekera, 1995, p112)

$$Pe = \frac{\rho u}{\mu / \delta x} \tag{4.99}$$

is a measure of the relative strengths of convection and diffusion at work in a mesh

cell. The cell Courant number (Ferziger and Peric, 2002, p144)

$$C = \frac{u\delta t}{\delta x} \tag{4.100}$$

is another key parameter in CFD. It compares the timestep δt with the characteristic convection time $\delta x/u$. $\delta x/u$ is the time required for the convection of a fluid particle a distance of mesh cell width δx by fluid of velocity u. The maximum values of these parameters over all cells and co-ordinate directions is of interest.

Although the non-linear simulation code is modified to work in terms of perturbations, the Peclet and Courant numbers are influenced by the base flow, and consequently here these numbers are therefore based on the total flow, i.e. base flow plus perturbation. The distinction between total flow and perturbation flow only occurs for the streamwise (x) direction. These numbers are calculated using quantities $\rho, u, \mu, \delta x, \delta t$ from the CFD analysis which are dimensionalised, as in section 4.3.3.

Figure 4.67 presents case 1 open-loop transient energy against time, starting from the worst initial conditions, for a variety of mesh and timestep combinations. It can be seen that for approximately the first 60 non-dimensional time units, the $N = 100$ mesh results are very close for timesteps δt 0.001 and 0.0001 seconds, and thereafter the results remain relatively close. It can therefore be assumed that the timestep independence has been achieved for this mesh at timestep $\delta t = 0.001s$. A finer mesh of $N = 150$, (with timestep $\delta t = 0.0005s$, to maintain approximately the same peak Courant number as $N = 100$ at timestep $\delta t = 0.001s$, as shown in figure 4.68), produces results close to those of the $N = 100$ mesh at timestep $\delta = 0.001s$ for approximately the first 27 time units. The agreement is better in terms of velocity, since this is proportional to the square root of the energy, as shown in figure 4.69 for the u velocity component at monitoring points at 25% channel height intervals. The channel centre-line is at $y = 0$, and the walls are at $y = \pm 1$, where, in the open-loop case, all velocities are zero. In terms of velocity, results from the two meshes agree very well for approximately 20 time units, and fairly well until around 60 time units. The results for velocity component v are similar. It may be concluded that reasonable mesh independence has been achieved between the $N = 100$ and $N = 150$ results, i.e. for $N = 100$ and above.

The $N = 150$, timestep $\delta t = 0.0005$ results are themselves timestep independent, as can be seen by the close agreement with $N = 150$ timestep $\delta t = 0.0001$ energy results, shown in figure 4.67. This might be expected by the maintenance of the Courant number for the $N = 150$, $\delta t = 0.0005s$ results. It may be concluded that the $N = 100$, $\delta t = 0.001s$ discretisation is both mesh and timestep independent for case 1.

Results from a variety of mesh and timestep combinations for case 2 open-loop transient energy against time, starting from the worst initial conditions, are shown in figure 4.70. It can be seen that the $N = 100$ mesh results are very close for timesteps $0.01s$ and $0.003s$. It can therefore be assumed that the timestep independence has been achieved for this mesh at timestep $\delta t = 0.01s$. A finer mesh of $N = 150$, (with timestep $\delta t = 0.005s$, to maintain approximately the same peak Courant number as $N = 100$ at $\delta t = 0.01s$, as shown in figure 4.71),

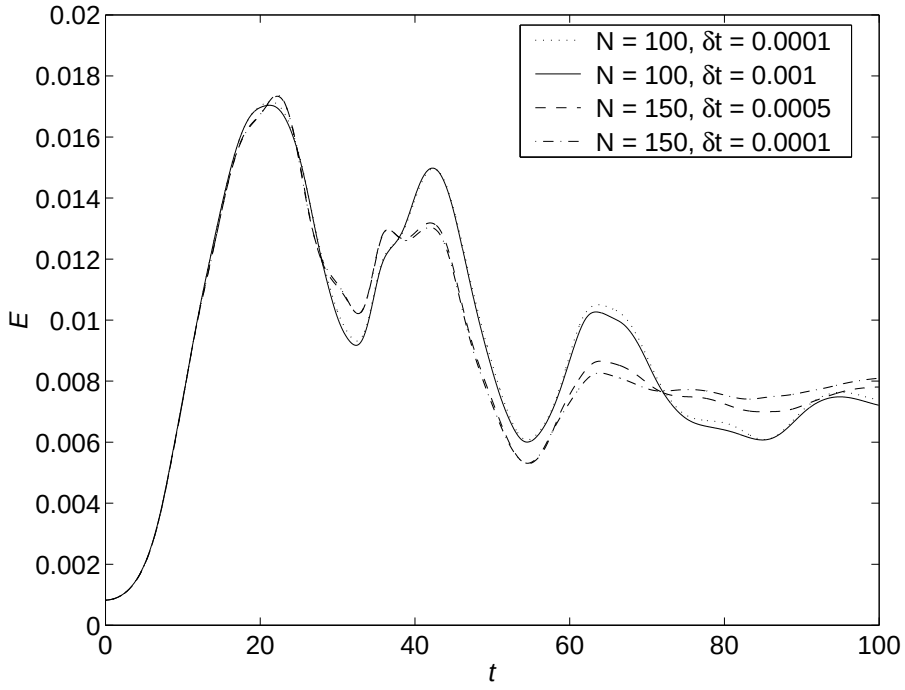

Figure 4.67: Case 1 Open-Loop Transient Energy E from Initial Conditions $\mathcal{X}_{Worst}$ Scaled to Energy $10^4 E_{C1}$, for Various Discretizations N and Timesteps δt

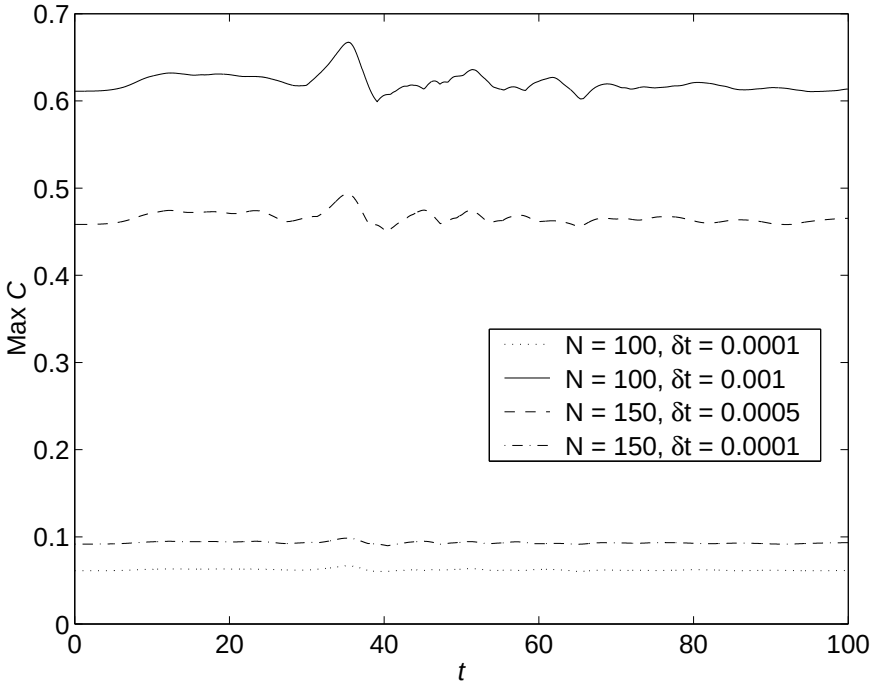

Figure 4.68: Case 1 Open-Loop Courant Number from Initial Conditions $\mathcal{X}_{Worst}$ Scaled to Energy $10^4 E_{C1}$, for Various Discretizations N and Timesteps δt

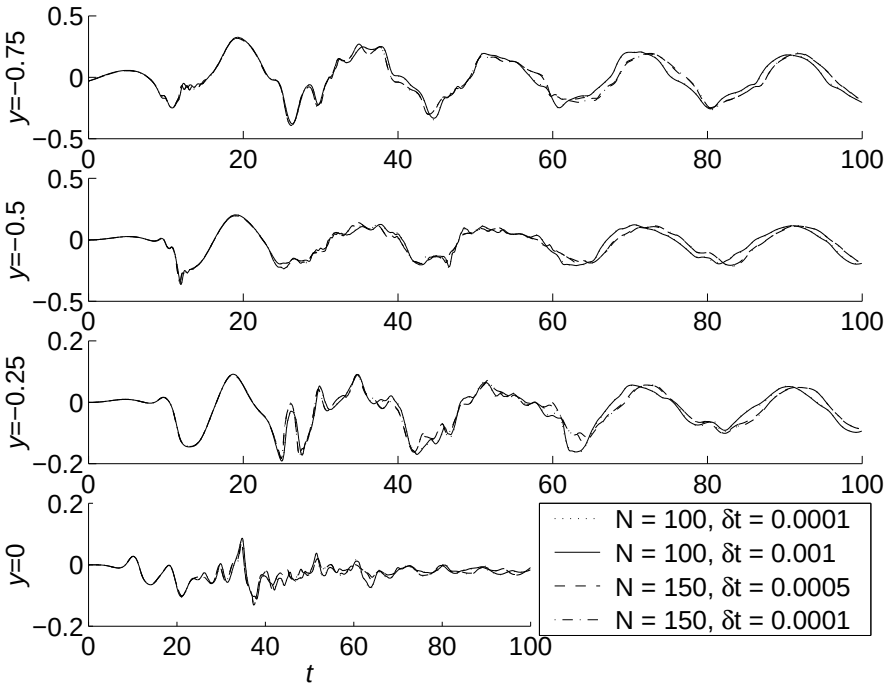

Figure 4.69: Case 1 Open-Loop u at Heightwise Monitoring Points from Initial Conditions $\mathcal{X}_{Worst}$ Scaled to Energy $10^4 E_{C1}$, for Various Discretizations N and Timesteps δt

produces results very close to those of the $N = 100$ mesh. The agreement is better than for case 1, and in terms of velocity better still (not shown), and reflects case 2 being more amenable to simulation in general. It may be concluded that mesh independence has been achieved between the $N = 100$ and $N = 150$ results, i.e. for $N = 100$ and above. It may be concluded that the $N = 100$, $\delta t = 0.01s$ discretisation is both mesh and timestep independent for case 2.

The Peclet numbers of the simulations of both test cases are very high, as shown in figures 4.72 and 4.73, and may lead to spatial oscillations, which are investigated in section 4.4.7.

Large Perturbation Results

Results are now presented for transient simulations, from initial conditions which are the worst for the particular eigensystem, with energy corresponding to that of a $v_{max} = 10^{-2} U_{cl}$ open-loop worst initial perturbation. For case 1 this energy is $10^4 E_{C1} = 0.00082$, and for case 2 it is $10^4 E_{C2} = 0.000023$. Contour plots of velocity after the first timestep from these increased energy initial conditions are close to scaled versions of the linear results, and thus no substantial non-linear effects are initially present and these scaled solutions to the linearised Navier-Stokes equations remain good solutions to the full Navier-Stokes equations, and are valid initial conditions. $10^4 E_{C2}$ is approximately a hundred times the open-loop streamwise vortices transition threshold for the test case, $2.56 - 2.65 \times 10^{-7}$, as determined by Reddy et al. (1998, p292), confirming that transition and its

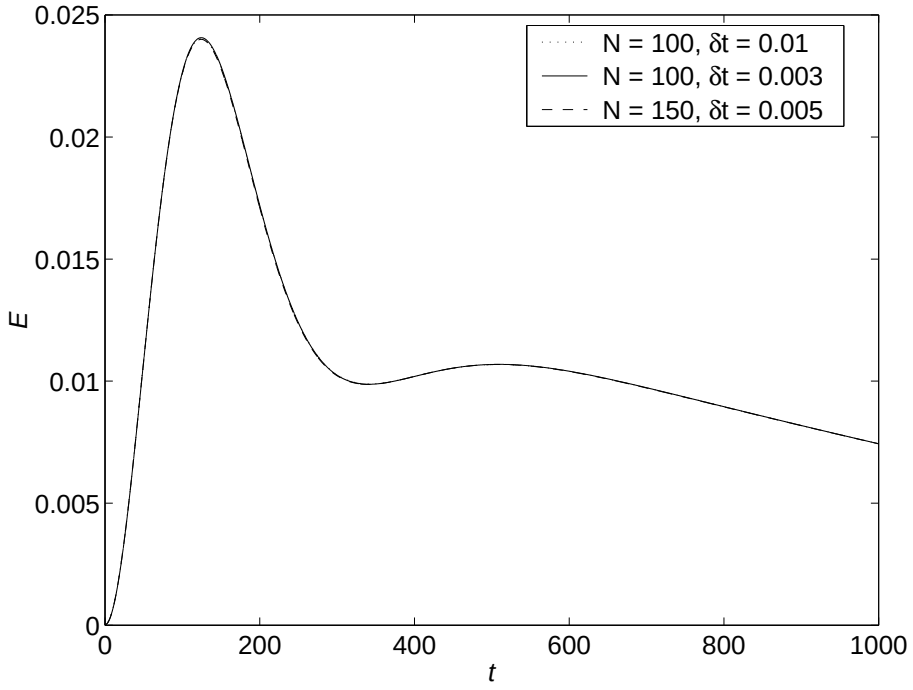

Figure 4.70: Case 2 Open-Loop Transient Energy E from Initial Conditions $\mathcal{X}_{Worst}$ Scaled to Energy $10^4 E_{C2}$, for Various Discretizations N and Timesteps δt

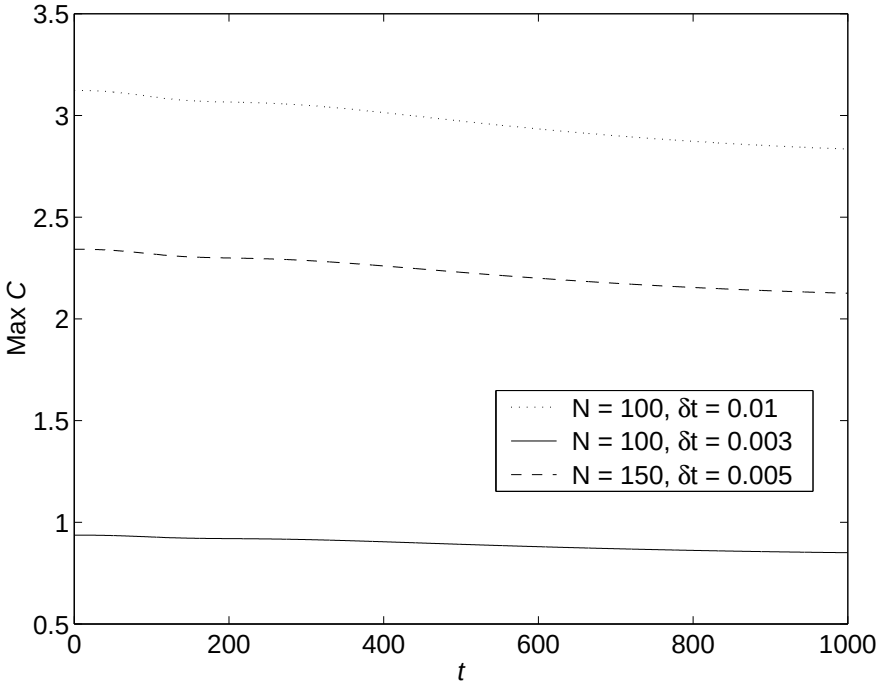

Figure 4.71: Case 2 Open-Loop Courant Number from Initial Conditions $\mathcal{X}_{Worst}$ Scaled to Energy $10^4 E_{C2}$, for Various Discretizations N and Timesteps δt

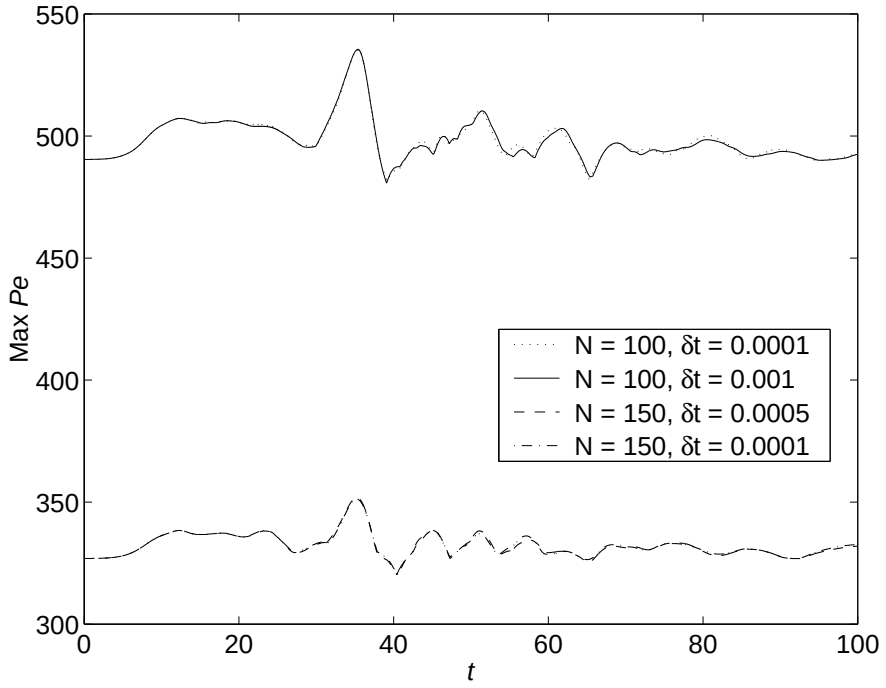

Figure 4.72: Case 1 Open-Loop Peclet Number from Initial Conditions $\mathcal{X}_{Worst}$ Scaled to Energy $10^4 E_{C1}$, for Various Discretizations N and Timesteps δt

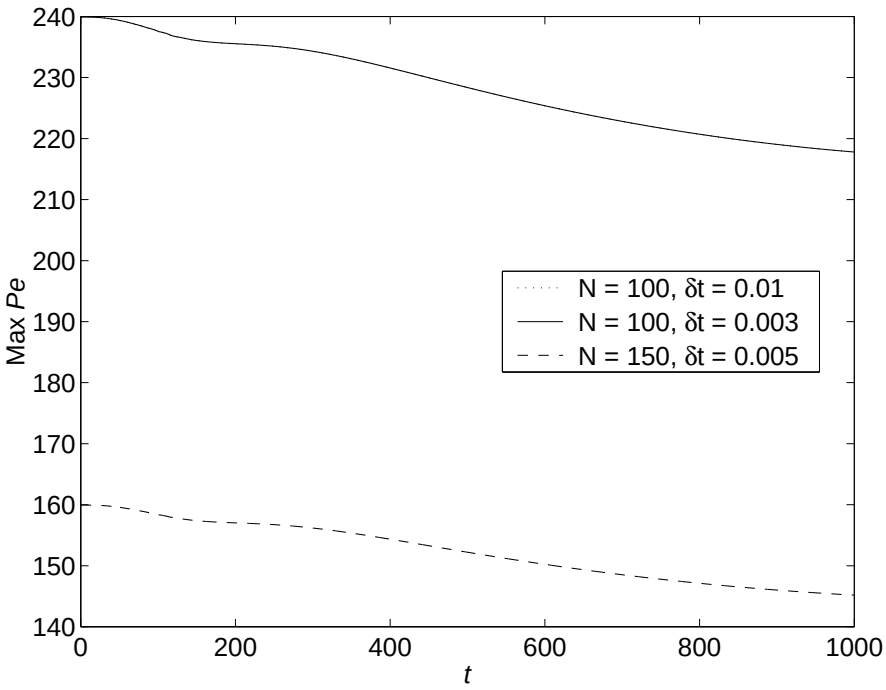

Figure 4.73: Case 2 Open-Loop Peclet Number from Initial Conditions $\mathcal{X}_{Worst}$ Scaled to Energy $10^4 E_{C2}$, for Various Discretizations N and Timesteps δt. The dotted and solid curves are identical.

associated non-linear behaviour may occur from this initial energy level of the case 2 initial conditions. The base flow energy density is $4/15 \approx 0.2667$. Thus $10^4 E_{C1}$ has approximately 3.1×10^{-3}, and $10^4 E_{C1}$ has 8.5×10^{-5}, of the base flow energy density.

Plots of transient energy against time these for larger initial perturbations are presented with logarithmic energy axes, as these axes show the initial energy growth and final decay in more detail. Logarithmic axes tend to compress results of similar magnitude, however, the non-linear results remain distinct from the scaled linear ones. Plots with linear axes are provided in appendix B.

Case 1 Open-Loop Non-Linear Simulation Figure 4.74 shows case 1 open-loop transient energy against time, from this larger initial perturbation, for both linear and non-linear simulations. The linear and non-linear simulations agree initially for a period of non-normal growth up to time approximately 10 units. Thereafter the linear simulation increases swiftly to complete the non-normal growth, and thence continues with modal growth, but the non-linear simulation undergoes an oscillatory transient, and reaches a saturated state, in which the transient energy grows relatively slowly, the value at time 150 being 0.0084 and later at 300 being just 0.0122 (not shown). Although the non-linear simulation deviates from the linear results during the initial non-modal phase, the earliest growth appears to be at a rate identical to that of the linear system non-modal phase. The non-linear analysis deviates as the extra terms in the non-linear simulation (discarded from the linear model in section 2.2.4) couple the equations for different modes, so that energy can be transferred between modes, which is not the case even for the non-normal behaviour of a linear system. Also, the non-linear analysis allows the presence of harmonics of the wavenumbers α and β, since, for example, wavenumber 2α (wavelength π/α) will also fit between the wavenumber α periodic boundary conditions imposed at a streamwise separation of $2\pi/\alpha$, whereas the Fourier assumption in the spectral analysis allows only the presence of disturbances at spatial frequencies α and β. In the non-linear simulations, the non-linear coupling terms may therefore excite disturbances at harmonics of the wavenumbers α and β.

As for LQE state estimation, figure 4.74 also presents the case 1 open-loop estimated transient energy against time. The performance of the linear estimator on the non-linear plant model is poor, achieving a peak energy of only 0.0014 as compared to the plant which reaches 0.017. The estimator is unable to match the final slow energy growth of the plant, and is effectively diverging.

Case 2 Open-Loop Non-Linear Simulation The case 2 open-loop transient energy time history, from this larger initial perturbation, for both linear and non-linear simulations, is displayed in figure 4.75. The linear and non-linear simulations agree initially for a period of non-normal growth up to time approximately 50 units. Thereafter the linear simulation increases to complete the non-normal growth to transient energy of 0.111, corresponding to an diachronic transient energy bound of 4896.94, and thence continue with decay, but the non-linear simulation reaches a saturated state with peak transient energy of 0.0240 at time approximately 124.5

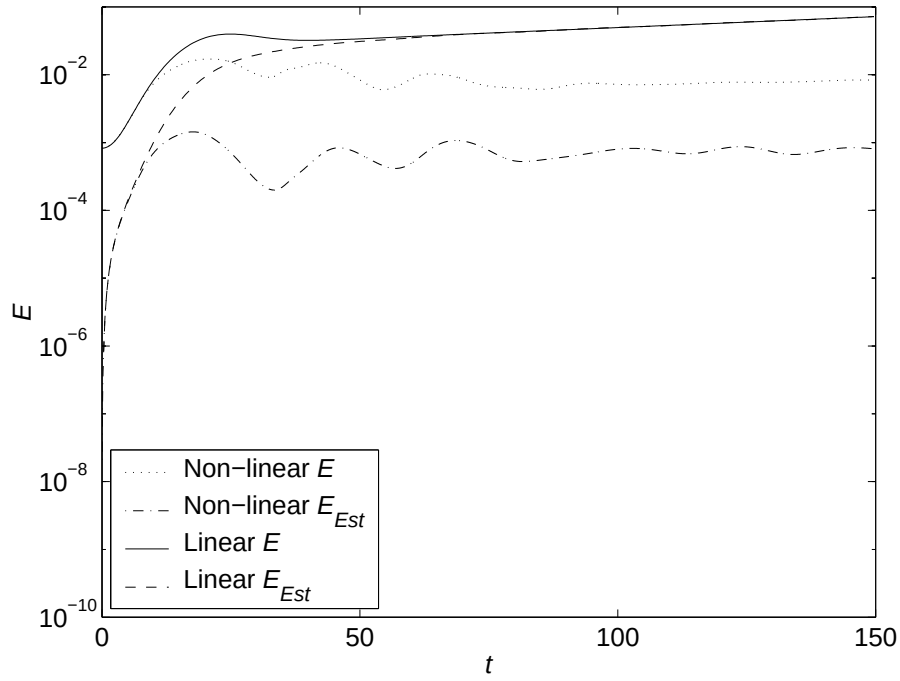

Figure 4.74: Case 1 Open-Loop Transient Energy E vs Time t, from Initial Conditions $\mathcal{X}_{Worst}$ Scaled to Energy $10^4 E_{C1}$

units, and thereafter decays. The decay continues beyond $t = 1500$ (not shown), at approximately the same rate as at $t = 1000$. As for case 1, although the non-linear simulation soon deviates from the linear results, the earliest growth appears to be at a rate identical to that of the linear system.

Regarding estimation, figure 4.75 also shows the open-loop estimated transient energy against time. In this case, the performance of the linear estimator on the non-linear plant model overshoots, and it reaches almost twice the peak plant energy level, and thereafter slowly converges with the plant's gradual decay. The overshoot of the linear estimator is consistent with the non-linear plant saturating.

Case 1 LQR State Feedback Non-Linear Simulation Case 1 closed-loop LQR transient energy versus time, for both linear and non-linear simulations, is presented in figure 4.76, and also in linear form as B.2. The controller reduces the transient energy, and thus the difference between the linear and non-linear simulation is much reduced, as compared to the open-loop case. The controller is able to stabilise the non-linear simulation, but it takes significantly longer than in the linear simulation.

Figure 4.77 displays the upper wall transpiration velocities at location $x = \pi$, the mid point of the domain in x, for the same perturbation. The wall transpiration velocities required in the non-linear simulation are lower than in the linear one, but are required for longer, which is consistent with the transient energy.

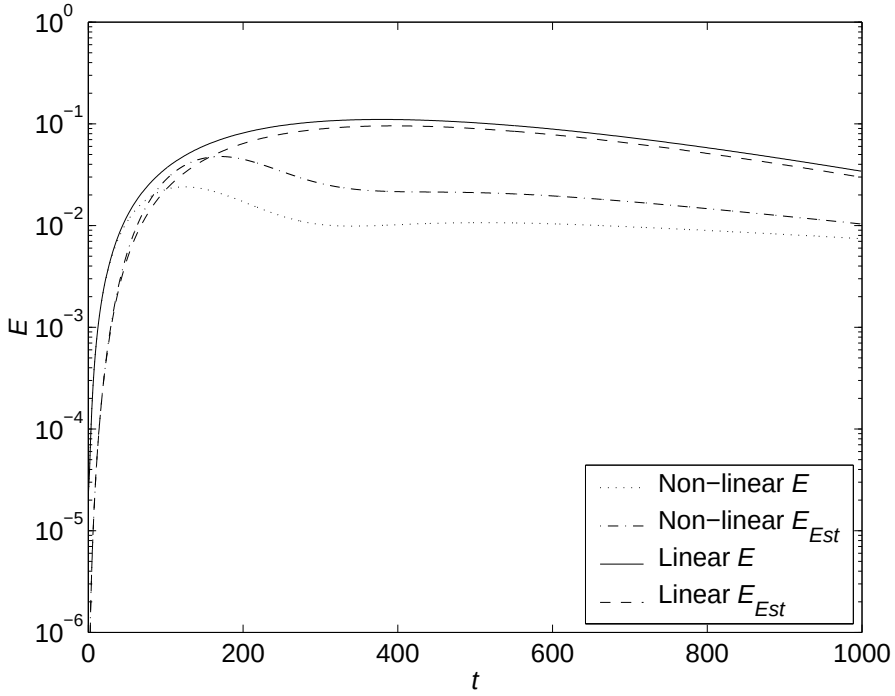

Figure 4.75: Case 2 Open-Loop Transient Energy E vs Time t, from Initial Conditions $\mathcal{X}_{Worst}$ Scaled to Energy $10^4 E_{C2}$

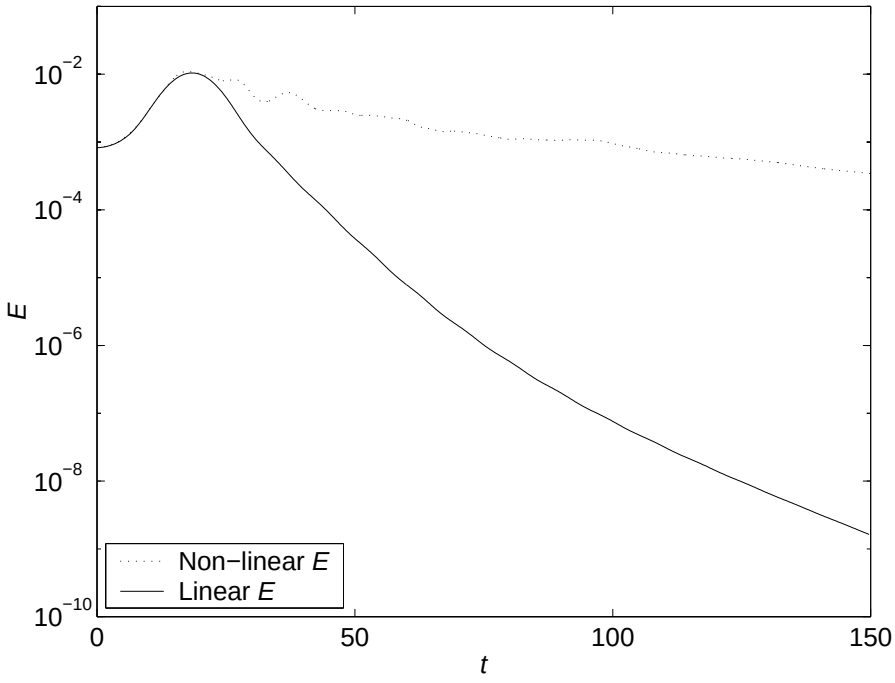

Figure 4.76: Case 1 LQR Transient Energy E vs Time t, from Initial Conditions $\mathcal{X}_{Worst}$ Scaled to Energy $10^4 E_{C1}$

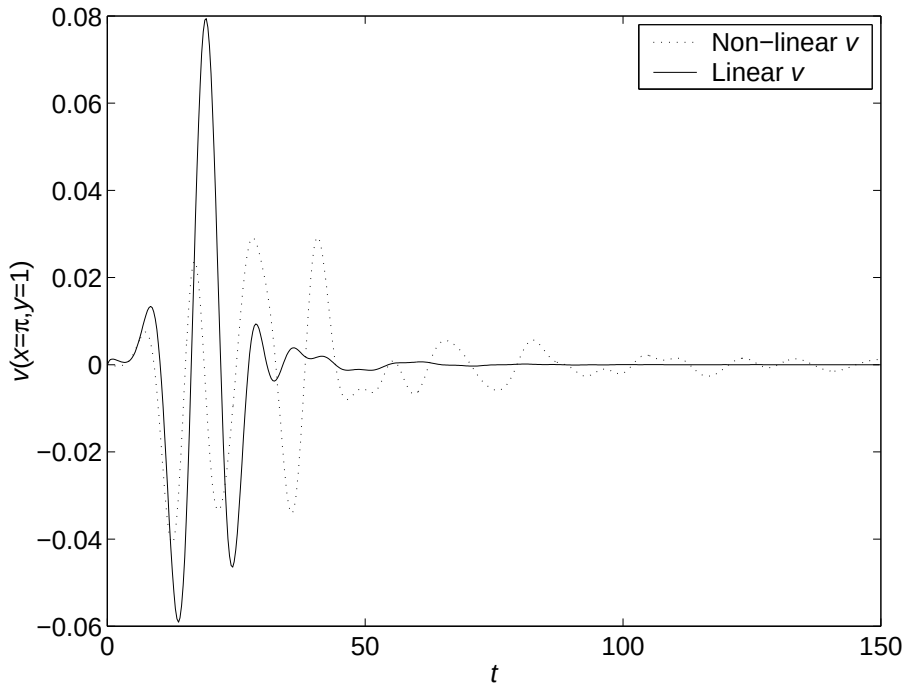

Figure 4.77: Case 1 LQR Wall Transpiration Velocity at $x = \pi$ vs Time t, from Initial Conditions $\mathcal{X}_{Worst}$ Scaled to Energy $10^4 E_{C1}$

Case 2 LQR State Feedback Non-Linear Simulation Regarding case 2, figure 4.78 presents the closed-loop LQR transient energy versus time, from this larger initial perturbation, for both linear and non-linear simulations. The controller reduces the transient energy, and the difference between the linear and non-linear simulation is somewhat reduced, as compared to the open-loop case. The controller has reduced the open-loop non-linear peak transient energy from 0.024 to 0.0095, a reduction of approximately 60% which is not nearly such a great reduction as that in the linear simulation where the diachronic transient energy bound falls from 4896.94 to 848.80, a reduction of approximately 83%. The peak non-linear LQR transient energy of 0.0095 is approximately half the linear value. The controller is acheiving a lower energy density on the non-linear simulation, as energy levels are in general lower in the non-linear simulation.

Figure 4.79 shows the wall transpiration velocities at location $z = 0.768$ for the same perturbation. This z value is the quarter point of the domain in z, and is chosen since the linear model velocity variation in z for case 2 is imaginary, and thus a sine wave and zero at the mid point of the domain. The wall transpiration velocities required in the non-linear simulation are slightly lower than those in the linear one. By integration, the magnitude of the harmonic transpiration fluid quantity required was found to be 2.07, as compared to 2.45 by scaling of the linear simulation results to $10^4 E_{C2}$.

The large perturbation CFD simulations for both case 1 and case 2 LQR systems showed poor agreement between peak transient energy as computed from the state variables by $E = \mathcal{X}^T \mathcal{Q} \mathcal{X}$ from (4.23) and as calculated by direct integration

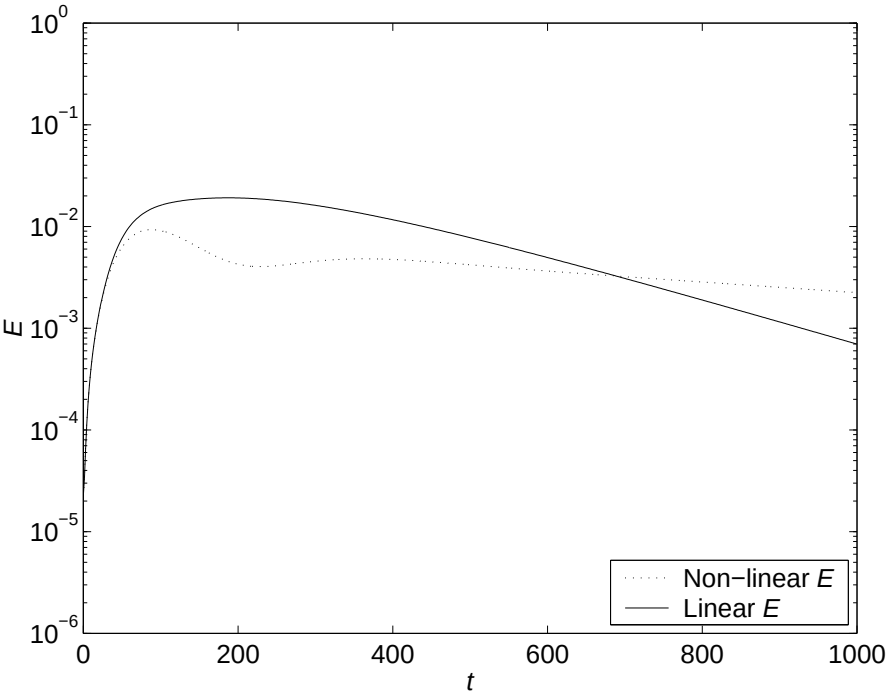

Figure 4.78: Case 2 LQR Transient Energy E vs Time t, from Initial Conditions $\mathcal{X}_{Worst}$ Scaled to Energy $10^4 E_{C2}$

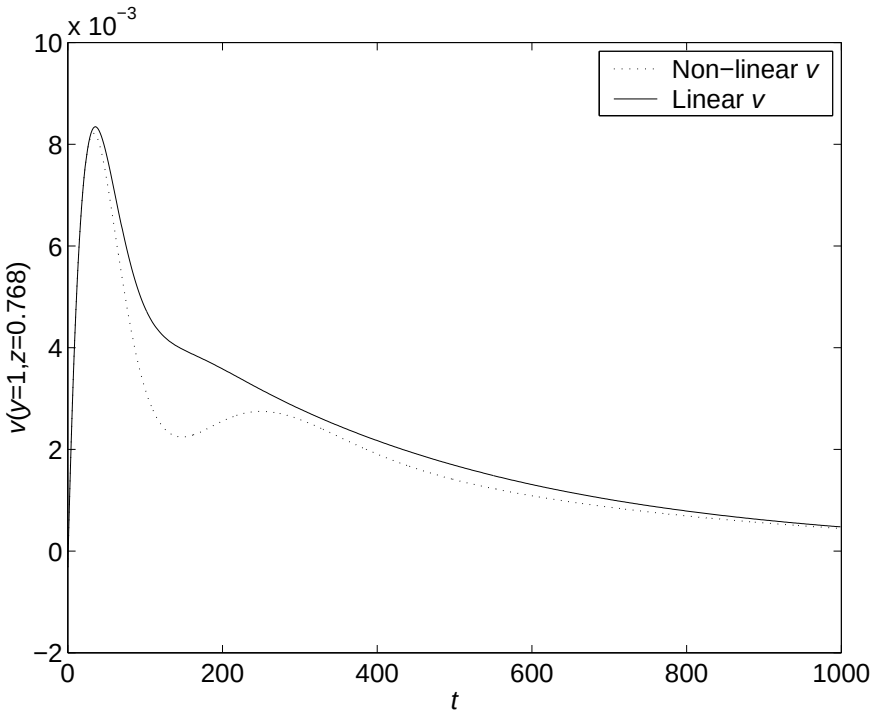

Figure 4.79: Case 2 LQR Wall Transpiration Velocity at $z = 0.768$ vs Time t, from Initial Conditions $\mathcal{X}_{Worst}$ Scaled to Energy $10^4 E_{C2}$

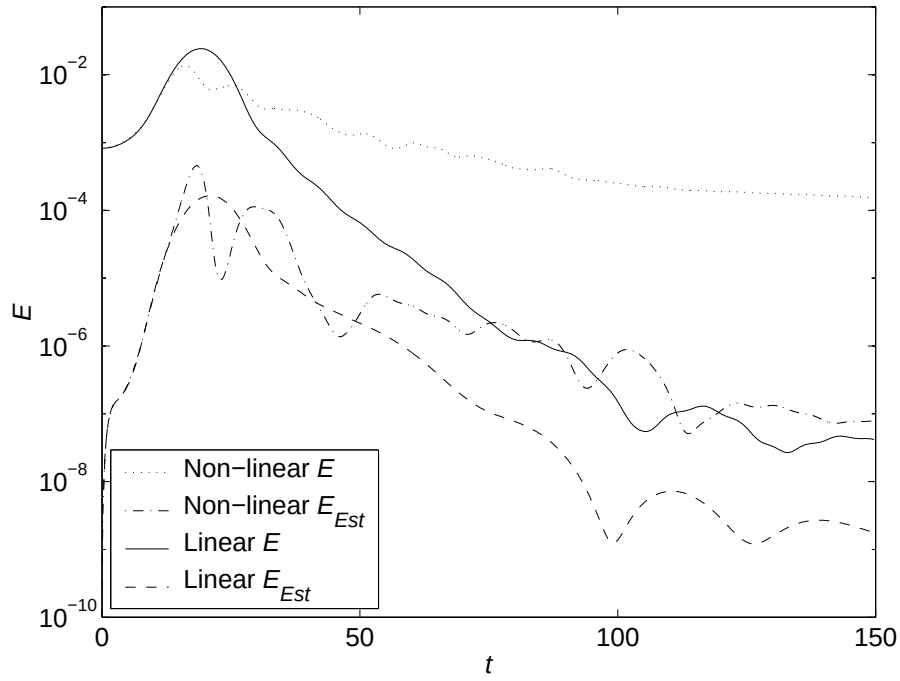

Figure 4.80: Case 1 LQG Transient Energy E vs Time t, from Initial Conditions $\mathcal{X}_{Worst}$ Scaled to Energy $10^4 E_{C1}$

over the mesh using (4.5), repeated here

$$E = \frac{1}{V} \int_{vol=V} \rho \frac{\vec{u}^T \vec{u}}{2} \, dvol \tag{4.101}$$

For case 1, $\mathcal{X}^T \mathcal{Q} \mathcal{X}$ under estimates E from direct integration by 77% and for case 2 it under estimates E by 44% . This is thought to be due to disturbances at wave numbers other than α, β being present at peak E in the non-linear magnitude CFD simulation, since the non-linear term in the Navier-Stokes equations (see section 2.2.4) couples wavenumbers and is capable of transferring energy between them.

Case 1 LQG Output Feedback Non-Linear Simulation Figure 4.80 presents case 1 LQG transient energy versus time. As might be expected, the estimator performs poorly. Surprisingly the estimates it provides are sufficient for the LQR state feedback to stabilise the plant, and at a lower peak transient energy than on the linear plant (0.014), and only a slightly higher value than the LQR controller achieves on the non-linear plant (0.011). The wall transpiration velocities required in the non-linear simulation are comparable to those required in the linear one, as shown in figure 4.81 of the wall transpiration velocities at location $x = \pi$ for the same perturbation.

Case 2 LQG Output Feedback Non-Linear Simulation Figure 4.82 shows case 2 LQG transient energy versus time. The linear controller is unable to stabilize the non-linear plant model at this level of initial disturbance, even though the

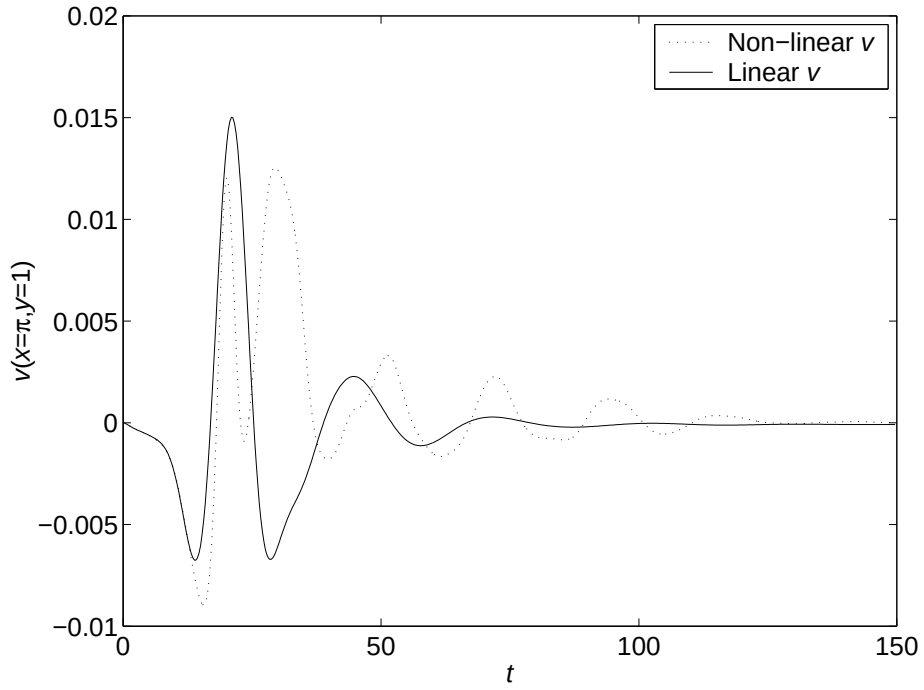

Figure 4.81: Case 1 LQG Wall Transpiration Velocity at $x = \pi$ vs Time t, from Initial Conditions $\mathcal{X}_{Worst}$ Scaled to Energy $10^4 E_{C1}$

initial energy of 0.000023 is much less than the energy of case 1 (0.00082), which is stabilised by its controller. Since the LQR controller is able to stabilise case 2 at this energy level, the deficiency appears to be in the estimator, and indeed its behaviour is poor, as its estimated energy overshoots the plant energy, and diverges erratically from time 720 onwards. Since an implicit method is employed, to circumvent stiffness problems, the estimator integration scheme is guaranteed to be stable, and thus integration instability is not the cause of this erratic behaviour. It is more likely that once the linear estimator overshoots the saturated non-linear plant, the control signals generated destabilise the plant.

Results from a smaller initial disturbance corresponding to an open-loop worst initial condition with $v_{max} = 7.5 \times 10^{-3} U_{cl}$, i.e. energy of $5625 E_{C2}$ are presented in figure 4.83. This energy is still approximately 50 times the transition threshold for streamwise vortices as determined by Reddy et al. (1998, p292). The linear controller is able to stabilize the non-linear plant model at this smaller level of initial disturbance, approximately half that of the level which could not be stabilised. This time the estimated energy overshoots but not sufficiently to destabilise the system. The transient energy is limited to 0.0075, as compared to the open-loop plant which reaches approximately 0.012 (not shown).

Flow-Field Results

The CFD flow-field results are scrutinised to determine the existence of oscillations in the contours, which may occur due to the use of a second order central differencing scheme for spatial terms and implicit Euler scheme for time marching

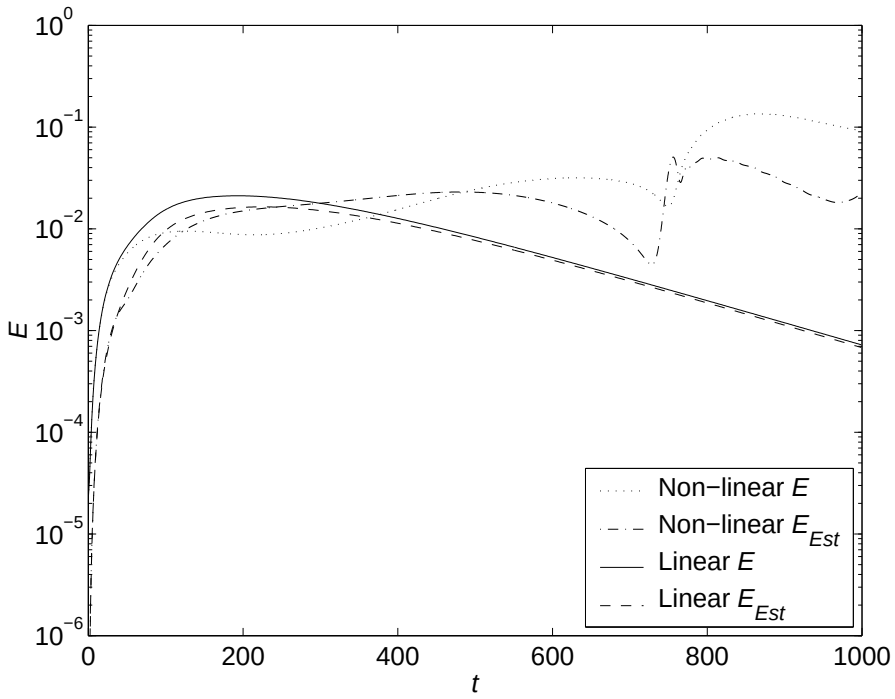

Figure 4.82: Case 2 LQG Transient Energy E vs Time t, from Initial Conditions $\mathcal{X}_{Worst}$ Scaled to Energy $10^4 E_{C2}$

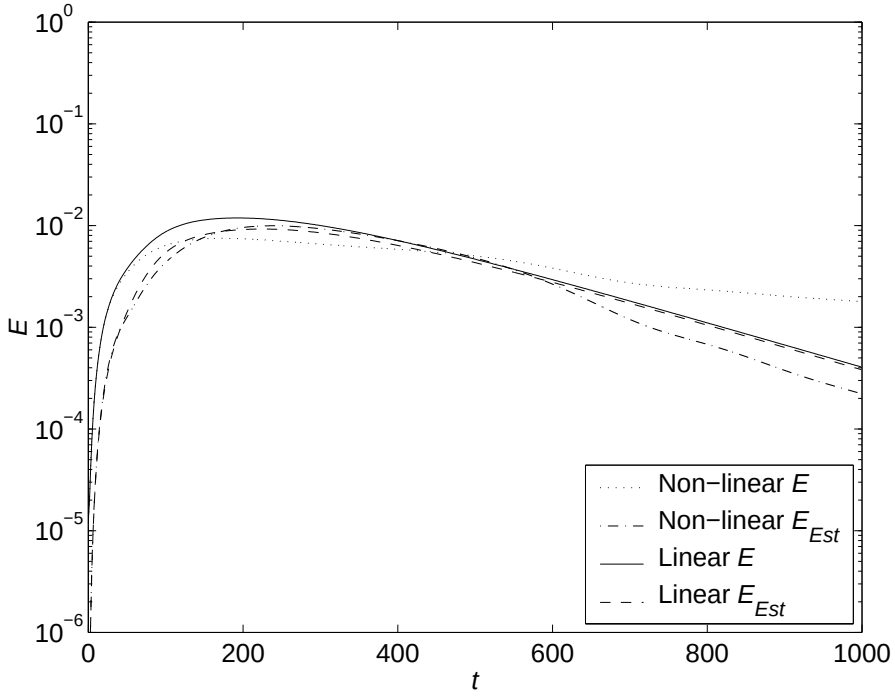

Figure 4.83: Case 2 LQG Transient Energy E vs Time t, from Initial Conditions $\mathcal{X}_{Worst}$ Scaled to Energy $5625 E_{C2}$

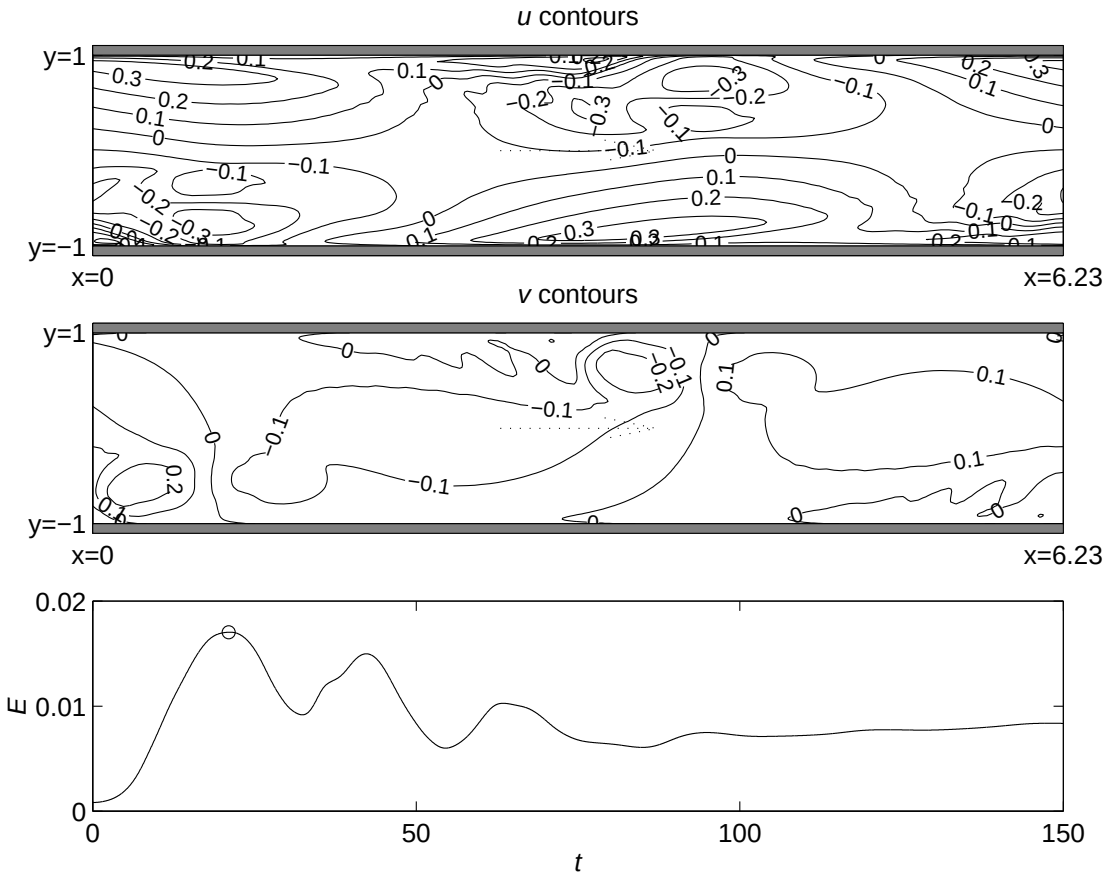

Figure 4.84: Case 1 Open-Loop Peak u and v Velocity Contours, from Initial Conditions $\mathcal{X}_{Worst}$ Scaled to Energy $10^4 E_{C1}$, at $t = 21$, Circled in E vs Time t

(Ferziger and Peric, 2002, p148).

Figure 4.84 displays the flow-field velocity contours near the peak transient energy of the non-linear simulation of initial energy $10^4 E_{C1}$ for case 1, open loop, on the mesh of figure 4.4. Spatial oscillations are apparent but only in the zero v velocity contour to any degree (e.g. near $x = 2.6, y = 0.8$). These are not thought to affect the accuracy of the simulation significantly. Figure 4.85 shows the same results with the mesh refined in the streamwise direction by a factor of 4, reducing the streamwise Peclet number by a factor of 4, making the oscillations much less apparent.

Figure 4.86 shows the final ($t = 150$) spanwise vorticity, $\partial v/\partial x - \partial u/\partial y$. Periodic ejections from alternate walls are seen, similar to those found by Jimenez (1990, p275) from random initial perturbations allowed to grow.

The flow-field velocity contours near the peak transient energy of the non-linear simulation of initial energy $10^4 E_{C1}$ for case 1, with the LQG controller, are presented in figure 4.87, which shows that no spatial oscillations are apparent. The peak transient energy is lower than for the open-loop case, and the LQR case is lower still.

Figure 4.88 shows the flow-field velocity contours near the peak transient energy of the non-linear simulation of initial energy $10^4 E_{C2}$ for case 2, open loop, on the

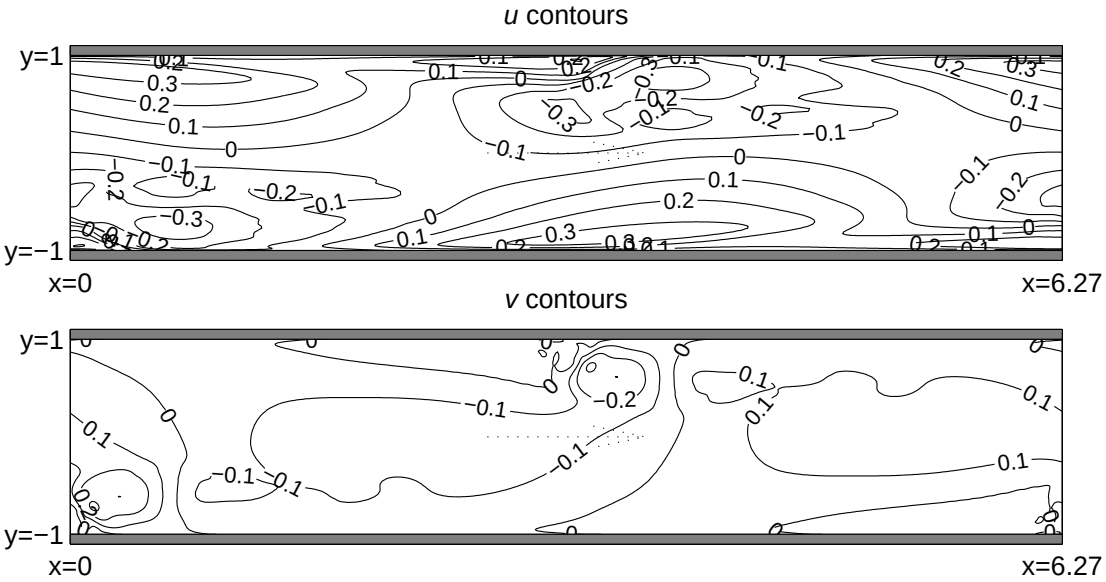

Figure 4.85: Case 1 Open-Loop Peak u and v Velocity Contours, from Initial Conditions $\mathcal{X}_{Worst}$ Scaled to Energy $10^4 E_{C1}$, at $t = 21$, Mesh Refined in Streamwise Direction

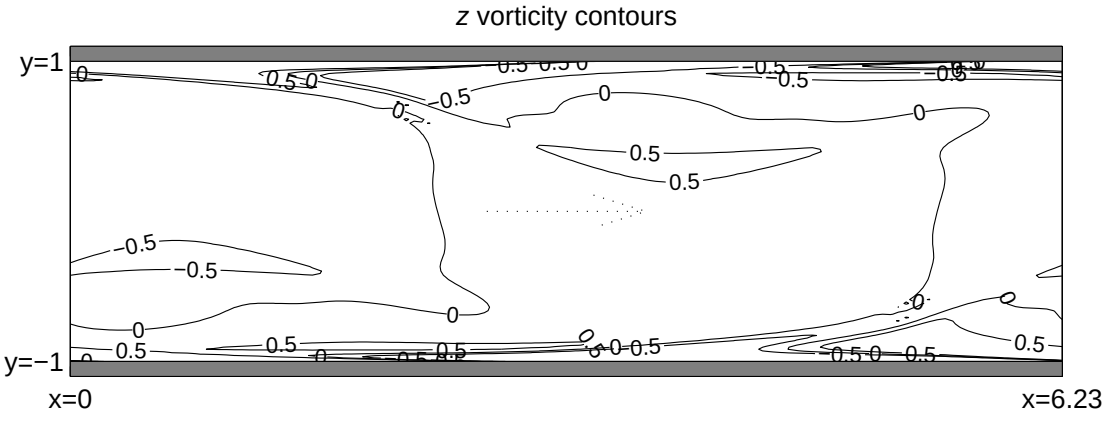

Figure 4.86: Case 1 Open-Loop Final Spanwise Vorticity Contours, from Initial Conditions $\mathcal{X}_{Worst}$ Scaled to Energy $10^4 E_{C1}$, at $t = 150$

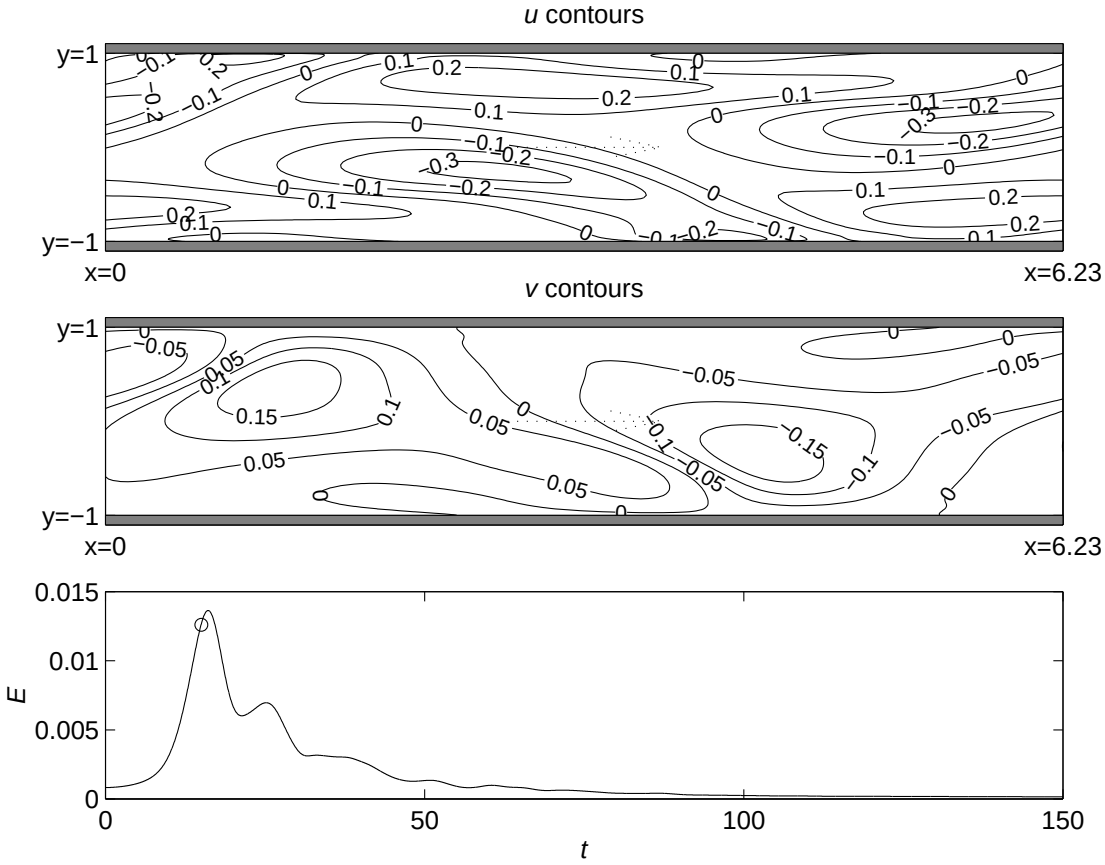

Figure 4.87: Case 1 LQG Near Peak u and v Velocity Contours, from Initial Conditions $\mathcal{X}_{Worst}$ Scaled to Energy $10^4 E_{C1}$, at $t = 15$, Circled in E vs Time t

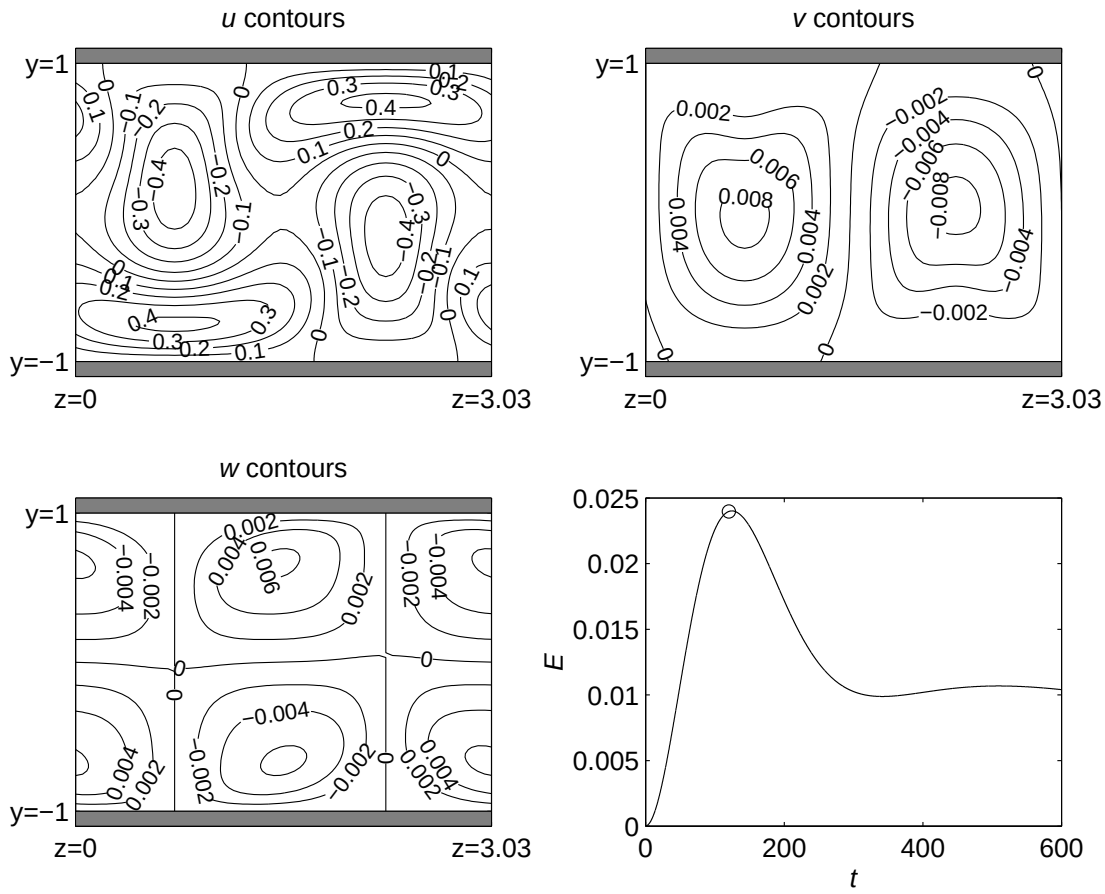

Figure 4.88: Case 2 Open-Loop Peak u, v, w Velocity Contours, from Initial Conditions $\mathcal{X}_{Worst}$ Scaled to Energy $10^4 E_{C2}$, at $t = 120$, Circled in E vs Time t

mesh of figure 4.5. No spatial oscillations are apparent.

The flow-field velocity contours near the peak transient energy of the non-linear simulation of initial energy $5625E_{C2}$ for case 2 with the LQG controller, are presented in figure 4.89. This magnitude of initial conditions was the largest able to be stabilised by the LQG controller. Again, no spatial oscillations are apparent. Sinusoidal transpiration at the walls can be clearly seen in the v flow-field.

Thus no successfully controlled non-linear simulation results exhibit spatial oscillations. The energy results from the case 1 open-loop simulations which do show spatial oscillations are not thought to be adversely affected.

4.4.8 Summary of Simulation Results

Tables 4.4 and 4.5 show a summary of the linear and non-linear simulation results. At the perturbation sizes used here, non-linear effects reduce the energy of large perturbation simulations below the level of scaled small perturbation results, with the exception of case 1 LQR state-feedback, where the levels are comparable, and the case 2 LQG unstable large perturbation simulation.

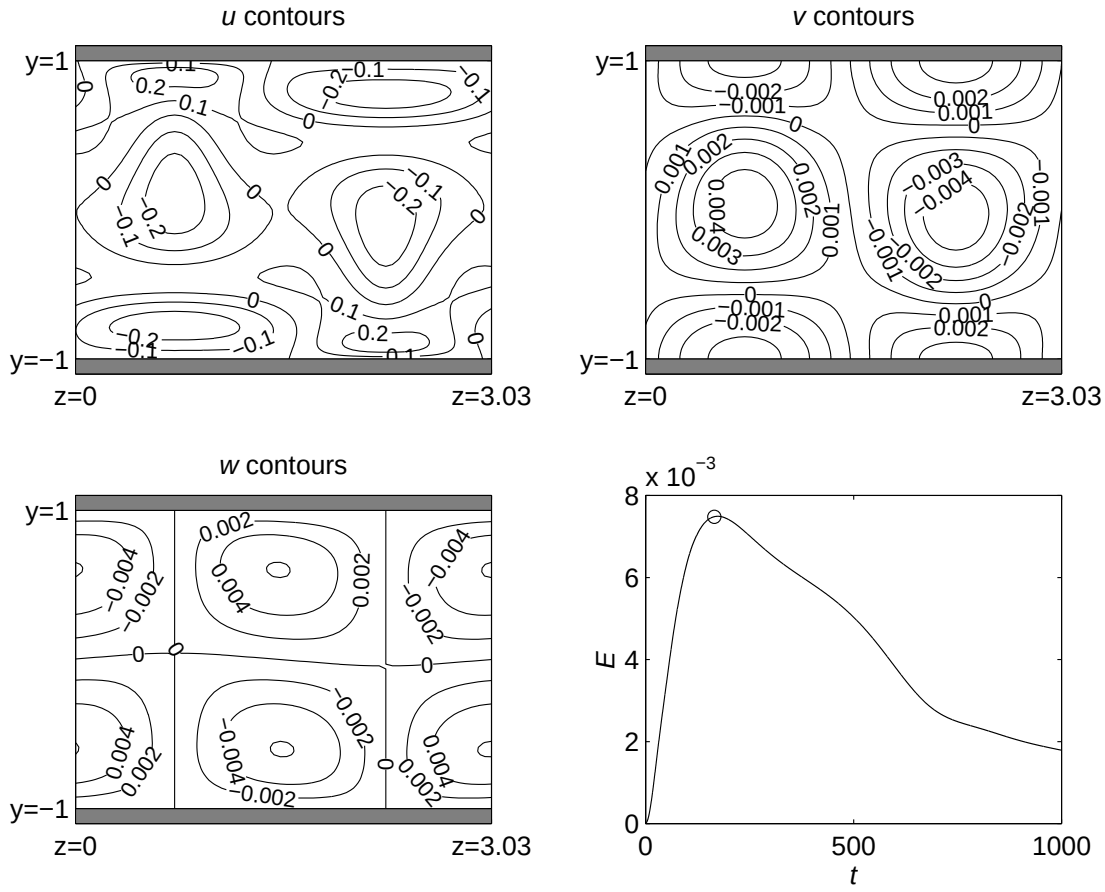

Figure 4.89: Case 2 LQG Peak u, v, w Velocity Contours, from Initial Conditions $\mathcal{X}_{Worst}$ Scaled to Energy $5625E_{C2}$, at $t = 165$, Circled in E vs Time t

Table 4.4: Case 1 Transient Energy E from Non-linear Simulations from Small and Large Initial Disturbances. (* indicates unstable.)

System	$\max_y \tilde{v}(t=0)$	$E(t=0)$	$\max_{t<150} E$	$\max_{t<150} E_{est}$
OL/	10^{-4}	E_{C1}	$7.16 \times 10^{-6}@t = 150^*$	$7.08 \times 10^{-6}@t = 150$
LQE	10^{-2}	$10^4 E_{C1}$	$1.70 \times 10^{-2}@t = 21.2$	$1.44 \times 10^{-3}@t = 17.6$
LQR		E_{C1}	$9.99 \times 10^{-7}@t = 18.3$	-
		$10^4 E_{C1}$	$1.10 \times 10^{-2}@t = 17.5$	-
LQG		E_{C1}	$2.45 \times 10^{-6}@t = 19.2$	$1.68 \times 10^{-8}@t = 21.0$
		$10^4 E_{C1}$	$1.36 \times 10^{-2}@t = 16.1$	$4.58 \times 10^{-4}@t = 18.4$

Table 4.5: Case 2 Transient Energy E from Non-linear Simulations from Small and Large Initial Disturbances (* indicates unstable.)

System	$\max_y \tilde{v}(t=0)$	$E(t=0)$	$\max_{t<600} E$	$\max_{t<600} E_{est}$
OL/	10^{-4}	E_{C2}	$1.10 \times 10^{-5}@t = 378.6$	$9.16 \times 10^{-6}@t = 383.2$
LQE	7.5×10^{-3}	$5625E_{C2}$	$1.20 \times 10^{-2}@t = 161.2$	$3.15 \times 10^{-2}@t = 204.9$
	10^{-2}	$10^4 E_{C2}$	$2.40 \times 10^{-2}@t = 124.5$	$4.77 \times 10^{-2}@t = 170.4$
LQR		E_{C2}	$1.90 \times 10^{-6}@t = 187.0$	-
		$10^4 E_{C2}$	$9.51 \times 10^{-3}@t = 89.7$	-
LQG		E_{C2}	$2.12 \times 10^{-6}@t = 196.3$	$1.79 \times 10^{-6}@t = 227.7$
		$5625E_{C2}$	$7.49 \times 10^{-3}@t = 173.8$	$9.96 \times 10^{-3}@t = 238.2$
		$10^4 E_{C2}$	$3.12 \times 10^{-2}@t = 600^*$	$2.30 \times 10^{-2}@t = 481.3$

4.4.9 Engineering Practicalities

It is appropriate to consider the practicalities of an engineering application of the controllers synthesized and simulated in this chapter, noting that the control of single wavenumbers of periodic disturbances is in itself a severe limitation in controller performance.

The peaks of closed-loop LQG disturbances, as shown in figures 4.80 and 4.83, are at non-dimensional times of approximately 20 and 200 units for test cases 1 and 2 respectively. With air as a working fluid, in a channel of half-height h equal to 0.01m, moving at the low speed of 15m/s as described in section 2.7, the peak times become 0.013s and 0.13s for cases 1 and 2 respectively, and for water as a working fluid moving at the low speed of 1m/s, they become 0.2s and 2s respectively. These time intervals need to be discretised into sufficiently small timesteps for the controller to act reliably (which may require a controller synthesized in discrete rather than continuous time, for example see Zhou et al. (1996, chapter 21)), and yet also enable sufficient computation time in each timestep for the measurement fast Fourier transform (2.47) and calculation of the actuation signal (see section 4.2), where the controllers described in this chapter are based on a discretisation of $N = 100$, and are of order approximately $2N$. The actuation signal must also be converted to its physical sinusoidal form (4.92) and distributed to the independent actuators by the beginning of the next timestep.

In a channel of half-height 0.01m, the wavelengths would be approximately 0.06m in the streamwise direction for test case 1, and approximately 0.03m in the spanwise direction for test case 2. These distances would need to contain both discrete sensors and actuators in sufficient quantities to accurately detect disturbances and control them, in two-dimensions to cover the general case, and hence the need for MEMs type devices. Significant progress has occurred in the development of MEMs wall shear sensors (Ho and Tai, 1998, p597-600), but the requirements placed on actuators by the controllers synthesised in this chapter are formidable. Their diaphragms or pistons must provide not only the velocities and quantities of transpiration fluid calculated in section 4.4.4 by means of sufficient power and capacity, but significantly more, since their orifices may only cover a

limited proportion of the channel walls, to leave room for measurement sensors and the material of the wall. For case 2, the controller synthesis model has assumed a particular phase for the disturbances in section 2.7, in order to halve the model dimensions, and this is unlikely to occur in practice. Use of a full model will require longer computation times for both controller synthesis and operation.

Thus physical implementation presents significant difficulties, even for low fluid centreline velocities as compared to typical engineering fluid velocities. It is more viable to consider an experimental research laboratory implementation, where the use of a larger channel half-height reduces velocities still further. For a channel half-height ten times as large i.e. $h = 0.1$m, for the same Reynolds numbers, time scales and length scales would increase tenfold, providing more time to discretise and compute control signals, and providing more room for sensors and actuators, which could thus be larger and easier to manufacture, although with larger inertia. Regarding the base flow, any channel would require careful design, and in the first instance operation below the critical Reynolds number (with controllers designed for such operation), so that the performance of the controllers on introduced disturbances, rather than spontaneous ones, could be investigated. An extra initial channel length of several half-heights and wavelengths would be necessary in order to fully develop channel flow and periodicity respectively. The appropriate degree of discretisation of measurement and actuation would also need to be determined and implemented, since too coarse a discretisation is likely to lead to interactions with other unmodelled wavenumbers and a deterioration in performance, and too fine increases complexity and difficulty of manufacture. It is unlikely that the worst initial conditions could be accurately set up, but these being the worst, others would suffice, although they would need to be at the correct periodicity. For research purposes, the actuators themselves could be used to introduce initial disturbances, which would then be of the appropriate periodicity, and of the phase expected in section 2.7 for test case 2.

4.5 Conclusions

Section 4.2 described the synthesis of optimal feedback controllers (LQR) and optimal estimators (LQE) for the state-space model derived in chapter 2. Curtis-Clenshaw quadrature for integration of the perturbation energy was introduced, as a method of generating LQR state variable weights. Tuned process noise weights for the optimal estimator synthesis were chosen to reflect the possible size variations in disturbances across the channel, as an alternative to uniform weights.

Section 4.3 described the linear and non-linear simulations undertaken on the open- and closed-loop systems. Following a restatement of the method for determining the 'worst' initial conditions which lead to the highest transient energy in linear systems, the modal and non-modal components of the transient energy were identified, the condition for its monotonic decay in the current system correctly identified, and an upper bound dependent on the initial conditions found.

For the non-linear simulations, the boundary conditions required to simulate the chosen test cases as two dimensional models were introduced, and the modifi-

cations to the CFD code required to accurately simulate small perturbations were derived. The implementation of the controller and estimator into the CFD code was also described.

Section 4.4 presented and discussed the results obtained during the synthesis of controllers and estimators, and during the linear simulations. An ARE solver based on the Hamiltonian matrix produced the lowest relative residuals for controller and estimator synthesis, except for case 2 estimator where a solver based on the eigenstructure approach proved the best in this respect. Convergence of the LQR controlled system diachronic transient energy bound with discretisation N proved fast, by $N = 30$, but for the LQE estimator, convergence required $N = 70$, implying that convergence of the combined closed-loop LQG estimator and controller system would also require $N = 70$. Although there exist procedures for reducing the order of controllers, the results are no longer optimal, as noted by Anderson and Liu (1989, p803), and the effect on non-normal transient energy growth is unclear.

The tuned estimator provided the faster estimator poles, and proved better at following the plant worst case initial conditions from zero initial estimates, than the uniform estimator. The uniform estimator provided a lower diachronic error energy bound, but even this appears unrealistically high. Consequently, further simulations were primarily based on the tuned estimator provided with zero initial estimates. The determination of the plant diachronic transient energy bound lay within bounds provided by the Frobenius norm, and for the open-loop case 2, agreed closely with published data. Careful scrutiny showed that the plant worst initial conditions suffered from non-physical oscillations at the wall, which were easily cured by filtering by the 2/3 rule. Such oscillations cause no problem for the linear (spectral) simulations, but were detrimental to the low-order wall shear stress calculations in the non-linear (finite volume) simulations. The filtering had a very small effect on the energy content, and on the velocity profiles, other than at the wall.

The plant worst initial conditions for case 2, open loop, were investigated regarding their potential for generating non-modal growth. Consecutive mode pairs were found to be highly non-normal, but only mode pair $4, 5$ was found to have any great potential for non-modal growth, as measured by the upper bound developed earlier. The closed-loop (LQR) mode pairs were not found to be significantly less non-normal, although the potential for non-modal growth was reduced, and more mode pairs were involved.

The linear simulations from the worst plant initial conditions were able to accurately reproduce the diachronic transient energy bound predicted. A discretisation of $N = 30$ was adequate, except where an estimator was involved, when $N = 50$ was required. For case 2 open loop, mode pair $4, 5$ indeed provided most of the transient energy growth. The tuned estimator was able to follow the open-loop non-normal growth better than the uniform one in both test cases 1 and 2. Closed loop, the case 2 estimator performed better than the case 1, which provided poor estimates in the output feedback controller, but this was able to stabilise the flow nonetheless.

Although the sinusoidal transpiration was guaranteed to have a zero net flux

over whole streamwise or spanwise periods, and thus also over any time interval, its magnitude was such that at any particular point the transpiration of comparatively large quantities of fluid were required. For an initial perturbation energy of 1% of base flow in linearised case 1 under LQR state feedback control, the velocity of fluid transpired would peak at 0.15 times the base flow centreline velocity, and the quantity of fluid transpired locally would peak at approximately 0.30 times the channel half-height, albeit on a temporary basis. For case 2 the velocity of fluid transpired would peak at 0.090 times the base flow centreline velocity, and the quantity of fluid transpired locally would peak at approximately 26.6 times the channel half-height. Furthermore, for case 2, this quantity of fluid is transpired permanently, i.e. any reservoirs would not return to their initial levels.

This volume of fluid would require a large associated reservoir or redistribution system within each spatial period. Controller implementation schemes mooted, for example as described by Ho and Tai (1998), envisage the use of microelectrical machines (MEMs) based on small reservoirs, but these schemes would appear unable to provide the quantities of fluid required for optimal control of the test cases based on early transition considered here.

The modelling (chapter 2) and linear results were scrutinised prior to the non-linear simulations, in order to determine the appropriate level of discretisation for the controller and estimator. The overriding requirement appeared to be the need for accurate modelling of the wall gradients in the estimator plant model, and thus $N = 100$ was selected for all configurations. LQR state feedback required less, but was given the same value for overall consistency.

The magnitude of linear sized perturbations was determined from case 1 open-loop spectral results at $v_{max} = 10^{-4}U_{cl}$, by estimating the size of the non-linear terms omitted. The transpiration flow-field was also determined from the integrator modes of the linear results. The modified non-linear code was able to accurately reproduce the transpiration flow-field for linear sized levels of transpiration, thus proving that the transpiration boundary conditions were correctly implemented.

Non-linear simulations on linear sized perturbations faithfully reproduced the linear simulation results, with the exception of small discrepancies in the open-loop estimation for case 2, caused by the use of implicit estimator integration to avoid problems with stiffness. The overall agreement between the linear spectral results and the independent finite volume results at low levels of disturbance provides good evidence that both are correct under these conditions.

A mesh and time step sensitivity study was performed before proceeding to full non-linear simulations. The open-loop results for cases 1 and 2 from non-linear sized perturbations ($v_{max} = 10^{-2}U_{cl}$) were shown to be both mesh and time step independent, although case 1 proved more difficult, requiring a 2nd order implicit scheme in time. Flow-field plots showed the presence of spatial oscillations in the velocity contours for case 1 open-loop, as might be expected at such high Peclet numbers. These were merely in the zero contour and were not regarded as a source significant error, especially since the closed-loop behaviour is of more interest in this thesis. The closed-loop simulations reached lower energy levels and did not show oscillations, nor did any case 2 simulations.

Non-linear simulations of the open-loop plant from large (non-linear sized,

$v_{max} = 10^{-2}U_{cl}$) worst initial perturbations showed that the flow saturates in case 1, but is nonetheless unstable, albeit on a long timescale. Case 2 also saturates, but appears stable. Although both simulations soon deviate from the linear results, initially they both grow at the non-normal rate of the linear simulations. On the open-loop plant, the case 1 estimator effectively diverges, but the case 2 estimator behaves well.

Non-linear simulations of the plant with LQR state feedback from large worst initial perturbations again saturate but remain stable. The state feedback reduces the peak transient energy below open-loop values. Thus the linear and non-linear results are closer than the open-loop results. The transient energy as calculated from the state variables is well below that of the non-linear flow-field for both test cases, and the discrepancy is believed to be due to non-linear terms transferring energy to other wavenumbers, which the linear controller has no knowledge of. By integration, the magnitude of the harmonic transpiration fluid quantity required for case 2 from large initial perturbations was found to be 2.07, as compared to 2.45 by extrapolation of the linear simulation results to the energy level used, which is consistent with saturation and diversion of energy to other wavenumbers leading to lower control actuation.

In non-linear simulations of the output feedback LQG system, from large worst initial perturbations, the case 1 estimator barely registers any energy, but its estimates are sufficient for the controller to stabilise the non-linear plant. For case 2, the LQG controller is unable to stabilise the non-linear plant at this level of initial perturbation. The estimator initially behaves well, but overshoots and diverges, leading the controller to destabilise the plant. This result is surprising, since the initial energy of case 2 is significantly less than that of case 1. A possible explanation is that the poor estimation in case 1 LQG simulations at linear perturbation levels leads to no overshoot at larger levels despite saturation occurring, but the good estimation in case 2 at linear perturbation levels leads to an overshoot at larger levels. From an initial perturbation of half this energy level, the estimator energy again overshoots the plant energy, but it does not diverge, and the controlled plant keeps the transient energy well below the open-loop value.

This study has not investigated the effects of uncertainty such as modelling errors, plant disturbances and measurement noise, on closed-loop performance. Although LQG control contains a specific model for disturbances and noise, this model does not adequately address their uncertainty, for example see Zhou et al. (1996, p214). Further study would require investigation of controller robustness to modelling uncertainty as performed by Bewley and Liu (1998) and Baramov et al. (2004).

To summarise, this chapter has described the synthesis and simulation of optimal controllers and estimators for the spectral state-space model of linearised plane Poiseuille flow developed in chapter 2, which uses the bases investigated in chapter 3 to impose the boundary conditions. The optimal controllers were synthesized using a correct formulation of the energy matrix for state variable weights, and the estimators were synthesized using novel process noise weights which resulted in better estimation of non-modal growth than estimation using uniform weights. Significantly higher levels of discretisation were required for con-

vergence of the estimator synthesis in terms of transient energy growth than for convergence of the controller, a confirmation of results found in chapter 2 for the convergence of the model dynamical properties. Linear simulations from the worst initial conditions confirmed the synthesis results of stabilisation and reduced transient energy growth, and also showed that significant velocities and local volumes of transpiration fluid were required for both test cases, indicating the need for further investigations into actuation. Thus chapter 5 investigates tangential transpiration, and chapter 6 describes the synthesis and simulation of controllers with limited control effort.

An independently derived finite-volume Navier-Stokes solver was employed for open- and close-loop non-linear simulations of the controllers and estimators. The magnitude of linear-sized initial worst perturbations was determined by examining the size of the non-linear terms in the Navier-Stokes equations. Once the non-linear solver was modified to compute just the flow perturbation, it was able to accurately reproduce the steady-state transpiration flow field for small transpiration, as determined in chapter 2, and when supplied with small initial conditions, it accurately reproduced the results of the linear simulations of the open and closed-loop systems, and thus validated the results independently. Careful mesh and timestep sensitivity studies were performed to ensure that the non-linear solver produced accurate results from larger initial worst perturbations which would generate significant non-linearity. Non-linear simulations from these larger initial conditions showed initial growth at the non-normal rate from linear simulations, and thus the relevance of linear control, but the flow soon saturated. The state feedback controllers were able to maintain stability and reduced transient energy growth, thus providing loci in the basin of attraction of the full closed loop system. The state estimators sometimes over-estimated the saturated flow, which could lead to destabilisation of the flow when controlled by output feedback. The non-linear flow energy density was greater than that indicated by the state feedback controller state variables, indicating the probable diversion of energy to harmonics of the wavenumbers considered, and motivating further work to control the harmonics.

Chapter 5

Tangential Actuation

5.1 Introduction

This chapter shows how the existing controller synthesis model, described in chapter 2, can be modified to include independent tangential actuation in addition to wall-normal actuation, thus providing extra control degrees of freedom. Simultaneous tangential and wall-normal actuation may be interpreted as directable or vectored transpiration. Few results exist regarding the application of LQR state feedback via tangential or vectored actuation to plane Poiseuille flow. Balogh et al. (1999, 2000, 2001) prove global Lyapunov stabilisation with tangential actuation for very low Reynolds number flow (R <1/8). Jovanovic and Bamieh (2005) indicate that wall-normal and spanwise body forces have a stronger influence on velocity than do streamwise body forces. For the test cases considered in this thesis, the Reynolds number is much higher (5000-10000), and linear stabilisation via wall boundary conditions is investigated. Tangential actuation may be achieved by wall mounted jets or rollers (Balogh et al., 2001). Although rollers, like jets, have constraints on acceleration and velocity due to inertia and friction, they have no constraint on cumulative displacement, unlike jets which must draw fluid from a source.

Section 5.2 describes the additional basis functions and control inputs required for simultaneous wall-normal and tangential actuation. Section 5.3 presents changes to the model dynamics arising from tangential actuation, and the results of controller synthesis. Subsequently, the worst initial conditions which generate the diachronic transient energy bound with tangential actuation are computed, and the results of linear simulations are described. Section 5.4 shows the results of non-linear simulations on small and large worst initial conditions under LQR control via tangential actuation. Finally section 5.5 draws conclusions about tangential actuation as compared to wall-normal actuation.

5.2 Modifications to the State-Space Model

5.2.1 The Velocity and Vorticity Representation

The state-space model developed in chapter 2 represents wall-normal velocity and wall-normal vorticity as (2.87,2.88), repeated here

$$\begin{aligned}\tilde{v}(y,t) &= \sum_{0}^{N} \Gamma_n^{DN}(y) a_{v,n}(t) + f_u(y)\tilde{q}_u(t) + f_l(y)\tilde{q}_l(t) \\ \tilde{\eta}(y,t) &= \sum_{0}^{N} \Gamma_n^{D}(y) a_{\eta,n}(t)\end{aligned} \tag{5.1}$$

where Γ^D are homogeneous combinations of Chebyshev polynomials, and Γ^{DN} are homogeneous combinations of Chebyshev polynomials with zero wall derivative, as described in section 2.5. $f_u(y)$ is a function which is unit at the upper wall and zero at the lower wall respectively, and with zero derivatives at both walls, and similarly but reversed for $f_l(y)$. Thus the velocity-vorticity formulation boundary conditions for wall transpiration with no-slip, i.e. zero tangential velocity (2.76,2.28)

$$\begin{aligned}\tilde{v}(y=1,t) &= \tilde{q}_u(t) \\ \tilde{v}(y=-1,t) &= \tilde{q}_l(t) \\ \tilde{v}'(y=1,t) &= 0 \\ \tilde{v}'(y=-1,t) &= 0 \\ \tilde{\eta}(y=1,t) &= 0 \\ \tilde{\eta}(y=-1,t) &= 0\end{aligned} \tag{5.2}$$

are fulfilled. $\tilde{q}_u(t)$ and $\tilde{q}_l(t)$ are the time integrals of the control inputs at the upper and lower walls respectively, on the wall-normal velocity $\tilde{v}$, as described in section 2.6.1.

5.2.2 Simultaneous Wall-Normal and Tangential Wall Velocity Boundary Conditions

Non-zero tangential wall velocity boundary conditions, $\tilde{u} \neq 0, \tilde{w} \neq 0$, lead to modified velocity-vorticity boundary conditions, as a result of the continuity equation and Fourier assumptions.

Boundary Conditions on Velocity Components $\tilde{u}, \tilde{v}, \tilde{w}$

If the normal ($\tilde{v}$) and tangential ($\tilde{u}, \tilde{w}$) fluid velocities at the wall are each independently set by the controller, the boundary conditions in terms of velocity

components become

$$\begin{aligned}
\tilde{u}(y=1,t) &= \tilde{p}_u(t) \\
\tilde{u}(y=-1,t) &= \tilde{p}_l(t) \\
\tilde{v}(y=1,t) &= \tilde{q}_u(t) \\
\tilde{v}(y=-1,t) &= \tilde{q}_l(t) \\
\tilde{w}(y=1,t) &= \tilde{r}_u(t) \\
\tilde{w}(y=-1,t) &= \tilde{r}_l(t)
\end{aligned} \tag{5.3}$$

where $\tilde{p}_u$ to $\tilde{r}_l$ are the Fourier coefficients of the velocities at the walls, at wavenumber pair α, β. Physically $u(y=1,t) = \Re(\tilde{p}_u e^{\jmath(\alpha x+\beta z)})$ by analogy with (2.32), i.e. the distribution of the u velocity is sinusoidal, and similarly for the other wall and other velocity components. These boundary conditions must be recast in terms of the wall-normal velocity and vorticity.

Relationships between Velocity Components and Vorticity

From section 2.4.2, equations (2.42), (2.44) and (2.45) state

$$\jmath\alpha\tilde{u} + \frac{\partial\tilde{v}}{\partial y} + \jmath\beta\tilde{w} = 0 \tag{5.4}$$

$$\tilde{\eta}(y,t) = \jmath\beta\tilde{u} - \jmath\alpha\tilde{w} \tag{5.5}$$

$$\begin{aligned}
\tilde{u} &= \frac{\jmath}{\alpha^2+\beta^2}\left(\alpha\frac{\partial\tilde{v}}{\partial y} - \beta\tilde{\eta}\right) \\
\tilde{w} &= \frac{\jmath}{\alpha^2+\beta^2}\left(\beta\frac{\partial\tilde{v}}{\partial y} + \alpha\tilde{\eta}\right)
\end{aligned} \tag{5.6}$$

5.2.3 Case 1

For case 1 only velocity components u and v exist, and only the equations in $\tilde{v}$ are modelled. Furthermore $\beta = 0$, so (5.4) becomes

$$\frac{\partial\tilde{v}}{\partial y} = -\jmath\alpha\tilde{u} \tag{5.7}$$

and the boundary conditions (5.3) become

$$\begin{aligned}
\tilde{u}(y=1,t) &= \tilde{p}_u(t) \\
\tilde{u}(y=-1,t) &= \tilde{p}_l(t) \\
\tilde{v}(y=1,t) &= \tilde{q}_u(t) \\
\tilde{v}(y=-1,t) &= \tilde{q}_l(t)
\end{aligned} \tag{5.8}$$

Substituting $\tilde{u}$ from (5.7) in these boundary conditions gives

$$\begin{aligned}
\tilde{v}'(y=1,t) &= -\jmath\alpha\tilde{p}_u(t) \\
\tilde{v}'(y=-1,t) &= -\jmath\alpha\tilde{p}_l(t) \\
\tilde{v}(y=1,t) &= \tilde{q}_u(t) \\
\tilde{v}(y=-1,t) &= \tilde{q}_l(t)
\end{aligned} \tag{5.9}$$

in the velocity-vorticity formulation. Thus the boundary conditions on $\tilde{u}$ are replaced by boundary conditions on the gradient of $\tilde{v}$. Thus in the code $\tilde{v}$ can be represented by

$$\begin{aligned}\tilde{v}(y,t) &= \sum_{0}^{N} \Gamma_n^{DN}(y) a_{v,n}(t) + f_u(y) q_u(t) + f_l(y) q_l(t) \\ &\quad + g_u(y) q_u^u(t) + g_l(y) q_l^u(t) \end{aligned} \tag{5.10}$$

where g_u is a function which is homogeneous at both walls, but has unit derivative at the upper wall, and zero derivative at the lower wall, and vice versa for g_l, and

$$\begin{aligned} q_u^u(t) &= -\jmath\alpha\tilde{p}_u(t) \\ q_l^u(t) &= -\jmath\alpha\tilde{p}_l(t) \end{aligned} \tag{5.11}$$

so in (5.8)

$$\begin{aligned} \tilde{u}(y=1,t) &= \jmath q_u^u(t)/\alpha \\ \tilde{u}(y=-1,t) &= \jmath q_l^u(t)/\alpha \end{aligned} \tag{5.12}$$

Control inputs q_u and q_l on v are joined by q_u^u and q_l^u on u. To implement the extra control inputs, functions f_u and f_l are joined by g_u and g_l in (2.91), which ultimately form the input matrix $\mathcal{B}$.

5.2.4 Case 2

For case 2, velocity components u, v and w exist, and both equations in $\tilde{v}$ and $\tilde{\eta}$ are modelled. Furthermore $\alpha = 0, \beta \neq 0$, so (5.5) and (5.4) become

$$\tilde{\eta}(y,t) = \jmath\beta\tilde{u} \tag{5.13}$$

$$\frac{\partial\tilde{v}}{\partial y} = -\jmath\beta\tilde{w} \tag{5.14}$$

and the boundary conditions remain as in (5.3)

$$\begin{aligned} \tilde{u}(y=1,t) &= \tilde{p}_u(t) \\ \tilde{u}(y=-1,t) &= \tilde{p}_l(t) \\ \tilde{v}(y=1,t) &= \tilde{q}_u(t) \\ \tilde{v}(y=-1,t) &= \tilde{q}_l(t) \\ \tilde{w}(y=1,t) &= \tilde{r}_u(t) \\ \tilde{w}(y=-1,t) &= \tilde{r}_l(t) \end{aligned} \tag{5.15}$$

Substituting $\tilde{u}$ and $\tilde{w}$ from (5.13,5.14,) in these boundary conditions gives

$$\begin{aligned} \tilde{\eta}(y=1,t) &= \jmath\beta\tilde{p}_u(t) \\ \tilde{\eta}(y=-1,t) &= \jmath\beta\tilde{p}_l(t) \\ \tilde{v}(y=1,t) &= \tilde{q}_u(t) \\ \tilde{v}(y=-1,t) &= \tilde{q}_l(t) \\ \tilde{v}'(y=1,t) &= -\jmath\beta\tilde{r}_u(t) \\ \tilde{v}'(y=-1,t) &= -\jmath\beta\tilde{r}_l(t) \end{aligned} \tag{5.16}$$

in the velocity-vorticity formulation. Thus in the code $\tilde{v}$ and $\tilde{\eta}$ can be represented by

$$\tilde{v}(y,t) = \sum_0^N \Gamma_n^{DN}(y)a_{v,n}(t) + f_u(y)q_u(t) + f_l(y)q_l(t) + g_u(y)q_u^w(t) + g_l(y)q_l^w \tag{5.17}$$

$$\tilde{\eta}(y,t) = \sum_0^N \Gamma_n^{D}a_{\eta,n} + f_u(y)q_u^u(t) + f_l(y)q_l^u(t) \tag{5.18}$$

where g_u and g_l are as previously in section 5.2.3 and

$$\begin{aligned} q_u^u(t) &= \jmath\beta\tilde{p}_u(t) \\ q_l^u(t) &= \jmath\beta\tilde{p}_l(t) \\ q_u^w(t) &= -\jmath\beta\tilde{r}_u(t) \\ q_l^w(t) &= -\jmath\beta\tilde{r}_l(t) \end{aligned} \tag{5.19}$$

so in (5.15)

$$\begin{aligned} \tilde{u}(y=1,t) &= -\jmath q_u^u(t)/\beta \\ \tilde{u}(y=-1,t) &= -\jmath q_l^u(t)/\beta \\ \tilde{v}(y=1,t) &= \tilde{q}_u(t) \\ \tilde{v}(y=-1,t) &= \tilde{q}_l(t) \\ \tilde{w}(y=1,t) &= \jmath q_u^w(t)/\beta \\ \tilde{w}(y=-1,t) &= \jmath q_l^w(t)/\beta \end{aligned} \tag{5.20}$$

Control inputs q_u and q_l on v are joined by q_u^u and q_l^u on u and q_u^w and q_l^w on w.

Although the modifications to the representations of v and η appear straightforward, the practical problems of enforcing 3 velocity boundary conditions at the walls would be formidable. Also, control on the vorticity equations requires substantial changes to the spectral model. Accordingly actuation on u for case 2 is no longer considered, leaving just actuation by v and w

$$\tilde{v}(y,t) = \sum_0^N \Gamma_n^{DN}(y)a_{v,n}(t) + f_u(y)q_u(t) + f_l(y)q_l(t) + g_u(y)q_u^w(t) + g_l(y)q_l^w \tag{5.21}$$

$$\tilde{\eta}(y,t) = \sum_0^N \Gamma_n^{D}(y)a_{\eta,n}(t) \tag{5.22}$$

5.2.5 The Functions g_u and g_l

As g_u is a function which is homogeneous at both walls, but has unit derivative at the upper wall, and zero derivative at the lower wall, and vice versa for g_l, the

Case		v-actuation	u-actuation	w-actuation
1	f_u	$(-y^3+3y+2)/4$	0	
	f_l	$-f_u(-y)$	0	
	g_u	0	$(y^3+y^2-y-1)/4$	
	g_l	0	$-g_u(-y)$	
2	f_u	$(-y^3+3y+2)/4$		0
	f_l	$-f_u(-y)$		0
	g_u	0		$(y^3+y^2-y-1)/4$
	g_l	0		$-g_u(-y)$

Table 5.1: Comparison of v- and u/w-Actuation Basis Functions

function g_u must satisfy

$$\begin{aligned} g_u(y=1) &= 0 \\ g_u(y=-1) &= 0 \\ g_u'(y=1) &= 1 \\ g_u'(y=-1) &= 0 \end{aligned} \tag{5.23}$$

and g_l must satisfy

$$\begin{aligned} g_l(y=1) &= 0 \\ g_l(y=-1) &= 0 \\ g_l'(y=1) &= 0 \\ g_l'(y=-1) &= 1 \end{aligned} \tag{5.24}$$

Suitable functions for g_u and g_l are

$$\begin{aligned} g_u(y) &= \frac{y^3+y^2-y-1}{4} \\ g_l(y) &= -g_u(-y) \end{aligned} \tag{5.25}$$

5.2.6 Comparison of v and u, w Actuation

Henceforth v-actuation will be compared with u-actuation for case 1 and w-actuation for case 2, as this simplification allows a direct comparison with earlier v-actuation results. Table 5.1 shows a summary of the actuation basis functions used. For v-actuation, function f_u provides a unit $\tilde{v}$ value with zero derivative at the upper wall, whereas for u, w actuation function g_u provides zero value but unit derivative at the upper wall. Functions f_l and g_l are mirror images of f_u and g_u about the centreline and thus provide unit value and derivative at the lower wall, respectively.

Figure 5.1 shows the basis functions associated with the state variables for case 1 with u-actuation. As compared to figure 2.2 of the basis function for v-actuation, those $\tilde{v}$ basis functions associated with actuation, g_u and g_l, have Dirichlet boundary conditions, with unit gradient at the upper and lower walls respectively, as compared to f_u and f_l in figure 2.2 which have Neumann boundary conditions and unit magnitude at the upper and lower walls respectively.

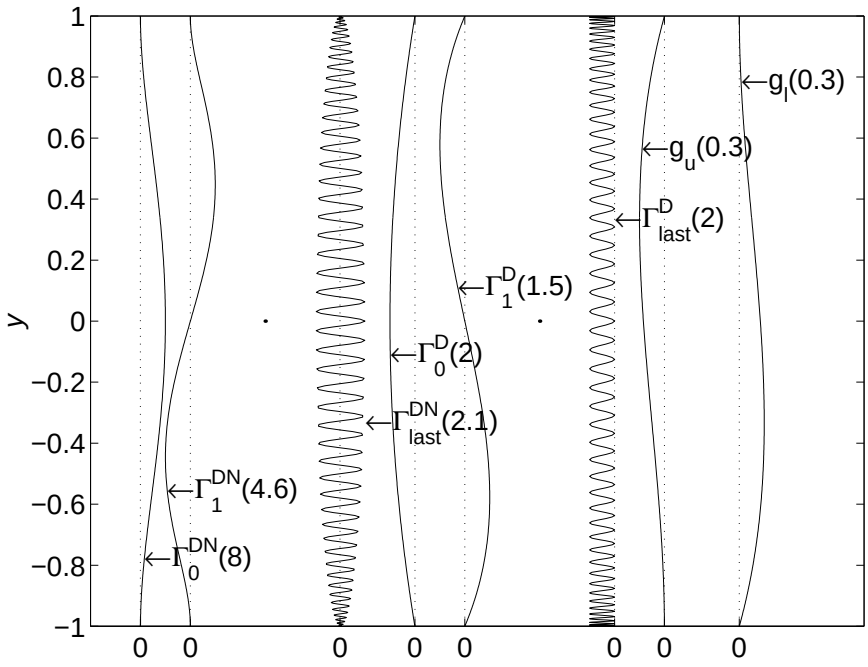

Figure 5.1: The u-Actuation Control Basis Functions Associated with the State Variables (Peak magnitudes over system for $N = 100$ in parenthesis)

5.3 Results from Linear Simulations and Discussion

This section investigates the model dynamics, and the synthesis of controllers, when tangential actuation is employed. Subsequently results from the calculation of the worst initial conditions and from linear simulations are presented. Tangential actuation is by u velocity for case 1 and w velocity for case 2, drawing comparisons with previous results for v-actuation from sections 2.8.2 and 4.4.

5.3.1 u- and w-Actuation Model Dynamics

Figure 5.2 shows the controllability of case 1 by u- and v-actuation. It can be seen that u-actuation has lower controllability than actuation by v, initially by more than an order of magnitude, but less so with increasing mode number. Lower controllability is consistent with basis functions g_u and g_l being less 'full' than f_u and f_l, in the sense that they have a lower peak value (0.3 cf. 1) and both have little effect close to both walls, whereas f_u and f_l each have a large effect at one wall or other. The controllability of case 2 by w- and v-actuation is shown in figure 5.3. It can be seen that w-actuation has lower controllability than actuation by v for modes that have a velocity component (1,2,4,6,8,...), which is again consistent with g_u and g_l being less 'full' than f_u and f_l.

The convergence of u- and w-actuation singular values with discretisation N is very similar to that for v-actuation, shown in figures 2.4 and 2.6, and similar conservative logic to that applied in section 2.8.1 would dictate the use of $N = 100$

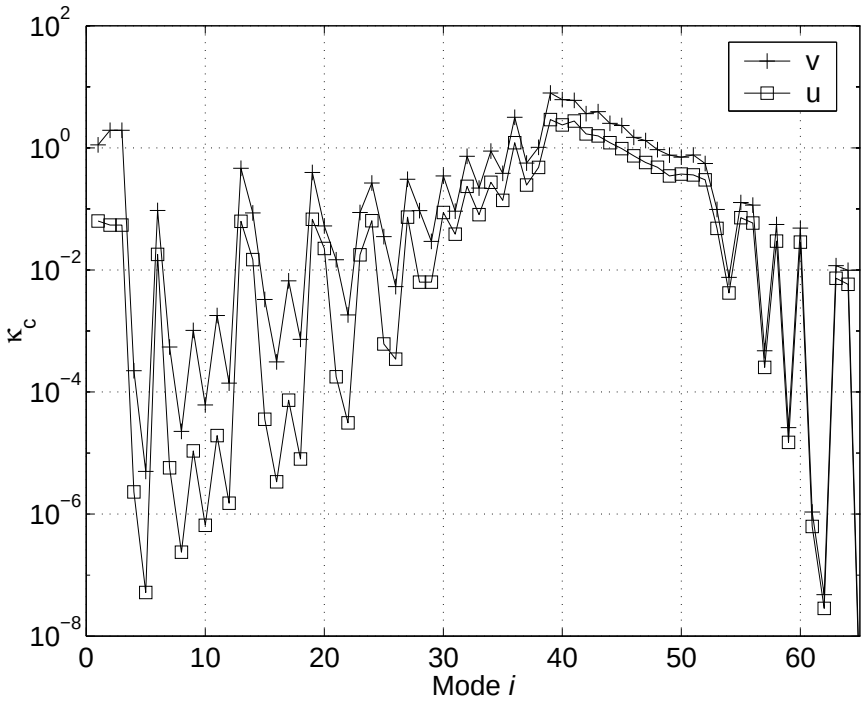

Figure 5.2: Case 1 u- and v-Actuation Controllability, $N = 100$

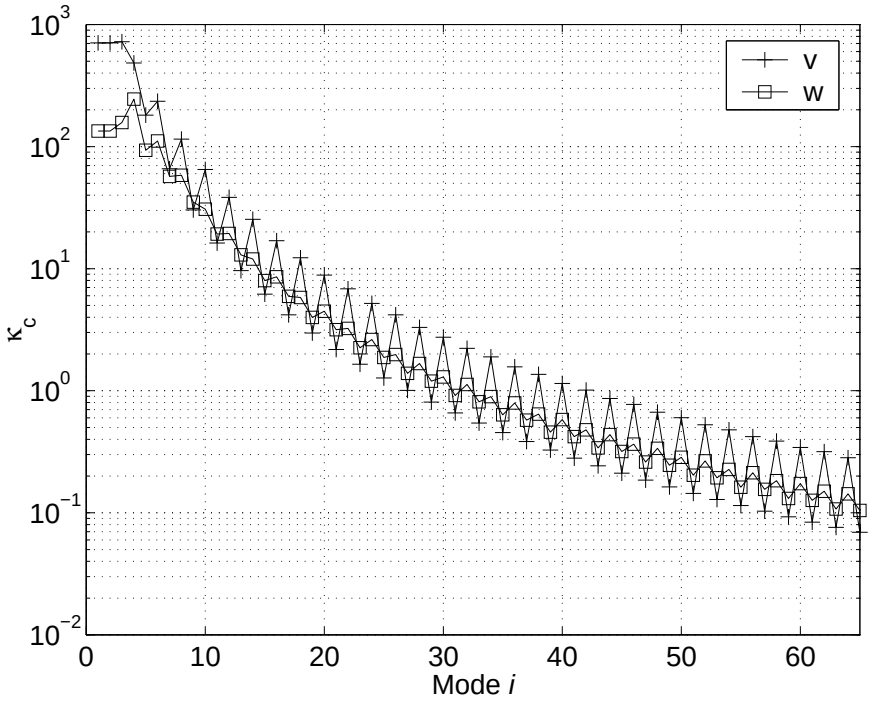

Figure 5.3: Case 2 w- and v-Actuation Controllability, $N = 100$

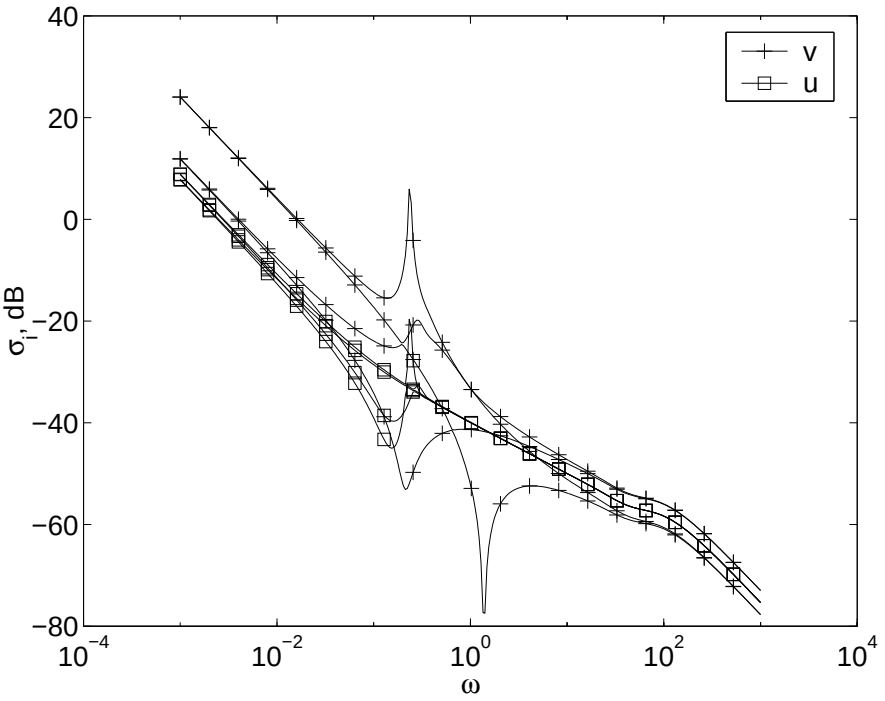

Figure 5.4: Case 1 u- and v-Actuation Open-Loop Singular Values vs Frequency, $N = 100$

for model accuracy above the closed-loop bandwidth.

Figure 5.4 shows a plot of the singular values of the case 1 system with u- and v-actuation. u-actuation results in a system with closer maximum and minimum singular values, i.e. the system is less sensitive to input direction. This is consistent with g_u and g_l being more symmetric about the centreline $y = 0$ than f_u and f_l. The singular values of the case 2 system with w- and v-actuation are presented in figure 5.5. Both w- and v-actuation are insensitive to direction, probably because the vorticity dominates the eigenvectors, and neither actuation acts directly upon it. w-actuation results in lower singular values, which is again consistent with g_u and g_l being less 'full' than f_u and f_l.

5.3.2 u- and w-Actuation Controller Synthesis

Figure 5.6 shows the relative residuals from the solution of the LQR algebraic Riccati equation (4.3) for a case 1 controller with u- and v-actuation. A larger range of weights r is shown than previously for v-actuation in figure 4.8. The u-actuation residuals are comparable with that for v-actuation for all but the largest control weights r and are acceptable. The relative residuals from the solution of the equation (4.3) for a case 2 controller with w- and v-actuation is given in figure 5.7. Again, a larger range of weights r is shown than previously for v-actuation in figure 4.10. The w residual is generally better than that for v-actuation at high r, and is acceptable. At the low r values shown here (corresponding to a large control effort) both w and v residuals show cause for concern.

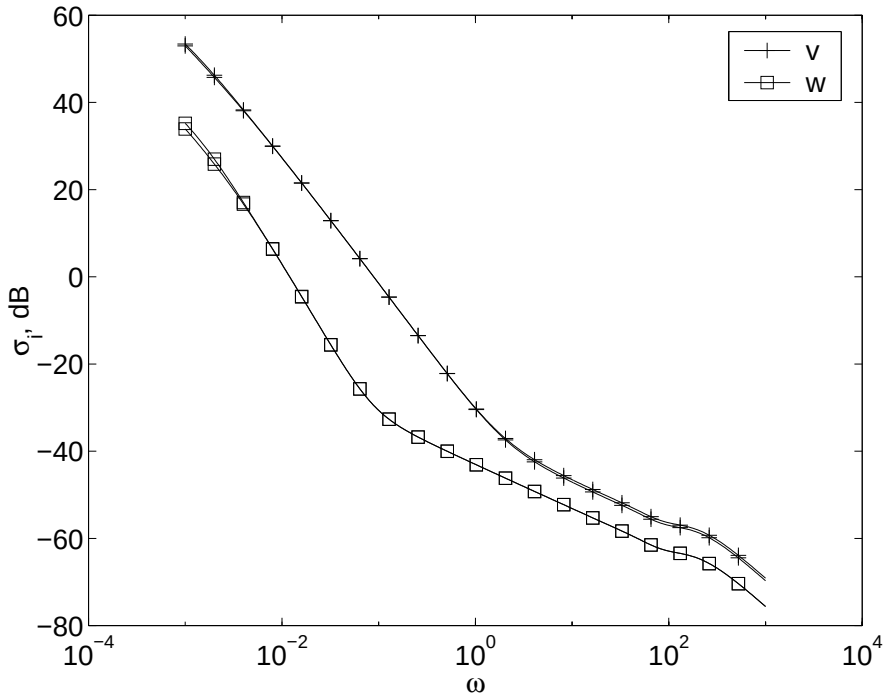

Figure 5.5: Case 2 w- and v-Actuation Open-Loop Singular Values vs Frequency, $N = 100$

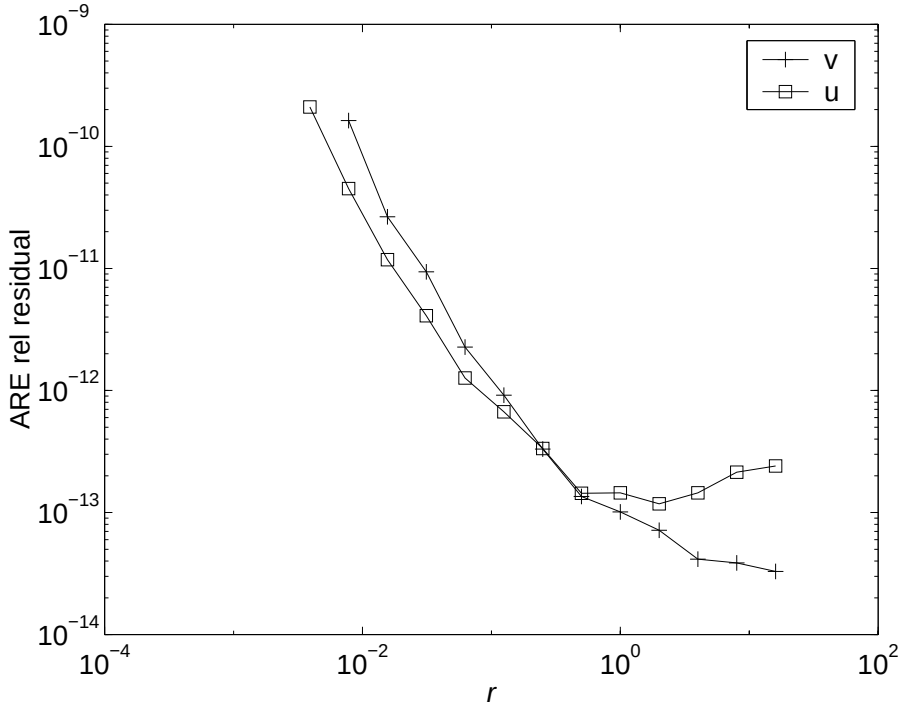

Figure 5.6: Case 1 u- and v-Actuation LQR ARE Relative Residual vs Control Weight r, $N = 100$

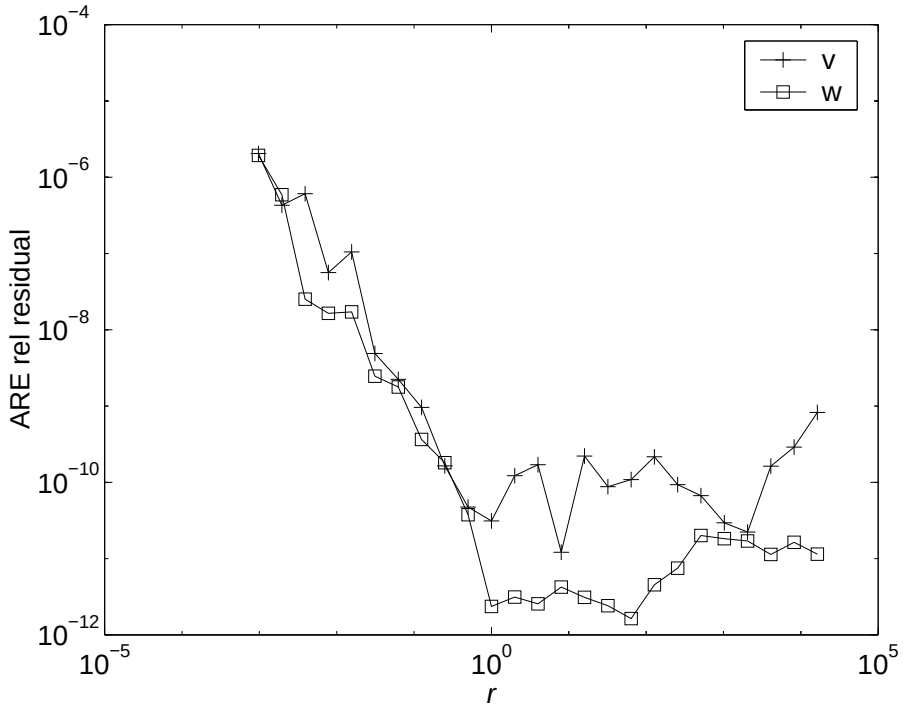

Figure 5.7: Case 2 w- and v-Actuation LQR ARE Relative Residual vs Control Weight r, $N = 100$

5.3.3 u- and w-Actuation Diachronic Transient Energy Bound θ and Initial Conditions

The variation of closed-loop diachronic transient energy bound with control weight is calculated for u- and w-actuation, as in section 4.3.1. Gross spatial oscillations are found to occur in the initial conditions associated with diachronic transient energy bound, as shown in figure 5.8 for case 1, and figure 5.9 for case 2, and both marked 'All Evecs'. The oscillations do not appear on the low frequency system eigenvectors as shown in figure 5.10 and no spurious eigenmodes are evident in plots of ordinal differences as formulated by Boyd (2001, p138) (not shown). The oscillations are peculiar to the solution of the eigensystem (4.41) repeated here

$$e^{\Lambda^T t}\Psi^T\mathcal{Q}\Psi e^{\Lambda t}\chi_{0,i} = \zeta_i\Psi^T\mathcal{Q}\Psi\chi_{0,i} \tag{5.26}$$

The anti-aliasing technique employed on the v-actuation initial conditions which generate the diachronic transient energy bound (see section 4.4.3) fails to remove these gross spatial oscillations. That technique discards the highest 1/3 Chebyshev coefficients, and thus removes noise with high spatial frequencies.

It is also possible to remove noise with high temporal frequencies by discarding the high frequency eigenvectors during the diachronic transient energy bound calculation (4.41), and it is reasonable to assume that high temporal frequency noise is associated with high frequency spatial noise. The procedure truncates the set of system eigenvectors Ψ and eigenvalues Λ in (5.26) by replacing them with just

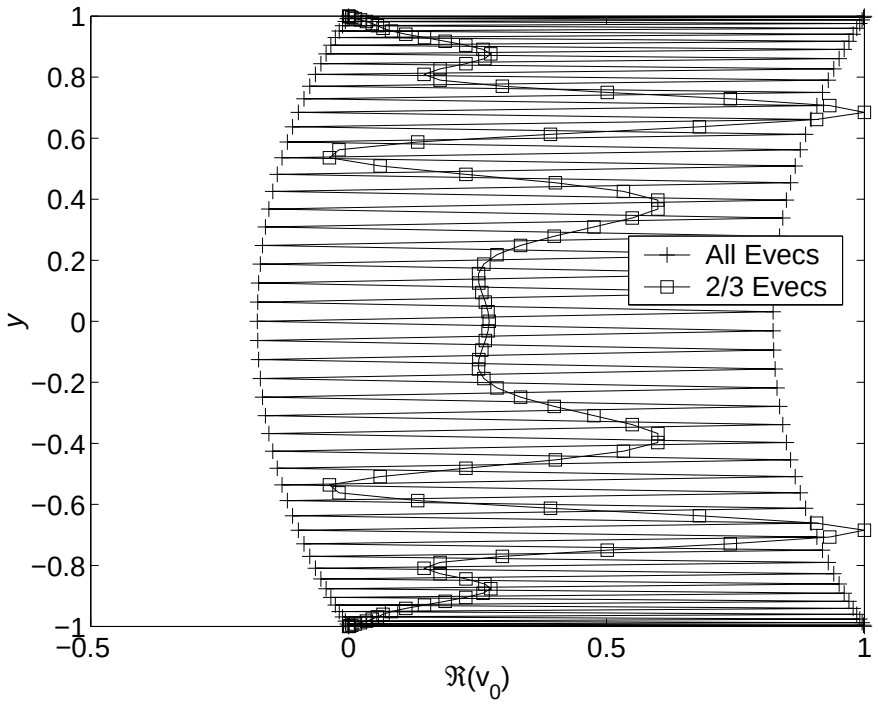

Figure 5.8: Case 1 u-Actuation LQR Worst $\Re(\tilde{v}(t=0))$ vs y, with and without Eigenvector Truncation, $N = 100$

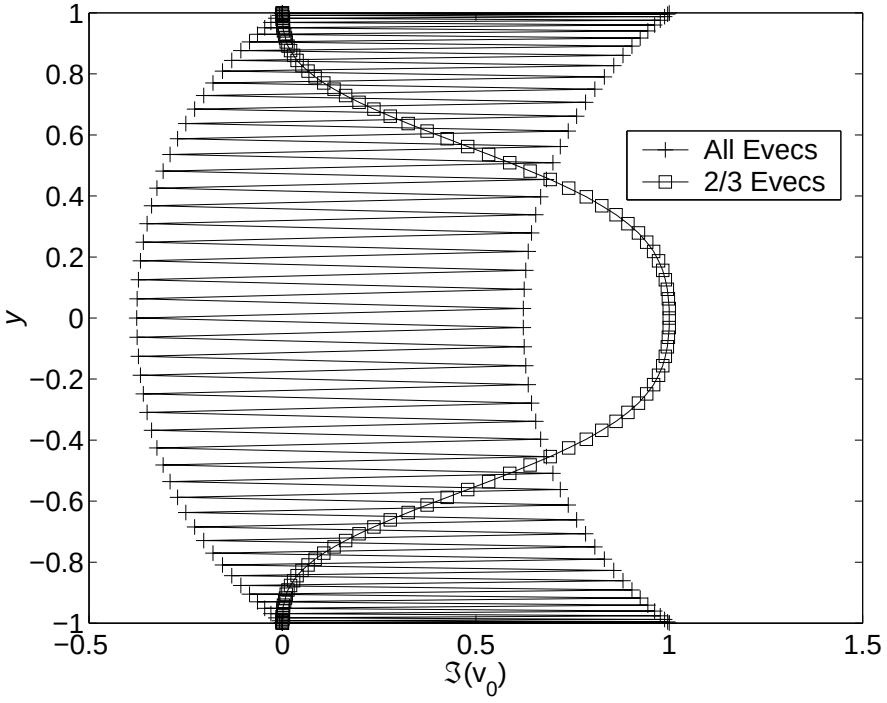

Figure 5.9: Case 2 w-Actuation LQR Worst $\Im(\tilde{v}(t=0))$ vs y, with and without Eigenvector Truncation, $N = 100$

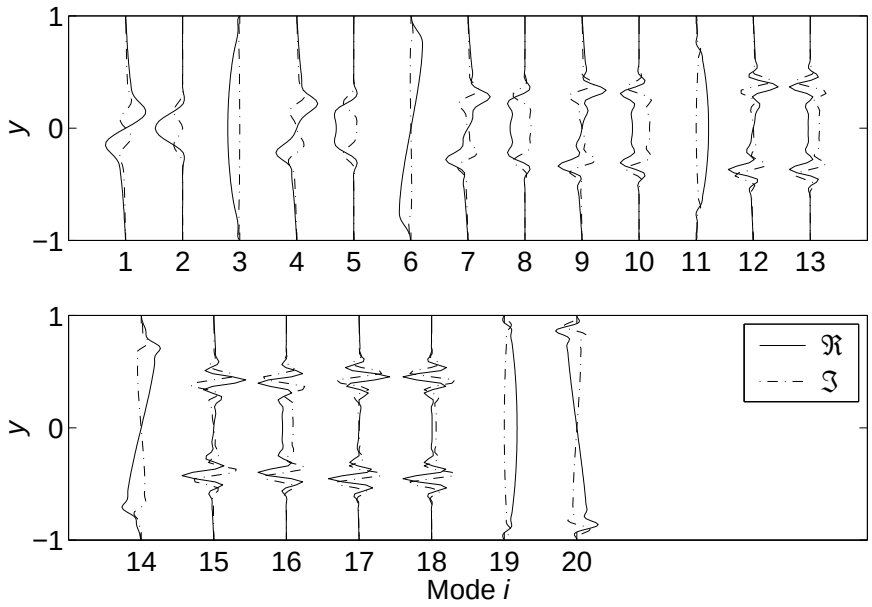

Figure 5.10: Case 1 u-Actuation LQR Eigenvectors, $N = 100$

the lowest frequency 2/3 i.e.

$$\begin{aligned} \Psi &= (\psi_1 \dots \psi_N) \\ \Lambda &= \operatorname{diag}(\lambda_1 \dots \lambda_N) \end{aligned} \tag{5.27}$$

becomes

$$\begin{aligned} \Psi_R &= \left(\psi_1 \dots \psi_{2/3N}\right) \\ \Lambda_R &= \operatorname{diag}\left(\lambda_1 \dots \lambda_{2/3N}\right) \end{aligned} \tag{5.28}$$

The resulting system is smaller

$$e^{\Lambda_R^T t}\Psi_R^T \mathcal{Q}\Psi_R e^{\Lambda_R t}\chi_{0,i,R} = \zeta_i \Psi_R^T \mathcal{Q}\Psi_R \chi_{0,i,R} \tag{5.29}$$

and the initial modal amplitudes $\chi_{0,i,R}$, which result from the solution of the smaller eigensystem, must be augmented with zeros representing the discarded modes

$$\chi_{0,i} = \left(\chi_{0,i,R}^T \mathbf{0}\right)^T \tag{5.30}$$

The effect of this procedure on the initial conditions for case 1 is shown in figure 5.8 and on case 2 in figure 5.9, both marked '2/3 Evecs'. It can be seen that the oscillations for both case 1 and case 2 have been removed.

To check the effect of the procedure, it is also applied to case 1 v-actuation LQR diachronic transient energy bound calculation, and the results are shown in figure 5.11. It can be seen that the procedure has little effect on the diachronic transient energy bound variation with control weight r. However, figure 5.12 shows the initial conditions for control weight $r = 2^{-2}$, as used for the case 1 LQR linear simulations, and it can be seen that the procedure has a marked effect. The initial

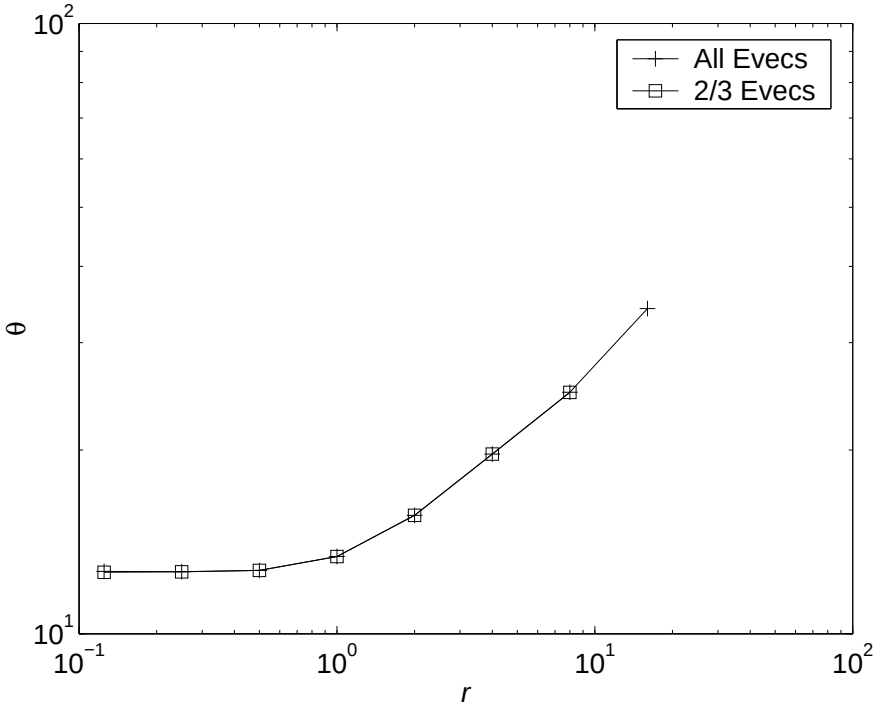

Figure 5.11: Case 1 v-Actuation LQR Diachronic Transient Energy Bound θ vs control weight r, with and without Eigenvector Truncation, $N = 100$

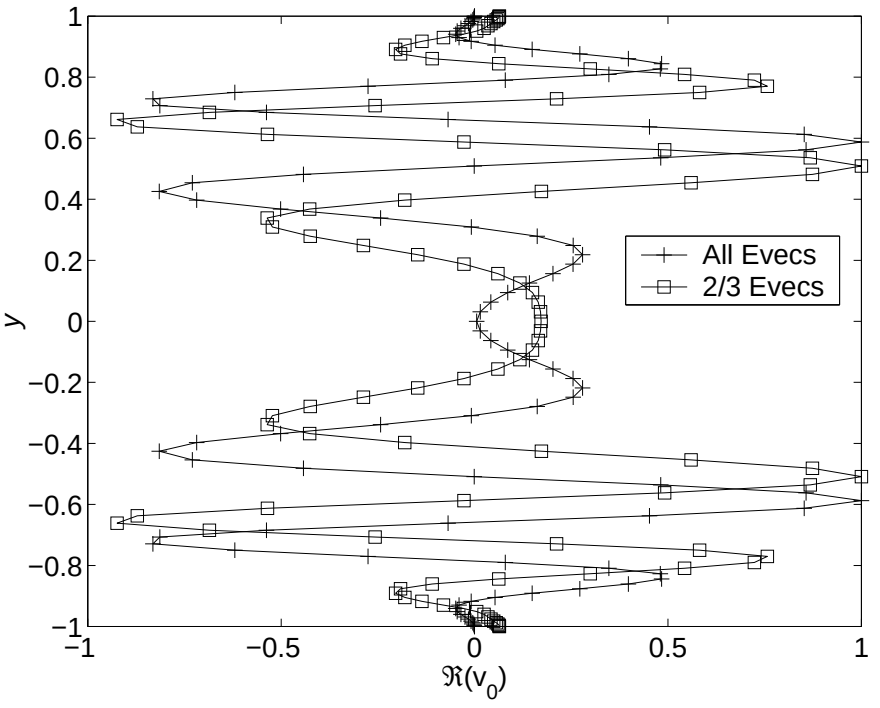

Figure 5.12: Case 1 v-Actuation LQR Worst $\Re(\tilde{v}(t = 0))$ vs y, with and without Eigenvector Truncation, $N = 100$

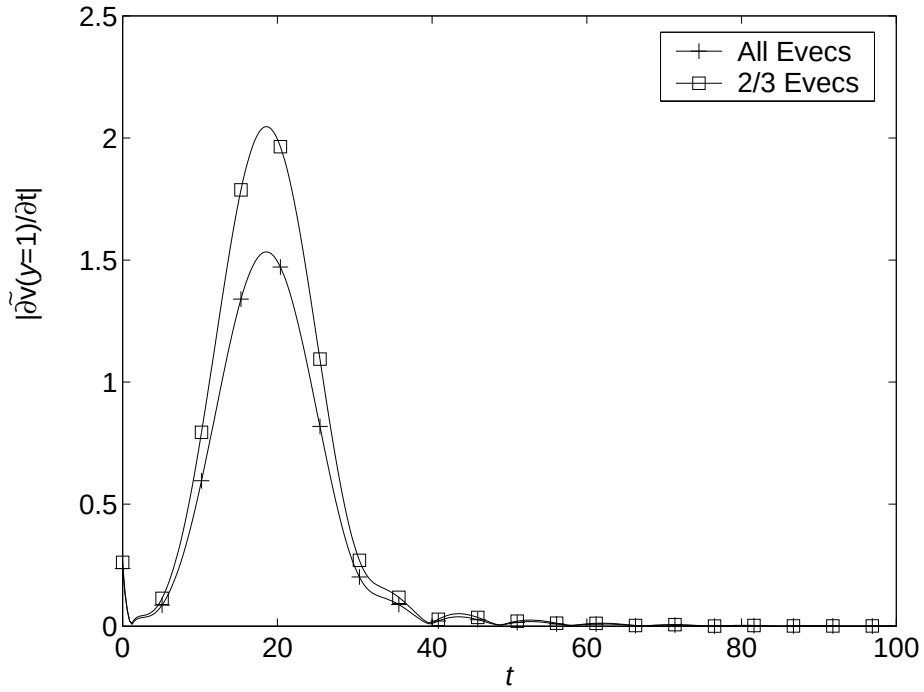

Figure 5.13: Case 1 v-Actuation LQR Upper Wall Control $\mathcal{U}(1)$ vs Time t, from Initial Conditions $\mathcal{X}_{worst}$ Scaled to $E = 1$, $N = 100$

conditions are changed, and thus the control actuation is also changed, as shown in figure 5.13. As the diachronic transient energy bound is the same with and without the eigenvector truncation procedure, it is evident that different initial conditions may generate very similar diachronic transient energy bounds, and simulations will show different control effort required. It would seem possible that the initial magnitude of modes that do not contribute significantly to the maximum transient energy could vary, but why the eigensystem (5.26) excites these modes at all is not as clear. This result casts some doubt on the uniqueness of the actuation results presented in section 4.4.4, although the degree of doubt can be quantified in that discarding 33% of the eigenvectors here only changes the actuation in figure 5.13 by approximately 25%. For consistency with previous results shown in section 4.4.4, all v-actuation results presented hereafter are without the eigenvector truncation procedure.

Figure 5.14 shows case 1 u-actuation diachronic transient energy bound θ against control weight r, with and without eigenvector truncation. Several results without eigenvector truncation are not shown, since those initial conditions do not produce the calculated diachronic transient energy bound in a linear simulation. The results without eigenvector truncation produce unrealistically large diachronic transient energy bound with initial conditions containing gross oscillations, hence the need for the truncation. Bearing in mind that the system singular values converge nicely, and that the LQR algebraic Riccati equation has acceptable residuals, it would appear that the eigensystem (5.26) is the cause of this poor numerical behaviour. Eigenvector truncation reduces the diachronic transient energy

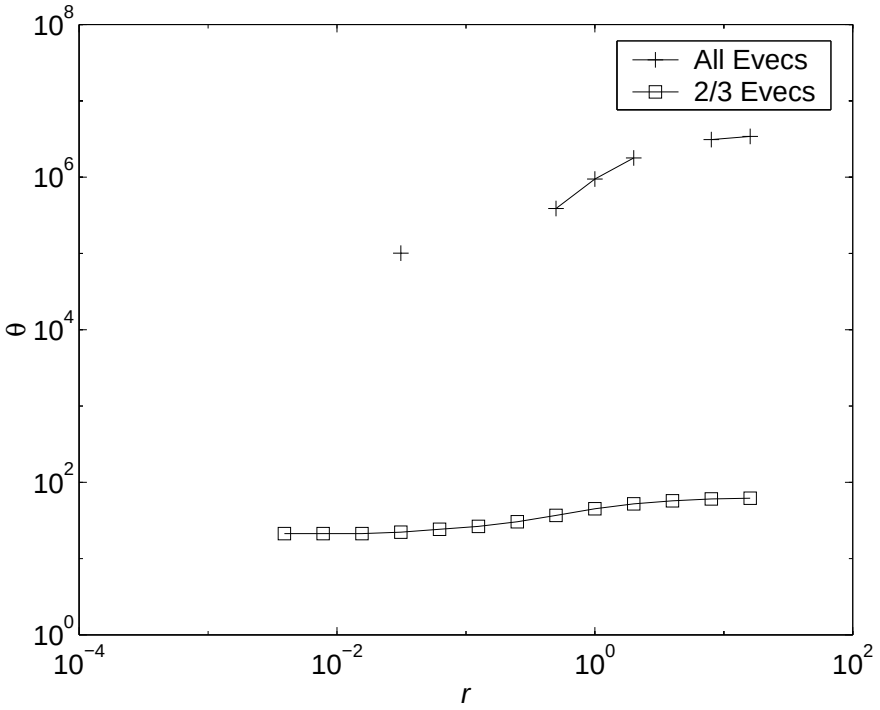

Figure 5.14: Case 1 u-Actuation LQR Diachronic Transient Energy Bound θ vs Control Weight r, with and without Eigenvector Truncation, $N = 100$

bound values significantly and removes the gross oscillations.

Case 2 w-actuation diachronic transient energy bound θ against control weight r, with and without eigenvector truncation, is presented in figure 5.15. Without eigenvector truncation most values of r produce transient energy in a linear simulation in agreement with the diachronic transient energy bound, but the diachronic transient energy bound values appear unrealistically large at high r values, and the associated worst initial conditions have the aforementioned gross oscillations. As for case 1, eigenvector truncation reduces the diachronic transient energy bound values significantly and removes the gross oscillations.

A further problem, encountered in Matlab, is that the initial state variables $\mathcal{X}_0 = \Psi\chi_{0,i}$, which are ideally real, since they have been decomposed into real and imaginary parts $\mathcal{X}_0^T = \left(\mathcal{X}_{real,0}^T \mathcal{X}_{imag,0}^T\right)^T$ in section 2.7, are found to be complex. An equivalent real form is given by $\left(\Re(\mathcal{X}_{real,0} + \jmath\mathcal{X}_{imag,0})^T, \Im(\mathcal{X}_{real,0} + \jmath\mathcal{X}_{imag,0})^T\right)^T$, which produces the same velocity and vorticity $(\tilde{v}^T, \tilde{\eta}^T)^T = \mathbf{T}\mathcal{X}$ (2.106). This problem, although solved, highlights the possibility of the states representing a particular velocity and vorticity distribution not being unique unless strict type checking is imposed, i.e. variables expected to be real must be checked that they are indeed real.

Figure 5.16 shows the convergence of case 1 u-actuation diachronic transient energy bound θ against control weight r with discretisation N. It can be seen that full convergence only occurs at the very beginning of the range for $N = 100$ with respect to $N = 150$. This result is surprising given the fast and uniform convergence of v-actuation at $N = 30$ as shown in figure 4.9. The convergence of

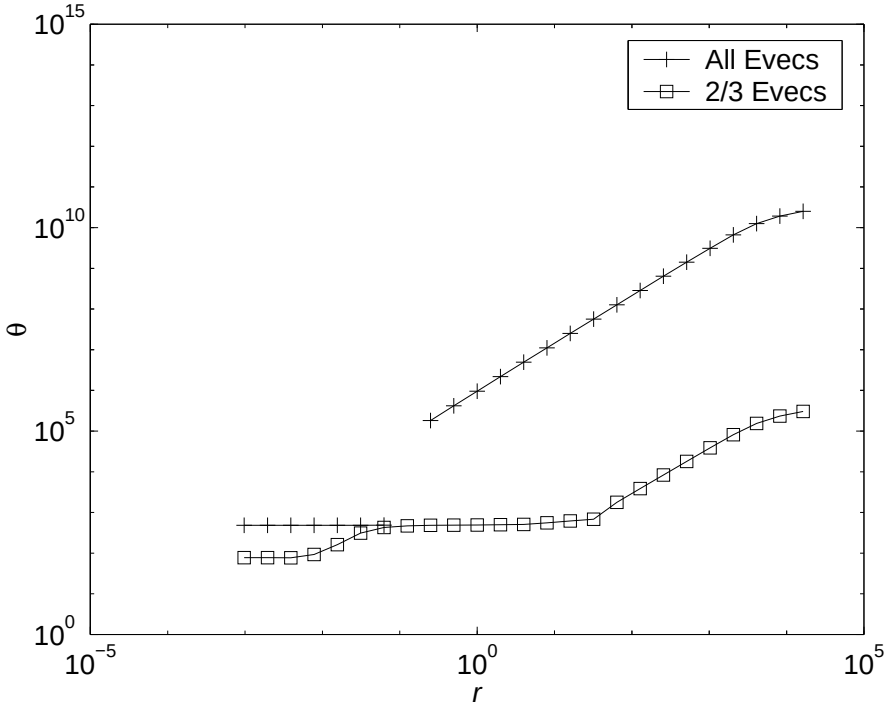

Figure 5.15: Case 2 w-Actuation LQR Diachronic Transient Energy Bound θ vs Control Weight r, with and without Eigenvector Truncation, $N = 100$

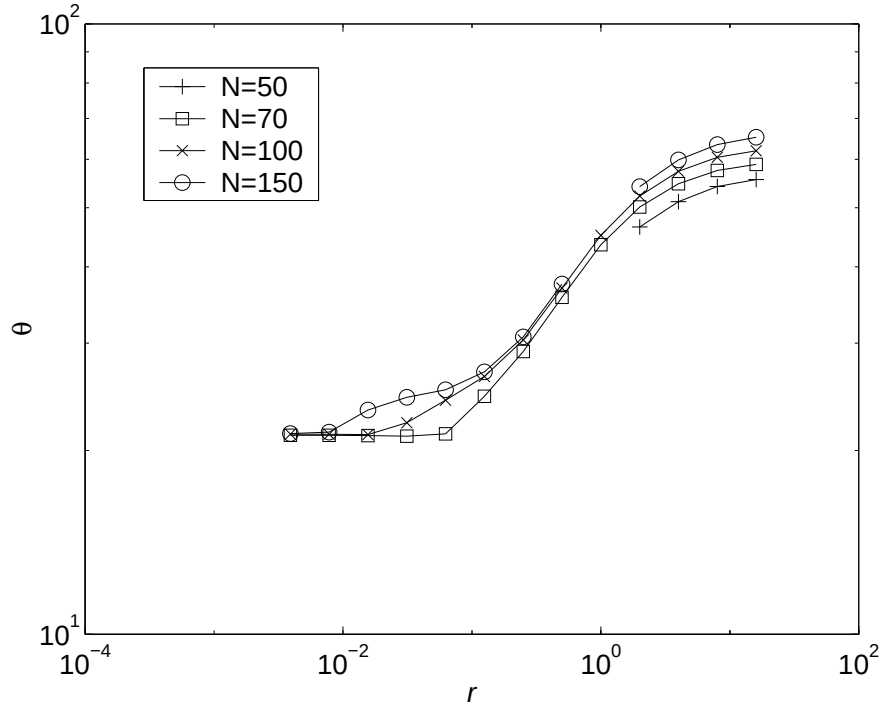

Figure 5.16: Case 1 u-Actuation LQR Diachronic Transient Energy Bound θ vs Control Weight r, for Different Discretisations N

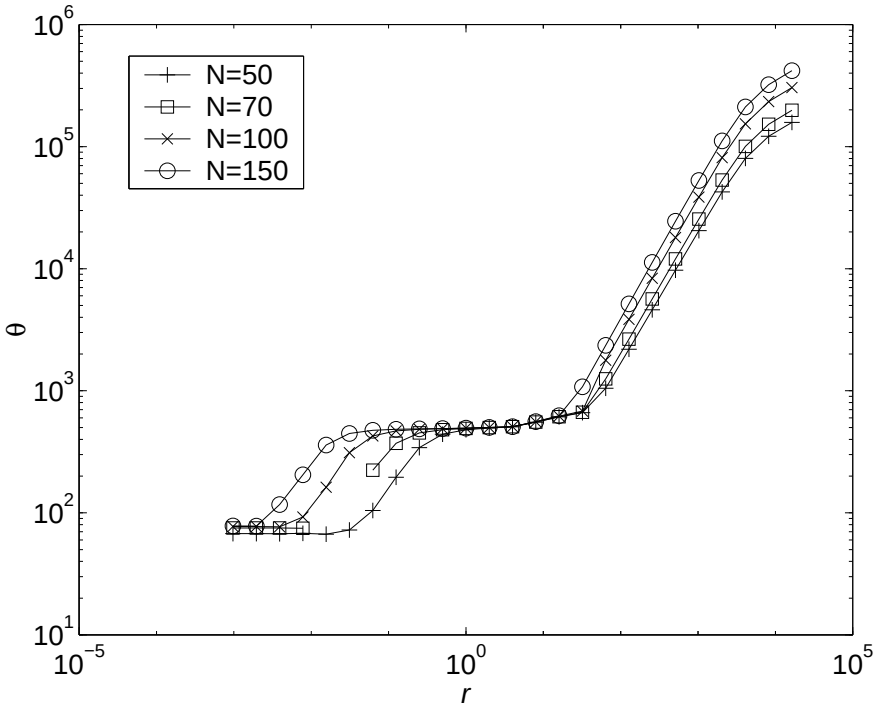

Figure 5.17: Case 2 w-Actuation LQR Diachronic Transient Energy Bound θ vs Control Weight r, for Different Discretisations N

case 2 w-actuation diachronic transient energy bound θ against control weight r with discretisation N is shown in figure 5.17. Convergence only occurs for limited values of r. Again this is at variance with the v-actuation convergence results shown in figure 4.11.

Figure 5.16 presents case 1 u- and v-actuation diachronic transient energy bound θ against control weight r, for discretisation $N = 100$. It can be seen that u-actuation produces a diachronic transient energy bound approximately twice as great as that produced by v-actuation. This is consistent with u-actuation resulting in a less controllable plant, as seen in figure 5.2.

Case 2 v and w-actuation diachronic transient energy bound θ against control weight r appears in figure 5.17. It can be seen that w-actuation produces a diachronic transient energy bound much greater than that from u-actuation at high r (low control effort). At moderate r, the w-actuation produces a 40% lower diachronic transient energy bound, and at low r w-actuation would appear to generate significantly lower diachronic transient energy bound, approximately one tenth, although these results are tempered by w-actuation requiring eigenvector truncation, and the LQR ARE residuals being poor at the lowest r values.

Figure 5.20 shows case 1 diachronic transient energy bound θ against maximum control magnitude (from linear simulations from the worst initial conditions), for both u- and v-actuation. It can be seen that v-actuation is better in a Pareto optimal sense, it achieves lower diachronic transient energy bound and lower control effort than u-actuation. Case 2 diachronic transient energy bound θ against maximum control magnitude (from linear simulations from the worst initial conditions),

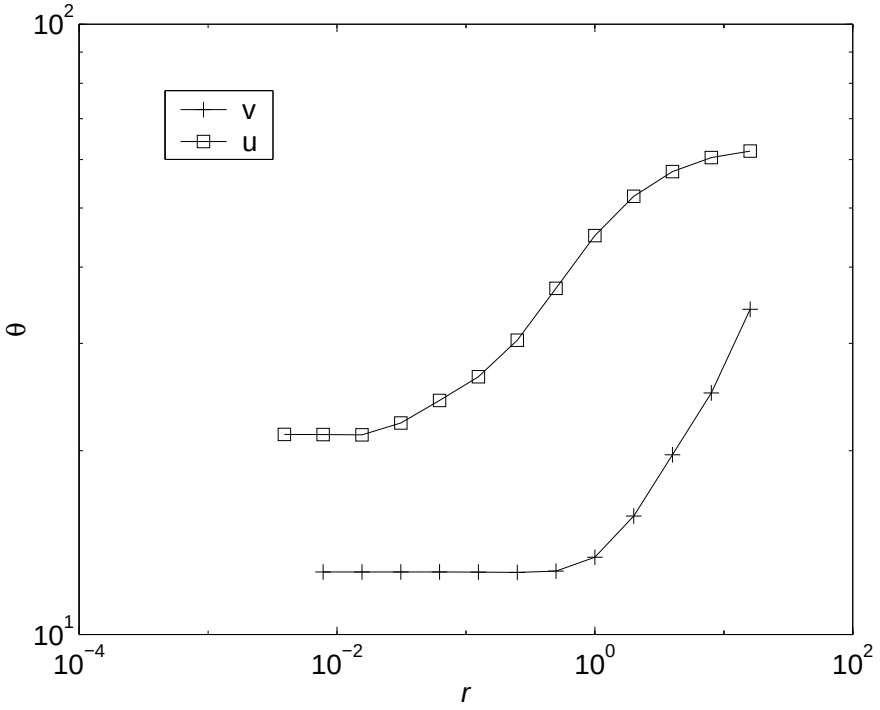

Figure 5.18: Case 1 u- and v-Actuation LQR Diachronic Transient Energy Bound θ vs Control Weight r, $N = 100$

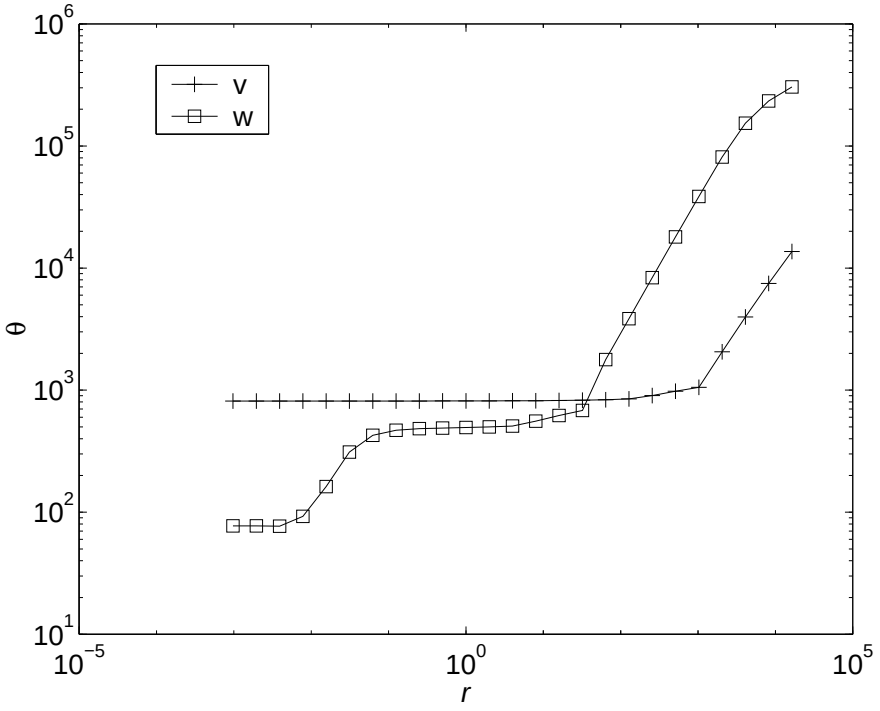

Figure 5.19: Case 2 w- and v-Actuation LQR Diachronic Transient Energy Bound θ vs Control Weight r, $N = 100$

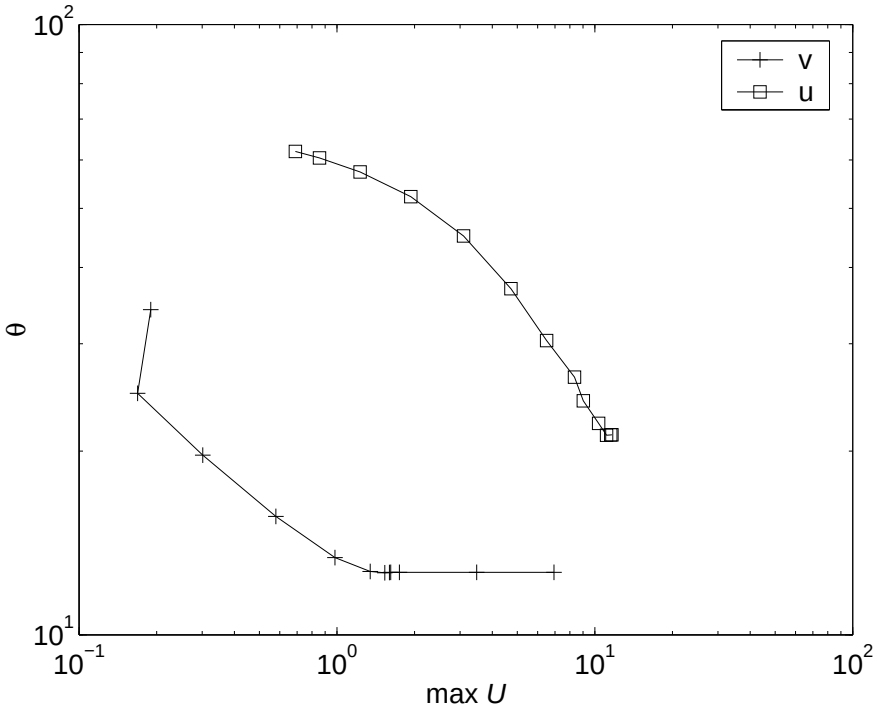

Figure 5.20: Case 1 u- and v-Actuation LQR Diachronic Transient Energy Bound θ vs Maximum Control $\mathcal{U}$, $N = 100$

for both w- and v-actuation, is given in figure 5.21. Again it can be seen that v-actuation is better in a Pareto optimal sense, at high diachronic transient energy bound, but w-actuation may reach a lower diachronic transient energy bound.

For case 1 simulations of control by u-actuation, a value of $r = 2^{-7} \approx 7.8e-3$ is selected, since it results in the lowest diachronic transient energy bound, and convergence with N has occurred at this value, as shown in figure 5.16. For case 2 simulations of control by w-actuation, a value of $r = 2^0$ is selected, since figure 5.7 shows an acceptable ARE residual and figure 5.17 shows convergence has occurred at this value, although it does not result in the lowest calculated diachronic transient energy bound. Figure 5.22 shows that the corresponding initial vorticity is far from smooth. Although the magnitude of the initial vorticity is much lower than that of the initial velocity, simulations from these initial conditions may be of doubtful value, and only the results from linear simulations are presented.

5.3.4 u- and w-Actuation Transient Simulations

Transient simulations are performed from the worst initial conditions for both u- and w-actuation, using the weights r selected in section 5.3.3. Figure 5.23 shows case 1 u-actuation transient energy E against time for various discretisations N. It can be seen that convergence has indeed occurred for $N \geq 70$ at the value of $r = 2^{-7}$ selected from figure 5.16. Case 2 w-actuation transient energy E against time is shown in figure 5.24, for various discretisations N. Again it can be seen that convergence has indeed occurred for $N \geq 100$ at the value of $r = 2^0$ selected.

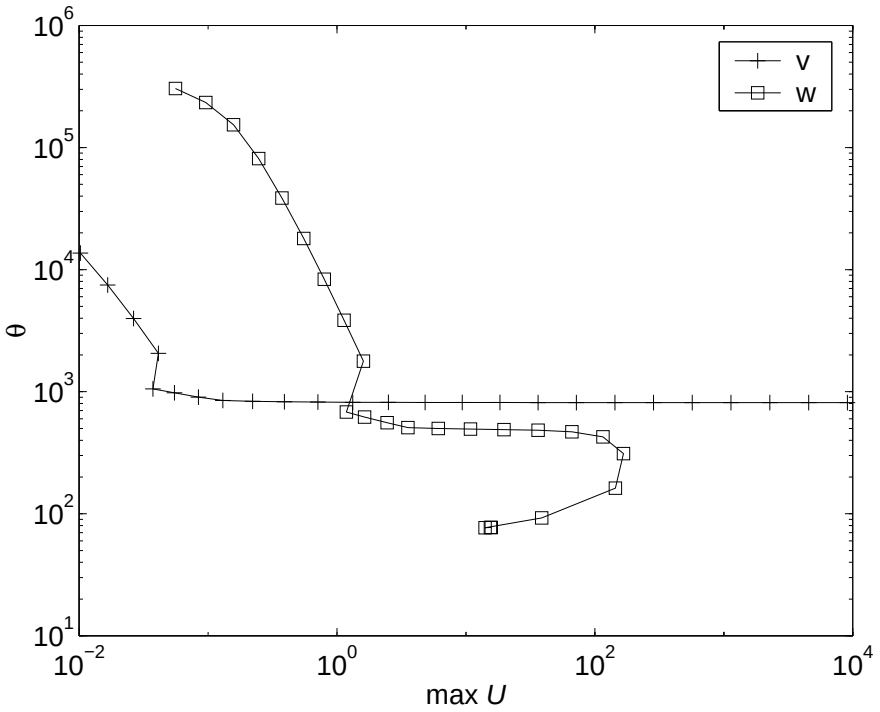

Figure 5.21: Case 2 w- and v-Actuation LQR Diachronic Transient Energy Bound θ vs Maximum Control $\mathcal{U}$, $N = 100$

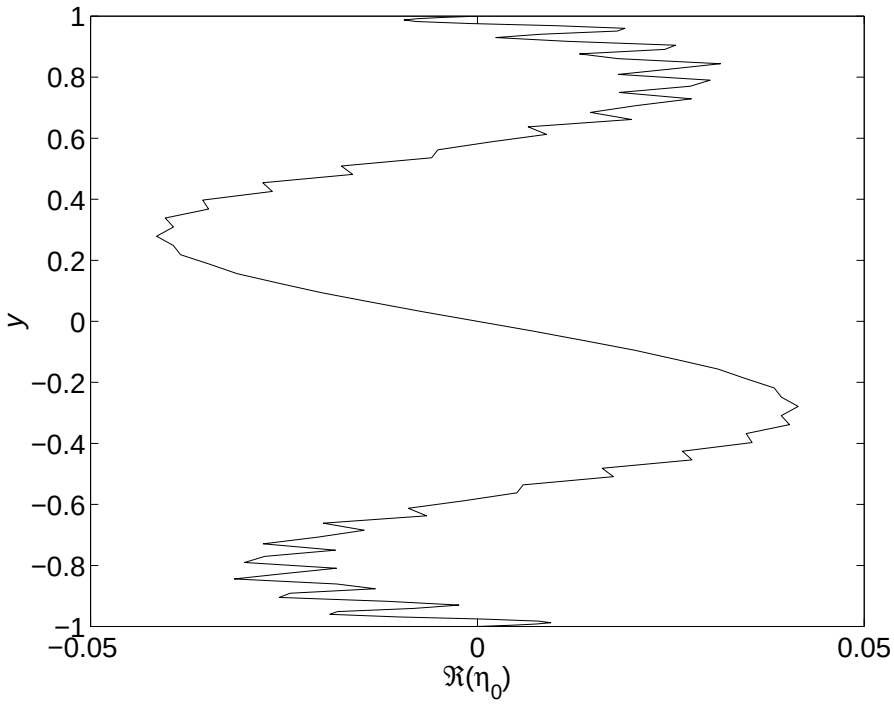

Figure 5.22: Case 2 w-Actuation LQR Worst $\Re(\tilde{\eta}(t = 0))$ vs y, after Eigenvector Truncation, $N = 100$

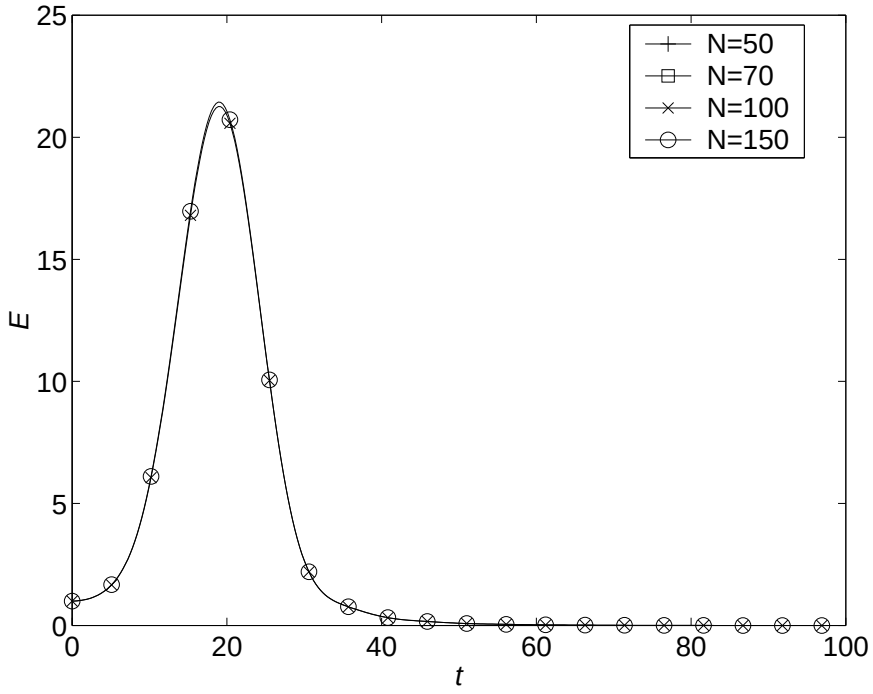

Figure 5.23: Case 1 u-Actuation LQR Transient Energy E vs Time t, for Various Discretisations N, from Initial Conditions $\mathcal{X}_{worst}$ Scaled to $E = 1$

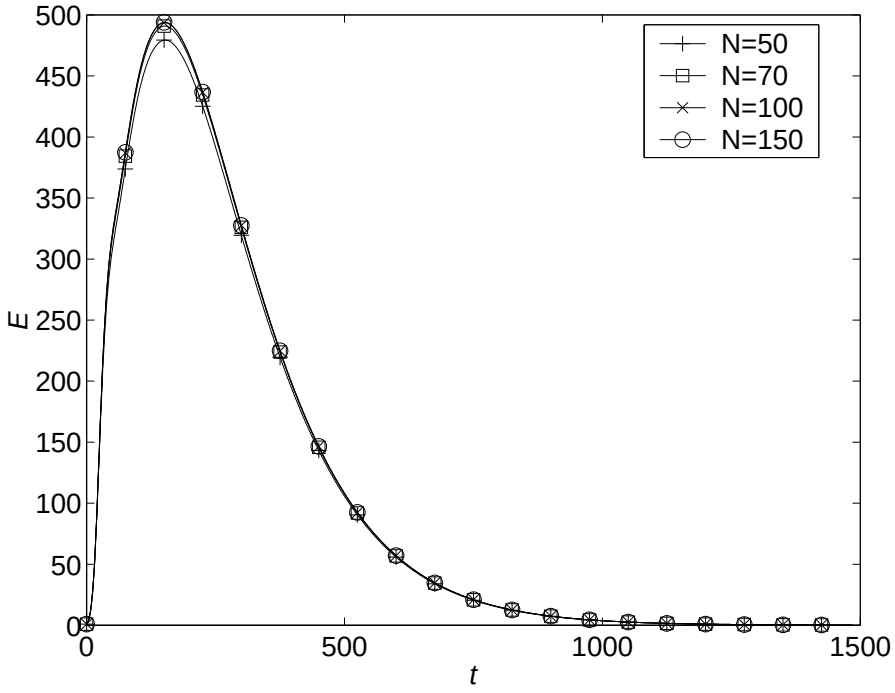

Figure 5.24: Case 2 w-Actuation LQR Transient Energy E vs Time t, for Various Discretisations N, from Initial Conditions $\mathcal{X}_{worst}$ Scaled to $E = 1$

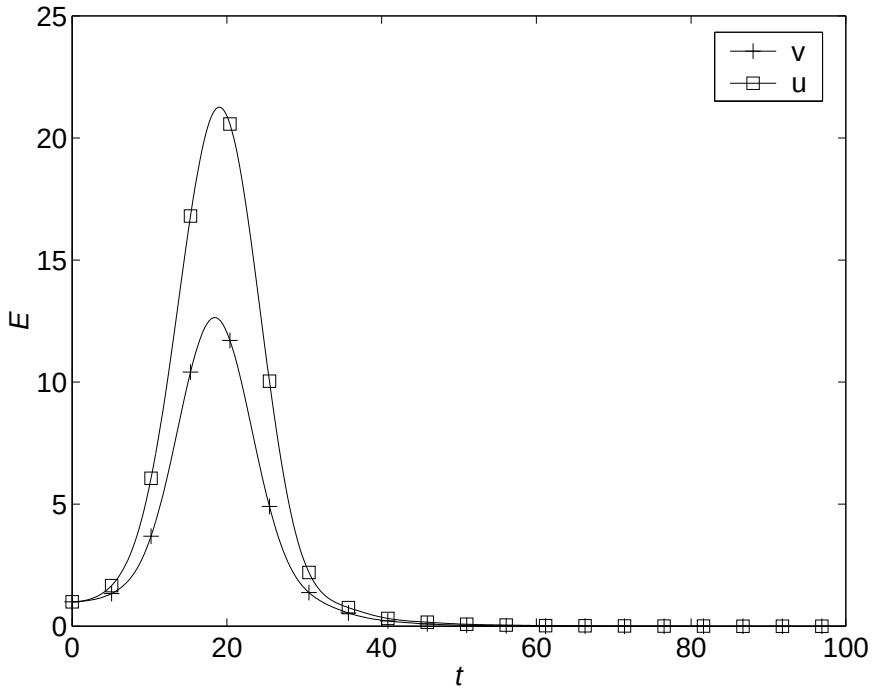

Figure 5.25: Case 1 u- and v-Actuation LQR Transient Energy E vs Time t, from Initial Conditions $\mathcal{X}_{worst}$ Scaled to $E = 1$, $N = 100$

Figure 5.25 shows case 1 transient energy E against time for both u- and v-actuation. It is evident that wall-normal v-actuation achieves approximately 40% lower peak transient energy than tangential u-actuation, as predicted by figure 5.18. Case 2 transient energy E against time for both w- and v-actuation appears in figure 5.26, which shows that tangential w-actuation achieves 40% lower peak transient energy than wall-normal v-actuation, which is consistent with figure 5.19 at $r = 2^0$. Figure 5.27 shows the magnitude of the case 1 u- and v-actuation LQR control signals at the upper wall, $\dot{\tilde{u}}(y = 1)$ and $\dot{\tilde{v}}(y = 1)$ respectively, against time. The peak u-actuation magnitude is approximately 7 times as large as that from v-actuation. The time integral of the case 1 LQR control signal at the upper wall, namely the Fourier coefficient of the upper wall velocities $\tilde{u}(y = 1)$ and $\tilde{v}(y = 1)$ respectively, appears in figure 5.28. The peak u-actuation velocity is more than 8 times as large as that from v-actuation. The double time integral of the case 1 LQR control signal at the upper wall for u- and v-actuation, namely the Fourier coefficient of the upper wall fluid quantity displaced, versus time is displayed in figure 5.29. The peak u-actuation displacement is approximately 9 times larger than that from v-actuation.

Figure 5.30 shows the magnitude of the case 2 w- and v-actuation LQR control signals at the upper wall i.e. $\dot{\tilde{w}}(y = 1)$ and $\dot{\tilde{v}}(y = 1)$ respectively, against time. The peak w-actuation magnitude is approximately 70 times as large as that from v-actuation. Figure 5.31 shows the time integral of the case 2 LQR control signal at the upper wall, namely the Fourier coefficient of the upper wall velocities $\tilde{w}(y = 1)$ and $\tilde{v}(y = 1)$ respectively. The peak u-actuation velocity is around 24 times as

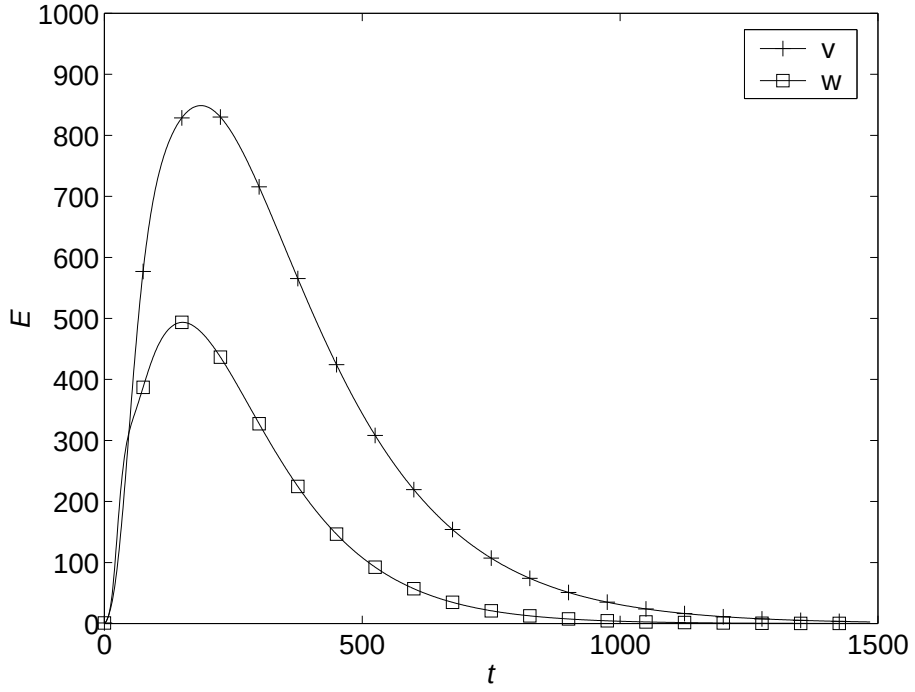

Figure 5.26: Case 2 w- and v-Actuation LQR Transient Energy E vs Time t, from Initial Conditions $\mathcal{X}_{worst}$ Scaled to $E = 1$, $N = 100$

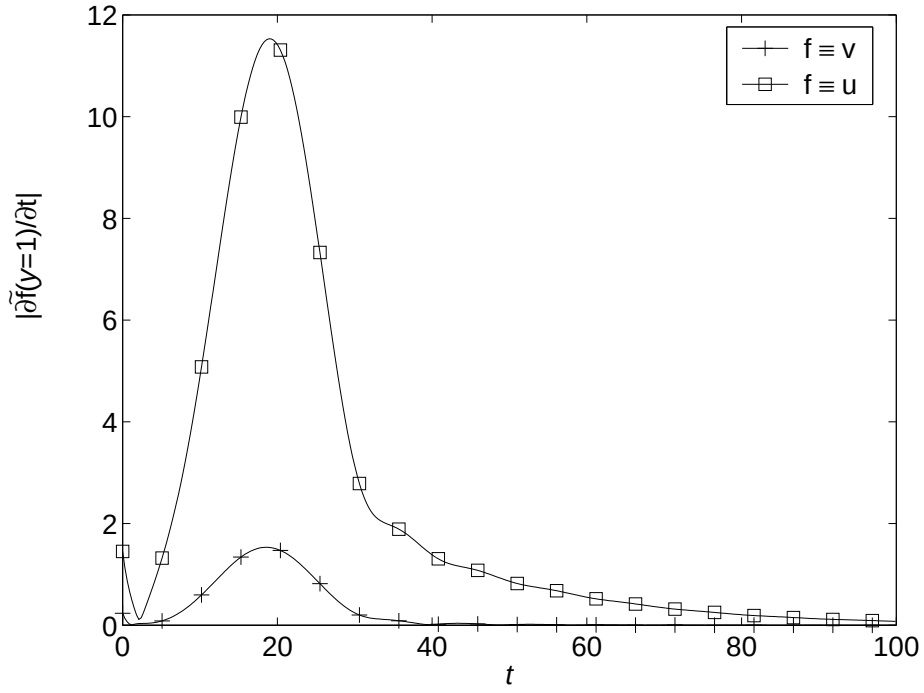

Figure 5.27: Case 1 u- and v-Actuation LQR Upper Wall Control $\mathcal{U}(1)$ vs Time t, from Initial Conditions $\mathcal{X}_{worst}$ Scaled to $E = 1$, $N = 100$

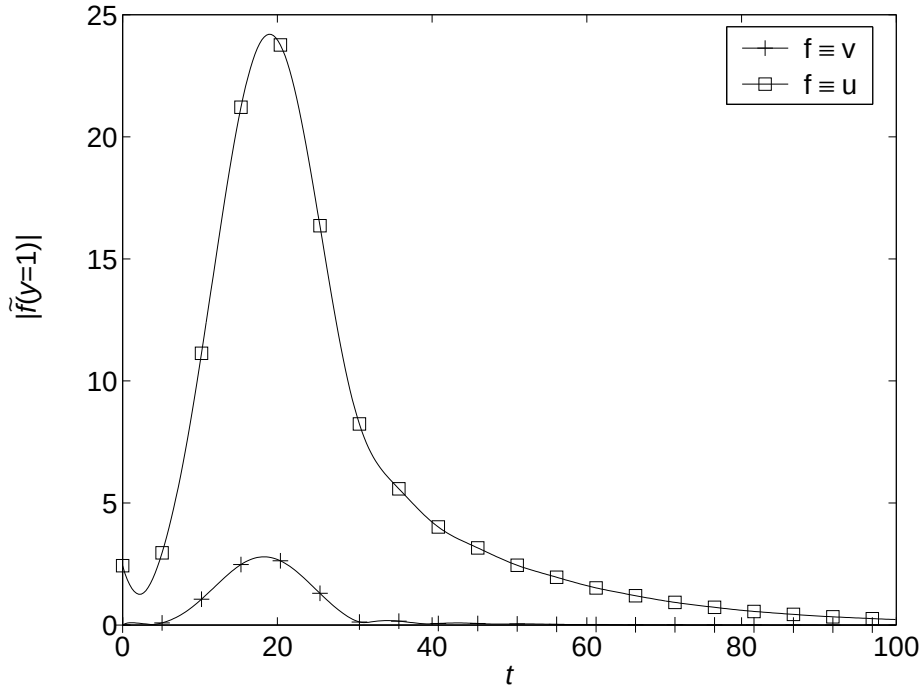

Figure 5.28: Case 1 u- and v-Actuation LQR Wall Velocity Coefficient, $\tilde{u}(y = 1), \tilde{v}(y = 1)$ vs Time t, from Initial Conditions $\mathcal{X}_{worst}$ Scaled to $E = 1$, $N = 100$

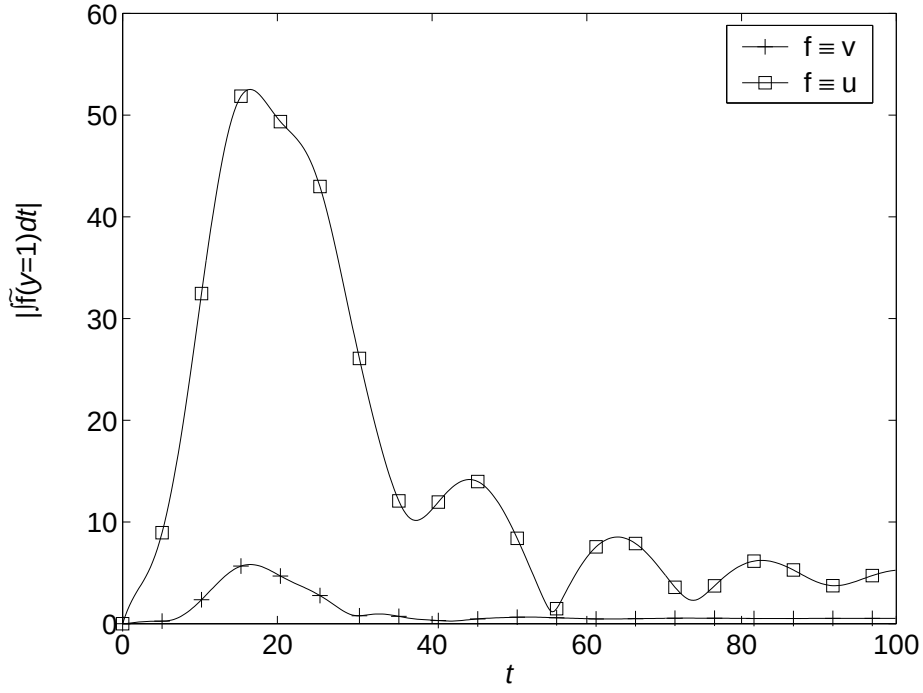

Figure 5.29: Case 1 u- and v-Actuation LQR Fluid Depth Transpired on Upper Wall vs Time t, from Initial Conditions $\mathcal{X}_{worst}$ Scaled to $E = 1$, $N = 100$

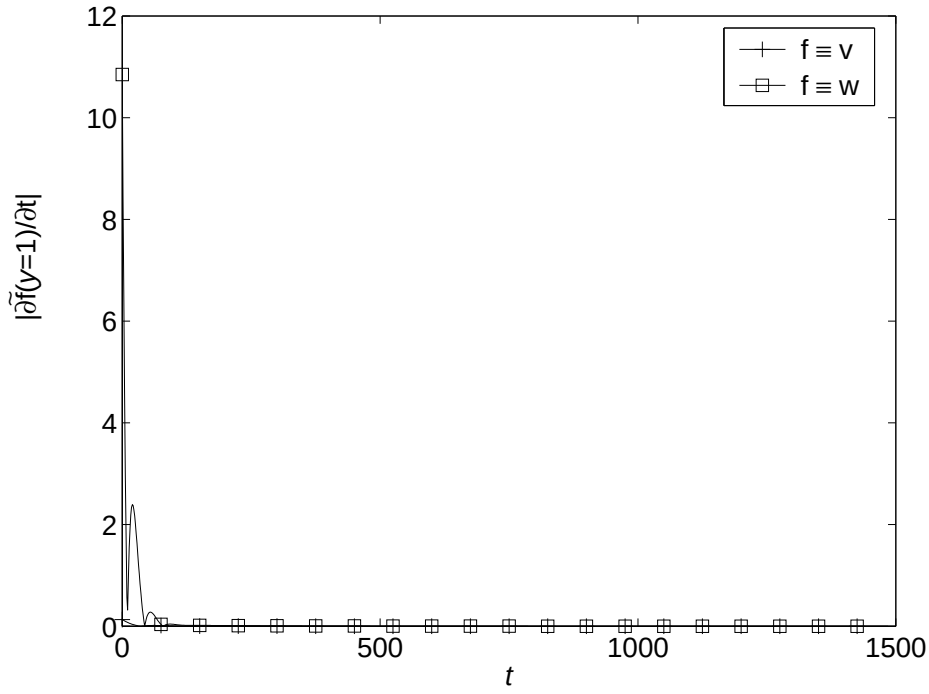

Figure 5.30: Case 2 w- and v-Actuation LQR Upper Wall Control $\mathcal{U}(1)$ vs Time t, from Initial Conditions $\mathcal{X}_{worst}$ Scaled to $E = 1$, $N = 100$

large as that from v-actuation.

The double time integral of the case 2 LQR control signal at the upper wall for w- and v-actuation, namely the Fourier coefficient of the upper wall fluid quantity displaced, versus time is displayed in figure 5.32. The final and peak w-actuation displacement is approximately 5 times larger than that from v-actuation, and thus the final accumulated displacement is even further from zero than the v-actuation.

5.4 Results from Non-linear Simulations and Discussion

This section describes results from non-linear simulations of LQR control by u-actuation on case 1. The CFD code is modified to enforce u tangential velocity boundary conditions rather than wall-normal v ones. The state variables q_u^u and q_l^u, which are the upper and lower wall $\partial\tilde{v}/\partial y$, are computed by three point unequal interval forward and backward finite difference methods respectively. Otherwise, the code and discretisation are as used in chapter 4.

5.4.1 u-Actuation on Small Initial Perturbations

Figure 5.33 presents the u-actuation case 1 LQR state feedback transient energy E, from worst initial perturbations of energy E_{C1}, for both linear (solid) and non-linear (dotted) simulations, for case 1. The results from both the linear and

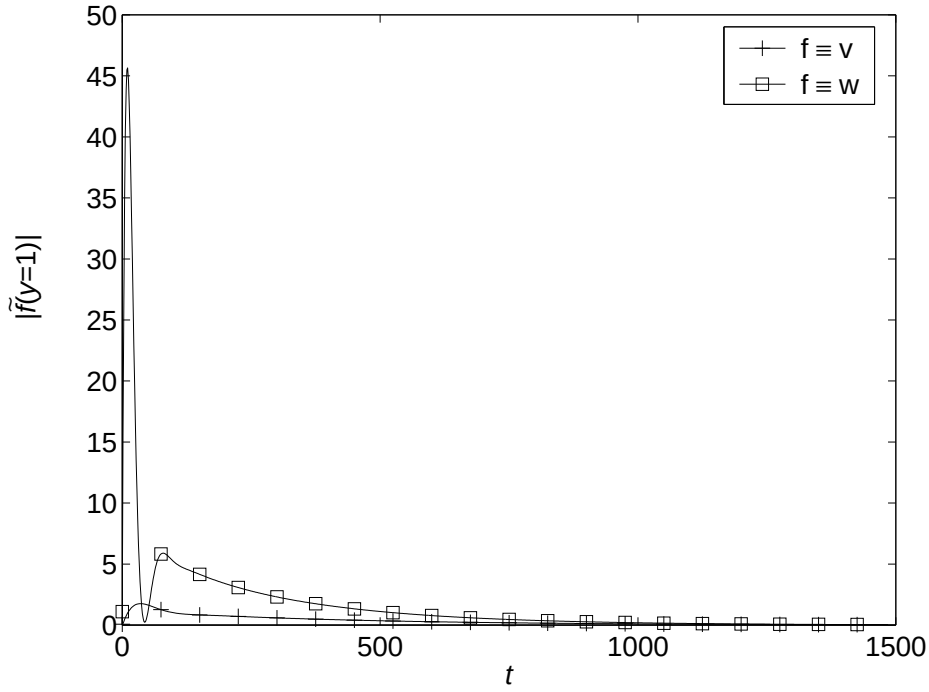

Figure 5.31: Case 2 w- and v-Actuation LQR Wall Velocity Coefficient, $\tilde{v}(y = 1), \tilde{w}(y = 1)$ vs Time t, from Initial Conditions $\mathcal{X}_{worst}$ Scaled to $E = 1$, $N = 100$

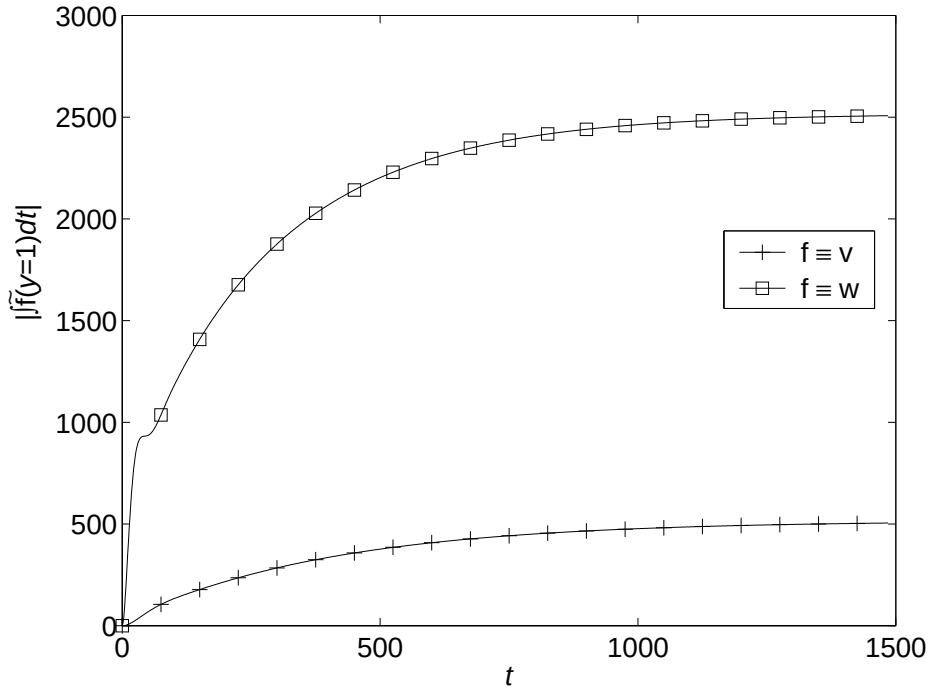

Figure 5.32: Case 2 w- and v-Actuation LQR Fluid Depth Transpired on Upper Wall vs Time t, from Initial Conditions $\mathcal{X}_{worst}$ Scaled to $E = 1$, $N = 100$

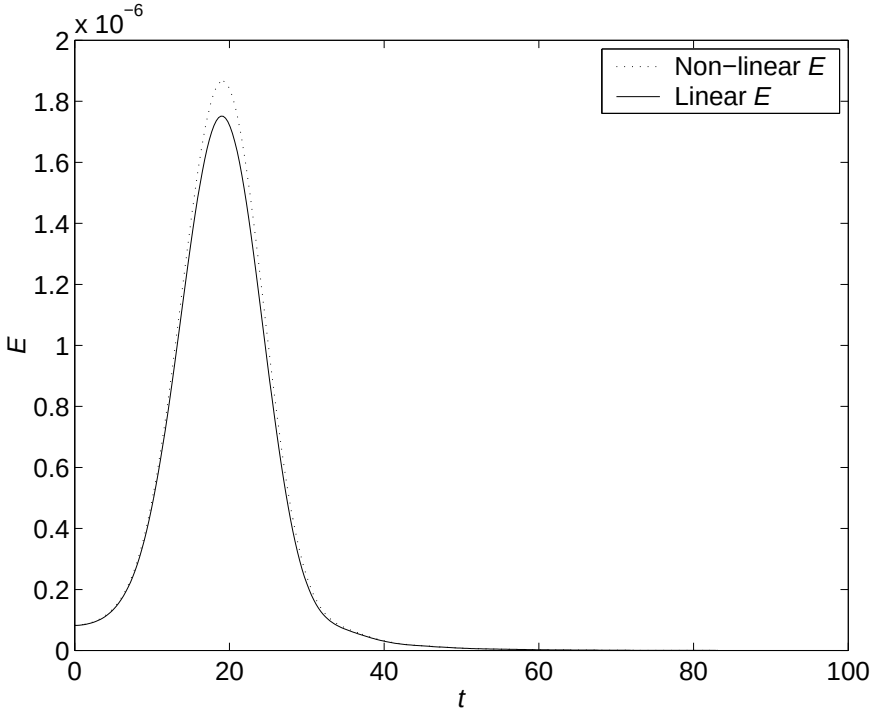

Figure 5.33: Case 1 u-Actuation LQR Transient Energy E vs Time t, from Initial Conditions $\mathcal{X}_{Worst}$ Scaled to Energy E_{C1}

non-linear simulations agree reasonably well, and show the stabilization of the flow by the LQR controller. Thus it may be assumed that the non-linear finite volume and linear spectral simulations are both modelling the linear problem correctly.

Figure 5.33 shows the case 1 u-actuation wall tangential velocity as a fraction of U_{cl} for both linear (solid) and non-linear (dotted) simulations. Again linear and non-linear simulations agree reasonably well.

5.4.2 u-Actuation on Large Initial Perturbations

Figure 5.35 presents the u-actuation case 1 LQR state feedback transient energy E, from worst initial perturbations of energy $10^4 E_{C1}$, for both linear (solid) and non-linear (dotted) simulations, for case 1. The non-linear simulation saturates at approximately 46% of the linear peak linear transient energy, and then decays relatively slowly. The peak non-linear transient energy is approximately 0.0081 and is slightly better than the value for v-actuation from table 4.4 of 0.011, despite v-actuation having better performance on linearly sized perturbations, as shown in figure 5.25.

Figure 5.35 shows the case 1 u-actuation wall tangential velocity as a fraction of U_{cl} for both linear (solid) and non-linear (dotted) simulations, from this larger initial perturbation. Non-linear actuation has a lower peak and persists longer than linear actuation, which is consistent with the transient energy in figure 5.35, since the state variables contribute to the transient energy and drive the LQR state-feedback actuation.

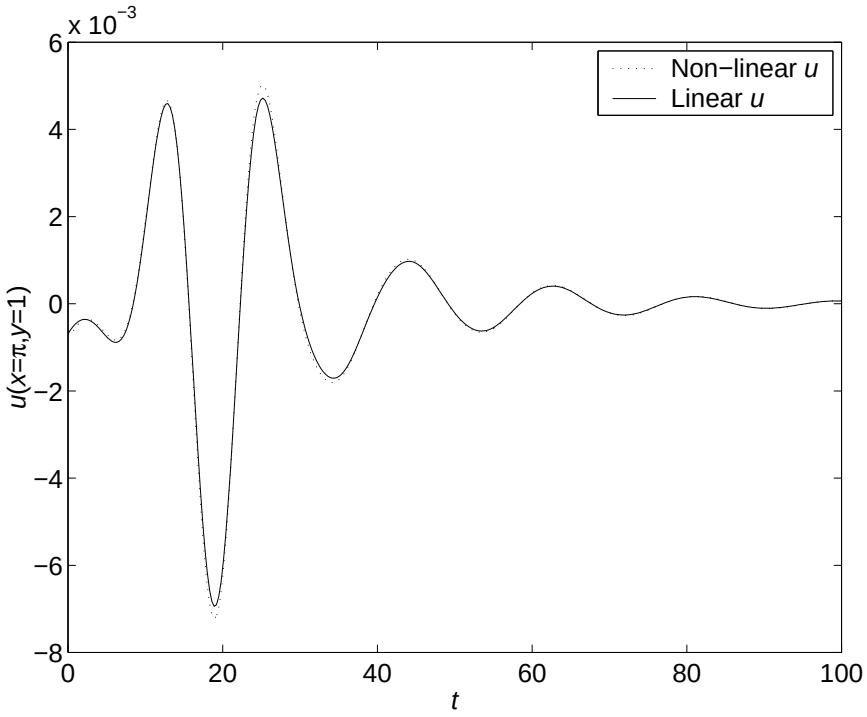

Figure 5.34: Case 1 u-Actuation LQR Wall Velocity at $x = \pi$ vs Time t, from Initial Conditions $\mathcal{X}_{Worst}$ Scaled to Energy E_{C1}

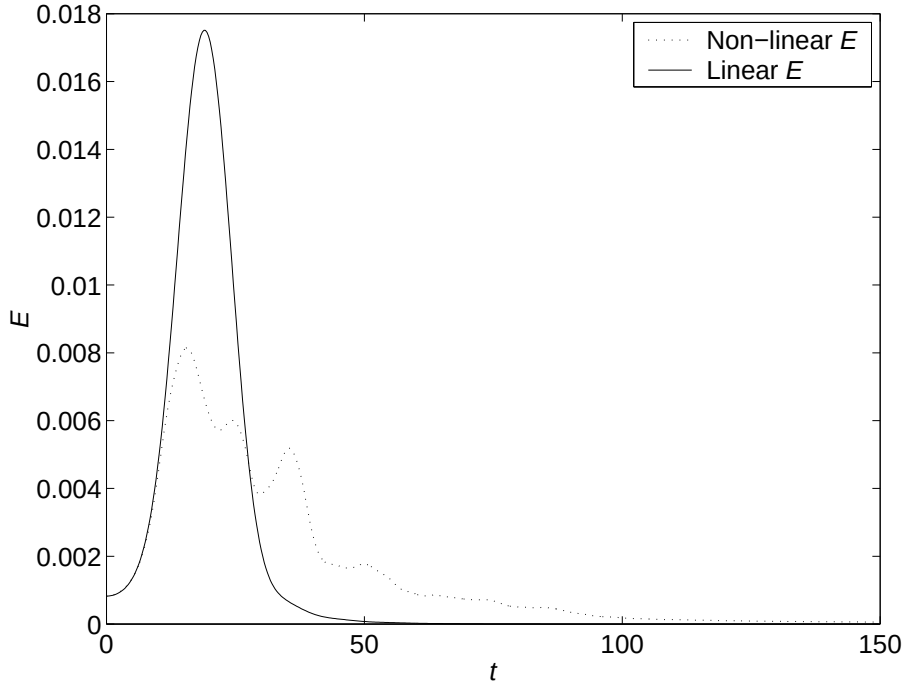

Figure 5.35: Case 1 u-Actuation LQR Transient Energy E vs Time t, from Initial Conditions $\mathcal{X}_{Worst}$ Scaled to Energy $10^4 E_{C1}$

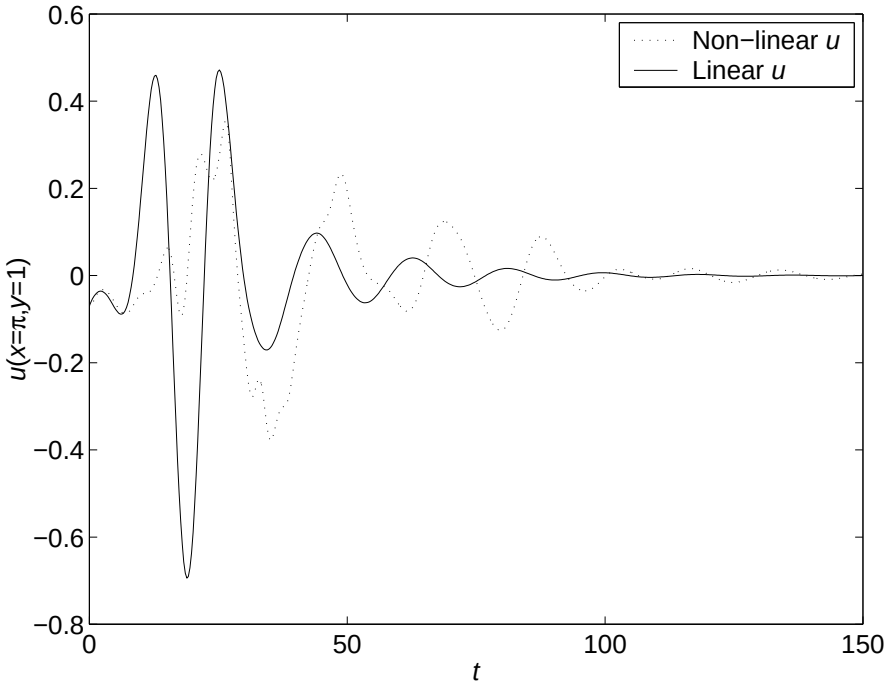

Figure 5.36: Case 1 u-Actuation LQR Wall Velocity at $x = \pi$ vs Time t, from Initial Conditions $\mathcal{X}_{Worst}$ Scaled to Energy $10^4 E_{C1}$

5.5 Conclusions

Section 5.2 described the implementation of simultaneous wall-normal and tangential actuation in the state-space model of linearised plane Poiseuille flow, by the addition of velocity and vorticity basis functions with non-zero derivatives at the walls.

Section 5.3 presented results from investigations of the model dynamics and synthesis of LQR controllers for case 1 with u-actuation and case 2 with w-actuation. u-actuation results in a less controllable plant than v-actuation, since the basis functions are less 'full', and similarly w-actuation results in less controllable modes when the velocity is non-zero. The singular values for u- and w-actuation converged with discretisation N as for v-actuation, and the residuals from the LQR ARE calculation were acceptable, other than for very high control w-actuation.

Difficulties were encountered in the calculation of the diachronic transient energy bound θ and associated worst initial conditions. If the full set of system eigenvectors was used, gross oscillations were seen in the initial conditions for both case 1 with u-actuation and case 2 with w-actuation, for which the anti-aliasing procedure described in section 4.4.3 provided no remedy. However, reducing the set of eigenvectors to the slowest two-thirds in a procedure termed eigenvector truncation removed the oscillations. As a check the procedure was applied to the earlier v-actuation results, and little effect was seen on the diachronic transient energy bound. However, the initial conditions did change as a result of the procedure, and thus the control applied. It would therefore appear that although the

diachronic transient energy bound of a controlled system is effectively unique, the initial conditions which generate it and control magnitudes applied are not unique (i.e. the initial conditions vary outside of the range allowed by consistent normalisation). In support of this, Criminale et al. (1997, p66) show that any symmetric $\tilde{v}$ initial condition yields close to the three-dimensional open-loop diachronic transient energy bound. It is of interest that for case 2, the vorticity eigenvectors are larger than the velocity ones, but the initial conditions, which are composed of eigenvectors, has larger velocity than vorticity, indicating the possibility of ill-conditioning. Ill-conditioning may be inherent in non-modal growth, as the worst initial conditions combine modes which almost cancel one another.

The convergence of the u- and w-actuation diachronic transient energy bound calculation with discretisation N was found to be erratic, and only occurred for certain ranges of control weight r, in contrast to v-actuation which converges uniformly over r and quickly with N. u-actuation produces approximately double the diachronic transient energy bound that v-actuation does, although, if the results are valid, moderate control weight w-actuation leads to a smaller diachronic transient energy bound than v-actuation (40% less), and very low control weight w-actuation leads to a significantly smaller diachronic transient energy bound (one tenth). The provisos are that w-actuation requires eigenvector truncation, and even after truncation w-actuation initial vorticity, although small compared to velocity, is not smooth, and furthermore very low control weight w-actuation has poor ARE residuals. The poor behaviour of the diachronic transient energy bound eigensystem (5.26) for u- and w-actuation is worthy of further investigation.

Control weight values which did lead to reasonable diachronic transient energy bound convergence were selected, and the associated u- and w-actuation controllers were subject to closed-loop linear simulations. The linear simulations confirmed the convergence with discretisation N, and the transient energy as compared to v-actuation. Regarding the diachronic transient energy bound itself, linear simulations cannot substantiate the peak value, but rather can merely show if the supplied initial conditions will generate the expected value, and the simulations did so. The simulations showed that the u- and w-actuation controllers produced substantially higher control effort, fluid velocity and fluid displacement than the v-actuation controllers did. However, tangential u-actuation and w-actuation may be realised via different actuation technologies to wall-normal v-actuation, e.g. by mechanical rollers, which have no constraint on cumulative displacement, as compared to fluid transpiration by jets which require a source of fluid. This advantage may outweigh the higher case 1 diachronic transient energy bound, and generally higher control effort, that results from tangential actuation.

Section 5.4 described non-linear simulations of u-actuation on case 1. Small perturbations showed that the linear simulation results were validated, and large perturbations showed that the flow field saturated but was stabilized, as it was for v-actuation.

In summary, this chapter has described the novel addition of tangential actuation to the wall-normal actuation of the state-space model of linearised plane Poiseuille flow developed in chapter 2. Tangential actuation was seen to result in lower controllability than wall-normal actuation, and suffer from numerical difficul-

ties. The calculation of initial conditions which yield the largest transient energy growth suffered from poor convergence with wall-normal discretisation, and the initial conditions themselves were prone to oscillations, which were ameliorated by eigenvector truncation. These difficulties indicate the need for further work in this area. The first test case yielded larger transient energy growth with tangential actuation than with wall-normal actuation, but the second yielded significantly lower worst transient energy growth with tangential actuation, and thus better performance in terms of avoiding transition to turbulence, although this is subject to caveats arising from the numerical difficulties which merit further investigation. Linear simulations showed that larger velocities and displacements of transpiration fluid were required for tangential actuation than for wall-normal actuation, although tangential actuation may be implemented with rollers, which have no constraint on fluid displacement, unlike the reservoirs mooted for wall-normal actuation. Closed-loop simulations using a non-linear finite-volume model of plane Poiseuille flow validated the linear results from small initial conditions, and showed saturation with continued stabilization from larger initial conditions.

Chapter 6

LMI Controller Synthesis and Simulations

6.1 Introduction

The diachronic transient energy bound θ (4.36) of a stable linear system is the largest transient energy it attains from unit initial energy. Even though the system is stable, θ may be large, and if the system is the result of linearisation the energy growth may take the non-linear system outside its domain of attraction, as noted by Hinrichsen and Pritchard (2005, p648). Bewley and Liu (1998) use θ as a performance index on systems for fluid flow control such as that described in chapter 2. An upper bound for θ has been derived by Whidborne et al. (2004), who also provide linear matrix inequality (LMI) methods for synthesizing state feedback controllers which minimise the upper bound, but without any constraint on control effort. Whidborne et al. (2005) and Whidborne and McKernan (2006) have derived output feedback controllers which minimise θ itself, using advanced optimisation techniques. Hinrichsen et al. (2002) and Boyd et al. (1994, p.89) have derived a constraint on the rate of transient energy decay.

θ is related to the orthogonality of the system eigenvectors, for example a normal system cannot have θ above unity as shown by Whidborne et al. (2004). Trefethen and Embree (2005, p48) note that there are many possible measures of non-normality. How θ depends upon system non-normality has been investigated via pseudospectra, for example by Reddy et al. (1993) and Trefethen and Embree (2005), although direct correlations between the degree of system eigenvector non-normality and θ for controlled linearised plane Poiseuille flow are limited. In Bewley and Liu (1998, figs 2(b) and 10), the control does not appear to have made the modes significantly more orthogonal, and similarly in this thesis in figures 4.29 and 4.30.

The equations derived by Lorenz (1963) are a small coupled set of non-linear differential equations representing a simplified model of fluid convection as ordinary rather than partial differential equations, and they exhibit deterministic but non-periodic chaotic behaviour. In the context of fluid flow control under investigation in this thesis, the transition of the Lorenz system from a steady linearly unstable state to bounded chaotic behaviour may be seen as an analogue of the

transition from laminar flow to turbulent flow, for example as used by Bewley (1999). As for the linearised Poiseuille flow system, the eigenvectors of the linearised Lorenz system are non-normal, so the system exhibits transient energy growth. Since the Lorenz equations do not require discretisation, the size of the Lorenz model is significantly smaller than that of the plane Poiseuille flow model, and thus requires much smaller computational resources for controller synthesis and simulation, bearing in mind that the solution of LMI systems requires large quantities of memory.

The aims of this chapter are to investigate the synthesis of controllers which minimize upper bounds on the diachronic transient energy bound θ and peak control effort, and further, by comparison with the performance of these controllers, to assess standard LQR controllers in reducing θ for fluid control systems. Since LQR controllers include control effort in their cost functions, a constraint on peak control effort will be incorporated into the LMI controller synthesis system. The relationship between the non-normality of the system eigenvectors and θ will also be examined. The plane Poiseuille model of chapter 2 is extremely complex and of high order, and so the linearised Lorenz system is used to obtain initial results.

The organisation of this chapter is as follows: section 6.2 describes a method of extending Whidborne et al. (2004) LMI based controllers, which minimise an upper bound on θ, to use limited peak control effort. Section 6.3 introduces and linearises the Lorenz equations and subsequently compares the performance of LMI controllers with LQR ones when applied to the linearised Lorenz system. This section also investigates aspects of the relationship between system normality and θ as control effort varies, and subsequently describes the results of simulations of the controllers applied to the full Lorenz equations. Section 6.4 compares the transient performance of LMI controllers with LQR ones when applied to the linearised plane Poiseuille flow system. This section also describes the results of simulations of the LMI controllers applied to the full flow equations. Finally section 6.5 draws conclusions regarding LMI controller synthesis, and LMI and LQR controller performance on the full and linearised Lorenz and plane Poiseuille flow systems, and the correlation between non-normality and diachronic transient energy bound θ.

6.2 Synthesis of LMI Controllers

6.2.1 Transient Growth

From chapter 4 the transient energy (4.34, repeated here)

$$E(t) = \mathcal{X}^T(t)\mathcal{Q}\mathcal{X}(t) \tag{6.1}$$

is defined as measure of how far the system state is from the equilibrium point. For the remainder of this chapter it is convenient to transform the state variables such that

$$E(t) = \hat{\mathcal{X}}^T(t)\hat{\mathcal{X}}(t) \tag{6.2}$$

where $\hat{\mathcal{X}}(t) = \mathcal{Q}^{1/2}\mathcal{X}(t)$. Hereafter the subscript $\hat{}$ will also be dropped for convenience. The synchronic transient energy bound is largest possible value at time t, after starting from unit initial transient energy but otherwise unknown state variables $\mathcal{X}(0)$ (4.35, repeated here)

$$\epsilon(t) = \max_{E(0)=1} E(t) \tag{6.3}$$

and the diachronic transient energy bound θ is defined as the largest synchronic transient energy bound possible over all time (4.36, repeated here)

$$\theta = \max_{t \geq 0} \epsilon(t) \tag{6.4}$$

Whidborne et al. (2004) demonstrate that there is a lower bound of unity on θ, since $\epsilon(t = 0) = 1$, and an upper bound is given by an ellipsoid through the initial conditions which bounds the trajectory in phase space. As the energy is represented by the squared distance from the origin (6.2), a bound on the largest energy growth possible is the ratio of the squared shortest ellipsoid semi-axis length to the squared longest semi-axis length.

If $\mathcal{F} = \mathcal{X}^T\mathcal{P}\mathcal{X}$ is a Lyapunov function i.e. $\mathcal{P}$ is positive definite ($\mathcal{P} = \mathcal{P}^T$ and $\mathcal{X}^T\mathcal{P}\mathcal{X} > 0 \, \forall \mathcal{X} \neq 0$ or more succinctly $\mathcal{P} > 0$) and

$$\mathcal{P}\mathcal{A} + \mathcal{A}^T\mathcal{P} < 0 \tag{6.5}$$

then $\dot{\mathcal{F}} < 0$ on all trajectories (e.g. p210-214 Jacobs, 1974), and all trajectories $\mathcal{X}(t)$ which begin inside or on the ellipsoid $\mathcal{M}^T\mathcal{P}\mathcal{M} = \mathcal{F}_0, \mathcal{M} \in \mathbb{R}^n$, i.e. $\mathcal{X}_0^T\mathcal{P}\mathcal{X}_0 \leq \mathcal{F}_0$, remain within it.

Thus $\mathcal{M}^T\mathcal{P}\mathcal{M} = \mathcal{F}_0 = \mathcal{X}_0^T\mathcal{P}\mathcal{X}_0$ is a trajectory bounding ellipsoid through the initial conditions. The squared lengths of the semi-axes are the extremal values of $\mathcal{M}^T\mathcal{M}$, subject to $\mathcal{M}^T\mathcal{P}\mathcal{M} - \mathcal{F}_0 = 0$. By the method of Lagrange multipliers, the extremes are given by

$$\frac{\partial \left(\mathcal{M}^T\mathcal{M} + l \left(\mathcal{M}^T\mathcal{P}\mathcal{M} - \mathcal{F}_0 \right) \right)}{\partial \mathcal{M}} = 0 \tag{6.6}$$

where l is a Lagrange multiplier. Hence the eigenproblem $2\mathcal{M}_i + 2l_i\mathcal{P}\mathcal{M}_i = 0$ or $\mathcal{P}\mathcal{M}_i = \lambda_i(\mathcal{P})\mathcal{M}_i$. So $\mathcal{F}_0 = \lambda_i(\mathcal{P})\mathcal{M}_i^T\mathcal{M}_i$ and the squared length of the ith semi-axis of the ellipsoid is $\mathcal{F}_0/\lambda_i(\mathcal{P})$. Therefore an upper bound on the maximum transient growth is given by $\theta_u = \lambda_{max}(\mathcal{P}) / \lambda_{min}(\mathcal{P})$.

6.2.2 Closed Loop Transient Growth

Whidborne et al. (2004) have established conditions for the existence of a monotonically decreasing transient energy controller, and characterised all such controllers. The work also proposes a linear matrix inequality (LMI) method to find controllers which minimise an upper bound θ_u on the diachronic transient energy bound. The linearised Lorenz equations and case 2 plane Poiseuille flow fail to meet the monotonically decreasing transient energy conditions, and thus only controllers which minimise θ_u are considered here.

Expanding $\mathcal{A}$ as $\mathcal{A}+\mathcal{B}\mathcal{K}$ in (6.5), to represent closed loop feedback control $\mathcal{U}=\mathcal{K}\mathcal{X}$ of $\mathcal{A}$ via input matrix $\mathcal{B}$, gives

$$\mathcal{P}\mathcal{A}+\mathcal{P}\mathcal{B}\mathcal{K}+\mathcal{A}^T\mathcal{P}+\mathcal{K}^T\mathcal{B}^T\mathcal{P}<0 \tag{6.7}$$

Now if matrix $\mathcal{M}$ is positive definite, $\mathcal{M}>0$, a congruence transformation $\mathcal{S}\mathcal{M}\mathcal{S}^T$ leaves $\mathcal{S}\mathcal{M}\mathcal{S}^T>0$ (Skogestad and Postlethwaite, 2005, p481). Thus, transforming (6.7) by $\mathcal{P}^{-1}$, noting $\mathcal{P}=\mathcal{P}^T$, yields

$$\mathcal{A}\mathcal{P}^{-1}+\mathcal{B}\mathcal{K}\mathcal{P}^{-1}+\mathcal{P}^{-1}\mathcal{A}^T+\mathcal{P}^{-1}\mathcal{K}^T\mathcal{B}^T<0 \tag{6.8}$$

which is a bilinear matrix inequality in $\mathcal{P}^{-1}$ and $\mathcal{K}$. Substituting $\mathcal{S}=\mathcal{P}^{-1}$ and $\mathcal{Z}=\mathcal{K}\mathcal{S}$ (Skogestad and Postlethwaite, 2005, p480) results in an equivalent linear matrix inequality for $\mathcal{S}$ and $\mathcal{Z}$

$$\mathcal{A}\mathcal{S}+\mathcal{S}\mathcal{A}^T+\mathcal{B}\mathcal{Z}+\mathcal{Z}^T\mathcal{B}^T<0 \tag{6.9}$$

Since $\lambda(\mathcal{P})=1/\lambda(\mathcal{S})$, the upper bound becomes $\theta_u=\lambda_{max}(\mathcal{S})/\lambda_{min}(\mathcal{S})$. Now if $\mathcal{M}\geq\mathcal{N}$, then for their ordered eigenvalues $\lambda_i(\mathcal{M})\geq\lambda_i(\mathcal{N})$ (Horn and Johnson, 1985, p471). Thus the LMI $\mathcal{I}\leq\mathcal{S}\leq\gamma\mathcal{I}$ ensures that $\lambda_{min}(\mathcal{S})\geq 1$ and $\lambda_{max}(\mathcal{S})\leq\gamma$, so $\theta_u\leq\gamma$. Hence a controller that minimises the upper bound θ_u is given by a solution to the LMI generalized eigenvalue problem

$$\begin{aligned}&\min\gamma\\&s.t.\\&\mathcal{I}\leq\mathcal{S}\leq\gamma\mathcal{I},\mathcal{A}\mathcal{S}+\mathcal{S}\mathcal{A}^T+\mathcal{B}\mathcal{Z}+\mathcal{Z}^T\mathcal{B}^T<0\end{aligned} \tag{6.10}$$

where the resulting state feedback controller is given by $\mathcal{K}=\mathcal{Z}\mathcal{S}^{-1}$.

6.2.3 Limited Control Effort

In addition, a limit on the expenditure of control effort can be set by simultaneously solving the LMI described by Boyd et al. (1994, p.103) and recommended by Hinrichsen et al. (2002).

A norm on the control input $\mathcal{U}=\mathcal{K}\mathcal{X}$ is

$$\max_{t\geq 0}\|\mathcal{U}\|^2=\max_{t\geq 0}\left\|\mathcal{Z}\mathcal{S}^{-1}\mathcal{X}(t)\right\|^2 \tag{6.11}$$

If $\mathcal{S}$ and $\mathcal{Z}$ satisfy (6.10) and $\mathcal{X}(0)^T\mathcal{S}^{-1}\mathcal{X}(0)\leq 1$, then $\mathcal{X}$ remains on or inside the ellipsoid $\mathcal{M}^T\mathcal{S}^{-1}\mathcal{M}=1$ for all $t\geq 0$, since $\mathcal{M}^T\mathcal{P}\mathcal{M}=1$ is a trajectory bounding ellipsoid for all trajectories which start on or within it. Thus $\mathcal{X}^T\mathcal{S}^{-1}\mathcal{X}\leq 1$ and the maximum over t may be replaced by one over the ellipsoid in phase space

$$\max_{t\geq 0}\|\mathcal{U}\|^2\leq\max_{\mathcal{X}^T\mathcal{S}^{-1}\mathcal{X}\leq 1}\left\|\mathcal{Z}\mathcal{S}^{-1}\mathcal{X}\right\|^2 \tag{6.12}$$

Splitting $\mathcal{S}^{-1}$ into its square roots gives

$$\max_{t\geq 0}\|\mathcal{U}\|^2\leq\max_{\mathcal{X}^T\mathcal{S}^{-1/2}\mathcal{S}^{-1/2}\mathcal{X}\leq 1}\left\|\mathcal{Z}\mathcal{S}^{-1/2}\mathcal{S}^{-1/2}\mathcal{X}\right\|^2 \tag{6.13}$$

which is the square of an induced 2-norm on matrix $\mathcal{Z}\mathcal{S}^{-1/2}$. This norm is equal to the largest singular value of $\mathcal{Z}\mathcal{S}^{-1/2}$ (Skogestad and Postlethwaite, 2005, p533), thus

$$\max_{t\geq 0} \|\mathcal{U}\|^2 \leq \lambda_{max}\left(\mathcal{S}^{-1/2}\mathcal{Z}^T\mathcal{Z}\mathcal{S}^{-1/2}\right) \tag{6.14}$$

Thus $\lambda_{max}\left(\mathcal{S}^{-1/2}\mathcal{Z}^T\mathcal{Z}\mathcal{S}^{-1/2}\right)$ is an upper bound on the control effort $\|\mathcal{U}\|^2$. A constraint on the upper bound

$$\lambda_{max}\left(\mathcal{S}^{-1/2}\mathcal{Z}^T\mathcal{Z}\mathcal{S}^{-1/2}\right) \leq \nu^2 \tag{6.15}$$

implies

$$\mathcal{S}^{-1/2}\mathcal{Z}^T\mathcal{Z}\mathcal{S}^{-1/2} \leq \nu^2\mathcal{I} \tag{6.16}$$

i.e. by a congruence transformation

$$\mathcal{Z}^T\mathcal{I}/\nu^2\mathcal{Z} \leq \mathcal{S} \tag{6.17}$$

which can be enforced by a solution of the LMI

$$\begin{bmatrix} \mathcal{S} & \mathcal{Z}^T \\ \mathcal{Z} & \nu^2\mathcal{I} \end{bmatrix} \geq 0 \tag{6.18}$$

as shown by Boyd et al. (1994, p28), noting $\mathcal{I} > 0$ and $\mathcal{I}$ is invertible. The constraint on the initial conditions $\mathcal{X}(0)^T\mathcal{S}^{-1}\mathcal{X}(0) \leq 1$ can similarly be enforced by a solution of the LMI

$$\begin{bmatrix} 1 & \mathcal{X}(0)^T \\ \mathcal{X}(0) & \mathcal{S} \end{bmatrix} \geq 0, \tag{6.19}$$

as shown by Boyd et al. (1994, p28), noting $\mathcal{S} > 0$ and $\mathcal{S}$ is invertible. The constraint on the initial conditions $\mathcal{X}(0)^T\mathcal{S}^{-1}\mathcal{X}(0) \leq 1$ can be replaced by the constraint $\mathcal{X}(0)^T\mathcal{X}(0) \leq 1$, providing it is more restrictive. The sphere $\mathcal{M}^T\mathcal{M} = 1$ lies within the ellipsoid $\mathcal{M}^T\mathcal{S}^{-1}\mathcal{M} = 1$ if the shortest ellipsoid semi-axis $1/\sqrt{\lambda_{max}(\mathcal{S}^{-1})}$ is larger than or equal to one, i.e. $\lambda_{min}(\mathcal{S}) \geq \mathcal{I}$ or $\mathcal{S} \geq \mathcal{I}$. Thus the system of LMIs to be solved to restrict the control effort to ν^2 from initial conditions $\mathcal{X}(0)^T\mathcal{X}(0) \leq 1$ becomes

$$\mathcal{S} \geq \mathcal{I}, \begin{bmatrix} \mathcal{S} & \mathcal{Z}^T \\ \mathcal{Z} & \nu^2\mathcal{I} \end{bmatrix} \geq 0 \tag{6.20}$$

as per Boyd et al. (1994, p 103), and the complete LMI to stabilise the system, minimise the upper bound on the transient growth and limit the control effort becomes

$$\begin{aligned} &\min \gamma \\ &s.t. \\ &\mathcal{I} \leq \mathcal{S} \leq \gamma\mathcal{I}, \mathcal{A}\mathcal{S} + \mathcal{S}\mathcal{A}^T + \mathcal{B}\mathcal{Z} + \mathcal{Z}^T\mathcal{B}^T < 0 \\ &\begin{bmatrix} \mathcal{S} & \mathcal{Z}^T \\ \mathcal{Z} & \nu^2\mathcal{I} \end{bmatrix} \geq 0 \end{aligned} \tag{6.21}$$

where the resulting state feedback controller is given by $\mathcal{K} = \mathcal{Z}\mathcal{S}^{-1}$. Hinrichsen et al. (2002) and Boyd et al. (1994, p.89) have derived a constraint on the rate of transient decay, which could be simultaneously incorporated into this expression. Note that (6.21) cannot be solved using the Matlab LMI toolbox, to so do the inequalities given by $\mathcal{I} \leq \mathcal{S} \leq \gamma\mathcal{I}$ and

$$\begin{bmatrix} \mathcal{S} & \mathcal{Z}^T \\ \mathcal{Z} & \nu^2\mathcal{I} \end{bmatrix} \geq 0 \tag{6.22}$$

need to be modified to a strict inequality. The conservatism this introduces is very slight.

6.3 Example Problem - The Lorenz Equations

Although initially developed as a simple model of atmospheric convection, the Lorenz equations may be interpreted as the elementary one-dimensional behaviour of fluid whose density varies with temperature, in a torus in a vertical plane heated from below and cooled from above (Tritton, 1988, p246). Once steady fluid convection has been established (either clockwise or anticlockwise around the torus), for certain fluid parameters and a large enough or critical heating, perturbations in the system about the steady convection are linearly unstable, and furthermore the perturbations vary chaotically i.e. they are very sensitive to initial conditions and never repeat their behaviour periodically. Both the Lorenz and Poiseuille flow equations are derived from the Navier-Stokes equations, and both are non-linear and deterministic.

The analogy of the onset of chaotic behaviour in the Lorenz system with transition in plane Poiseuille flow follows if the steady but unstable convection represents steady laminar flow, and the critical heat flow represents the critical Reynolds number above which transition occurs, and if the chaotic convection is analogous to the chaotic nature of turbulence, noting that the simplified convection is not itself capable of being turbulent, since turbulence is a three-dimensional phenomenon over many length scales. This analogy justifies the investigation of control of the onset of chaotic behaviour in the Lorenz equations as a preliminary to the investigation of control of transition in Poiseuille flow. In particular, it justifies investigating the control of the transient energy growth of the linearised Lorenz equations by LMI controller synthesis, which requires far less computing resources than such control of linearised Poiseuille flow, since no discretisation is involved.

The equations derived by Lorenz (1963) represent simplified convection and may be cast as (Tritton, 1988, p394)

$$\begin{aligned} \dot{X}_1 &= -pX_1 + pX_2 \\ \dot{X}_2 &= UX_1 - X_2 - X_1X_3 \\ \dot{X}_3 &= -bX_3 + X_1X_2 \end{aligned} \tag{6.23}$$

where state variable X_1 represents fluid velocity, and X_2 and X_3 represent horizontal and vertical temperature gradients respectively. Parameter p is related

to the fluid properties, b is related to the geometry and U is related to the heat source. The equations have three steady-state solutions: $X_{1s} = X_{2s} = X_{3s} = 0$ (no convection) and $X_{1s} = X_{2s} = \pm (U_s - 1)^{1/2}, X_{3s} = U_s - 1$ (steady clockwise and anticlockwise convection respectively). After linearisation, the equations for small perturbations $\mathcal{X} = (x_1, x_2, x_3)^T$ about a non-zero steady-state solution are

$$\begin{aligned}
\dot{x}_1 &= -px_1 + px_2 \\
\dot{x}_2 &= (U_s - X_{3s})\, x_1 - x_2 - X_{1s}x_3 + X_{1s}\mathcal{U} \\
\dot{x}_3 &= X_{2s}x_1 + X_{1s}x_2 - bx_3
\end{aligned} \tag{6.24}$$

where input $\mathcal{U}$ is a small perturbation in the steady heat source U_s. The control problem is to determine a state feedback controller $\mathcal{U} = \mathcal{K}\mathcal{X}$, which will stabilise the plant, and minimise its worst transient growth, subject to a limit on control effort $\mathcal{U}^T\mathcal{U}$.

LQR controllers as described in section 4.2 are also synthesized, to enable comparison with the performance of the LMI controllers. For the purposes of controlling the linearised Lorenz equations, the LQR state weights $\mathcal{Q}$ are an identity matrix and the control weights $\mathcal{R}$ are the scalar r.

6.3.1 Simulations

The chaotic regime Lorenz parameters $p = 4, U_s = 48, b = 1$ as used by Bewley (1999) are employed, and yield the three eigenvalues $-6.66, 0.33 \pm 7.50\jmath$, upon linearisation of the system about steady clockwise convection.

LQR and LMI controllers are synthesized for a range of controller weights r and control effort limits ν, using the Matlab Control and LMI toolboxes, respectively. Although the LMI toolbox solves strict inequalities rather than the non-strict control effort inequality in 6.21, the consequences are minimal. Linear and nonlinear simulations are performed, using the `lsim` and `ode15s` functions, from the worst initial conditions as calculated using the eigensystem (4.41).

6.3.2 Results of Linear Simulations and Discussion

Figure 6.1 shows the transient behaviour of the linearised Lorenz equations controlled by LQR controllers with varying control weight r. At low control weight, i.e. high control effort, there is a large fast initial transient. At high control weight, i.e. low control effort, there is a slower and moderately sized transient. In between there is an optimum control weight which results in the smallest transient. This is apparent in figure 6.2 which shows that the diachronic transient energy bound θ plotted against LQR control weight r is not monotonic. The lowest diachronic transient energy bound occurs at a control weight $r \approx 1$. The upper bound on diachronic transient energy bound θ_u is also plotted, and is a reasonably close bound at high control weights (low control effort), but poor at low control weights.

Figure 6.3 shows the transient behaviour of the linearised Lorenz equations controlled by LMI controllers with varying control upper bound limit ν. At high control limit there is a very fast but small magnitude initial transient. At low control limit there is a slow transient with a moderately sized maximum perturbation.

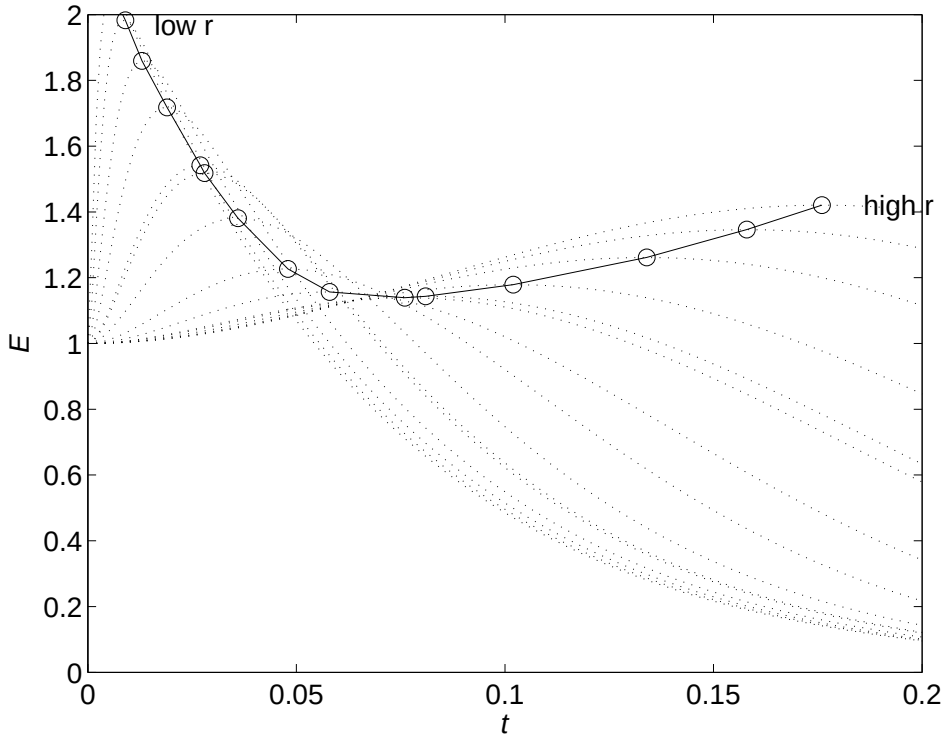

Figure 6.1: Transient Behaviour of the Linearised Lorenz Equations with Varying LQR Control Weight (dotted). Peak Transients are also shown (solid).

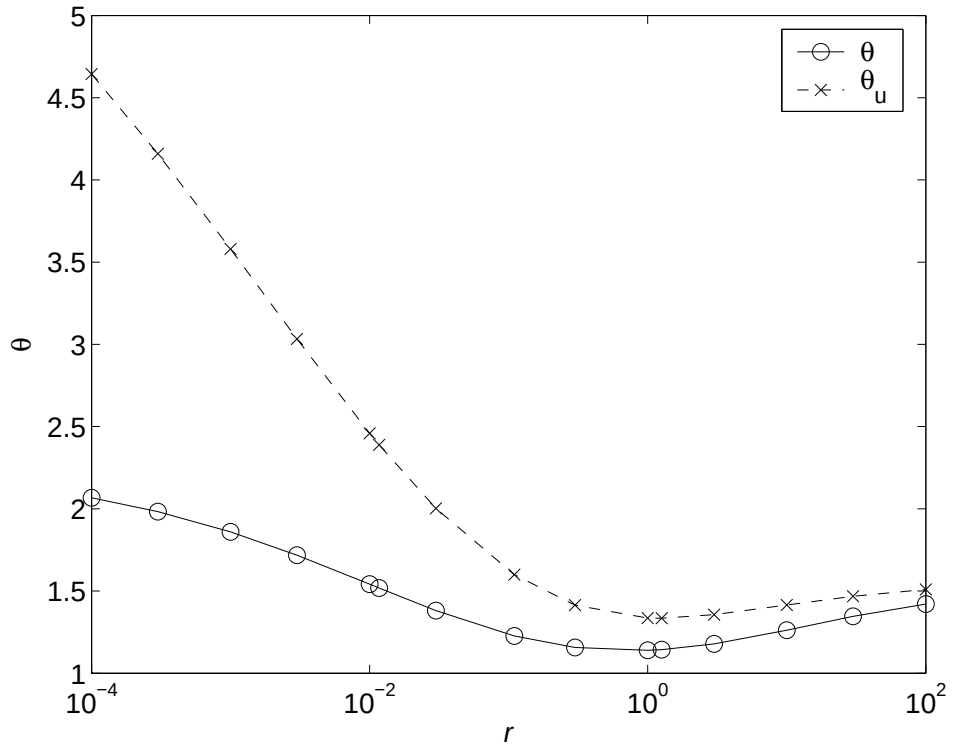

Figure 6.2: Diachronic Transient Energy Bound θ of the Linearised Lorenz Equations vs LQR Control Weight r

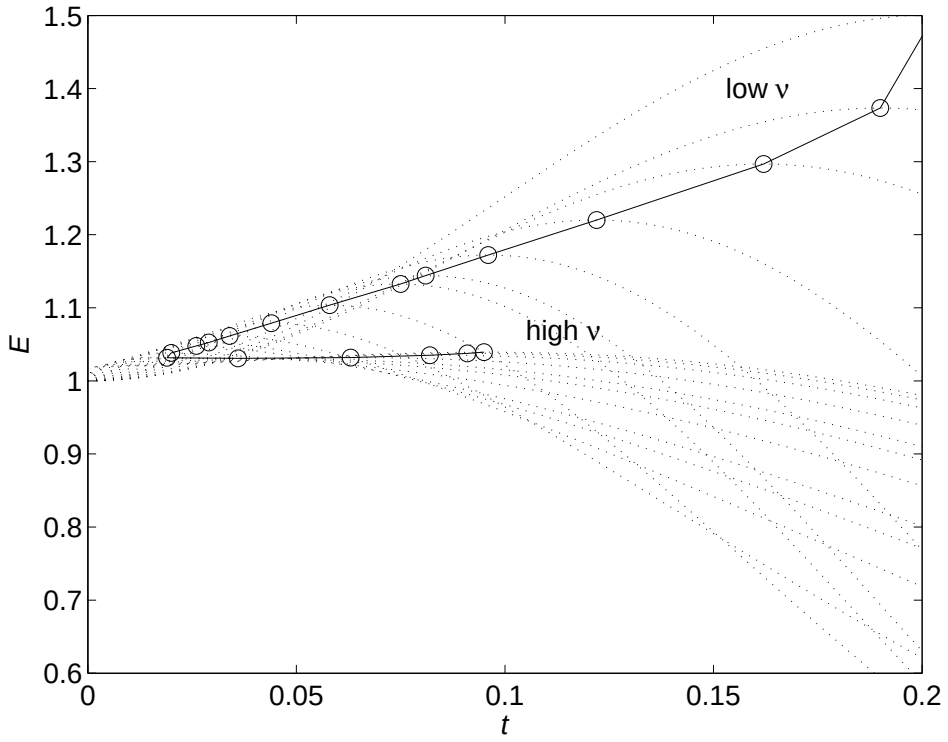

Figure 6.3: Transient Behaviour of Linearised Lorenz Equations for a Range of LMI Control Limits (dotted) with Peak Transients (solid).

The diachronic transient energy bound plotted against LMI control limit is shown in figure 6.4. The lowest diachronic transient energy bound occurs at a control limit $\nu^2 \approx 10^4$. The upper bound on diachronic transient energy bound θ_u is also plotted, and, as for the LQR case, is a close bound only at low control effort.

Figure 6.5 shows diachronic transient energy bound versus peak control effort for both LMI and LQR controllers. At low control effort both controllers have a similar value. The LQR controller reaches its minimum near $\max_{t\geq 0}(\mathcal{U}^T\mathcal{U}) = 1$, and then has an increasing value with control effort, as the control is causing the peak. However, the LMI controller continues to produce smaller diachronic transient energy bound for increasing control effort, until a shallow minimum near $\max_{t\geq 0}(\mathcal{U}^T\mathcal{U}) = 10^2$. The very similar transient behaviour of LQR and LMI controllers, with $\max_{t\geq 0}(\mathcal{U}^T\mathcal{U}) = 1$ and from their worst initial conditions, is apparent in figure 6.6. Figure 6.7 shows the transient behaviour of LQR and LMI controllers with $\max_{t\geq 0}(\mathcal{U}^T\mathcal{U}) = 10^2$. The LMI controller produces a transient perturbation around 3% above unity, much less that of the LQR controller (52%), although the overall perturbation lasts at least twice as long. How the low LMI transient is achieved is shown in figure 6.8, where for the same initial negative peak control effort ($\mathcal{U}(0) = -10$), the LMI controller is able to deliver a faster positive control effort.

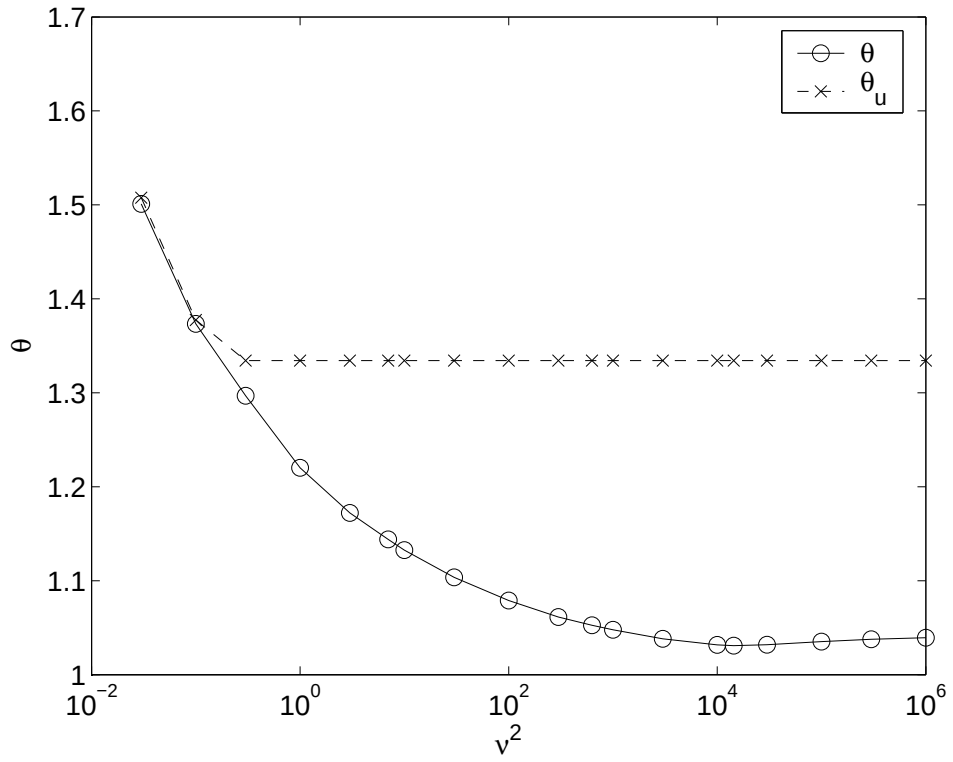

Figure 6.4: Diachronic Transient Energy Bound θ of Linearised Lorenz Equations vs LMI Control Limit ν^2

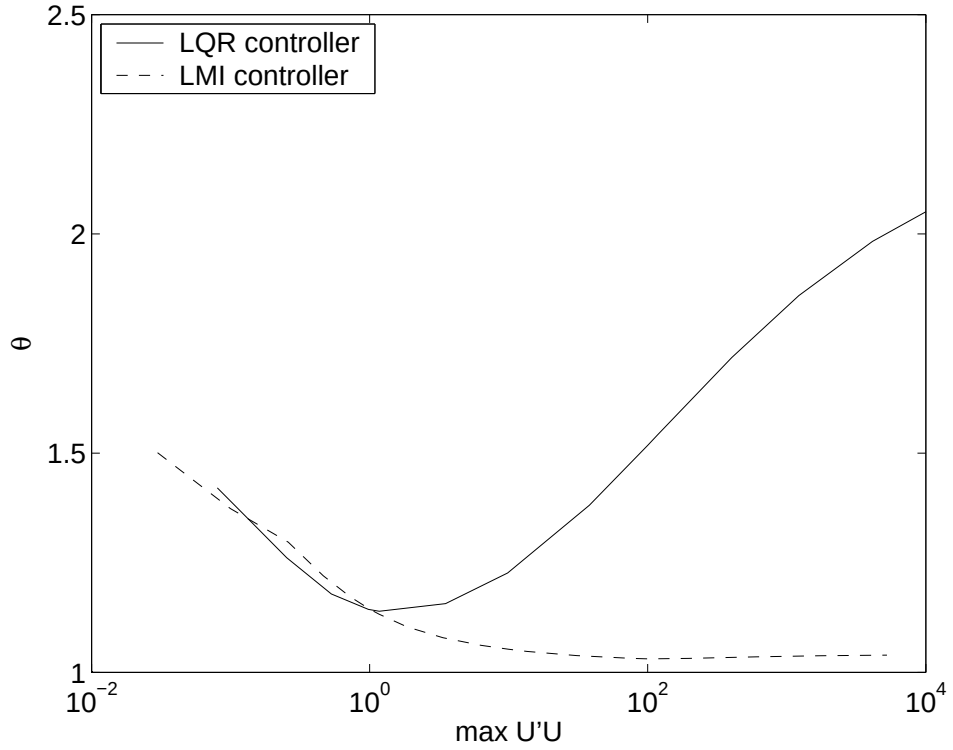

Figure 6.5: Diachronic Transient Energy Bound vs Maximum Control Effort for LQR and LMI Controllers acting on the Linearised Lorenz Equations

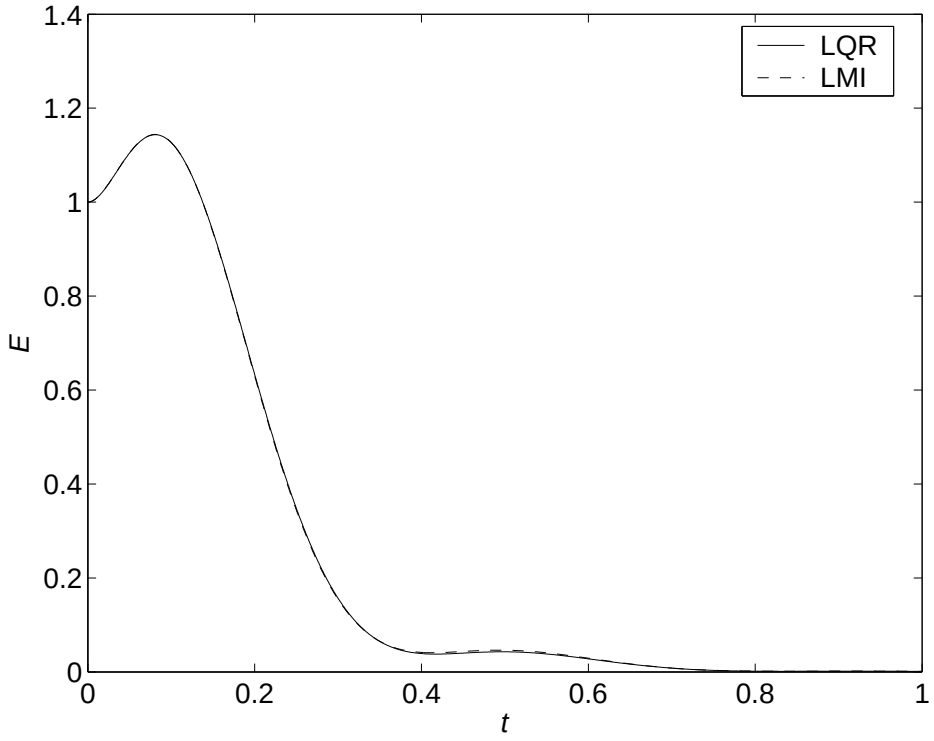

Figure 6.6: Transient Behaviour of the Linearised Lorenz Equations with Low Effort LQR and LMI Controllers, $\max_t(\mathcal{U}^T\mathcal{U}) = 1$

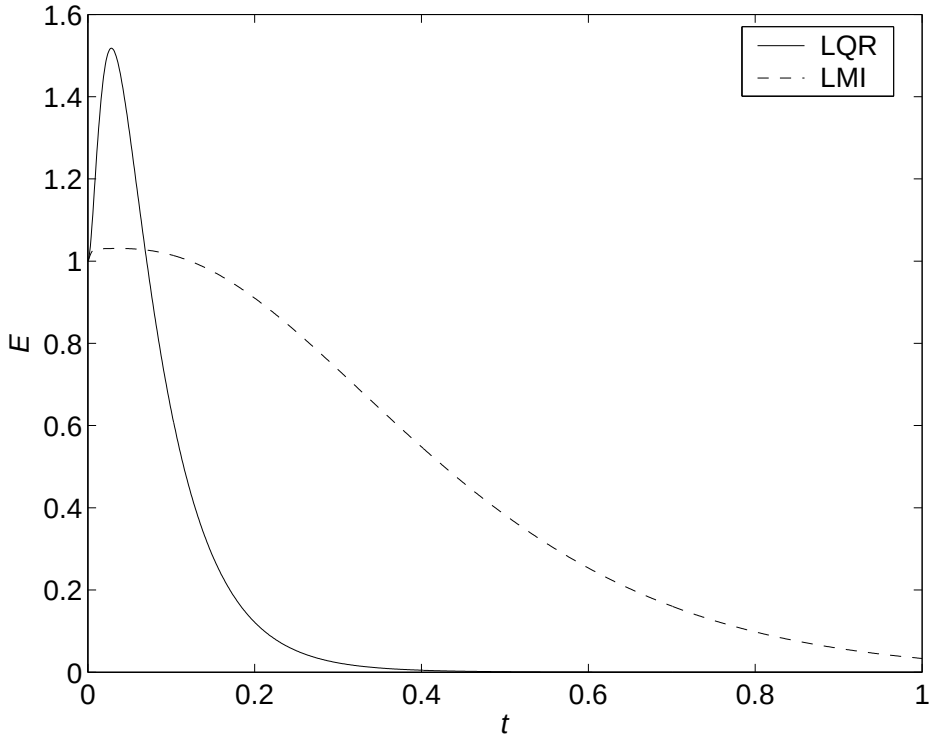

Figure 6.7: Transient Behaviour of the Linearised Lorenz Equations with High Effort LQR and LMI Controllers $\max_t(\mathcal{U}^T\mathcal{U}) = 100$

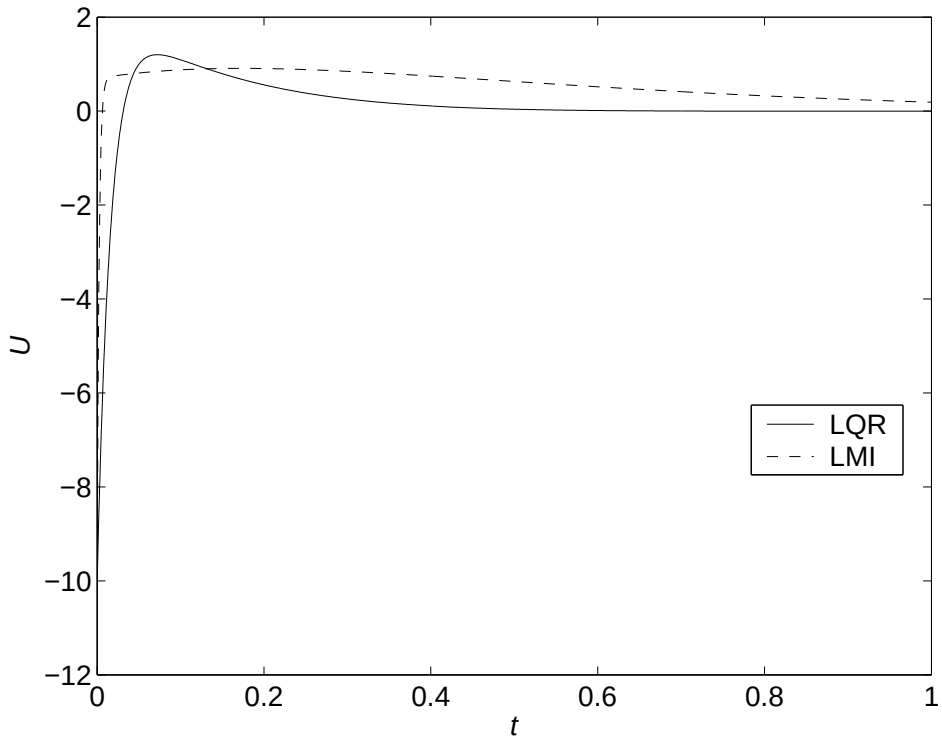

Figure 6.8: High Effort LQR and LMI Control, $\max_t(\mathcal{U}^T\mathcal{U}) = 100$, acting on the Linearised Lorenz Equations

6.3.3 Investigation of Diachronic Transient Energy Bound θ, as Determined by Eigenvector Non-normality and Eigenvalues

To investigate the relationship between the non-normality of the system eigenvectors and the transient growth, the closed-loop system dissimilar eigenvector dot products $(\psi_i \cdot \psi_j)$ and diachronic transient energy bound are plotted against LMI control limit in figure 6.9. The similar eigenvector dot products $(\psi_i \cdot \psi_i)$ are unity. For the current system, two dissimilar dot products are identical. It is evident that the diachronic transient energy bound does not correlate with the maximum dissimilar eigenvector dot product, and the same is true of the LQR controller. In particular, the minimum diachronic transient energy bound does not correspond with the lowest maximum dot product. The reason can be inferred from the expression for transient energy in modal components (4.54), as derived in section 4.3.1, repeated here

$$E(t) = \sum_{i=1}^{N} c_i^T c_i e^{\left(\lambda_i^T + \lambda_i\right)t} + \sum_{i=1}^{N} \sum_{j=1}^{N, j \neq i} c_i^T c_j (\psi_i \cdot \psi_j) e^{\left(\lambda_i^T + \lambda_j\right)t} \tag{6.25}$$

As noted in section 4.3.1, the terms of the first summation of (6.25)

$$\sum_{i=1}^{N} c_i^T c_i e^{\left(\lambda_i^T + \lambda_i\right)t} \tag{6.26}$$

are the modal terms. They are positive for all c_i and decay monotonically, and cannot lead to any energy increase. The terms of the second summation

$$\sum_{i=1}^{N} \sum_{j=1}^{N, j \neq i} c_i^T c_j (\psi_i \cdot \psi_j) e^{\left(\lambda_i^T + \lambda_j\right)t} \tag{6.27}$$

are non-modal. They decay in magnitude, at intermediate rates to the first summation, and can lead to energy increase when either they are negative, that is if $c_i^T c_j (\psi_i \cdot \psi_j)$ is negative or they oscillate, that is if $\Im(\lambda_i^T + \lambda_j) \neq 0$.

As stated in section 4.3.1, if the system eigenvectors cannot be made accurately orthogonal by the introduction of control, selecting instead a system with the lowest dot products $(\psi_i \cdot \psi_j)$ will not necessarily lead to the lowest diachronic transient energy bound due to the presence of the other factors $c_i^T c_j$ and $e^{\left(\lambda_i^T + \lambda_j\right)t}$ in (6.25), and since, for the bound, c_i are selected to maximise the transient energy growth, within the overall constraint $E(0) = (c_0, \ldots, c_N)^T \Psi^T \Psi (c_0, \ldots, c_N) = 1$.

A closed form solution for the diachronic transient energy bound θ from (6.25) in terms of ψ_i and λ_i is elusive, even for a 2×2 system, the smallest stable system capable of $\theta > 1$, although Plischke (2005, p92) presents an expression for the synchronic transient energy bound in terms of the entries of 2×2 upper triangular system matrices. To investigate further, figure 6.10 shows the effect of independently varying system normality and eigenvalue speed, on the synchronic transient energy bound against time and its peak value (the diachronic transient

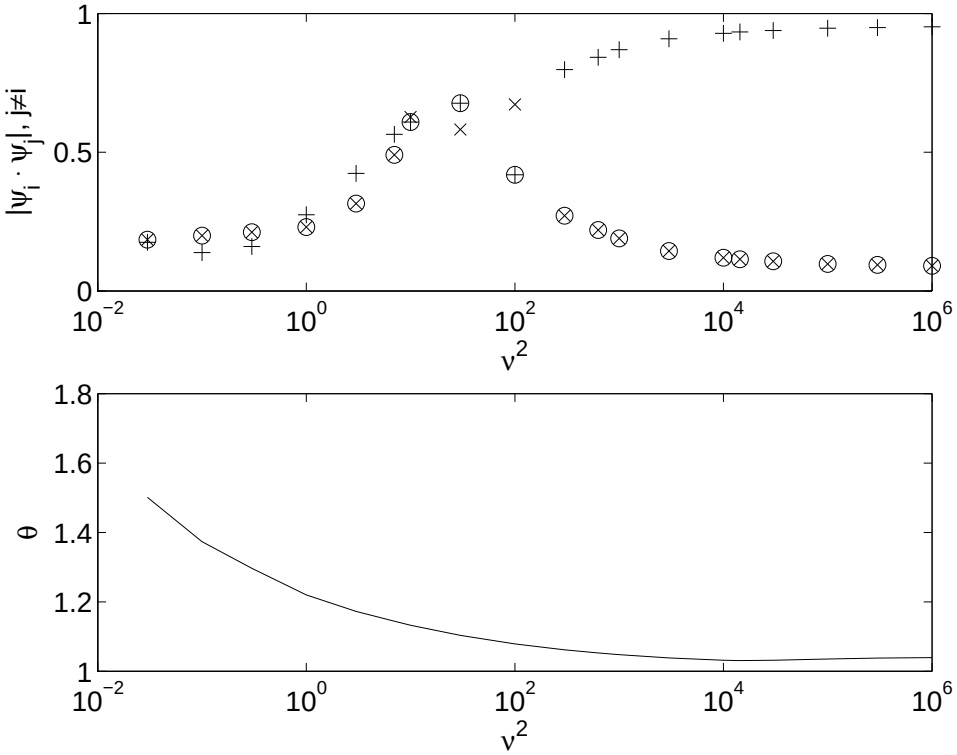

Figure 6.9: Dissimilar Eigenvector Dot Product and θ vs LMI Control Limit ν^2, for the Linearised Lorenz Equations

energy bound), for a synthetic system. The synthetic system is $\mathcal{A} = \Psi\Lambda\Psi^{-1}$ and has stable baseline eigenvalues $\Lambda = -1, -2, -3$ and eigenvectors

$$\Psi = \begin{pmatrix} a, & b, & b \\ b, & a, & b \\ b, & b, & a \end{pmatrix} \tag{6.28}$$

where $a = \delta + 1/\sqrt{(3)}$ and $b = \sqrt{(1-a^2)/2}$, i.e. the eigenvectors are each perturbed in different directions about direction $1, 1, 1$ by a small amount δ and normalised. The synchronic transient energy bound is calculated using eigensystem (4.41). For the baseline curve (shown solid) $\delta = \sin(\alpha\pi), \alpha = 0.001$. As α is increased in steps of 0.001, the system becomes more normal, and the curve of synchronic transient energy bound against time falls, and thus also the maximum value, the diachronic transient energy bound (circled) also falls. Alternatively, as the baseline eigenvalues Λ are made slower by incrementing them to $\Lambda + k$ by $k = 0.1, 0.2, 0.3, 0.4$, the synchronic transient energy bound curve peaks later and also increases in magnitude, and thus the diachronic transient energy bound increases. If the eigenvalues Λ are made slower by scaling them to Λk by $k = 0.9, 0.8, 0.7, 0.6$, the synchronic transient energy bound curve peaks later but does not change appreciably in magnitude. This is to be expected as such scaling merely scales the time axis.

The figure shows if non-normality can be reduced independently of altering the system eigenvalues, then the diachronic transient energy bound may fall, but if the

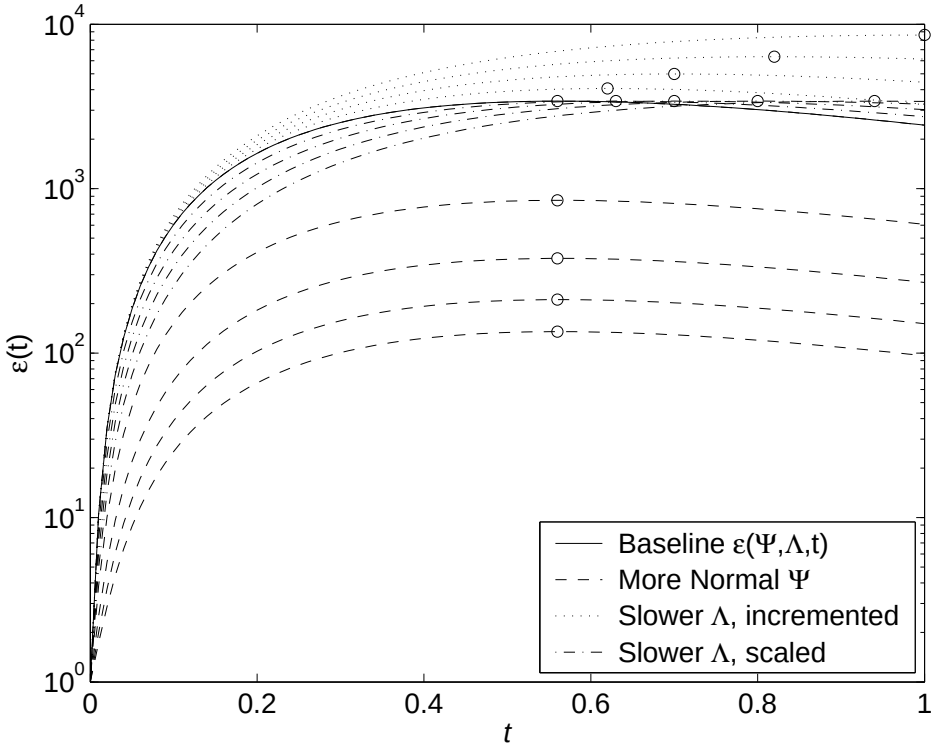

Figure 6.10: Variation Synchronic Transient Energy Bound ϵ vs Time t, and Diachronic Transient Energy Bound (circled), with Non-normality and Speed, for a Synthesized System $\mathcal{A} = \Psi\Lambda\Psi^{-1}$

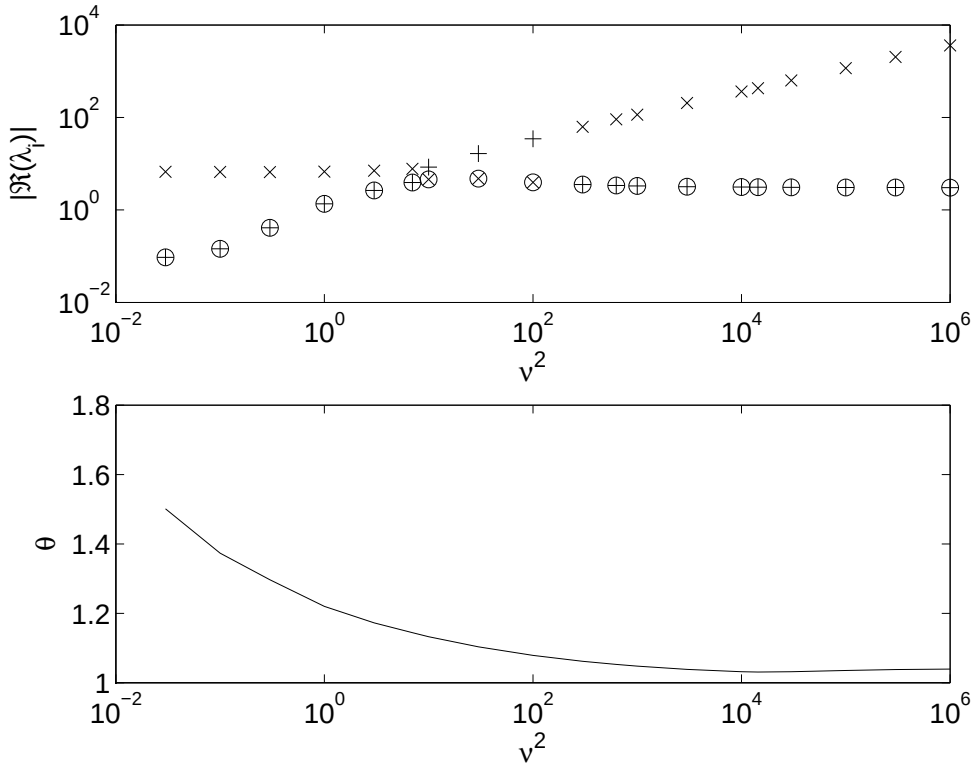

Figure 6.11: Lorenz System Eigenvalue Magnitude and θ vs LMI Control Limit

system eigenvalues become slower for any reason, the diachronic transient energy bound may rise.

For the Lorenz system, the diachronic transient energy bound correlates reasonably well with the inverse of the speed of the slowest eigenvector, as shown in figure 6.11. Slow slowest eigenvectors occur in conjunction with large diachronic transient energy bound, and fast slowest eigenvectors occur with small diachronic transient energy bound. This correlation is better than that shown for non-normality in figure 6.9, indicating that for the Lorenz system controlled with limited effort, eigenvalue speed is possibly the critical factor in determining diachronic transient energy bound, rather than non-normality, although some non-normality must be present for the diachronic transient energy bound to be above one.

6.3.4 Results of Non-Linear Simulations and Discussion

Figure 6.12 shows the transient perturbation growth of the full Lorenz equations from an arbitrary initial condition $\mathcal{X} = (10, 0, 0)^T$, with respect to the linearisation point of stable clockwise convection, and figure 6.13 shows the trajectories in phase space. For the first 3 seconds the state spirals in towards one attractor, and then commences to orbit non-periodically about both. LMI and LQR controllers (both synthesised such that $\max_{t\geq 0, \|x(0)\|=1}(\mathcal{U}^T\mathcal{U}) = 10^2$ in section 6.3.2) are switched on at $t = 3s$ and stabilise the system. In this instance, the LMI controller is able to do this with a lower transient, and a more direct trajectory, albeit with a greater

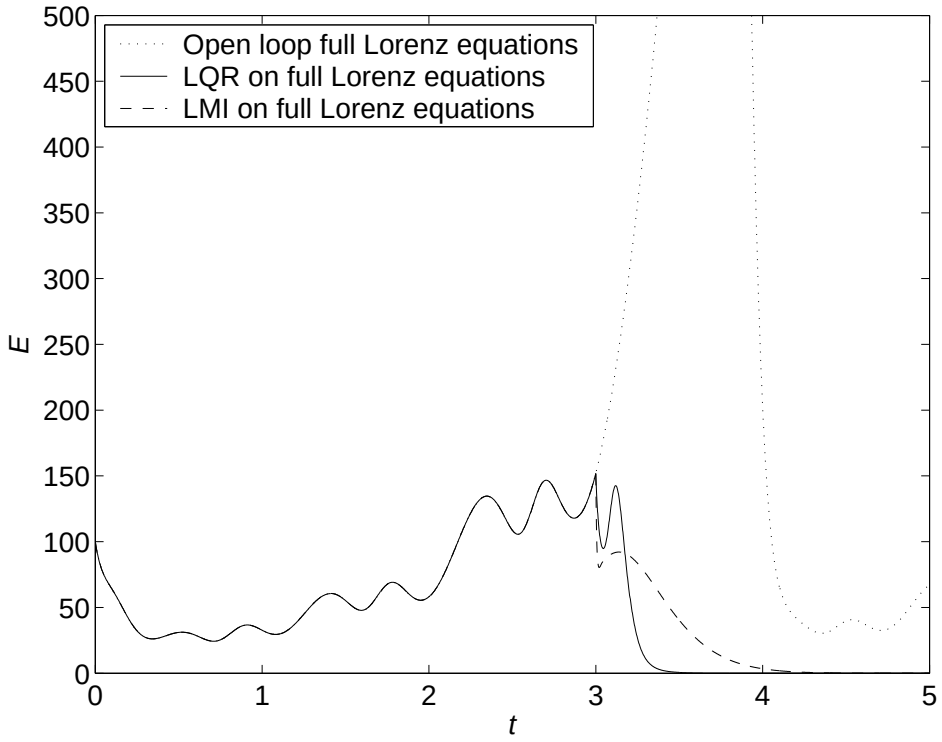

Figure 6.12: Effect of LQR and LMI Controllers on Non-linear Lorenz Equation Perturbation. Controllers Switched on at $t = 3.0$

control effort.

Neither controller is able to stabilise the Lorenz system if switched on at $t = 3.1s$, rather they cause the trajectory to be expelled from the ball of attraction (not shown) as described by Bewley (1999).

6.4 LMI Control of Plane Poiseuille Flow

6.4.1 LMI Controller Synthesis

Reduced Order Controller Synthesis

The Matlab LMI Control Toolbox version 1.0.8 is found only capable of synthesizing controllers for case 2 state-space plant model $\mathcal{G}(\mathcal{A}, \mathcal{B}, \mathcal{C})$ discretised at $N = 20$, before memory problems occur, as compared to $N = 100$ as used for LQR state feedback on grounds of convergence well beyond the anticipated closed-loop bandwidth in section 2.8.1. A reduced order plant model $\mathcal{G}_{N=20}$ is converged with respect to N, as shown in figure 4.39, unlike $N = 10$. Model reduction by coarser discretisation still provides a measure of system energy, as the state variables remain physically meaningful, as discussed in section 2.8.2. Figure 6.14 shows case 2 LQR transient energy against time from the worst initial conditions, for various plant discretisations and associated controllers. It is evident that the plant and controller performance are identical for $\mathcal{K}(\mathcal{G}_{N=100})$ on $\mathcal{G}_{N=100}$ (previous results

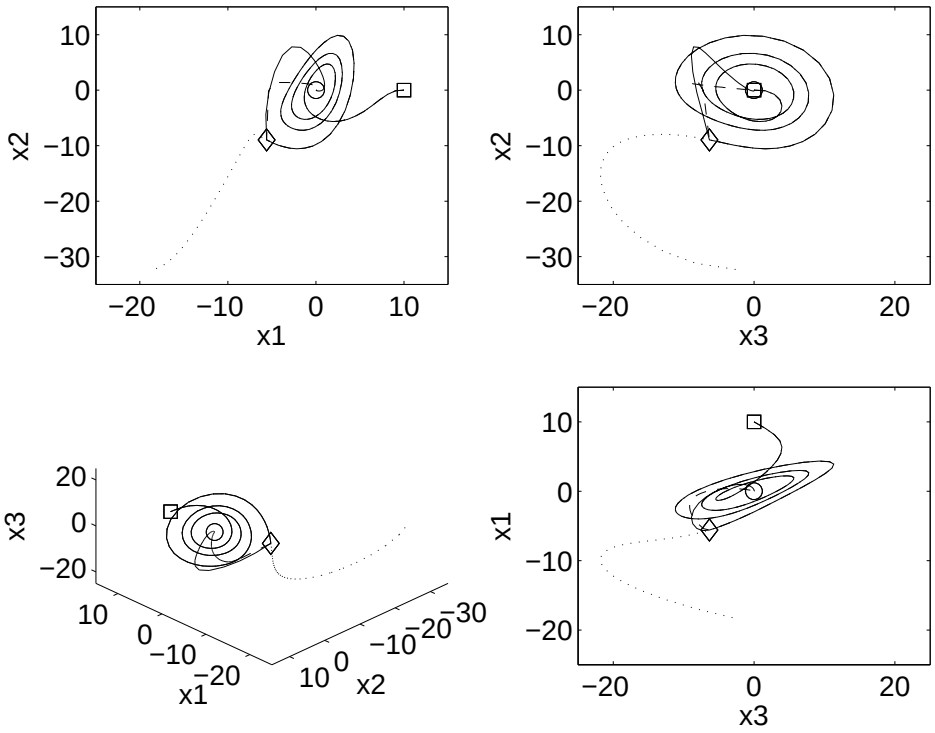

Figure 6.13: Effect of LQR and LMI Controllers on Non-linear Lorenz Equation Perturbation in Phase Space. (Initial conditions (□), controllers switched on at $t = 3.0$ (◇), and clockwise convection equilibrium at origin (○). Line styles as in figure 6.12.)

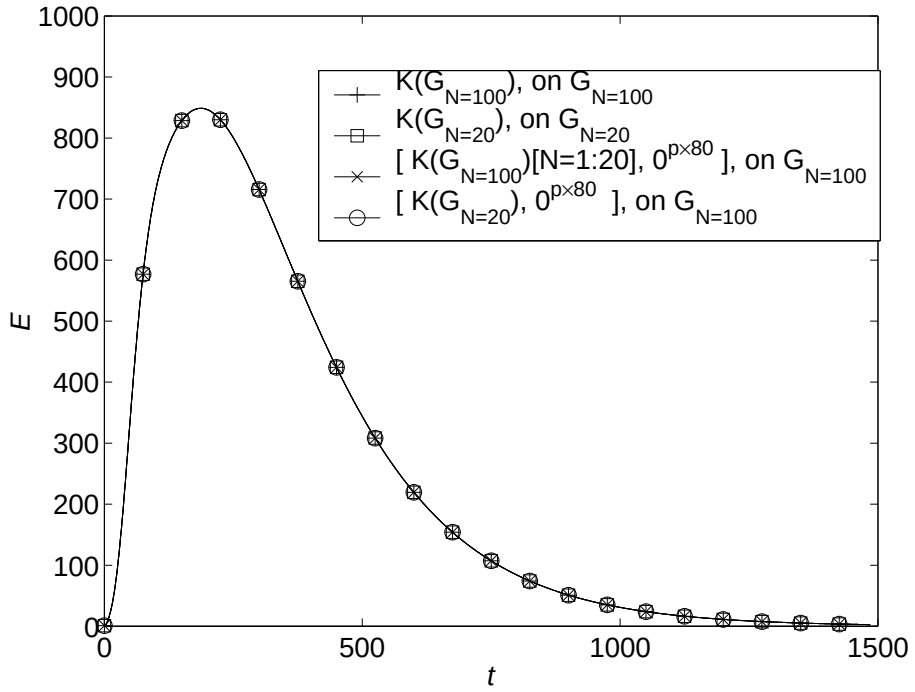

Figure 6.14: Case 2 LQR Transient Energy E vs Time t, for Various Controller Discretisations, from Initial Conditions $\mathcal{X}_{worst}$ Scaled to $E = 1$

from figure 4.50) and a controller $\mathcal{K}(\mathcal{G}_{N=20})$, synthesized using a lower discretisation plant model $\mathcal{G}_{N=20}$, on plant $\mathcal{G}_{N=20}$. This is to be expected from the fast convergence results shown in figure 4.50.

Plane Poiseuille flow is very high order, and figure 6.14 also shows the performance of a truncated and 'padded' high order controller $\mathcal{K}([\mathcal{G}_{N=100}(1:20), \mathbf{0}])$ on the high order plant $\mathcal{G}_{N=100}$. Only the variables corresponding to spectral state variables of the controller are truncated, and it performs as well as the full controller. The figure also shows the performance of a padded low order controller $\mathcal{K}([\mathcal{G}_{N=20}, \mathbf{0}])$ on a high order plant $\mathcal{G}_{N=100}$, and again it performs well, although balancing of the plants $\mathcal{G}_{N=20}$ and $\mathcal{G}_{N=100}$ is not performed in order to maintain consistency between them.

Thus it would appear feasible to synthesize a $\mathcal{K}(\mathcal{G}_{N=20})$ LMI controller and pad it with additional zero spectral state variables to become $\mathcal{K}([\mathcal{G}_{N=20}, \mathbf{0}])$ i.e. the same dimensions as $\mathcal{K}(\mathcal{G}_{N=100})$ controller, for comparison with the previous results from LQR $\mathcal{K}(\mathcal{G}_{N=100})$ controllers on plant $\mathcal{G}_{N=100}$.

Monotonically Decreasing Transient Energy Controller

There are two tests by Whidborne et al. (2004) for the existence of a monotonically decreasing transient energy controller

$$\mathcal{B}^{\perp}\left(\mathcal{A}+\mathcal{A}^{T}\right)\left(\mathcal{B}^{\perp}\right)^{T}<0 \tag{6.29}$$

or

$$\mathcal{B}\mathcal{B}^{T}>0 \tag{6.30}$$

where $\mathcal{B}^{\perp}$ denotes the left null space of $\mathcal{B}$ i.e. $\mathcal{B}^{\perp} = \mathcal{U}_2^T$ in the singular value decomposition

$$\mathcal{B} = \begin{bmatrix} \mathcal{U}_1 & \mathcal{U}_2 \end{bmatrix} \begin{bmatrix} \Sigma_{11} & \mathbf{0} \\ \mathbf{0} & \mathbf{0} \end{bmatrix} \begin{bmatrix} \mathcal{V}_1 \\ \mathcal{V}_2 \end{bmatrix} \tag{6.31}$$

The case 2 linearised plane Poiseuille flow system fails both of these tests, hence no state feedback controller exists that ensures the transient energy is monotonically decreasing. Therefore (6.10) and (6.21) are solved to synthesize controllers that minimise the upper bound θ_u on the diachronic transient energy bound.

LMI Controller Symmetry

LMI controllers are found not to be symmetric with respect to the centreline $y = 0$, unless forced to be so by new symmetric and anti-symmetric actuation basis functions, as follows. The control signal $\mathcal{U} = \mathcal{K}\mathcal{X}$ expanded in complex form (for clarity) is

$$\begin{bmatrix} u_u \\ u_l \end{bmatrix} = \begin{bmatrix} k_{u,v,0} & \dots & k_{u,v,N} & k_{u,\eta,0} & \dots & k_{u,\eta,N} & k_{u,qu}, & k_{u,ql} \\ k_{l,v,0} & \dots & k_{l,v,N} & k_{l,\eta,0} & \dots & k_{l,\eta,N} & k_{l,qu}, & k_{l,ql} \end{bmatrix} \begin{bmatrix} a_{v,1} \\ \vdots \\ a_{v,N} \\ a_{\eta,1} \\ \vdots \\ a_{\eta,N} \\ q_u \\ q_l \end{bmatrix} \tag{6.32}$$

where u_u and u_l are the upper and lower wall actuation signals. Now state variable $a_{v,0}$ represents the magnitude of a velocity component Γ_0^{DN} which is mathematically symmetric about the centreline $y = 0$, and $a_{v,1}$ represents that of an anti-symmetric velocity component Γ_1^{DN}, and so on alternating in symmetry, as shown in figure 2.2. Note that the mathematical symmetry shown in this figure is the opposite of physical symmetry, e.g. positive v above and below the centreline is mathematically symmetric, but physically it corresponds to fluid above the centreline traveling towards the upper wall, but below the centreline fluid travels away from the lower wall, which may be regarded as anti-symmetric in a velocity vector plot. State variable $a_{\eta,0}$ represents the magnitude of a vorticity component Γ_0^{D} which is symmetric about the centreline $y = 0$, and $a_{\eta,1}$ represents that of an anti-symmetric vorticity component Γ_1^{DN}, and so on alternating in symmetry. Symmetrical wall-normal vorticity corresponds to anti-symmetric wall-normal velocity, and vice versa, as shown in figure 2.16. The wall transpiration velocity state variables q_u and q_l represent the magnitude of inhomogeneous asymmetric velocity components f_u and f_l which are reflections of one another about the centreline.

The control actuation is on wall-normal velocity, and it should respond symmetrically to a symmetric wall-normal velocity disturbance, and anti-symmetrically to

an anti-symmetric wall-normal velocity disturbance, i.e.

$$\begin{aligned} k_{u,v,0} &= k_{l,v,0} \\ k_{u,v,1} &= -k_{l,v,1} \\ &\vdots \\ k_{u,\eta,0} &= -k_{l,\eta,0} \\ k_{u,\eta,1} &= k_{l,\eta,1} \\ &\vdots \\ k_{u,qu} &= k_{l,ql} \\ k_{u,ql} &= k_{l,qu} \end{aligned} \tag{6.33}$$

This symmetrical structure occurs in LQR controllers (actually $\mathcal{U} = -\mathcal{K}\mathcal{X}$) but not LMI ones. The correct symmetry structure is enforced on the basis functions f_u and f_l, associated with control by wall-normal transpiration velocity, by making them symmetric and anti-symmetric respectively i.e.

$$\begin{aligned} f_u^{lmi} &= 1 \\ f_l^{lmi} &= \frac{-y^3 + 3y}{2} \end{aligned} \tag{6.34}$$

This is found to generate LMI gain matrices $\mathcal{K}$ with a structure of the correct symmetry. Figure 6.15 shows the new basis functions associated with the state variables.

The effect of this procedure on the transient behaviour of the LQR controller synthesised in section 4.4.1 is shown figures C.1 and C.2 in appendix C. There is a change of 1% in the diachronic transient energy bound shown in figure C.1, and of 30% in the maximum upper wall control signal shown in figure C.2, for discretisation $N = 100$, and the results are similar for $N = 20$ (not shown). These changes are unexpected, since the symmetric/anti-symmetric actuation basis functions impose identical boundary conditions as the original asymmetric actuation basis functions. The changes indicate sensitivity in the solution of the ARE (4.3) or the diachronic transient energy bound eigensystem (4.41) to the exact formulation of the problem, which is particularly manifest in the peak control magnitude. Inspection of the new LQR controller $\mathcal{K}$ shows that its structure no longer has the correct symmetry. As the peak control magnitude occurs at time $t = 0$, the sensitivity is also apparent in the wall-normal velocity values of the initial conditions at the walls (not shown). The changes should be borne in mind when comparing LQR and LMI controller results. Subsequent LQR controller synthesis results use the symmetric/anti-symmetric actuation basis functions for consistency with LMI controller synthesis. The open loop worst initial conditions transient behaviour is independent of the choice of actuation basis functions (not shown), although it does not contain zero eigenvalue modes associated with actuation (see section 4.3.1).

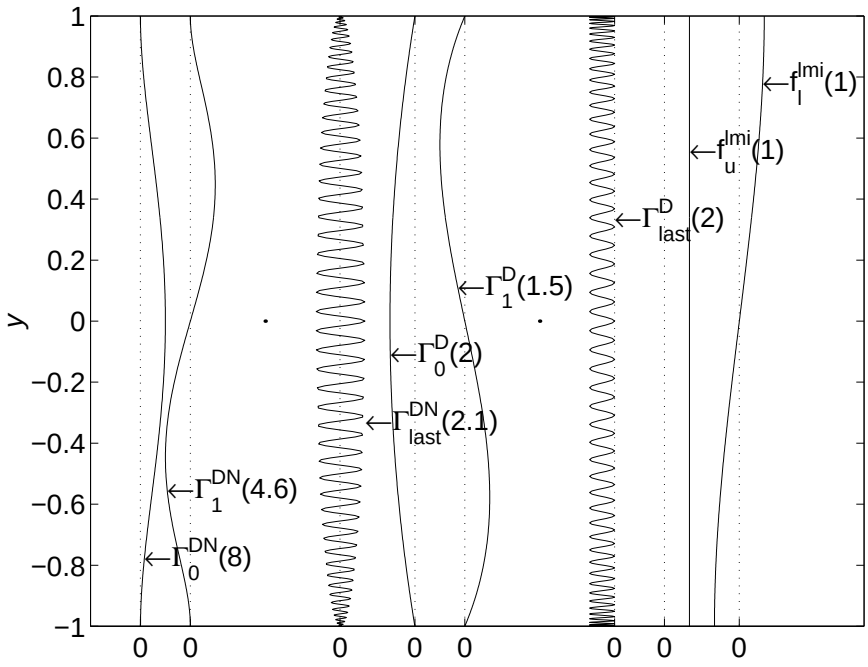

Figure 6.15: The LMI Basis Functions Associated with the State Variables (Peak magnitudes over system for $N = 100$ in parenthesis)

6.4.2 Results of Linear Simulations and Discussion

Unconstrained Control Effort

For synthesis of the LQR controller, zero control weight ($r = 0$) and thus unconstrained control effort, is not possible as $\mathcal{R}$ must be invertible in (4.3). An LMI controller with unconstrained control effort is synthesised using (6.10), and the results of a transient simulation from the worst initial conditions are shown in figure 6.16. The figure shows a diachronic transient energy bound of 893.4 and the unconstrained LMI upper wall control magnitude is approximately 2430 (not shown). Since the initial wall-normal velocity conditions are symmetric with respect to the centreline, similar to those in figure 4.46, the LMI anti-symmetric control signal is negligible throughout, and the upper and lower actuations are equal to the symmetric control signal.

Large Control Effort

Low LQR control weights $r = 2, \mathcal{R} = r\mathbf{I}$, generating a large control effort, are selected from earlier figure 4.11, and a linear simulation performed from the worst initial conditions, as shown in figure 6.17. The peak magnitude of upper wall control $\mathcal{U}$ is 6.71 and occurs at time zero. By iterating on the LMI control magnitude limit ν, an LMI controller is synthesized using (6.21) which achieves a peak magnitude of upper wall control of 6.76 in a linear simulation, as also shown in figure 6.17. The control limit required is $\nu = 32$.

Figure 6.18 shows case 2 LMI and LQR transient energy against time, for these

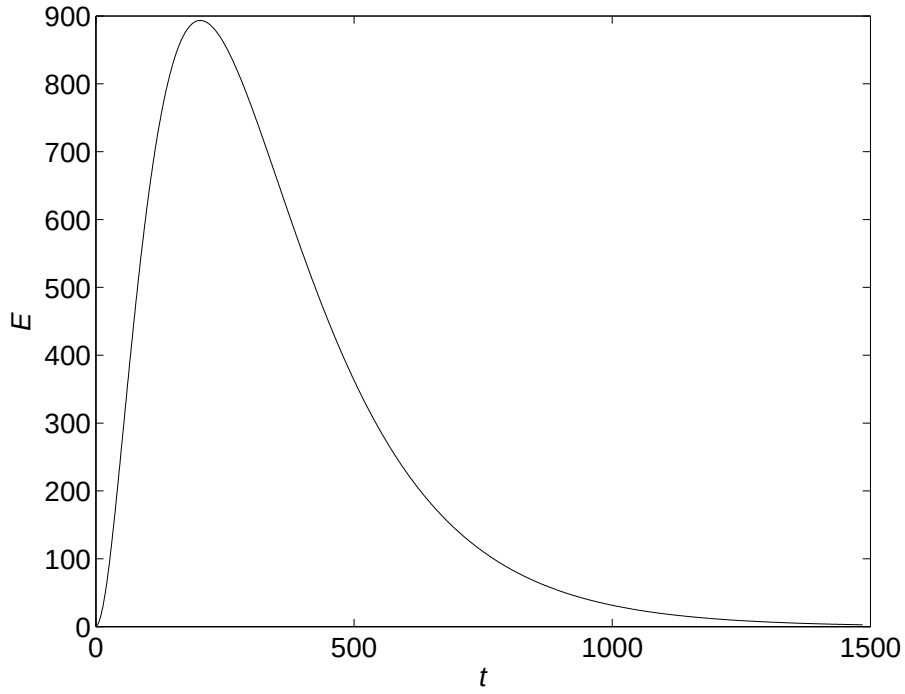

Figure 6.16: Case 2 LMI Transient Energy E vs Time t, Unconstrained Control Effort, from Initial Conditions $\mathcal{X}_{worst}$ Scaled to $E = 1$

LQR control weights and LMI control limit, from the worst initial conditions. The LMI controller has a slightly higher diachronic transient energy bound (823.8) than the LQR (815.9), whether on a lower order plant model, or padded spectrally and on a high order plant model. Since the initial wall-normal velocity conditions are symmetric with respect to the centreline, the LQR and LMI anti-symmetric control signals are negligible throughout.

Small Control Effort

Larger LQR control weights $r = 2^7, \mathcal{R} = r\mathbf{I}$, are selected as in section 4.4.1 for earlier simulations, and a linear simulation performed from the worst initial conditions, as shown in figure 6.19. The peak magnitude of upper wall control $\mathcal{U}$ is reduced to 0.169, as compared to 6.71 for $r = 2$. An LMI controller is synthesized using (6.21) and a control limit of $\nu = 0.8$ which achieves a peak magnitude of upper wall control of 0.177, as also shown in figure 6.19.

Case 2 LMI and LQR transient energy against time, for these LQR control weights and LMI control limit, from the worst initial conditions is shown in figure 6.20. The LMI controller achieves a slightly lower diachronic transient energy bound (839.1) than the LQR (840.4), again whether on a lower order plant model, or padded spectrally and on a high order plant model.

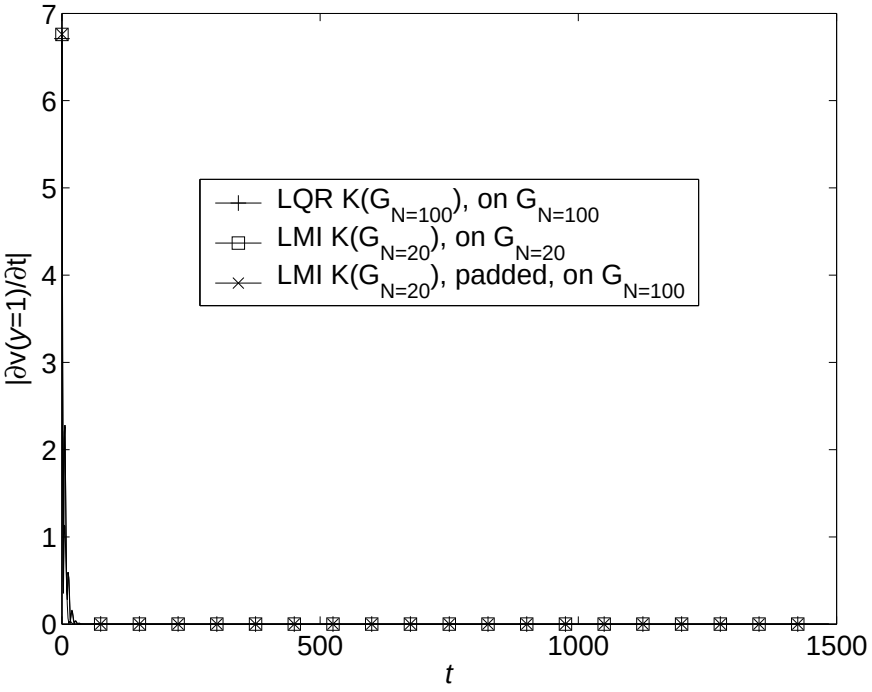

Figure 6.17: Case 2 LMI and LQR Upper Wall Control $\mathcal{U}(1)$ vs Time t, Large Control Effort, from Initial Conditions $\mathcal{X}_{worst}$ Scaled to $E = 1$, $N = 100$

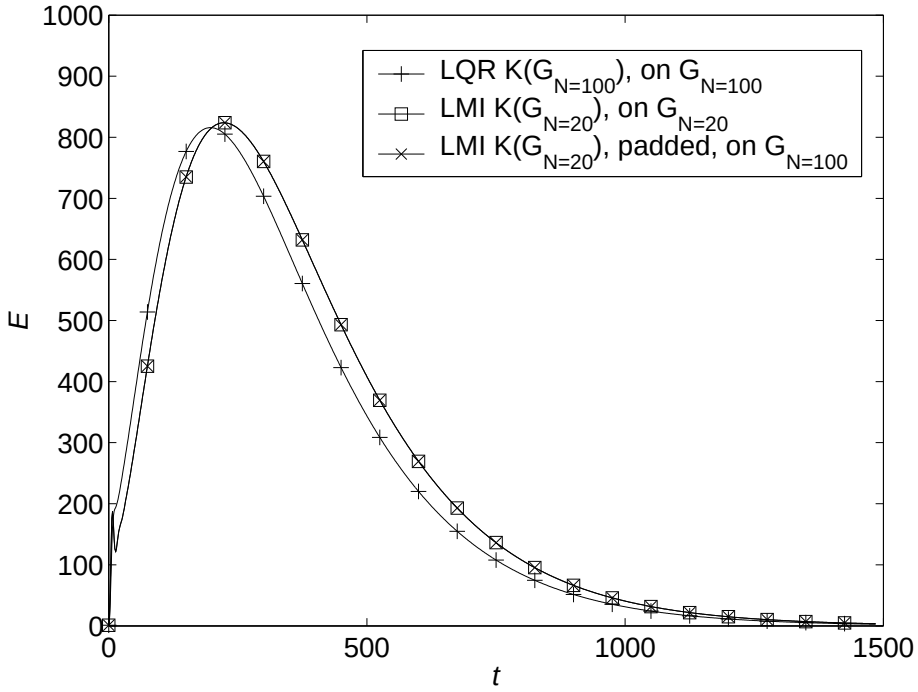

Figure 6.18: Case 2 LMI and LQR Transient Energy E vs Time t, Large Control Effort, from Initial Conditions $\mathcal{X}_{worst}$ Scaled to $E = 1$

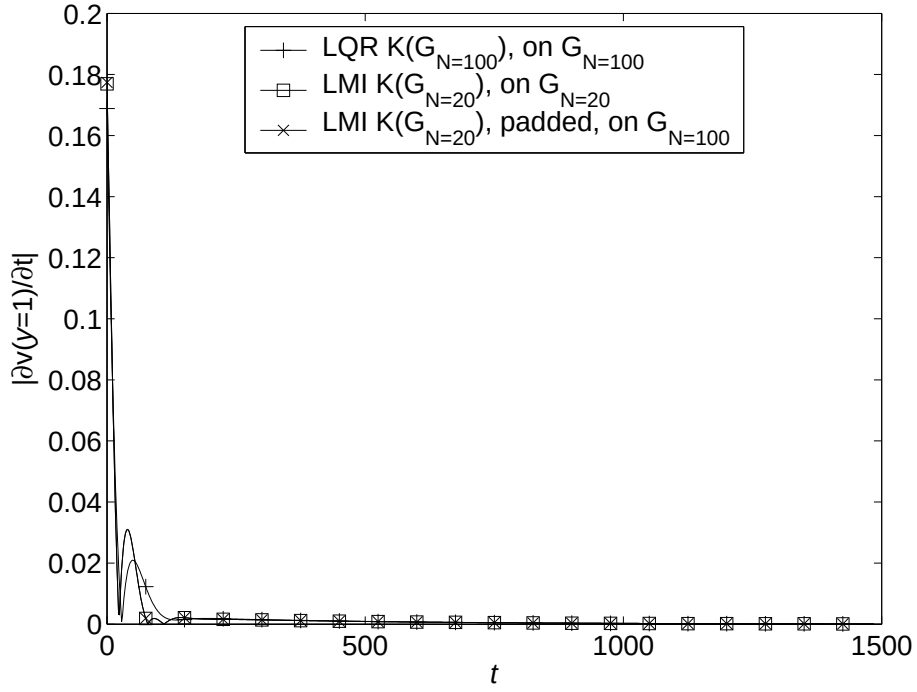

Figure 6.19: Case 2 LMI and LQR Upper Wall Control $\mathcal{U}(1)$ vs Time t, Small Control Effort, from Initial Conditions $\mathcal{X}_{worst}$ Scaled to $E = 1$, $N = 100$

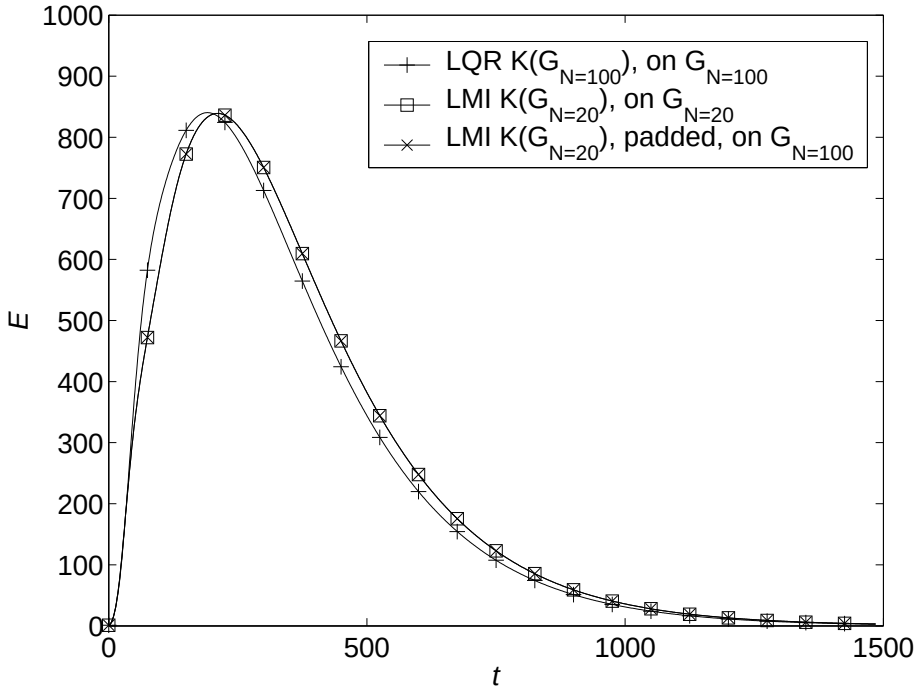

Figure 6.20: Case 2 LMI and LQR Transient Energy E vs Time t, Small Control Effort, from Initial Conditions $\mathcal{X}_{worst}$ Scaled to $E = 1$, $N = 100$

Table 6.1: Diachronic Transient Energy Bound of LQR and LMI Control on Case 2

	LQR			LMI			
Control Effort	LQR r	$\max_t \|\mathcal{U}\|^2$	θ	ν^2	$\max_t \|\mathcal{U}\|^2$	θ	θ_u
Unlimited	-	-	-	-	1.18e7	893.4	1722.4
Large	2	90.0	815.9	1024	91.4	823.8	1722.4
Small	128	0.0571	840.4	0.64	0.0626	839.1	1722.4

Discussion

Table 6.1 shows a summary of the diachronic transient energy bound and control effort from the linear simulations on the LQR and LMI controllers, together with the upper bound on the diachronic transient energy bound, θ_u, which is minimised by the LMI controllers. It is evident that the upper bound is loose for plane Poiseuille flow, as it was for the Lorenz system. The LMI control limit ν is also seen to be a loose bound on the peak control effort. The LMI diachronic transient energy bound is smallest for large control effort, intermediate between unconstrained and small effort. The Lorenz system also showed the lowest diachronic transient energy bound for intermediate control effort, although the minimum in figure 6.5 is very shallow.

The diachronic transient energy bound achieved by the LMI and LQR controllers for similar control effort are similar, and within the changes to the LQR results caused by the symmetric/anti-symmetric actuation basis functions. The table shows that there is no penalty on LQR diachronic transient energy bound for the larger control effort used here, unlike for the Lorenz system in figure 6.1 where large control effort increases the diachronic transient energy bound significantly. This may be due to control being by rate of change of wall transpiration velocity in the plane Poiseuille flow system, rather than velocity itself.

6.4.3 Results of Non-Linear Simulations and Discussion

Results are presented from non-linear simulations of the small control effort LMI controller on the full Navier-Stokes equations. Non-linear simulations of the unconstrained control effort LMI controller are unsuccessful, due to the high control magnitudes involved. No changes to the CFD code described in section 4.3.3 are necessary, other than to read in the LMI controller state feedback gain matrix $\mathcal{K}$ rather than the LQR one.

Small Initial Perturbations

Case 2 LMI controlled transient energy against time t, from initial conditions $\mathcal{X}_{Worst}$ scaled to energy E_{C2}, is presented in figure 6.21. The linear and non-linear simulation transient energy agree well, with peak values of 1.90×10^{-6} and 1.89×10^{-6} respectively, as do wall transpiration velocities (not shown).

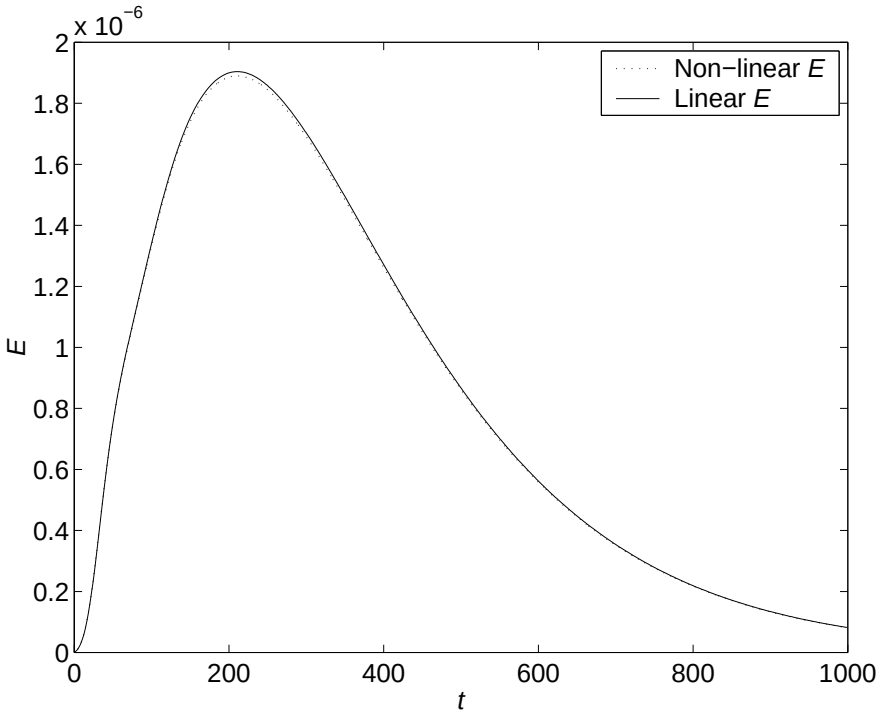

Figure 6.21: Case 2 LMI Transient Energy E vs Time t, from Initial Conditions $\mathcal{X}_{Worst}$ Scaled to Energy E_{C2}

Large Initial Perturbations

Figure 6.22 shows case 2 LMI controlled transient energy against time, from initial conditions $\mathcal{X}_{Worst}$ scaled to energy $10^4 E_{C2}$. The non-linear simulation saturates, and reaches a peak transient energy of only 0.00751 as compared to the linear value of 0.0194. The LMI peak transient energy is lower than the LQR value of 0.00951 in table 4.5, from worst conditions of identical initial energy.

6.5 Conclusions

Section 6.2 described an extension of an LMI based method to obtain controllers with a minimised closed-loop upper bound on diachronic transient energy bound θ, in order to limit the control effort. An upper bound on the control effort was derived, and a further LMI was incorporated into the LMI controller synthesis system to minimise it.

Subsequently section 6.3 introduced and linearised the Lorenz equations and subsequently compared the performance of LMI and LQR controllers on the linearised form. The LQR controllers minimised the time integral of the transient energy plus weighted control effort, from any initial conditions, rather than θ itself, although θ was reduced as a consequence. Whereas the LQR controllers were found to have a pronounced minimum achievable peak transient over control effort, since high control effort contributes to the peak transient, the LMI controllers were found to deliver ever smaller peak transients for a wide range of controller effort,

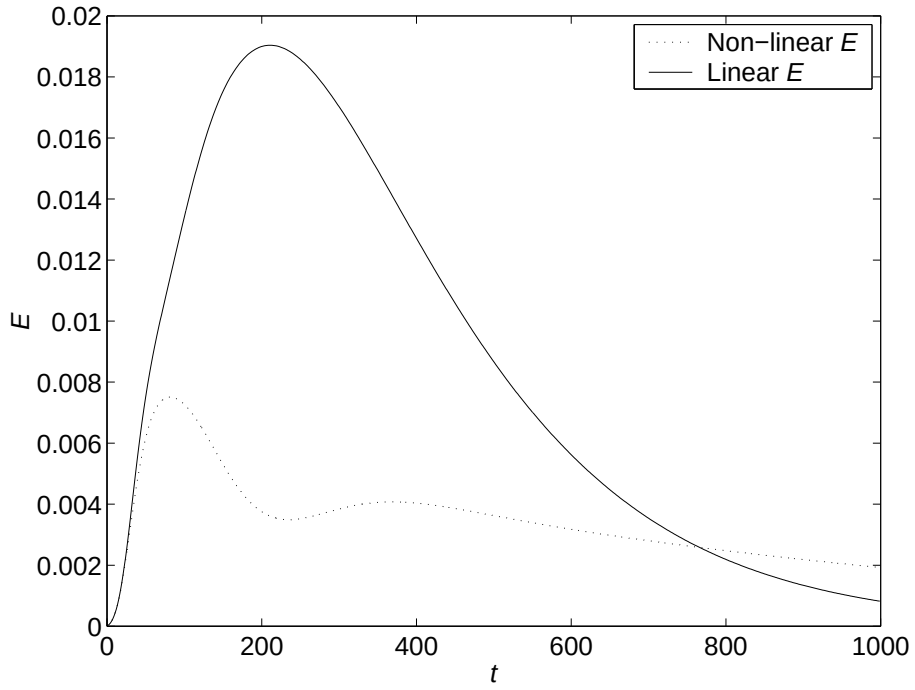

Figure 6.22: Case 2 LMI Transient Energy E vs Time t, from Initial Conditions $\mathcal{X}_{Worst}$ Scaled to Energy $10^4 E_{C2}$

until a shallow minimum was reached. It was also seen that for high-effort LMI controllers, the upper bound on the peak transient could be very conservative.

Whilst the presence of non-orthogonality of system eigenvectors has been shown to be an important factor in transient growth by Trefethen et al. (1993), evidence was presented that when perfect orthogonality cannot be achieved, simply selecting controllers with the lowest non-orthogonality (in terms of eigenvector dot products) will not necessarily lead to the lowest θ. For a simple example system with specified non-orthogonality, a correlation was seen between slow closed-loop eigenvalue speed and high θ. This correlation also occurred for the Lorenz system, and it was supposed that this effect was causing θ not to correlate with non-orthogonality.

The LMI controllers led to relatively large settling times when compared to the LQR controllers. An exponential time weighting could be incorporated into the LMI to improve the convergence rate, as proposed by Hinrichsen et al. (2002) and Boyd et al. (1994, p.89). Both LMI and LQR controllers were able to stabilise a simulation of the full non-linear Lorenz equations from limited initial conditions, the LMI controller producing a more direct trajectory to the origin in phase space.

Section 6.4 compared the performance of LMI controllers with LQR ones when applied to the linearised plane Poiseuille flow system. Memory problems necessitated a maximum system size for LMI controller synthesis of $N = 20$. A case 2 model discretisation $N = 20$ was found to be capable of producing LQR controllers capable of controlling an $N = 100$ plant model as well as a controller synthesized from the full $N = 100$ model, and thus LMI controllers synthesized with $N = 20$ would also be suitable. Symmetric and anti-symmetric actuation basis functions were found necessary to produce LMI controllers with the correct symmetry with

respect to the physical problem, although the use of these basis functions caused the LQR controller symmetry to be lost, and also caused some variation in the LQR results, especially in the magnitude of the initial control effort.

An LMI controller with no control effort constraint was able to stabilise the system, albeit with very large control effort. For large control effort the LQR and LMI controllers achieved the best diachronic transient energy bound θ, and the difference between them was less than the variation in the LQR system caused by the symmetric and anti-symmetric actuation basis functions. No apparent penalty on the LQR system θ at large control effort (caused by the control itself contributing to the transient) was found on the linearised plane Poiseuille flow system, unlike on the Lorenz system. At smaller control effort both LMI and LQR controllers produced similar but larger θ. Thus LQR controllers which minimise the time integral of the transient energy and weighted control effort and LMI controllers which minimise upper bounds on the θ and control effort were found to be equally effective at minimising linearised plane Poiseuille flow θ at both large and small control effort. Neither the upper bound on the LMI θ nor the upper bound on the LMI control effort was found to be tight.

The small control effort LMI controller was able to stabilise non-linear simulations from both small and large worst initial conditions. For small initial perturbations the linear simulation results were closely reproduced. For the larger initial perturbations the transient energy saturated, and the flow was stabilised with a lower peak transient energy than the LQR controller achieved on worst initial conditions of equal energy.

To summarise, this chapter has described the addition of a minimised bound on control effort to a system of LMI's for the synthesis of controllers with a minimised bound on transient energy growth, in order to limit both transient energy growth and the control effort applied to achieve it. Novel controllers have then been synthesised for the linearised Lorenz equations, a simple analogue of flow transition, and the state-space system of linearised plane Poiseuille flow developed in chapter 2. For the linearised Lorenz system, the LMI based controllers were found to deliver lower transient energy growth as controller effort is increased over a wide range, as compared to LQR controllers for which high controller effort contributed to the transient energy growth and thus to the incidence of non-linearity. No correlation was seen between lower (but non-zero) controlled eigenvector non-orthogonality and lower transient energy growth, i.e. low controlled eigenvector non-orthogonality is not beneficial in terms of reduced transient energy growth *per se*, although there was a correlation between faster eigenvalues and lower transient energy growth. In simulations, LMI and LQR controllers were found to stabilise the full Lorenz system from limited initial conditions.

For the linearised Poiseuille flow system, LMI and LQR controllers behaved similarly in terms of transient energy growth, for similar control effort, i.e. controllers which minimise a bound on transient energy behave similarly to those which minimise the time integral of transient energy. Neither the LMI bound on transient energy nor on control effort was seen to be tight, motivating further work to minimise the transient energy and control effort themselves. The results from linear closed-loop simulations of the LMI controller were validated by non-

linear finite-volume simulations from small worst initial conditions. In non-linear simulations from larger initial conditions, saturation occurred and stability was maintained.

Chapter 7

Conclusions and Future Work

This chapter describes the main findings from the work carried out in this thesis, and suggests future work that might be performed.

7.1 Conclusions

This thesis has described work undertaken to spectrally model linearised plane Poiseuille flow, with wall transpiration actuation and wall shear measurements, and to synthesise controllers using modern control approaches. An account has been given of the results from open- and closed-loop, linear and independently derived non-linear simulations, with particular emphasis on transient energy growth. The performance of alternative actuation has been investigated, and of alternative controllers which minimise the transient energy growth. The major results from this thesis are summarised chapter by chapter as follows.

7.1.1 Chapter 2

A spectral wall-normal polynomial-form state-space velocity-vorticity representation of linearised plane Poiseuille flow with control by rate of change of wall-normal velocity has been derived. This representation combines beneficial features from several previously published spectral state-space models. A wall-normal polynomial form allows approximation of the wall-normal variation by truncation of the series, unlike an interpolating form. Velocity-vorticity formulation allows three-dimensional perturbations to be modeled, unlike the stream function formulation which allows only two-dimensional perturbations. The transformation to an inhomogeneous system with homogeneous boundary conditions allows the correct boundary conditions to be imposed more easily, without the subsequent generation of spurious modes. The transformation leads to the formation of the state-space system by partition then inversion of the Laplacian, and ultimately produces control by rate of change of wall-normal velocity.

An interpolating state-space form derived by partition-then-inversion and leading to control by rate of change of wall transpiration velocity has been shown to be consistent with a published interpolating form performing inversion-then-partition and leading to control by wall transpiration velocity (Bewley and Liu, 1998). The

two forms have been shown to be consistent by use of the Schur complement, at the point before the integrators are introduced into the partition-then-inversion form in order to regularise the inputs.

The linear flow field of steady harmonic transpiration has been determined. The eigenvectors associated with the integrators, which control by rate of change of wall-normal velocity introduces, have been shown to represent steady transpiration.

Pressure measurements for the state-space model have been derived. Previous authors suggest performing the inversion of a Laplacian in order to determine pressure (Bewley and Liu, 1998, p309), but the assumption of periodicity allows the derivation of a simple expression for wall pressures (2.51). The expression contains higher wall-normal derivatives than wall shear stress measurements require, and hence need finer model discretisation.

The size of a real system for controlling streamwise vorticities may be halved. Two test cases, case 1 (Tollmien-Schlichting waves) and test case 2 (streamwise vortices) were considered, representing the earliest stages of transition to turbulence. For test case 2, examination of the governing equations shows that the real velocity and imaginary vorticity may be discarded, leading to a system reduced in dimension by approximately 50% when expanded into components for the solution of the algebraic Riccati equations for LQR controller synthesis.

Good agreement was found with previously published observability results. Using particular observability and controllability measures, observabilities were found to be close to those of Bewley and Liu (1998). A discrepancy in the controllability results was shown to be due to variations in the order of partitioning and inversion, and the associated integrators.

Convergence of observability needs high discretisation. A direct correlation was shown between modal observability and wall velocity gradient, which was seen to require a high level of discretisation for convergence. For streamwise vortices, spanwise wall shear, dw/dy, contributes little to observability, as compared to streamwise wall shear, du/dy.

Integrators placed directly on the inputs of a state-space system cause the controllability of existing modes λ_i to change by a factor $1/\sqrt{\lambda_i^T \lambda_i}$ (2.154). The modal observability is unchanged by the integrators. An algorithm for the computation of individual left eigenvectors has also been proposed. It has also been demonstrated that for consistently normalised right eigenvectors, non-normality leads to left eigenvectors being larger, and thus greater modal controllability.

7.1.2 Chapter 3

Valid bases have been established for imposing Dirichlet and Neumann boundary conditions. From a linear algebraic point of view, several published practices for forming bases that impose the boundary conditions were shown to be not strictly correct. Valid bases have been established in polynomial form. A novel recombination is proposed for the simultaneous Neumann and Dirichlet boundary conditions, that extends a published Dirichlet boundary condition method.

The condition number of bases is a complex interplay of maximum and min-

imum singular values. The conditioning of four bases and their derivatives have been compared. Of the matrices required for plane Poiseuille flow without wall equations, Heinrichs' method, which modulates the bases, has best conditioning on 2 specific matrices where it reduces the maximum element magnitude, but in general other bases which do not cause low minimum singular values are better, in particular for the Laplacian which is inverted.

Preconditioning by postmultiplying by diag($[1, 1/n_{n=1:N}^{\text{derivative order}}]$) *generally improves conditioning markedly.* This is because the system has the wall equations removed, and this preconditioning matrix is inversely proportional to the channel interior derivative magnitude. With this preconditioning, the novel extended basis proposed for the simultaneous Neumann and Dirichlet boundary conditions has the best conditioning for inversion of the Laplacian. Preconditioning by postmultiplying by $\text{diag}([1, 1/n_{n=1:N}^{2\times\text{derivative order}}])$, which is inversely proportional to the wall derivative magnitude, improves conditioning but less so.

7.1.3 Chapter 4

LQR state feedback controllers and LQE state estimators have been synthesized for the model of linearised plane Poiseuille flow. The controllers and estimators were also combined into LQG output feedback controllers. The worst initial conditions, generating the diachronic transient energy bound (the highest transient energy possible from unit energy initial conditions), were also computed, and linear simulations performed. The controllers were seen to stabilise the flow for test case 1 (open-loop linearly unstable), and reduce the diachronic transient energy bound of test case 2.

Convergence of the performance of LQE estimators was found to require higher levels of wall-normal discretisation than did LQR controllers. The level of discretisation for convergence of state feedback of linearised plane Poiseuille flow is lower than that required for state estimation, which is consistent with the estimators being dependent upon accurate modelling of velocity gradients close to the walls.

The boundary truncation of interpolating-form derivative matrices on a system with inhomogeneous boundary conditions is inaccurate. Previously published work performs this truncation on the energy matrix used for LQR state weighting (Bewley and Liu, 1998, p311-313), and thus no comparison is possible with the associated closed-loop (inhomogeneous boundary condition) results.

Tuned estimator weights were found to have lower estimated energy bound and faster convergence than uniform weights. Tuned estimator weights, which assumed that disturbances near the centreline are larger and more variable than those near the walls, were found to have lower estimated energy bound (from the worst plant initial conditions and zero initial estimates), and faster convergence than estimators which made no assumptions regarding the physical distribution of disturbances. Uniform estimators had lower worst diachronic error energy bound, but it was nonetheless unrealistically high and difficult to see how it could occur in practice.

Small oscillations were found at the walls in the worst initial conditions. These small oscillations were produced by the solution of the transient growth eigensys-

tem, and although difficult to see, they had a marked effect on the initial wall velocity gradient and thus state estimation, particularly in subsequent finite-volume simulations. The oscillations were removed by 2/3 dealiasing, with negligible effect on the flow energy density.

The system eigenvectors were found not to be made appreciably more normal by the application of control. Although some non-normality is required for transient energy growth, and the application of control reduces diachronic transient energy bound, the application of control did not reduce eigenvector non-normality in terms of eigenvector dot products. Inspection of the energy growth in modal and non-modal terms shows a complex relationship between non-normality and diachronic transient energy bound.

Linear simulations showed that significant amounts of transpiration fluid were required locally. Although the transpiration considered is harmonic, and thus zero net mass flow, the magnitude of the transpiration required for the test cases considered is such that locally large amounts of fluid are required, much greater than the size of reservoirs provided by MEMs devices.

Simulations of the controller were performed on a full non-linear model of plane Poiseuille flow. The magnitude of linear sized perturbations was determined by inspection of the non-linear terms in the worst initial conditions. A finite-volume Navier-Stokes solver was modified to work in terms of flow perturbations, in order to accurately model the evolution of linear sized initial conditions. Close agreement was found between linear and non-linear simulation results on linear sized perturbations for both open and closed-loop systems.

State feedback controllers were generally able to stabilise the flow and reduce the transient energy growth from large perturbation worst initial conditions. Mesh insensitivity was harder to prove for test case 1 (Tollmien-Schlichting waves) than test case 2 (streamwise vortices). Simulations were found to saturate but closed-loop transient energy growth was lower than open-loop growth. On saturated streamwise vortices (test case 2), the state estimators tended to overshoot, and could destabilise the system when it was controlled by output feedback.

For large perturbations, the energy as computed from the state feedback controller state variables was found to be significantly less than that of the non-linear flow field. This is believed to occur because the state variables only represent energy at one wavenumber pair, and the non-linear flow terms are able to transfer energy to other wavenumber pairs.

7.1.4 Chapter 5

Simultaneous wall-normal and tangential actuation for a state-space model of linearised plane Poiseuille flow has been derived. Simultaneous wall-normal and tangential actuation represents generalised transpiration in any direction. The appropriate control boundary conditions were derived in velocity-vorticity form, and the additional basis functions required were selected, for use in the system input matrix.

Tangential actuation was found to produce lower controlability than wall-normal actuation. This is consistent with the tangential actuation basis functions being

less 'full' than the wall-normal actuation basis functions.

LQR state feedback via tangential actuation, as compared to wall-normal actuation, was found to produce a higher diachronic transient energy bound on test case 1, but a lower diachronic transient energy bound on test case 2. LQR State feedback controllers using tangential actuation were synthesized and the diachronic transient energy bound calculated. Oscillations in the worst initial conditions had to be removed by truncation of the eigenvalues in the transient energy eigensystem, and convergence with discretisation was found to be erratic over the range of control weights. With these caveats, tangential actuation was found to produce lower diachronic transient energy bound for test case 2. Truncation on earlier wall-normal actuation results showed that although the worst transient energy growth appears to be unique, the associated initial conditions, and thus also the control effort, are not.

Linear simulations showed that tangential actuation requires higher control effort. This is the case for control effort in terms of fluid acceleration, velocity and displacement, although tangential actuation opens up the possibility of utilising different technologies for actuators, e.g. rollers, which have no constraint on displacement.

Non-linear simulations of control via tangential actuation showed saturation but also stabilisation of test case 1. LQR controlled non-linear simulations from small initial perturbations produced results in agreement with linear simulations, for test case 1, Tollmien-Schlichting waves. Non-linear simulations from large initial perturbations led to saturation, but the controller stabilised the flow nonetheless.

7.1.5 Chapter 6

A method for synthesizing linear controllers with minimised upper bounds on diachronic transient energy bound and peak control effort has been developed. Additional terms which minimise an upper bound on peak control effort have been incorporated into a linear matrix inequality (LMI) system that already synthesizes state feedback controllers which minimise an upper bound on diachronic transient energy bound.

LMI controllers with minimised upper bounds on diachronic transient energy bound and control effort have been synthesized for the linearised Lorenz equations. The upper bound on diachronic transient energy bound was seen to be conservative at high control effort. LQR controllers were also synthesized and found to have similar performance in terms of diachronic transient energy bound at low levels of control, but at high levels of control their performance was poorer as the control tended to contribute to the transient energy. The LMI controllers were able to stabilise the full Lorenz equations from limited initial conditions.

The worst transient energy was found not to correlate well with non-normality for variable effort controllers acting on the linearised Lorenz system. Although some non-normality is required for transient growth, reduced transient energy growth was not seen to correlate with lower system least normal eigenvector dot product. On an artificial system with constant non-normality, an inverse correlation between the eigenvalue speed and the worst transient energy growth was seen.

This correlation also occurred for the controlled Lorenz system.

LMI controllers with minimised upper bounds on worst transient energy and control effort have been synthesized for the linearised plane Poiseuille flow system. It was found necessary to recast the actuation into symmetric and anti-symmetric components in order to produce a controller structure with the correct symmetry with respect to the walls.

The performance of LQR and LMI controllers on linear simulations of plane Poiseuille flow were seen to be similar. For similar control effort, LQR controllers which minimise the time integral of the transient energy plus control effort, and LMI controllers which minimise upper bounds on the diachronic transient energy bound and peak control effort were seen to have similar diachronic transient energy bound. As found for the LQR controllers, the LMI controllers were able to stabilise non-linear simulations of plane Poiseuille flow.

7.1.6 Summary

The conclusions drawn in this thesis may be summarised as follows. An eclectic state-space model of linearised plane Poiseuille flow has been shown to be consistent with previous models, although improved techniques for wall-normal discretisation have been suggested. Closed-loop non-linear simulations of linear optimal controllers using a solver derived independently from the state-space model show agreement with it for small initial perturbations, and generally saturation and stabilisation from larger perturbations. Despite numerical difficulties and high control effort, tangential actuation may produce lower transient energy growth than wall-normal actuation. Linear optimal controllers which minimise the time integral of transient energy perform similarly to controllers which minimise an upper bound on the peak transient energy growth. No obvious positive correlation between closed-loop system non-normality and highest transient energy growth was seen.

7.2 Further Work

The main findings from this thesis motivate the following possibilities for future work in the field of practical control of early transition in Poiseuille flow, and in flow about more relevant geometries. Items of future work in various areas are divided into short, medium and long term categories, as an indication of the relative effort required for each individual item.

7.2.1 Short Term Work

Flow Conditions

In practice, the exact base flow conditions would not be known precisely, and disturbances would occur over all time, and not just in the initial conditions. It would therefore be appropriate to consider the stability and performance robustness of the controllers synthesized, with regard to uncertainty in the flow model and with

regard to flow disturbance models. This may be addressed by the synthesis of H_∞ controllers, for instance by using the Matlab Robust Control Toolbox.

Practical initial disturbances are likely to be larger than those considered in this thesis, which contained 3.1×10^{-3}, and 8.5×10^{-5}, of the base flow energy density, for test cases one and two respectively. The performance of the controllers in non-linear simulations from larger initial perturbations would show the extent to which linearisation at a single wavenumber is able to control more non-linear flow.

Although the initial condition test cases considered in this thesis covered both unstable perturbations and those which generate the highest subsequent transient energy, neither was fully three-dimensional. It would be straightforward to synthesize controllers for α and β being non-zero, for example to represent oblique waves, although non-linear finite-volume simulations would require fully 3-dimensional meshes, and would require significantly longer computational times.

Assumption of Periodicity

The assumption of periodic behaviour in the unbounded directions has proved useful, but is somewhat unrealistic in practice. Evidence has been found for the presence of other wavenumbers during non-linear simulations, and these are likely to be harmonics of the fundamental wavenumbers, due to the periodic boundary conditions imposed. The synthesis of controllers to control harmonic wavenumbers would be a straightforward minor relaxation of the assumption of purely periodic behaviour, and lead to the possibility of controlling the non-linear flow simply by controlling sufficient harmonics, since the non-linear terms just transfer energy between modes.

Measurement and Actuation

The linearised and discretised expression for pressure derived in this thesis could be employed to synthesize controllers based on wall pressure measurements, rather than wall shear stress, which may be more suitable in practice.

Regarding actuation, the optimal controllers simulated in this thesis have are those that result in the lowest diachronic transient energy bound, regardless of actuation level. Since actuation is limited in practice, it would be worthwhile to investigate the deterioration of performance, in terms of diachronic transient energy bound, if actuation levels were reduced, for example by increasing the control weighting.

7.2.2 Medium Term Work

Controller Synthesis

The LMI controller synthesized in chapter 6 minimised an upper bound on the diachronic transient energy bound by state feedback. The upper bound was found to be loose, and for practical implementation state estimators would be required. This could be improved by the synthesis of controllers as described by Whidborne

and McKernan (2006) which directly minimise the diachronic transient energy bound itself by output feedback.

As large amounts of transpiration were found to be required to achieve control, it would be appropriate to introduce constraints on the transpiration fluid velocity and quantity, rather than on the control effort as in this thesis, which is the time derivative of velocity.

The initial condition oscillations at the wall for wall-normal actuation, and widespread oscillations and numerical difficulties encountered for tangential actuation, during the calculation of the diachronic transient energy bound, are also worthy of further investigation.

In order to synthesise controllers of a realistic order, it would be advantageous to investigate the effects of standard model and controller reduction techniques on the transient energy growth of non-normal systems, and to determine appropriate reduction techniques with minimal effect on transient energy growth.

Assumption of Periodicity

In order to further relax the assumption of periodicity in the unbounded directions, the work described in this thesis could be applied to spatially developing perturbations in channel flow. Calculating the spatial development of perturbations varying periodically in time is a related problem which generates a non-linear eigensystem, as shown by Danabasoglu and Biringen (1990). This eigensystem may be linearised, and although it leads to a larger computational problem, flow control may be introduced by similar procedures to those described in this thesis.

Alternatively, by replacing the use of periodic expressions in the streamwise and spanwise directions with spectral collocation by Chebyshev series similar to that performed in the wall-normal direction, it may be possible to use the methods described in this thesis for the synthesis of controllers for spatially developing channel flow perturbations as modelled by Liou and Fitzmaurice (1995), who do not assume a periodic time variation, but do however impose Dirichlet boundary conditions in the streamwise direction. Thus it would be advantageous to also apply techniques that exist for the spectral collocation modelling of an infinite domain in the streamwise direction, as presented by Boyd (2001, p338), in order to model isolated disturbances in an infinite channel. The use of spectral collocation in 2 or more dimensions leads to a large increase in system size and would require techniques for model reduction.

Flow Conditions

The modification of the model described in this thesis to cover disturbances in a more realistic slowly developing boundary layer base flow, rather than in Poiseuille base flow, would require the imposition of free-stream boundary conditions at the upper wall, and an appropriate boundary layer base-flow profile, and might be achieved by using techniques for the spectral collocation modelling of a semi-infinite domain in the wall-normal direction, as described by Boyd (2001, p326).

7.2.3 Long Term Work

Flow Conditions

It may also be possible to apply the methods described in this thesis to flow in more complex two-dimensional, and three-dimensional geometries, for example in curved channels, to study the effects of curvature, and in cavities, which are rich in flow phenomena. Modelling curved channels could be achieved by employing a cylindrical co-ordinate system and additional acceleration terms. Controllers as described here might be applied to cavities by using some of two-dimensional techniques suggested for spatially developing Poiseuille flow, and would be more feasible than the computationally intensive adjoint control investigated by Spasov and Kunisch (2006).

Linear controllers for the flow around around cylinders and spheroids might also be synthesised, for example on the flow as modelled by Mittal (1999), noting that in cylindrical and spherical co-ordinate systems the geometry and flow shows periodicity. The performance of such controllers on the initial stages of vortex shedding could thus be established. Regarding controller verification, the finite-volume non-linear simulation employed in this thesis is well-known to able to simulate the flow associated with varied geometries such as these.

References

Aamo, O.M. (2002). *Modelling and Control of Flows and Marine Structures*, PhD thesis, Department of Engineering Cybernetics, Norwegian University of Science and Technology.

Aamo, O.M. and Fossen, T.I. (2002). Tutorial on feedback control of flows, Part I: Stabilization of fluid flows in channels and pipes, *Modelling, Identification and Control* **23**(3): 161–226.

Aamo, O.M., Krstic, M. and Bewley, T.R. (2003). Control of mixing by boundary feedback in 2D channel flow, *Automatica* **39**(9): 1597–1606.

Abergel, F. and Temam, R. (1990). On some control problems in fluid mechanics, *Theoretical and Computational Fluid Dynamics* **1**: 303–325.

Anderson, B.D.O. and Liu, Y. (1989). Controller reduction: Concepts and approaches, *IEEE Transactions on Automatic Control* **34**(8): 802–812.

Anton, H (1991). *Elementary Linear Algebra*, sixth edn, Wiley, New York.

Baker, J. and Christofides, P.D. (1999). Nonlinear control of incompressible fluid flows, *Proc. 38th IEEE Conference on Decision and Control, Dec, 1999*, Phoenix, Arizona, pp. 2881–2886.

Baker, J. and Christofides, P.D. (2002). Drag reduction in transitional linearized channel flow using distributed control, *International Journal of Control* **75**(15): 1213–1218.

Baker, J., Armaou, A. and Christofides, P.D. (2000a). Drag reduction in incompressible channel flow using electromagnetic forcing, *Proc. 2000 American Control Conference (ACC 2000), Jun 28-30, 2000*, Chicago, Illinois, pp. 4269–4273.

Baker, J., Armaou, A. and Christofides, P.D. (2000b). Nonlinear control of incompressible fluid flow: Application to Burgers' equation and 2D channel flow, *Journal of Mathematical Analysis and Applications* **252**(1): 230–255.

Balogh, A., Liu, W-J. and Krstic, M. (1999). Stability enhancement by boundary control in 2D channel flow - Part I: Regularity of solutions, *Proc. 38th Conference on Decision and Control, December, 1999*, Phoenix, Arizona, pp. 2869–2874.

Balogh, A., Liu, W-J. and Krstic, M. (2000). Stability enhancement by boundary control in 2D channel flow - Part II: Numerical implementation and stability, *Proc. 2000 American Control Conference (ACC 2000), Jun 28-30, 2000*, Chicago, Illinois, pp. 4259–4263.

Balogh, A., Liu, W.J. and Krstic, M. (2001). Stability enhancement by boundary control in 2-D channel flow, *IEEE Transactions on Automatic Control* **46**(11): 1696–1711.

Bamieh, B. and Dahleh, M. (1999). Disturbance energy amplification in three-dimensional channel flows, *Proc. 1999 American Control Conference (ACC 1999), Jun, 1999*, San Diego, California, pp. 4532–4537.

Bamieh, B. and Dahleh, M. (2001). Energy amplification in channel flows with stochastic excitation, *Physics of Fluids* **13**(11): 3258–3269.

Bamieh, B., Paganini, F. and Dahleh, M.A. (2002). Distributed control of spatially invariant systems, *IEEE Transactions on Automatic Control* **47**(7): 1091–1107.

Baramov, L., Tutty, O.R. and Rogers, E. (2000). Further results on robust control of 2d Poiseuille flow, *Proc. UKACC International Conference on Control Sep 04-07, 2000*, Cambridge, UK.

Baramov, L., Tutty, O.R. and Rogers, E. (2001). H-infinity control for non-periodic planar channel flows, *Proc. 40th IEEE Conference on Decision and Control, Dec 04-07, 2001*, Orlando, Florida, pp. 4950–4955.

Baramov, L., Tutty, O.R. and Rogers, E. (2002). Robust control of linearized Poiseuille flow, *Journal of Guidance, Control and Dynamics* **25**(1): 145–151.

Baramov, L., Tutty, O.R. and Rogers, E. (2003). Robust control of a nonlinear fluidics problem, *in* A. Zinober and D. Owens (eds), *Nonlinear and Adaptive Control: NCN4 2001*, Vol. 281 of *Lecture Notes in Control and Information Sciences*, Springer, Berlin, pp. 21–31.

Baramov, L., Tutty, O.R. and Rogers, E. (2004). H-infinity control of nonperiodic two-dimensional channel flow, *IEEE Transactions on Control Systems Technology* **12**(1): 111–122.

Benner, P., Mehrmann, V., Sima, V., Van Huffel, S. and Varga, A (1999). SLICOT — A subroutine library in systems and control theory, *in* B. Datta (ed.), *Applied and Computational Control, Signals, and Circuits*, Vol. 1, chapter 10, Birkhauser, Boston, pp. 499–539.

Bewley, T.R. (1999). Linear control and estimation of nonlinear chaotic convection: Harnessing the butterfly effect, *Physics of Fluids* **11**(5): 1169–1186.

Bewley, T.R. (2001). Flow control: New challenges for a new Renaissance, *Progress in Aerospace Sciences* **37**(1): 21–58.

Bewley, T.R. and Aamo, O.M. (2004). A 'win-win' mechanism for low-drag transients in controlled two-dimensional channel flow and its implications for sustained drag reduction, *Journal of Fluid Mechanics* **499**: 183–196.

Bewley, T.R. and Liu, S. (1998). Optimal and robust control and estimation of linear paths to transition, *Journal of Fluid Mechanics* **365**: 305–349.

Bewley, T.R. and Protas, B. (2004). Skin friction and pressure: The 'footprints' of turbulence, *Physica D* **196**(1-2): 28–44.

Bewley, T.R., Moin, P. and Temam, R. (2001). DNS-based predictive control of turbulence: An optimal benchmark for feedback algorithms, *Journal of Fluid Mechanics* **447**: 179–225.

Bewley, T.R., Teman, R. and Ziane, M. (2000). A general framework for robust control in fluid mechanics, *Physica D* **138**(3-4): 360–392.

Boyd, J.P. (2001). *Chebyshev and Fourier Spectral Methods*, second edn, Dover, Mineola, New York.

Boyd, S., El Ghaoui, L., Feron, E. and Balakrishnan, V. (1994). *Linear Matrix Inequalities in System and Control Theory*, Vol. 15 of *SIAM Studies in Applied Mathematics*, SIAM, Philadelphia.

Bushnell, D.M. (2003). Aircraft drag reduction-a review, *Proceedings of The Institution of Mechanical Engineers. Part G: Journal of Aerospace Engineering* **217**: 1–18.

Butler, K.M. and Farrell, B.F. (1992). Three-dimensional optimal perturbations in viscous shear flow, *Physics of Fluids* **4**(8): 1637–1650.

Calvert, J.R. and Farrar, R.A. (1999). *An Engineering Data Book*, Palgrave, Houndmills, Basingstoke, Hampshire RG21 6XS.

Cameron, P.J. (1998). *Introduction to Algebra*, OUP, Oxford.

Campbell, S.L. and Marszalek, W. (1999). The index of an infinite dimensional implicit system, *Mathematical and Computer Modelling of Dynamical Systems* **5**(1): 18–42.

Carlson, D.R., Widnall, S.E. and Peeters, M.F. (1982). A flow-visualization study of transition in plane Poiseuille flow, *Journal of Fluid Mechanics* **121**: 487–505.

Chevalier, M., Hœpffner, J., Bewley, T.R. and Henningson, D.S. (2004). Turbulent channel flow estimation, *Proc. Tenth European Turbulence Conference, 2004*, Barcelona, pp. 1–4, paper 268H.

Collis, S.C., Joslin, R.D., Seifert, A. and Theofilis, V. (2004). Issues in active flow control: Theory, control, simulation, and experiment, *Progress in Aerospace Sciences* **40**: 237–289.

Cortelezzi, L. and Speyer, J.L. (1998). Robust reduced-order controller of laminar boundary layer transitions, *Physical Review E* **58**(2): 1906–1910.

Cortelezzi, L., Lee, K.H., Kim, J. and Speyer, J.L. (1998a). Skin-friction drag reduction via robust reduced-order linear feedback control, *International Journal of Computational Fluid Dynamics* **11**(1-2): 79–96.

Cortelezzi, L., Speyer, J.L., Lee, K.H. and Kim, J. (1998b). Robust reduced-order control of turbulent channel flows via distributed sensors and actuators, *Proc. 37th IEEE Conference on Decision and Control, Dec 16-18, 1998*, pp. 1906–1911.

Criminale, W.O., Jackson, T.L., Lasseigne, D.G. and Joslin, R.D. (1997). Perturbation dynamics in viscous channel flows, *Journal of Fluid Mechanics* **339**: 55–75.

Danabasoglu, G. and Biringen, S (1990). A Chebyshev matrix method for the spatial modes of the Orr-Sommerfeld equation, *International Journal for Numerical Methods in Fluids* **11**: 1033–1037.

Dongarra, J.J., Straughan, B. and Walker, D.W. (1996). Chebyshev tau-qz algorithm methods for calculating spectra of hydrodynamic stability problems, *Applied Numerical Mathematics* **22**(4): 399–434.

Drikakis, D. (2001). The issue of numerical accuracy in computational fluid dynamics, *Computational Fluid Dynamics in Practice*, Professional Engineering Publishing Limited, Northgate Avenue, Bury St. Edmunds, Suffolk, IP32 6BW, UK, chapter 1, pp. 1–22.

Ferziger, J.H. and Peric, M. (2002). *Computational Methods for Fluid Dynamics*, 3rd edn, Springer-Verlag, Berlin.

Fletcher, C.A.J. (1991). *Computational Techniques for Fluid Dynamics*, Vol. 1 Fundamental and General Techniques, Springer-Verlag, Berlin.

Fox, L. and Parker, I.B. (1968). *Chebyshev Polynomials in Numerical Analysis*, Oxford Mathematical Handbooks, OUP, Oxford.

Gad-el-Hak, M. (1998). Introduction to flow control, *in* M. Gad-el-Hak, A. Pollard and J.-P. Bonnet (eds), *Flow Control Fundamentals and Practices*, Lecture Notes in Physics, Springer-Verlag, Berlin.

Gad-el-Hak, M. (1999). The fluid mechanics of microdevices - The Freeman scholar lecture, *Journal of Fluids Engineering-Transactions of ASME* **121**(1): 5–33.

Gad-el-Hak, M. (2000). *Flow Control - Passive, Active, and Reactive Flow Management*, CUP, Cambridge, UK.

Gaster, M. (2000). Active control of boundary layer instabilities using MEMs, *Current Science* **79**(6): 774–780.

Golub, G.H. and Van Loan, C.F. (1990). *Matrix Computations*, 2nd edn, The John Hopkins University Press, Baltimore.

Gottlieb, D. and Orszag, S. A. (1993). *Numerical Analysis of Spectral Methods: Theory and Applications*, Regional Conference Series in Applied Mathematics, sixth edn, SIAM, Philadelphia.

Gottlieb, D., Hussaini, M.Y. and Orszag, S.A. (1984). Theory and Applications of Spectral Methods, *in* R. Voight, D. Gottlieb and M. Hussaini (eds), *Spectral Methods for Partial Differential Equations*, SIAM, Philadelphia, pp. 1–54.

Hamming, R.W. (1973). *Numerical Methods for Scientists and Engineers*, International Series in Pure and Applied Mathematics, second edn, McGraw-Hill, New York.

Heinrichs, W. (1989). Improved condition number for spectral methods, *Mathematics of Computation* **53**(187): 103–119.

Heinrichs, W. (1991). A stabilized treatment of the biharmonic operator with spectral methods, *SIAM Journal on Scientific and Statistical Computing* **12**(5): 1162–1172.

Hinrichsen, D. and Pritchard, A.J. (2000). On the transient behaviour of stable linear systems, *Proc. International Symposium on Mathematical Theory of Networks and Systems MTNS-2000, Jun 19-23, 2000*, Perpignan, France, pp. CDROM – paper B218.

Hinrichsen, D. and Pritchard, A.J. (2005). *Mathematical Systems Theory I: Modelling, State Space Analysis, Stability and Robustness*, Springer-Verlag, Berlin.

Hinrichsen, D., Plischke, E. and Wirth, F. (2002). State feedback stabilization with guaranteed transient bounds, *Proc. Symposium on Mathematical Theory of Networks and Systems MTNS-2002*, South Bend, Indiana, pp. CDROM – paper 2132.

Ho, C.M. and Tai, Y.C. (1998). Micro-electro-mechanical-systems (MEMS) and fluid flows, *Annual Review of Fluid Mechanics* **30**: 579–612.

Hœpffner, J., Chevalier, M., Bewley, T.R. and Henningson, D.S. (2005). State estimation in wall-bounded flow systems. Part 1. Perturbed laminar flows, *Journal of Fluid Mechanics* **534**: 263–294.

Hœpffner, J., Chevalier, M., Bewley, T.R. and Henningson, D.S. (2006). Linear feedback control of transition in shear flows, *in* R. Govindarajan (ed.), *Fluid Mechanics and its Applications*, Springer, pp. 213–281.

Hogberg, M. and Bewley, T.R. (2000). Spatially localized convolution kernels for feedback control of transitional flows, *Proc. 39th IEEE Conference on Decision and Control, Dec 12-15, 2000*, pp. 3278–3283.

Hogberg, M. and Henningson, D.S. (2002). Linear optimal control applied to instabilities in spatially developing boundary layers, *Journal of Fluid Mechanics* **470**: 151–179.

Hogberg, M., Bewley, T.R. and Henningson, D.S. (2003a). Linear feedback control and estimation of transition in plane channel flow, *Journal of Fluid Mechanics* **481**: 149–175.

Hogberg, M., Bewley, T.R. and Henningson, D.S. (2003b). Relaminarization of re-tau=100 turbulence using gain scheduling and linear state-feedback control, *Physics of Fluids* **15**(11): 3572–3575.

Hogberg, M., Bewley, T.R., Berggren, M. and Henningson, D.S. (2001). Optimal control of transition initiated by oblique waves in channel flow, *Proc. 2nd International Symposium on Turbulence and Shear Flow Phenomena, Jun 2001*, Stockholm.

Horn, R.A. and Johnson, C. R. (1985). *Matrix Analysis*, CUP, Cambridge.

Hu, H.H. and Bau, H.H. (1994). Feedback-control to delay or advance linear loss of stability in planar Poiseuille flow, *Proceedings of The Royal Society London A* **447**(1930): 299–312.

Jacobs, O.L.R. (1974). *Introduction to Control Theory*, OUP, Oxford.

Jimenez, J. (1990). Transition to turbulence in two-dimensional Poiseuille flow, *Journal of Fluid Mechanics* **218**: 265–297.

Joshi, S.S. (1996). *A Systems Theory Approach to the Control of Plane Poiseuille Flow*, PhD thesis, Department of Electrical Engineering, UCLA.

Joshi, S.S., Speyer, J.L. and Kim, J. (1995). Modelling and control of two dimensional Poiseuille flow, *Proc. 34th IEEE Conference on Decision and Control, Dec 13-15, 1995*, New Orleans, LA, pp. 921–927.

Joshi, S.S., Speyer, J.L. and Kim, J. (1997). A systems theory approach to the feedback stabilization of infinitesimal and finite-amplitude disturbances in plane Poiseuille flow, *Journal of Fluid Mechanics* **332**: 157–184.

Joshi, S.S., Speyer, J.L. and Kim, J. (1999). Finite dimensional optimal control of Poiseuille flow, *Journal of Guidance, Control and Dynamics* **22**(2): 340–348.

Joslin, R.D. (1998). Aircraft laminar flow control, *Annual Review of Fluid Mechanics* **30**: 1–29.

Jovanovic, M.R. and Bamieh, B. (2005). Componentwise energy amplification in channel flows, *Journal of Fluid Mechanics* **534**: 145–183.

Kim, J. (2003). Control of turbulent boundary layers, *Physics of Fluids* **15**(5): 1093–1105.

Kim, J. and Lim, J. (2000). A linear process in wall-bounded turbulent shear flows, *Physics of Fluids* **12**(8): 1885–1888.

Lauga, E. and Bewley, T.R. (2004). Performance of a linear robust control strategy on a nonlinear model of spatially developing flows, *Journal of Fluid Mechanics* **512**: 343–374.

Lee, K.H., Cortelezzi, L., Kim, J. and Speyer, J. (2001). Application of reduced-order controller to turbulent flows for drag reduction, *Physics of Fluids* **13**(5): 1321–1330.

Lewis, F.L. and Syrmos, V.L. (1995). *Optimal Control*, 2nd edn, Wiley, New York.

Lim, J. and Kim, J. (2004). A singular value analysis of boundary layer control, *Physics of Fluids* **16**(6): 1980–1988.

Liou, M.-F. and Fitzmaurice, N. (1995). An implicit boundary spectral collocation method for eigenvalue problem in two Chebyshev directions, *Proc. AIAA 12th Computational Fluid Dynamics Conference, June 19-22, 1995*, San Diego, CA.

Lofdahl, L. and Gad-el-Hak, M. (1999). MEMs applications in turbulence and flow control, *Progress in Aerospace Sciences* **35**(2): 101–203.

Lorenz, E.N. (1963). Deterministic nonperiodic flow, *Journal of the Atmospheric Sciences* **20**: 130–141.

Lumley, J. and Blossey, P. (1998). Control of turbulence, *Annual Review of Fluid Mechanics* **30**: 311–327.

MathWorks Inc. (1998). *Control System Toolbox User's Guide*, Matlab 5.2 edn, The MathWorks Inc., Natick, MA.

Mittal, R. (1999). A Fourier-Chebyshev spectral collocation method for simulating flow past spheres and spheroids, *International Journal for Numerical Methods in Fluids* **30**: 921–937.

Moin, P. and Bewley, T.R. (1994). Feedback control of turbulence, *Applied Mechanics Review* **47**(6): 3–13. part 2.

Moler, C. and Van Loan, C. (2003). Nineteen dubious ways to compute the exponential of a matrix, twenty-five years later, *SIAM Review* **45**(1): 3–49.

Morris, K.A. and Navasca, C. (2005). Solution of algebraic Riccati equations arising in control of partial differential equations, *in* J. Cagnol and J. Zolesio (eds), *Control and Boundary Analysis*, Vol. 240 of *Lecture Notes in Pure and Applied Mathematics*, CRC Press, Boca Raton, Fl, pp. 257–280.

Orr, W.M.F. (1907). The stability or instability of the steady motions of a perfect liquid and of a viscous liquid, *Proceedings of The Royal Irish Academy A* **27**: 9–138.

Orszag, S.A. (1971). Accurate solution of the Orr-Sommerfeld stability equation, *Journal of Fluid Mechanics* **50**(4): 689–703.

Pabiou, H., Liu, J. and Benard, C. (2004). Linear stability analysis for the wall temperature feedback control of planar Poiseuille flows, *Journal of Dynamic Systems, Measurement, and Control* **124**: 617–624.

Peyret, R. (2002). *Spectral Methods for Incompressible Viscous Flow*, Applied Mathematical Sciences, second edn, Springer, Berlin.

Plischke, E (2005). *Transient Effects of Linear Dynamical Systems*, PhD thesis, Fachbereich 3 (Mathematik & Informatik) der Universitat Bremen.

Plischke, E. and Wirth, F. (2004). Stabilization of linear systems with prescribed transient bounds, *Proc. Symposium on Mathematical Theory of Networks and Systems MTNS-2004*, Leuven, Belgium.

Press, W.H., Flannery, B.P., Teukolsky, S.A. and Vetterling, W.T. (1986). *Numerical Recipes*, CUP, Cambridge.

Reddy, S.C. and Henningson, D.S. (1993). Energy growth in viscous channel flows, *Journal of Fluid Mechanics* **252**: 209–238.

Reddy, S.C., Schmid, P.J. and Henningson, D.S (1993). Pseudospectra of the Orr-Sommerfeld operator, *SIAM Journal on Applied Mathematics* **53**(1): 15–47.

Reddy, S.C., Schmid, P.J., Baggett, J.S. and Henningson, D.S. (1998). On stability of streamwise streaks and transition thresholds in plane channel flows, *Journal of Fluid Mechanics* **365**: 269–303.

Rempfer, D. (2003). Low-dimensional modeling and numerical simulation of transition in simple shear flows, *Annual Review of Fluid Mechanics* **35**: 229–265.

Reynolds, W. C. and Kassinos, S.C (1995). One-point modelling of rapidly deformed homogeneous turbulence, *Proceedings of The Royal Society London A* **451**: 87–104.

Råde, L. and Westergren, B. (1999). *Mathematics Handbook for Science and Engineering*, fourth edn, Springer-Verlag, Berlin.

Schmid, P.J. and Henningson, D.S. (2001). *Stability and Transition in Shear Flows*, Vol. 142 of *Applied Mathematical Sciences*, Springer-Verlag, New York.

Skogestad, S. and Postlethwaite, I. (1996). *Multivariable Feedback Control*, Wiley, Chichester, England.

Skogestad, S. and Postlethwaite, I. (2005). *Multivariable Feedback Control*, 2nd edn, Wiley, Chichester, England.

Spasov, Y. and Kunisch, K. (2006). Dynamical system based optimal control of incompressible fluids. Boundary control, *European Journal of Mechanics Part B/Fluids* **25**: 153–163.

Sturzebecher, D. and Nitsche, W. (2003). Active cancellation of Tollmien-Schlichting instabilities on a wing using multi-channel sensor actuator systems, *International Journal of Heat and Fluid Flow* **24**(4): 572–583.

Sykes, J.B. (ed.) (1976). *The Concise Oxford Dictionary*, 6th edn, OUP, Oxford.

Thomas, L.H. (1953). Stability of plane Poiseuille flow, *Physical Review* **91**(1): 780–785.

Trefethen, L.N. (2000). *Spectral Methods in Matlab*, Software Environments Tools, SIAM, Philadelphia.

Trefethen, L.N. and Embree, M. (2005). *Spectra and Pseudospectra*, Princeton University Press, Princeton, NJ.

Trefethen, L.N., Trefethen, A.E., Reddy, S.C. and Driscoll, T.A. (1993). Hydrodynamic stability without eigenvalues, *Science* **261**: 578–584.

Tritton, D.J. (1988). *Physical Fluid Dynamics*, 2nd edn, OUP, Oxford.

Van Dyke, M. (1982). *An Album of Fluid Motion*, The Parabolic Press, Stanford, California.

Van Huffel, S., Sima, V., Varga, A, Hammarling, S. and Delebecque, F. (2004). High-performance numerical software for control, *IEEE Control Systems Magazine* **24**(1): 60–76.

Veres, S.M., Baramov, L., Tutty, O.R. and Rogers, E. (2003). Iterative design for active control of fluid flow, *International Journal of Control* **76**(14): 1375–1386.

Versteeg, H.K. and Malalasekera, W (1995). *An Introduction to Computational Fluid Dynamics*, Longman, Edinburgh Gate, Harlow, Essex CM20 2JE, U.K.

Weideman, J.A.C. and Reddy, S.C. (2000). A MATLAB differentiation matrix suite, *ACM Transactions on Mathematical Software* **26**(4): 465–519.

Whidborne, J.F. and McKernan, J. (2006). On the minimization of maximum transient energy growth, *IEEE Transactions on Automatic Control*. Submitted.

Whidborne, J.F., McKernan, J. and Papadakis, G. (2004). Minimization of maximum transient energy growth, *Proc. UKACC International Conference Control 2004, Sep 06-09, 2004*, Bath, UK.

Whidborne, J.F., McKernan, J. and Steer, A.J. (2005). On minimizing maximum transient energy growth, *Technical Report COA No 0501*, Dynamics, Simulation and Control Group, Department of Aerospace Sciences, School of Engineering, Cranfield University.

Wood, R.M. (2003). Aerodynamic drag and drag reduction: Energy and energy savings, *Proc. 41st AIAA Aerospace Sciences Meeting & Exhibit, 6-9 Jan 2003*, Reno, NV.

Yeoh, S.L., Papadakis, G. and Yianneskis, M. (2004). Large eddy simulation of turbulent flow in a Rushton impeller stirred reactor with sliding-deforming mesh methodology, *Chemical Engineering Technology* **27**(3): 257–263.

Zhou, K., Doyle, J.C. and Glover, G. (1996). *Robust and Optimal Control*, Prentice-Hall, Upper Saddle River, NJ.

Appendix A

Y-Discretisation Conditioning

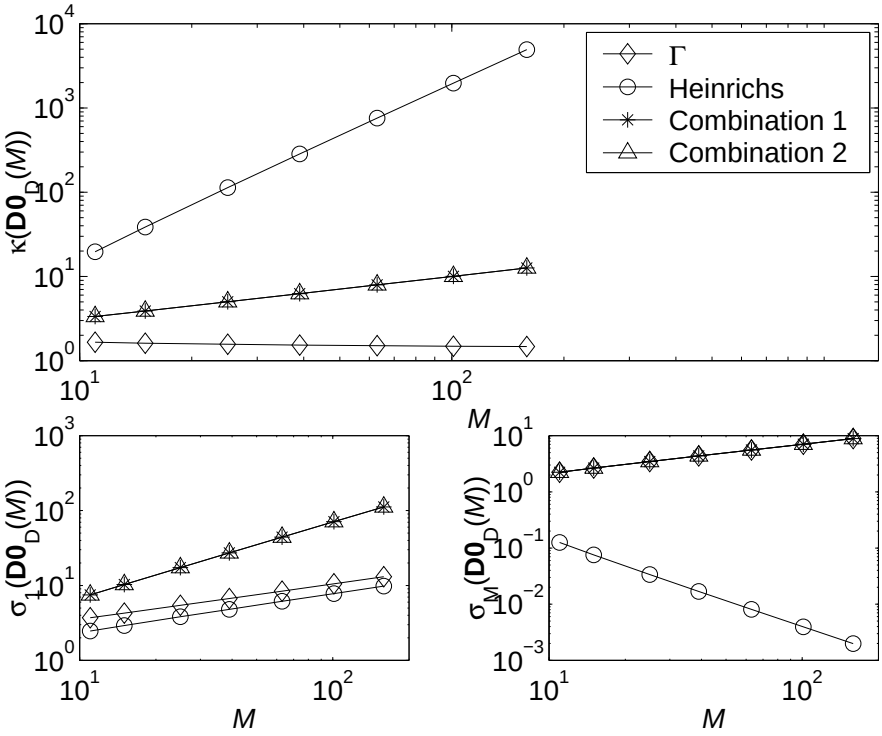

Figure A.1: Conditioning of $\mathbf{D0}_D$ Matrix

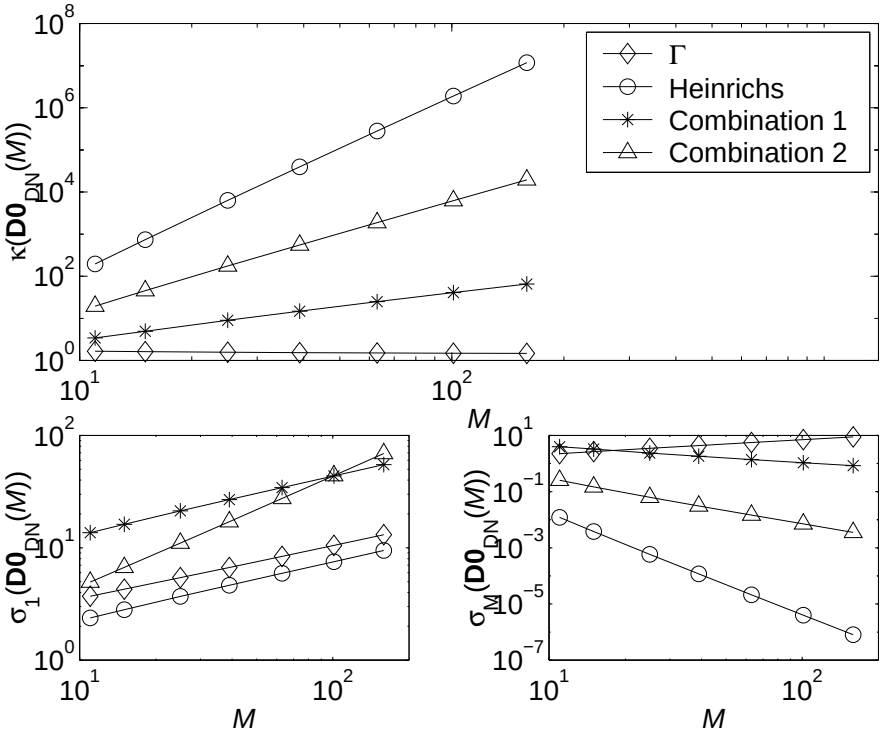

Figure A.2: Conditioning of $\mathbf{D0}_{DN}$ Matrix

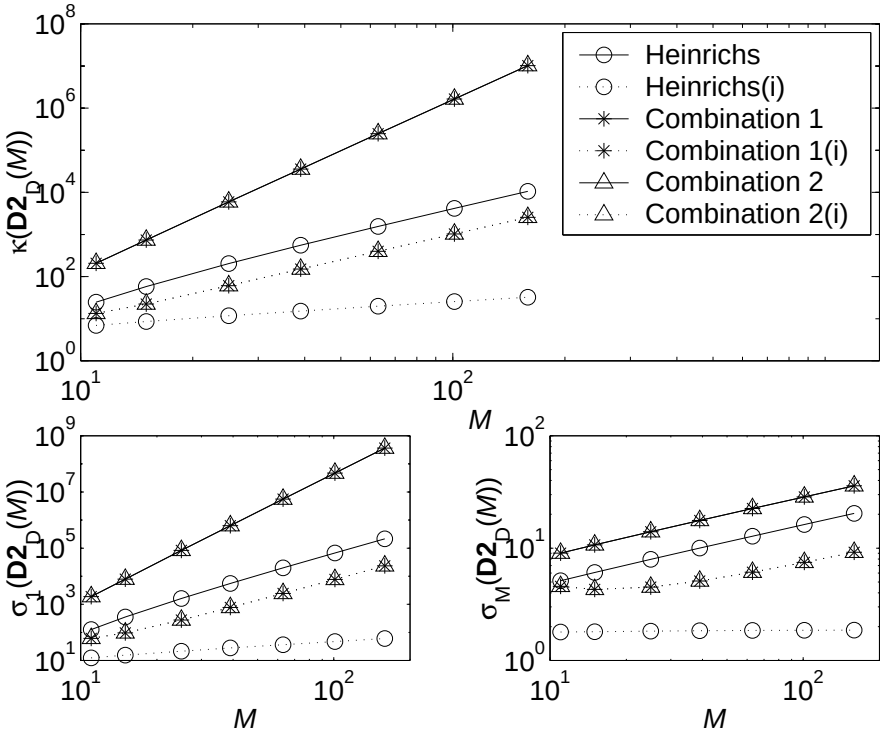

Figure A.3: Conditioning of $\mathbf{D2}_D$ Matrix ((i) indicates interior preconditioned)

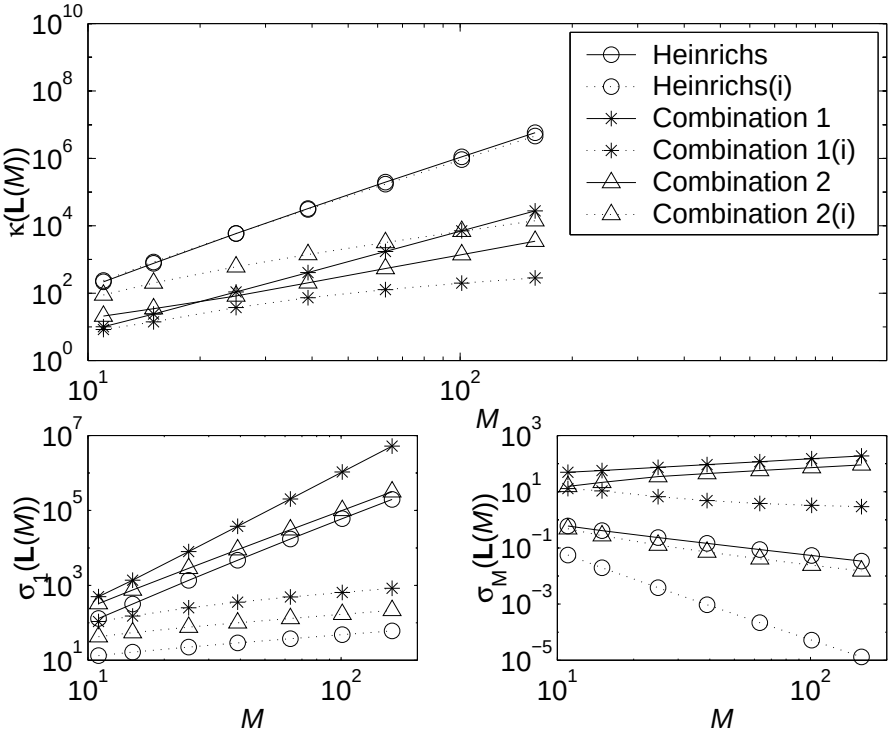

Figure A.4: Conditioning of $\mathbf{L}$ Matrix ((i) indicates interior preconditioned)

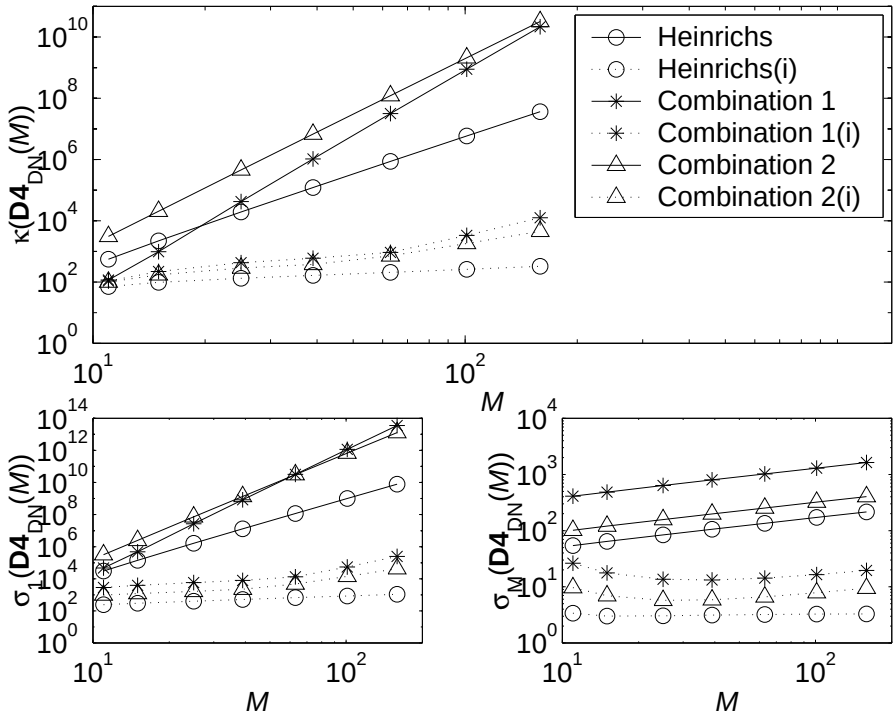

Figure A.5: Conditioning of $\mathbf{D4}_{DN}$ Matrix ((i) indicates interior preconditioned)

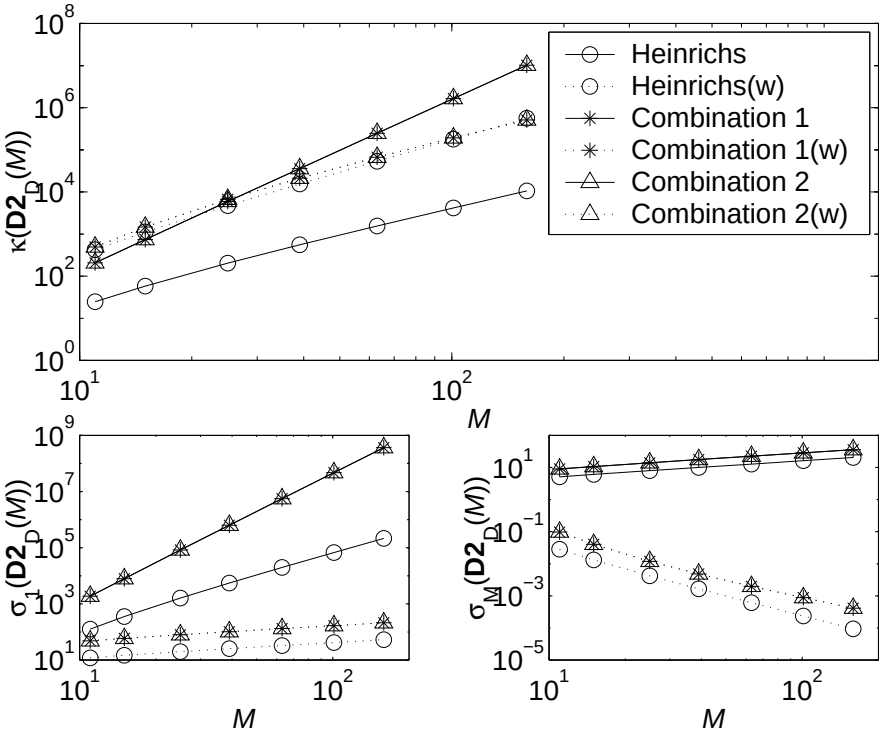

Figure A.6: Conditioning of $\mathbf{D2}_{D}$ Matrix ((w) indicates wall preconditioned)

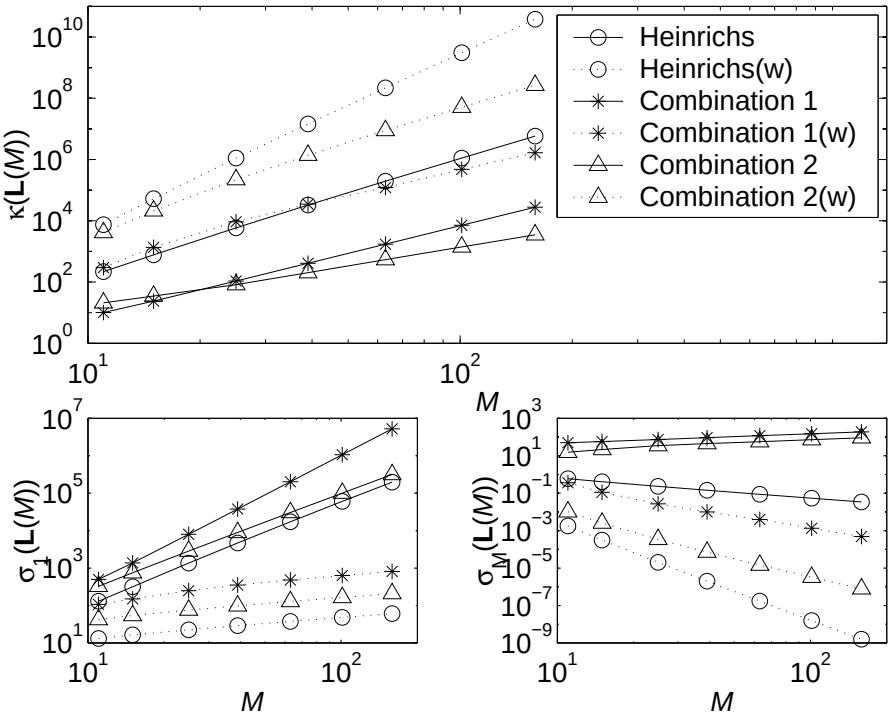

Figure A.7: Conditioning of $\mathbf{L}$ Matrix ((w) indicates wall preconditioned)

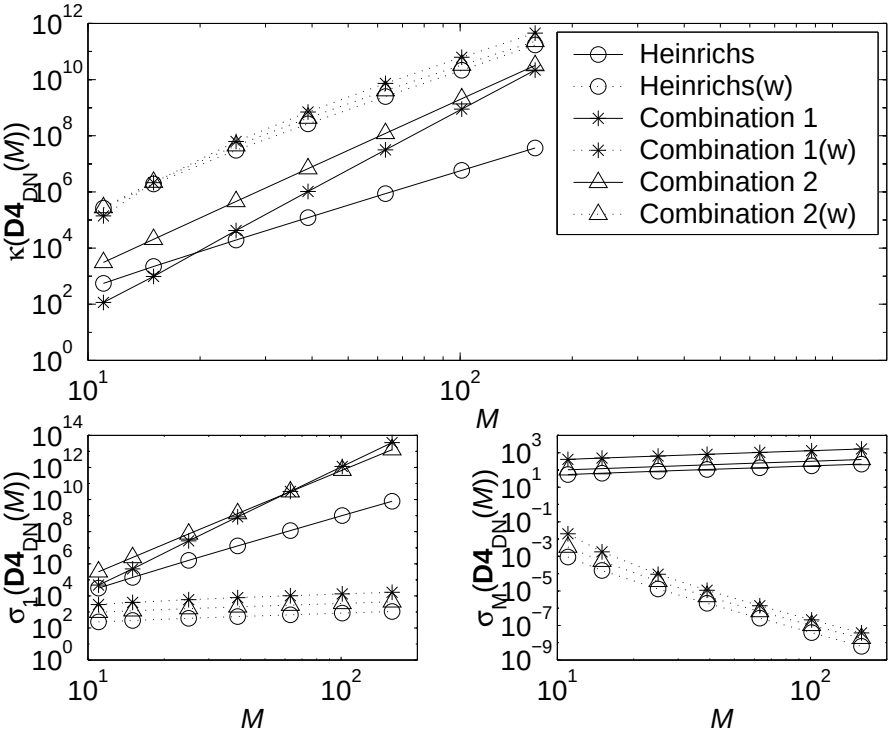

Figure A.8: Conditioning of $\mathbf{D4}_{DN}$ Matrix ((w) indicates wall preconditioned)

Appendix B

Linear Transient Energy E Plots

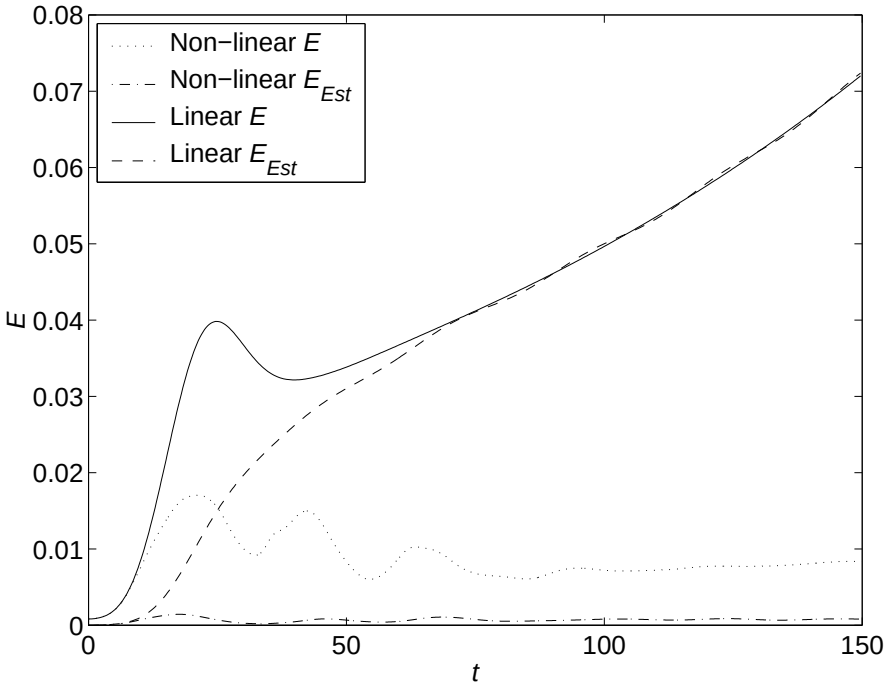

Figure B.1: Case 1 LQE Transient Energy E vs Time t, from Initial Conditions $\mathcal{X}_{Worst}$ Scaled to Energy $10^4 E_{C1}$

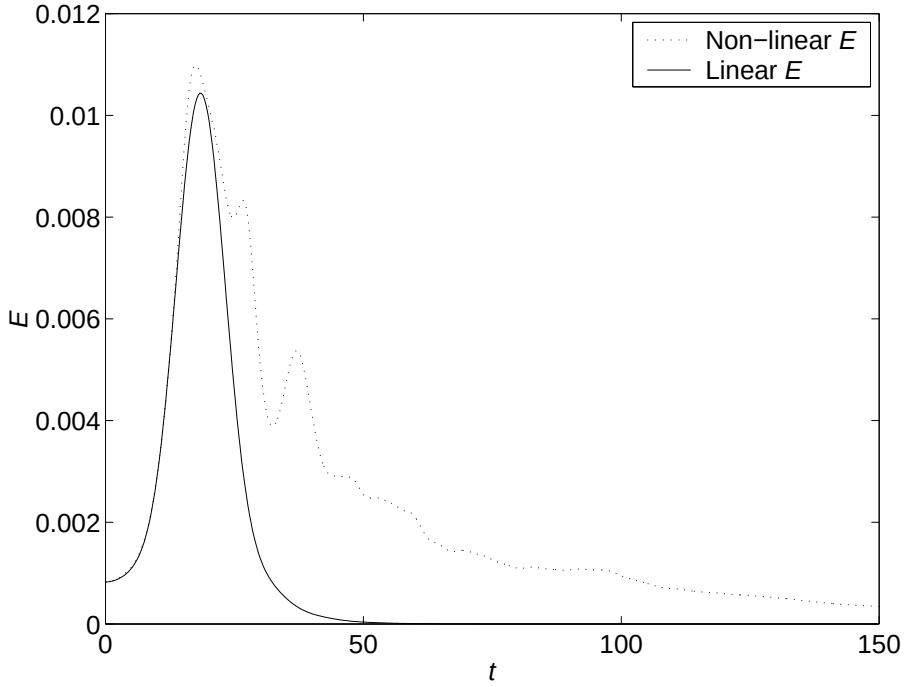

Figure B.2: Case 1 LQR Transient Energy E vs Time t, from Initial Conditions $\mathcal{X}_{Worst}$ Scaled to Energy $10^4 E_{C1}$

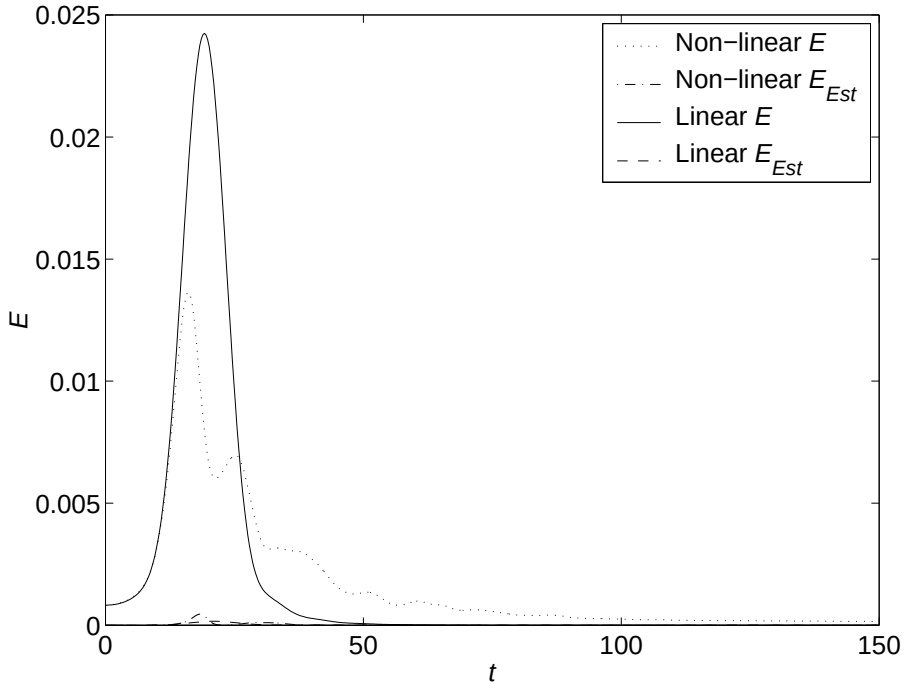

Figure B.3: Case 1 LQG Transient Energy E vs Time t, from Initial Conditions $\mathcal{X}_{Worst}$ Scaled to Energy $10^4 E_{C1}$

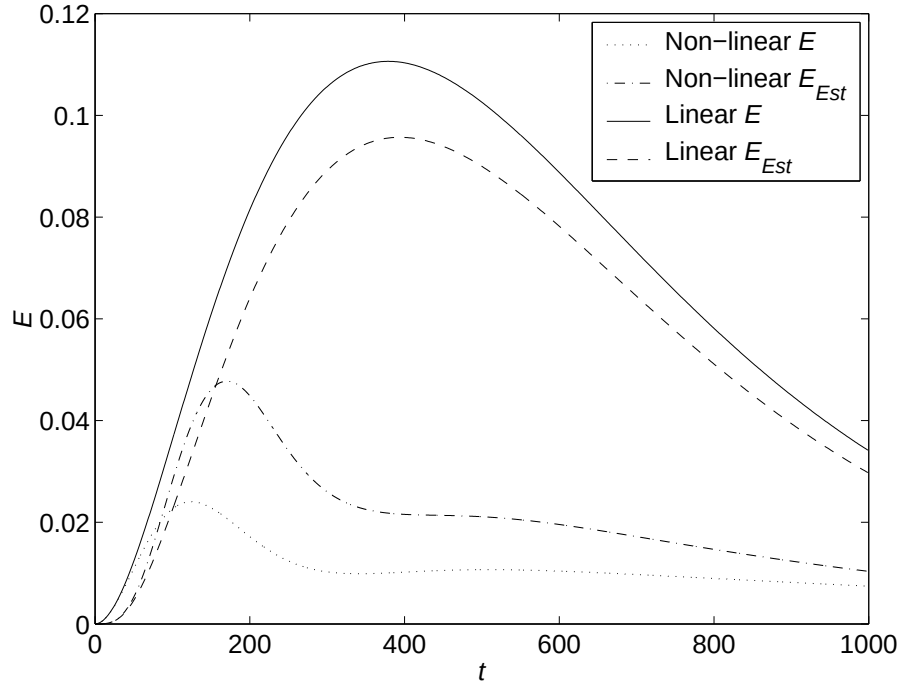

Figure B.4: Case 2 LQE Transient Energy E vs Time t, from Initial Conditions $\mathcal{X}_{Worst}$ Scaled to Energy $10^4 E_{C2}$

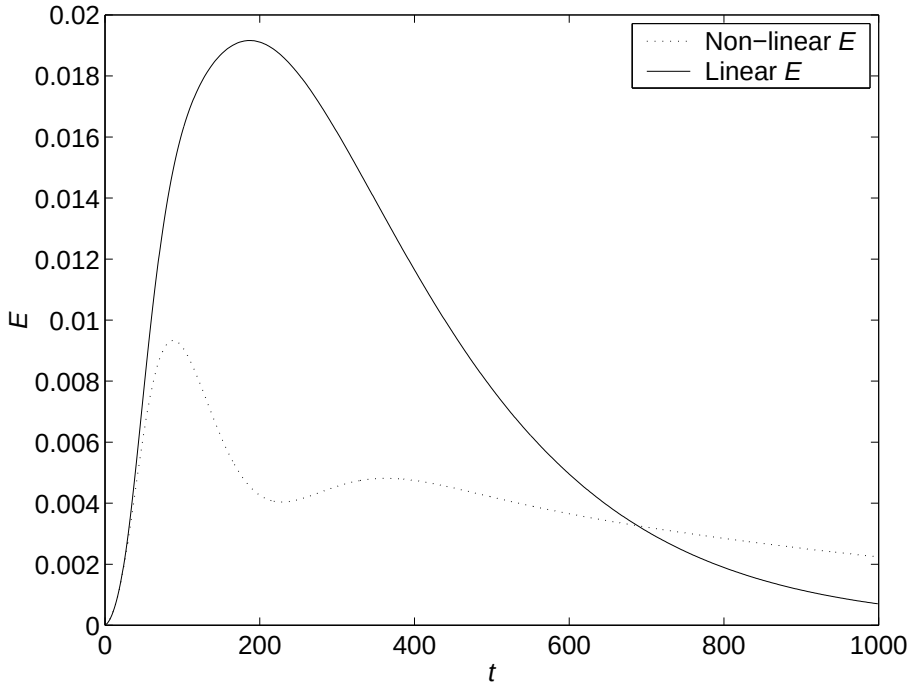

Figure B.5: Case 2 LQR Transient Energy E vs Time t, from Initial Conditions $\mathcal{X}_{Worst}$ Scaled to Energy $10^4 E_{C2}$

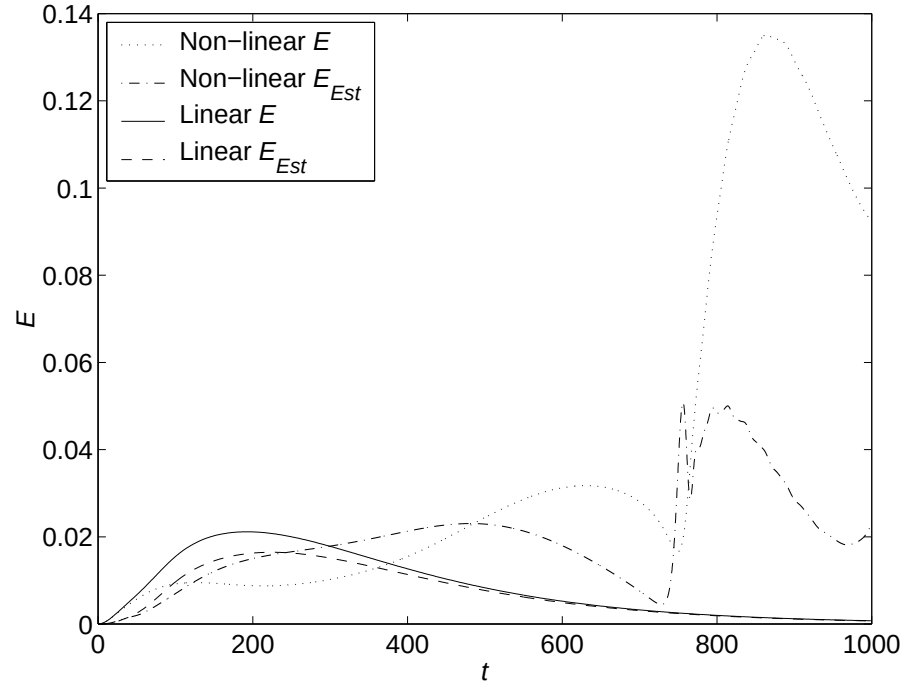

Figure B.6: Case 2 LQG Transient Energy E vs Time t, from Initial Conditions $\mathcal{X}_{Worst}$ Scaled to Energy $10^4 E_{C2}$

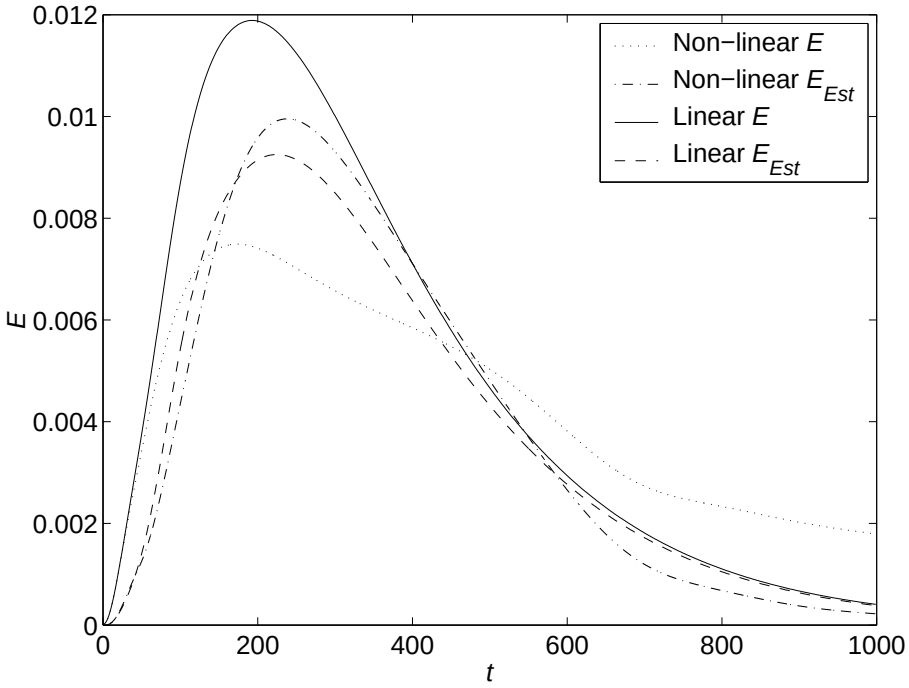

Figure B.7: Case 2 LQG Transient Energy E vs Time t, from Initial Conditions $\mathcal{X}_{Worst}$ Scaled to Energy $5625E_{C2}$

Appendix C

Effect of Symmetric and Anti-Symmetric Control Signals

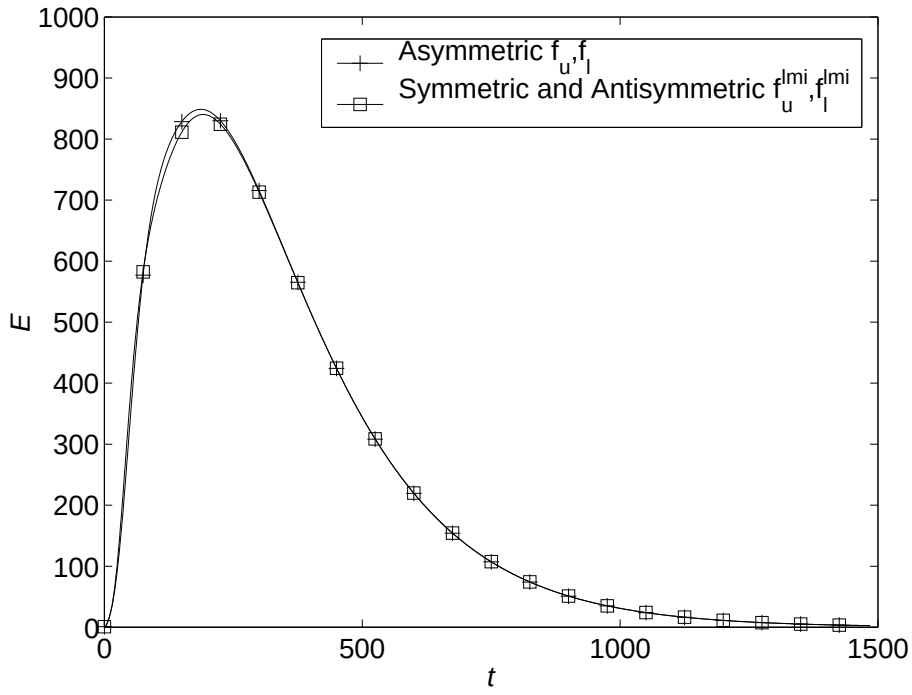

Figure C.1: Case 2 LQR Transient Energy E vs Time t, with Asymmetric and Symmetric/Antisymmetric Control, from Initial Conditions $\mathcal{X}_{worst}$ Scaled to $E = 1$, $N = 100$

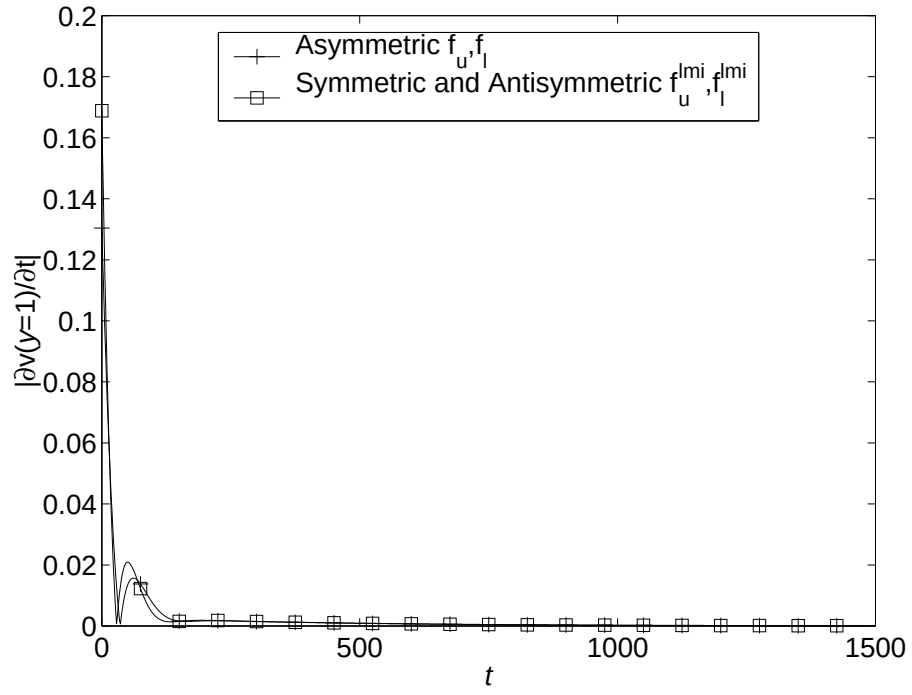

Figure C.2: Case 2 LQR Upper Wall Control $\mathcal{U}(1)$ vs Time t, with Asymmetric and Symmetric/Antisymmetric Control, from Initial Conditions $\mathcal{X}_{worst}$ Scaled to $E = 1$, $N = 100$